frontiers | Research Topics

Electronic and nuclear quantum dynamics of molecules in intense laser fields

Edited by
Yuichi Fujimura, Andre Bandrauk and Leticia González

Published in
Frontiers in Chemistry
Frontiers in Physics

ISSN 1664-8714
ISBN 978-2-8325-2211-0
DOI 10.3389/978-2-8325-2211-0

About Frontiers

Frontiers is more than just an open access publisher of scholarly articles: it is a pioneering approach to the world of academia, radically improving the way scholarly research is managed. The grand vision of Frontiers is a world where all people have an equal opportunity to seek, share and generate knowledge. Frontiers provides immediate and permanent online open access to all its publications, but this alone is not enough to realize our grand goals.

Frontiers journal series

The Frontiers journal series is a multi-tier and interdisciplinary set of open-access, online journals, promising a paradigm shift from the current review, selection and dissemination processes in academic publishing. All Frontiers journals are driven by researchers for researchers; therefore, they constitute a service to the scholarly community. At the same time, the *Frontiers journal series* operates on a revolutionary invention, the tiered publishing system, initially addressing specific communities of scholars, and gradually climbing up to broader public understanding, thus serving the interests of the lay society, too.

Dedication to quality

Each Frontiers article is a landmark of the highest quality, thanks to genuinely collaborative interactions between authors and review editors, who include some of the world's best academicians. Research must be certified by peers before entering a stream of knowledge that may eventually reach the public - and shape society; therefore, Frontiers only applies the most rigorous and unbiased reviews. Frontiers revolutionizes research publishing by freely delivering the most outstanding research, evaluated with no bias from both the academic and social point of view. By applying the most advanced information technologies, Frontiers is catapulting scholarly publishing into a new generation.

What are Frontiers Research Topics?

Frontiers Research Topics are very popular trademarks of the *Frontiers journals series*: they are collections of at least ten articles, all centered on a particular subject. With their unique mix of varied contributions from Original Research to Review Articles, Frontiers Research Topics unify the most influential researchers, the latest key findings and historical advances in a hot research area.

Find out more on how to host your own Frontiers Research Topic or contribute to one as an author by contacting the Frontiers editorial office: frontiersin.org/about/contact

Electronic and nuclear quantum dynamics of molecules in intense laser fields

Topic editors
Yuichi Fujimura — Tohoku University, Japan
Andre Bandrauk — Université de Sherbrooke, Canada
Leticia González — University of Vienna, Austria

Citation
Fujimura, Y., Bandrauk, A., González, L., eds. (2023). *Electronic and nuclear quantum dynamics of molecules in intense laser fields*. Lausanne: Frontiers Media SA. doi: 10.3389/978-2-8325-2211-0

Table of contents

frontiers in Chemistry

ORIGINAL RESEARCH
published: 31 January 2022
doi: 10.3389/fchem.2022.809137

Electron Dynamics and Correlations During High-Order Harmonic Generation in Be

*Eric Kutscher, Anton N. Artemyev and Philipp V. Demekhin**

Institut für Physik und CINSaT, Universität Kassel, Kassel, Germany

We investigate theoretically the high-order harmonic generation in beryllium atom irradiated by a short 1850 nm linearly polarized laser pulse in the intermediate strong-field ionization regime with the Keldysh parameter of 0.85. To this end, the respective time-dependent Schrödinger equation is solved by the time-dependent restricted-active-space configuration-interaction (TD-RASCI) method. By systematically increasing the active space of included configurations, we demonstrate an individual effect of different physical processes evoked by the pulse, which, all together, significantly enrich and extend the computed high-order harmonic generation spectrum.

Keywords: light-matter interaction, strong-field ionisation, high-harmonic generation, electron correlations, restricted-active-space, theoretical and numerical methods

Edited by:
Yuichi Fujimura,
Tohoku University, Japan

Reviewed by:
Laura Kelly McKemmish,
University of New South Wales, Australia
Marzio Rosi,
University of Perugia, Italy

****Correspondence:***
Philipp V. Demekhin
demekhin@physik.uni-kassel.de

Specialty section:
This article was submitted to Theoretical and Computational Chemistry, a section of the journal Frontiers in Chemistry

Received: *04 November 2021*
Accepted: *10 January 2022*
Published: *31 January 2022*

Citation:
Kutscher E, Artemyev AN and Demekhin PV (2022) Electron Dynamics and Correlations During High-Order Harmonic Generation in Be. Front. Chem. 10:809137. doi: 10.3389/fchem.2022.809137

INTRODUCTION

The high-order harmonic generation (HHG (Corkum, 1993)) is one of the most fascinating processes arising due to the nonlinear response of matter to strong laser pulses. It gave rise to a new efficient way of generating high-frequency XUV laser pulses (Brabec and Krausz, 2000) and opened up a door to the area of attosecond physics (Kienberger et al., 2004). Many efforts have been spent to provide a detailed theoretical explanation of the HHG processes. Already the semi-classical three-step model (Lewenstein et al., 1994) explains the well-known cutoff law (Krause et al., 1992) in the harmonic spectra, as is confirmed by numerous successful calculations of HHG spectra performed within the single-active electron (SAE) approximation (Bandrauk et al., 2009; Frolov et al., 2009; Ivanov and Kheifets, 2009; Le et al., 2009; Han and Madsen, 2010; Chelkowski et al., 2012; Fu et al., 2017). Going beyond the SAE approximation and solving fully the many-body time-dependent Schrödinger equation (TDSE) is a formidable computational task. Nevertheless, several attempts to study dynamics and correlations of inactive electrons have been performed (Gordon et al., 2006; Miyagi and Madsen, 2013; Sato et al., 2016; Artemyev et al., 2017a; Tikhomirov et al., 2017) by either reducing dimensionality of the problem or simplifying many-body interactions. More details on the HHG phenomenon and key concepts of the strong-field attosecond science can be found, e.g., in the review article (Krausz and Ivanov, 2009).

In order to accurately describe the three-dimensional four-electron beryllium atom exposed to a strong infrared laser pulse, which is a subject of the present theoretical study, several approaches were already reported. For instance, a model approach of Ref. (NgokoDjiokap and Starace, 2013). introduces an effective potential which replaces the two innermost $1s^2$ electrons. The HHG spectra obtained in the multiphoton regime exhibit a strong resonant enhancement due to doubly-excited intermediate autoionizing states. The two accurate approaches designed to describe the full dimensional correlated dynamics of the electrons are the well-known time-dependent configuration-interaction (TDCI (Klamroth, 2003; Krause et al., 2005)) and multiconfigurational time-dependent Hartree-Fock (MCTDHF (Zanghellini et al., 2003; Kato and Kono, 2004; Nest et al., 2005; Alon et al., 2007; Haxton et al., 2011; Hochstuhl and Bonitz, 2011)) methods. In the former approach, the many-electron wave function is expanded over a basis of chosen configurations described by an optimized Slater determinant with a time-dependent expansion coefficient. In the latter, the basis functions are time-dependent in addition and optimized at each time step. Main concepts of the time-dependent formulation of the computational methods can be found, e.g., in the book (Meyer et al., 2009).

Unfortunately, computational efforts of TDCI and MCTDHF methods increase very rapidly with the number of included basis states. Therefore, more efficient methods, such as time-dependent complete-active-space self-consistent-field theory (TD-CASSCF (Sato et al., 2016; Tikhomirov et al., 2017)), the time-dependent restricted-active-space self-consistent-field theory (TD-RASSCF (Miyagi and Madsen, 2013)), and the time-dependent two-particle reduced-density-matrix theory (TD-2RDM (Lackner et al., 2017)), were used to study HHG spectra in beryllium atom. All HHG spectra of Be, computed by these methods beyond the SAE approximation, demonstrate a significance of electron dynamics and correlations in the generation of high-order harmonic spectra. While the HHG spectra obtained in Refs. (Sato et al., 2016; Lackner et al., 2017). on three-dimensional beryllium atom are most accurate and yield reliable predictions, it is rather difficult to extract from those calculations individual impacts of important physical effects on HHG spectra in a transparent way.

In the present work, we aim at revealing those physical effects. To this end, we employ the time-dependent restricted-active-space configuration-interaction (TD-RASCI (Hochstuhl and Bonitz, 2012)) method, adopted in our previous works (Artemyev et al., 2016; Artemyev et al., 2017a; Artemyev et al., 2017b; Artemyev et al., 2019) to study interaction of two electrons of helium atom with intense laser pulses. In this method, a preselected optimized set of single-particle orbitals is used as a basis for the time-independent Slater determinants and a chosen number of electrons is allowed to occupy excited and continuum single-particle states, where the latter are sought as the time-dependent wave packets. By systematically enhancing the active space and thus enabling specific physical processes step by step, one can differentiate individual contributions to the electron dynamics and correlation, and can thus explore the physical role of relevant processes and their impact on the HHG. For the present needs, we extend our realization of the TD-RASCI method to study dynamics and correlations of arbitrary number of electrons.

THEORY

The present realization of the TD-RASCI method was introduced in detail in our previous works on He (Artemyev et al., 2016; Artemyev et al., 2017a; Artemyev et al., 2017b). Therefore, only developments of the method which are necessary to describe field-driven electron dynamics in Be are discussed below.

We describe the light-matter interaction in the velocity gauge, where a fast convergence over the angular momentum of photoelectron wave packets is inherent (Cormier and Lambropoulos, 1996). Thereby, in the electric dipole approximation, the total Hamiltonian $\hat{H}$ of Be atom interacting with a linearly polarized laser pulse reads (atomic units are used throughout this paper)

$$\hat{H} = \sum_{j=1}^{4}\left(-\frac{1}{2}\vec{\nabla}_j^2 - \frac{4}{r_j} - i\nabla_{z_j} A_0 g(t)\sin(\omega t)\right) + \sum_{i<j}\frac{1}{|\vec{r}_i - \vec{r}_j|} \quad . \qquad (1)$$

Here, the first sum accounts for kinetic energy, potential energy of the nuclear-electron interaction, and light-matter interaction for all electrons, while the second one describes the Coulomb repulsion between electrons. The vector potential of the pulse is described by its carrier frequency ω, time envelope $g(t)$ and peak amplitude A_0, which is related to the peak intensity I_0 via $I_0 = A_0^2 \frac{\omega^2}{8\pi\alpha}$ ($\alpha \approx 1/137.036$ is the fine-structure constant).

The present calculations were performed for illustrative laser pulses with peak intensity $I_0 = 2 \times 10^{13}\,\mathrm{W/cm^2}$ and wavelength $\lambda = 1850\,\mathrm{nm}$. The corresponding Keldysh (Keldysh, 1965) parameter $\gamma = 0.85$ indicates that the strong-field ionization of Be takes place in the intermediate regime between tunnel and multiphoton ionization, and far from a barrier suppression regime. With such a choice of the pulse parameters, the probability of double-ionization of Be atom is low, as compared to that of its single-ionization. Thereby, one can neglect any double-ionization of Be atom and assume that only one of its four electrons can populate continuum states. Nevertheless, electron dynamics in the ionic core (i.e., excitation caused by electron correlations or induced by interaction with the pulse) are not negligible and need to be considered. Therefore, we make the following ansatz for the total four-electron wave function of Be:

$$\Psi\left(\vec{r}_1, \vec{r}_2, \vec{r}_3, \vec{r}_4, t\right) = \sum_{ijkl} a_{ijkl}(t)|\phi_i\phi_j\phi_k\phi_l\rangle + \sum_{pqrs}|\phi_p\phi_q\phi_r\psi_s(t)\rangle. \qquad (2)$$

In the ansatz (2), two kinds of contributions in the total wave function are explicitly separated. The first sum over the $|\phi_i\phi_j\phi_k\phi_l\rangle$ configurations with the time-dependent expansion coefficients $a_{ijkl}(t)$ contains only preselected bound one-particle orbitals ϕ, while the second sum over $|\phi_p\phi_q\phi_r\psi_s(t)\rangle$ configurations contains three bound orbitals ϕ and one photoelectron wave packet $\psi(t)$, which is either excited beyond the basis of preselected bound orbitals ϕ or belongs to continuum states. Configurations of both kinds are given by linear combinations of Slater determinants constructed following angular momentum summation rules. The two one-particle basis sets $\{\phi_\alpha \equiv \phi_{n\ell m}\}$ and $\{\psi_s(t) \equiv \psi_{\varepsilon\ell m}(t)\}$ are mutually orthogonal (Artemyev et al., 2016). Both summations in **Eq. 2** run over all possible combinations which can be formed within the selected basis sets. In order to describe one-electron orbitals, we use the finite-element discrete-variable representation (FEDVR) scheme (Manolopoulos and Wyatt, 1988; Rescigno and McCurdy, 2000; McCurdy et al., 2004; Demekhin et al., 2013; Artemyev et al., 2015). Thereby, the radial coordinate of the three-dimensional basis element $\xi_\lambda(\vec{r})$

is represented in the basis set of the normalized Lagrange polynomials, which are constructed over a Gauss-Lobatto grid. The normalized stationary orbitals $\phi_\alpha = \sum_\lambda c_\lambda^\alpha \xi_\lambda$ and the time-dependent wave packets $\psi_s(t) = \sum_\lambda b_\lambda^s(t) \xi_\lambda$ are expanded with respect to the FEDVR basis elements ξ_λ. The matrix elements containing one- and two-particle contributions can then be identified using symmetry properties and selection rules, and their analytical expressions can be found in Refs. (McCurdy et al., 2004; Artemyev et al., 2016; Artemyev et al., 2017a).

Within the TD-RASCI method, the full configuration-interaction character of the TDCI method is relaxed by allowing only a selected set of bound states to be included into the basis (Artemyev et al., 2016; Artemyev et al., 2017a; Artemyev et al., 2017b). In the case of Be atom, the method is also designed to choose a type of configurations which can be built out of a selected basis, of course, in a complete manner. In this way, we are able to study different levels of approximations and their influence on HHG spectrum, catching thereby the essential physics of the problem without losing accuracy. The simplest case is the SAE approximation, where three electrons are fixed in the configuration $1s^2\,2s$ and only one of the electrons is allowed to participate in the dynamics. More complex calculations incorporate a frozen-core approximation which keeps two electrons in the $1s^2$ state, and thus single and double excitations of the two outermost electrons are allowed (hereafter referred to as 2FC). In beryllium, one can also consider further excitations of $1s$ and $2s$ electrons, which will be referred to as 2DC (dynamical-core) approximation. Depending on the allowed type of included configurations, this gives rise to the additional $1s^2$ ionization or $2s^2$ relaxation. In the former case, the active space included additional configurations with two electrons kept frozen in the $2s^2$ state, whereas in the latter case, additional $3s^2$ excitations in the presence of all former effects were allowed. The last step in complexity included in this study is the 1FC approximation. Here, only one electron is kept frozen in the $1s$ orbital, and all possible triple excitations are considered. This allows one to study the influence of three-electron dynamics and correlations on the HHG spectra. We stress again that in all considered approximations, the condition of a singly-occupied continuum is fulfilled. Summarizing, starting from SAE approximation, we consider the mentioned physical effects by going to 2FC, further to 2DC, and finally to 1FC approximations.

Time evolution of the total wave function (2) is given by the vector of the time-dependent expansion coefficients $\vec{B}(t) = \{a_{ijkl}(t); b_\lambda^s(t)\}$. $\vec{B}(t)$ was propagated according to Hamiltonian (1). The propagation was carried out by the short-iterative Lanczos method (Park and Light, 1986). The initial ground state $\vec{B}(t=0)$ was obtained by the propagation in imaginary time (relaxation) in the absence of the external field. Finally, the HHG spectrum $I(\omega)$ was computed as the squared modulus of the Fourier-transformed acceleration of the total electric dipole moment as

$$I(\omega) = \frac{1}{(2\pi)^{1/2}} \left| \int \frac{\mathrm{d}^2 D(t)}{\mathrm{d}t^2} e^{-i\omega t} \mathrm{d}t \right|^2, \tag{3}$$

with $D(t)$ given by

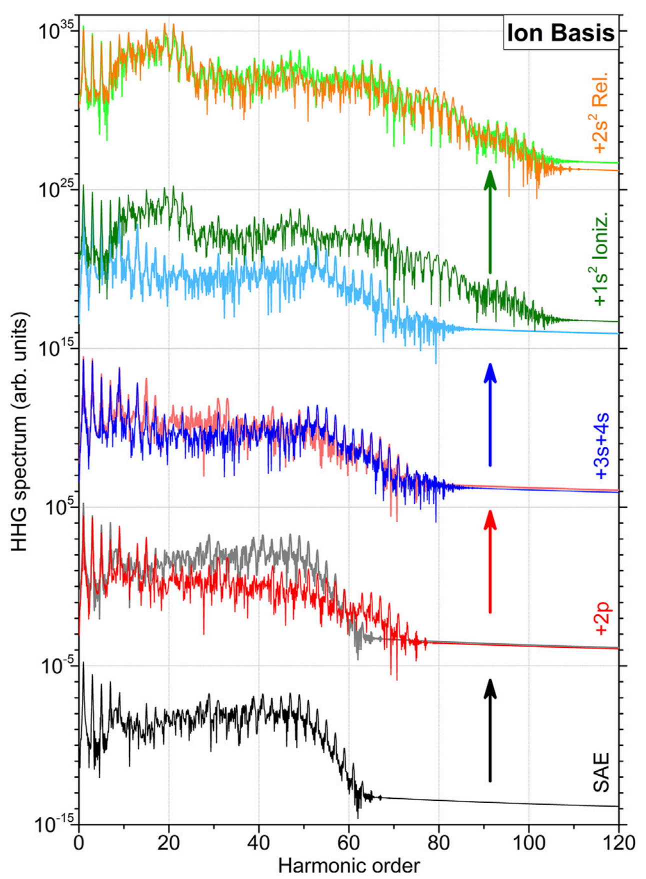

FIGURE 1 | High-order harmonic generation spectra of beryllium atom computed in the basis set $\{\phi_\alpha\}$ of ionic orbitals. The calculations are performed in a systematic series of improving approximations used to incorporate dynamics of the bound electrons (indicated at the right-hand vertical axis). For a better comparison, the spectra in each row are compared with the ones calculated in the previous level of approximation (as indicated by the colored arrows) and are vertically shifted upwards by multiplying successively with 10^{10} starting with the lowermost spectrum, obtained in the SAE approximation. The next two spectra (from bottom to top) are obtained within the 2FC approximation, by sequentially extending the basis set of discrete orbitals $\{n\ell_+\}$, first with $2p_+$ and then additionally with $3s_+$ and $4s_+$. The spectra shown in the two uppermost rows represent results obtained within the 2DC approximation, by additionally allowing first $1s_+^2$ ionization and then $2s_+^2$ relaxation.

$$D(t) = \langle \Psi(\vec{r}_1, \vec{r}_2, \vec{r}_3, \vec{r}_4, t) | \sum_{i=1}^{4} \vec{r}_i | \Psi(\vec{r}_1, \vec{r}_2, \vec{r}_3, \vec{r}_4, t) \rangle. \tag{4}$$

The present study was conducted for a trapezoidal pulse with a linearly growing front edge, a constant plateau with unit height, and a linearly falling back edge, each supporting 4 optical cycles. Thereby, an asymmetry due to the carrier-envelope phase can be neglected. The propagation was therefore performed in the time interval of $[0, T_f]$ with $T_f \approx 74$ fs. The size of the radial box was chosen to be $R_{max} = 4500$ a.u. The radial interval $[0, R_{\max}]$ was divided into 2250 equidistant finite elements of 2 a.u. size, each covered by 10 Gauss-Lobatto points. The photoelectron wave

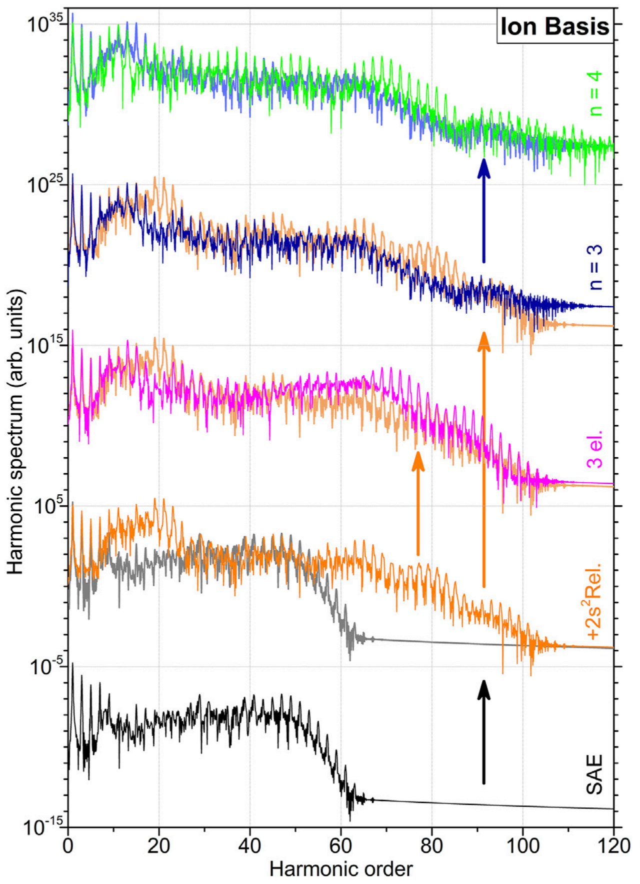

FIGURE 2 | High-order harmonic generation spectra of beryllium atom computed in the basis set $\{\phi_\alpha\}$ of ionic states at higher levels of approximations (indicated at the right-hand vertical axis, see also caption of **Figure 1** for details on the data representation). The two lowermost spectra, obtained in the SAE approximation and in the 2DC approximation by including physical effects up to $2s_+^2$ relaxation, are the same as the respective spectra in **Figure 1**. The spectrum in the middle, obtained in the 1FC approximation, illustrates an impact of the three-electron correlations, as compared to that of the 2DC approximation (also indicated by the respective colored arrow). The spectra shown in the two uppermost rows represent results obtained within the 2DC approximation by additionally (as compared to that of the 2DC approximation, see also respective colored arrows) extending the ionic basis set $\{\phi_\alpha\}$ first with all $n\ell_+$ orbitals with principal quantum $n = 3$ and then with $n = 4$.

packets $\{\psi_s(t)\}$ were described by the partial harmonics with $\ell \le 50$. Because the photoelectron wave packet is initially localized within a relatively small box and its size gradually increases with time according to the TDSE, we could save computation efforts by incorporating a so-called "running grid." To this end, the outermost wave-packet-free region of the grid with $r > R_{cut}(t)$ was neglected during the propagation. In this region, each harmonics of the wave packet must be smaller than a predefined accuracy parameter $\epsilon = 10^{-10}$, and the dynamical edge of this region $R_{cut}(t)$ must be updated at each time step. Finally, when $R_{\max}$ was reached, the wave packets are multiplied at each time step by a mask function (Artemyev et al., 2017a) to avoid any reflection from the boundary.

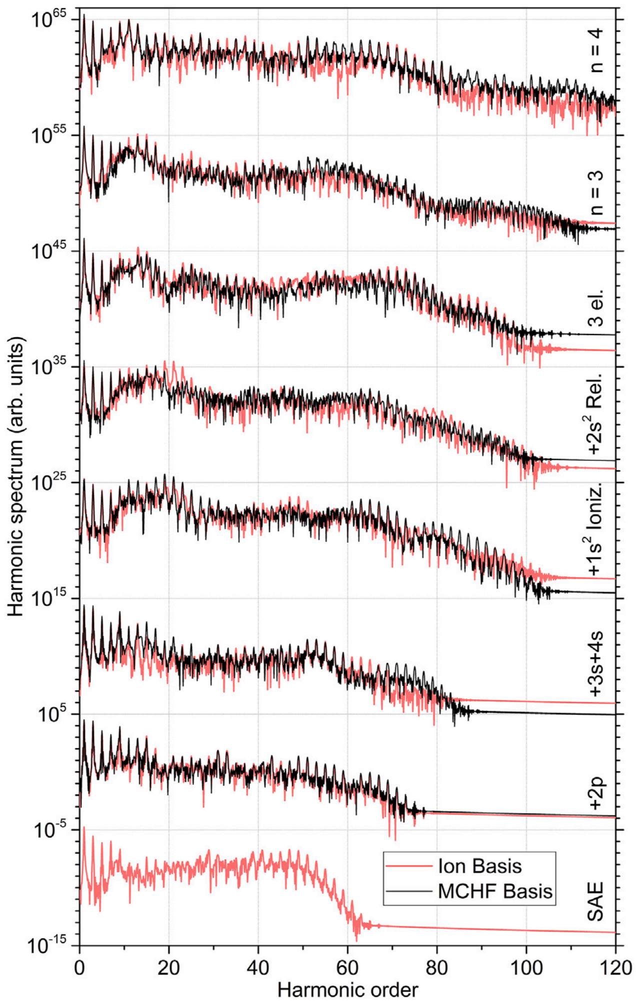

FIGURE 3 | Comparison of the high-order harmonic generation spectra of beryllium atom computed using the ionic and MCHF basis sets in different level of systematically improving approximations (indicated at the right-hand vertical axis, see also captions of **Figures 1**, **2** for details on the data representation). The five lowermost spectra obtained in the ionic basis set correspond to those depicted **Figure 1**, while the three uppermost ones to the three uppermost spectra shown in **Figure 2**.

RESULTS AND DISCUSSION

In the present calculations, we used two different basis sets for the description of the bound orbitals $\{\phi_\alpha\}$. The first one is composed of the Hartree-Fock (HF) orbitals obtained by solving the stationary Schrödinger equation of the singly charged beryllium ion in the configuration of $1s_+^2 2s_+^1$ (hereafter referred to as $\{n\ell_+\}$ ion basis set). This choice is natural for an accurate description of the final ionic state of the system. Here, we use all ionic orbitals with $n \le 4$ and $\ell \le 3$ (i.e., up to $4f_+$ orbital). The initial neutral ground state of beryllium atom is built mainly from two configurations $1s^2\,2s^2$ and $1s^2\,2p^2$ (Fischer and Jönsson, 1994) and, thus, is accurately described by the multiconfigurational Hartree-Fock (MCHF) method. As the second basis set of the bound orbitals $\{\phi_\alpha\}$, we used the minimal MCHF basis containing

{1*s*, 2*s*, 2*p*} orbitals. Here, in order to describe the whole ionization process accurately, we extended it successively by adding all ionic orbitals $n\ell_+$ and implying mutual orthogonalisation. In what follows, the HHG spectra obtained with the ionic basis set are depicted in **Figures 1**, **2**, while comparison between the spectra obtained in different basis sets is shown in **Figure 3**. **Figure 1** illustrates results of the lower-level 2FC and 2DC calculations, as obtained in the basis set with all ionic orbitals with the principal quantum number $n = 2$. In **Figure 2**, higher-level 2DC (with $n = 3$ and $n = 4$) and 1FC (3el.) calculations are compared with the best lower-level 2DC result.

The simplest calculations in the SAE approximation can be performed only in the ionic basis set of $\{1s_+, 2s_+\}$ oribitals. Here, we allow one of the $2s_+$ electrons to be ionized, but include direct and exchange interactions between all bound and continuum electrons. The respective HHG spectrum is shown in the lowermost row of **Figure 1**. This spectrum exhibits a plateau of harmonics up to an order of about 50 and a sharp cutoff up to harmonic order of about 60. These results agree with the three step model predicting the respective cutoff at the harmonic order of about $(IP + 3.17 \cdot U_p)/\omega \approx 45$ (Lewenstein et al., 1994), where IP, U_p, and ω are the respective ionization potential, ponderomotive potential, and carrier frequency.

As the next step, we apply the 2FC approximation and allow the second $2s_+$ electron to be excited, first only in the $2p_+$ orbital (note that this approximation is analogous to using the minimal {1*s*, 2*s*, 2*p*} MCHF basis set). The respective HHG spectrum is shown in the second-from-the-bottom row of **Figure 1** by a red curve. For a better comparison, the spectrum obtained in the previous SAE approximation is plotted in gray (note that this style of comparison of the result obtained in the two successive approximations will be kept thereafter, if not stated otherwise). As one can see, inclusion of the $2p_+$ orbital results in a decrease of the intensity of harmonics higher than about $k > 15$ by one to two orders of magnitude. Nevertheless, one can already see an appearance of harmonics beyond the SAE-cutoff up to about an order of 70. The middle panel of **Figure 1** depicts the HHG spectrum computed in the 2FC approximation by additionally extending the ionic basis set with $3s_+$ and $4s_+$ orbitals. By comparing this spectrum (blue curve) with that obtained in the previous approximation (also shown in this panel), we observe an additional loss of the harmonic intensity in the range of $15 < k < 50$.

Next, we allow the $1s_+^2$ electrons to be excited and ionized (2DC approximation). The respective HHG spectrum is plotted in the second-from-the-top row of **Figure 1** against the previous result. A dramatic increase of intensity by a few orders of magnitude at almost all harmonic orders can be recognized. In addition, the computed spectrum exhibits now harmonics up to an order of about 100. Allowing in addition the $2s_+^2$ shell to relax does not significantly change the computed HHG spectrum (see the uppermost panel of **Figure 1**). An additional comparison of the spectrum computed in this approximation with that from the SAE calculations is given in the second-from-the-bottom row of **Figure 2**. While allowing the second $2s_+$ electron to be active significantly decreases the intensity of the computed HHG spectrum, ionization of the $1s_+^2$ shell recovers the intensity of harmonics to that computed in the SAE approximation. In addition, a prominent increase of intensity of $15 < k < 25$ harmonics and an appearance of prominent $60 < k < 100$ harmonics beyond the former cutoff can be recognized.

At the following step, we allow for the three-electron dynamics and correlations. The HHG spectrum computed in the 1FC approximation is compared to that obtained in the most complete 2DC approximation in the middle row of **Figure 2**. One can observe a slight attenuation of lower $15 < k < 25$ and an amplification of higher $k > 50$ harmonic. Finally, the two uppermost rows of **Figure 2** represent calculations obtained in the 2DC approximation by including all ionic orbitals with the principal quantum number $n = 3$ (the second-from-the-top row) and subsequently with $n = 4$ (the top row). The latter results employ the most complete basis set of ionic orbitals, but neglect the effect of three-electron dynamics and correlation (as indicated by the long vertical arrow in orange colour). As one can see, extension of the one-particle basis set further influences intensities of all harmonics with $k > 15$, but, importantly, it does not alter the extension of HHG spectrum up to an order of about 100, caused by allowing $1s^2$ ionization and excitation.

As the last point of our study, we ensure that the effect observed here is independent of the basis set $\{\phi_\alpha\}$ of the bound orbitals. For this purpose, we perform analogous calculations employing the MCHF basis set described above. The results of those calculations (black curves) are compared in **Figure 3** with the respective results from the ionic basis (red curves). In each step of subsequently improving approximations (note that SAE calculations are not possible in the MCHF basis set), the HHG spectra computed with the two chosen basis sets agree well with each other in overall. We thus conclude that the individual impacts of different physical processes, discussed above on the example of the ionic basis set, persist also in the MCHF basis set.

CONCLUSION

Generation of high-order harmonics in the beryllium atom exposed to an intense linearly polarized 1850 nm laser pulse is studied beyond the single-active-electron approximation by the time-dependent restricted-active-space configuration-interaction method. In the calculations, we allowed only one of the electrons to be ionized and kept the other three electrons always bound to the nucleus, thereby neglecting the double-ionization process. This photoelectron was described in time-dependent wave packets with angular momenta $\ell \leq 50$. The dynamics of the remaining bound electrons was described by a set of discrete orbitals obtained either via Hartree-Fock or multiconfigurational Hartree-Fock methods in ionic or neutral beryllium, respectively. The active space of included configurations was systematically improved by allowing either specific basis states or specific types of configurations (or both) to be included. As soon as dynamics and correlations of the bound electrons are enabled, the computed spectrum of HHG exhibits considerably more harmonics of a higher order (as compared to that obtained in the SAE approximation). The richness of generated harmonics systematically increases with increasing the level of accuracy of the calculations. In particular, the HHG spectra computed in the most accurate approximations exhibit harmonics of up to an order of 100, and that in the SAE approximation only up to 60. Among the other included effects, excitation and ionization of the doubly-occupied 1*s* shell causes the most prominent effect on the computed spectrum of HHG. The presently obtained results are found to be independent of the basis set representing bound orbitals. As demonstrated in our previous work on HHG in He atom (Artemyev et al., 2017a), the effect of electron dynamics and correlations is also independent of the time envelope of employed laser pulses.

DATA AVAILABILITY STATEMENT

The original contributions presented in the study are included in the article/**Supplementary Material**, further inquiries can be directed to the corresponding author.

AUTHOR CONTRIBUTIONS

All authors listed have made a substantial, direct, and intellectual contribution to the work and approved it for publication.

FUNDING

AA and PD acknowledge support from the Deutsche Forschungsgemeinschaft: DFG—Projects No. 328 961 117—SFB 1319 ELCH and No. DE 2366/1-2. Funds to publish in open access were received from the Open Access Publikationsfonds of the University of Kassel.

SUPPLEMENTARY MATERIAL

The Supplementary Material for this article can be found online at: https://www.frontiersin.org/articles/10.3389/fchem.2022.809137/full#supplementary-material

REFERENCES

Alon, O. E., Streltsov, A. I., and Cederbaum, L. S. (2007). Unified View on Multiconfigurational Time Propagation for Systems Consisting of Identical Particles. *J. Chem. Phys.* 127, 154103. doi:10.1063/1.2771159

Artemyev, A. N., Cederbaum, L. S., and Demekhin, P. V. (2017a). Impact of Intense Laser Pulses on the Autoionization Dynamics of the 2*s*2*p* Doubly Excited State of He. *Phys. Rev. A.* 96, 033410. doi:10.1103/PhysRevA.96.033410

Artemyev, A. N., Cederbaum, L. S., and Demekhin, P. V. (2017b). Impact of Two-Electron Dynamics and Correlations on High-Order-Harmonic Generation in He. *Phys. Rev. A.* 95, 033402. doi:10.1103/PhysRevA.95.033402

Artemyev, A. N., Müller, A. D., Hochstuhl, D., Cederbaum, L. S., and Demekhin, P. V. (2016). Dynamic Interference in the Photoionization of He by Coherent Intense High-Frequency Laser Pulses: Direct Propagation of the Two-Electron Wave Packets on Large Spatial Grids. *Phys. Rev. A.* 93, 043418. doi:10.1103/PhysRevA.93.043418

Artemyev, A. N., Müller, A. D., Hochstuhl, D., and Demekhin, P. V. (2015). Photoelectron Circular Dichroism in the Multiphoton Ionization by Short Laser Pulses. I. Propagation of Single-Active-Electron Wave Packets in Chiral Pseudo-potentials. *J. Chem. Phys.* 142, 244105. doi:10.1063/1.4922690

Artemyev, A. N., Streltsov, A. I., and Demekhin, P. V. (2019). Controlling Dynamics of Postcollision Interaction. *Phys. Rev. Lett.* 122, 183201. doi:10.1103/PhysRevLett.122.183201

Bandrauk, A. D., Chelkowski, S., Diestler, D. J., Manz, J., and Yuan, K.-J. (2009). Quantum Simulation of High-Order Harmonic Spectra of the Hydrogen Atom. *Phys. Rev. A.* 79, 023403. doi:10.1103/PhysRevA.79.023403

Brabec, T., and Krausz, F. (2000). Intense Few-Cycle Laser fields: Frontiers of Nonlinear Optics. *Rev. Mod. Phys.* 72, 545–591. doi:10.1103/RevModPhys.72.545

Chelkowski, S., Bredtmann, T., and Bandrauk, A. D. (2012). High-order-harmonic Generation from Coherent Electron Wave Packets in Atoms and Molecules as a Tool for Monitoring Attosecond Electrons. *Phys. Rev. A.* 85, 033404. doi:10.1103/physreva.85.033404

Corkum, P. B. (1993). Plasma Perspective on strong Field Multiphoton Ionization. *Phys. Rev. Lett.* 71, 1994–1997. doi:10.1103/PhysRevLett.71.1994

Cormier, E., and Lambropoulos, P. (1996). Optimal Gauge and Gauge Invariance in Non-Perturbative Time-Dependent Calculation of Above-Threshold Ionization. *J. Phys. B: Mol. Opt. Phys.* 29, 1667–1680. doi:10.1088/0953-4075/29/9/013

Demekhin, P. V., Hochstuhl, D., and Cederbaum, L. S. (2013). Photoionization of Hydrogen Atoms by Coherent Intense High-Frequency Short Laser Pulses: Direct Propagation of Electron Wave Packets on Large Spatial Grids. *Phys. Rev. A.* 88, 023422. doi:10.1103/PhysRevA.88.023422

Fischer, C. F., and Jönsson, P. (1994). MCHF Calculations for Atomic Properties. *Computer Phys. Commun.* 84, 37–58. doi:10.1016/0010-4655(94)90202-X

Frolov, M. V., Manakov, N. L., Sarantseva, T. S., Emelin, M. Y., Ryabikin, M. Y., and Starace, A. F. (2009). Analytic Description of the High-Energy Plateau in Harmonic Generation by Atoms: Can the Harmonic Power Increase with Increasing Laser Wavelengths? *Phys. Rev. Lett.* 102, 243901. doi:10.1103/PhysRevLett.102.243901

Fu, Y., Zeng, J., and Yuan, J. (2017). PCTDSE: A Parallel Cartesian-Grid-Based TDSE Solver for Modeling Laser-Atom Interactions. *Computer Phys. Commun.* 210, 181–192. doi:10.1016/j.cpc.2016.09.016

Gordon, A., Kärtner, F. X., Rohringer, N., and Santra, R. (2006). Role of many-Electron Dynamics in High Harmonic Generation. *Phys. Rev. Lett.* 96, 223902. doi:10.1103/PhysRevLett.96.223902

Han, Y.-C., and Madsen, L. B. (2010). Comparison between Length and Velocity Gauges in Quantum Simulations of High-Order Harmonic Generation. *Phys. Rev. A.* 81, 063430. doi:10.1103/PhysRevA.81.063430

Haxton, D. J., Lawler, K. V., and McCurdy, C. W. (2011). Multiconfiguration Time-Dependent Hartree-Fock Treatment of Electronic and Nuclear Dynamics in Diatomic Molecules. *Phys. Rev. A.* 83, 063416. doi:10.1103/PhysRevA.83.063416

Hochstuhl, D., and Bonitz, M. (2011). Two-photon Ionization of Helium Studied with the Multiconfigurational Time-dependent Hartree-Fock Method. *J. Chem. Phys.* 134, 084106. doi:10.1063/1.3553176

Hochstuhl, D., and Bonitz, M. (2012). Time-Dependent Restricted-Active-Space Configuration-Interaction Method for the Photoionization of many-electron Atoms. *Phys. Rev. A.* 86, 053424. doi:10.1103/PhysRevA.86.053424

Ivanov, I. A., and Kheifets, A. S. (2009). Harmonic Generation for Atoms in Fields of Varying Ellipticity: Single-Active-Electron Model with Hartree-Fock Potential. *Phys. Rev. A.* 79, 053827. doi:10.1103/PhysRevA.79.053827

Kato, T., and Kono, H. (2004). Time-Dependent Multiconfiguration Theory for Electronic Dynamics of Molecules in an Intense Laser Field. *Chem. Phys. Lett.* 392, 533–540. doi:10.1016/j.cplett.2004.05.106

Keldysh, L. V. (1965). Ionization in the Field of a strong Electromagnetic Wave. *Sov. Phys. JETP.* 20, 1307–1314. Available at: https://inspirehep.net/files/6697e05d52e411291acc8238a780db45.

Kienberger, R., Goulielmakis, E., Uiberacker, M., Baltuska, A., Yakovlev, V., Bammer, F., et al. (2004). Atomic Transient Recorder. *Nature.* 427, 817–821. doi:10.1038/nature02277

Klamroth, T. (2003). Laser-Driven Electron Transfer through Metal-Insulator-Metal Contacts: Time-dependent Configuration Interaction Singles Calculations for a Jellium Model. *Phys. Rev. B.* 68, 245421. doi:10.1103/PhysRevB.68.245421

Krause, J. L., Schafer, K. J., and Kulander, K. C. (1992). High-order Harmonic Generation from Atoms and Ions in the High Intensity Regime. *Phys. Rev. Lett.* 68, 3535–3538. doi:10.1103/PhysRevLett.68.3535

Krause, P., Klamroth, T., and Saalfrank, P. (2005). Time-Dependent Configuration-Interaction Calculations of Laser-Pulse-Driven many-Electron Dynamics: Controlled Dipole Switching in Lithium Cyanide. *J. Chem. Phys.* 123, 074105. doi:10.1063/1.1999636

Krausz, F., and Ivanov, M. (2009). Attosecond Physics. *Rev. Mod. Phys.* 81, 163–234. doi:10.1103/RevModPhys.81.163

Lackner, F., Březinová, I., Sato, T., Ishikawa, K. L., and Burgdörfer, J. (2017). High-harmonic Spectra from Time-Dependent Two-Particle Reduced-Density-Matrix Theory. *Phys. Rev. A.* 95, 033414. doi:10.1103/PhysRevA.95.033414

Le, A.-T., Lucchese, R. R., Tonzani, S., Morishita, T., and Lin, C. D. (2009). Quantitative Rescattering Theory for High-Order Harmonic Generation from Molecules. *Phys. Rev. A.* 80, 013401. doi:10.1103/PhysRevA.80.013401

Lewenstein, M., Balcou, P., Ivanov, M. Y., L'Huillier, A., and Corkum, P. B. (1994). Theory of High-Harmonic Generation by Low-Frequency Laser fields. *Phys. Rev. A.* 49, 2117–2132. doi:10.1103/PhysRevA.49.2117

Manolopoulos, D. E., and Wyatt, R. E. (1988). Quantum Scattering via the Log Derivative Version of the Kohn Variational Principle. *Chem. Phys. Lett.* 152, 23–32. doi:10.1016/0009-2614(88)87322-6

McCurdy, C. W., Baertschy, M., and Rescigno, T. N. (2004). Solving the Three-Body Coulomb Breakup Problem Using Exterior Complex Scaling. *J. Phys. B: Mol. Opt. Phys.* 37, R137–R187. doi:10.1088/0953-4075/37/17/r01

Meyer, H-D., Gatti, F., and Worth, G. A. (2009). *Multidimensional Quantum Dynamics: MCTDH Theory and Applications*. Weinheim: Wiley VCH. doi:10.1002/9783527627400

Miyagi, H., and Madsen, L. B. (2013). Time-Dependent Restricted-Active-Space Self-Consistent-Field Theory for Laser-Driven many-electron Dynamics. *Phys. Rev. A.* 87, 062511. doi:10.1103/PhysRevA.87.062511

Nest, M., Klamroth, T., and Saalfrank, P. (2005). The Multiconfiguration Time-dependent Hartree-Fock Method for Quantum Chemical Calculations. *J. Chem. Phys.* 122, 124102. doi:10.1063/1.1862243

Ngoko Djiokap, J. M., and Starace, A. F. (2013). Resonant Enhancement of the Harmonic-Generation Spectrum of Beryllium. *Phys. Rev. A.* 88, 053412. doi:10.1103/PhysRevA.88.053412

Park, T. J., and Light, J. C. (1986). Unitary Quantum Time Evolution by Iterative Lanczos Reduction. *J. Chem. Phys.* 85, 5870–5876. doi:10.1063/1.451548

Rescigno, T. N., and McCurdy, C. W. (2000). Numerical Grid Methods for Quantum-Mechanical Scattering Problems. *Phys. Rev. A.* 62, 032706. doi:10.1103/PhysRevA.62.032706

Sato, T., Ishikawa, K. L., Březinová, I., Lackner, F., Nagele, S., and Burgdörfer, J. (2016). Time-Dependent Complete-Active-Space Self-Consistent-Field Method for Atoms: Application to High-Order Harmonic Generation. *Phys. Rev. A.* 94, 023405. doi:10.1103/PhysRevA.94.023405

Tikhomirov, I., Sato, T., and Ishikawa, K. L. (2017). High-harmonic Generation Enhanced by Dynamical Electron Correlation. *Phys. Rev. Lett.* 118, 203202. doi:10.1103/PhysRevLett.118.203202

Zanghellini, J., Kitzler-Zeiler, M., Fabian, C., Brabec, T., and Scrinzi, A. (2003). An MCTDHF Approach to Multi-Electron Dynamics in Laser fields. *Laser Phys.* 13, 1064–1068. Available at: https://www.researchgate.net/profile/Juergen-Zanghellini/publication/236985711_An_MCTDHF_approach_to_multi-electron_dynamics_in_laser_fields/links/5a109127458515cc5aa80341/An-MCTDHF-approach-to-multi-electron-dynamics-in-laser-fields.pdf.

Conflict of Interest: The authors declare that the research was conducted in the absence of any commercial or financial relationships that could be construed as a potential conflict of interest.

frontiers in Chemistry

ORIGINAL RESEARCH
published: 16 March 2022
doi: 10.3389/fchem.2022.857348

Systematic Investigation of the Reliability of the Frozen Nuclei Approximation for Short-Pulse Excitation: The Example of HCCl$^+$

Dongming Jia[1] *and Yonggang Yang*[2,3]*

[1]*MOE Key Laboratory for Non-equilibrium Synthesis and Modulation of Condensed Matter, School of Physics, Xi'an Jiaotong University, Xi'an, China,* [2]*State Key Laboratory of Quantum Optics and Quantum Optics Devices, Institute of Laser Spectroscopy, Shanxi University, Taiyuan, China,* [3]*Collaborative Innovation Center of Extreme Optics, Shanxi University, Taiyuan, China*

In this work we quantitatively study the reliability of the frozen nuclei approximation for ultrafast dynamics. Specifically we study laser excitation of HCCl$^+$ from its ground state to the first electronically excited state. The population of the first excited state is obtained by both the frozen nuclei approximation and by multidimensional nuclear dynamics. Detailed comparison of the results by the two methods are performed to provide quantitative criteria for the reliability of the frozen nuclei approximation for this system.

Keywords: frozen nuclei approximation, ultrashort laser pulses, nuclear quantum dynamics, electronic excitation, population transfer

Edited by:
Yuichi Fujimura,
Tohoku University, Japan

Reviewed by:
Hirobumi Mineo,
Ton Duc Thang University, Vietnam
Manabu Kanno,
Tohoku University, Japan

Correspondence:
Yonggang Yang
ygyang@sxu.edu.cn

Specialty section:
This article was submitted to Physical Chemistry and Chemical Physics,
a section of the journal Frontiers in Chemistry

Received: *18 January 2022*
Accepted: *07 February 2022*
Published: *16 March 2022*

Citation:
Jia D and Yang Y (2022) Systematic Investigation of the Reliability of the Frozen Nuclei Approximation for Short-Pulse Excitation: The Example of HCCl$^+$.
Front. Chem. 10:857348.
doi: 10.3389/fchem.2022.857348

1 INTRODUCTION

The rapid advances of ultrafast science and technology have made it possible to manipulate electron dynamics in molecular systems with ultrashort laser pulses. In particular, laser induced electron density redistribution such as charge transfer (Marcus, 1956; May and Kühn, 2008) and charge migration (Weinkauf et al., 1996, 1997; Cederbaum and Zobeley, 1999; Calegari et al., 2014; Kraus et al., 2015) have been extensively investigated. In general, charge migration prefers frozen nuclei or small amplitude nuclear motions, while charge transfer is typically accompanied by large amplitude nuclear motions. The research of charge transfer processes has a relatively long history. While ultrafast charge migration emerged as a hot topic during the past two decades (Weinkauf et al., 1996, 1997; Remacle et al., 1998; Cederbaum and Zobeley, 1999; Remacle and Levine, 1999; Barth and Manz, 2006; Kanno et al., 2006; Yudin et al., 2006; Remacle et al., 2007; Kanno et al., 2010; Mineo et al., 2012; Calegari et al., 2014; Kraus et al., 2015; Li et al., 2015; Yamaki et al., 2016; Wörner et al., 2017; Mineo et al., 2021). It should be noted that the first attosecond charge migration phenomenon was already introduced in 1944 (Eyring et al., 1944) and was largely forgotten during the next decades. Surveys of the literature on ultrafast charge migration can be found in Ref. (Jia et al., 2017a; Wörner et al., 2017). Below we summarize some typical features of ultrafast charge migration and its connection to the frozen nuclei approximation (FNA).

Ultrafast charge migration typically represents quantum dynamics of a coherent superposition of more than one electronic state. The typical time scale of ultrafast charge migration ranges from several hundred attoseconds to a few femtoseconds which makes the experimental observation (Kraus et al., 2015) rather difficult. For such a short time, the frozen nuclei approximation has been widely used for theoretical work of ultrafast charge migration. There are also several theoretical investigations which include the effects of nuclear motions (Bandrauk et al., 2009; Kanno et al., 2010; Ulusoy and Nest, 2012; Mendive-Tapia et al., 2013; Mineo et al., 2014; Despré et al., 2015; Mineo et al., 2021). The amplitude of charge migration can be significantly modulated by nuclear motions, in particular for relatively long-time dynamics (Mendive-Tapia et al., 2013; Mineo et al., 2014; Jia et al., 2019a,b). In general, the FNA is widely believed to be only valid for short time pulses, but there are no quantitative criteria for how short the pulses should be. This serves as the motivation for the present work: to seek quantitative criteria for the reliability of the FNA. Specifically, we will investigate short-pulse excitations of $HCCI^+$ by systematically varying the laser parameters in a sufficiently wide region.

The choice of $HCCI^+$ as our model of interest is based on the availability of experimental data (Heilbronner et al., 1971; Kraus et al., 2015) and theoretical techniques (Jia et al., 2019b). The combined experimental and theoretical reconstruction of attosecond charge migration has been reported for ultrafast ionization of HCCI (Kraus et al., 2015). Coherent superposition of the ground and first excited states has been created and analyzed. Subsequent theoretical investigations of ultrafast charge migration in $HCCI^+$ (Jia et al., 2017b; Ding et al., 2017) related to the experimental observation (Kraus et al., 2015) exploit the FNA. In-depth investigations of simulations and manipulations of charge migration in $HCCI^+$ including multidimensional nuclear dynamics have been reported recently (Jia et al., 2019a,b). However, no comparisons between the results of multidimensional nuclear dynamics and the ones of the FNA are available.

In the present work, we will investigate the reliability of the FNA by comparing the FNA and multidimensional nuclear dynamics. The remainder parts of the paper are organized as follows. **Section 2** contains the model and methods for numerical calculations. **Section 3** presents the results and discussion. The conclusions are drawn in **Section 4**.

2 MODEL AND METHODS

We focus on laser excitations of $HCCI^+$ from its ground state. Full dimensional simulations of the system involve sets of electronic coordinates $\boldsymbol{r} = \{\boldsymbol{r}_1, \boldsymbol{r}_2, \ldots\}$ and nuclear coordinates $\boldsymbol{R} = \{\boldsymbol{R}_1, \boldsymbol{R}_2, \ldots\}$. Here $\boldsymbol{r}_i$ and $\boldsymbol{R}_j$ are the spatial coordinates of the i-th electron and the j-th nucleus, respectively. It is convenient to use the Dirac notation for the electronic degrees of freedom. The total wavefunction of the system is thus

$$\Psi(\boldsymbol{r}, \boldsymbol{R}, t) = \langle \boldsymbol{r} | \Psi(\boldsymbol{R}, t) \rangle. \tag{1}$$

Using the Born-Huang expansion (Born and Oppenheimer, 1927; Born and Huang, 1954), the total wavefunction can be expressed in terms of the electronic eigenstates $|k(\boldsymbol{R})\rangle$ which are the solutions of the standard time-independent electronic schrödinger equation

$$H_{\mathrm{el}}(\boldsymbol{R}) |k(\boldsymbol{R})\rangle = V_k(\boldsymbol{R}) |k(\boldsymbol{R})\rangle. \tag{2}$$

The corresponding electronic eigenenergy $V_k(\boldsymbol{R})$ is the k-th potential energy surface (PES). Here $V_k(\boldsymbol{R})$ and $\langle \boldsymbol{r} | k(\boldsymbol{R})\rangle$ are the same as the ones used in Refs. (Jia et al., 2019a,b) which are calculated by Molpro (Werner et al., 2012) using the state-averaged CASSCF(15,13) with cc-pVQZ basis set (cc-pVQZ-pp for iodine).

According to (Kraus et al., 2015; Jia et al., 2019a,b), nonadiabatic couplings between different electronic states $|k(\boldsymbol{R})\rangle$ are negligible. The total Hamiltonian for $HCCI^+$ in an external laser field $\boldsymbol{E}(t)$ can be approximated as

$$H(t) = \sum_{kk'} |k(\boldsymbol{R})\rangle \left[T(\boldsymbol{R})\delta_{kk'} + V_k(\boldsymbol{R})\delta_{kk'} - \boldsymbol{\mu}_{kk'}(\boldsymbol{R}) \cdot \boldsymbol{E}(t) \right] \langle k'(\boldsymbol{R})|, \tag{3}$$

where $T(\boldsymbol{R})$ is the nuclear kinetic energy and $\boldsymbol{\mu}_{kk'}(\boldsymbol{R}) = \langle k(\boldsymbol{R}) | \boldsymbol{\mu} | k'(\boldsymbol{R})\rangle$ is the transition (or permanent) dipole moment. The laser pulse has a Gaussian shape with maximum amplitude $E_{\max}$ and carrier frequency ω

$$\begin{aligned} \boldsymbol{E}(t) &= \boldsymbol{e}_z\, E_{\max} s(t) \sin(\omega t), \\ s(t) &= e^{-at^2/T^2}, \end{aligned} \tag{4}$$

where $\boldsymbol{e}_z$ is the direction of the electric field. For convenience, the electric field and the molecules are oriented along the z-axis. In the literature, there are different choices of the parameter a in **Eq. 4**. For the present work we set

$$a = 4 \ln 2 \tag{5}$$

for easier characterization of the pulse duration. We define the pulse duration as the full width at half maximum (FWHM) of $s(t)$, which is just T in **Eq. 4**.

The quantum dynamics of the system can be simulated by the time-dependent schrödinger equation subject to initial condition at $t = -\infty$

$$\begin{aligned} i\hbar \frac{\mathrm{d}}{\mathrm{d}t} |\Psi(\boldsymbol{R}, t)\rangle &= H |\Psi(\boldsymbol{R}, t)\rangle, \\ |\Psi(\boldsymbol{R}, t = -\infty)\rangle &= \chi_{g,\nu=0}(\boldsymbol{R}) |g(\boldsymbol{R})\rangle, \end{aligned} \tag{6}$$

where $\chi_{g,\nu=0}(\boldsymbol{R})$ is the vibrational ground state wavefunction of the lowest potential energy surface $V_g(\boldsymbol{R})$. For convenience we use $k = g, e$ to represent the lowest and first excited electronic states, respectively. The wave packet is numerically propagated by means of the split operator method (Leforestier et al., 1991).

Subsequently, we can obtain the population of the electronic state $|k(\boldsymbol{R})\rangle$ according to

$$\begin{aligned} P_k(t) &= \int \langle \Psi(\boldsymbol{R}, t) | k(\boldsymbol{R})\rangle \langle k(\boldsymbol{R}) | \Psi(\boldsymbol{R}, t)\rangle \mathrm{d}\boldsymbol{R} \\ &\equiv \int \chi_k^*(\boldsymbol{R}, \boldsymbol{t}) \chi_k(\boldsymbol{R}, \boldsymbol{t}) \mathrm{d}\boldsymbol{R}, \end{aligned} \tag{7}$$

where $\chi_k(\boldsymbol{R}, \boldsymbol{t}) = \langle k(\boldsymbol{R}) | \Psi(\boldsymbol{R}, t)\rangle$ is the nuclear wave packet on the k-th PES $V_k(\boldsymbol{R})$. It contains seven vibrational coordinates. According to Ref. (Jia et al., 2019a,b), one-dimensional (1D), three-dimensional (3D), and seven-dimensional (7D) calculations lead to essentially the same results. In the 3D calculations, the H-C, C-C and C-I bond lengths are explicitly taken into account and the four bending degrees of freedom are neglected. This kind of approximation is reasonable for linear molecules, such as $HCCI^+$. In the present work we use the same

3D calculations for the nuclear wave packet $\chi_k(\boldsymbol{R},t)$ as in Ref. (Jia et al., 2019b). Then we mainly focus on the population of the first electronically excited state $P_k(t)$ for $k = e$.

To check the reliability of the FNA, we further calculated the population of the first electronically excited state $P_e^{\rm FNA}$ using the FNA. Accordingly, the molecular structure is fixed at the minimum of the lowest PES $V_g(\boldsymbol{R})$. This structure is called equilibrium structure $\boldsymbol{R}_{\rm eq}$. The corresponding transition dipole moment is $\boldsymbol{\mu}_{\rm eq} \equiv \boldsymbol{\mu}_{ge}(\boldsymbol{R} = \boldsymbol{R}_{\rm eq})$. The electronic wavefunction of the FNA is expanded as

$$|\Psi^{\rm FNA}(t)\rangle = \sum_k c_k(t)|k(\boldsymbol{R} = \boldsymbol{R}_{\rm eq})\rangle. \quad (8)$$

the time dependent coefficient $c_k(t)$ can be obtained subject to the initial condition $c_k(t = -\infty) = \delta_{kg}$. The corresponding population is

$$P_k^{\rm FNA}(t) = |c_k(t)|^2. \quad (9)$$

Throughout this work we fix the carrier frequency of the laser in **Eq. 4** as $\hbar\omega = V_e(\boldsymbol{R}_{\rm eq}) - V_g(\boldsymbol{R}_{\rm eq})$. We only focus on the final population at $t = t_f$ when the laser pulse is off. This leads to the following analytical expression (Jia et al., 2017a)

$$P_e^{\rm FNA}\left(t = t_f\right) \approx \sin^2\left(\frac{\sqrt{\pi}\,E_{\max}\mu_{\rm eq}^z T}{\sqrt{a}\,\hbar}\right), \quad (10)$$

where $\mu_{\rm eq}^z$ denotes the z component of the transition dipole at $\boldsymbol{R}_{\rm eq}$. The relative error of the FNA with respect to multi-dimensional nuclear dynamic is defined as

$$\frac{\delta P_e}{P_e} = \frac{\left|P_e^{\rm FNA}\left(t = t_f\right) - P_e\left(t = t_f\right)\right|}{P_e\left(t = t_f\right)} \times 100\%. \quad (11)$$

For all the subsequent numerical calculations we set $t_f = 5T$. However, this should not be wrongly interpreted as the FNA is valid even for $t = 5T$. We choose $t_f = 5T$ just to make use of the property that the results presented in this work do not depend on different choices of t_f as long as $t_f \geq T$.

3 RESULTS AND DISCUSSION

The equilibrium structure $\boldsymbol{R}_{\rm eq}$ of HCCI$^+$ is linear with bond lengths $R_{\rm HC} = 1.06$ Å, $R_{\rm CC} = 1.21$ Å and $R_{\rm CI} = 1.95$ Å. The corresponding vertical excitation energy from ground state $|g(\boldsymbol{R}_{\rm eq})\rangle$ to the first excited state $|e(\boldsymbol{R}_{\rm eq})\rangle$ is $\hbar\omega = 2.41$ eV. For typical pulse durations, there are sufficient numbers of cycles in $\boldsymbol{E}(t)$ to make the electronic transition resonant. The corresponding transition dipole has only a z-component, which is $\mu_{\rm eq}^z = 3.21$ Debye. Subsequently we calculated the population of the first electronically excited state $P_e^{\rm FNA}(t = t_f)$ according to **Eq. 10** by the FNA. Convergence tests are performed for nuclear dynamics simulations such that the corresponding population of the first electronically excited state $P_e(t)$ does not change subject to further increase of the grid-region or decrease of the spatial or temporal steps. We first analyze the dependence of the results on the pulse durations with the other parameters fixed. Specifically, the maximum amplitude of the electric field $E_{\max}$ is fixed at 2.0×10^9 V/m. The detailed comparison between $P_e(t = t_f)$ and $P_e^{\rm FNA}(t = t_f)$ is shown in **Figure 1** for $T \leq 20$ fs.

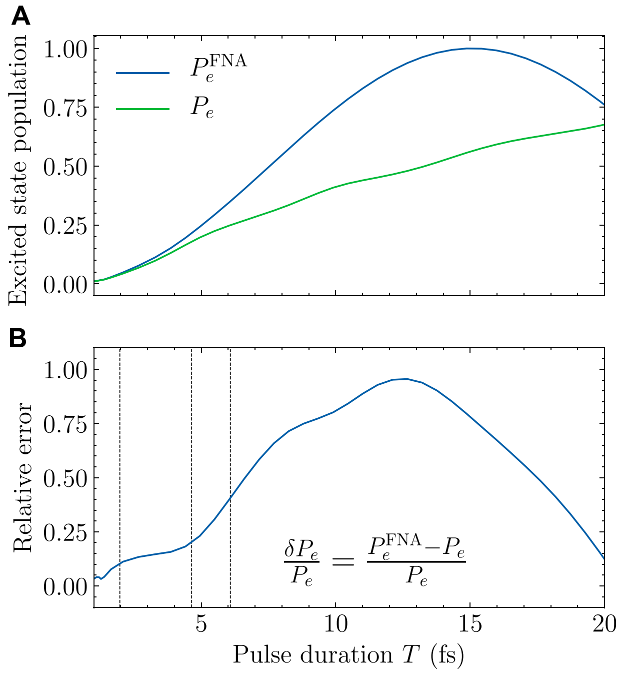

FIGURE 1 | Population of the first electronically excited state of HCCI$^+$ versus the pulse duration T, at $t = t_f$ when the laser pulse is switched off. The maximum-amplitude of the electric field $E_{\max}$ is 2 GV/m. **(A)** $P_e(t_f)$ and $P_e^{\rm FNA}(t_f)$ obtained by multidimensional nuclear dynamics (green) and by the frozen nuclei approximation (blue), respectively. **(B)** The relative error $\frac{\delta P_e}{P_e}$ of $P_e^{\rm FNA}(t_f)$ with respect to $P_e(t_f)$. Vertical lines show the positions of $\frac{\delta P_e}{P_e} = 10\%$, 20%, and 40%, respectively.

As can be seen from **Figure 1A**, the deviation between $P_e^{\rm FNA}(t_f)$ and $P_e(t_f)$ gradually increases with the pulse duration T, for the region of short pulses. For $T \leq 20$ fs, $P_e(t)$ keeps increasing with T. However, $P_e^{\rm FNA}(t)$ first increases and then decreases for $T \leq 20$ fs. This kind of qualitative deviation will be further discussed below. According to **Eq. 10** $P_e^{\rm FNA}(t_f)$ will oscillate periodically with the pulse duration T. In **Figure 1A**, $P_E^{\rm FNA}(t_f)$ reaches its maximum $P_{e,\max}^{\rm FNA} = 1$ for $T = 15.45$ fs. However, $P_e(t_f)$ is still substantially below one even for $T = 20$ fs.

To quantitatively compare $P_e^{\rm FNA}(t_f)$ and $P_e(t_f)$, the relative error $\frac{\delta P_e}{P_e}$ defined in **Eq. 11** is shown in **Figure 1B**. The relative error increases relatively slowly when the pulse duration T is smaller than 5 fs, and increases rapidly when T is larger than 5 fs. For long pulses, say $T \geq 15$ fs, **Figure 1B** shows significant decrease of $\frac{\delta P_e}{P_e}$. However, this is pure coincidence. As can be identified from **Figure 1A**, the trend of $P_e^{\rm FNA}(t_f)$ is already qualitatively wrong for $T > 15.45$ fs. Smaller relative error in this region does not imply better agreement between the frozen nuclei approximation and real physics. Consequently, we focus on short pulses for which the FNA is expected to be reasonable. Accordingly, we add three vertical lines in **Figure 1B** for relative errors of 40, 20, and 10%, respectively. The corresponding pulse

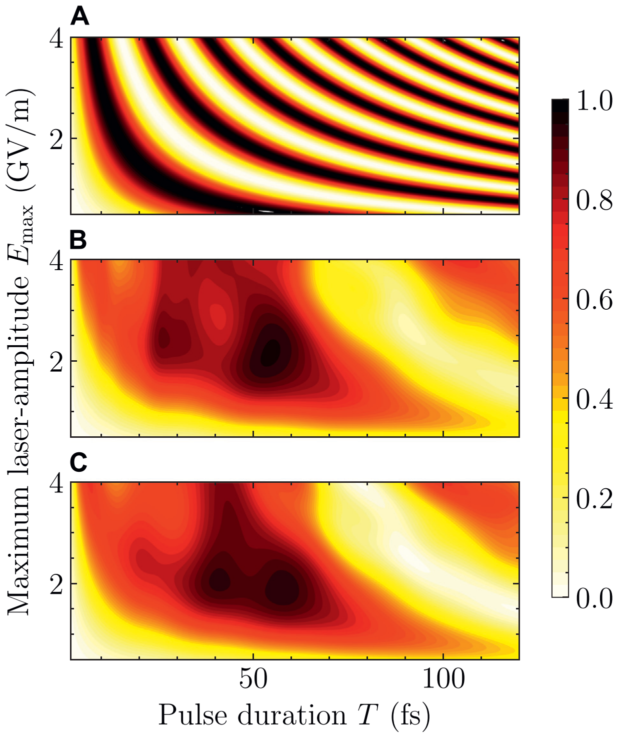

FIGURE 2 | Population of the first electronically excited state of HCCI$^+$ *versus* $E_{\max}$ and T illustrated by color-coded contour plots. **(A)** $P_e^{\mathrm{FNA}}(t_f)$ calculated by the FNA. **(B)** $P_e(t_f)$ obtained by 3D nuclear dynamics simulations. **(C)** Same as **(B)** but the nuclear dynamics is one-dimensional.

durations with fixed value of $E_{\max} = 2.0\times10^9$ V/m are $T = 6.09$, 4.65, and 1.97 fs, respectively.

Figure 2 shows the color-coded contour plots for the dependence of $P_e^{\mathrm{FNA}}(t_f)$ and $P_e(t_f)$ on the amplitude of the electric field $E_{\max}$ and the pulse duration T. The full set of the involved parameters span the region 0.5 GV/m $\le E_{\max} \le$ 4.0 GV/m and $T \le 120$ fs. The region of $E_{\max}$ more or less covers the reported amplitudes of lasers exploited in typical applications in the literature. The region of T reaches the first revival of charge migration in HCCI$^+$ reported in Ref. (Jia et al., 2019b). As can be seen from **Figure 2A**, $P_e^{\mathrm{FNA}}(t_f)$ oscillates between 1 and 0 periodically with $E_{\max}$ or T. Larger values of $E_{\max}$ or T corresponds to smaller oscillation period of $P_e^{\mathrm{FNA}}(t_f)$, c.f., **Eq. 10**. **Figure 2B** is the same as **Figure 2A** except that $P_e^{\mathrm{FNA}}(t_f)$ is replaced by $P_e(t_f)$ which is obtained by performing 3D nuclear dynamics simulations. We can immediately identify that **Figures 2A,B** are qualitatively different for relatively long laser lulses (e.g., for $T \ge 20$ fs). We therefore consider the results for the FNA are not meaningful for relatively long laser pulses. This is quite natural. Even if $P_e^{\mathrm{FNA}}(t_f)$ is coincidentally very close to $P_e(t_f)$ for $T \ge 20$ fs, the nuclear wave packet is quite different from the initial one as has been reported in Ref. (Jia et al., 2019b). Accordingly, the basic assumption of the FNA breaks down for $T \ge 20$ fs. We further plot **Figure 2C** which is the same with **Figure 2B** except that the population of the first electronically excited state is obtained by performing 1D nuclear dynamics simulations which explicitly treats the C-I stretch (Jia et al., 2019a). The results of 1D and 3D simulations agree well with each other, which confirms the findings in Refs. (Jia et al., 2019a,b).

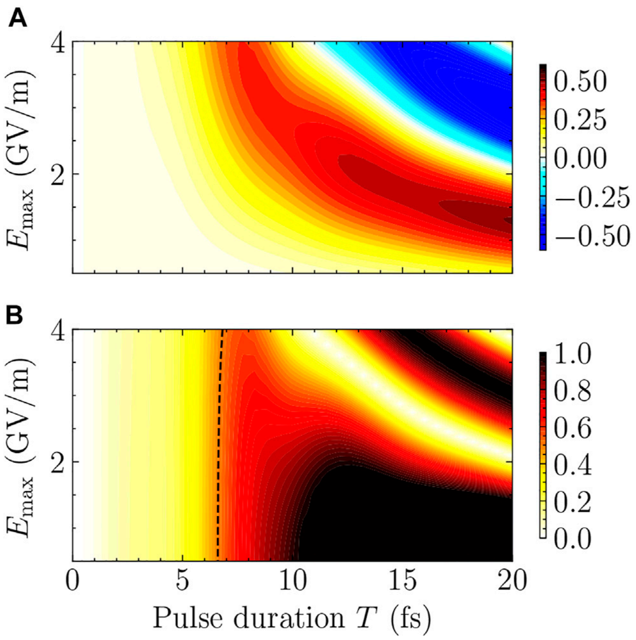

FIGURE 3 | (A) Color-coded contour plots for the deviation $P_e^{\mathrm{FNA}}(t_f) - P_e(t_f)$ between $P_e^{\mathrm{FNA}}(t_f)$ in **Panel 2A** and $P_e(t_f)$ in **Panel 2B** for $T \le 20$ fs. **(B)** Color-coded contour plots for the relative error $\frac{\delta P_e}{P_e}$ of $P_e^{\mathrm{FNA}}(t_f)$ with respect to $P_e(t_f)$. The black dashed curve indicates $\frac{\delta P_e}{P_e} = 50\%$.

To systematically study the reliability of the FNA for short pulses, the difference between $P_e^{\mathrm{FNA}}(t_f)$ in **Figure 2A** and $P_e(t_f)$ in **Figure 2B** is shown in **Figure 3A**, for the region $T \le 20$ fs when the FNA may be expected to work. The dependence of $P_e^{\mathrm{FNA}}(t_f) - P_e(t_f)$ on $E_{\max}$ and T is shown by color-code contour plots. Results for which $|P_e^{\mathrm{FNA}}(t_f) - P_e(t_f)| \ge 0.5$ are not resolved, since results with errors larger than 50 percent are in general not helpful. For any fixed value of $E_{\max}$, the deviation between $P_e^{\mathrm{FNA}}(t_f)$ and $P_e(t_f)$ first increases then decreases with T after reaching a maximum. More complicated features can be found for relatively large $E_{\max}$ combined with relatively long T. However, as discussed above for **Figure 1**, the results of $P_e^{\mathrm{FNA}}(t_f)$ in this complicated region in **Figure 3A** (specifically, after reaching maximum deviations) can agree better with $P_e(t_f)$ by coincidence. In the following we only focus on the left bottom region of **Figure 3A** before the corresponding deviation $P_e^{\mathrm{FNA}}(t_f) - P_e(t_f)$ reaches its maximum for any fixed value of $E_{\max}$. As can be seen from **Figure 3A**, the deviations are rather small for $T \le 5$ fs for all the different values of $E_{\max}$ involved in the present work. This implies that we may roughly use $T \le 5$ fs as the criterion for the reliability of the FNA. The deviation not only increases with T for any given $E_{\max}$, but also increases with $E_{\max}$ for any given T. According to **Eq. 10**, $P_e^{\mathrm{FNA}}(t_f)$ increases with the product of $E_{\max}$ and T before reaching its maximum. From

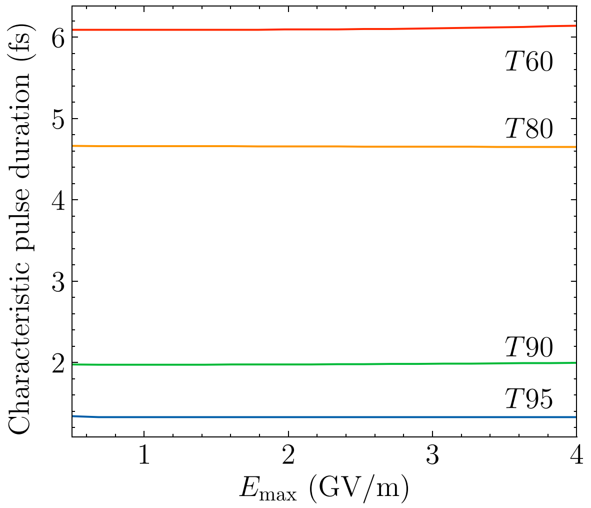

FIGURE 4 | Characteristic pulse durations *T*95, *T*90, *T*80, and *T*60 for relative error $\frac{\delta P_e}{P_e}$ = 5, 10, 20, and 40%, respectively. See the text for more details.

Figure 3A we can also find that the deviation $P_e^{\mathrm{FNA}}(t_f) - P_e(t_f)$ essentially increases with the product of $E_{\max}$ and T before reaching its maximum. Better criteria for the reliability of the FNA can be obtained by analyzing the relative error of $P_e^{\mathrm{FNA}}(t_f)$ with respect to $P_e(t_f)$ shown in **Figure 3B**. In the same spirit, we only need to focus on the left region of **Figure 3B** indicated by the dashed curve in which the relative error $\frac{\delta P_e}{P_e}$ never exceeds 50%. For relatively long pulses, say $T = 7$ fs, the relative error of the FNA is already larger than 50% for any value of $E_{\max}$ shown in **Figure 3B**. In this case, the FNA is no longer reliable for $T \geq 7$ fs.

In the short pulse region, the relative error $\frac{\delta P_e}{P_e}$ increases with the pulse duration T. To give quantitative criteria for the reliability of the FNA, we define certain characteristic pulse durations as follows:

$$TN:\ \frac{\delta P_e}{P_e} \leq (100-N)\% \text{ if } T \leq TN. \quad (N = 60, 80, 90, 95)$$

For example, if we want to use the FNA to obtain results with relative errors smaller than 5%, we need to set the pulse durations of the lasers to be smaller than *T*95. Similarly for the meanings of *T*90, *T*80, and *T*60. According to our model the characteristic pulse durations *T*95, *T*90, *T*80, and *T*60 only depend on one parameter $E_{\max}$, which will be investigated subsequently.

The detailed dependence of *T*95, *T*90, *T*80, and *T*60 on the maximum amplitude of the electric field $E_{\max}$ is shown in **Figure 4**. A quite good property for the characteristic pulse durations is that *T*95, *T*90, and *T*80 almost do not depend on $E_{\max}$. The corresponding values are *T*95 = 1.32 fs, *T*90 = 1.97 fs, and *T*80 = 4.65 fs respectively. The value of *T*60 increases with $E_{\max}$ extremely slightly from 6.09 to 6.14 fs. For relatively high standard criteria, say relative errors below 20%, the corresponding characteristic pulse durations are quite robust with respect to different amplitudes of lasers. This greatly simplifies the criteria for choosing proper lasers for applications of short pulse excitations of HCCI$^+$. Essentially, we only need to care about the durations of the laser pulses with quantitative guidance derived from **Figure 4** for the reliability of the FNA.

The FNA only considers the electronic degrees of freedom and neglects the nuclear motions. Mathematically this corresponds to a large overlap of the time-dependent and the initial nuclear wave packets. The overlap can be estimated as the product of the corresponding overlap for each normal mode. The overlap for a normal mode may be approximated as $e^{-f^2(t)}$ for short time dynamics. Here $f(t)$ is the displacement of the normal coordinate with respect to its initial value in units of the standard deviation of the initial wave packet for this normal mode. Typically, there will be only one or a few modes with $f^2(t)$ substantially above zero, which are called active modes. The overall overlap is thus mainly determined by the active modes. For the present case, there is only one active mode which is the C-I stretch with period 86 fs (Jia et al., 2019b). Due to the relatively large amplitude of the C-I stretch mode, the function $e^{-f^2(t)}$ quickly decreases to zero (Jia et al., 2019a,b). In this case, the duration of the pulse must be much shorter than a vibrational period to keep the overlap large enough. According to the results of **Figure 4**, all the characteristic pulse durations of HCCI$^+$ are smaller than $\frac{1}{10}$ of a vibrational period. However, for some molecules with sufficiently small vibrational amplitudes for all the active modes, the overlap can be relatively large for a rather long time. For such cases, the effects of nuclear dynamics can be neglected for a longer time than just a few femtoseconds (Kanno et al., 2010; Ulusoy and Nest, 2012; Despré et al., 2015).

4 CONCLUSION

We have systematically investigated the population of the first electronically excited state of HCCI$^+$ excited by different laser pulses. The amplitudes and durations of the laser pulses span a rather large domain for typical applications. The deviations between the results obtained by the frozen nuclei approximation and the ones obtained by multidimensional nuclear dynamics are calculated and analyzed in detail to check the reliability of the FNA. As expected the validity of the FNA can be admitted for sufficiently short laser pulses. Quantitative criteria for the reliability of the FNA are obtained. Specifically if we want to limit the relative errors of the FNA within 5% (or 10, or 20, or 40%), the durations of the laser pulses should be less than *T*95 = 1.3 fs (or *T*90 = 2.0 fs, or *T*80 = 4.7 fs, or *T*60 = 6.1 fs). For example, ultrafast charge migration in HCCI$^+$ is reconstructed in Ref. (Kraus et al., 2015). for the first period of 1.85 fs. By extrapolation of our results, the error of the reported charge migration in HCCI$^+$ for the first period is less than 10%. For short pulses with durations up to *T*60, the relative errors of the FNA are found to be almost independent of the amplitudes of the laser pulses. The results of the present work are expected to provide valuable guidance to future investigations of short pulse excitations of HCCI$^+$.

DATA AVAILABILITY STATEMENT

The original contributions presented in the study are included in the article/supplementary material, further inquiries can be directed to the corresponding author.

AUTHOR CONTRIBUTIONS

YY proposed the conception and design of the study. DJ carried out all the quantum chemical calculations and the quantum dynamics simulations, and prepared all Figures. YY wrote the zero-order draft. All the authors contributed to the submitted version of the manuscript.

FUNDING

This work was supported by the National Key Research and Development Program of China (2017YFA0304203), the Program for Changjiang Scholars and Innovative Research Team (IR_17R70), the National Natural Science Foundation of China (11904215), the 111 project (Grant No. D18001), the Fund for "Shanxi 1331 Project," and the Hundred Talent Program of Shanxi Province.

ACKNOWLEDGMENTS

We would like to express our gratitude to Professor Jörn Manz (Berlin) for stimulating discussions and careful reading of the manuscript.

REFERENCES

Bandrauk, A. D., Chelkowski, S., Corkum, P. B., Manz, J., and Yudin, G. L. (2009). Attosecond Photoionization of a Coherent Superposition of Bound and Dissociative Molecular States: Effect of Nuclear Motion. *J. Phys. B: Mol. Opt. Phys.* 42, 134001. doi:10.1088/0953-4075/42/13/134001

Barth, I., and Manz, J. (2006). Periodic Electron Circulation Induced by Circularly Polarized Laser Pulses: Quantum Model Simulations for Mg Porphyrin. *Angew. Chem. Int. Ed.* 45, 2962–2965. doi:10.1002/anie.200504147

Born, M., and Huang, K. (1954). Dynamical Theory of crystal Lattices. Clarendon Press, Oxford.

Born, M., and Oppenheimer, R. (1927). Zur Quantentheorie der Molekeln. *Ann. Phys.* 389, 457–484. doi:10.1002/andp.19273892002

Calegari, F., Ayuso, D., Trabattoni, A., Belshaw, L., De Camillis, S., Anumula, S., et al. (2014). Ultrafast Electron Dynamics in Phenylalanine Initiated by Attosecond Pulses. *Science* 346, 336–339. doi:10.1126/science.1254061

Cederbaum, L. S., and Zobeley, J. (1999). Ultrafast Charge Migration by Electron Correlation. *Chem. Phys. Lett.* 307, 205–210. doi:10.1016/S0009-2614(99)00508-4

Despré, V., Marciniak, A., Loriot, V., Galbraith, M. C. E., Rouzée, A., Vrakking, M. J. J., et al. (2015). Attosecond Hole Migration in Benzene Molecules Surviving Nuclear Motion. *J. Phys. Chem. Lett.* 6, 426–431. doi:10.1021/jz502493j

Ding, H., Jia, D., Manz, J., and Yang, Y. (2017). Reconstruction of the Electronic Flux during Adiabatic Attosecond Charge Migration in HCCI+. *Mol. Phys.* 115, 1813–1825. doi:10.1080/00268976.2017.1287967

Eyring, H., Walter, J., and Kimball, G. E. (1944). *Quantum Chemistry*. New York: Wiley.

Heilbronner, E., Muszkat, K. A., and Schäublin, J. (1971). An Estimate of the Interatomic Distances in Monohaloacetylene Radical Cations from Photoelectron-Spectroscopic Data. *Hca* 54, 58–76. doi:10.1002/hlca.19710540107

Jia, D., Manz, J., Paulus, B., Pohl, V., Tremblay, J. C., and Yang, Y. (2017a). Quantum Control of Electronic Fluxes during Adiabatic Attosecond Charge Migration in Degenerate Superposition States of Benzene. *Chem. Phys.* 482, 146–159. doi:10.1016/j.chemphys.2016.09.021

Jia, D., Manz, J., and Yang, Y. (2019a). De- and Recoherence of Charge Migration in Ionized Iodoacetylene. *J. Phys. Chem. Lett.* 10, 4273–4277. doi:10.1021/acs.jpclett.9b01687

Jia, D., Manz, J., and Yang, Y. (2017b). Generation of Electronic Flux during the Femtosecond Laser Pulse Tailored to Induce Adiabatic Attosecond Charge Migration in. *J. Mod. Opt.* 64, 960–970. doi:10.1080/09500340.2016.1269216

Jia, D., Manz, J., and Yang, Y. (2019b). Timing the Recoherences of Attosecond Electronic Charge Migration by Quantum Control of Femtosecond Nuclear Dynamics: A Case Study for HCCI+. *J. Chem. Phys.* 151, 244306. doi:10.1063/1.5134665

Kanno, M., Kono, H., and Fujimura, Y. (2006). Control of π-Electron Rotation in Chiral Aromatic Molecules by Nonhelical Laser Pulses. *Angew. Chem. Int. Ed.* 45, 7995–7998. doi:10.1002/anie.200602479

Kanno, M., Kono, H., Fujimura, Y., and Lin, S. H. (2010). Nonadiabatic Response Model of Laser-Induced Ultrafastπ-Electron Rotations in Chiral Aromatic Molecules. *Phys. Rev. Lett.* 104, 108302. doi:10.1103/physrevlett.104.108302

Kraus, P. M., Mignolet, B., Baykusheva, D., Rupenyan, A., Horný, L., Penka, E. F., et al. (2015). Measurement and Laser Control of Attosecond Charge Migration in Ionized Iodoacetylene. *Science* 350, 790–795. doi:10.1126/science.aab2160

Leforestier, C., Bisseling, R. H., Cerjan, C., Feit, M. D., Friesner, R., Guldberg, A., et al. (1991). A Comparison of Different Propagation Schemes for the Time Dependent Schrödinger Equation. *J. Comput. Phys.* 94, 59–80. doi:10.1016/0021-9991(91)90137-a

Li, H., Mignolet, B., Wachter, G., Skruszewicz, S., Zherebtsov, S., Süßmann, F., et al. (2015). Coherent Electronic Wave Packet Motion inC60Controlled by the Waveform and Polarization of Few-Cycle Laser Fields. *Phys. Rev. Lett.* 114, 123004. doi:10.1103/PhysRevLett.114.123004

Marcus, R. A. (1956). On the Theory of Oxidation-Reduction Reactions Involving Electron Transfer. I. *J. Chem. Phys.* 24, 966–978. doi:10.1063/1.1742723

May, V., and Kühn, O. (2011). *Charge and Energy Transfer Dynamics in Molecular Systems*, Third, Revised and Enlarged Edition. Wiley-VCH, Weinheim.

Mendive-Tapia, D., Vacher, M., Bearpark, M. J., and Robb, M. A. (2013). Coupled Electron-Nuclear Dynamics: Charge Migration and Charge Transfer Initiated Near a Conical Intersection. *J. Chem. Phys.* 139, 044110. doi:10.1063/1.4815914

Mineo, H., Lin, S. H., and Fujimura, Y. (2014). Vibrational Effects on UV/Vis Laser-Driven π-electron Ring Currents in Aromatic Ring Molecules. *Chem. Phys.* 442, 103–110. doi:10.1016/j.chemphys.2014.02.011

Mineo, H., Phan, N.-L., La, D.-K., and Fujimura, Y. (2021). Theoretical Study of Dynamic Stark-Induced π-Electron Rotations in Low-Symmetry Aromatic Ring Molecules beyond the Frozen Nuclear Approximation. *J. Phys. Chem. A.* 125, 1476–1489. doi:10.1021/acs.jpca.0c10216

Mineo, H., Yamaki, M., Teranishi, Y., Hayashi, M., Lin, S. H., and Fujimura, Y. (2012). Quantum Switching of π-Electron Rotations in a Nonplanar Chiral Molecule by Using Linearly Polarized UV Laser Pulses. *J. Am. Chem. Soc.* 134, 14279–14282. doi:10.1021/ja3047848

Remacle, F., and Levine, R. D. (1999). Charge Migration and Control of Site Selective Reactivity: The Role of Covalent and Ionic States. *J. Chem. Phys.* 110, 5089–5099. doi:10.1063/1.478406

Remacle, F., Levine, R. D., and Ratner, M. A. (1998). Charge Directed Reactivity:. *Chem. Phys. Lett.* 285, 25–33. doi:10.1016/S0009-2614(97)01314-6

Remacle, F., Nest, M., and Levine, R. D. (2007). Laser Steered Ultrafast Quantum Dynamics of Electrons in LiH. *Phys. Rev. Lett.* 99, 183902. doi:10.1103/PhysRevLett.99.183902

Ulusoy, I. S., and Nest, M. (2012). Remarks on the Validity of the Fixed Nuclei Approximation in Quantum Electron Dynamics. *J. Phys. Chem. A.* 116, 11107–11110. doi:10.1021/jp304140r

Weinkauf, R., Schanen, P., Metsala, A., Schlag, E. W., Bürgle, M., and Kessler, H. (1996). Highly Efficient Charge Transfer in Peptide Cations in the Gas Phase: Threshold Effects and Mechanism. *J. Phys. Chem.* 100, 18567–18585. doi:10.1021/jp960926m

Weinkauf, R., Schlag, E. W., Martinez, T. J., and Levine, R. D. (1997). Nonstationary Electronic States and Site-Selective Reactivity. *J. Phys. Chem. A.* 101, 7702–7710. doi:10.1021/jp9715742

Werner, H.-J., Knowles, P. J., Knizia, G., Manby, F. R., Schütz, M., Celani, P., et al. (2012). Molpro, Version 2012.1, a Package of Ab Initio Programs. Available at http://www.molpro.net (accessed Feb 18, 2016)

Wörner, H. J., Arrell, C. A., Banerji, N., Cannizzo, A., Chergui, M., Das, A. K., et al. (2017). Charge Migration and Charge Transfer in Molecular Systems. *Struct. Dyn.* 4, 061508. doi:10.1063/1.4996505

Yamaki, M., Mineo, H., Teranishi, Y., Lin, S. H., and Fujimura, Y. (2016). Quantum Control of Coherent ρρ-Electron Dynamics in Chiral Aromatic Molecules. *Jnl Chin. Chem. Soc* 63, 87–92. doi:10.1002/jccs.201500043

Yudin, G. L., Bandrauk, A. D., and Corkum, P. B. (2006). Chirped Attosecond Photoelectron Spectroscopy. *Phys. Rev. Lett.* 96, 063002. doi:10.1103/PhysRevLett.96.063002

Conflict of Interest: The authors declare that the research was conducted in the absence of any commercial or financial relationships that could be construed as a potential conflict of interest.

Frontiers in Chemistry

ORIGINAL RESEARCH
published: 05 April 2022
doi: 10.3389/fchem.2022.859095

Coherent Control of Molecular Dissociation by Selective Excitation of Nuclear Wave Packets

*Hugo A. López Peña, Jacob M. Shusterman, Derrick Ampadu Boateng, Ka Un Lao and Katharine Moore Tibbetts**

Department of Chemistry, Virginia Commonwealth University, Richmond, VA, United States

We report on pump-probe control schemes to manipulate fragmentation product yields in *p*-nitrotoluene (PNT) cation. Strong field ionization of PNT prepares the parent cation in the ground electronic state, with coherent vibrational excitation along two normal modes: the C–C–N–O torsional mode at 80 cm^{-1} and the in-plane ring-stretching mode at 650 cm^{-1}. Both vibrational wave packets are observed as oscillations in parent and fragment ion yields in the mass spectrum upon optical excitation. Excitation with 650 nm selectively fragments the PNT cation into $C_7H_7^+$, whereas excitation with 400 nm selectively produces $C_5H_5^+$ and $C_3H_3^+$. In both cases the ion yield oscillations result from torsional wave packet excitation, but 650 and 400 nm excitation produce oscillations with opposite phases. Ab initio calculations of the ground and excited electronic potential energy surfaces of PNT cation along the C–C–N–O dihedral angle reveal that 400 nm excitation accesses an allowed transition from D_0 to D_6 at 0° dihedral angle, whereas 650 nm excitation accesses a strongly allowed transition from D_0 to D_4 at a dihedral angle of 90°. This ability to access different electronic excited states at different locations along the potential energy surface accounts for the selective fragmentation observed with different probe wavelengths. The ring-stretching mode, only observed using 800 nm excitation, is attributed to a D_0 to D_2 transition at a geometry with 90° dihedral angle and elongated C–N bond length. Collectively, these results demonstrate that strong field ionization induces multimode coherent excitation and that the vibrational wave packets can be excited with specific photon energies at different points on their potential energy surfaces to induce selective fragmentation.

Keywords: coherent control, strong field ionization, mass spectrometry, pump-probe, nuclear wave packet

Edited by:
Andre Bandrauk,
Université de Sherbrooke, Canada

Reviewed by:
Riccardo Conte,
University of Milan, Italy
Chaoyuan Zhu,
National Chiao Tung University, Taiwan

****Correspondence:***
Katharine Moore Tibbetts
kmtibbetts@vcu.edu

Specialty section:
This article was submitted to Physical Chemistry and Chemical Physics,
a section of the journal Frontiers in Chemistry

Received: *20 January 2022*
Accepted: *18 March 2022*
Published: *05 April 2022*

Citation:
López Peña HA, Shusterman JM, Ampadu Boateng D, Lao KU and Tibbetts KM (2022) Coherent Control of Molecular Dissociation by Selective Excitation of Nuclear Wave Packets. Front. Chem. 10:859095. doi: 10.3389/fchem.2022.859095

1 INTRODUCTION

Chemists have sought to control molecular dissociation with lasers for decades. Tunable monochromatic laser light was believed to enable "bond-selective chemistry" through resonant energy absorption at the vibrational frequency of the targeted bond Bloembergen and Yablanovitch (1978). However, early attempts to control bond-cleavage by tuning the laser frequency failed due to rapid intramolecular vibrational energy redistribution (IVR) across coupled vibrational modes Bloembergen and Zewail (1984). Effective control of

---

Abbreviations: BBO, β-barium borate; DFT, density functional theory; EOM-EE-CCSD, equation-of-motion excitation-energies coupled cluster singles and doubles; OPA, optical parametric amplifier; PES, potential energy surface; PNT, *p*-nitrotoluene; TDDFT, time-dependent density functional theory; IVR, intramolecular vibrational energy redistribution.

unimolecular dissociation was only achieved with the development of high-intensity ultrashort pulsed lasers and coherent control techniques that operate on timescales faster than IVR.

Coherent control over molecular dissociation has primarily been achieved by the "closed-loop" scheme of optimally designing shaped laser pulses with automated learning algorithms, initially proposed by Judson and Rabitz (1992). Gerber and co-workers reported the first experimental implementation of closed-loop control over ionization and dissociation of $CpFe(CO)_2Cl$ (Cp = cyclopentadienyl) into $CpFeCOCl^+$ or $FeCl^+$ Assion et al. (1998). This success spurred the application of closed-loop control to selectively dissociate various molecules including halogenated alkanes Damrauer et al. (2002), Langhojer et al. (2005), Plenge et al. (2011), Moore Tibbetts et al. (2013) and acetones Langhojer et al. (2005), Cardoza et al. (2006). However, shaped pulse control fails to enhance specific dissociation pathways in certain molecules including *p*-nitrotoluene Lozovoy et al. (2008). Moreover, the "black box" nature of closed-loop control makes it difficult to fully understand the physical mechanisms by which an optimal pulse shape achieves product selectivity, even using additional specialized pulse shaping procedures Xing et al. (2017).

Understanding the physical mechanisms underlying coherent control of molecular dissociation can be achieved using two-pulse "pump-probe" excitation schemes Tannor and Rice (1985), Zewail (1988). Pump-probe measurements with complementary quantum chemical calculations of the relevant electronic potential energy surfaces (PESs) have revealed bond-cleavage mechanisms facilitated by coherent vibrational motions in numerous organic cations Moore Tibbetts (2019). For instance, coherent excitation of the I–C–Br bending mode in CH_2IBr^+ upon strong-field ionization facilitates dissociation into CH_2Br^+ upon excitation of the $D_0 \rightarrow D_3$ transition at a specific point on the D_0 PES Nichols et al. (2009). Similarly, coherent vibrational motions along the phenyl–substituent torsional coordinate in the molecular cations of acetophenone Bohinski et al. (2014), Tibbetts et al. (2015) and nitrobenzene López Peña et al. (2021) facilitate CH_3 and NO_2 loss, respectively, upon excitation of the vibrational wave packet at 90° phenyl–substituent dihedral angle. Although pump-probe measurements advance understanding of molecular dissociation facilitated by coherent vibrational dynamics, they enable only limited control over relative fragment yields because the probe wavelength typically excites resonantly to a single electronic excited state. As a result, one preferential fragment or a specific distribution of fragments is usually observed.

In this work, we demonstrate selective coherent excitation to three different electronic excited states from ground-state *p*-nitrotoluene (PNT) cation using probe pulses at 800, 650, and 400 nm. This selective excitation results in different relative yields of the $C_7H_7^+$, $C_5H_5^+$, and $C_3H_3^+$ fragment ions depending on the probe wavelength. Strong field adiabatic ionization prepares a superposition of two vibrational wave packets in the D_0 PES of PNT cation: the first along the C–C–N–O torsional coordinate identified in earlier work Ampadu Boateng et al. (2018) and the second along the in-plane phenyl ring-stretching mode that includes C–N bond stretching. The torsional wave packet can be selectively excited to D_4 at a C–C–N–O dihedral angle of 90° with 650 nm photons to produce primarily $C_7H_7^+$, or to D_6 at a 0° dihedral angle with 400 nm photons to produce $C_5H_5^+$ and $C_3H_3^+$. The ring-stretching wave packet can be selectively excited to D_2 at a geometry with slightly elongated C–N bond length and 90° dihedral angle using 800 nm photons, producing exclusively $C_7H_7^+$. These results indicate that careful choice of excitation wavelengths in two-pulse schemes can effectively control dissociation pathways in a complex organic molecule.

2 MATERIALS AND METHODS

2.1 Experiments

Portions of the experimental setup have been described in our previous works Ampadu Boateng et al. (2018), Ampadu Boateng et al. (2019a). Briefly, a commercial Ti:sapphire regenerative amplifier (Astrella, Coherent, Inc.) producing 30 fs, 800 nm, 2.2 mJ pulses was used to pump an optical parametric amplifier (OPA, TOPAS Prime) to produce sub-20 fs 1,300 nm or 1,500 nm pump pulses. The pump wavelength was 1,300 nm for measurements with the 400 and 650 nm probes, whereas the pump wavelength was 1,500 nm for measurements with the 800 nm probe for reasons that will be discussed in the Results section. The 650 nm probe pulse was obtained from OPA output split with a 50:50 (r:t) beam splitter and frequency doubled with a β-barium borate (BBO) crystal. The 800 nm probe pulse was obtained from the transmitted portion of the incident laser beam from a 90:10 (r:t) beam splitter prior to the OPA and down-collimated using a reflective telescope with reduction factor 2. The 400 nm probe pulse was obtained by down-collimating the 800 nm beam with a telescope with reduction factor 3.33 comprised of a plano-convex lens (f = 250 mm) and a plano-concave lens (f = –75 mm) placed on a linear translation stage, followed by frequency doubling with a BBO crystal. The transmissive telescope geometry was necessary to allow for fine adjustment of the focal spot of the 400 nm probe beam to overlap with the focal spot of the 1,300 nm pump beam when both are focused with the same plano-convex lens (f = 200 mm). Both the 800 and 650 nm probe pulses have duration of ~25 fs as measured by frequency-resolved optical gating Ampadu Boateng et al. (2018), Ampadu Boateng et al. (2019a). The 400 nm probe pulse duration was estimated at 70 fs as measured by the cross-correlation of the O_2 signal from air in the mass spectrometer with 1,300 nm pump/400 nm probe excitation (**Supplementary Figure S1**). PNT (Sigma Aldrich, 99%) was introduced into the time-of-flight mass spectrometer (Jordan TOF) *via* an effusive inlet under gentle heating. Pump-probe measurements were taken over the delay range of –500 fs (probe before pump) to +2,500 fs (pump before probe) in steps of 5 fs for the 800 nm probe and 10 fs otherwise. Mass spectra were recorded at each pump-probe delay and averaged over 1,000 laser shots with a 1 GHz digital oscilloscope (LeCroy WaveRunner 610Zi).

2.2 Computations

Density functional theory (DFT) calculations were conducted using Gaussian 16 software Frisch et al. (2016) employing the restricted Kohn-Sham formalism for neutral species and the unrestricted formalism for cationic species. A previous work on PNT from our group Ampadu Boateng et al. (2018a) has identified the hybrid

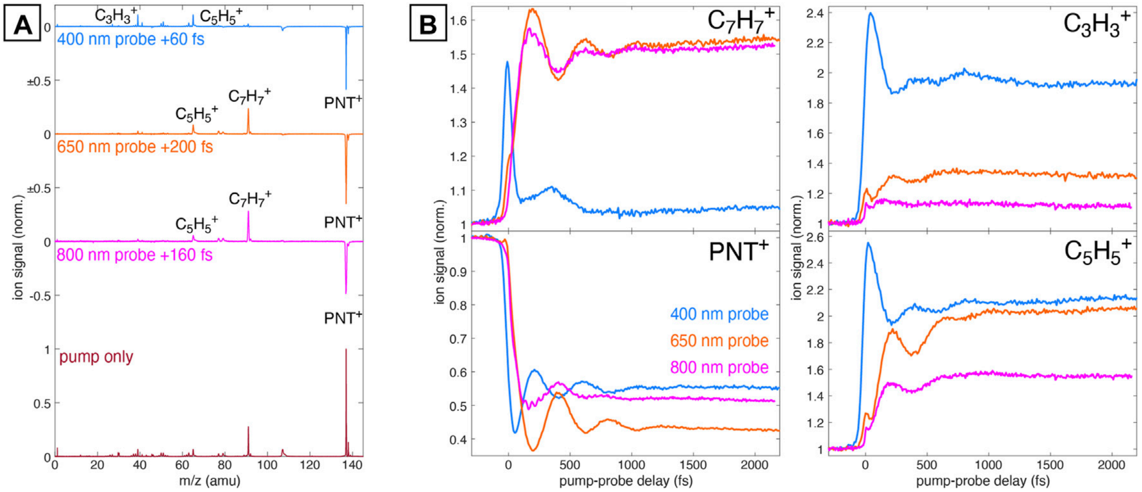

FIGURE 1 | (A) Mass spectrum of PNT$^+$ taken with 1,300 nm pump only (dark red) and the difference spectra relative to the pump-only spectrum taken with 800 nm (magenta), 650 nm (orange), and 400 nm (blue) probe pulses at the indicated delays. **(B)** Transient ion signals for PNT$^+$, $C_7H_7^+$, $C_5H_5^+$, and $C_3H_3^+$ taken at each probe wavelength. Each signal is normalized to its yield at negative pump-probe delay.

generalized gradient approximation (GGA) B3LYP functional Becke (1993), Stephens et al. (1994) in combination with the def2-TZVPP Weigend and Ahlrichs (2005) basis set as an adequate level of theory to describe this molecular system. Both the neutral and cation geometries of PNT were optimized within this level of theory. The convergence threshold for total energy was set to 10^{-8} eV while the force threshold was set to 10^{-3} eV/Å. Each geometric optimization was followed by harmonic frequency computations in order to confirm the stationary character of the state obtained.

To determine the excited-state energies of the PNT cation at different geometries, we performed single-point time-dependent DFT (TDDFT) Bauernschmitt and Ahlrichs (1996) calculations using Gaussian 16. For each cation geometry, we calculated the first 10 doublet-doublet transitions at the B3LYP/def2-TZVPP level of theory. In **section 3.2** we will present TDDFT excited-state calculations for PNT radical cation at the B3LYP/def2-TZVPP level but those calculations will be further supported with selected calculations at the equation-of-motion excitation-energies coupled-cluster singles and doubles (EOM-EE-CCSD) Krylov, (2008) level. Due to the high computational cost of EOM methods, we employ the smaller 6–311+G* basis set. These EOM calculations were performed using Q-Chem 5.3 Epifanovsky et al. (2021). It is important to clarify that both TDDFT and EOM calculations on the cation are done under field-free conditions, i.e., after the strong-field pump pulse is over (see further discussion on **Section 3.1**).

3 RESULTS

3.1 Pump-Probe Measurements

Pump-probe measurements were conducted with pump intensity of 6×10^{13} W cm^{-2}. **Figure 1A** shows the mass spectra of PNT$^+$ taken with only the 1,300 nm pump pulse (bottom) and with pump-probe excitation using 6×10^{12} W cm^{-2} probe pulses at 800, 650, and 400 nm (top). The pump-only spectrum is dominated by the intact PNT$^+$ cation at *m*/*z* 137, with minor contribution from the $C_7H_7^+$ fragment at *m*/*z* 91. The greatest depletion in PNT$^+$ signal was observed at pump-probe delays of +160 fs for 800 nm probe, +200 fs for 650 nm probe, and +60 fs for 400 nm probe. As seen in **Figure 1A**, a substantial depletion in PNT$^+$ signal and concomitant rise in fragment ion signals occurs at the selected pump-probe delay for each probe wavelength. Whereas both the 800 and 650 nm probe wavelengths primarily enhance the yield of $C_7H_7^+$ and to a lesser extent $C_5H_5^+$ (*m*/*z* 65), the 400 nm probe enhances only $C_5H_5^+$ and $C_3H_3^+$ (*m*/*z* 39). This change in fragmentation pattern with different probe wavelengths indicates that selective fragmentation is possible using pump-probe excitation.

Figure 1B displays the transient ion signals of the PNT$^+$, $C_7H_7^+$, $C_5H_5^+$, and $C_3H_3^+$ fragments as a function of pump-probe delay using 800 nm (magenta), 650 nm (orange), and 400 nm (blue) probe wavelengths. Each ion signal is normalized to its respective yield at negative pump-probe delay. The large-amplitude oscillations in the PNT$^+$ and fragment ion signals with period 420 fs arise from the vibrational wave packet along the C–C–N–O torsional coordinate in PNT$^+$, which we previously reported from pump-probe measurements with only 800 nm probe wavelength Ampadu Boateng et al. (2018a). The present results show that the 650 nm probe wavelength produces larger-amplitude oscillations in PNT$^+$ with the same phase, which indicates that 650 nm more effectively excites the PNT$^+$ torsional wave packet than 800 nm. In contrast, the PNT$^+$ oscillations with the 400 nm probe have the opposite phase, which indicates 400 nm probe selectively excites the PNT$^+$ torsional wave packet at a different location on the PES along the torsional coordinate than the lower-energy probe wavelengths. Finally, additional low-amplitude fast oscillations with a period of ~55 fs are observed in the PNT$^+$ and $C_7H_7^+$ signals only for the 800 nm probe. These oscillations were best resolved using a 1,500 nm pump wavelength (shown in

TABLE 1 | Curve fitting coefficients for coherent dynamics of ion signals: oscillation amplitude (a), coherent lifetime (T_1), oscillation period (t), and phase (ϕ).

λ_{probe} (nm)	Ion	a	T_1 (fs)	t (fs)	ϕ (rad)
400	PNT^+	0.10 ± 0.01	345 ± 33	410 ± 7	3.1 ± 0.1
—	$C_5H_5^+$	0.03 ± 0.01	370 ± 120	421 ± 20	0.3 ± 0.3
650	PNT^+	0.25 ± 0.01	308 ± 15	425 ± 4	0.05 ± 0.04
—	$C_7H_7^+$	0.15 ± 0.01	290 ± 12	417 ± 3	3.1 ± 0.03
—	$C_5H_5^+$	0.09 ± 0.01	252 ± 17	438 ± 9	3.3 ± 0.1
800	PNT^+	0.15 ± 0.02	210 ± 16	464 ± 11	0.45 ± 0.07
—	$C_7H_7^+$	0.13 ± 0.01	212 ± 12	438 ± 7	3.3 ± 0.1

Figure 1B), although they are also visible using a 1,300 nm pump wavelength (**Supplementary Figure S2**).

To further interpret the oscillatory dynamics, transient ion signals as a function of pump-probe delay, τ, were fit to the equation

$$S(\tau) = ae^{-\tau/T_1}\cos\left(\frac{2\pi}{t}\tau + \phi\right) + be^{-\tau/T_2} + c \tag{1}$$

where a and b are amplitude coefficients, t is the oscillation period, T_1 is the coherence lifetime, T_2 is a second lifetime not associated with oscillations, and c is the ion yield as $\tau \to \infty$. Each transient signal at $\tau \geq 70$ fs (i.e., after the pump pulse is over so the instrument response function can be ignored) was fit to **Eq. 1** using nonlinear least-squares curve fitting in MATLAB. A full description of the extracted coefficients can be found in the Supplementary Material, **Supplementary Figure S3** and **Supplementary Tables S1–S3**. Although the strong-field pump pulse can populate multiple electronic states of the cation, it is reasonable to assume that, when the probe beam arrives after a delay ≥ 70 fs, it will find the cation in the ground electronic state after electronic relaxation. The validity of this assertion can be supported with the work of Kraus and coworkers Kraus et al. (2015), in which charge migration processes leading to relaxation of the electronic wave packet in iodoacetylene occur within 5 fs, well below the initial measurement of dynamics at 70 fs delay used for our analysis. The fit coefficients corresponding to the oscillatory dynamics shown in **Table 1** confirm both that each fragment ion oscillates π radians out of phase with respect to PNT^+ and that the phase of the PNT^+ signal shifts from approximately 0 radians for 650 nm excitation to π radians for 400 nm excitation. The oscillation period is ~420 fs for both 650 and 400 nm probes, whereas the somewhat longer ~460 fs oscillation period using the 800 nm probe arises from a poorer fit quality (**Supplementary Figure S3**).

Subtraction of the incoherent dynamics (second and third terms in **Eq. 1**) allows for clearer visualization of the oscillatory dynamics and frequency analysis via fast Fourier Transform (FFT). **Figure 2A** displays the coherent transient ion dynamics of PNT^+ and oscillatory fragment ions for each probe wavelength. A clear π phase shift in the PNT^+ signals (red) between the 400 nm probe and 650 nm or 800 nm probes is visible, as indicated by the dotted lines at 200, 620, and 1,040 fs. **Figure 2B** displays the FFT amplitude of the signals shown in **Figure 2A**. For all probe wavelengths the FFT spectra exhibit a strong peak at 80 cm^{-1} assigned to the previously reported C–N–N–O torsional mode of PNT^+ Ampadu Boateng et al. (2018). A closer inspection of the oscillations using the 800 nm probe (bottom panel of **Figure 2A**) reveals what seems to be the superposition of two coherent oscillations: one corresponding to the torsional mode already discussed and smaller amplitude oscillations corresponding to a faster vibrational mode. In line with these observations is the presence of two frequencies, at 80 and 650 cm^{-1}, in the FFT of the 800 nm probe signal (bottom panel of **Figure 2B**). Additionally, it is worth noting that the superposition of vibrational modes is more evident around the first minimum of the oscillatory ion signal in PNT^+. This fact will be further discussed in **Section 3.3** with the aid of computational results.

In order to motivate forthcoming computational results, we present the optimized structures of neutral and cationic PNT at the B3LYP/def2-TZVPP level of theory in **Figure 3**. The corresponding coordinates are available within the Supplementary Material (**Supplementary Tables S4, S5**). Relevant to this work are the following changes after electron detachment: the C–C–N–O dihedral angle goes from 0.1 to 52.7° and a moderate distortion of the ring occurs. Additionally, the frequencies and corresponding intensities of the normal modes for PNT^+ are presented in the Supplementary Material (**Supplementary Table S6**). A careful analysis of these vibrational modes shows that the C–C–N–O torsional mode has a calculated frequency of 58.96 cm^{-1}, in reasonable agreement with the experimental frequency of 80 cm^{-1} (**Figure 2B**). **Figure 3B** shows the 12th normal mode calculated for the PNT cation. The relevance of this ring-stretching mode will be further discussed in **Section 3.3**. At this moment, it is enough to say that the calculated frequency of 604.32 cm^{-1} fairly matches the experimental frequency of 650 cm^{-1} shown in **Figure 2B** for the 800 nm probe.

3.2 Coherent Control of Torsional Wave Packet Excitation

As mentioned in the previous section, a former work from our group has assigned the main coherent oscillations of PNT^+ to a torsional wave packet involving the C–C–N–O dihedral angle Ampadu Boateng et al. (2018). In order to explain the observation of different fragment distributions and ion yield dynamics depending on the wavelength of the probe beam, we used the following approach: starting from the optimized cation geometry with a C–C–N–O dihedral angle of 52.7° we performed a relaxed scan of this torsional mode using the ModRedundant keyword in Gaussian 16. This procedure generated a collection of geometries that span all the torsional mode, which were used to perform single-point TDDFT calculations. The resulting potential energy surfaces (PESs) can be seen in **Figure 4A**. In line with previous findings on the closely related nitrobenzene cation López Peña et al. (2021), we found that the PESs can be classified into two groups: the first one comprising from D_1 to D_4 with all the surfaces showing a marked dependence on the dihedral angle, and a second group comprising from D_5 to D_7 with a less marked dependence on the dihedral angle. The influence of the dihedral angle on the excitation probability, quantified by means of a harmonic estimate of the oscillator strength, can be observed in **Figure 4B**. It is noteworthy that the oscillator strength for the $D_0 \rightarrow D_4$ transition (f_{04}) is particularly high

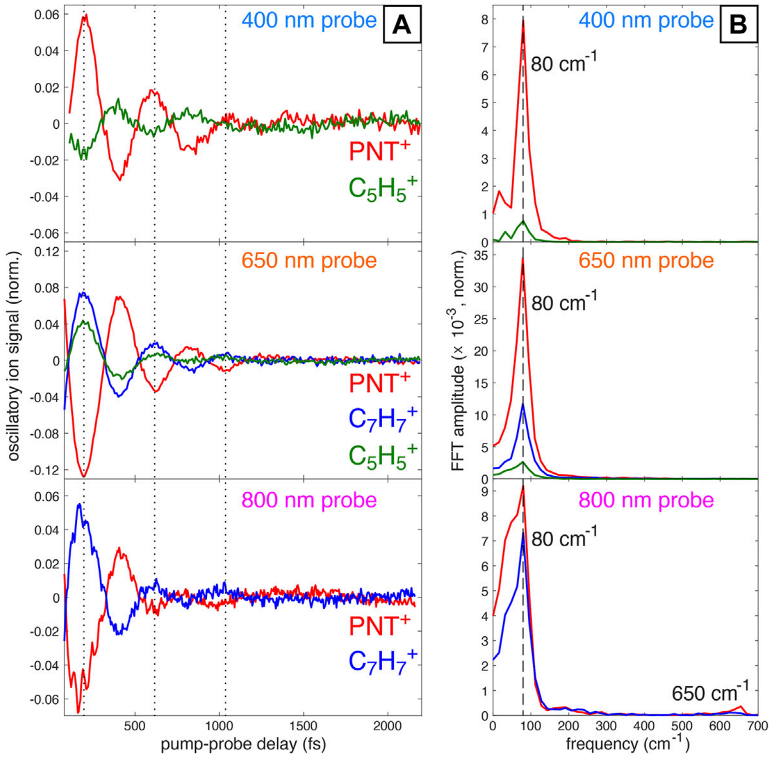

FIGURE 2 | (A) Oscillatory ion signals for PNT^+ and selected fragment ions obtained by subtracting off the incoherent contributions to signal fitting *via* **Eq. 1**. **(B)** FFT amplitudes obtained from the signals in **(A)** with indicated frequencies at 80 cm^{-1} and 650 cm^{-1} (for 800 nm probe).

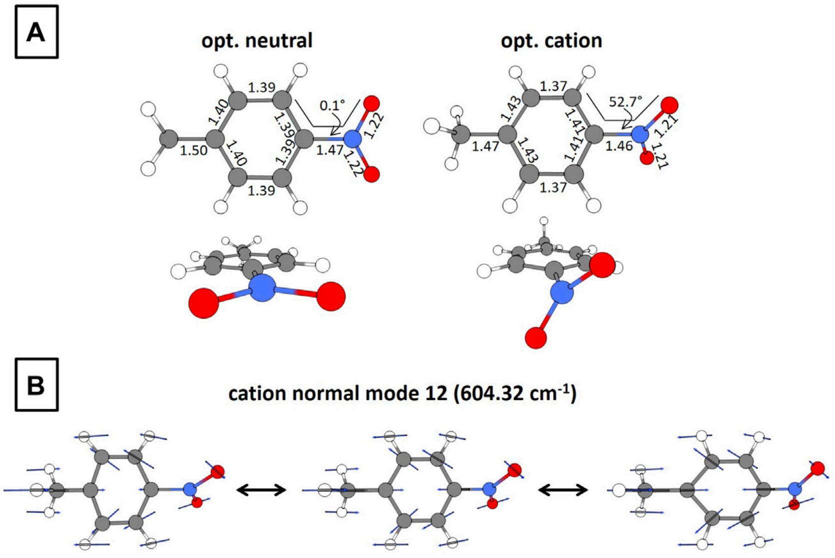

FIGURE 3 | (A) Geometrical structures for optimized neutral and cationic PNT. Bond lengths are in Å and torsional angles in degrees. **(B)** Normal mode at 604.32 cm^{-1} for the optimized PNT cation. The calculations were performed at the B3LYP/def2-TZVPP level of theory.

and dependent on the geometry, reaching its maximum value at 90°. Moreover, this transition is the only one that has a substantial oscillator strength at 90°. Also notable is the parabolic shape of f_{06} centered at 90° dihedral angle. As a consequence, there is higher probability for the $D_0 \rightarrow D_6$ transition at geometries where PNT^+ is nearly planar, i.e., near the neutral PNT geometry. **Figure 4A** also

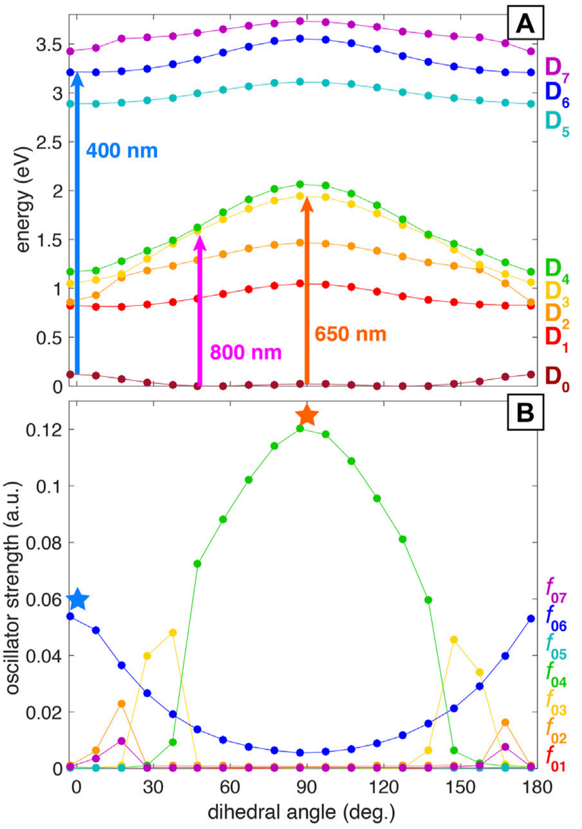

FIGURE 4 | Computed potential energy surfaces **(A)** and oscillator strengths **(B)** for PNT$^+$ along the C–C–N–O dihedral angle.

shows the energies corresponding to 400, 650, and 800 nm photons for comparison (3.1, 1.91, and 1.55 eV respectively). A careful evaluation of all the information contained in **Figure 4** as a whole reveals that the 400 nm probe can selectively access an allowed transition from D_0 to D_6 at dihedral angles close to 0°, whereas the 650 nm probe can selectively access a strongly allowed transition from D_0 to D_4 at a dihedral angle of 90°. This ability to access different electronic excited states at different locations along the potential energy surface accounts for the selective fragmentation observed with different probe wavelengths at different time delays. Additionally, the 800 nm probe should be capable of promoting the $D_0 \rightarrow D_n$, $n = 1, 2$ transitions at any dihedral angle.

In order to support our TDDFT calculations we also performed single-point computations at three selected geometries calculated at the B3LYP/def2-TZVPP level using the EOM-EE-CCSD method. The geometries considered were the optimized neutral and cationic species (**Figure 3A**; **Supplementary Tables S4, S5**) and the geometry with a dihedral angle of 87.4° obtained by means of the relaxed scan previously described (**Supplementary Table S7**). **Table 2** shows the excitation energies and harmonic estimates of oscillator strengths calculated at both levels of theory for PNT cation with a C–C–N–O dihedral angle of 87.4°. These methodologies produced qualitatively similar results but there are some differences that are worth noting: EOM calculations introduce a larger energetic gap between D_1 and D_2 states of ~1.2 eV. Consequently, states D_2, D_3, and D_4 from EOM computations are shifted upwards when compared with TDDFT results. Also, according to the oscillator strength values, EOM method points towards D_3 as the bright state while TDDFT locates the D_4 state as the bright one. Despite this disagreement in the ordering of states, the relevant fact is that both methodologies confirm the presence of an excited state with substantial oscillator strength at 90° dihedral angle and with excitation energy around 2 eV. Possible sources for the disagreement between both levels of theory will be briefly discussed on **Section 4**. **Supplementary Tables S8, S9** of Supplementary Material show analogous comparisons between the two methodologies for PNT$^+$ at the optimized neutral and cation geometries respectively.

3.3 Assignment of 650 cm^{-1} Wave Packet

In **Section 3.1** we showed experimental evidence of the superposition of two vibrational wave packets and identified the associated frequencies as 80 and 650 cm^{-1}. The 80 cm^{-1} has previously been assigned to the C–C–N–O torsional mode but the identity of the vibrational mode associated with the 650 cm^{-1} frequency remains to be fully elucidated. The match between the experimental frequency of 650 cm^{-1} (**Figure 2B**) and the computationally calculated frequency of 604.32 cm^{-1} (**Figure 3B** and **Supplementary Table S6**) lays the foundation for the hypothesis that this ring-stretching mode is the one supporting the additional nuclear wave packet found in this work.

In order to test this hypothesis we simulated the superposition of the two vibrational modes by considering three geometries within the torsional mode with 0.1, 52.7, and 87.4 C–C–N–O dihedral angles. Then, from these three geometries we performed frequency calculations to identify the ring-stretching mode in each case. The geometry with 0.1° torsional angle corresponds to the vertical cation, i.e., the cation under the optimized neutral geometry, while the structure with 52.7° dihedral angle corresponds to the optimized cation with a ring-stretching mode at 604.32 cm^{-1} (**Supplementary Table S6**). Having identified the ring-stretching modes for each of the three geometries we made the additional hypothesis that the $D_0 \rightarrow D_2$ transition is the one allowing the observation of the ring-stretching wave packet. This hypothesis is supported by our TDDFT calculations showing that 800 nm is nearly resonant

TABLE 2 | Excitation energies (EE) and oscillator strengths (*f*) for PNT$^+$ with a C–C–N–O dihedral angle of 87.4° at the B3LYP/def2-TZVPP and EOM-EE-CCSD/6-311+G* levels of theory.

	B3LYP/ def2-TZVPP		EOM-EE-CCSD/ 6–311 + G*	
Transition	EE (eV)	*f* (a.u.)	EE (eV)	*f* (a.u.)
$D_0 \rightarrow D_1$	1.02	0.0000	1.12	0.000049
$D_0 \rightarrow D_2$	1.44	0.0007	2.35	0.000654
$D_0 \rightarrow D_3$	1.92	0.0000	2.59	0.132253
$D_0 \rightarrow D_4$	2.04	0.1201	2.87	0.000112
$D_0 \rightarrow D_5$	3.09	0.0001	3.49	0.000003
$D_0 \rightarrow D_6$	3.53	0.0055	3.56	0.000051
$D_0 \rightarrow D_7$	3.71	0.0004	3.84	0.001330

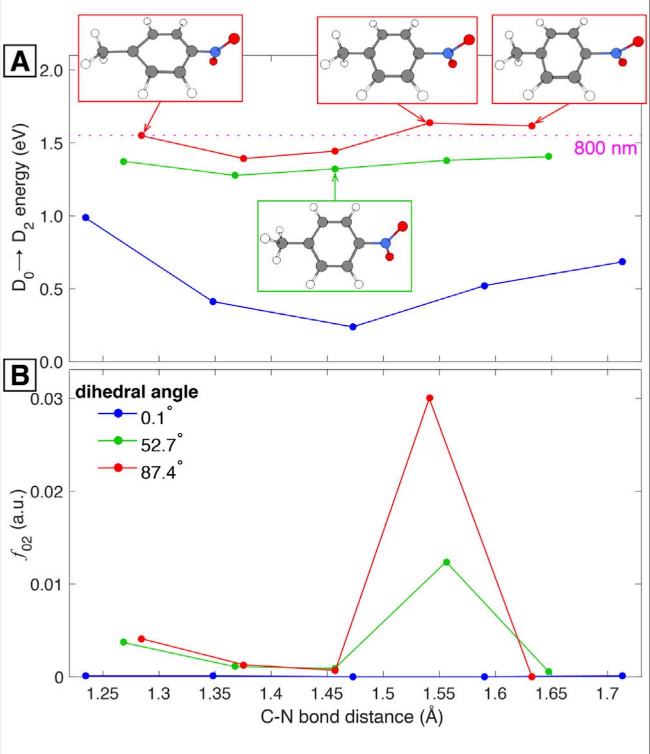

FIGURE 5 | Computed potential energy surfaces **(A)** and oscillator strengths **(B)** for PNT^+ along C–N bond distance under different C–C–N–O dihedral angles.

with the $D_0 \rightarrow D_2$ transition at any dihedral angle (**Figure 4A**) and by the experimental fact that the superposition of vibrational wave packets is only observable with 800 nm excitation. With these ideas in mind we took five "snapshots" within each of the three ring-stretching modes and retrieve the corresponding geometries. Those 15 geometries, five per each ring-stretching mode, served as the basis for single-point TDDFT calculations to obtain the $D_0 \rightarrow D_2$ excitation energies and the corresponding harmonic estimates for the oscillator strengths.

The results of these calculations are shown in **Figure 5**. It is important to offer some clarification regarding the abscissa axis of this figure: since the ring-stretching mode involves the collective motion of many atoms as can be seen in **Figure 3B**, the description of the mode in terms of a single parameter is not an easy task. Due to this complication we show the C–N bond distance as a signature of the mode, but it should be kept in mind that the abscissa axis represents the whole ring-stretching mode, as highlighted in the structures shown in **Figure 5**. This being said, **Figure 5A** shows the excitation energy for the $D_0 \rightarrow D_2$ transition as a function of the C–N bond distance for three different torsional geometries with 0.1, 52.7, and 87.4 dihedral angles. The figure also shows that 800 nm (1.55 eV) provides enough energy to promote the $D_0 \rightarrow D_2$ transition for all the C–N bond lengths under all torsional geometries. Additionally, 800 nm is nearly resonant with the excitation energy corresponding to the torsional geometry of 87.4° at all C–N bond distances. This last observation might explain why the superposition of vibrational modes is more evident around the first minimum of PNT^+ and the first maximum of $C_7H_7^+$ oscillatory ion signals (bottom panel of **Figure 2A**). The reasons behind the association of the minimum in the oscillatory ion signal of PNT^+ with a dihedral angle ~90° are two-fold: first, our TDDFT calculations show that there is a strong probability of a $D_0 \rightarrow D_4$ transition as the dihedral angle approaches 90° (**Figure 4**). While it is true that 800 nm excitation is not capable of promoting the $D_0 \rightarrow D_4$ at all dihedral angles it is also true that it can promote such transition at different torsional angles. The second reason is motivated by a previous work from our group regarding an analogous torsional wave packet within nitrobenzene cation, a cation closely related to PNT^+. In that work we estimated the time taken for the wave packet to reach a 90° dihedral angle as approximately 200 fs by means of classical wave packet trajectory calculations and pump-probe measurements. This finding is consistent with the maximum depletion of PNT^+ at 160 fs pump-probe delay with 800 nm excitation (the maximum depletion with 650 nm excitation occurs at a delay of 200 fs). **Figure 5B** shows the oscillator strength for the $D_0 \rightarrow D_2$ transition (f_{02}) as a function of the C–N bond under the same torsional geometries as panel A. Here we can observe a sharp increase in f_{02} at an elongated C–N bond lenth of 1.54 Å (the equilibrium bond length is 1.46 Å for the optimized cation, **Figure 3A**). This increase is very large for the geometry with 87.4° dihedral angle but it is also visible, although to a lesser extent, for the geometry with dihedral angle of 52.7°. All this facts as a whole strengthen the assignment of the additional wave packet found in this work to the ring-stretching vibrational mode.

4 DISCUSSION

This study represents the first demonstration of selective excitation to different electronic excited states upon coherent vibrational motion in a large organic cation. The motion of the two nuclear wave packets in PNT^+ produces three distinct transient electronic transitions amenable to optical excitation: 1) $D_0 \rightarrow D_6$ transition with energy 3.1 eV at C–C–N–O dihedral angle of 0°, 2) $D_0 \rightarrow D_4$ (or D_3) transition with energy 2.0 eV at a 90° dihedral angle, and 3) $D_0 \rightarrow D_2$ transition with energy 1.6 eV at 90° dihedral angle with elongated C–N bond length of 1.54 Å. The electronic structure of PNT^+ along both the torsional and ring-stretching coordinates enables selective excitation to different excited states at specific geometries. The electronic structure was mainly explored by means of TDDFT calculations and further supported at the EOM-CCSD level. The upwards energetic shift observed for the D_2, D_3, and D_4 states at the EOM level when compared with TDDFT results can be rationalized by the small 6–311+G* basis set being used for EOM computations (in contrast with the def2-TZVPP basis set for TDDFT calculations). Different groups had found that, as the basis set is expanded by adding diffuse and polarization functions, the excitation energies computed at the EOM-CCSD level decrease Cristian and Krylov (2003), Laurent et al. (2015). Therefore, a closer match between the excitation energies predicted by both levels of theory would be expected if a bigger basis set is employed for EOM calculations. Additionally, the discrepancy in which

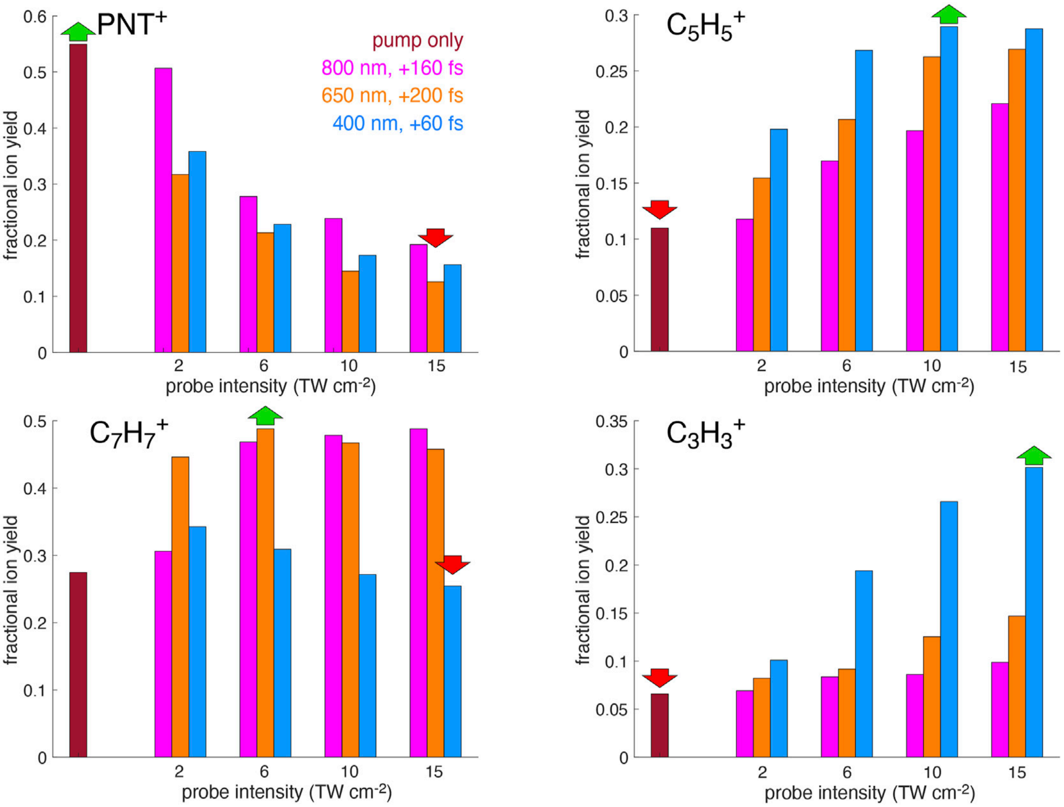

FIGURE 6 | Fractional yields of PNT^+, $C_7H_7{}^+$, $C_5H_5{}^+$, and $C_3H_3{}^+$ from **Eq. 2** obtained using 800 nm, 650 nm, and 400 nm probe wavelengths at intensities from 2–15 TW cm^{-2}.

EOM identifies D_3 as the bright state while TDDFT points to D_4 has been previously observed for various systems Grimme and Parac (2003), Lopata et al. (2011), Prlj et al. (2015), Prlj et al. (2016), Acharya et al. (2018), López Peña et al. (2021) Nevertheless, both levels of theory confirm the presence of an excited state with substantial oscillator strength at 90° dihedral angle and with excitation energy around 2 eV. Overall, we conclude that the computationally inexpensive TDDFT level of theory is adequate enough for aiding and rationalizing the design of pump-probe control schemes.

The finding that 400 nm excitation of PNT^+ selectively produces $C_5H_5{}^+$ and $C_3H_3{}^+$, whereas 650 nm or 800 nm excitation produces $C_7H_7{}^+$ (**Figure 1**) indicates that population of the higher-energy D_6 state causes more extensive fragmentation than population of the lower D_2–D_4 states. This finding is consistent with the reported higher dissociation energy of $C_5H_5{}^+$ and its formation by further dissociation of $C_7H_7{}^+$ Zhang et al. (2012). We can quantify the selectivity to $C_7H_7{}^+$, $C_5H_5{}^+$, or $C_3H_3{}^+$ formation by examining the fractional yield of a specific target ion relative to the sum of the ion yields,

$$Y = \frac{\text{target ion}}{PNT^+ + C_7H_7{}^+ + C_5H_5{}^+ + C_3H_3{}^+} \qquad (2)$$

for each probe wavelength at the pump-probe delay producing the greatest PNT^+ signal depletion identified in **Figure 1**. The fractional yields for each ion at a series of probe intensities from 2 to 15 TW cm^{-2} are shown in **Figure 6**. Although greater enhancement of fragment ion yields is observed at higher probe intensities, 15 TW cm^{-2} represents a practical upper limit because at higher intensity the probe pulse creates ions even in the absence of the pump pulse. Examination of **Figure 6** shows that $C_7H_7{}^+$ is selectively enhanced using 650 and 800 nm, whereas $C_3H_3{}^+$ is selectively enhanced using 400 nm. Hence, we can conclude that population of D_2–D_4 selectively produces $C_7H_7{}^+$ whereas population of D_6 selectively produces $C_3H_3{}^+$. Although the $C_5H_5{}^+$ yield is most enhanced by 400 nm excitation, its weaker dependence on the probe wavelength suggests that it can be formed by excitation to any of the excited states and is therefore less amenable to selective enhancement with pump-probe control. Overall, pump-probe excitation is found to enable a similar degree of control over the $C_7H_7{}^+/C_3H_3{}^+$ ion ratios as attained using shaped 800 nm pulses Lozovoy et al. (2008): the maximum $C_7H_7{}^+/C_3H_3{}^+$ ratio of 5.6 attained with 800 nm, 5 TW cm^{-2} probe pulses is 40% higher than the maximum ratio of ~4 obtained with transform-limited 800 nm pulses, although the minimum ratio of 0.8 attained with 400 nm, 15 TW cm^{-2} is somewhat higher than the minimum ratio of ~0.2 reported with pulse shaping.

Finally, the observation that strong field ionization of PNT launches nuclear wave packets along two distinct vibrational modes is of particular interest. Numerous previous pump-probe studies of other substituted benzenes including nitrobenzene López Peña et al. (2021), *o*-nitrotoluene Ampadu Boateng et al. (2019a), azobenzene Munkerup et al. (2017) and alkyl phenyl ketones Konar et al. (2014), Bohinski et al. (2014), Tibbetts et al. (2015) have observed only torsional wave packet motion upon strong-field ionization. To the best of our knowledge, the only previous study to definitively observe multimode coherent vibrational motion in a cation prepared by strong field ionization found a superposition of the C–I stretch and I–CH_3 umbrella modes in CH_3I^+ Wei et al. (2017). Although in a previous work we had proposed multimode coherent excitation in diisopropyl methylphosphonate ion to explain observed ion yield oscillations at two different frequencies Ampadu Boateng et al. (2019b), no PES calculations were performed to confirm distinct excitation pathways. Hence, we recommend the combined strategy of pump-probe measurements with multiple probe wavelength and PES computations along possible coherently excited coordinates as performed in this work to identify possible multimode coherent excitation in other organic cations prepared by strong-field ionization.

DATA AVAILABILITY STATEMENT

The original contributions presented in the study are included in the article/**Supplementary Material**, further inquiries can be directed to the corresponding author.

AUTHOR CONTRIBUTIONS

KT designed and directed the research. HL, JS, and DA conducted the experiments. HL performed the calculations with input from KL. KL contributed calculation codes. HL, JS, and KT analyzed the data and wrote the manuscript with input from all authors.

FUNDING

This work was supported by the U.S. Army Research Office through Contract W911NF-19-1-0099. DA and HL acknowledge generous financial support from Altria Graduate Research Fellowships.

ACKNOWLEDGMENTS

High Performance Computing resources provided by the High Performance Research Computing (HPRC) Core Facility at Virginia Commonwealth University (https://chipc.vcu.edu) were used for conducting portions of the research reported in this work.

SUPPLEMENTARY MATERIAL

The Supplementary Material for this article can be found online at: https://www.frontiersin.org/articles/10.3389/fchem.2022.859095/full#supplementary-material

REFERENCES

Acharya, A., Chaudhuri, S., and Batista, V. S. (2018). Can Tddft Describe Excited Electronic States of Naphthol Photoacids? a Closer Look with EOM-CCSD. *J. Chem. Theor. Comput.* 14, 867–876. doi:10.1021/acs.jctc.7b01101

Ampadu Boateng, D., Gutsev, G. L., Jena, P., and Tibbetts, K. M. (2018). Dissociation Dynamics of 3- and 4-nitrotoluene Radical Cations: Coherently Driven C-NO_2 bond Homolysis. *J. Chem. Phys.* 148, 134305. doi:10.1063/1.5024892

Ampadu Boateng, D., Word, M. K. D., Gutsev, L. G., Jena, P., and Tibbetts, K. M. (2019a). Conserved Vibrational Coherence in the Ultrafast Rearrangement of 2-nitrotoluene Radical Cation. *J. Phys. Chem. A.* 123, 1140–1152. doi:10.1021/acs.jpca.8b11723

Ampadu Boateng, D., Word, M. K., and Tibbetts, K. (2019b). Probing Coherent Vibrations of Organic Phosphonate Radical Cations with Femtosecond Time-Resolved Mass Spectrometry. *Molecules* 24, 509. doi:10.3390/molecules24030509

Assion, A., Baumert, T., Bergt, M., Brixner, T., Kiefer, B., Seyfried, V., et al. (1998). Control of Chemical Reactions by Feedback-Optimized Phase-Shaped Femtosecond Laser Pulses. *Science* 282, 919–922. doi:10.1126/science.282.5390.919

Bauernschmitt, R., and Ahlrichs, R. (1996). Treatment of Electronic Excitations within the Adiabatic Approximation of Time Dependent Density Functional Theory. *Chem. Phys. Lett.* 256, 454–464. doi:10.1016/0009-2614(96)00440-X

Becke, A. D. (1993). Density-functional Thermochemistry. III. The Role of Exact Exchange. *J. Chem. Phys.* 98, 5648–5652. doi:10.1063/1.464913

Bloembergen, N., and Yablonovitch, E. (1978). Infrared-laser-induced Unimolecular Reactions. *Phys. Today* 31, 23–30. doi:10.1063/1.2995035

Bloembergen, N., and Zewail, A. H. (1984). Energy Redistribution in Isolated Molecules and the Question of Mode-Selective Laser Chemistry Revisited. *J. Phys. Chem.* 88, 5459–5465. doi:10.1021/j150667a004

Bohinski, T., Moore Tibbetts, K., Tarazkar, M., Romanov, D. A., Matsika, S., and Levis, R. J. (2014). Strong Field Adiabatic Ionization Prepares a Launch State for Coherent Control. *J. Phys. Chem. Lett.* 5, 4305–4309. doi:10.1021/jz502313f

Cardoza, D., Pearson, B. J., Baertschy, M., and Weinacht, T. (2006). Charge-transfer as a Mechanism for Controlling Molecular Fragmentation. *J. Photochem. Photobiol. A: Chem.* 180, 277–281. doi:10.1016/j.jphotochem.2006.02.007

Cristian, A.-M. C., and Krylov, A. I. (2003). Electronic Structure of the π-bonded Al-C_2H_4 Complex: Characterization of the Ground and Low-Lying Excited States. *J. Chem. Phys.* 118, 10912–10918. doi:10.1063/1.1576212

Damrauer, N. H., Dietl, C., Krampert, G., Lee, S.-H., Jung, K.-H., and Gerber, G. (2002). Control of Bond-Selective Photochemistry in CH_2 BrCl Using Adaptive Femtosecond Pulse Shaping. *Eur. Phys. J. D - At. Mol. Opt. Phys.* 20, 71–76. doi:10.1140/epjd/e2002-00101-8

Epifanovsky, E., Gilbert, A. T. B., Feng, X., Lee, J., Mao, Y., Mardirossian, N., et al. (2021). Software for the Frontiers of Quantum Chemistry: An Overview of Developments in the Q-Chem 5 Package. *J. Chem. Phys.* 155, 084801. doi:10.1063/5.0055522

[Dataset] Frisch, M. J., Trucks, G. W., Schlegel, H. B., Scuseria, G. E., Robb, M. A., Cheeseman, J. R., et al. (2016). *Gaussian 16 revision c.01.* Wallingford CT: Gaussian Inc.

Grimme, S., and Parac, M. (2003). Substantial Errors from Time-dependent Density Functional Theory for the Calculation of Excited States of Large π Systems. *ChemPhysChem* 4, 292–295. doi:10.1002/cphc.200390047

Judson, R. S., and Rabitz, H. (1992). Teaching Lasers to Control Molecules. *Phys. Rev. Lett.* 68, 1500–1503. doi:10.1103/PhysRevLett.68.1500

Konar, A., Shu, Y., Lozovoy, V. V., Jackson, J. E., Levine, B. G., and Dantus, M. (2014). Polyatomic Molecules under Intense Femtosecond Laser Irradiation. *J. Phys. Chem. A.* 118, 11433–11450. doi:10.1021/jp505498t

Kraus, P. M., Mignolet, B., Baykusheva, D., Rupenyan, A., Horný, L., Penka, E. F., et al. (2015). Measurement and Laser Control of Attosecond Charge Migration in Ionized Iodoacetylene. *Science* 350, 790–795. doi:10.1126/science.aab2160

Krylov, A. I. (2008). Equation-of-Motion Coupled-Cluster Methods for Open-Shell and Electronically Excited Species: The Hitchhiker's Guide to Fock Space. *Annu. Rev. Phys. Chem.* 59, 433–462. doi:10.1146/annurev.physchem.59.032607.093602

Langhojer, F., Cardoza, D., Baertschy, M., and Weinacht, T. (2005). Gaining Mechanistic Insight from Closed Loop Learning Control: The Importance of Basis in Searching the Phase Space. *J. Chem. Phys.* 122, 014102. doi:10.1063/1.1826011

Laurent, A. D., Blondel, A., and Jacquemin, D. (2015). Choosing an Atomic Basis Set for TD-DFT, SOPPA, ADC(2), CIS(D), CC2 and EOM-CCSD Calculations of Low-Lying Excited States of Organic Dyes. *Theor. Chem. Acc.* 134, 76. doi:10.1007/s00214-015-1676-9

Lopata, K., Reslan, R., Kowalska, M., Neuhauser, D., Govind, N., and Kowalski, K. (2011). Excited-state Studies of Polyacenes: A Comparative Picture Using EOMCCSD, CR-EOMCCSD(T), Range-Separated (LR/RT)-TDDFT, TD-PM3, and TD-ZINDO. *J. Chem. Theor. Comput.* 7, 3686–3693. doi:10.1021/ct2005165

López Peña, H. A., Ampadu Boateng, D., McPherson, S. L., and Tibbetts, K. M. (2021). Using Computational Chemistry to Design Pump-Probe Schemes for Measuring Nitrobenzene Radical Cation Dynamics. *Phys. Chem. Chem. Phys.* 23, 13338–13348. doi:10.1039/D1CP00360G

Lozovoy, V. V., Zhu, X., Gunaratne, T. C., Harris, D. A., Shane, J. C., and Dantus, M. (2008). Control of Molecular Fragmentation Using Shaped Femtosecond Pulses. *J. Phys. Chem. A.* 112, 3789–3812. doi:10.1021/jp071691p

Moore Tibbetts, K., Xing, X., and Rabitz, H. (2013). Optimal Control of Molecular Fragmentation with Homologous Families of Photonic Reagents and Chemical Substrates. *Phys. Chem. Chem. Phys.* 15, 18012–18022. doi:10.1039/C3CP52664J

Moore Tibbetts, K. (2019). Coherent Vibrational and Dissociation Dynamics of Polyatomic Radical Cations. *Chem. Eur. J.* 25, 8431–8439. doi:10.1002/chem.201900363

Munkerup, K., Romanov, D., Bohinski, T., Stephansen, A. B., Levis, R. J., and Sølling, T. I. (2017). Conserving Coherence and Storing Energy during Internal Conversion: Photoinduced Dynamics of Cis- and Trans-azobenzene Radical Cations. *J. Phys. Chem. A.* 121, 8642–8651. doi:10.1021/acs.jpca.7b09185

Nichols, S., Weinacht, T., Rozgonyi, T., and Pearson, B. (2009). Strong-field Phase-dependent Molecular Dissociation. *Phys. Rev. A.* 79, 043407. doi:10.1103/physreva.79.043407

Plenge, J., Wirsing, A., Wagner-Drebenstedt, I., Halfpap, I., Kieling, B., Wassermann, B., et al. (2011). Coherent Control of the Ultrafast Dissociative Ionization Dynamics of Bromochloroalkanes. *Phys. Chem. Chem. Phys.* 13, 8705–8714. doi:10.1039/C0CP02742A

Prlj, A., Curchod, B. F. E., Fabrizio, A., Floryan, L., and Corminboeuf, C. (2015). Qualitatively Incorrect Features in the TDDFT Spectrum of Thiophene-Based Compounds. *J. Phys. Chem. Lett.* 6, 13–21. doi:10.1021/jz5022087

Prlj, A., Sandoval-Salinas, M. E., Casanova, D., Jacquemin, D., and Corminboeuf, C. (2016). Low-Lying ππ* States of Heteroaromatic Molecules: A Challenge for Excited State Methods. *J. Chem. Theor. Comput.* 12, 2652–2660. doi:10.1021/acs.jctc.6b00245

Stephens, P. J., Devlin, F. J., Chabalowski, C. F., and Frisch, M. J. (1994). Ab Initio calculation of Vibrational Absorption and Circular Dichroism Spectra Using Density Functional Force fields. *J. Phys. Chem.* 98, 11623–11627. doi:10.1021/j100096a001

Tannor, D. J., and Rice, S. A. (1985). Control of Selectivity of Chemical Reaction via Control of Wave Packet Evolution. *J. Chem. Phys.* 83, 5013–5018. doi:10.1063/1.449767

Tibbetts, K. M., Tarazkar, M., Bohinski, T., Romanov, D. A., Matsika, S., and Levis, R. J. (2015). Controlling the Dissociation Dynamics of Acetophenone Radical Cation through Excitation of Ground and Excited State Wavepackets. *J. Phys. B: Mol. Opt. Phys.* 48, 164002. doi:10.1088/0953-4075/48/16/164002

Wei, Z., Li, J., Wang, L., See, S. T., Jhon, M. H., Zhang, Y., et al. (2017). Elucidating the Origins of Multimode Vibrational Coherences of Polyatomic Molecules Induced by Intense Laser fields. *Nat. Commun.* 8, 735. doi:10.1038/s41467-017-00848-2

Weigend, F., and Ahlrichs, R. (2005). Balanced Basis Sets of Split Valence, Triple Zeta Valence and Quadruple Zeta Valence Quality for H to Rn: Design and Assessment of Accuracy. *Phys. Chem. Chem. Phys.* 7, 3297–3305. doi:10.1039/B508541A

Xing, X., Rey-de-Castro, R., and Rabitz, H. (2017). Gaining Mechanistic Insight with Control Pulse Slicing: Application to the Dissociative Ionization of CH2BrI. *J. Phys. Chem. A.* 121, 8632–8641. doi:10.1021/acs.jpca.7b08835

Zewail, A. H. (1988). Laser Femtochemistry. *Science* 242, 1645–1653. doi:10.1126/science.242.4886.1645

Zhang, Q., Fang, W., Xie, Y., Cao, M., Zhao, Y., Shan, X., et al. (2012). Photoionization and Dissociation Study of P-Nitrotoluene: Experimental and Theoretical Insights. *J. Mol. Struct.* 1020, 105–111. doi:10.1016/j.molstruc.2012.03.059

Conflict of Interest: The authors declare that the research was conducted in the absence of any commercial or financial relationships that could be construed as a potential conflict of interest.

frontiers | Frontiers in Chemistry

ORIGINAL RESEARCH
published: 08 April 2022
doi: 10.3389/fchem.2022.859750

Post-Ionization Dynamics of the Polar Molecule OCS in Asymmetric Laser Fields

Tomoyuki Endo[1,2], *Karl Michael Ziems*[3,4], *Martin Richter*[3], *Friedrich G. Fröbel*[3], *Akiyoshi Hishikawa*[5,6], *Stefanie Gräfe*[3,4], *François Légaré*[1]* and *Heide Ibrahim*[1]*

[1]Institut national de la recherche scientifique, Centre Énergie Matériaux et Télécommunications, Varennes, QC, Canada, [2]Kansai Photon Science Institute, National Institutes for Quantum Science and Technology, Kizugawa, Japan, [3]Institute of Physical Chemistry and Abbe Center of Photonics, Friedrich Schiller University Jena, Jena, Germany, [4]Max Planck School of Photonics, Jena, Germany, [5]Department of Chemistry, Graduate School of Science, Nagoya University, Nagoya, Japan, [6]Research Center for Materials Science, Nagoya University, Nagoya, Japan

We have investigated the dissociation mechanisms of the prototypical heavy polar molecule OCS into the two break-up channels of the dication, $OCS^{2+} \rightarrow O^+ + CS^+$ and $OC^+ + S^+$, in phase-locked two-color intense laser fields. The branching ratio of the breaking of the C–O and C–S bonds followed a pronounced 2π-oscillation with a modulation depth of 11%, depending on the relative phase of the two-color laser fields. The fragment ejection direction of both break-up channels reflects the anisotropy of the tunneling ionization rate, following a 2π-periodicity, as well. The two dissociation pathways in the C–S bond breaking channel show different phase dependencies of the fragment ejection direction, which are assigned to post-ionization dynamics. These observations, resulting from the excitation with asymmetric two-color intense laser fields, supported by state-of-the-art theoretical simulations, reveal the importance of post-ionization population dynamics in addition to tunneling ionization in the molecular fragmentation processes, even for heavy polar molecules.

Keywords: two-color laser field, coherent control experiment, post-ionization dynamics, real-time real-space time-dependent density functional theory, Coulomb explosion imaging

Edited by:
Andre Bandrauk,
Université de Sherbrooke, Canada

Reviewed by:
Bernd Von Issendorff,
University of Freiburg, Germany
Tomás González-Lezana,
Spanish National Research Council (CSIC), Spain

***Correspondence:**
François Légaré
francois.legare@inrs.ca
Heide Ibrahim
heide.ibrahim@inrs.ca

Specialty section:
This article was submitted to Physical Chemistry and Chemical Physics,
a section of the journal Frontiers in Chemistry

Received: *21 January 2022*
Accepted: *07 March 2022*
Published: *08 April 2022*

Citation:
Endo T, Ziems KM, Richter M, Fröbel FG, Hishikawa A, Gräfe S, Légaré F and Ibrahim H (2022) Post-Ionization Dynamics of the Polar Molecule OCS in Asymmetric Laser Fields.
Front. Chem. 10:859750.
doi: 10.3389/fchem.2022.859750

1 INTRODUCTION

Coherent control of molecular dynamics in real-time is one of the ultimate goals of chemistry. One can envision the production of novel chemical substances and chemical reactions without undesired side-products. Coherent reaction control with photons such as the pump-dump technique (Tannor and Rice, 1985; Shen et al., 1999) adapting the field to the instantaneous dynamics (Malinovsky et al., 1997; Gräfe et al., 2005) or interference between reaction pathways (Brumer and Shapiro, 1986; Wang et al., 1996) have been demonstrated in the past decades. Though these methods are powerful to achieve desired chemical reactions, possible reaction outcomes are limited by the structures of the potential energy surface (PES) along the reaction coordinates.

The development of ultrashort laser techniques opened-up new paths for direct reaction control by tailored intense laser fields (Rabitz, 2006). In intense laser fields (typically ~ 10^{14} W/cm^2), the PESs of molecules are distorted due to strong light-matter interactions. By using feed-back loop optimization of the shape of the laser electric fields, previous studies have demonstrated coherent control of photo-chemical reactions such as selective bond scission (Assion et al., 1998; Bergt et al., 1999; Brixner et al., 2001; Levis et al., 2001; Cardoza et al., 2005), intramolecular cyclization (Kotur et al., 2009), and electron localization (Wells et al., 2009). However, the complex relationships between the optimized laser fields and the obtained products hinder understanding of the fundamental driving mechanisms. Alternatively, one can control a chemical reaction by directly addressing its spectral signature (Ibrahim et al., 2009a,b).

Recently, simple pulse shaping techniques based on breaking the inversion symmetry of an electric field have been employed instead of complex tailored laser fields. Carrier-envelope-phase (CEP) stabilized few-cycle laser fields and phase-locked two-color laser fields are widely used to investigate the underlying mechanisms of such reaction control (Alnaser and Litvinyuk, 2017). Control of the fragment ejection direction has been demonstrated for a wide range of *non-polar* (symmetric) molecules, from the simplest diatomic molecule H_2 (D_2) (Kling et al., 2006; Roudnev and Esry, 2007; Ray et al., 2009; Znakovskaya et al., 2012; Wanie et al., 2016), summarized in (Ibrahim et al., 2018), to poly-atomic hydrocarbons (Xie et al., 2012, 2014; Alnaser et al., 2014; Miura et al., 2014; Song et al., 2015; Doblhoff-Dier et al., 2016), the tri-atomic CO_2 molecule (Endo et al., 2016, 2017), as well as CF_4 as part of this special issue (Hasegawa et al., 2022). Several mechanisms have been proposed such as the interference of dissociation pathways for H_2^+ and D_2^+ (Kling et al., 2006; Roudnev and Esry, 2007; Ray et al., 2009; Znakovskaya et al., 2012; Wanie et al., 2016; Ibrahim et al., 2018), coherent superposition of vibrational states and electron recollisional excitation for $C_2H_2^+$ (Alnaser et al., 2014; Xie et al., 2014; Song et al., 2015; Doblhoff-Dier et al., 2016), laser induced bond-weakening for $C_2D_2^+$ (Miura et al., 2014), or potential deformation for CO_2^{2+} (Sato et al., 2003; Endo et al., 2016, 2017). The important roles of post-ionization interactions such as the interference between ionic states and potential deformation in doubly charged states as well as the ionization step in the fragmentation processes of non-polar molecules have been discussed and clarified by using such simple asymmetric laser fields.

In the case of *polar* (asymmetric) molecules on the contrary, the fragment ejection direction in asymmetric laser fields has been exclusively explained by the anisotropy of the tunneling ionization rate, which is determined by the shape of the ionizing molecular orbital (usually the highest occupied molecular orbital, HOMO) and the molecule's permanent dipole moment (Ohmura and Tachiya, 2008; Holmegaard et al., 2010; Dimitrovski et al., 2011; Li et al., 2011; Wu et al., 2012; Ohmura et al., 2014; Li et al., 2016; Wustelt et al., 2018; Yue et al., 2018; Endo et al., 2019; Ohmura et al., 2019), rather than by post-ionization interactions. Although post-ionization interactions should be important even for the dissociation of polar molecules, their contributions are generally buried under the strong anisotropy of the tunneling ionization rate. A deeper understanding of both the ionization step and post-ionization interactions is required to achieve flexible and mighty reaction control.

In the present study, we investigated the break-up processes of carbonyl sulfide, OCS, in phase-locked two-color intense laser fields by using the Coulomb explosion imaging technique (Wales et al., 2014; Endo et al., 2020; Zhao et al., 2021). OCS is the prototype of a heavy polar molecule (not containing hydrogen atoms) and has been widely investigated, including a molecular movie of its alignment (Karamatskos et al., 2019). In addition, we have demonstrated the applicability of reaction control based on post-ionization interactions to the dynamics of heavy atoms by using a simple pulse shaping technique. The effects of post-ionization interactions between polar molecules and phase-locked two-color intense laser fields, and the resulting molecular dynamics are discussed on the basis of the two dissociation channels OCS^{2+}, $OCS^{2+} \rightarrow O^+ + CS^+$/$OC^+ + S^+$, and compared to state-of-the-art theoretical simulations using real-time real-space time-dependent density functional theory (rtTDDFT) and semi-classical surface-hopping dynamics.

2 METHODS

2.1 Experimental Section

The 2.5 kHz Titanium-Sapphire laser beam line of the Advanced Laser Light Source (ALLS) user facility in Varennes, Canada, was used to perform ion coincidence three-dimensional (3D) momentum imaging measurements. Two-color laser fields were obtained in a Mach-Zehnder interferometer after second harmonic generation, as schematically shown in **Figure 1**.

The electric field of the resulting two-color laser field, composed of the fundamental (carrier frequency of ω) and parallel polarized second harmonic (2ω) pulses, can be expressed as

$$F(t) = F_\omega \cos(\omega t) + F_{2\omega} \cos(2\omega t + \phi) \quad (1)$$

where F_ω and $F_{2\omega}$ are the electric field amplitudes of the fundamental and second harmonic fields, respectively, and ϕ is the relative phase between both fields. The relative phase was determined keeping the fragment ejection direction consistent with previous OCS studies (Ohmura and Tachiya, 2008; Ohmura et al., 2014, 2019); ϕ is zero when the maximum amplitude side of $F(t)$ points towards the positive x direction in the laboratory frame (see **Figure 1**).

To stabilize ϕ during long data acquisition times, the obtained two-color pulses were partly reflected by a CaF_2 wedge. The reflected pulses were subsequently introduced into a second β-BBO crystal (Type I). The interference spectrum of both second harmonics generated by the first and the second BBO crystals was used to lock ϕ by a feedback loop with a pair of fused silica wedges mounted on a motorized translational stage (Endo et al., 2016, 2017). The root mean square of the measured phase deviation was less than 14°, corresponding to 0.05 fs over 24 h. The intensity of each laser field, $I_\omega \propto F_\omega^2$ and $I_{2\omega} \propto F_{2\omega}^2$, at the focal spot was estimated by measuring pulse energy, pulse duration, and focal spot size of each beam. The pulse energy on target was estimated from the measured pulse energy in front of the chamber and the reflectivity of the chamber window and focussing mirror. The pulse durations of ω and 2ω pulses were measured to be 100 fs and 250 fs by second harmonic generation frequency-resolved optical gating (SHG-FROG) and transient grating FROG (TG-FROG) techniques, respectively (Kane and Trebino, 1993; Schmidt et al., 2008). The focal spot size was measured by a charge-coupled-device (CCD) camera using a second concave mirror of identical focal length in air. The total laser field peak intensity is defined as $I_{\omega+2\omega} \propto (F_\omega + F_{2\omega})^2$ and the intensity ratio is defined as $\alpha = I_{2\omega}/I_\omega = (F_{2\omega}/F_\omega)^2$.

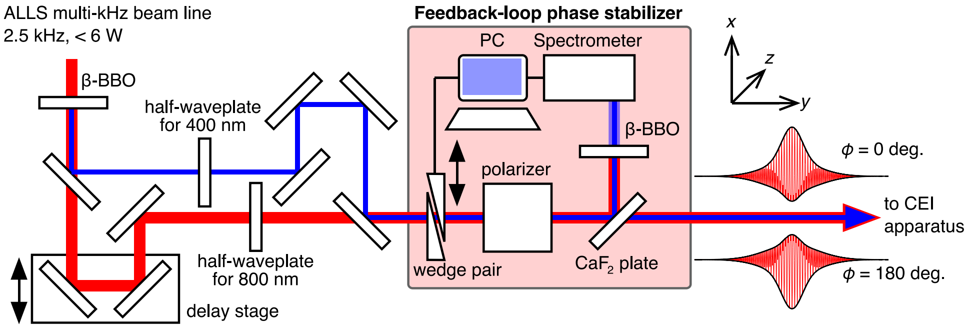

FIGURE 1 | Schematic of the experimental setup to generate phase-locked two-color laser fields. The output of a Ti:Sapphire laser amplifier system (ω, 800 nm, 2.5 kHz) was introduced into a β-barium borate (BBO, Type I) crystal to generate second-harmonic pulses (2ω, 400 nm). ω and 2ω pulses were separated by a dielectric mirror. The polarization direction of both pulses was rotated by a half-waveplate and extracted by a polarizer to parallelize the polarization directions along the x-axis in the laboratory frame and tune the field intensity individually. The time-delay between both pulses was controlled by a linear delay stage before ω and 2ω pulses were collinearly re-combined. A pair of fused silica wedges was used to fine-tune the relative phase ϕ, which was locked by a feedback loop utilizing the interference spectrum of the 2ω pulses. Schematic shapes of the phase-locked two-color laser electric fields ($\phi = 0^\circ$ and 180°) are shown.

The obtained two-color laser fields were focused on an effusive molecular beam of a gas mixture (He 95% + OCS 5%) by a concave mirror (f = 100 mm) placed in an ultrahigh vacuum chamber. The generated ions were accelerated by electrodes in velocity map configuration to a position sensitive detector with delay-line anodes (RoentDek Handels GmbH). The 3D momentum of the ith ion $\mathbf{p}_i = (p_i^x, p_i^y, p_i^z)$ was calculated from the position (x_i, y_i) and the arrival time (t_i) at the detector. We used the Waterloo algorithm (Wales et al., 2012) to determine true coincidence events. The total kinetic energy release (KER) E_{kin} of each event was calculated from the 3D momenta as

$$E_{\text{kin}} = \sum_i \frac{|\mathbf{p}_i|^2}{2m_i}, \tag{2}$$

with m_i being the mass of the ith fragment ion.

2.2 Computational Section

Numerical simulations based on rtTDDFT and semi-classical surface-hopping dynamics were performed separately for the ionization and dissociation steps. First, we simulated the ionization of OCS in two-color laser fields under the fixed nuclei approximation, since the effects of bond stretching during ionization is not significant in the present experimental conditions. Second, to consider nuclear dynamics of OCS^{2+} in two-color laser fields, we simulated the dissociation processes starting from the selected electronic states.

2.2.1 Ionization Step

We employed a state-of-the-art numerical description of the strong-field response of OCS (and OCS^{+}) based on the rtTDDFT as realized in the *Octopus* program package (Andrade et al., 2012; Tancogne-Dejean et al., 2020). Shortly, the 16 outermost electrons, within the time-dependent Kohn–Sham orbitals, are propagated numerically in real-time and real-space using finite element methods. From these orbitals, the time-dependent electron density is constructed. For the calculations, a spherical box with a radius of R = 20 a. u. was used, including a complex absorbing potential at its boundary with r_{abs} = 5 a.u. We confirmed that increasing the box radius to R = 30 a. u. did not change the results substantially (a maximum deviation in the total number of emitted electrons $\Delta n_{\text{emit}} \sim 0.002$, $< 0.2\%$ of the total number of emitted electrons n_{emit}). We employed an equidistant grid of 0.28 a.u. resolution in three spatial dimensions each, resulting in more than 7,000,000 mesh points. The propagation is done in short (attosecond) time steps, requiring several ten-thousand consecutive propagation steps for covering a short excitation pulse of about 50 fs duration. Electron dynamics were propagated for > 150 fs (211,667 steps of about 0.7 as). The molecule is fixed in space and lies on the x-axis. The electric field is polarized likewise along the x-axis. The coordinate system is such that the carbon atom is at the origin, the oxygen at positive coordinate values, and the sulfur atom at negative ones ((x, y, z) positions: C (0,0,0); O (1.17,0,0); S (-1.57,0,0) a.u.).

For the exchange-correlation potential, we chose the local-density approximation (LDA) functional with average-density self-interaction correction (ADSIC). The highest occupied DFT Kohn–Sham orbitals included in our calculations can be specified as follows: the HOMO-5, HOMO-4, HOMO-3, and HOMO-2 are of σ-type, while the (doubly degenerate) HOMO-1 and HOMO are of π-type. We performed five different calculations for relative phases of $\phi = 0^\circ, 45^\circ, 90^\circ, 135^\circ, 180^\circ$. The laser pulses were implemented as in **Eq. 1**, with F_ω = 0.0755 a.u. (corresponding to an intensity $I_\omega = 2 \times 10^{14}\ \text{W/cm}^2$), a pulse width of 20 fs, and a wavelength of 800 nm. For the 2ω field, a field strength of 0.0407 a.u. (corresponding to an intensity $I_{2\omega} = 0.29 I_\omega = 0.58 \times 10^{14}\ \text{W/cm}^2$), a pulse width of 50 fs, and a wavelength of 400 nm are chosen. The pulse duration used in the simulation is shorter than that in the experiment due to the limitation of computational costs. However, as mentioned below in **Section 3**, since ionization mainly occurs around the peak of the laser electric field and dissociation from the excited state of OCS^{2+} proceeds in a few tens of femtoseconds, the pulse durations of 20 and 50 fs are long enough to compare with the experiment quantitatively. As the orbitals strongly mix in the presence of the laser field, we focus our evaluation on the projection of time-dependent Kohn–Sham wavefunctions on ground-state wavefunctions at the end of the simulation time, when the pulse has vanished. By doing so, we can monitor the fraction of ionized electrons that originated from σ and π orbitals, respectively.

This procedure allows us to assign, which orbitals are depopulated in the field, and, consequently, which cationic (and dicationic) electronic states are formed upon ionization.

2.2.2 Nuclear Dynamics of the Dication

The ground state equilibrium structure of neutral OCS was optimized by means of CASSCF(12, 10)/aug-cc-pVTZ level of theory (Aquilante et al., 2016) state-averaged over the first six singlet roots using the OpenMolcas suite program (Roos et al., 1980; Godbout et al., 1992). A subsequent vibrational analysis was carried out to verify that a minimum on the PES was obtained. The active orbitals were chosen by using the full set of valence orbitals (16 electrons in 12 orbitals) and omitting the two lowest σ orbitals with main contributions from 1*s* atomic orbitals of the oxygen and sulfur atom.

For the dynamical calculations of OCS^{2+}, the semi-classical program package SHARC 2.1 (Richter et al., 2011; Mai et al., 2018) interfaced with OpenMolcas (Aquilante et al., 2016) was employed. The electronic structure properties were calculated using state-average CASSCF(10, 10)/cc-pVDZ for the first 20 roots in the triplet manifold, while the nuclei are treated classically. Non-adiabatic effects are realized in the SHARC code via jumps between electronic surfaces, and the two-color field is incorporated explicitly as off-diagonal element in the electronic Hamiltonian used for the propagation of the electronic wave function. The initial trajectories were Wigner sampled around the equilibrium structure (obtained as described above) of the neutral OCS and started in the triplet ground state of OCS^{2+}, $X^3\Sigma^-$, and the excited $1^3\Pi$ state assuming an instantaneous excitation. For each of the three investigated relative phases of $\phi = 0^\circ, 180^\circ, 270^\circ$, an ensemble of 20 trajectories was started. The classic propagation was carried out for 75 fs with a time step of 0.1 fs centred around the light pulse. The KER was calculated by tracking the relevant mass-weighted molecular fragment in position space.

For all calculations, a reproducible and transferable computational environment was set up with the Nix package manager using NixOS-QChem (Kowalewski and Seeber, 2022) (commit 206dcba) and Nixpkgs (NixOS, 2021) (commit 9775b39).

3 RESULTS AND DISCUSSION

The electronic configuration of neutral OCS in the ground state is $(\text{core})^{14}(6\sigma)^2(7\sigma)^2(8\sigma)^2(9\sigma)^2(2\pi)^4(3\pi)^4(4\pi)^0$. The potential energy curves of the lower lying electronic states, relevant to the two dissociation channels, $OC^+ + S^+$ and $O^+ + CS^+$, are depicted as a function of the bond lengths in **Figure 2**. The double ionization potential of OCS at the equilibrium structure (Franck-Condon region), reached by removing two valence electrons from the 3π orbital, is 30.3 eV (Langford et al., 1991). Since the electronic ground state of OCS^{2+} is the metastable $X^3\Sigma^-$ state (Kaneyasu et al., 2015) and its lifetime is theoretically predicted to be on the order of 10^{160} s (Ridard et al., 1988), the dissociation does not occur directly from the ground state of OCS^{2+}. In our nuclear dynamics simulation in intense laser fields, dissociation from the $(3\pi)^{-2}$ states does not occur within our simulation time. Note that the molecular states are described in terms of single orbital occupations, which correspond to the dominant contributions.

As observed in the previous experiments of OCS in one-color intense laser fields (Bryan et al., 2006; Ma et al., 2019), OCS^{2+} preferentially dissociates into $OC^+ + S^+$ rather than $O^+ + CS^+$. The total yield of the $OC^+ + S^+$ channel is more than one order of magnitude larger than that of the $O^+ + CS^+$ channel in our experimental conditions. This can be explained by the fact that the products of the C–S bond breaking are more stable than the ones of the C–O bond breaking (Masuoka et al., 1992). The potential energies of the lowest state at the dissociation limits are 27.5 eV for OC^+ ($X^2\Sigma^+$) + S^+ (^4S) vs 31.3 eV for O^+ (^4S) + CS^+ ($X^2\Sigma^+$) (Brites et al., 2008). In addition, the potential barrier for the C–S bond breaking is much smaller than the one for the C–O bond breaking, as shown in **Figure 2**. According to photoionization experiments by Masuoka and Koyano (Masuoka and Koyano, 1991), the onset of the major $OC^+ + S^+$ dissociation channel is at a threshold energy of 33.5 eV, while more than 40 eV are necessary for the $O^+ + CS^+$ dissociation channel.

We start the discussion with the major dissociation channel, $OCS^{2+} \rightarrow OC^+ + S^+$, compare it to previous studies of OCS in intense laser fields (Holmegaard et al., 2010; Dimitrovski et al., 2011; Ohmura et al., 2014, 2019; Ma et al., 2019; Zhao et al., 2021), and discuss its dissociation mechanisms. Next, we focus on the minor dissociation channel, $OCS^{2+} \rightarrow O^+ + CS^+$. We then investigate the newly observed shoulder peak in the major dissociation channel and discuss the effects of post-ionization interactions. Lastly, we discuss the control of the branching ratio between the C–O and C–S bond breaking channels.

3.1 The Major Dissociation Channel: C–S Bond Breaking

The phase-averaged total KER (E_{kin}) spectrum of the $OC^+ + S^+$ channel in phase-locked two-color intense laser fields ($I_{\omega+2\omega} = 2 \times 10^{14}$ W/cm^2, $\alpha = 0.19$) is shown in **Figure 3A**. The E_{kin} spectrum shows a main peak at 5.2 eV (highlighted in green) and a shoulder structure at 4 eV (highlighted in orange).

The peak around 5 eV was also observed in a synchrotron experiment (Masuoka et al., 1992) and assigned to the fragments generated via the electronically excited states of OCS^{2+} such as $(9\sigma)^{-1}(3\pi)^{-1}$ or $(2\pi)^{-1}(3\pi)^{-1}$. Note that in a previous study using intense laser fields (Ma et al., 2019), the largest peak was however observed at a smaller KER of 4 eV instead of the 5.2 eV in our work. This difference can be attributed to the fact that different double ionization channels open up depending on the laser field intensity. In high intensity fields ($\geq 5 \times 10^{14}$ W/cm^2), doubly charged OCS^{2+} ions would be produced by sequential double ionization (SDI), which involves bond stretching on the singly charged OCS^+ ion,

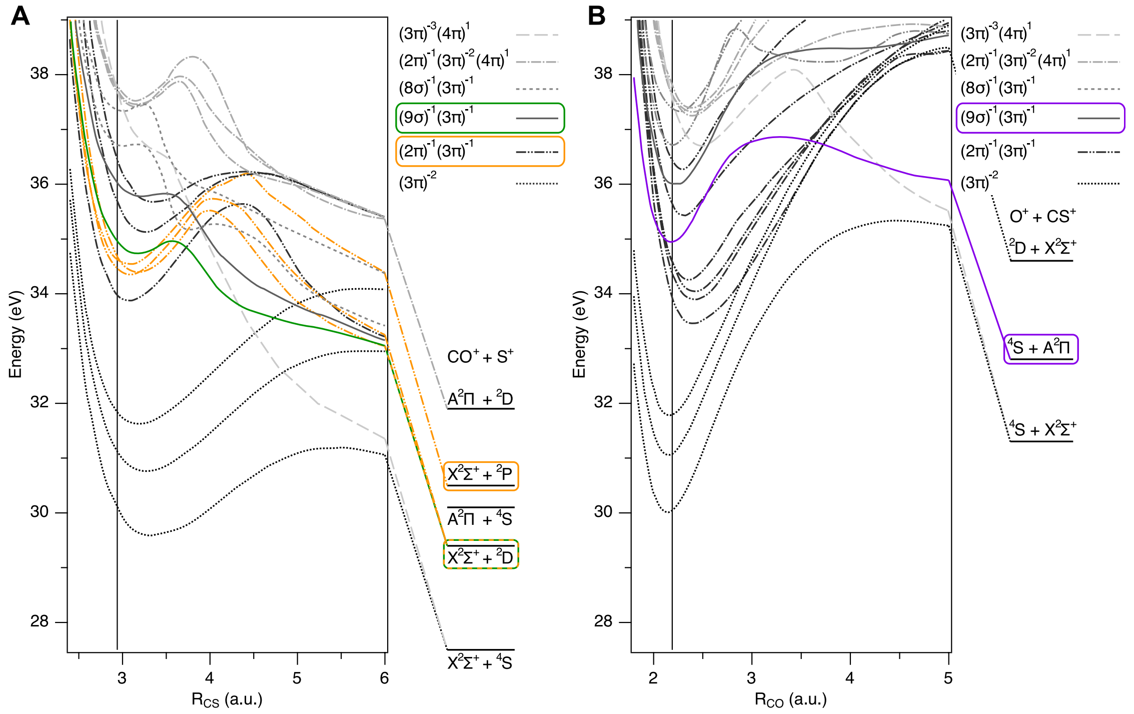

FIGURE 2 | Potential energy curves of lower lying electronic states of OCS^{2+} and corresponding dissociation limits, dissociating to **(A)** $OC^+ + S^+$ (R_{CO} =2.185 a. u.) and **(B)** $O^+ + CS^+$ (R_{CS} =2.95 a. u.) (Brites et al., 2008). The bending angle is fixed at 180°. Vertical lines correspond to the equilibrium geometry of neutral OCS in the ground state. Dotted lines correspond to $(3\pi)^{-2}$ states ($X\,^3\Sigma^-$, $a\,^1\Delta$, $b\,^1\Sigma^+$), dash-double dotted lines correspond to $(2\pi)^{-1}(3\pi)^{-1}$ states ($1^1\Sigma^-$, $1^3\Delta$, $1^1\Sigma^+$, $2^3\Sigma^-$, $2^1\Delta$, $2^1\Sigma^+$), solid lines correspond to $(9\sigma)^{-1}(3\pi)^{-1}$ states ($1^3\Pi$, $1^1\Pi$), broken lines correspond to $(8\sigma)^{-1}(3\pi)^{-1}$ states ($2^3\Pi$, $2^1\Pi$), dash-dotted lines correspond to $(2\pi)^{-1}(3\pi)^{-2}(4\pi)^1$ states ($2^1\Sigma^-$, $2^3\Delta$, $2^3\Sigma^+$), and dashed lines correspond to $(3\pi)^{-3}(4\pi)^1$ states ($1^5\Sigma^-$). The latter two states include electron excitation to a vacant 4π orbital. The potential energy curves and corresponding dissociation limits mainly responsible for the KER peaks in **Figure 3** are highlighted in green, orange, and purple.

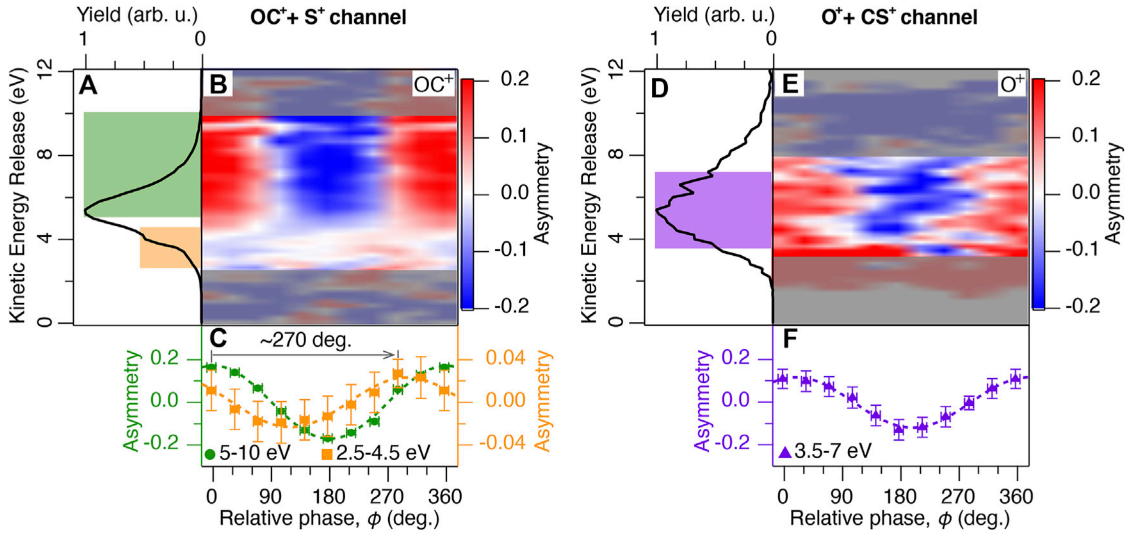

FIGURE 3 | (A) The total kinetic energy release E_{kin} spectrum of the $OC^+ + S^+$ channel averaged over the relative phase ϕ between the ω and 2ω laser fields. The KER spectrum is calculated from the fragments ejected within 45 deg. with respect to the laser polarization direction. The colored areas are linked to the different dissociation pathways indicated in **Figure 2**. **(B)** Two-dimensional plot of the asymmetry parameter as a function of E_{kin} and ϕ. The asymmetry parameter is calculated from the OC^+ fragment yields. Noisy data outside of the region of interest is masked grey shaded. **(C)** Asymmetry parameter of the OC^+ fragments integrated over 5–10 eV (green circles) and 2.5–4.5 eV (orange squares) are plotted as a function of ϕ. The dotted lines are sine fits. **(D)** Same as **(A)**, but for the $O^+ + CS^+$ channel. **(E)** Same as **(B)**, but calculated from the O^+ fragment yields. **(F)** Same as **(C)**, but the O^+ fragments are integrated over 3.5–7 eV (purple triangles).

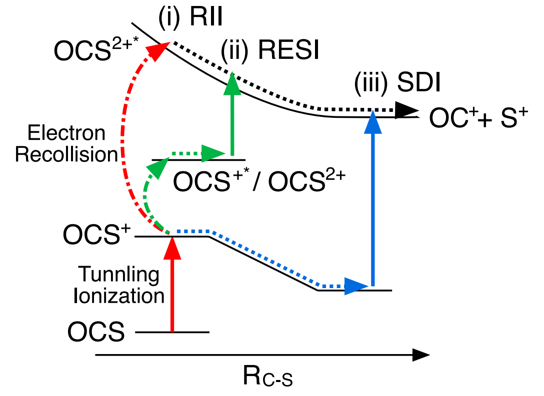

FIGURE 4 | Schematic of sequential and non-sequential double ionization and dissociation processes of OCS along the C-S bond stretching coordinate. Three possible pathways for population to the excited states of OCS^{2+} (OCS^{2+*}); (i) Recollision impact ionization (RII) leading to direct ionization to OCS^{2+*} by electron recollision, (ii) recollisional excitation with subsequent ionization (RESI) causing indirect population to OCS^{2+*} via intermediate states (OCS^{+*} or OCS^{2+}), and (iii) sequential double ionization (SDI) leading to ionization from OCS$^+$, involving bond stretching. Due to the different bond stretching in the intermediate states and the shape of the PES of OCS^{2+*}, the observed KERs appear in the order (i) > (ii) > (iii). Vertical solid arrows indicate ionization or excitation by laser fields. Curved dash-dotted arrows show ionization or excitation by electron recollision, dotted arrows represent bond stretching.

resulting in a smaller KER of 4 eV. In the present study, other mechanisms would be dominant due to the lower intensities.

Three possible double ionization mechanisms in intense laser fields have been widely accepted, as indicated in **Figure 4**. One of them is SDI as mentioned above, others are identified as non-sequential double ionization (NSDI). SDI plays an important role in a higher intensity regime, because the first ionization step can occur on the rising edge of laser pulses and the residual laser fields are intense enough to remove the second electron by field ionization. However, in a lower intensity regime, the first ionization step occurs around the peak of the laser pulse. The residual field is not strong enough to lead to a second field ionization, therefore subsequent ionization is assisted by an electron recollision process. The simplest type of NSDI is recollision impact ionization (RII), in which the recolliding electron has gained sufficient energy to ionize the second electron. In the RII mechanism, since electron impact ionization occurs within half an optical cycle (1.3 fs at 800 nm) after the first ionization step, there is no time for bond stretching to occur. Another NSDI mechanism is known as recollision excitation with subsequent tunneling ionization (RESI), in which the recolliding electron can promote molecular ions to the excited states. The second electron will be subsequently ionized by the residual laser fields because of a smaller effective ionization potential. Due to the time delay between the first and second ionization step, the bond can slightly stretch in the RESI mechanism. Xu et al. (2020) clarified that NSDI is the dominant mechanism to generate OCS^{2+} at a laser field intensity below 1×10^{14} W/cm^2 and SDI becomes dominant as the laser intensity increases.

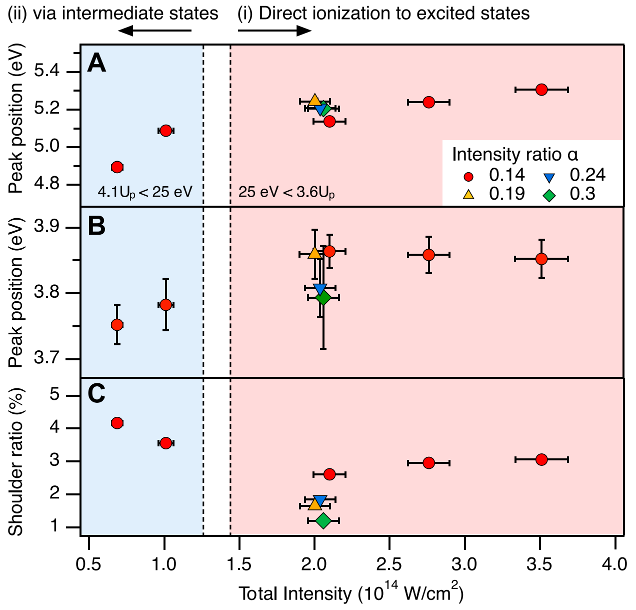

FIGURE 5 | Intensity dependence of the KER spectrum. **(A)** Position of the main peak in the OC$^+$ + S$^+$ channel as a function of the total laser field intensity ($I_{\omega+2\omega}$). **(B)** Position of the shoulder peak in the OC$^+$ + S$^+$ channel. **(C)** Ratio of the shoulder peak in the OC$^+$ + S$^+$ channel. Circles, triangles, up-side down triangles, and diamonds indicate the different intensity ratios of α = 0.14, 0.19, 0.24, and 0.3, respectively. Colored areas correspond to the intensity of (i) direct ionization to the $1^3\Pi$ state of OCS^{2+} from the ground state of OCS$^+$ by electron recollision ($I_{\omega+2\omega}$ >1.44×10^{14} W/cm^2) and (ii) indirect excitation via the electronically excited states of OCS$^+$ or the electronic ground state of OCS^{2+} ($I_{\omega+2\omega}$ <1.26×10^{14} W/cm^2) in two-color laser fields at α = 0.14 (see the text for details).

In the present study, we observed the generation of fragments via the excited states of OCS^{2+} (OCS^{2+*}) instead of the yields of the parent ion OCS^{2+}. Therefore, the threshold intensity for SDI would be shifted towards larger intensity due to the larger potential energy of OCS^{2+*} compared to the ground state of OCS^{2+}. Here, three double ionization mechanisms, including the population of the excited state of OCS^{2+}, should be considered as shown in **Figure 4**: i) direct ionization to the excited states of OCS^{2+*} by electron recollision, that is RII to the excited states, ii) recollisional excitation (ionization) to OCS^{+*} (OCS^{2+}) with subsequent ionization (excitation) to OCS^{2+*}, in analogy to RESI, and iii) SDI to the excited states of OCS^{2+}.

To clarify contributions of these mechanisms, the laser field intensity dependence of the main peak position is shown in **Figure 5A**. We observe a larger peak shift in the lower field intensity region ($< 1 \times 10^{14}$ W/cm^2) than in the higher intensity region ($> 2 \times 10^{14}$ W/cm^2), which indicates switching of the major ionization mechanism from (ii) indirect via intermediate states to (i) direct ionization to the excited states between 1–2 × 10^{14} W/cm^2. This switch is understood on the basis of the kinetic energy of the recolliding electron in intense laser fields. In two-color laser fields, this energy depends on the relative phase and the intensity ratio α as well as the laser field intensity (Endo et al., 2017). At α = 0.14, the maximum kinetic energy of the recolliding electron is between 3.6–4.1 U_p depending on the relative phase. Hereby, U_p is the ponderomotive energy in the fundamental laser fields and proportional to the laser field intensity. For example, the energy difference from the ground state of OCS^+ to the excited $1^3\Pi$ state of OCS^{2+}, which has the smallest potential barrier along the C–S bond breaking, is about 25 eV at the equilibrium geometry of neutral OCS, so the corresponding intensity range is $1.26–1.44 \times 10^{14}$ W/cm^2. When the total laser field intensity is larger than the upper threshold, the maximum kinetic energy of the recolliding electron exceeds the vertical excitation energy regardless of the relative phase. In this intensity regime, the direct mechanism (RII to the excited states) contributes to populate the $1^3\Pi$ states of OCS^{2+}. As discussed above, the double ionization by RII occurs within half an optical cycle, which does not lead to distortion of the molecular geometry during ionization. On the other hand, at a total laser intensity below the lower threshold, the energy of the recolliding electron does not exceed the excitation energy. Therefore, the RII-type direct mechanism cannot contribute and RESI-type indirect mechanisms via the excited state of OCS^+ or the ground state of OCS^{2+} play important roles. In the indirect mechanisms, bond stretching on intermediate states can occur, which may cause the lower KER. The observed KER shift in **Figure 5A** is well explained by this picture.

In addition, Wales et al. (2014) showed that the peak position of the KER spectra of the $O^+ + C^+ + S^+$ channel from OCS^{3+} did not change with pulse duration below 200 fs; in contrast to the peak position from the OCS^{4+} break-up channel, which strongly depended on the pulse duration. The effects of bond stretching during ionization would be larger in higher charged states, because the bond can stretch at each charged state, causing further ionization of the molecules to an even higher charged state. Since the intensity of the fundamental pulse is much stronger than that of the second harmonic pulse in the present study, the pulse duration of the resulting two-color laser fields can be considered to be comparable to that of the fundamental pulse (100 fs). Bending is likely to occur under the present experimental condition, however, it would play a minor role in the two-body breaking channel we focused on in this study. Another concern might be the effect of photo-absorption of the 2ω field, due to its higher photon energy. We observe however, that the KER spectra in one-color and two-color laser fields show the same main and shoulder structure independent of α (see **Supplementary Figure S3**). Moreover, in longer wavelength (1700 nm + 850 nm) laser fields, similar main and shoulder peaks are observed at identical position compared to the shorter wavelength (800 nm + 400 nm). These results suggest that field ionization is the dominant mechanism and photo-absorption can be excluded.

From the discussion above and based on the PESs in **Figure 2**, we assign the main peak at 5.2 eV to dissociation via the electronically excited states $1^1\Pi$ and $1^3\Pi$ of OCS^{2+}, populated by the RII mechanism. The electronic configuration of these states is $(9\sigma)^{-1}(3\pi)^{-1}$, leading to OC^+ ($X^2\Sigma^+$) and S^+ (^2D) highlighted in green in **Figure 2A**. The states highlighted in **Figure 2** represent the ones mainly contributing to the dynamics observed. We point out that, in general, for almost every triplet state, there is a corresponding singlet state of almost identical electronic configuration and similar fragmentation behavior (leading to almost identical KERs). Experimentally, we can not distinguish between singlet and triplet states, thus, also for the theoretical analysis, we concentrate on one spin species only (the triplet states). The shoulder peak is discussed in the separate **Subsection 3.3**.

To evaluate the fragment ejection direction quantitatively, the asymmetry parameter A is defined as a function of E_{kin} and ϕ,

$$A(E_{\mathrm{kin}}, \phi) = \frac{Y_+(E_{\mathrm{kin}}, \phi) - Y_-(E_{\mathrm{kin}}, \phi)}{Y_+(E_{\mathrm{kin}}, \phi) + Y_-(E_{\mathrm{kin}}, \phi)}, \tag{3}$$

where Y_+ and Y_- are the fragment yields with positive and negative momenta along the laser polarization direction (x-axis), respectively. Here, the fragment yields are evaluated by the counts of fragments ejected within 45° with respect to the laser polarization direction to reduce artificial blurring of the asymmetry due to the molecular rotation around the boundary of Y_+ and Y_-. The two-dimensional plot of the asymmetry parameter calculated from the OC^+ fragment yields is shown in **Figure 3B**. A clear asymmetry was observed above 5 eV which showed a 2π-oscillatory behavior when changing the relative phase as observed in previous studies based on the fragments' flight time measurements without coincidence detection (Ohmura et al., 2014, 2019). When a dissociation process is fast enough, the orientation of the parent ions generated by tunneling ionization reflects the ejection direction of fragment ions. Therefore, such strong asymmetry of the fragment ejection direction can be explained by the asymmetry of the ionization rate, which is determined by the shape of the HOMO and the effective ionization potential (Holmegaard et al., 2010). When the laser field is parallel to the difference in permanent dipole moment vectors of neutral and ionized states, the effective ionization potential becomes lower than in the field-free case and the ionization rate increases. Vice versa, in the case of an anti-parallel electric field, the ionization rate decreases since the effective ionization potential becomes higher than the field-free one. As a result of this competition between the shape of the HOMO and the effective ionization potential, the ionization rate increases when the laser field points to the O atom side and the electron ejects from the S atom side in circularly polarized laser fields (Holmegaard et al., 2010). However, in linearly polarized two-color laser fields (Ohmura et al., 2014, 2019), the effects of the permanent dipole moment are not strong enough to flip the ionization rate of OCS, as can be deduced from the shape of the HOMO (see **Figure 6C**), with larger electron density on the S atom than on the O atom side. That is, the ionization rate increases when the laser field points towards the O atom, and the electron ejects from the S atom side. Then, the OC^+ fragments are preferentially ejected to the larger amplitude side of the two-color laser fields (positive direction of x-axis at $\phi = 0°$).

3.2 The Minor Dissociation Channel: C–O Bond Breaking

The total KER spectrum of the $O^+ + CS^+$ channel is shown in **Figure 3D**. In contrast to the $OC^+ + S^+$ channel, no low-energy shoulder peak is observed. The two-dimensional plot of the

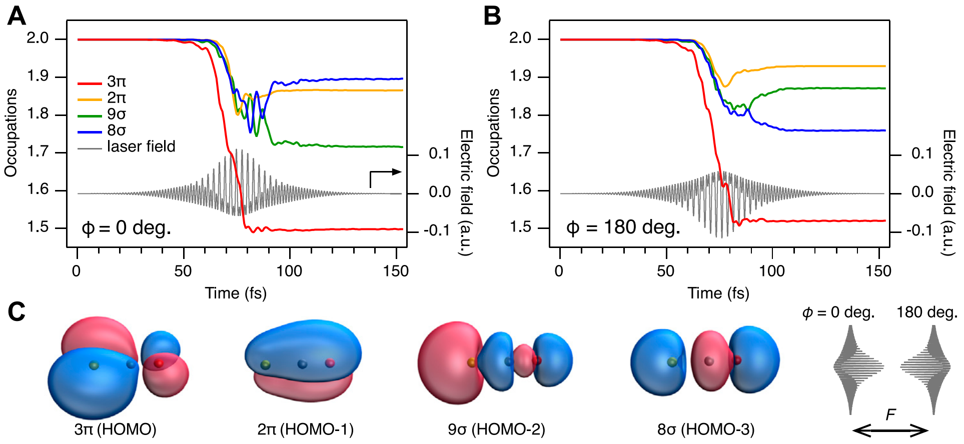

FIGURE 6 | Results of the rtTDDFT calculations. **(A)** Time-dependent orbital occupations for $\phi = 0^\circ$. **(B)** same for $\phi = 180^\circ$. The temporal shapes of the electric fields are shown as solid grey lines. Note that 3π and 2π are doubly degenerate. **(C)** Orbitals of HOMO to HOMO-3. HOMO and HOMO-1 are π orbitals, while HOMO-2 and HOMO-3 are σ orbitals. For π orbitals, only one variant is shown, the other variant is a simple rotation around the molecular axis by 90°. Yellow atom indicate sulfur, blue atoms = carbon and red atoms = oxygen. *F* denotes the laser polarization direction. Schematic shapes of the phase-locked two-color laser electric fields (ϕ =0° and 180°) are shown.

asymmetry parameter calculated from the O^+ fragment yields is shown in **Figure 3E**. No clear dependence on the KER is observed. The integrated asymmetry between 3.0 and 7.5 eV follows a similar phase dependence as the main peak of the $OC^+ + S^+$ channel, as shown in **Figure 3F**. Such similarity indicates that this broad peak can be assigned to the fragments originating from the excited $1^1\Pi$ or $1^3\Pi$ states. These states are the same ones contributing to the main peak of the $OC^+ + S^+$ channel, and dissociate to e.g. O^+ (^4S) and CS^+ ($A^2\Pi$) highlighted in purple in **Figure 2B**. The anisotropy of fragments from the excited $1^1\Pi$ or $1^3\Pi$ states reflects the angular dependence of the ionization rate because of the prompt dissociation through small potential barriers. Although the asymmetry amplitude slightly decreases compared to the main peak in the $OC^+ + S^+$ channel, which we attribute to the effects of molecular rotation due to a higher potential barrier along the O–C bond breaking. This result indicates that the orientation of the parent OCS^{2+} ions is mainly determined by the ionization step, even for different dissociation channels as discussed in the previous studies of polar molecules (Ohmura and Tachiya, 2008; Holmegaard et al., 2010; Dimitrovski et al., 2011; Li et al., 2011; Wu et al., 2012; Ohmura et al., 2014; Li et al., 2016; Wustelt et al., 2018; Yue et al., 2018; Endo et al., 2019; Ohmura et al., 2019).

3.3 Post-ionization Interaction: The Shoulder Peak in the Major Dissociation Channel

In the main $OC^+ + S^+$ dissociation channel, we have observed a shoulder peak at around 4 eV, next to the main peak, as indicated in orange in **Figure 3A**. This shoulder structure was not observed in synchrotron radiation experiments (Masuoka and Koyano, 1991; Masuoka et al., 1992). From the following discussion and nuclear dynamics simulation, we assign this peak to dissociation via the $(2\pi)^{-1}(3\pi)^{-1}$ states highlighted in orange in **Figure 2A**.

The peak position of the shoulder peak shifts in lower intensity region rather than in higher intensity region as well as the main peak. This shift indicates that the shoulder peak can be assigned to dissociation via the excited states of OCS^{2+}, in a way similar to the main peak. To identify the origin of this shoulder peak from another point of view, we compare its ratio to the main peak depending on the laser field intensity in **Figure 5C**. From Xu et al. (2020) we know, that the SDI mechanism becomes dominant at higher intensities. If the shoulder peak can be attributed to fragments generated by the SDI process, its yield would significantly increase with increasing intensity. However, we observe that the yield in the $OC^+ + S^+$ channel remains almost constant as the total laser field increases. We therefore conclude that the occurrence of both the shoulder peak and the main peak are mainly caused by the RII mechanism that does not involve bond stretching.

Another possible pathway for the occurrence of the shoulder peak would be due to interactions in neutral states such as enhanced ionization induced by structural deformation. In general, enhanced ionization causes a decrease of the observed KER (Ibrahim et al., 2018); the main peak, however, appears at the same energy here and also in the case of a synchrotron experiment (Masuoka et al., 1992) and bond stretching in neutral states was not observed in previous studies (Wales et al., 2014; Ma et al., 2019). From these observations, we conclude that interactions in neutral states are not significant here and that the ionization process, vertical ionization in the Franck-Condon region, is essentially the same as in previous studies. However, interactions after ionization/during dissociation, such as potential deformation or population transfer play important roles in the dissociation of polar molecules, as we discuss in the next sections.

The shoulder peak is not only present, it also shows a different phase dependence in its asymmetry parameter *A*, compared to the main peak. Its asymmetry amplitude is about 5 times weaker, and the relative phase leading to maximum asymmetry is shifted by 270° (-90°). This shift is directly apparent in the integrated asymmetry parameters between 5 and 10 eV for the main peak and between 2.5 and 4.5 eV for the shoulder peak in **Figure 3C**. Such shift indicates that contributions from two (or more) components are present whose phase difference is not an integer multiple of 180°. We draw this conclusion, because two components, phase-shifted by 180°, would only cause a dependence of the overall asymmetry amplitude on their ratio but no phase shift would occur.

The weak amplitude can be attributed to competition between the contributions from the main and shoulder peaks with different phase dependence, leading to a cancellation in modulation contrast. The observed phase shift, however, cannot be explained by the simple tunneling ionization picture discussed above for the main peak. The ionization rate becomes largest at a relative phase of 0° or 180°, where the peak of the electric field amplitude is maximum. In the extreme case of diametrical effects of the orbital shapes and dipole moments, e.g. ionization from lower lying orbitals, the asymmetry would be shifted by 180°. The observed phase shift of 270° therefore means that other mechanisms, occurring after the actual ionization, such as electron recollisional excitation, potential deformation, or population transfer between electronic states determine the fragment's asymmetry. One of the possible scenarios is based on electron recolliding excitation and potential deformation as suggested in the asymmetric dissociation of CO_2 (Endo et al., 2017): The excitation probability due to electron impact depends on the kinetic energy and the incident direction of the recollisional electron, which are determined by both the field intensity and the relative phase (Endo et al., 2019). This means that the population distribution among electronic states in the ionic states manifold depends on the relative phase. In addition, potential deformations would be more prominent in higher electronic states, which have diffuse wavefunctions. The sum of these contributions from different electronic states can lead to the observed phase shift of 270° in the fragment ejection direction. However, in the case of CO_2, the asymmetry amplitudes are on the order of a few percent, while in this study, they reach values of up to 0.16 ($E_{\text{kin}} > 5$ eV) and decrease to 0.03 ($E_{\text{kin}} < 4.5$ eV). This suggests that both shoulder- and main peak have comparable asymmetry amplitudes. In addition to that, the intensity dependence of the asymmetry amplitudes of CO_2 (Endo et al., 2017) plateaus, while in OCS a monotonic decrease with increasing intensity is observed as shown in **Supplementary Figure S4** of the SM. We therefore suggest another possible scenario; a population transfer between electronic states after ionization, as will be discussed later.

To summarize these results, the shoulder peak of the $OC^+ + S^+$ channel occurring around 4 eV exhibits a distinct phase dependence compared to the two channels directly dissociating from the excited states. We assign its origin to post-ionization dynamics; through this observed phase dependence, we are able to indicate that this shoulder peak arises from a population transfer between electronic excited states in doubly charged states, as supported by the computational results discussed in the following.

3.4 Computational Results

To further analyse the contribution of different electronic states to the observed asymmetry in both ionization and post-ionization interactions, we now discuss the computational results of the rtTDDFT calculations. Results are summarized in **Table 1** and **Supplementary Figure S1** of the SM, listing the total number of emitted electrons n_{emit}, the number of electrons originating from 3π and 2π orbitals (HOMO and HOMO-1), n_π, and from 9σ and 8σ orbitals (HOMO-2 and HOMO-3), n_σ, as well as the fraction of electrons originating from σ orbitals, $f_\sigma = n_\sigma/n_{\text{emit}}$. The results show that for phase $\phi = 0°$, ionization is most efficient: 1.67 electrons are removed in total. This is not surprising, as the peak of the field amplitude $|F_{\omega+2\omega}|$ is maximum for that phase. However, for a relative phase of $\phi = 180°$, the ionization is less, as only 1.48 electrons, about 90% of $\phi = 0°$, leave the numerical grid. Thus, as the molecule in the simulation is perfectly aligned with the laser polarization direction, at phase $\phi = 0°$, ionization preferentially occurs from the sulfur atom, as the electric field vector pointing towards the oxygen atom allows the electrons to acquire momentum in the opposite direction. For phase $\phi = 180°$, the situation is reversed and ionization preferentially occurs from the oxygen side. As shown by Ohmura et al. (Ohmura and Tachiya, 2008; Ohmura et al., 2014, 2019), the ionization efficiency is larger when emitting electrons from the large lobe of the 3π HOMO located at the sulfur (see **Figure 6C**), explaining the observed difference in n_{emit} for the cases $\phi = 0°$ and $\phi = 180°$. Note, that the preference of ionization from the S or the O side at specific ϕ is identical between our work and the ones of Ohmura et al. (Ohmura and Tachiya, 2008; Ohmura et al., 2014, 2019), both obtained with linear polarized light. It is however opposite to the work of Holmegaard et al. (Holmegaard et al., 2010) using circularly polarized light.

TABLE 1 | Summary over the numerical results obtained from the rtTDDFT calculations. Listed are the number n_{emit} of emitted electrons originating from 3π and 2π orbitals (HOMO and HOMO-1), n_π, and from 9σ and 8σ orbitals (HOMO-2 and HOMO-3), n_σ, as well as the fraction of electrons originating from σ orbitals, f_σ, for different relative phases ϕ. Additionally, the maximum field strength of the (combined) applied laser field, $|F_{\text{max}}|$, is given in atomic units (a.u.).

phase ϕ	0°	45°	90°	135°	180°
n_{emit}	1.67	1.61	1.48	1.46	1.48
n_π	1.27	1.25	1.16	1.11	1.10
n_σ	0.40	0.36	0.32	0.34	0.38
f_σ	0.24	0.23	0.22	0.24	0.26
$\|F_{\text{max}}\|$	0.1157	0.1117	0.1004	0.1120	0.1160

Next, we consider the amount of σ electrons being emitted for different relative phases. **Figure 6A,B** provide an overview over the time-dependent occupations of the respective orbitals for ϕ = 0° and 180°. Overviews of other phases are provided in the SM. It should be noted that the π orbitals are doubly degenerate. We can read from **Figure 6** and **Table 1** that the number of electrons emitted from σ orbitals n_σ is 0.40 for $\phi = 0°$, while $n_\sigma = 0.38$ for ϕ = 180°. Emission of σ electrons corresponds to a depopulation of the 9σ and 8σ orbitals, which leads, together with the also very pronounced depopulation of the 3π orbitals, to a final electron configuration of $(9\sigma)^{-1}(3\pi)^{-1}$ and $(8\sigma)^{-1}(3\pi)^{-1}$, and thus to the $1^1\Pi$, $1^3\Pi$, $2^1\Pi$, and $2^3\Pi$ states. These states feature a small barrier towards dissociation into $OC^+ + S^+$ (**Figure 2A**). Thus, upon pronounced ionization of σ orbitals, the dication ultimately fragments into $OC^+ + S^+$. As a side notice, fragmentation of these electronic states into the $O^+ + CS^+$ channel is less likely, as the barrier towards dissociation is still around 2 eV (see also **Figure 2B**). This explains the difference of the yields between the channels observed in the experiment, and also why the main peaks at 5 eV in the two different fragment channels follow the same phase dependence (green line in **Figure 3C** and purple line in (f)).

The rtTDDFT calculations also provide another possible post-ionization origin to explain the shoulder peak in the $OC^+ + S^+$ channel: taking a closer look again on the population dynamics in **Figure 6A**, we observe a strong mixing between the 9σ and 8σ orbitals for $\phi = 0^\circ$. This can be traced back, because the $2^1\Pi$ and $2^3\Pi$ states (corresponding to ionization from 8σ) are, at the equilibrium structure of the neutral OCS, only about 2 eV above the $1^1\Pi$ and $1^3\Pi$ states (corresponding to ionization from 9σ, see **Figure 2**). As can be gathered from the time-dependent populations in **Figure 6**, mixing of these states starts around $t = 70$ fs and continues up to 100 fs, a time well after the maximum of the electric field and also after the main ionization event between $t = 60$–80 fs. This state mixing after the main ionization events provides another strong indication for post-ionization dynamics. **Figure 2** shows that at slightly stretched geometries ($R = 3.5$ a. u.), the pairs of the two mixing states, $1^3\Pi$ and $2^3\Pi$, or $1^1\Pi$ and $2^1\Pi$, come energetically very close and the efficiency of population transfer can be expected to further increase at the wing of the pulse compared to the rtTDDFT calculations, which do not take such stretching into account. This is similar to the strong coupling of the σ_g and σ_u states in H_2^+ at a bond distance larger than the equilibrium geometry (Kling et al., 2006; Roudnev and Esry, 2007; Ray et al., 2009; Znakovskaya et al., 2012; Wanie et al., 2016; Ibrahim et al., 2018). This "late" population transfer is expected to lead to fragments with smaller kinetic energies, around 3–4 eV. Post-ionization interactions, such as electron recollisional excitation, potential deformation, and population transfer, would contribute to the shoulder peak and the competitions of these effects determine the effective phase dependence. We have therefore demonstrated here post-ionization interactions of heavy polar molecules in both experiment and calculation.

Since the rtTDDFT calculations already strongly suggested the contribution of several excited states, we performed separate semi-classical surface-hopping calculations, in order to trace possible post-ionization dynamics beyond the fixed-nuclei approximation. As outlined in **Section 2.2.2**, in these calculations, the electronic states are calculated on-the-fly with the quantum chemical program package OpenMolcas including the two-color laser field, while the nuclei are treated classically.

We have investigated the following initial conditions upon double ionization: 1) all trajectories are launched in the electronic ground state of the dication, $X^3\Sigma^-$; 2) all trajectories start initially in the excited state $1^3\Pi$ ($(9\sigma)^{-1}(3\pi)^{-1}$), as suggested by rtTDDFT.

Our calculations show that for (i), double ionization occurring to the electronic ground state of the dication, none of the trajectories showed dissociation during the calculation time. These results will not be discussed any more in what follows. For (ii), ionization into the excited electronic state of OCS^{2+*}, several pathways were identified for a relative phase of $\phi = 0^\circ$, leading to break up into $OC^+ + S^+$ (4 of 20 trajectories), $O^+ + CS^+$ (5 of 20 trajectories), and $[O+ C + S]^{2+}$ (11 of 20 trajectories), the latter one being not visible experimentally. Similar values concerning the relative number of trajectories are obtained for the other relative phases of the two-color field. When looking at the population dynamics, we gather a complex behavior for all cases, including population transfer between several excited electronic states (see also **Figure 7** for representative trajectories). Changes in the relative phase of the two-color field lead to changes in the ratio between the population of the electronic states. With these trajectories at hand, we focus on the $OC^+ + S^+$ channel and the question concerning the shoulder peak. In our calculations, we identify for this break-up channel trajectories which would end up at higher KER (> 5 eV), as well as a substantial number of trajectories ending up at lower KER (< 5 eV). **Figure 7** shows the population dynamics of two representative trajectories; panel A) displays the population dynamics of a trajectory leading to fragmentation at higher KER corresponding to the main peak of the $OC^+ + S^+$ channel. Panel B) shows the respective scenario for a trajectory leading to fragmentation at lower KER. Panel C) shows the population dynamics of a trajectory leading to the $O^+ + CS^+$ channel. We can see that the dissociation leading to higher KERs (main peak) proceeds either directly from the $(9\sigma)^{-1}(3\pi)^{-1}$ state (green line) or involves the mixed-character $(2\pi)^{-0.4}(3\pi)^{-2.6}(4\pi^*)^1$ state (red line), while the dissociation leading to lower KERs (shoulder peak) proceeds with pronounced coupling to the $(2\pi)^{-1}(3\pi)^{-1}$ state (orange line). Moreover, the dynamics involving population transfer seems to occur at later times. Or, in other words, the dynamics associated to the shoulder peak at low KER seems to proceed slower and it takes slightly longer to achieve the same C–S elongation. Thus, our semi-classical surface-hopping calculations emphasize the importance of post-ionization population dynamics.

3.5 Control of the Branching Ratio

To discuss the effects of post-ionization interactions from another point of view, the inter-channel branching ratio between the OC^+ and the O^+ fragments is defined as

$$B(\phi) = \frac{Y_{+,O^+}(\phi)}{Y_{+,OC^+}(\phi)}, \tag{4}$$

where Y_{+,OC^+} and Y_{+,O^+} are the OC^+ and O^+ fragment yields with positive momentum along the laser polarization direction, respectively. The fragment yields are evaluated in the same way as Y_+ in **Eq. (3)**, but integrated over the entire KER range. Those fragments were detected by ion-ion coincidence measurements, as in the previous sections. In other words, this parameter compares the yields of OC^+ and the O^+ fragments ejected to the same direction and evaluates whether the O–C or the C–S bond is preferentially broken in the dication. The branching ratio is shown as a function of the relative phase in **Figure 8**. The total peak intensity $I_{\omega+2\omega} =$

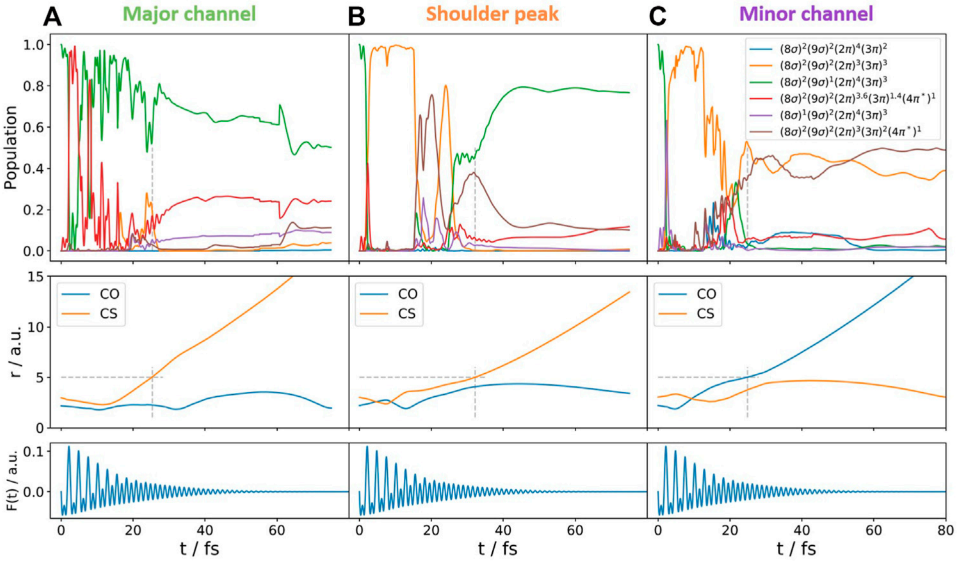

FIGURE 7 | Quantum amplitudes (in the limit of infinite trajectories, this would correspond to populations) of different excited states (top), bond length C-O and C-S (middle), and the temporal shapes of the applied electric fields (bottom) during the dissociation of selected trajectories. These represent typical trajectories following **(A,B)** the $OC^+ + S^+$ channel and **(C)** the $O^+ + CS^+$ channel. A KER > 5 eV **(A)** is associated with the main peak of the $OC^+ + S^+$ channel in the experiment, while a KER < 4.5 eV **(B)** is attributed to the shoulder peak. The KERs at the end of these specific trajectories correspond to 7.9 eV **(A)**, 3.9 eV **(B)**, and 5.8 eV **(C)**. Dashed gray lines indicate the time when the (arbitrarily chosen) value of $r = 5$ a. u. is reached. We note that such dissociation is reached at a later time for the shoulder peak compared to the main peak; another strong indication for post-ionization dynamics.

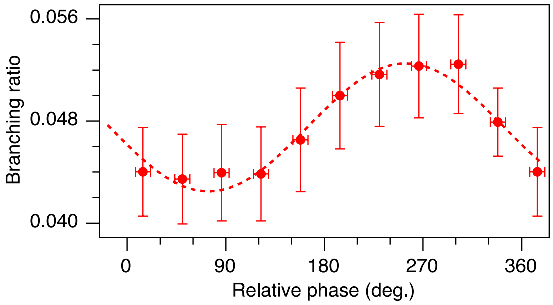

FIGURE 8 | Inter-channel branching ratio between the OC^+ and the O^+ fragments ejected to the same direction as a function of the relative phase at a total peak intensity of 2×10^{14} W/cm^2 and a ratio $\alpha = 0.14$. Red circles correspond to experimental data points, the dotted line is a sine fit.

2×10^{14} W/cm^2 is the same as in **Figure 3**, but the intensity ratio, $\alpha = 0.14$, is smaller. The branching ratio shows a clear 2π-oscillation with a modulation depth of 11%. This oscillation indicates that the O–C bond-breaking is more likely to occur at 255° than at 75°. As discussed above, we consider NSDI to be the dominant process in the present experimental conditions. Moreover, we could exclude contributions of bond stretching in neutral states because such effects are not observed even in higher intensity laser fields (Ma et al., 2019). Therefore, the origin of this phase dependence can be attributed to post-ionization interaction rather than to the ionization step. Dissociation from the $2^3\Pi$ state would enhance the C–S bond breaking due to a smaller potential barrier of the $2^3\Pi$ state compared to the $1^3\Pi$ state along this bond and almost similar potential barriers of these states along the C–O bond. Therefore, the C–S bond breaking is more likely to occur and the branching ratio decreases when population transfers from the $1^3\Pi$ state to the $2^3\Pi$ state or electron recollisional excitation to the $2^3\Pi$ state occurs. In two-color laser fields, the recolliding electron energy has minimum and maximum values at relative phases of around 25° and 110°, so the population distribution in the doubly charged states would depend on the relative phase as well as on the dynamics after the ionization. In the rtTDDFT calculations, 8σ occupations, which correspond to populating the $2^3\Pi$ state at the end of the simulation, show a clear phase dependence. Thus, this population transfer scenario can explain both the observation of the shoulder peak and the phase dependencies of the asymmetry parameters and the branching ratio.

We have thus demonstrated the selective bond scission of polar molecules by changing the relative phase of phase-locked two-color intense laser fields and attributed the origin of such selectivity to post-ionization interactions.

4 CONCLUSION

To summarize, we have investigated the Coulomb explosion of the polar molecule OCS in phase-locked two-color intense laser fields. A clear 2π-oscillation was observed in both the $OC^+ + S^+$ and $O^+ + CS^+$ channels. We have succeeded in the observation of a shoulder peak that has not been discovered previously, because it is a dark channel for synchrotron radiation that opens however up due to strong light-matter interactions in intense laser fields. In the $OC^+ + S^+$ channel, a clear dependency of the asymmetry on the kinetic energy was found due to this dissociation pathway. The phase shift of 270° between both sub-channels of $OC^+ + S^+$ is attributed to a population transfer between the involved electronic states in the applied intense laser fields as demonstrated by rtTDDFT calculations. In addition, the inter-channel branching ratio (when breaking the C–O and C–S bonds oriented to the same direction with respect to the laser polarization direction) also oscillated with 2π, depending on the relative phase. The selective scission of chemical bonds in polar molecules has been demonstrated by using a simple pulse shaping technique. Here presented results indicate that not only the ionization step, but also post-ionization interactions play important roles even for heavy polar molecules, where the anisotropy of the fragments is mainly dominated by tunneling ionization. Two-color phase-locked laser fields provide a variety of controllable parameters, such as the total intensity, the intensity ratio, the relative phase and the polarization, while not involving a complex experimental implementation. This approach is therefore useful to investigate the mechanisms of coherent reaction control for a wide variety of molecular systems by tailored intense laser fields.

DATA AVAILABILITY STATEMENT

The raw data supporting the conclusions of this article will be made available by the authors, without undue reservation.

AUTHOR CONTRIBUTIONS

TE performed all experiments and data analysis. FL was responsible for the ALLS facility at INRS in Canada. KMZ, MR, FF, and SG performed all simulations. AH, FL, SG, TE, and HI discussed results. HI conceived and directed the project, supervised experiments, and analyzed data. TE, SG, and HI wrote the original draft. All authors contributed to the discussions of the results and to the production of the manuscript.

FUNDING

We sincerely thank the Canada Foundation for Innovation, NSERC and FRQNT. TE and AH acknowledges support from the JSPS Program for Advancing Strategic International Networks to Accelerate the Circulation of Talented Researchers (S2602). FF and SG highly acknowledge support by the German Science Foundation (DFG) provided via the International Research Training Group (IRTG 2101) “Guided Light, Tightly Packed”. MR and SG highly acknowledge support from the European Research Council via the Consolidator Grant QUEM-CHEM (772676). KMZ and SG are part of the Max Planck School of Photonics supported by BMBF, Max Planck Society, and Fraunhofer Society.

ACKNOWLEDGMENTS

We thank Philippe Lassonde for technical support, as well as Dr. Benji Wales and Prof. Joseph Sanderson for providing the analysis software for the CEI measurement files.

SUPPLEMENTARY MATERIAL

The Supplementary Material for this article can be found online at: https://www.frontiersin.org/articles/10.3389/fchem.2022.859750/full#supplementary-material

REFERENCES

Alnaser, A. S., Kübel, M., Siemering, R., Bergues, B., Kling, N. G., Betsch, K. J., et al. (2014). Subfemtosecond Steering of Hydrocarbon Deprotonation through Superposition of Vibrational Modes. *Nat. Commun.* 5, 3800. doi:10.1038/ncomms4800

Alnaser, A. S., and Litvinyuk, I. V. (2017). Subfemtosecond Directional Control of Chemical Processes in Molecules. *J. Phys. B: Mol. Opt. Phys.* 50, 032002. doi:10.1088/1361-6455/50/3/032002

Andrade, X., Alberdi-Rodriguez, J., Strubbe, D. A., Oliveira, M. J. T., Nogueira, F., Castro, A., et al. (2012). Time-dependent Density-Functional Theory in Massively Parallel Computer Architectures: the octopus Project. *J. Phys. Condens. Matter* 24, 233202. doi:10.1088/0953-8984/24/23/233202

Aquilante, F., Autschbach, J., Carlson, R. K., Chibotaru, L. F., Delcey, M. G., De Vico, L., et al. (2016). Molcas 8: New Capabilities for Multiconfigurational Quantum Chemical Calculations across the Periodic Table. *J. Comput. Chem.* 37, 506–541. doi:10.1002/jcc.24221

Assion, A., Baumert, T., Bergt, M., Brixner, T., Kiefer, B., Seyfried, V., et al. (1998). Control of Chemical Reactions by Feedback-Optimized Phase-Shaped Femtosecond Laser Pulses. *Science* 282, 919–922. doi:10.1126/science.282.5390.919

Bergt, M., Brixner, T., Kiefer, B., Strehle, M., and Gerber, G. (1999). Controlling the Femtochemistry of Fe(CO)5. *J. Phys. Chem. A.* 103, 10381–10387. doi:10.1021/jp992541k

Brites, V., Eland, J. H. D., and Hochlaf, M. (2008). $OCS2^+$ Dication Spectroscopy and Electronic States. *Chem. Phys.* 346, 23–33. doi:10.1016/j.chemphys.2007.11.009

Brixner, T., Kiefer, B., and Gerber, G. (2001). Problem Complexity in Femtosecond Quantum Control. *Chem. Phys.* 267, 241–246. doi:10.1016/S0301-0104(01)00223-3

Brumer, P., and Shapiro, M. (1986). Control of Unimolecular Reactions Using Coherent Light. *Chem. Phys. Lett.* 126, 541–546. doi:10.1016/S0009-2614(86)80171-3

Bryan, W. A., Newell, W. R., Sanderson, J. H., and Langley, A. J. (2006). Observation of Multiple Ionization Pathways for OCS in an Intense Laser Field Resolved by Three-Dimensional Covariance Mapping and Visualized by Hierarchical Ionization Topology. *Phys. Rev. A.* 74, 053409. doi:10.1103/physreva.74.053409

Cardoza, D., Baertschy, M., and Weinacht, T. (2005). Understanding Learning Control of Molecular Fragmentation. *Chem. Phys. Lett.* 411, 311–315. doi:10.1016/j.cplett.2005.06.044

Dimitrovski, D., Abu-samha, M., Madsen, L. B., Filsinger, F., Meijer, G., Küpper, J., et al. (2011). Ionization of Oriented Carbonyl Sulfide Molecules by Intense Circularly Polarized Laser Pulses. *Phys. Rev. A.* 83, 023405. doi:10.1103/physreva.83.023405

Doblhoff-Dier, K., Kitzler, M., and Gräfe, S. (2016). Theoretical Investigation of Alignment-dependent Intense-Field Fragmentation of Acetylene. *Phys. Rev. A.* 94, 013405. doi:10.1103/PhysRevA.94.013405

Endo, T., Fujise, H., Hasegawa, H., Matsuda, A., Fushitani, M., Tolstikhin, O. I., et al. (2019). Angle Dependence of Dissociative Tunneling Ionization of NO in Asymmetric Two-Color Intense Laser fields. *Phys. Rev. A.* 100, 053422. doi:10.1103/PhysRevA.100.053422

Endo, T., Fujise, H., Kawachi, Y., Ishihara, A., Matsuda, A., Fushitani, M., et al. (2017). Selective Bond Breaking of CO_2 in Phase-Locked Two-Color Intense Laser fields: Laser Field Intensity Dependence. *Phys. Chem. Chem. Phys.* 19, 3550–3556. doi:10.1039/C6CP07471E

Endo, T., Fujise, H., Matsuda, A., Fushitani, M., Kono, H., and Hishikawa, A. (2016). Coincidence Momentum Imaging of Asymmetric Coulomb Explosion of CO_2 in Phase-Locked Two-Color Intense Laser fields. *J. Electron Spectrosc. Relat. Phenomena* 207, 50–54. doi:10.1016/j.elspec.2015.12.010

Endo, T., Neville, S. P., Wanie, V., Beaulieu, S., Qu, C., Deschamps, J., et al. (2020). Capturing Roaming Molecular Fragments in Real Time. *Science* 370, 1072–1077. doi:10.1126/science.abc2960

Godbout, N., Salahub, D. R., Andzelm, J., and Wimmer, E. (1992). Optimization of Gaussian-type Basis Sets for Local Spin Density Functional Calculations. Part I. Boron through Neon, Optimization Technique and Validation. *Can. J. Chem.* 70, 560–571. doi:10.1139/v92-079

Gräfe, S., Meier, C., and Engel, V. (2005). Instantaneous Dynamics and Quantum Control fields: Principle and Numerical Applications. *J. Chem. Phys.* 122, 184103. doi:10.1063/1.1891728

Hasegawa, H., Walmsley, T., Matsuda, A., Morishita, T., Madsen, L. B., Jensen, F., et al. (2022). Asymmetric Dissociative Ionization of Tetrafluoromethane in ω-2ω Intense Laser fields. *Front. Chem.*. doi:10.3389/fchem.2022.857863

Holmegaard, L., Hansen, J. L., Kalhøj, L., Louise Kragh, S., Stapelfeldt, H., Filsinger, F., et al. (2010). Photoelectron Angular Distributions from strong-field Ionization of Oriented Molecules. *Nat. Phys* 6, 428–432. doi:10.1038/nphys1666

Ibrahim, H., Héjjas, M., Fushitani, M., and Schwentner, N. (2009a). Phase Sensitive Control of Vibronic Guest–Host Interaction: Br_2 in Ar Matrix. *J. Phys. Chem. A.* 113, 7439–7450. doi:10.1021/jp900287m

Ibrahim, H., Héjjas, M., and Schwentner, N. (2009b). Tracing, Amplifying, and Steering Chromophore-Bath Coherences by Ultrashort Pulse Trains. *Phys. Rev. Lett.* 102, 088301. doi:10.1103/PhysRevLett.102.088301

Ibrahim, H., Lefebvre, C., Bandrauk, A. D., Staudte, A., and Légaré, F. (2018). H2: the Benchmark Molecule for Ultrafast Science and Technologies. *J. Phys. B: Mol. Opt. Phys.* 51, 042002. doi:10.1088/1361-6455/aaa192

Kane, D. J., and Trebino, R. (1993). Characterization of Arbitrary Femtosecond Pulses Using Frequency-Resolved Optical Gating. *IEEE J. Quan. Electron.* 29, 571–579. doi:10.1109/3.199311

Kaneyasu, T., Ito, M., Soejima, K., Hikosaka, Y., and Shigemasa, E. (2015). Site-specific Formation of Metastable OCS^{2+}studied by Auger-Electron-Ion Coincidence Method. *J. Phys. B: Mol. Opt. Phys.* 48, 125101. doi:10.1088/0953-4075/48/12/125101

Karamatskos, E. T., Raabe, S., Mullins, T., Trabattoni, A., Stammer, P., Goldsztejn, G., et al. (2019). Molecular Movie of Ultrafast Coherent Rotational Dynamics of Ocs. *Nat. Commun.* 10, 3364. doi:10.1038/s41467-019-11122-y

Kling, M. F., Siedschlag, C., Verhoef, A. J., Khan, J. I., Schultze, M., Uphues, T., et al. (2006). Control of Electron Localization in Molecular Dissociation. *Science* 312, 246–248. doi:10.1126/science.1126259

Kotur, M., Weinacht, T., Pearson, B. J., and Matsika, S. (2009). Closed-loop Learning Control of Isomerization Using Shaped Ultrafast Laser Pulses in the Deep Ultraviolet. *J. Chem. Phys.* 130, 134311. doi:10.1063/1.3103486

Kowalewski, M., and Seeber, P. (2022). Sustainable Packaging of Quantum Chemistry Software with the Nix Package Manager. *Int. J. Quan. Chem.* doi:10.1002/qua.26872

Langford, M. L., Harris, F. M., Reid, C. J., Ballantine, J. A., and Parry, D. E. (1991). Triplet-state Energy Levels of $CO_2{}^{+2}$, COS^{2+} and CS^{2+}. *Chem. Phys.* 149, 445–457. doi:10.1016/0301-0104(91)90044-T

Levis, R. J., Menkir, G. M., and Rabitz, H. (2001). Selective Bond Dissociation and Rearrangement with Optimally Tailored, strong-field Laser Pulses. *Science* 292, 709–713. doi:10.1126/science.1059133

Li, H., Ray, D., De, S., Znakovskaya, I., Cao, W., Laurent, G., et al. (2011). Orientation Dependence of the Ionization of CO and NO in an Intense Femtosecond Two-Color Laser Field. *Phys. Rev. A.* 84, 043429. doi:10.1103/PhysRevA.84.043429

Li, H., Tong, X. M., Schirmel, N., Urbasch, G., Betsch, K. J., Zherebtsov, S., et al. (2016). Intensity Dependence of the Dissociative Ionization of DCl in Few-Cycle Laser fields. *J. Phys. B: Mol. Opt. Phys.* 49, 015601. doi:10.1088/0953-4075/49/1/015601

Ma, P., Wang, C., Luo, S., Li, X., Hu, W., Yu, J., et al. (2019). Bond-breakage-dependent Dissociative Ionization of an Asymmetric Molecule in an Intense Femtosecond Laser Field. *Phys. Rev. A.* 99, 023423. doi:10.1103/physreva.99.023423

Mai, S., Marquetand, P., and González, L. (2018). Nonadiabatic Dynamics: The SHARC Approach. *Wires Comput. Mol. Sci.* 8, e1370. doi:10.1002/wcms.1370

Malinovsky, V. S., Meier, C., and Tannor, D. J. (1997). Optical Paralysis in Electronically Congested Systems: Application to Large-Amplitude Vibrational Motion of Ground State Na_2. *Chem. Phys.* 221, 67–76. doi:10.1016/s0301-0104(97)00126-2

Masuoka, T., and Koyano, I. (1991). Dissociative Single, Double, and Triple Photoionization of OCS in the Region hν=20-100 eV Studied by Mass Spectrometry and the Photoion-Photoion Coincidence Method. *J. Chem. Phys.* 95, 909–917. doi:10.1063/1.461099

Masuoka, T., Koyano, I., and Saito, N. (1992). Kinetic-energy Release in the Dissociative Double Photoionization of OCS. *J. Chem. Phys.* 97, 2392–2399. doi:10.1063/1.463078

Miura, S., Ando, T., Ootaka, K., Iwasaki, A., Xu, H., Okino, T., et al. (2014). Carrier-envelope-phase Dependence of Asymmetric C D Bond Breaking in C_2D_2 in an Intense Few-Cycle Laser Field. *Chem. Phys. Lett.* 595-596, 61–66. doi:10.1016/j.cplett.2014.01.045

NixOS (2021). *Nixpkgs 21.05 Manual*. Available at: https://nixos.org/manual/nixpkgs/stable/(Accessed December 29, 2021).

Ohmura, H., Saito, N., and Morishita, T. (2014). Molecular Tunneling Ionization of the Carbonyl Sulfide Molecule by Double-Frequency Phase-Controlled Laser fields. *Phys. Rev. A.* 89, 013405. doi:10.1103/PhysRevA.89.013405

Ohmura, H., and Tachiya, M. (2008). Robust Quantum Control of Molecular Tunneling Ionization in the Space Domain by Phase-Controlled Laser fields. *Phys. Rev. A.* 77, 023408. doi:10.1103/PhysRevA.77.023408

Ohmura, H., Yoshida, T., and Saito, N. (2019). Four-mode Multi-Selection in the Dual Phase Control of a Molecular Ionization Induced by Fourier-Synthesized Laser fields. *Appl. Phys. Lett.* 114, 054101. doi:10.1063/1.5082578

Rabitz, H. (2006). Strong-arming Molecular Dynamics. *Science* 314, 264–265. doi:10.1126/science.1134083

Ray, D., He, F., De, S., Cao, W., Mashiko, H., Ranitovic, P., et al. (2009). Ion-Energy Dependence of Asymmetric Dissociation of D_2 by a Two-Color Laser Field. *Phys. Rev. Lett.* 103, 223201. doi:10.1103/PhysRevLett.103.223201

Richter, M., Marquetand, P., González-Vázquez, J., Sola, I., and González, L. (2011). SHARC: Ab Initio Molecular Dynamics with Surface Hopping in the Adiabatic Representation Including Arbitrary Couplings. *J. Chem. Theor. Comput.* 7, 1253–1258. doi:10.1021/ct1007394

Ridard, J., Levy, B., and Millié, P. (1988). Theoretical Investigation of the Dissociation of OCS^{2+} in the Process $OCS(X^1\Sigma^+) + h\nu \rightarrow OCS^{2+} \rightarrow CO^+ (X^2\Sigma^+) + S^+ (^4S)$. *Chem. Phys.* 122, 403–412. doi:10.1016/0301-0104(88)80022-3

Roos, B. O., Taylor, P. R., and Sigbahn, P. E. M. (1980). A Complete Active Space SCF Method (CASSCF) Using a Density Matrix Formulated Super-CI Approach. *Chem. Phys.* 48, 157–173. doi:10.1016/0301-0104(80)80045-0

Roudnev, V., and Esry, B. D. (2007). General Theory of Carrier-Envelope Phase Effects. *Phys. Rev. Lett.* 99, 220406. doi:10.1103/PhysRevLett.99.220406

Sato, Y., Kono, H., Koseki, S., and Fujimura, Y. (2003). Description of Molecular Dynamics in Intense Laser Fields by the Time-dependent Adiabatic State Approach: Application to Simultaneous Two-Bond Dissociation of CO_2 and its Control. *J. Am. Chem. Soc.* 125, 8019–8031. doi:10.1021/ja0344819

Schmidt, B. E., Unrau, W., Mirabal, A., Li, S., Krenz, M., Wöste, L., et al. (2008). Poor Man's Source for Sub 7 Fs: a Simple Route to Ultrashort Laser Pulses and Their Full Characterization. *Opt. Express* 16, 18910–18921. doi:10.1364/OE.16.018910

Shen, Z., Yan, Y., Cheng, J., Shuang, F., Zhao, Y., and He, G. (1999). Pump-dump Control and the Related Transient Absorption Spectroscopies. *J. Chem. Phys.* 110, 7192–7201. doi:10.1063/1.478623

Song, Q., Gong, X., Ji, Q., Lin, K., Pan, H., Ding, J., et al. (2015). Directional Deprotonation Ionization of Acetylene in Asymmetric Two-Color Laser fields. *J. Phys. B: Mol. Opt. Phys.* 48, 094007. doi:10.1088/0953-4075/48/9/094007

Tancogne-Dejean, N., Oliveira, M. J. T., Andrade, X., Appel, H., Borca, C. H., Le Breton, G., et al. (2020). Octopus, a Computational Framework for Exploring Light-Driven Phenomena and Quantum Dynamics in Extended and Finite Systems. *J. Chem. Phys.* 152, 124119. doi:10.1063/1.5142502

Tannor, D. J., and Rice, S. A. (1985). Control of Selectivity of Chemical Reaction via Control of Wave Packet Evolution. *J. Chem. Phys.* 83, 5013–5018. doi:10.1063/1.449767

Wales, B., Bisson, É., Karimi, R., Beaulieu, S., Ramadhan, A., Giguère, M., et al. (2014). Coulomb Imaging of the Concerted and Stepwise Break up Processes of Ocs Ions in Intense Femtosecond Laser Radiation. *J. Electron Spectrosc. Relat. Phenomena* 195, 332–336. doi:10.1016/j.elspec.2014.05.003

Wales, B., Bisson, E., Karimi, R., Kieffer, J.-C., Légaré, F., and Sanderson, J. (2012). A Coincidence Detection Algorithm for Improving Detection Rates in Coulomb Explosion Imaging. *Nucl. Instr. Methods Phys. Res. Section A: Acc. Spectrometers, Detectors Associated Equipment* 667, 11–15. doi:10.1016/j.nima.2011.11.082

Wang, X., Bersohn, R., Takahashi, K., Kawasaki, M., and Kim, H. L. (1996). Phase Control of Absorption in Large Polyatomic Molecules. *J. Chem. Phys.* 105, 2992–2997. doi:10.1063/1.472172

Wanie, V., Ibrahim, H., Beaulieu, S., Thiré, N., Schmidt, B. E., Deng, Y., et al. (2016). Coherent Control of D_2/H_2 dissociative Ionization by a Mid-infrared Two-Color Laser Field. *J. Phys. B: Mol. Opt. Phys.* 49, 025601. doi:10.1088/0953-4075/49/2/025601

Wells, E., Todt, M., Jochim, B., Gregerson, N., Averin, R., Wells, N. G., et al. (2009). Examining the Feedback Signals Used in Closed-Loop Control of Intense Laser Fragmentation of CO^+. *Phys. Rev. A.* 80, 063402. doi:10.1103/PhysRevA.80.063402

Wu, J., Schmidt, L. P. H., Kunitski, M., Meckel, M., Voss, S., Sann, H., et al. (2012). Multiorbital Tunneling Ionization of the CO Molecule. *Phys. Rev. Lett.* 108, 183001. doi:10.1103/PhysRevLett.108.183001

Wustelt, P., Oppermann, F., Yue, L., Möller, M., Stöhlker, T., Lein, M., et al. (2018). Heteronuclear Limit of Strong-Field Ionization: Fragmentation of HeH^+ by Intense Ultrashort Laser Pulses. *Phys. Rev. Lett.* 121, 073203. doi:10.1103/PhysRevLett.121.073203

Xie, X., Doblhoff-Dier, K., Roither, S., Schöffler, M. S., Kartashov, D., Xu, H., et al. (2012). Attosecond-recollision-controlled Selective Fragmentation of Polyatomic Molecules. *Phys. Rev. Lett.* 109, 243001–243005. doi:10.1103/PhysRevLett.109.243001

Xie, X., Doblhoff-Dier, K., Xu, H., Roither, S., Schöffler, M. S., Kartashov, D., et al. (2014). Selective Control over Fragmentation Reactions in Polyatomic Molecules Using Impulsive Laser Alignment. *Phys. Rev. Lett.* 112, 163003. doi:10.1103/PhysRevLett.112.163003

Xu, Q.-y., Ben, S., Sun, Y., Xu, H.-f., Liu, X.-s., Lv, H., et al. (2020). Non-sequential Double Ionization of Triatomic Molecules OCS in Intense Laser fields. *Chem. Phys. Lett.* 747, 137326. doi:10.1016/j.cplett.2020.137326

Yue, L., Wustelt, P., Sayler, A. M., Oppermann, F., Lein, M., Paulus, G. G., et al. (2018). Strong-field Polarizability-Enhanced Dissociative Ionization. *Phys. Rev. A.* 98, 043418. doi:10.1103/PhysRevA.98.043418

Zhao, X., Xu, T., Yu, X., Ren, D., Zhang, X., Li, X., et al. (2021). Tracking the Nuclear Movement of the Carbonyl Sulfide Cation after strong-field Ionization by Time-Resolved Coulomb-Explosion Imaging. *Phys. Rev. A.* 103, 053103. doi:10.1103/PhysRevA.103.053103

Znakovskaya, I., von den Hoff, P., Marcus, G., Zherebtsov, S., Bergues, B., Gu, X., et al. (2012). Subcycle Controlled Charge-Directed Reactivity with Few-Cycle Midinfrared Pulses. *Phys. Rev. Lett.* 108, 063002. doi:10.1103/PhysRevLett.108.063002

Conflict of Interest: The authors declare that the research was conducted in the absence of any commercial or financial relationships that could be construed as a potential conflict of interest.

frontiers | Frontiers in Chemistry

ORIGINAL RESEARCH
published: 14 April 2022
doi: 10.3389/fchem.2022.857863

Asymmetric Dissociative Tunneling Ionization of Tetrafluoromethane in $\omega - 2\omega$ Intense Laser Fields

Hiroka Hasegawa[1], Tiffany Walmsley[1,2], Akitaka Matsuda[1], Toru Morishita[3], Lars Bojer Madsen[4], Frank Jensen[5], Oleg I. Tolstikhin[6] and Akiyoshi Hishikawa[1,7]*

[1]Graduate School of Science, Nagoya University, Nagoya, Japan, [2]School of Chemistry, University of Edinburgh, Edinburgh, United Kingdom, [3]Institute for Advanced Science, The University of Electro-Communications, Chofu-shi, Tokyo, Japan, [4]Department of Physics and Astronomy, Aarhus University, Aarhus, Denmark, [5]Department of Chemistry, Aarhus University, Aarhus, Denmark, [6]Moscow Institute of Physics and Technology, Dolgoprudny, Russia, [7]Research Center for Materials Science, Nagoya University, Nagoya, Japan

Dissociative ionization of tetrafluoromethane (CF_4) in linearly polarized ω-2ω ultrashort intense laser fields (1.4×10^{14} W/cm^2, 800 and 400 nm) has been investigated by three-dimensional momentum ion imaging. The spatial distribution of CF_3^+ produced by $CF_4 \rightarrow CF_3^+ + F + e^-$ exhibited a clear asymmetry with respect to the laser polarization direction. The degree of the asymmetry varies by the relative phase of the ω and 2ω laser fields, showing that 1) the breaking of the four equivalent C-F bonds can be manipulated by the laser pulse shape and 2) the C-F bond directed along the larger amplitude side of the ω-2ω electric fields tends to be broken. Weak-field asymptotic theory (WFAT) shows that the tunneling ionization from the $4t_2$ second highest-occupied molecular orbital (HOMO-1) surpasses that from the $1t_1$ HOMO. This predicts the enhancement of the tunneling ionization with electric fields pointing from F to C, in the direction opposite to that observed for the asymmetric fragment ejection. Possible mechanisms involved in the asymmetric dissociative ionization, such as post-ionization interactions, are discussed.

Keywords: coherent control, intense laser fields, tunneling ionization, molecular dissociation, tetrafluoromethane

Edited by:
Yuichi Fujimura,
Tohoku University, Japan

Reviewed by:
Hideki Ohmura,
National Institute of Advanced Industrial Science and Technology (AIST), Japan
Hirohiko Kono,
Tohoku University, Japan

***Correspondence:**
Akiyoshi Hishikawa
hishi@chem.nagoya-u.ac.jp

Specialty section:
This article was submitted to Physical Chemistry and Chemical Physics,
a section of the journal Frontiers in Chemistry

Received: *19 January 2022*
Accepted: *22 February 2022*
Published: *14 April 2022*

Citation:
Hasegawa H, Walmsley T, Matsuda A, Morishita T, Madsen LB, Jensen F, Tolstikhin OI and Hishikawa A (2022) Asymmetric Dissociative Tunneling Ionization of Tetrafluoromethane in ω − 2ω Intense Laser Fields. Front. Chem. 10:857863. doi: 10.3389/fchem.2022.857863

1 INTRODUCTION

Shaped intense laser fields with a field intensity of ~ 10^{14} W/cm^2 have attracted considerable attention in the last decades for their capability to manipulate ultrafast electronic and nuclear dynamics of atoms, molecules, and solids. Armed with the electric field exerting a force on the electrons comparable to that of the Coulomb potential in a molecule, shaped laser pulses enable us to drive electrons in a nonperturbative manner to exploit unique properties from the targets. The application has been demonstrated in controls of high-order harmonic generation (Bartels et al., 2000; Pfeifer et al., 2005; Winterfeldt et al., 2008), photoemission (Bardeen et al., 1997; Wollenhaupt and Baumert, 2011; Eickhoff et al., 2021), and chemical reactions (Levis et al., 2001; Assion et al., 1998; Levis and Rabitz, 2002; Hishikawa et al., 2020).

Laser pulse shaping can be accomplished by a spatial amplitude and phase modulator placed on a Fourier transform plane in a 4*f* setup (Bardeen et al., 1997; Levis et al., 2001; Assion et al., 1998; Eickhoff et al., 2021). Alternatively, one can synthesize the laser waveform by coherent superposition of pulses with different colors (Chan et al., 2011; Manzoni et al., 2015), which has been used to control high harmonic generation (Takahashi et al., 2010; Neyra et al., 2018) and multiphoton and tunneling ionization of atoms and molecules (Eickhoff et al., 2021; Ohmura and Saito, 2020; Ohmura et al., 2021). Among others, the ω-2ω laser fields, consisting of the fundamental and the second harmonics, have been

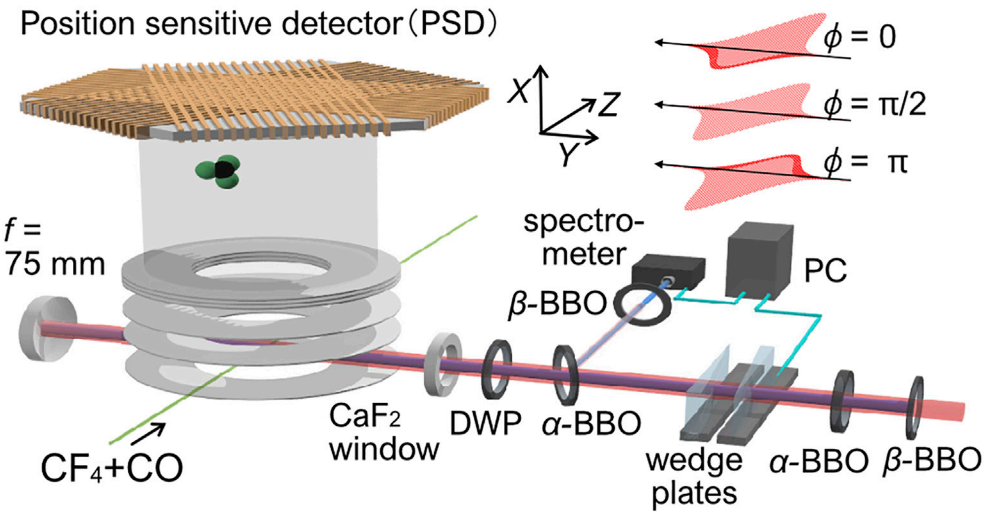

FIGURE 1 | Schematic of the experimental setup. The output from a Ti: Sapphire regenerative laser amplifier system (800 nm, 1 kHz, 50 fs) was introduced to a β-BBO crystal (type-I) to generate a second-harmonic pulse (400 nm). The time delay between the fundamental (ω) and the second harmonics (2ω) pulse was compensated by two birefringent α-BBO crystals. The two-color relative phase was stabilized by a pair of fused-silica wedge plates controlled by the active feedback locking to the 2ω-2ω interference spectrum. The polarization of the fundamental and the second harmonic pulse was set parallel by a dual-wavelength plate (DWP). For the phase calibration, CO gas is mixed with the sample gas of CF_4.

widely used for understanding the mechanisms of laser tunneling ionization and chemical reaction control in intense laser fields. In the case of linear polarization along the Z direction, the ω-2ω electric fields may be expressed as follows (Endo et al., 2019):

$$\mathbf{F}(t) = F(t)\mathbf{e}_Z, \tag{1}$$

$$F(t) = \bar{F}_\omega(t)\cos(\omega t) + \bar{F}_{2\omega}(t)\cos(2\omega t + \phi), \tag{2}$$

where $\bar{F}_\omega(t)$ and $\bar{F}_{2\omega}(t)$ represent the envelopes of the fundamental and the second harmonic pulses, respectively, and ϕ is the two-color relative phase. The unit vector along the Z-axis is denoted as $\mathbf{e}_Z$. Typical ω-2ω electric fields are illustrated in **Figure 1**, showing that the direction and degree of asymmetry vary by phase ϕ for a given ratio of the ω and 2ω field intensities.

Asymmetric fragment ejection through directional bond-breaking has been observed for various molecules in the ω-2ω intense laser fields. For HD (Sheehy et al., 1995), NO (Endo et al., 2019; Li et al., 2011), CO (Li et al., 2011; Ohmura et al., 2011; Ohmura et al., 2014), OCS (Ohmura et al., 2014; Endo et al., 2022), and CH_3X (X = F, Cl, Br, I) (Ohmura et al., 2006a; Ohmura et al., 2006b; Walt et al., 2015), the directional fragment ejection has been observed. The observed asymmetric distribution of fragment ions is interpreted as a result of orientation-selective tunneling ionization followed by dissociation in intense ω-2ω laser fields. Molecular tunneling ionization has been discussed intensively in the last decade, showing that many of the characteristic properties can be understood in terms of the shape of molecular orbitals (MOs) and their direction of electric dipole moments. Because of the asymmetric MOs and the non-zero dipole moments of the linear heteronuclear molecules mentioned above, tunneling ionization is enhanced in one direction along the molecular axis compared to the other, resulting in orientation-selective ionization.

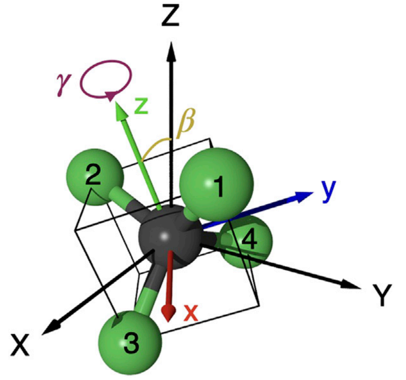

FIGURE 2 | Molecular orientation of CF_4 in the laboratory frame (X, Y, Z), where the polarization direction of the linearly polarized $\omega-2\omega$ laser fields is directed along the Z-axis. The molecular principal axis (C_2 axis) is along the z-axis of the molecular frame (x, y, z). The orientation is specified by the Euler angles (α, β, γ). Because of the axial symmetry around the electric field F one can set α=0 without losing generality.

The asymmetric fragment ejection is also observed with symmetric molecules such as D_2 (Ray et al., 2009; Wanie et al., 2015), H_2O (Kechaoglou et al., 2019), CO_2 (Endo et al., 2016; Endo et al., 2017), and C_2H_2 (Song et al., 2015). For D_2 (Ray et al., 2009; Wanie et al., 2015), electron localization is induced by the coherent superposition of two cationic states through interaction with two kinds of photons of the fundamental and second harmonic, resulting in asymmetric D^+ ejection. For C_2H_2 (Song et al., 2015), H^+ ejection associated with breaking the C-H bond shows clear asymmetry with respect to the laser polarization. The observed selectivity is suggested to be produced

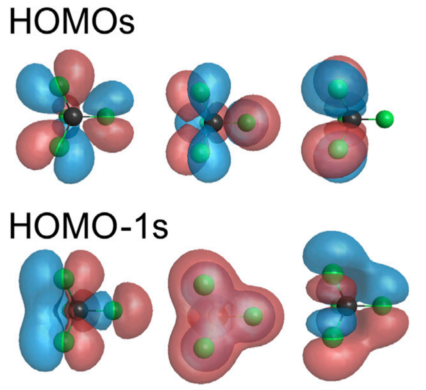

FIGURE 3 | Highest-occupied molecular orbitals HOMO ($1t_1$) and HOMO-1 ($4t_2$). Both HOMO and HOMO-1 are triply degenerated.

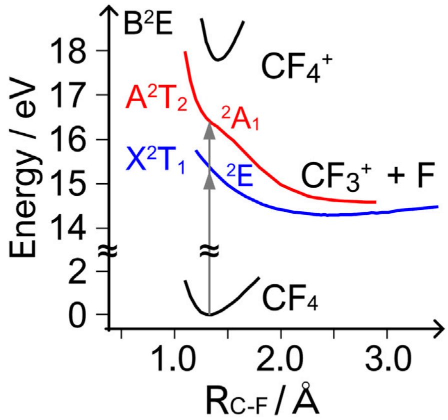

FIGURE 4 | Schematic potential energy curves of selected electronic states of CF$_4$ and CF$_4^+$ as a function of the internuclear distance $R_{\text{C-F}}$ between F and C in the CF$_3$ group [reproduced from Tang et al. (2013)].

by laser-induced coupling of HOMO and HOMO-1, 2 states. For CO$_2$ (Endo et al., 2016; Endo et al., 2017), asymmetric ejection of O$^+$ was observed on the larger amplitude side of the ω-2ω laser fields. This is consistent with the results of a theoretical calculation of nuclear wave packet dynamics on the potential energy surfaces (PES) of CO$_2^{2+}$ in ω-2ω intense laser fields (Sato et al., 2003), demonstrating the chemical reaction control by laser manipulation of PES.

This study discusses the feasibility of applying the ω-2ω reaction control to more complex symmetric molecules. More specifically, we study a tetrahedral molecule, tetrafluoromethane (CF$_4$), which has four equivalent C-F bonds in the equilibrium structure in T_d symmetry (**Figure 2**) to see if directional ejection of the fragment can be induced by asymmetric laser fields. The electronic configuration is $\ldots\ (1e)^4(4t_2)^6(1t_1)^6$ in the ground state. The highest-occupied MO (HOMO), $1t_1$, is triply degenerated (see **Figure 3**). We discuss dissociative ionization in ω-2ω intense laser fields:

$$\mathrm{CF_4 \rightarrow CF_3^+ + F + e^-}. \tag{3}$$

The dissociative ionization has been subjected to single-photon (Brehm et al., 1974; Creasey et al., 1990; Hikosaka and Shigemasa, 2006; Tang et al., 2013; Larsen et al., 2018; Pertot et al., 2017) and electron impact (Hossen et al., 2018) studies. The process is characterized by the ultrashort lifetime (< 40 fs) (Pertot et al., 2017) on the repulsive PESs leading to the CF$_3^+$ + F asymptote in both the ground and the first excited states of CF$_4^+$ as shown in **Figure 4**. The repulsive PESs imply that the CF$_4$ can serve as a unique benchmark to elucidate how the tunneling ionization of polyatomic molecules proceeds in intense laser fields because fragments can be produced by direct dissociation without additional interaction with the laser fields (Fujise et al., 2022).

The paper is organized as follows. We first describe the experimental setup for the three-dimensional momentum imaging of CF$_3^+$ fragment ions produced by dissociative ionization in **Eq. 3** in linearly polarized ω-2ω intense laser fields (50 fs, 1.4 × 10^{14} W/cm^2, 800 and 400 nm). Then, we present the experimental results on the asymmetry in the ejection of CF$_3^+$ and its dependence on the relative phase ϕ between the ω and 2ω laser fields. Finally, the obtained results are compared with theoretical predictions by the weak-field asymptotic theory (WFAT) (Tolstikhin et al., 2011) for tunneling ionization.

2 EXPERIMENT

The schematic of the experimental setup is shown in **Figure 1**. Details have been described previously (Endo et al., 2019). Briefly, the output from a Ti: Sapphire regenerative laser amplifier system (800 nm, 1 kHz, 50 fs) was introduced to an inline ω-2ω pulse generator. After generation of the second-order harmonics (400 nm, ~80 fs) by a type-I β-BBO crystal, the time delay between the ω and 2ω pulses was compensated by two birefringent α-BBO crystals. The relative phase between the two-color was controlled by a pair of fused silica wedge plates. The relative phase of the two-color laser pulses was stabilized by active feedback control of the wedge plate utilizing the 2ω-2ω interference spectrum. The polarization direction of the fundamental and second harmonic pulses was set parallel with each other by a true zero-order dual-wavelength plate and introduced into an ultrahigh vacuum chamber. The ω-2ω laser pulse was focused onto a diffusive molecular beam by a focusing mirror (f = 75 mm). Fragment ions generated by the interaction with ω-2ω intense laser fields were guided to a delay-line anode position-sensitive detector (PSD) by a static electric field. The three-dimensional momentum (p_X, p_Y, p_Z) of each fragment ion was obtained from the arrival position (Y, Z) at the detector and the time of flight (t). The kinetic energy release (KER) was calculated from the momentum of CF$_3^+$, $\mathbf{p}_{\text{CF}_3^+}$, where we assume the momentum conservation between CF$_3^+$ and the counterpart fragment F atom, $\mathbf{p}_\text{F} = -\mathbf{p}_{\text{CF}_3^+}$. Under this approximation, the KER is expressed as

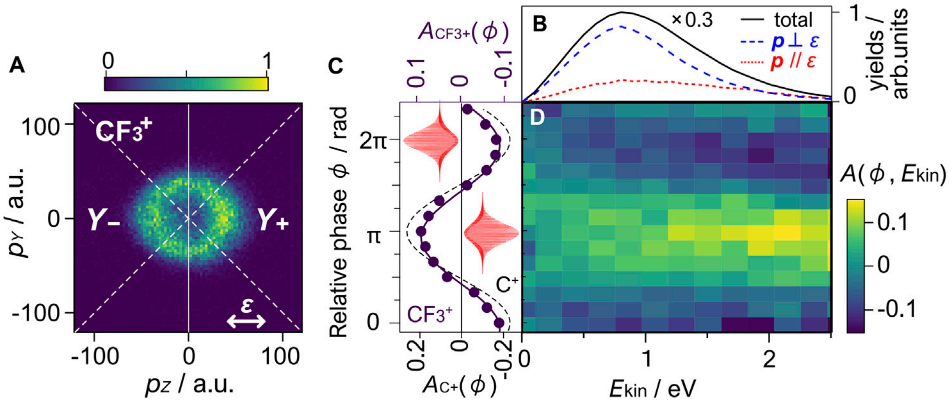

FIGURE 5 | (A) Momentum image of CF_3^+ fragment ions produced in ω-2ω intense laser fields (50 fs, 1.4×10^{14} W/cm^2, 800 and 400 nm), averaged over the relative phase ($0 \le \phi \le 2\pi$). The image is a slice of the three-dimensional ion momentum distribution in the Y-Z plane with a thickness of $|p_X| < 10$ a.u. The arrow represents the direction of the laser polarization. **(B)** Total kinetic energy release spectra of $CF_4^+ \to CF_3^+ + F$ (solid) plotted together with the parallel (dotted) and perpendicular (dashed) components, defined by the polar angles of $0^\circ \le \theta \le 20^\circ$ and $75^\circ \le \theta \le 90^\circ$, respectively. The total spectrum is multiplied by 0.3. **(C)** The asymmetry parameter $A_{CF_3^+}(\phi)$ for the CF_3^+ fragment ions with an acceptance angle of 45°(solid circle) and the results of the least-square fitting (solid line) (see text). The fitting results for the C^+ ion produced by the Coulomb explosion of CO (4 eV $\le E_{kin} \le$ 8 eV) are also plotted (dashed line). The laser pulse shapes at $\phi = 0$ and π are shown. **(D)** Two-dimensional plot of the asymmetry parameter $A(\phi, E_{kin})$ for CF_3^+.

$$E_{kin} = \frac{m_F + m_{CF_3^+}}{2 m_F m_{CF_3^+}} |\mathbf{p}_{CF_3^+}|^2, \qquad (4)$$

where $m_{CF_3^+}$ and m_F are the masses of the CF_3^+ fragment ions and F atoms, respectively.

The intensities of the laser fields were estimated to be $I_\omega = 1.15 \times 10^{14}$ W/cm^2 and $I_{2\omega} = 2.6 \times 10^{13}$ W/cm^2, respectively. The total field intensity is $I_{\omega+2\omega} = I_\omega + I_{2\omega} = 1.4 \times 10^{14}$ W/cm^2 with a ratio of $I_{2\omega}/I_\omega = 0.23$. A mixture of CF_4 and CO was used as the sample gas. The absolute phase difference ϕ between ω and 2ω pulses at the focal point was determined by the phase dependence of Coulomb explosion of CO, $CO \to C^+ + O^+ + 2e^-$, where C^+ is ejected more to the smaller amplitude side of the ω-2ω electric fields than to the opposite (Li et al., 2011).

3 RESULTS AND DISCUSSION

3.1 Fragment Momentum Distribution

Figure 5A shows the momentum image of CF_3^+ that dominates the time-of-flight spectrum, reflecting the repulsive nature of the PES of CF_4^+. The KER spectrum shows a broad single peak at E_{kin} = 0.8 eV as observed in the previous studies (Tang et al., 2013; Larsen et al., 2018; Hossen et al., 2018; Hikosaka and Shigemasa, 2006; Fujise et al., 2022). The CF_3^+ momentum image in **Figure 5A** shows an elliptic distribution. The peak momentum values along the Z-axis and Y-axis are 35 a.u. and 30 a.u., respectively, showing that CF_3^+ is emitted with a larger momentum along the laser polarization direction. **Figure 5B** shows the KER spectra obtained for parallel ($0^\circ \le \theta \le 20^\circ$) and perpendicular ($75^\circ \le \theta \le 90^\circ$) components to the laser polarization direction, where θ is the polar angle from the Z-axis. The parallel component shows a broader peak at 0.9 eV extending to a higher KER region than the perpendicular component. The perpendicular component has a sharper peak at 0.8 eV, indicating that different pathways contribute to the dissociative ionization. The previous electron impact study at an energy of 67 eV (Hossen et al., 2018) shows that contributions from five different molecular orbitals $1t_1$, $4t_2$, $1e$, $3t_2$, and $4a_1$ overlap within the peak. The KER spectrum associated with the ionization from HOMO ($1t_1$) exhibits a peak at ~0.9 eV, while a broader peak appears at a slightly higher energy region for HOMO-1 ($4t_2$). This suggests that both the X^2T_1 ground state and A^2T_2 first excited state contribute to the dissociative ionization in the ω-2ω intense laser fields, although it is difficult to estimate the relative contributions from these orbitals by the present experimental results. It is worth noting that the dissociation from the $1e$ HOMO-2 state may also contribute to the KER spectrum (Larsen et al., 2018) through internal conversion from the B^2E to the A^2T_2 state (Maier and Thommen, 1980).

3.2 Asymmetric Dissociative Ionization of CF_4

To understand how CF_4 responds to different shapes of the laser pulse, we focus on the spatial asymmetry in the fragment distribution. For a quantitative discussion, the asymmetry parameter,

$$A(\phi) = \frac{Y_+(\phi) - Y_-(\phi)}{Y_+(\phi) + Y_-(\phi)}, \qquad (5)$$

is introduced, where Y_+ and Y_- represent the yields of ions with positive and negative momenta within a 45° acceptance angle along the laser polarization direction (Z-axis), respectively (see **Figure 5A**). **Figure 5C** plots the obtained asymmetry parameters for CF_3^+, $A_{CF_3^+}(\phi)$, together with those obtained for C^+ produced from the Coulomb explosion of CO used for the phase calibration. The asymmetry parameter shows a 2π periodic dependence on the two-color relative phase. The least-squares fitting to $A(\phi) = A_0\cos(\phi\text{-}\phi_0)$ provides $A_0 = 0.09(1)$ and $\phi_0 = 0.9(1)\ \pi$, where numbers in the parentheses represent uncertainties. The results show that CF_3^+ prefers being emitted on the smaller electric field side of the asymmetric laser fields. In other words, the dissociative tunneling ionization is enhanced when the lager amplitude side of the ω-2ω electric fields points from C to F. **Figure 5D** shows the KER-resolved asymmetry parameter,

$$A(\phi, E_{\text{kin}}) = \frac{Y_+(\phi, E_{\text{kin}}) - Y_-(\phi, E_{\text{kin}})}{Y_+(\phi, E_{\text{kin}}) + Y_-(\phi, E_{\text{kin}})}. \tag{6}$$

An increase in the asymmetry amplitude to $A_0 \sim 0.12$ is observed in higher KER region where contributions from the A^2T_2 state of CF_4^+ is observed. The maximum and minimum of the asymmetry parameter are seen at $\phi \sim \pi$ and 0, respectively, over the KER range investigated.

3.3 Comparison With Tunneling Ionization Theory

3.3.1 Tunneling Ionization Rates

Theoretical calculations of the tunneling ionization rate of CF_4 were carried out by WFAT (Tolstikhin et al., 2011). The tunneling ionization rate is expressed as (Madsen et al., 2012)

$$\Gamma(\beta, \gamma) = |G_{00}(\beta, \gamma)|^2 W_{00}(F). \tag{7}$$

The structure factor $G_{00}(\beta, \gamma)$ describes the dependence on the molecular orientation relative to the laser electric field F defined by the Euler angles (α, β, γ) (Zare, 1988). The field factor $W_{00}(F)$ is given as

$$W_{00}(F) = \frac{\varkappa}{2}\left(\frac{4\varkappa^2}{F}\right)^{2/\varkappa-1} \exp\left(-\frac{2\varkappa^3}{3F}\right), \tag{8}$$

which defines the dependence on the field strength F. Here, $\varkappa = \sqrt{-2E_0}$, with E_0 being the energy of the molecular orbital from which the electron is ionized, and the subscript 00 refers to the dominant ionization channel (Tolstikhin et al., 2011).

The HOMO ($1t_1$) and HOMO-1 ($4t_2$) of CF_4 are both triply degenerate (**Figure 3**). The Stark interaction with the ionizing field removes the degeneracy. Tunneling ionization occurs from eigenorbitals of the operator $-(\boldsymbol{\mu} \cdot \boldsymbol{F})$ within each degenerate subspace, where $\boldsymbol{\mu}$ is the electric dipole moment of the considered orbital (Kraus et al., 2015). We denote these eigenorbitals as ϕ_A, ϕ_B, and ϕ_C. The three eigenorbitals are the particular linear combinations of the three degenerate HOMOs shown in **Figure 3**, which diagonalize the Stark term $(\boldsymbol{\mu} \cdot \boldsymbol{F})$. The structure factors $G_{00}(\beta, \gamma)$ incorporating the effect of the dipole for the eigenorbitals are calculated using the integral representation of the WFAT (Dnestryan and Tolstikhin, 2016; Madsen et al., 2017; Dnestryan et al., 2018) implemented by means of the GAMESS package with a polarization consistent basis set at the pc-4 level (Jensen, 2001).

Figures 6A–C show the squared norms of the structure factors $|G_{00}(\beta, \gamma)|^2$ of the three eigenorbitals, ϕ_A, ϕ_B, and ϕ_C, in the subspace of HOMO ($E_0 = -18.66$ eV), where the orbitals are labeled with A, B, and C in the ascending order of the dipole, $\mu_A < \mu_B < \mu_C$. The orbital energy in the field to the first order is given as

$$E_{0,i}(\boldsymbol{F}) = E_0 - \boldsymbol{\mu}_i \cdot \boldsymbol{F}, \tag{9}$$

where i = A,B,C. **Figure 7** shows the energy of eigenorbitals calculated using **Eq. 9** at four different molecular orientations with respect to F. The structure factors for HOMO in **Figures 6A–C** show that the largest contribution to the tunneling ionization comes from eigenorbital ϕ_B because the field factor $W_{00}(F)$ is common for ϕ_A, ϕ_B, and ϕ_C (see **Eq. 7**). Each orbital has nodes along the C-F axis, which appear as the minima in the respective structure factors. The nodes remain visible in the sum of $|G_{00}(\beta, \gamma)|^2$ in **Figure 6D**.

The squared norms of the structure factors $|G_{00}(\beta, \gamma)|^2$ of HOMO-1 ($E_0 = -19.44$ eV) are shown in **Figures 6E–H**. The eigenorbital ϕ_A having the highest energy among the three orbitals has the largest contributions to the sum in **Figure 6H**. **Figure 6H** shows that the tunneling ionization is enhanced by the electric field pointing from F to C when the three degenerated eigenorbitals are equally populated. Because eigenenergy $E_{0,A}$ of ϕ_A at $(\beta, \gamma) = (124^\circ, 314^\circ)$ is slightly smaller than that at $(\beta, \gamma) = (54^\circ, 134^\circ)$, the large structure factors for the former orientation indicate that the shape of the molecular orbital is more important in determining the tunneling rate in the present case than the increase in the effective ionization potential by the Stark interaction with the dipole moment.

3.3.2 Fragment Angular Distribution

If the breaking of each of the four C-F bonds after ionization occurs with an equal probability, the angular distribution of the F fragment in the laboratory frame can be expressed as follows (Zare, 1988):

$$P(\theta_s, \phi_s) = \int_0^{2\pi} d\alpha \int_0^{\pi} \sin\beta d\beta \int_0^{2\pi} d\gamma P_{\text{mol}}(\alpha, \beta, \gamma) f(\theta_m, \phi_m), \tag{10}$$

where (θ_s, ϕ_s) and (θ_m, ϕ_m) are the spherical angles with respect to the laboratory and molecular frame, respectively, and $f(\theta_m, \phi_m)$ is the angular distribution of the fragment ion in the molecular frame. The orientation distribution of the molecular ion formed in the ω-2ω laser fields in the laboratory frame may be expressed as

$$P_{\text{mol}}(\alpha, \beta, \gamma) = \frac{1}{8\pi^2}\left\{1 - \exp\left[-\int_{-\infty}^{+\infty} \Gamma_s(\alpha, \beta, \gamma, F(t)) dt\right]\right\}, \tag{11}$$

where $\Gamma_s(\alpha, \beta, \gamma, F(t))$ represents the tunneling rate in the ω-2ω laser field $F(t)$ of **Eq. 2** for molecular orientation defined by the Euler angles (α, β, γ) relative to the Z-axis of the laboratory frame (see **Figure 2**). It can be expressed by $|G_{00}(\beta, \gamma)|^2$ and $W_{00}(F)$ as follows:

$$\Gamma_s(\alpha, \beta, \gamma, F(t)) = \begin{cases} |G_{00}(\beta, \gamma)|^2 W_{00}(|F(t)|) & (F(t) \geq 0) \\ |G_{00}(\pi - \beta, \gamma + \pi)|^2 W_{00}(|F(t)|) & (F(t) < 0) \end{cases}. \tag{12}$$

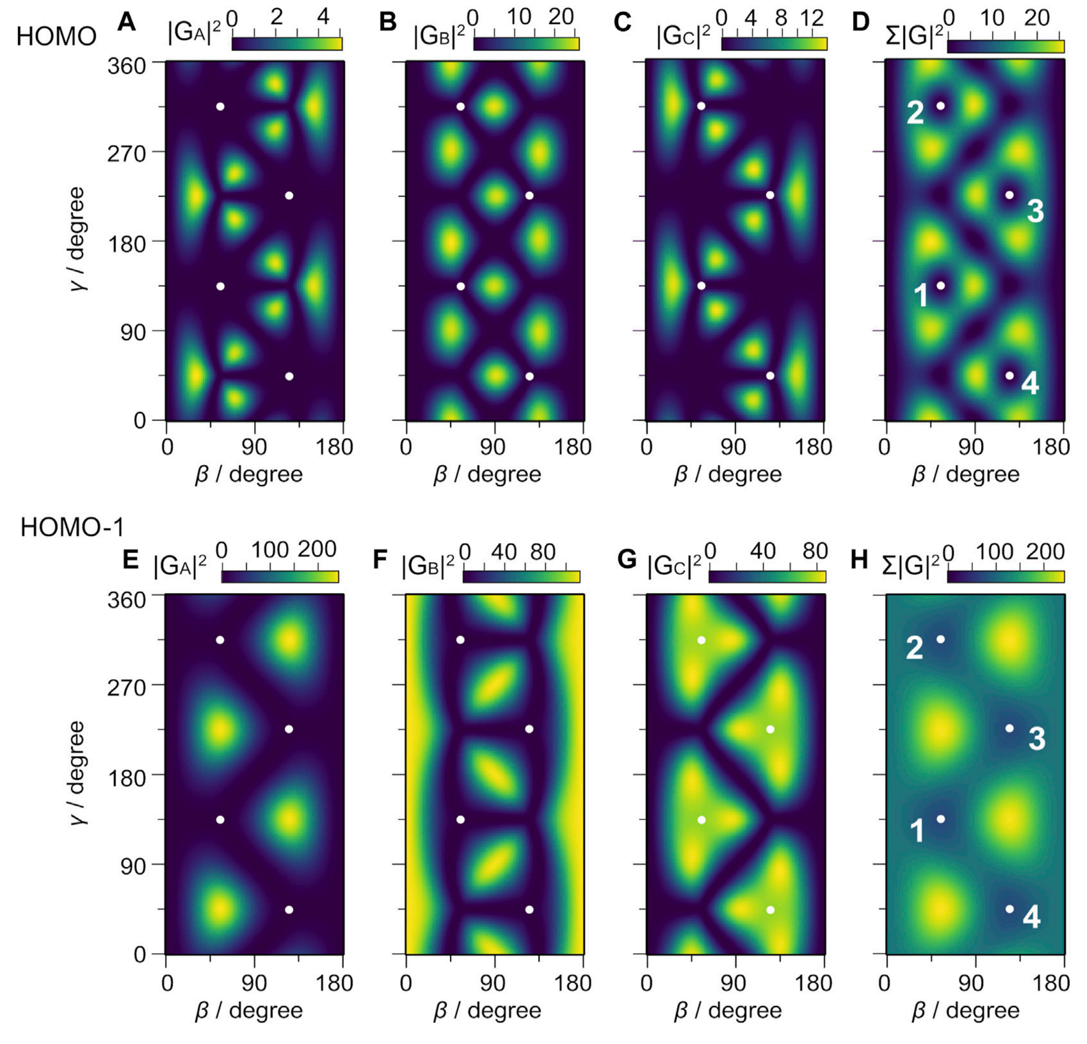

FIGURE 6 | Structure factors of eigenorbitals, **(A)** $|G_A|^2$, **(B)** $|G_B|^2$, **(C)** $|G_C|^2$, and **(D)** the sum, $\Sigma|G|^2 = |G_A|^2 + |G_B|^2 + |G_C|^2$ for HOMO, and **(E)** $|G_A|^2$, **(F)** $|G_B|^2$, **(G)** $|G_C|^2$ and **(H)** $\Sigma|G|^2$ for HOMO-1. The dots represent the Euler angles (β, γ) at which one of the C-F axes points to the Z direction. The numbers attached to the dots in panels **(D,H)** represent the labels of the respective F atoms in **Figure 2**. Note the difference in the scaling of the color bars in **(A–H)**.

When the ionization probability is sufficiently smaller than unity, **Eq. 11** reduces to

$$P_{\mathrm{mol}}(\alpha,\beta,\gamma) = \frac{1}{8\pi^2}\int_{-\infty}^{+\infty}\Gamma_s(\alpha,\beta,\gamma,F(t))\mathrm{d}t. \tag{13}$$

The angular distribution $P_{\mathrm{mol}}(\alpha, \beta, \gamma)$ can be expanded by the rotation matrices $D^k_{q'q}(R)$ as follows:

$$P_{\mathrm{mol}}(\alpha,\beta,\gamma) = \frac{1}{8\pi^2}\sum_{k,q,q'} a^k_{q'q} D^{k*}_{q'q}(\alpha,\beta,\gamma). \tag{14}$$

Here, the coefficients $a^k_{q'q}$ are given as follows:

$$a^k_{q'q} = (2k+1)\int P_{\mathrm{mol}}(\alpha,\beta,\gamma) D^k_{q'q}(R)\mathrm{d}\Omega. \tag{15}$$

The angular distribution of the fragment ion can be expressed using the spherical harmonics $Y_{jm}(\theta_m, \phi_m)$:

$$f(\theta_m,\phi_m) = \sum\nolimits_{j,m} b_{jm} Y_{jm}(\theta_m,\phi_m), \tag{16}$$

$$b_{jm} = \int_0^{2\pi}\mathrm{d}\phi_m\int_0^{\pi}\sin\theta_m\mathrm{d}\theta_m Y^*_{jm}(\theta_m,\phi_m) f(\theta_m,\phi_m). \tag{17}$$

Thus, we have

$$P(\theta_s,\phi_s) = \sum_{k,q,q'}\frac{a^k_{q'q} b_{kq}}{2k+1} Y_{kq'}(\theta_s,\phi_s). \tag{18}$$

Under the axial recoil approximation, the angle distribution $f(\theta_m, \phi_m)$ may be expressed as follows:

$$f(\theta_m,\phi_m) = \frac{1}{\sin\theta_m}\delta(\theta_m - \theta^0_m)\delta(\phi_m - \phi^0_m), \tag{19}$$

with $(\theta^0_m, \phi^0_m) = (54.7°, 45°)$ for CF_4 in T_d symmetry. By substituting to **Eq. 17**, we have

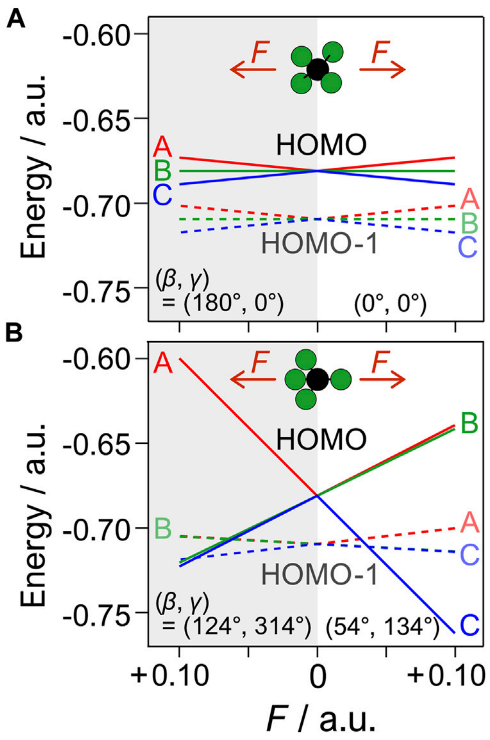

FIGURE 7 | Stark shifted energies of $E_{0,i}(\boldsymbol{F})$ of eigenorbitals, ϕ_i (i = A, B, C), of HOMO (solid line) and HOMO-1 (dashed line) as a function of the static field F (see **Eq. 9**) at four different molecular orientations with respect to F, defined by the Euler angles (β, γ) in **Figure 2**. **(A)** The electric field is parallel to the molecular principal axis (C_2), i.e., (β, γ) = (0°, 0°) (right) and (180°, 0°) (left). **(B)** The same as **(A)** but for (β, γ) = (54°,134°) (right) and (124°, 314°) (left), where the electric field is almost parallel to one of the C-F axes.

$$b_{jm} = Y^{*}_{jm}\left(\theta^{0}_{m}, \phi^{0}_{m}\right) = (-1)^{m} Y_{j-m}\left(\theta^{0}_{m}, \phi^{0}_{m}\right), \tag{20}$$

from which we obtain an expression for the fragment angular distribution as follows:

$$P\left(\theta_s, \phi_s\right) = P\left(\theta_s\right) = \frac{1}{\sqrt{4\pi}} \sum\nolimits_{k} c_k P_k\left(\cos\theta_s\right), \tag{21}$$

$$c_k = \frac{1}{\sqrt{2k+1}} \sum\nolimits_{q} a^{k}_{0q} Y^{*}_{kq}\left(\theta^{0}_{m}, \phi^{0}_{m}\right). \tag{22}$$

Figure 8 shows the fragment angular distributions obtained for the relative phase $\phi = 0$ of the ω - 2ω pulse ($I_{\omega+2\omega} = 1.4 \times 10^{14}$ W/cm^2 and $I_{2\omega}/I_{\omega} = 0.23$). The calculated fragment yields for HOMO-1 is larger than that of HOMO under the present experimental conditions ($F_{\omega} = 0.057$ a.u. and $F_{2\omega} = 0.027$ a.u.). This is attributed to the large structure factor $|G_{00}|^2$ for HOMO-1 (**Figure 6H**), which is about 10 times larger than $|G_{00}|^2$ for HOMO (**Figure 6D**), because of the small difference between the ionization potentials of these orbitals (~1 eV) giving rise to the relatively small field factor ratio of $W_{00}(1t_1)/W_{00}(4t_2) \sim 3$. The angular distribution calculated for each HOMO exhibits characteristic structures associated with the nodes of the molecular orbitals. The total fragment distribution carries the nodal pattern with a larger ionization probability on the larger amplitude side of the ω-2ω laser fields. In contrast, the angular distribution of HOMO-1 is more directional along the laser polarization direction, consistent with the fragment ion image and the KER spectra in **Figures 5A,B**, where the ionization from HOMO-1 contributes more to the parallel component than to the perpendicular one.

3.3.3 Asymmetry Parameter

The yields of the F fragment in a finite acceptance angle θ_0 around 0° and 180° can be expressed as follows:

$$Y^{\theta_0}_{+}(\phi) = 2\pi \int_{0}^{\theta_0} P\left(\theta_s\right) \sin\theta_s \mathrm{d}\theta_s, \tag{23}$$

$$Y^{\theta_0}_{-}(\phi) = 2\pi \int_{\pi-\theta_0}^{\pi} P\left(\theta_s\right) \sin\theta_s \mathrm{d}\theta_s. \tag{24}$$

The asymmetry parameters defined by **Eq. 5** are calculated using **Eqs 23**, **24**, where $\theta_0 = 45°$ compared with the experimental results. The asymmetry parameter $A_{\mathrm{F}}(\phi)$ thus obtained for HOMO shows a clear dependence on the relative phase ϕ between the ω and 2ω laser fields. The asymmetry parameter for HOMO (**Figure 9A**) is positive at $\phi = 0$, showing that tunneling ionization is more efficient when the larger amplitude side of the laser fields points from C to F. In contrast, the parameter for HOMO-1 exhibits the opposite dependence with negative values at $\phi = 0$. The difference originates essentially from the shape of the eigenorbitals dominating the tunneling ionization of the respective MOs.

Figure 9B plots the experimental asymmetry parameter $A_{\mathrm{F}}(\phi)$ for the counterpart fragment F produced by the dissociative ionization (**Eq. 3**), which is obtained from the asymmetry parameter for CF_3^+ by $A_{\mathrm{F}}(\phi) = -A_{\mathrm{CF}_3^+}(\phi)$. It is compared with the corresponding asymmetry parameter calculated with the contributions from the two orbitals, where the angular distribution is given as $P(\theta_s) = P_{\mathrm{HOMO}}(\theta_s) + P_{\mathrm{HOMO\text{-}1}}(\theta_s)$. The obtained amplitude of $A_0 = 0.1$ is slightly larger than the experimental results. The small experimental amplitude might be attributed to the contribution from HOMO-2 ($1e$), located ~1.4 eV below the HOMO-1. The B^2E state of CF_4^+ produced by the tunneling ionization from $1e$ has a lifetime of 10^{-10}–10^{-12} s (Maier and Thommen, 1980). This lifetime is longer than or comparable with the molecular rotational periods and could form an isotropic fragment distribution, which reduces the asymmetry of the fragmentation. **Figure 9B** plots the asymmetry parameter $A_{\mathrm{F}}(\phi)$ obtained at a higher field intensity 3.0×10^{14} W/cm^2 with a similar intensity ratio of $I_{2\omega}/I_{\omega} = 0.25$. The increase in the field intensity resulted in a small amplitude $A_0 \sim 0.04$, while the amplitude of the calculated results remained essentially the same. Because the relative contribution from the B^2E state is expected to increase by an increase in the field intensity, the experimental results support the involvement of the B^2E state in the dissociative ionization.

Interestingly, the calculated asymmetry parameter in **Figure 9B** has an opposite phase dependence to the experimental results, showing that the dissociative tunneling ionization of CF_4 in the ω-2ω laser fields cannot be explained by the angular distribution of the tunneling ionization from

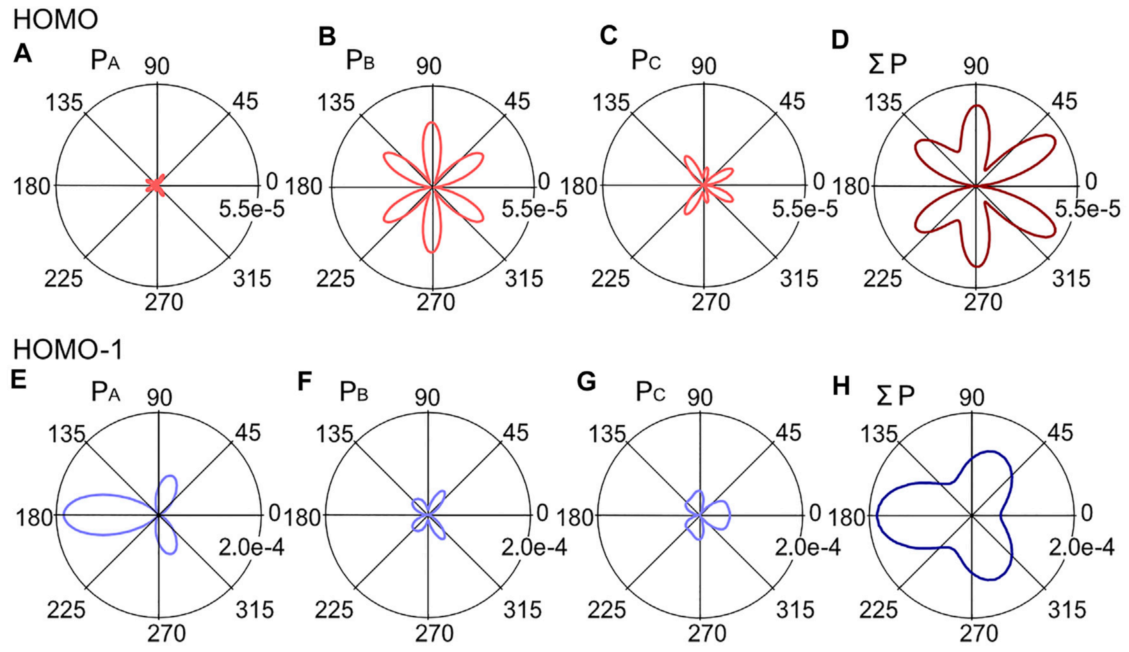

FIGURE 8 | Angular distributions $P(\theta_s)$ calculated for the eigenorbitals, ϕ_A, ϕ_B, and ϕ_C, in the ω-2ω laser field with the relative phase $\phi = 0$, **(A)** $P_A(\theta_s)$, **(B)** $P_B(\theta_s)$, **(C)** $P_C(\theta_s)$, and **(D)** the sum $\Sigma P(\theta_s)$ for HOMO and **(E)** $P_A(\theta_s)$, **(F)** $P_B(\theta_s)$, **(G)** $P_C(\theta_s)$ and **(H)** $\Sigma P(\theta_s)$, for HOMO-1. Note the difference in the scaling of the polar plots for HOMO and HOMO-1.

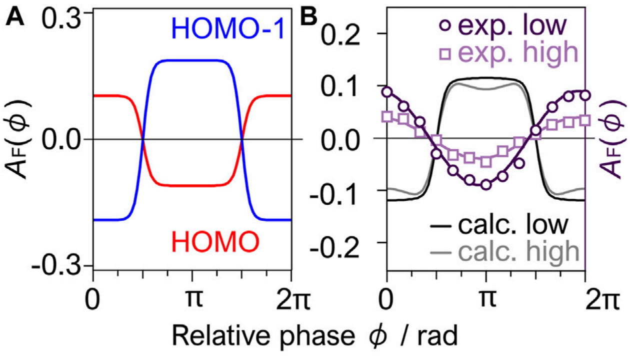

FIGURE 9 | (A) Phase dependence of the asymmetry parameter $A(\phi)$ calculated for HOMO and HOMO-1 with the acceptance angle of $\theta_0 = 45°$. **(B)** Total asymmetry parameter compared with the experimental parameter for F fragment, $A_F(\phi)$, calculated at $I_{\omega+2\omega} = 1.4 \times 10^{14}$ W/cm^2 (solid) and 3.0×10^{14} W/cm^2 (gray), in comparison with the corresponding experimental results (circle and square, respectively).

the HOMO and HOMO-1 alone, although the F (or CF_3^+) fragments are promptly ejected on the repulsive potentials of the X^2T_1 and A^2T_2 states after the tunneling ionization (**Figure 4**). The present experimental results show a marked contrast to those obtained by recent studies on the dissociative ionization of CF_4 in circularly polarized laser fields (35 fs, 0.8 × 10^{14} W/cm^2, 1,035 nm) (Fujise et al., 2022). The recoil-frame photoelectron angular distribution (RFPAD) showed that the dissociative tunneling ionization occurs more efficiently when the electric field points from F to C than the opposite, which is consistent with the prediction by WFAT for the tunneling ionization (see also **Figure 8**).

Previous studies on spatially oriented OCS showed that the tunneling ionization yields exhibit different angular dependence in linearly polarized and circularly polarized laser fields (Holmegaard et al., 2010; Hansen et al., 2012) as in the present case, where the tunneling ionization is enhanced at different directions of the applied electric fields in the molecular frame. For circularly polarized fields, a significant enhancement of tunneling ionization was observed when the electric fields were applied from C to S along the molecular axis, while the linearly polarized fields favor the tunneling ionization from the direction perpendicular to the axis. The discrepancy was discussed in terms of electron rescattering and the involvement of electronic excitation (Hansen et al., 2012), as well as orbital modification (Murray et al., 2010) and multielectron effects (Majety and Scrinzi, 2015) in the ionization process. These effects can, in principle, be involved in the present case of CF_4 to explain the deviation between the experimental and theoretical results in **Figure 9B**. Furthermore, **Figure 7** suggests that the energy shifts of eigenorbitals formed by the Stark interaction becomes large enough to induce mixing between HOMO and HOMO-1, for example, at a field intensity $F \geq 0.06$ a.u. in the molecular orientation in **Figure 7B**. This would result in additional polarization (field-induced deformation) of the ionizing orbitals, which affects the ionization rate (Matsui et al., 2021) but is not considered in the calculation of the structure factors in **Figure 6**.

Because the directional ejection of the fragments involves both ionization and fragmentation, post-ionization interaction with the laser fields (Endo et al., 2019; Endo et al., 2022) is another important factor to consider. The post-ionization interaction in ω-2ω laser fields has been extensively studied with H_2^+ (Ray et al., 2009; Wanie et al., 2015). The dissociative ionization shows a clear dependence on the relative phase ϕ. The H^+ ejection direction is determined by the quantum interference between the pathways associated with excitation and deexcitation between the $1s\sigma_g$ and $2p\sigma_u$ states of H_2^+ by absorption or emission of ω and 2ω photons. This results in the spatial asymmetry of H^+ ejection dependent on both phase ϕ and KER. The quantum interference effect can also manifest itself in circularly polarized laser fields when the tunneling electron is detected in coincidence with H^+ (Wu et al., 2013). It appears as the distortion of the molecular-frame photoelectron angular distribution (MFPAD). As for CF_4, the RFPADs recorded for the dissociative ionization in **Eq. 3** in circularly polarized fields exhibited clear dependences on both the helicity of circularly polarized laser fields and the KER [1]. The observed results are interpreted in terms of the laser-induced coupling between the electronic states, depending on the phase of the rotating electric fields in the molecular frame. The coupling between the ground state X^2T_1 and the excited state A^2T_2 through non-adiabatic population transfer in the alternating laser electric fields was suggested as a possible dynamics contributing to the helicity dependence. In the present case of the two-color laser fields consisting of 800 and 400 nm for ω and 2ω, the energy differences between the states and the A^2T_2 and B^2E states are close to the photon energy of $h\nu = 1.5$ and 3.1 eV of the present ω and 2ω fields (see **Figure 4**), which further facilitates such coupling to modify the asymmetry of the fragmentation through quantum interferences.

4 SUMMARY

In the present study, we investigated the directional fragment ejection of CF_4 in dissociative ionization, $CF_4 \rightarrow CF_3^+ + F + e^-$, in linearly polarized ω-2ω ultrashort intense laser fields (1.4×10^{14} W/cm^2, 800 and 400 nm) by three-dimensional ion momentum imaging. The CF_3^+ fragment distribution exhibited a clear dependence on the relative phase ϕ between the ω and 2ω laser fields, showing that the CF_3^+ ions tend to be ejected to smaller electric field sides of the two-color laser fields. The observed results indicated that the asymmetric ejection of the CF_3^+ ion or the F fragment can be manipulated by the relative phase of the ω-2ω intense laser fields. To understand the mechanism of the directional fragment ejection, the tunneling ionization rates were calculated by the weak-field asymptotic theory (WFAT) incorporating the Stark interaction in the triply degenerated orbitals of HOMO and HOMO-1. It was shown that the contributions from the HOMO-1 ($4t_2$) are even larger than those from HOMO ($1t_1$). The inverted order is attributed to the large structure factor of HOMO-1, which is governed essentially by the shape of the MO. The observed momentum distribution of CF_3^+ and the KER spectrum supported that both the X^1T_1 and A^2T_2 states contribute to the dissociative ionization of CF_4 in the ω-2ω intense laser fields.

In contrast, WFAT showed that the ionization yield sum becomes larger when the electric field points from F to C along the one of the C-F axis to predict a phase-dependent asymmetry parameter $A(\phi)$ being π out-of-phase to the experimental one. The difference between experimental and theoretical results could be attributed to additional distortion of molecular orbitals by mixing between HOMO and HOMO-1, as well as to the other processes proposed in the previous studies. The post-ionization process is another possible source of different phase dependence. The direct coupling between the electronic states of CF_4^+ by non-adiabatic transitions between the orbitals would cause constructive and destructive interference of the dissociating nuclear wavepackets to make the four C-F bonds inequivalent in dissociation. The present study demonstrated the feasibility of applying strong-field coherent control of directional fragment ejection to a symmetric polyatomic molecule in T_d symmetry. Several factors need to be considered to fully understand the selective breaking of C-F bonds in the dissociative tunneling ionization, even though ultrafast dissociation occurs on the repulsive potential surfaces after the ionization.

DATA AVAILABILITY STATEMENT

The original contributions presented in the study are included in the article/Supplementary Material. Further inquiries can be directed to the corresponding author.

AUTHOR CONTRIBUTIONS

HH, TW, and AM performed experiments and data analysis. TM, LBM, FJ, OIT, HH, and AH carried out theoretical calculations and simulations. AH conceived and directed the project, supervised the experiments, and analyzed data. HH and AH wrote the original draft. All authors contributed to the discussions of the results and to the production of the manuscript.

FUNDING

This work was supported by JSPS KAKENHI (Grant nos. JP19H00887, JP16H04029, and JP21K18929), MEXT Quantum Leap Flagship Program (MEXT Q-LEAP) (Grant no. JPMXS0118068681), and World Research Unit (B-1) of Reaction Infography (R-ing) at Nagoya University. This work was financially supported by JST SPRING, Grant Number JPMJSP2125. HH would like to take this opportunity to thank the "Interdisciplinary Frontier Next-Generation Researcher Program of the Tokai Higher Education and Research System." OIT was supported by the Ministry of Science and Higher Education of the Russian Federation (No.FSMG-2021-0005).

REFERENCES

Assion, A., Baumert, T., Bergt, M., Brixner, T., Kiefer, B., Seyfried, V., et al. (1998). Control of Chemical Reactions by Feedback-Optimized Phase-Shaped Femtosecond Laser Pulses. *Science* 282, 919–922. doi:10.1126/science.282.5390.919

Bardeen, C. J., Yakovlev, V. V., Wilson, K. R., Carpenter, S. D., Weber, P. M., and Warren, W. S. (1997). Feedback Quantum Control of Molecular Electronic Population Transfer. *Chem. Phys. Lett.* 280, 151–158. doi:10.1016/s0009-2614(97)01081-6

Bartels, R., Backus, S., Christov, I., Kapteyn, H., and Murnane, M. (2000). Attosecond Time-Scale Feedback Control of Coherent X-ray Generation. *Chem. Phys.* 267, 277. doi:10.1016/s0301-0104(01)00213-0

Brehm, B., Frey, R., Küstler, A., and Eland, J. (1974). Kinetic Energy Release in Ion Fragmentation: N_2O^+, COS^+ and CF_4^+ Decays. *Int. J. Mass Spectrom. Ion Phys.* 13, 251–260. doi:10.1016/0020-7381(74)80029-x

Chan, H.-S., Hsieh, Z.-M., Liang, W.-H., Kung, A. H., Lee, C.-K., Lai, C.-J., et al. (2011). Synthesis and Measurement of Ultrafast Waveforms from Five Discrete Optical Harmonics. *Science* 331, 6021. doi:10.1126/science.1198397

Creasey, J. C., Lambert, I. R., Tuckett, R. P., Codling, K., Frasinski, L. J., Hatherly, P. A., et al. (1990). Nonradiative Decay Pathways of Electronic States of Group IV Tetrafluoro and Tetrachloro Molecular Ions Studied with Synchrotron Radiation. *J. Chem. Phys.* 93, 3295–3306. doi:10.1063/1.458810

Dnestryan, A. I., and Tolstikhin, O. I. (2016). Integral-Equation Approach to the Weak-Field Asymptotic Theory of Tunneling Ionization. *Phys. Rev. A* 93, 033412. doi:10.1103/physreva.93.033412

Dnestryan, A. I., Tolstikhin, O. I., Madsen, L. B., and Jensen, F. (2018). Structure Factors for Tunneling Ionization Rates of Molecules: General Grid-Based Methodology and Convergence Studies. *J. Chem. Phys.* 149, 164107. doi:10.1063/1.5046902

Eickhoff, K., Englert, L., Bayer, T., and Wollenhaupt, M. (2021). Multichromatic Polarization-Controlled Pulse Sequences for Coherent Control of Multiphoton Ionization. *Front. Phys.* 9, 675258. doi:10.3389/fphy.2021.675258

Endo, T., Fujise, H., Hasegawa, H., Matsuda, A., Fushitani, M., Tolstikhin, O. I., et al. (2019). Angle Dependence of Dissociative Tunneling Ionization of NO in Asymmetric Two-Color Intense Laser Fields. *Phys. Rev. A* 100, 053422. doi:10.1103/physreva.100.053422

Endo, T., Fujise, H., Kawachi, Y., Ishihara, A., Matsuda, A., Fushitani, M., et al. (2017). Selective Bond Breaking of CO_2 in Phase-Locked Two-Color Intense Laser Fields: Laser Field Intensity Dependence. *Phys. Chem. Chem. Phys.* 19, 3550–3556. doi:10.1039/c6cp07471e

Endo, T., Fujise, H., Matsuda, A., Fushitani, M., Kono, H., and Hishikawa, A. (2016). Coincidence Momentum Imaging of Asymmetric Coulomb Explosion of CO_2 in Phase-Locked Two-Color Intense Laser fields. *J. Electron Spectrosc. Relat. Phenomena* 207, 50–54. doi:10.1016/j.elspec.2015.12.010

Endo, T., Ziems, K. M., Richter, M., Froebel, F. G., Hishikawa, A., and Gräfe, S. (2022). Post-Ionization Dynamics of Polar Molecules in Asymmetric Laser Fields. *Front. Chem.*. doi:10.3389/fchem.2022.859750

Hansen, J. L., Holmegaard, L., Nielsen, J. H., Stapelfeldt, H., Dimitrovski, D., and Madsen, L. B. (2012). Orientation-Dependent Ionization Yields from strong-field Ionization of Fixed-In-Space Linear and Asymmetric Top Molecules. *J. Phys. B: At. Mol. Opt. Phys.* 45, 015101. doi:10.1088/0953-4075/45/1/015101

Hikosaka, Y., and Shigemasa, E. (2006). Anisotropic Fragment Emission on Valence Photoionization of CF_4. *J. Electron Spectrosc. Relat. Phenomena* 152, 29–32. doi:10.1016/j.elspec.2006.02.005

Hishikawa, A., Matsuda, A., and Fushitani, M. (2020). Ultrafast Reaction Imaging and Control by Ultrashort Intense Laser Pulses. *Bull. Chem. Soc. Jpn.* 93, 1293–1304. doi:10.1246/bcsj.20200158

Holmegaard, L., Hansen, J. L., Kalhøj, L., Kragh, S. L., Stapelfeldt, H., Filsinger, F., et al. (2010). Photoelectron Angular Distributions from Strong-Field Ionization of Oriented Molecules. *Nat. Phys.* 6, 428–432. doi:10.1038/nphys1666

Hossen, K., Ren, X., Wang, E., Kumar, S. V. K., and Dorn, A. (2018). An (e, 2e + ion) Study of Electron-Impact Ionization and Fragmentation of Tetrafluoromethane at Low Energies. *Eur. Phys. J. D* 72, 43. doi:10.1140/epjd/e2017-80665-8

Fujise, H., Uemura, M., Hasegawa, H., Ikeya, D., Matsuda, A., Morishita, T., et al. (2022). Helicity-Dependent Dissociative Tunneling Ionization of CF_4 in Multicycle Circularly Polarized Intense Laser Fields. *Phys. Chem. Chem. Phys.*. doi:10.1039/d1cp05858d

Jensen, F. (2001). Polarization Consistent Basis Sets: Principles. *J. Chem. Phys.* 115, 9113–9125. doi:10.1063/1.1413524

Kechaoglou, E., Kaziannis, S., and Kosmidis, C. (2019). Controlling Intramolecular Hydrogen Migration by Asymmetric Laser Fields: the Water Case. *Phys. Chem. Chem. Phys.* 21, 11259–11265. doi:10.1039/c9cp01470e

Kraus, P. M., Tolstikhin, O. I., Baykusheva, D., Rupenyan, A., Schneider, J., Bisgaard, C. Z., et al. (2015). Observation of Laser-Induced Electronic Structure in Oriented Polyatomic Molecules. *Nat. Commun.* 6, 7039. doi:10.1038/ncomms8039

Larsen, K. A., Trevisan, C. S., Lucchese, R. R., Heck, S., Iskandar, W., Champenois, E., et al. (2018). Resonance Signatures in the Body-Frame Valence Photoionization of CF_4. *Phys. Chem. Chem. Phys.* 20, 21075–21084. doi:10.1039/c8cp03637c

Levis, R. J., Menkir, G. M., and Rabitz, H. (2001). Selective Bond Dissociation and Rearrangement with Optimally Tailored, Strong-Field Laser Pulses. *Science* 292, 709–713. doi:10.1126/science.1059133

Levis, R. J., and Rabitz, H. A. (2002). Closing the Loop on Bond Selective Chemistry Using Tailored strong Field Laser Pulses. *J. Phys. Chem. A* 106, 6427–6444. doi:10.1021/jp0134906

Li, H., Ray, D., De, S., Znakovskaya, I., Cao, W., Laurent, G., et al. (2011). Orientation Dependence of the Ionization of CO and NO in an Intense Femtosecond Two-Color Laser Field. *Phys. Rev. A* 84, 043429. doi:10.1103/physreva.84.043429

Madsen, L. B., Jensen, F., Dnestryan, A. I., and Tolstikhin, O. I. (2017). Structure Factors for Tunneling Ionization Rates of Molecules: General Hartree-Fock-Based Integral Representation. *Phys. Rev. A* 96, 013423. doi:10.1103/physreva.96.013423

Madsen, L. B., Tolstikhin, O. I., and Morishita, T. (2012). Application of the Weak-Field Asymptotic Theory to the Analysis of Tunneling Ionization of Linear Molecules. *Phys. Rev. A* 85, 053404. doi:10.1103/physreva.85.053404

Maier, J. P., and Thommen, F. (1980). Non-radiative Decay of Electronically Excited CF_4^+ (B^2E) and $CFCl_3^+$ (D^2E) Cations in the Gaseous Phase. *Chem. Phys. Lett.* 78, 54. doi:10.1016/0009-2614(81)85550-9

Majety, V. P., and Scrinzi, A. (2015). Static Field Ionization Rates for Multi-Electron Atoms and Small Molecules. *J. Phys. B: At. Mol. Opt. Phys.* 48, 245603. doi:10.1088/0953-4075/48/24/245603

Manzoni, C., Mücke, O. D., Cirmi, G., Fang, S., Moses, J., Huang, S., et al. (2015). Coherent Pulse Synthesis: Towards Sub-Cycle Optical Waveforms. *Laser Photon. Rev.* 9, 129–171. doi:10.1002/lpor.201400181

Matsui, H., Tolstikhin, O. I., and Morishita, T. (2021). Weak-Field Asymptotic Theory of Tunneling Ionization of the Hydrogen Molecule Including Core Polarization, Spectator Nucleus, and Internuclear Motion Effects. *Phys. Rev. A* 103, 033102. doi:10.1103/physreva.103.033102

Murray, R., Spanner, M., Patchkovskii, S., and Ivanov, M. Y. (2010). Tunnel Ionization of Molecules and Orbital Imaging. *Phys. Rev. Lett.* 106, 173001. doi:10.1103/physrevlett.106.173001

Neyra, E., Videla, F., Ciappina, M. F., Pérez-Hernández, J. A., Roso, L., and Torchia, G. A. (2018). Synthesis of Ultrashort Laser Pulses for High-Order Harmonic Generation. *Phys. Rev. A* 98, 013403. doi:10.1103/physreva.98.013403

Ohmura, H., Ito, F., and Tachiya, M. (2006a). Phase-Sensitive Molecular Ionization Induced by a Phase-Controlled Two-Color Laser Field in Methyl Halides. *Phys. Rev. A* 74, 043410. doi:10.1103/physreva.74.043410

Ohmura, H., Saito, N., and Morishita, T. (2014). Molecular Tunneling Ionization of the Carbonyl Sulfide Molecule by Double-Frequency Phase-Controlled Laser fields. *Phys. Rev. A* 89, 013405. doi:10.1103/physreva.89.013405

Ohmura, H., Saito, N., and Morishita, T. (2011). Quantum Control of Molecular Tunneling Ionization in the Spatiotemporal Domain. *Phys. Rev. A* 83, 063407. doi:10.1103/physreva.83.063407

Ohmura, H., and Saito, N. (2020). Sub-Optical-Cycle Attosecond Control of Molecular Ionization by Using Fourier-Synthesized Laser Fields. *Phys. Rev. A* 101, 043419. doi:10.1103/physreva.101.043419

Ohmura, H., Saito, N., and Tachiya, M. (2006b). Selective Ionization of Oriented Nonpolar Molecules with Asymmetric Structure by Phase-Controlled Two-Color Laser Fields. *Phys. Rev. Lett.* 96, 173001. doi:10.1103/physrevlett.96.173001

Ohmura, S., Ohmura, H., Kato, T., and Kono, H. (2021). Manipulation of Multielectron Dynamics of Molecules by Fourier-Synthesized Intense Laser Pulses: Effective Potential Analysis of CO. *Front. Phys.* 9, 677671. doi:10.3389/fphy.2021.677671

Pertot, Y., Schmidt, C., Matthews, M., Chauvet, A., Huppert, M., Svoboda, V., et al. (2017). Time-Resolved X-ray Absorption Spectroscopy with a Water Window High-Harmonic Source. *Science* 264, 355. doi:10.1126/science.aah6114

Pfeifer, T., Walter, D., Winterfeldt, C., Spielmann, C., and Gerber, G. (2005). Controlling the Spectral Shape of Coherent Soft X-Rays. *Appl. Phys. B* 80, 277–280. doi:10.1007/s00340-005-1754-0

Ray, D., He, F., De, S., Cao, W., Mashiko, H., Ranitovic, P., et al. (2009). Ion-Energy Dependence of Asymmetric Dissociation of D_2 by a Two-Color Laser Field. *Phys. Rev. Lett.* 103, 223201. doi:10.1103/physrevlett.103.223201

Sato, Y., Kono, H., Koseki, S., and Fujimura, Y. (2003). Description of Molecular Dynamics in Intense Laser Fields by the Time-Dependent Adiabatic State Approach: Application to Simultaneous Two-Bond Dissociation of CO_2 and its Control. *J. Am. Chem. Soc.* 125, 8019–8031. doi:10.1021/ja0344819

Sheehy, B., Walker, B., and DiMauro, L. F. (1995). Phase Control in the Two-Color Photodissociation of HD^+. *Phys. Rev. Lett.* 74, 4799. doi:10.1103/physrevlett.74.4799

Song, Q., Gong, X., Ji, Q., Lin, K., Pan, H., Ding, J., et al. (2015). Directional Deprotonation Ionization of Acetylene in Asymmetric Two-Color Laser Fields. *J. Phys. B: At. Mol. Opt. Phys.* 48, 094007. doi:10.1088/0953-4075/48/9/094007

Takahashi, E. J., Lan, P., Mücke, O. D., Nabekawa, Y., and Midorikawa, K. (2010). Infrared Two-Color Multicycle Laser Field Synthesis for Generating an Intense Attosecond Pulse. *Phys. Rev. Lett.* 104, 233901. doi:10.1103/physrevlett.104.233901

Tang, X., Zhou, X., Wu, M., Gao, Z., Liu, S., Liu, F., et al. (2013). Dissociation Limit and Dissociation Dynamic of CF_4^+ : Application of Threshold Photoelectron-Photoion Coincidence Velocity Imaging. *J. Chem. Phys.* 138, 094306. doi:10.1063/1.4792368

Tolstikhin, O. I., Morishita, T., and Madsen, L. B. (2011). Theory of Tunneling Ionization of Molecules: Weak-Field Asymptotics Including Dipole Effects. *Phys. Rev. A* 84, 053423. doi:10.1103/physreva.84.053423

Walt, S. G., Ram, N. B., Conta, A. v., Tolstikhin, O. I., Madsen, L. B., Jensen, F., et al. (2015). Role of Multi-Electron Effects in the Asymmetry of Strong-Field Ionization and Fragmentation of Polar Molecules: The Methyl Halide Series. *J. Phys. Chem. A* 119, 11772–11782. doi:10.1021/acs.jpca.5b07331

Wanie, V., Ibrahim, H., Beaulieu, S., Thiré, N., Schmidt, B. E., Deng, Y., et al. (2015). Coherent Control of D_2/H_2 Dissociative Ionization by a Mid-Infrared Two-Color Laser Field. *J. Phys. B: At. Mol. Opt. Phys.* 49, 025601. doi:10.1088/0953-4075/49/2/025601

Winterfeldt, C., Spielmann, C., and Gerber, G. (2008). Colloquium: Optimal Control of High-Harmonic Generation. *Rev. Mod. Phys.* 80, 117–140. doi:10.1103/revmodphys.80.117

Wollenhaupt, M., and Baumert, T. (2011). Ultrafast Laser Control of Electron Dynamics in Atoms, Molecules and Solids. *Faraday Discuss.* 153, 9–26. doi:10.1039/c1fd00109d

Wu, J., Magrakvelidze, M., Schmidt, L., Kunitski, M., Pfeifer, T., Schöffler, M., et al. (2013). Understanding the Role of Phase in Chemical Bond Breaking with Coincidence Angular Streaking. *Nat. Commun.* 4, 2177. doi:10.1038/ncomms3177

Zare, R. N. (1988). *Angular Momentum*. New York: Wiley.

Conflict of Interest: The authors declare that the research was conducted in the absence of any commercial or financial relationships that could be construed as a potential conflict of interest.

frontiers | Frontiers in Chemistry

ORIGINAL RESEARCH
published: 25 April 2022
doi: 10.3389/fchem.2022.866137

Ionization of HCCI Neutral and Cations by Strong Laser Fields Simulated With Time Dependent Configuration Interaction

H. Bernhard Schlegel*, Paul Hoerner and Wen Li

Department of Chemistry, Wayne State University, Detroit, MI, United States

Strong field ionization of neutral iodoacetylene (HCCI) can produce a coherent superposition of the X and A cations. This superposition results in charge migration between the CC π orbital and the iodine π-type lone pair which can be monitored by strong field ionization with short, intense probe pulses. Strong field ionization of the X and A states of HCCI cation was simulated with time-dependent configuration interaction using singly ionized configurations and singly excited, singly ionized configurations (TD-CISD-IP) and an absorbing boundary. Studies with static fields were used to obtain the 3-dimensional angular dependence of instantaneous ionization rates by strong fields and the orbitals involved in producing the cations and dications. The frequency of charge oscillation is determined by the energy separation of the X and A states; this separation can change depending on the direction and strength of the field. Furthermore, fields along the molecular axis can cause extensive mixing between the field-free X and A configurations. For coherent superpositions of the X and A states, the charge oscillations are characterized by two frequencies–the driving frequency of the laser field of the probe pulse and the intrinsic frequency due to the energy separation between the X and A states. For linear and circularly polarized pulses, the ionization rates show marked differences that depend on the polarization direction of the pulse, the carrier envelope phase and initial phase of the superposition. Varying the initial phase of the superposition at the beginning of the probe pulse is analogous to changing the delay between the pump and probe pulses. The charge oscillation in the coherent superposition of the X and A states results in maxima and minima in the ionization yield as a function of the superposition phase.

Keywords: HCCI+, iodoacetylene cation, strong field ionization, coherent superposition, time-dependent configuration interaction, pump-probe

Edited by:
Yuichi Fujimura,
Tohoku University, Japan

Reviewed by:
Yonggang Yang,
Shanxi University, China
Kenichi Ishikawa,
The University of Tokyo, Japan

****Correspondence:***
H. Bernhard Schlegel
hbs@chem.wayne.edu

Specialty section:
This article was submitted to Physical Chemistry and Chemical Physics, a section of the journal Frontiers in Chemistry

Received: *30 January 2022*
Accepted: *24 March 2022*
Published: *25 April 2022*

Citation:
Schlegel HB, Hoerner P and Li W (2022) Ionization of HCCI Neutral and Cations by Strong Laser Fields Simulated With Time Dependent Configuration Interaction. Front. Chem. 10:866137. doi: 10.3389/fchem.2022.866137

INTRODUCTION

Producing and probing ultrafast electronic wave packets are important topics of attosecond spectroscopy and have attracted much attention in the past decade. A few atomic and molecular systems have been shown to exhibit coherent electronic motions in the few to tens of femtoseconds range. (Smirnova et al., 2009; Goulielmakis et al., 2010; Calegari et al., 2014; Kraus et al., 2015). Various experimental techniques have been developed to achieve excellent temporal resolution and

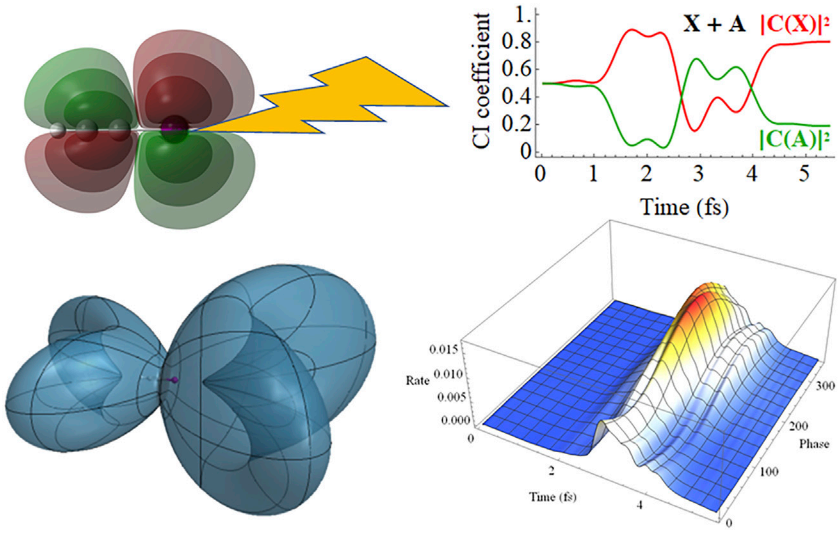

Graphical Abstract | Time-dependent configuration interaction simulations of the electron dynamics in coherent superpositions of the X and A cation states of HCCI show marked differences in the strong field ionization rates by intense, 2 cycle probe pulses that depend on the initial phase of the superposition and on the carrier envelope phase.

these include attosecond transient absorption, attosecond pump-IR probe, high harmonic spectroscopy, and attosecond streaking. (Kienberger et al., 2004; Eckle et al., 2008; Smirnova et al., 2009; Goulielmakis et al., 2010; Calegari et al., 2014; Winney et al., 2017). Strong field ionization (SFI) plays an important role in most of these developed techniques owing to its sub-cycle timing arising from the high nonlinearity of the process. SFI has been used either as a pump pulse to excite the electronic superposition or as a probe to detect the wavepacket motion. A simple extrapolation would suggest it might be possible to employ SFI in both steps to produce and probe electronic dynamics. In this article, computational simulations were carried out to explore SFI of a molecule undergoing coherent electronic dynamics. Iodoacetylene, HCCI, is selected as the model system. The superposition between the X and A states of HCCI cation has been studied previously using high harmonic spectroscopy and advanced modeling. (Kraus et al., 2015; Ding et al., 2017; Jenkins et al., 2018; Jia et al., 2019a; Jia et al., 2019b; Jia and Yang, 2022). However, due to the limited probing range of HHS, the wave packet motion beyond the first three femtoseconds has not been studied. Recent theoretical investigations suggested the coherence will rapidly dephase after 5 fs and even rephase at a later time. (Jia et al., 2019a; Jia et al., 2019b; Jia and Yang, 2022). Therefore, a new probing method with attosecond time resolution and a long probing range is needed. Here we show theoretically that SFI and second ionization implemented with few-cycle laser pulses can indeed follow the electronic wave packet motion and thus offer a long range attosecond probing method. Furthermore, our investigation reveals detailed and complex electronic dynamics associated with a SFI probe, which involves laser driven dynamics as well as intrinsic electronic dynamics.

Recent reviews discuss theoretical and computational methods for describing electron dynamics and ionization in strong laser fields. (Posthumus, 2004; Ishikawa and Sato, 2015; Nisoli et al., 2017; Goings et al., 2018; Li et al., 2020; Palacios and Martin, 2020). One and two electron systems can be treated accurately by solving the time dependent Schrodinger equation. For multi-electron systems, the single active electron (SAE) approximation and the strong field approximation (SFA) are often used. Orientation dependent ionization rates can be modelled with molecular Ammosov-Delone-Krainov (Tong et al., 2002) (MO-ADK) and weak-field asymptotic theory (Tolstikhin et al., 2011) (WFAT). More detailed descriptions of ionization by intense laser fields require numerical simulations of the electron dynamics. Methods for time dependent electronic structure methods have been reviewed recently. (Nisoli et al., 2017; Goings et al., 2018; Li et al., 2020; Palacios and Martin, 2020). Two approaches that have been used successfully to simulate strong field ionization for multi-electron polyatomic systems are real-time integration of time-dependent density functional theory (Chu and Chu, 2001; Chu, 2010; Hellgren et al., 2013; Lopata and Govind, 2013; Provorse and Isborn, 2016; Bruner et al., 2017; Sandor et al., 2018) (rt-TDDFT) and time-dependent configuration interaction (TD-CI). (Krause et al., 2005; Rohringer et al., 2006; Krause et al., 2007; Klinkusch et al., 2009; Greenman et al., 2010; Tremblay et al., 2011; Krause et al., 2014; Krause and Schlegel, 2015a). In these approaches, ionization is treated by removing the outgoing electron density using a complex absorbing potential. (Kosloff and Kosloff, 1986; Santra and Cederbaum, 2002; Muga et al., 2004; Krause et al., 2014; Krause and Schlegel, 2015a; Sommerfeld and Ehara, 2015).

In previous work, we have used time-dependent configuration interaction with a complex absorbing potential to study strong field ionization. (Krause et al., 2014; Krause and Schlegel, 2015a; Krause and Schlegel, 2015b; Hoerner and Schlegel, 2017; Hoerner and Schlegel, 2018; Winney et al., 2018; Lee et al., 2020). In particular, we have used TD-CIS to examine the angular dependence of strong field ionization of haloacetylenes, HCCX (X = F, Cl, Br, and I). (Hoerner and Schlegel, 2018). The present study examines some aspects of coherent electron dynamics in HCCI cations that can be generated by intense laser pump pulses and probed by strong field ionization using intense,ultra-short pulses. To provide some background of the electronic behavior of HCCI$^+$ in intense fields, the angular dependence of strong field ionization of the X and A states are studied with a static field and fixed nuclei. Next, the coherent superpositions of the X and A states of the cation are examined for the field free case and for strong field ionization by a static field. The purpose of the static field studies is to help understand the electronic response HCCI cations in strong fields. The time-dependent electron dynamics for strong field ionization by very short linearly and circularly polarized probe pulses are simulated for the X and A states of HCCI cation and their coherent superpositions. Nuclear dynamics leads to dephasing which modulates the electron dynamics. (Ding et al., 2017; Jenkins et al., 2018; Jia et al., 2019a; Jia et al., 2019b; Jia and Yang, 2022). This is addressed in a separate paper by Jia and Yang in this collection of articles on electronic and nuclear dynamics of molecules in intense laser fields. (Jia and Yang, 2022). The focus of the present paper is on the use of strong field ionization to probe the electron dynamics of HCCI$^+$. To minimize the effects of decoherence caused by nuclear motion during the pulse, the probe pulses are limited to two cycles (2.66 fs FWHM).

COMPUTATIONAL METHODS

The electronic wavefunction is propagated with the time-dependent Schrödinger equation (atomic units are used throughout the paper).

$$i\hbar\frac{\partial}{\partial t}\Psi(t) = \hat{\mathbf{H}}(t)\Psi(t) = [\hat{\mathbf{H}}_{el} - \hat{\vec{\mu}}\cdot\vec{E}(t) - i\,\hat{\mathbf{V}}^{absorb}]\Psi(t) \quad (1)$$

$\hat{\mathrm{H}}_{el}$ is the field-free non-relativistic electronic Hamiltonian. The interaction with the intense electric field is treated in the semiclassical dipole approximation, where $\hat{\vec{\mu}}$ is the dipole operator and $\vec{E}$ is the electric field. Ionization is modeled with a complex absorbing potential (CAP), $-i\mathbf{V}^{absorb}$, as described in our earlier papers. (Krause et al., 2014; Krause and Schlegel, 2015a; Krause and Schlegel, 2015b; Hoerner and Schlegel, 2017; Hoerner and Schlegel, 2018; Winney et al., 2018; Lee et al., 2020) The total absorbing potential for the molecule is equal to the minimum of the values of spherical absorbing potentials centered on each atom. Each spherical potential begins at 3.5 times the van der Waals radius of each element (R_{H} = 9.544 bohr, R_{C} = 12.735 bohr, R_{I} = 14.882 bohr), rises as $\sin((\pi/2)(R–R_0)/(R_1-R_0))^2$ to 10 hartree at approximately $R_1 = R_0 + 28$ bohr and is equal to 10 hartree for $R > R_1$. The decrease in the norm^2 of the wavefunction is taken as the total ionization yield. The instantaneous ionization rate is calculated as the rate of decrease in the norm^2 and can be related to the matrix elements of the absorbing potential.

$$\begin{aligned}\mathrm{rate}(t) &= -\partial\langle\Psi_{neutral}(t)|\Psi_{neutral}(t)\rangle/\partial t\\ &= \frac{2}{\hbar}\langle\Psi_{neutral}(t)|\mathbf{V}^{absorb}|\Psi_{neutral}(t)\rangle\end{aligned} \quad (2)$$

The matrix elements of $\mathbf{V}^{absorb}$ can be written in terms of the molecular orbitals to give the contribution of individual molecular orbitals to the total ionization rate. (Lee et al., 2020).

For simulations of the ionization of neutral HCCI with TD-CIS, the wavefunction includes the Hartree-Fock reference determinant and all distinct $\alpha\rightarrow\alpha$ and $\beta\rightarrow\beta$ single excitations from the active orbitals,

$$\Psi_{neutral}(t) = \sum_{I=0} C_I(t)|\Psi_I\rangle = c_0\Psi_0 + \sum_{ia} c_i^a\Psi_i^a + \sum_{\bar{i}\bar{a}} c_{\bar{i}}^{\bar{a}}\Psi_{\bar{i}}^{\bar{a}} \quad (3)$$

where β orbitals are indicated by an overbar. Simulations of the ionization of HCCI cations were carried out with TD-CISD-IP. (Lee et al., 2020) The CISD-IP wavefunction (Golubeva et al., 2009) includes singly ionized determinants, Ψ_x, constructed by removing an electron from each of the active orbitals of the neutral molecule and all $\alpha\rightarrow\alpha$ and $\beta\rightarrow\beta$ single excitations from these determinants,

$$\begin{aligned}\Psi_{cation}(t) = \sum_{I=0} C_I(t)|\Psi_I\rangle = \sum_{x} c_x\Psi_x + \sum_{\bar{x}} c_{\bar{x}}\Psi_{\bar{x}} +\\ \sum_{iax} c_{ix}^a\Psi_{ix}^a + \sum_{ia\bar{x}} c_{i\bar{x}}^a\Psi_{i\bar{x}}^a + \sum_{\bar{i}\bar{a}x} c_{\bar{i}x}^{\bar{a}}\Psi_{\bar{i}x}^{\bar{a}} + \sum_{\bar{i}\bar{a}\bar{x}} c_{\bar{i}\bar{x}}^{\bar{a}}\Psi_{\bar{i}\bar{x}}^{\bar{a}}\end{aligned} \quad (4)$$

The hole density for the cation is the difference of the one electron densities of the neutral and the cation. Movies of the hole density are useful for examining the electron dynamics in a laser field. Aspects of the electron dynamics of the cations can also be followed by looking at occupied-occupied elements of the density matrix (for the field strengths considered here, the other elements of the cation density matrix are much smaller). For a CISD-IP wavefunction, the occupied-occupied block of the one electron density matrix in terms of molecular spin orbitals is given by

$$\rho_{i,j}^{occ} = \delta_{i,j} - c_j^*c_i - \sum_{ka} c_{jk}^{a\,*}c_{ik}^a \quad (5)$$

As in our previous studies, (Krause et al., 2014; Krause and Schlegel, 2015a; Krause and Schlegel, 2015b; Hoerner and Schlegel, 2017; Hoerner and Schlegel, 2018; Winney et al., 2018; Lee et al., 2020), the exponential of the Hamiltonian is used to propagate the time-dependent wavefunction. For a linearly polarized pulse, a Trotter factorization is employed to compute the exponential.

$$\begin{aligned}\Psi(t+\Delta t) &= \exp(-i\,\hat{\mathbf{H}}\Delta t)\Psi(t)\\ \mathbf{C}(t+\Delta t) &= \exp(-i\,\mathbf{H}_{el}\Delta t/2)\exp(-\mathbf{V}^{absorb}\Delta t/2)\\ &\quad\times\mathbf{W}^T\exp(i\,E(t+\Delta t/2)\,\mathbf{d}\,\Delta t)\,\mathbf{W}\\ &\quad\times\exp(-\mathbf{V}^{absorb}\Delta t/2)\exp(-i\,\mathbf{H}_{el}\Delta t/2)\mathbf{C}(t)\end{aligned} \quad (6)$$

$\mathbf{WDW}^T = \mathbf{d}$ are the eigenvalues and eigenvectors of the transition dipole matrix $\mathbf{D}$ in the field direction. The matrices $\exp(-i\,\mathbf{H}_{el}\Delta t/2)$, $\exp(-\mathbf{V}^{absorb}\Delta t/2)$, $\mathbf{W}$ and $\mathbf{d}$ need to be calculated only once at the beginning of the propagation because they are time independent. Likewise, the product $\mathbf{U} = \exp(-\mathbf{V}^{absorb}\Delta t/2)\ \mathbf{W}^{\boldsymbol{T}}$ is formed once at the beginning of the

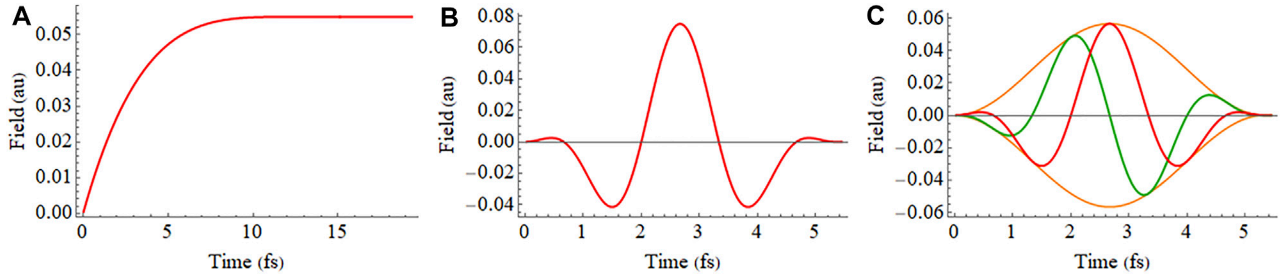

FIGURE 1 | (A) Shape of the electric field used to obtain the instantaneous ionization in a static field (**Eq. 8**), **(B)** 2 cycle linearly polarized 800 nm pulse with a $\sin^2$ envelope (**Eq. 9**), and **(C)** 2 cycle circularly polarized 800 nm pulse with a $\sin^2$ envelope (**Eq. 10**) showing x and z components in green and red, respectively.

propagation. The only time dependent factor is $\exp(i\,E\,(t+\Delta t/2)\,\mathbf{d}\,\Delta t)$; this exponential can be calculated easily because $\mathbf{d}$ is a diagonal matrix. A propagation step for a linearly polarized pulse with fixed nuclear positions involves two full matrix-vector multiplies ($\mathbf{U}$ and $\mathbf{U}^T$) and three diagonal matrix-vector multiplies ($\exp(-i\,\mathbf{H}_{el}\Delta t/2)$ and $\exp(i\,E\,(t+\Delta t/2)\,\mathbf{d}\,\Delta t)$).

The corresponding Trotter factorization for a circularly polarized pulse involves two oscillating fields

$$\begin{aligned}\mathbf{C}(t+\Delta t) = {} & \exp(-i\,\mathbf{H}_{el}\Delta t/2)\exp(-\mathbf{V}^{absorb}\Delta t/2)\\ & \times \mathbf{W}_2^T \exp(i\,E_2\,(t+\Delta t/2)\,\mathbf{d}_2\,\Delta t/2)\,\mathbf{W}_2\\ & \times \mathbf{W}_1^T \exp(i\,E_1\,(t+\Delta t/2)\,\mathbf{d}_1\,\Delta t)\,\mathbf{W}_1\\ & \times \mathbf{W}_2^T \exp(i\,E_2\,(t+\Delta t/2)\,\mathbf{d}_2\,\Delta t/2)\,\mathbf{W}_2\\ & \times \exp(-\mathbf{V}^{absorb}\Delta t/2)\exp(-i\,\mathbf{H}_{el}\Delta t/2)\mathbf{C}(t)\end{aligned} \tag{7}$$

where $\mathbf{W}_1\mathbf{D}_1{\mathbf{W}_1}^T = \mathbf{d}_1$ and $\mathbf{W}_2\mathbf{D}_2{\mathbf{W}_2}^T = \mathbf{d}_2$ are the eigenvalues and eigenvectors of the transition dipole matrix $\mathbf{D}_1$ and $\mathbf{D}_2$ in the two orthogonal field directions. A propagation step for a circularly polarized pulse with fixed nuclei involves four full matrix-vector multiplies and five diagonal matrix-vector multiplies.

The present methodology has been tested in an earlier paper (Krause et al., 2014) and satisfactory agreement was obtained in comparisons with the results for ionization of hydrogen atom and H_2^+ calculated with grid-based methods. (Hehenberger et al., 1974; Hermann and Fleck, 1988; Bandrauk et al., 2012). While grid-based methods are limited to one and two electron systems, the TDCI approach can be applied to many-electron, polyatomic molecules. Unlike the strong field approximation (SFA) and single active electron (SAE) approximation, the TDCI calculations include exchange interactions of the ionizing electron, and the dynamics of the remaining valence electrons. Because the propagation uses the exponential of the Hamiltonian, a fairly large time step of $\Delta t = 0.05$ au (1.2 as) can be used. In similar simulations, reducing the time step by a factor of 2 changed the ionization yield by less than 0.01%. (Hoerner and Schlegel, 2017). Once the initial eigenvectors and matrix exponentials are calculated, the cost of the propagation steps is $O(N^2)$ compared to $O(N^3)$ for real-time integration of TD-DFT. (Li et al., 2020).

Directional information for ionization was obtained by examining the ionization rate in a static field. Abruptly turning on a strong field can cause extensive non-adiabatic excitation. A practical approach to avoid non-adiabatic excitations involves ramping up the electric field slowly and calculating the instantaneous ionization rate when the field has reached a constant value. (Hermann and Fleck, 1988). The instantaneous ionization rate was calculated after 800 au (19.35 fs) using

$$\begin{aligned}E(t) &= E_{\max}\left(1-\left(1-\frac{t}{t_{ramp}}\right)^4\right) \quad \text{for } 0 \le t \le t_{ramp},\\ E(t) &= E_{\max} \text{ for } t \ge t_{ramp}\end{aligned} \tag{8}$$

with $t_{ramp} = 533$ au $= 12.90$ fs.

Simulations of strong field ionization of HCCI cations with linearly polarized light used a 2 cycle 800 nm ($\omega = 0.057$ au) pulse in the xz plane with a $\sin^2$ envelope,

$$\begin{aligned}E(t) &= E_{\max}\sin(\omega t/4)^2\cos(\omega t) \quad \text{for } 0 \le \omega t \le 4\pi,\\ E(t) &= 0 \text{ for } \omega t \ge 4\pi\end{aligned} \tag{9}$$

for HCCI aligned with the *z* axis. Simulations with circularly polarized light used a 2 cycle 800 nm pulse in the xz plane with a $\sin^2$ envelope (FWHM = 2.66 fs).

$$\begin{aligned}E_x(t) &= E_{\max}\sin(\omega\,t/4)^2\left[-\cos(\omega\,t)\cos(\gamma)-\sin(\omega\,t)\sin(\gamma)\right]\\ E_z(t) &= E_{\max}\sin(\omega\,t/4)^2\left[\cos(\omega\,t)\sin(\gamma)-\sin(\omega\,t)\cos(\gamma)\right]\\ &\text{for } 0 \le \omega\,t \le 4\pi,\ E_z(t) = E_x(t) = 0 \text{ for } \omega\,t \ge 4\pi\end{aligned} \tag{10}$$

E_{max} is the maximum value for the electric field and γ determines the direction of the field at the maximum of the pulse. The electric fields for **Eqs 8–10** are shown in **Figure 1**.

A locally modified version of the Gaussian software package (Frisch et al., 2019) was used to calculate the CAP integrals needed for the TDCI simulation. The TDCI simulations were carried out with an external Fortran95 code. Mathematica (Mathematica 12, 2019) was used to analyze the simulations and plot the results. Movies were prepared with VMD. (Humphrey et al., 1996). The CC, CH, and CI bond lengths used for HCCI were 1.0542, 1.1819, and 1.9982 Å, respectively. HCCI was placed on the *z* axis with the iodine in the -z direction. All of the simulations were

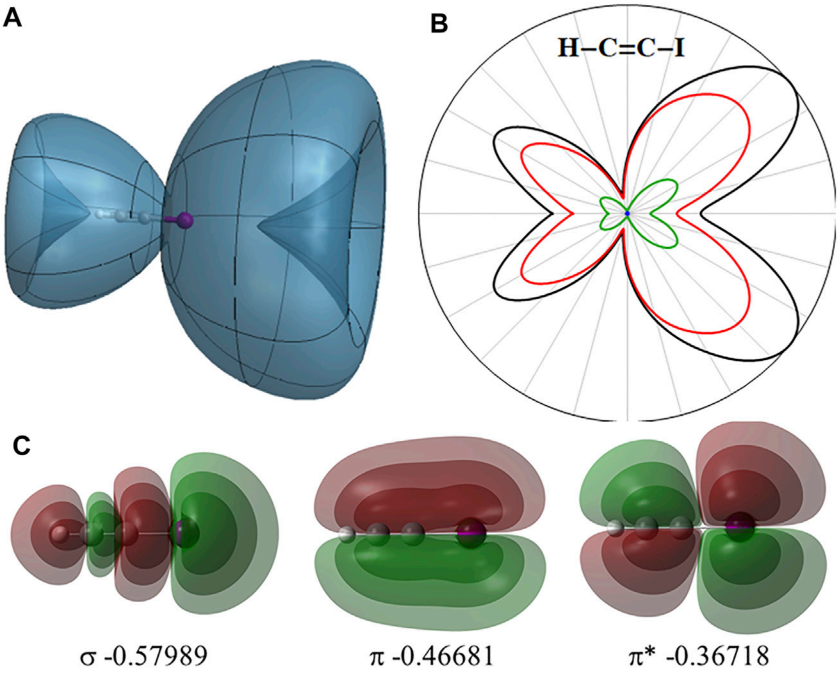

FIGURE 2 | (A) Angular dependence of the instantaneous ionization rate for neutral HCCI in static field of 0.033 au. **(B)** 2-Dimensional slice showing the total ionization rate (black) and contributions from the σ, π, and π^* orbitals (blue, green and red, respectively). **(C)** Highest occupied σ, π and π^* orbitals of HCCI and their orbital energies (in hartree).

carried out with fixed nuclei. The aug-cc-pVTZ basis set (Dunning, 1989; Woon and Dunning, 1993; Peterson et al., 2006) was used for H and C; the aug-cc-pVTZ-PP basis set with pseudopotential was used for iodine. (Peterson et al., 2003). These basis sets were augmented with a set of additional diffuse functions placed on each atom to describe the electron dynamics during the ionization process and to ensure adequate interaction with the CAP. (Krause et al., 2014; Hoerner and Schlegel, 2017). This "absorbing basis" consisted of four *s* functions with exponents of 0.0256, 0.0128, 0.0064, and 0.0032; four *p* functions with exponents of 0.0256, 0.0128, 0.0064, and 0.0032; five *d* functions with exponents of 0.0512, 0.0256, 0.0128, 0.0064, and 0.0032; and two *f* function with an exponent of 0.0256 and 0.0128. The time-dependent wavefunction for HCCI included all excitations from the highest σ orbital and two highest π and π* orbitals to all virtual orbitals with orbital energies less than 3 hartree, for a total of 2,621 configurations for HCCI neutral and 18,530 configurations for HCCI cations. For studies with a static field, $E_{\max}$ = 0.033 au was optimal for neutral HCCI and 0.055 au for the cation, while $E_{\max} = 0.075$ au and $0.080/\sqrt{2} = 0.0566$ au were used for ionization of the cation with linear and circularly polarized pulses, respectively. Smaller values of $E_{\max}$ yielded too little ionization of the neutral and the X state of the cation; larger values lead to artifacts in the angular dependence of the ionizations of the cations.

RESULTS AND DISCUSSION

The angular dependence of the instantaneous ionization rate of neutral HCCI in a static field obtained with TD-CIS simulations is shown in **Figure 2** along with the highest occupied σ, π and π^* orbitals of HCCI. The π and π^* orbitals are the in-phase and out-of-phase combinations of the CC π orbitals and the iodine π-type lone pairs. When the field has reached a constant value, the shape of the instantaneous ionization rate and the total ionization yield both resemble the nodal structure of the highest occupied π^* orbital. Similar shapes were found with WFAT calculations. (Tolstikhin et al., 2011). Partitioning the instantaneous ionization rate into orbital contributions (Lee et al., 2020) shows that ionization is predominantly from the π^* orbital leading to the ground state of the cation, the X state (see **Figure 2B**). The π orbital is 0.1 hartree lower in energy and contributes to a lesser extent. Removal of an electron from this orbital leads to the lowest excited state of the cation (the A state). The iodine σ-type lone pair orbital is 0.2 hartree lower in energy than the π^* orbital and does not contribute significantly to ionization at this field strength. Ionization of HCCI by a strong field can result in a coherent superposition of cation states, mainly the X and A states. The ratio of the calculated ionization rates of the X and A states is 3.9 when averaged over the angles, in good agreement with the experimental ratio of 4.3 for the populations of the superposition of the X and A states found in the analysis of the HHG spectra. (Kraus et al., 2015).

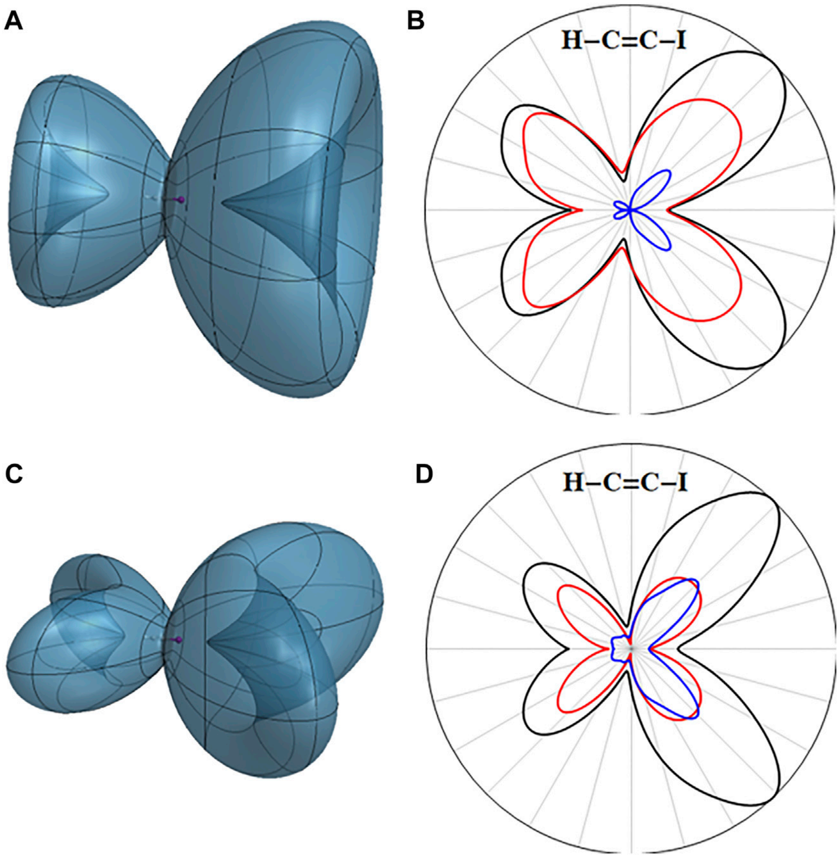

FIGURE 3 | Three-dimensional angular dependence of the instantaneous ionization rate for the ground state of the HCCI cation in a static field of 0.055 au for **(A)** the X ($\bar{\pi}_{+}^{*\,-1}$) cation and **(C)** the X ($\bar{\pi}_{x}^{*\,-1}$) cation. Total ionization rates in the xz plane in black and contributions from ionizing the π^* orbitals in red and from the π orbitals in blue for **(B)** the X ($\bar{\pi}_{+}^{*\,-1}$) cation and **(D)** the X ($\bar{\pi}_{x}^{*\,-1}$) cation.

The experimental energies for the vertical ionization from the neutral to the X and A states of the cation are 9.71 and 11.94 eV, respectively. (Allan et al., 1977). Ionization energies calculated by Koopmans theorem are just the negative of the orbital energies (9.99 and 12.70 eV, resp.); these values are in reasonably good agreement with experiment because of a cancellation of errors caused by the neglect of orbital relaxation and electron correlation effects. Electron propagator theory (Ortiz, 1996) (EPT) treats both relaxation and correlation, resulting in improved ionization potentials (9.89 and 12.22 eV, resp. with the aug-cc-pVTZ-PP basis set). EOMIP/CCSD calculations give even better agreement with experiment. (Kraus et al., 2015). However, EPT and EOMIP/CCSD cannot be used in TDCI simulations of the cations since thousands of excited states are needed to model the electron dynamics of strong field ionization. Spin unrestricted CIS could be employed, but this results in different orbitals for the X and A states. As an alternative, the TD-CISD-IP approach can be used to treat the dynamics of the ground and excited states of the cation on an equal footing. The CISD-IP ionization energies (8.55 and 10.76 eV with aug-cc-pVTZ-PP plus the absorbing basis) are about an eV too low because they include some orbital relaxation but little correlation. However, the difference in the energies of the X and A states is the most important factor for the dynamics of a superposition of these states. The difference in the CISD-IP ionization energies, 2.21 eV, is in very good agreement with the experimental difference, 2.23 eV.

The electron density of the field-free X cation is cylindrically symmetrical with a hole in one of the degenerate $\pi_{\pm}^{*}$ orbitals (**Figure 3A**). The ionization from the X cation to the dication is dominated by removing an electron from $\pi_{\mp}^{*}$, the other orbital of the degenerate pair (red curve in **Figure 3B**); contributions from the lower lying $\pi_{\pm}$ orbitals are smaller (blue curve). For HCCI aligned with the z axis, sequential strong field ionization of HCCI in a static field, or by linear and circular pulses with the electric field in the xz plane will favor cations and dications with electron hole densities localized in the xz plane, *i.e.* loss of electrons from the π_x and π_x^* orbitals. The three-dimensional angular dependence of the ionization rate for the X ($\bar{\pi}_{x}^{*\,-1}$) cation is shown in **Figure 3C**. The largest contribution comes from the $\bar{\pi}_y^*$ orbital. If only ionization in the xz plane is considered, removing an electron from the π_x^* orbital makes the largest contribution, yielding a ($\pi_x^{*\,-1}$, $\bar{\pi}_x^{*\,-1}$) dication (red curve in **Figure 3D**). Ionization from the π_x and $\bar{\pi}_x$ orbitals make somewhat smaller contributions (blue curve).

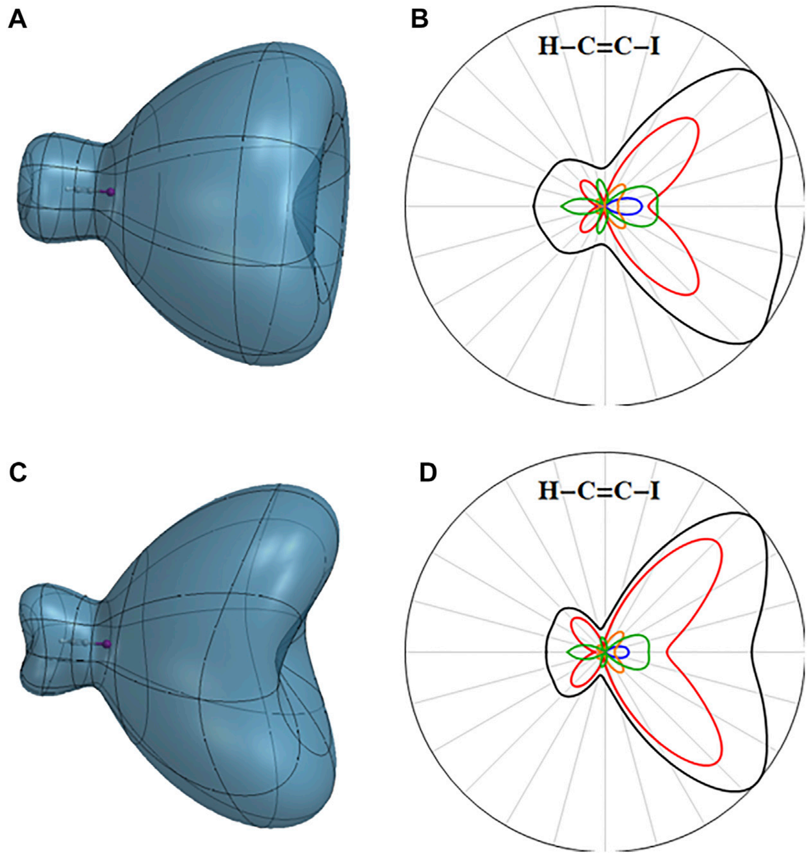

FIGURE 4 | Three-dimensional angular dependence of the instantaneous ionization rate for the first excited state of the HCCI cation in a static field of 0.055 au for **(A)** the A ($\bar{\pi}_+^{-1}$) cation and **(C)** the A ($\bar{\pi}_x^{-1}$) cation. Total ionization rates in black and contributions from ionizing the π^* and $\bar{\pi}^*$ orbitals in red (*i.e.* yielding the ($\bar{\pi}^{-1}$, π^{*-1}) and ($\bar{\pi}^{-1}$, $\bar{\pi}^{*-1}$) doubly ionized configurations), contributions yielding the (π^{*-1} , $\bar{\pi}_y^{-1}$), ($\bar{\pi}^{*-1}$, $\bar{\pi}_y^{-1}$), (π^{-1} , $\bar{\pi}_y^{*-1}$), and ($\bar{\pi}^{-1}$, $\bar{\pi}_y^{*-1}$) doubly ionized configurations in blue, the (π^{-1} , $\bar{\pi}_x^{*-1}$) configurations in orange and the (π^{*-1} , π^{*-1}), (π^{*-1} , $\bar{\pi}^{*-1}$), and ($\bar{\pi}^{*-1}$, $\bar{\pi}^{*-1}$) configurations in green for **(B)** the A ($\bar{\pi}_+^{-1}$) cation and **(D)** the A ($\bar{\pi}_x^{-1}$) cation.

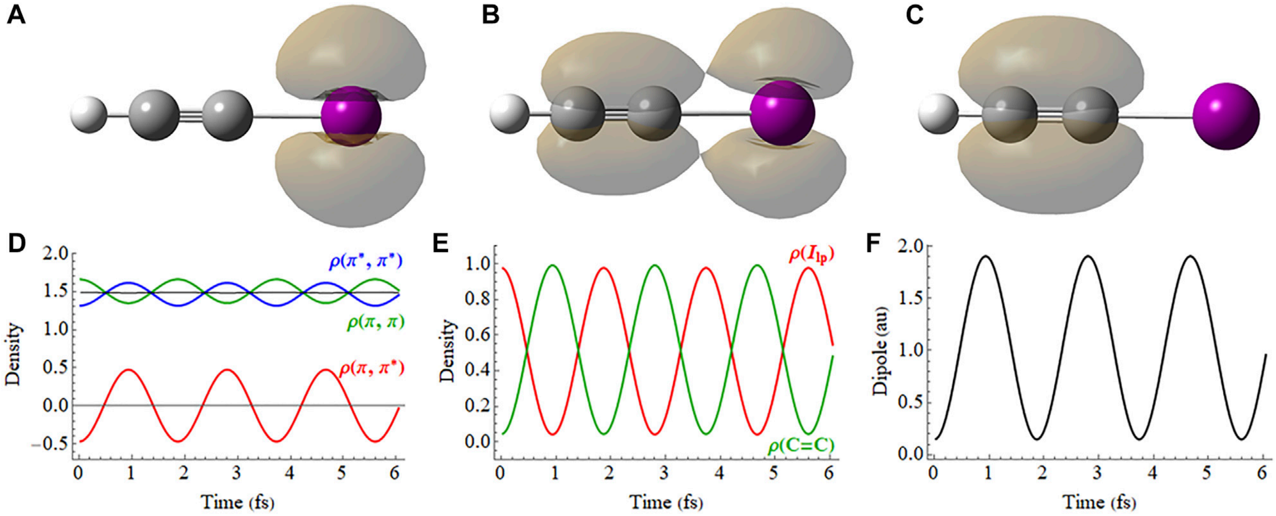

FIGURE 5 | Field-free coherent superposition of the X ($\bar{\pi}_x^{*-1}$) and A ($\bar{\pi}_x^{-1}$) cations of HCCI. Hole density for **(A)** X + A, **(B)** X + *i* A and **(C)** X – A (a movie of the hole density is available in **Supplementary Figure S1** of the Supporting Information). **(D)** Density matrix elements for the π_x and π_x^* orbitals. **(E)** Hole density for the C=C π orbital ($\pi - \pi^*$) and the I_{lp} orbital ($\pi + \pi^*$). **(F)** Z component of the dipole moment.

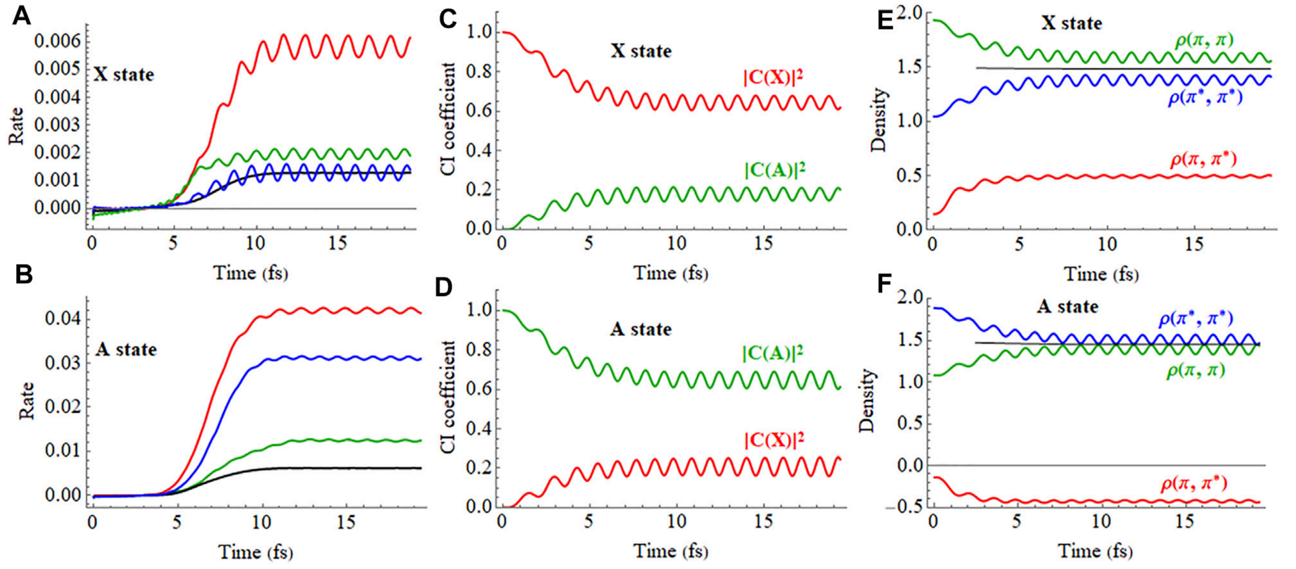

FIGURE 6 | Ionization of the X ($\bar{\pi}_x^{*\,-1}$) and A ($\bar{\pi}_x^{-1}$) states by static electric field ramped up to 0.055 au. **(A,B)** The ionization rate for the field along the molecular axis and ionization from the iodine end (blue) and the hydrogen end (green), perpendicular to the molecular axis (black) and at 45° to the molecular axis from the iodine end (red). **(C,D)** CI coefficients for the X and A configurations (red and green, resp.) in the normalized wavefunction for the time-dependent X and A states, for the field along the molecular axis and ionization from the iodine end. **(E,F)** Density matrix elements for the π_x and π_x^* orbitals for the field along the molecular axis and ionization from the iodine end for the X and A states, respectively. A movie of the hole density for the X state is available in **Supplementary Figure S2** of the Supporting Information.

The angular dependence of the ionization rate for the A state of the cation with a hole in the $\bar{\pi}$ orbital is shown in **Figure 4** along with the orbital contributions. Because the A state is 2.2 eV higher than the X state, its ionization rate is considerably higher. As expected, the largest contribution to ionization comes from removing an electron from the π^* orbitals (red curve in **Figures 4B,D**). Because of large transition dipole matrix elements between the π and π^* orbitals (0.88 au), the component of the electric field aligned with the molecular axis mixes the X and A field-free states. As discussed above, the component from the X state ionizes mainly from π^* orbitals, yielding a dication with 2 electrons removed from the π^* orbitals (green curve in **Figures 4B,D**). There is also some ionization of the A ($\bar{\pi}_x^{-1}$) cation along the molecular axis from the iodine end (blue curve). The partitioning of this ionization rate into orbital contributions indicates that it involves ionization from the π_y and π_y^* orbitals when the field is aligned with the molecular axis. This component becomes considerably larger for higher field strengths.

In the field-free case, the X ($\bar{\pi}_x^{*\,-1}$) and A ($\bar{\pi}_x^{-1}$) cations are stationary states, but a coherent superposition of these X and A cations results in a hole density that oscillates continuously between the iodine π-type lone pair and the CC π bond, as shown in **Figures 5A–C** (a movie is available in **Supplementary Figure S1** of the Supporting Information). The density for the π and π^* orbitals is shown in **Figure 5D**. The charge oscillation can be seen readily by examining the hole density for the C=C π orbital and the π-type I_{lp} orbital, plotted in **Figure 5E**. The charge

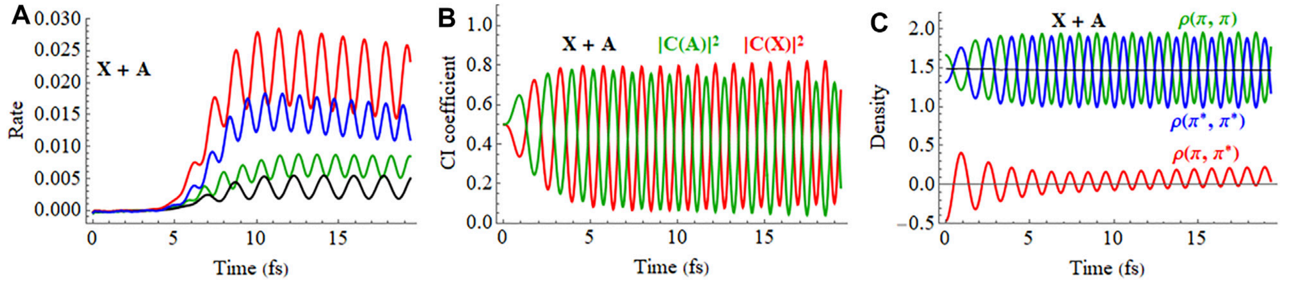

FIGURE 7 | Ionization of the X + A ($\bar{\pi}_x^{*\,-1} + \bar{\pi}_x^{-1}$) coherent superposition by a static electric field ramped up to 0.055 au. **(A)** The ionization rate for the field along the molecular axis and ionization from the iodine end (blue) and the hydrogen end (green), perpendicular to the molecular axis (black) and at 45° to the molecular axis from the iodine end (red). **(B)** CI coefficients for the X and A configurations (red and green, resp.) in the normalized wavefunction for the X + A coherent superposition for the field along the molecular axis and ionization from the iodine end. **(C)** Density matrix elements for the π_x and π_x^* orbitals for the field along the molecular axis and ionization from the iodine end (a movie of the hole density is available in **Supplementary Figure S2** of the Supporting Information).

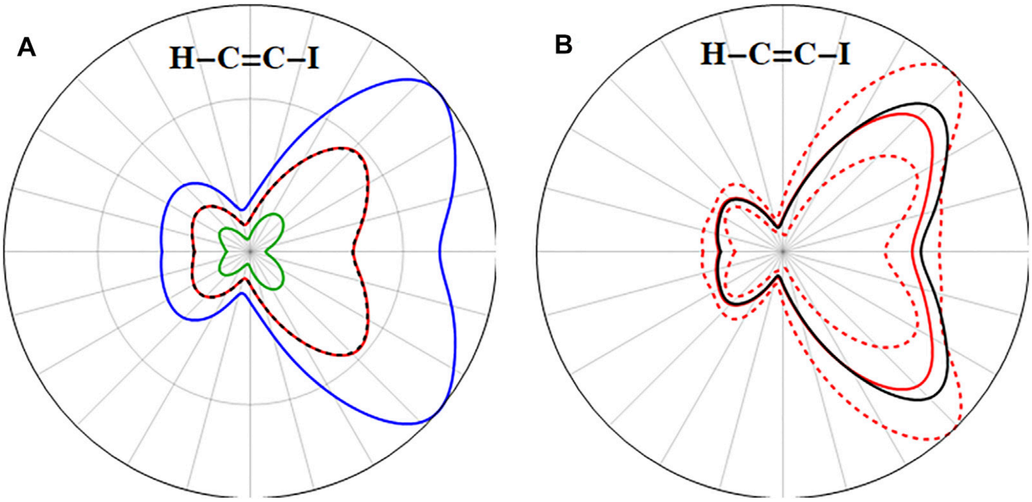

FIGURE 8 | (A) Comparison of the ionization yield (decrease in $|\Psi|^2$) for the X + A coherent superposition (red) with the incoherent superposition of X and A (black dashed); the ionization yields for X and A states individually are in green and blue, respectively. **(B)** Comparison of the instantaneous ionization rate for the X + A coherent superposition (red) with the incoherent superposition of X and A (1:0.9 ratio, black) averaged over the last 2 fs of the simulation; maximum and minimum rates for X + A during the last 2 fs of the simulation shown as dashed red lines (same simulation parameters as in **Figure 7**).

oscillation can also be seen by monitoring the dipole moment, **Figure 5F**. The period of the oscillation, 1.87 fs, is determined by the 2.21 eV energy difference between the X and A states. The CISD-IP wavefunctions for the field-free cations involve a small amount of mixing between the pure $(\bar{\pi}_x^{*\,-1})$ and $(\bar{\pi}_x^{-1})$ configurations $\Psi(\mathrm{X}) = 0.95\ (\bar{\pi}_x^{*\,-1})$ - $0.14\ (\bar{\pi}_x^{-1})$ and $\Psi(\mathrm{A}) = 0.93\ (\bar{\pi}_x^{-1}) + 0.16\ (\bar{\pi}_x^{*\,-1})$)

In a finite static field, the field-free X and A states are generally no longer stationary. **Figures 6A,B** show the X and A states for a number of directions of a static field that is ramped up to a constant value of 0.055 au (a movie of the hole density for the X state is available in **Supplementary Figure S2** of the Supporting Information). As expected, the ionization rate for the higher lying A state is considerably larger than for the X state. When the field has a component along the molecular axis, the X and A configurations interact through a large transition dipole matrix element. This mixing of the X and A states produces the oscillation of the ionization rate seen in **Figures 6A,B**. Because the X and A states have different dipole moments and polarizabilities, the finite field affects the energy difference between the two states and hence changes the oscillation frequency (*e.g.* compare the different directions shown **Figure 6A** and see **Supplementary Figure S12** of Kraus et al., 2015). The square of the CI coefficients shown in **Figures 6C,D** are the populations of the field-free configurations (see **Eq. 4**). For the field along the molecular axis and ionization from the iodine end, the CI coefficient squared for the X configuration decreases from an initial value of 1 to an average of 0.64 and the coefficient squared for the A configuration increases from 0 to an average of 0.18; complementary behavior is seen for the A state. The density matrix elements in terms of the field-free π and π^* molecular orbitals are shown in **Figures 6E,F**. The $\rho(\pi,\ \pi)$ and $\rho(\pi^*, \pi^*)$ matrix elements (*i.e.,* populations of the π and π^* molecular orbitals) become nearly equal and average to a constant value of 1.5. For the X state, the off-diagonal $\rho(\pi, \pi^*)$ rises to 0.5 and accounts for a shift of the electron density toward the CC π bond; the converse behavior is seen for the A state.

The coherent superposition of X + A in a static field is shown in **Figure 7** (a movie is available in **Supplementary Figure S2** of the Supporting Information). Similar results were found for the X − A superposition. As expected from the field-free case, the electron hole moves between the iodine π-type lone pair and the CC π bond resulting in oscillations of the ionization rate for all field directions. Like the X and A states individually, the oscillation frequency for X + A ionization rate depends on the magnitude and direction of the field. After the field has reached a constant value, there is a noticeable decrease in the ionization rate from the iodine end of the molecule (red and blue curves in **Figure 7A**). The CI coefficients of the X and A configurations for ionization from the iodine end are plotted in **Figure 7B**. The X:A ratio changes from an initial value of 1:1 to an average value of 1: 0.9 by the end of the simulation because the A state is ionized more rapidly than the X state. Since the ionization from the iodine end is 5–10 times higher for the A state than for the X state, (compare **Figures 6A,B**), the decrease in the relative population of the A state accounts for the decrease in the total ionization rate seen in **Figure 7A**. The density matrix elements are shown in **Figure 7C**. The average value of the off-diagonal $\rho(\pi, \pi^*)$ matrix element increases from 0 to 0.12 by the end of the simulation as a result of the increasing fraction of the X configuration. The amplitude of the oscillations of $\rho(\pi, \pi^*)$ decreases from ±0.5 at zero field strength to ±0.1 when the field reaches a constant value. When simulations of the coherent superposition of X + A are carried out in the absence of ionization (*e.g.,* no absorbing basis), the X:A ratio does not change and the average value of $\rho(\pi, \pi^*)$ remains zero; this supports the conclusion that the decrease in the rate observed in **Figure 7A** is due to the more rapid ionization of the A configuration.

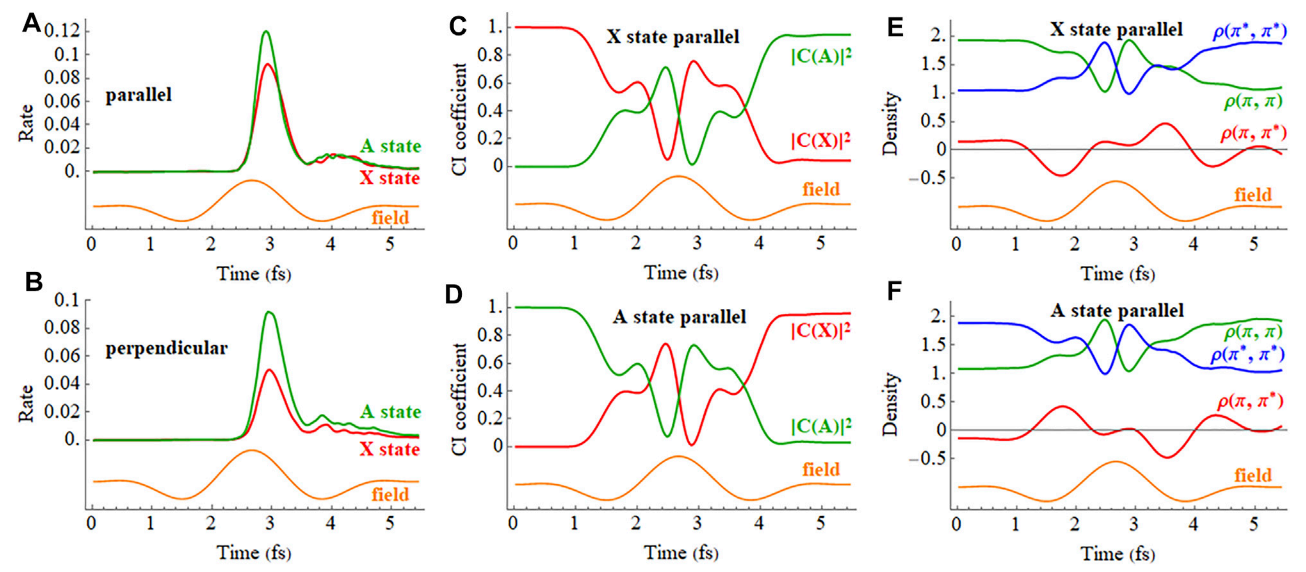

FIGURE 9 | (A,B) Ionization rate for the X and A cations in a 2 cycle linearly polarized 800 nm pulse with E_{max} = 0.075 au aligned parallel and perpendicular to the molecular axis (X in red, A in green). **(C,D)** CI coefficients for the X and A configurations (red and green, resp.) in the normalized wavefunctions for the X ($\bar{\pi}_x^{*\,-1}$) and A ($\bar{\pi}_x^{-1}$) states with the pulse aligned parallel to the molecular axis with ionization mainly from the iodine. **(E,F)** Density matrix elements for the π_x and π_x^* orbitals in the X and A states for the pulse aligned with the molecular axis (the orange traces are proportional to the electric field). A movie of the hole density is available in **Supplementary Figure S3** of the Supporting Information.

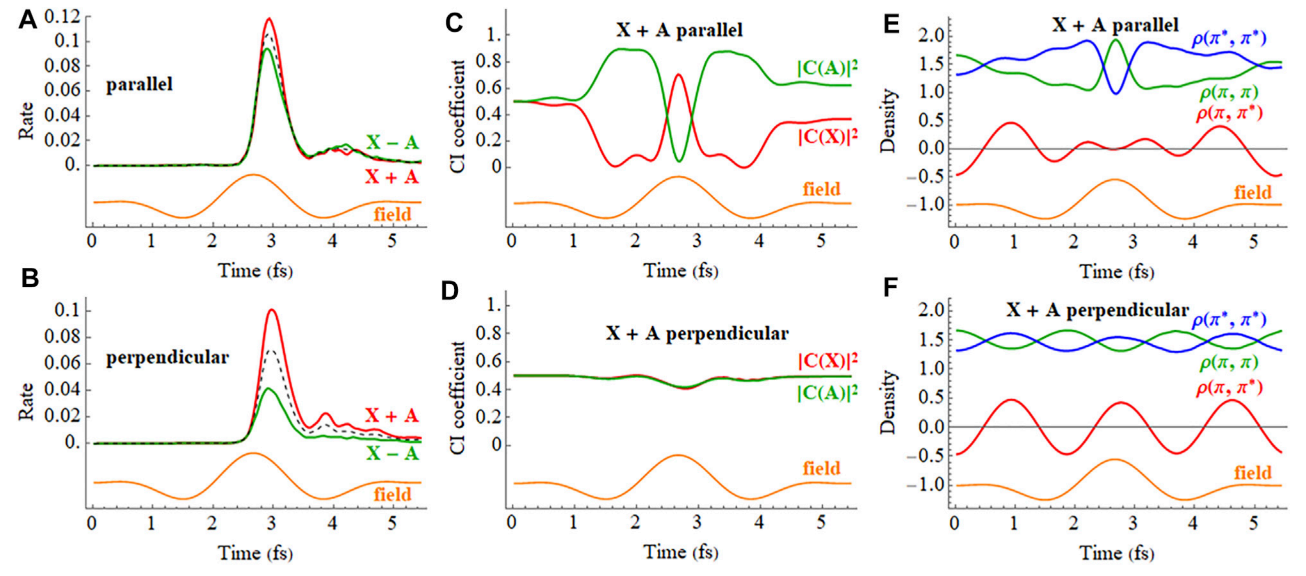

FIGURE 10 | (A,B) Ionization rate for coherent X + A and X − A superpositions for a 2 cycle, 800 nm linearly polarized pulse with E_{max} = 0.075 au aligned parallel and perpendicular to the molecular axis (incoherent average of X and A in black dashed). **(C,D)** CI coefficients for the X and A configurations (red and green, resp.) in the normalized wavefunction for polarizations parallel and perpendicular to the molecular axis. **(E,F)** Density matrix elements for the π_x and π_x^* orbitals for polarizations parallel and perpendicular to the molecular axis (the orange traces are proportional to the electric field). A movie of the X + A hole density for a pulse parallel to the molecular axis is available in **Supplementary Figure S3** of the Supporting Information.

The ionization yield (decrease in $|\Psi|^2$) for the X + A coherent superposition was found to be nearly equal to the ionization yield for the incoherent superposition of X and A, **Figure 8A**. Since the yield is the integration of the rate over the pulse, it is not very sensitive to fluctuations in the ionization rate caused by the coherent superposition of the states. The instantaneous rates for the superposition oscillate strongly and at different frequencies for different directions, as seen in **Figure 7A**. The

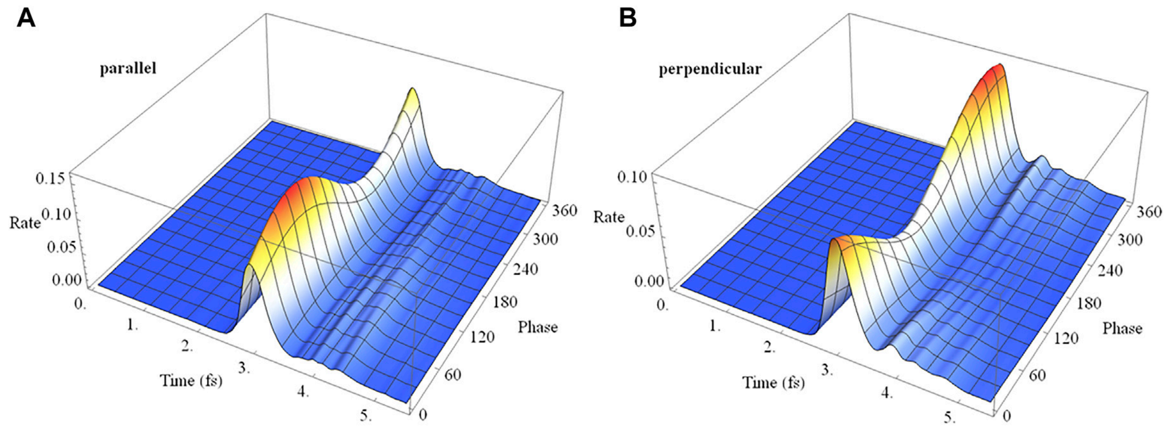

FIGURE 11 | Ionization rate as a function of time and the initial phase of the superposition (X + $e^{i\phi}$ A) for a 2 cycle linearly polarized 800 nm pulse with $E_{\max} = 0.075$ au for polarizations **(A)** parallel and **(B)** perpendicular to the molecular axis.

angular shape of the minimum and maximum of the instantaneous rates for X + A (shown as dashed red lines in **Figure 8B**, obtained from the last 2 fs of the simulation) have characteristics of the shapes for ionizing the π^* orbitals in the A state (see **Figure 4D**). The average of the ionization rates for the coherent superposition of X + A is in good agreement with the rates for the incoherent superposition of X and A, when accounting for the change in the relative populations of X and A at the end of the simulation.

A summary of the static field studies includes the following observations: 1) There is a strong directional dependence of the ionization rate and yield that is governed by the shape and energy of the orbitals being ionized. 2) The large transition dipole between the X and A states causes significant mixing between these states when the field has a component along the molecular axis. 3) The strong field alters the CI coefficients and electron density distribution for the X and A states. 4) For a coherent superposition of the X and A states, the field can alter both the magnitude and frequency of the charge oscillation. These observations can be used to help interpret the simulations of $HCCI^+$ subject to short, intense probe pulses that are linearly and circularly polarized.

The ionization rates of the X and A cations in a 2 cycle linearly polarized pulse oriented parallel and perpendicular to the molecular axis are plotted in **Figures 9A,B** (a movie of the hole density for the X state is available in **Supplementary Figure S3** of the Supporting Information). Like the static field case, a linearly polarized pulse along the molecular axis causes strong mixing between the X and A configurations in the time-dependent wavefunctions during the pulse, as can be seen in the plot of the CI coefficients and density matrix elements versus time in **Figures 9C–F**. The fact that the time dependence of the CI coefficients and density matrix elements of the A state are nearly mirror images of the X state indicates that $HCCI^+$ is behaving like a two-state system, as was found in earlier simulations. (Kraus et al., 2015). The strong fields in these very short pulses cause both polarization along the molecular axis during the pulse and the population transfer between the X and A configurations by the end of the pulse. **Figures 9C–F** show that the mixing between the X and A configurations and oscillations in the electron density do not simply follow the period of driving the laser pulse (2.66 fs) but also contain components arising from the superposition of the X and A states (period of 1.87 fs for the field-free case). This is more evident for longer pulses (see **Supplementary Figure S4** of the Supporting Information). Because the pulse produces a superposition of the X and A states, the oscillation in the $\rho(\pi, \pi^*)$ density matrix element continues after the pulse. Polarization and population transfer are considerably less for other alignments of the pulse that have smaller components along the molecular axis. When the pulse is perpendicular to the molecular axis, there is no mixing between the X and A states because the transition dipole between these states is zero by symmetry for this direction.

The response of the X + A and X − A coherent superpositions in a 2 cycle, linearly polarized pulse is shown in **Figure 10** (a movie for X + A is available in **Supplementary Figure S3** of the Supporting Information). The ionization rates for the X + A and X − A deviate quite noticeably from the X and A states averaged incoherently. Furthermore, simulations starting from the X + A and X − A superpositions differ significantly, indicating there is also a strong dependence on the initial phase of the superposition. The CI coefficients of the X + A coherent superposition for a pulse aligned parallel to the molecular axis, **Figure 10C**, show a combination of two oscillations, reflecting the frequency of the laser pulse and the intrinsic frequency of charge oscillation of the superposition seen in the field-free case. Like the CI coefficients, the density matrix elements (**Figure 10E**) also show a combination of two frequencies during the pulse but return to the single frequency seen for the superposition in the absence of a field. By the end of the pulse, the CI coefficients for the X and A configurations differ from their initial values because the pulse has caused significant population transfer between the states, as was seen earlier in both experiment and simulations. (Kraus et al., 2015). Calculations in the present study show that the nature of this population transfer depends

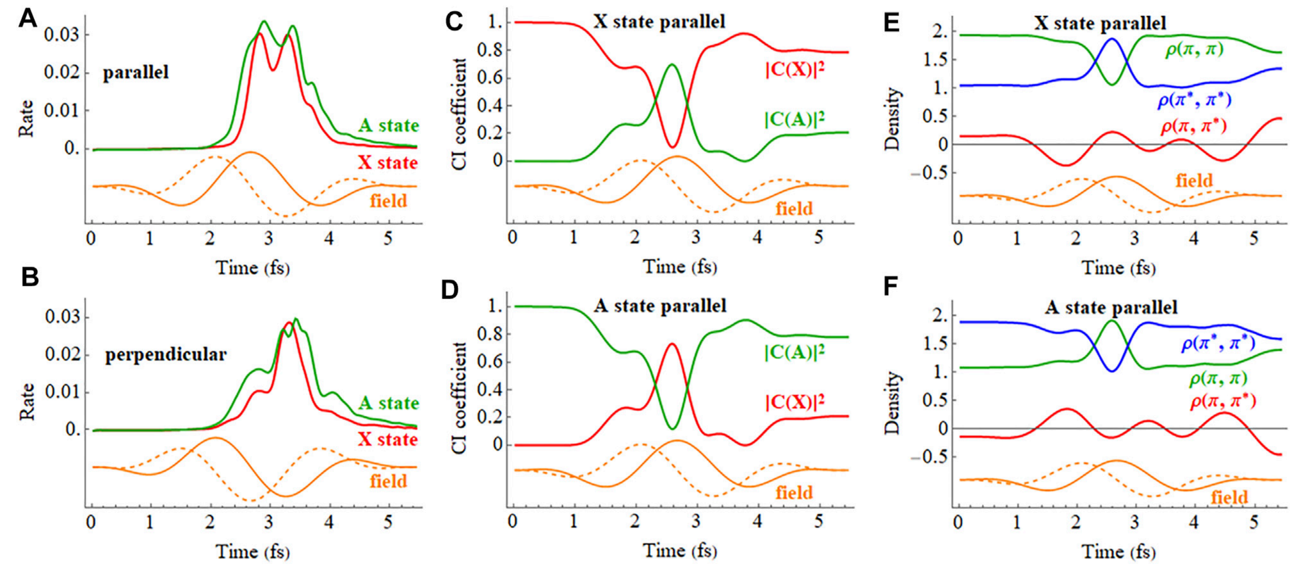

FIGURE 12 | (A,B) Ionization rate for the X and A cations in a 2 cycle circularly polarized 800 nm pulse with $E_{max} = 0.0566$ au with the carrier envelope maximum parallel and perpendicular to the molecular axis (X in red, A in green). **(C,D)** CI coefficients for the X and A configurations (red and green, resp.) in the normalized wavefunctions for the X ($\bar{\pi}_x^{*\,-1}$) and A ($\bar{\pi}_x^{-1}$) states with the carrier envelope maximum parallel and perpendicular to the molecular axis. **(E,F)** Density matrix elements for the π_x and π_x^* orbitals in the X and A states with the carrier envelope maximum parallel to the molecular axis (the orange traces are proportional to the electric field). A movie of the hole density is available in **Supplementary Figure S5** of the Supporting Information.

not only on the initial phase of the superposition, but also on the length of the pulse, the carrier envelope phase (CEP), the field strength, and the pulse orientation. For example, a pulse perpendicular to the molecular axis does not cause any interaction between the X and A states (**Figure 10D**). The small response in the CI coefficients reflects the polarization perpendicular to the molecular axis through interactions with higher lying states. Because the perpendicular field does not affect the X + A superposition, the oscillations of the density matrix elements (**Figure 10F**) and the dipole moment (not

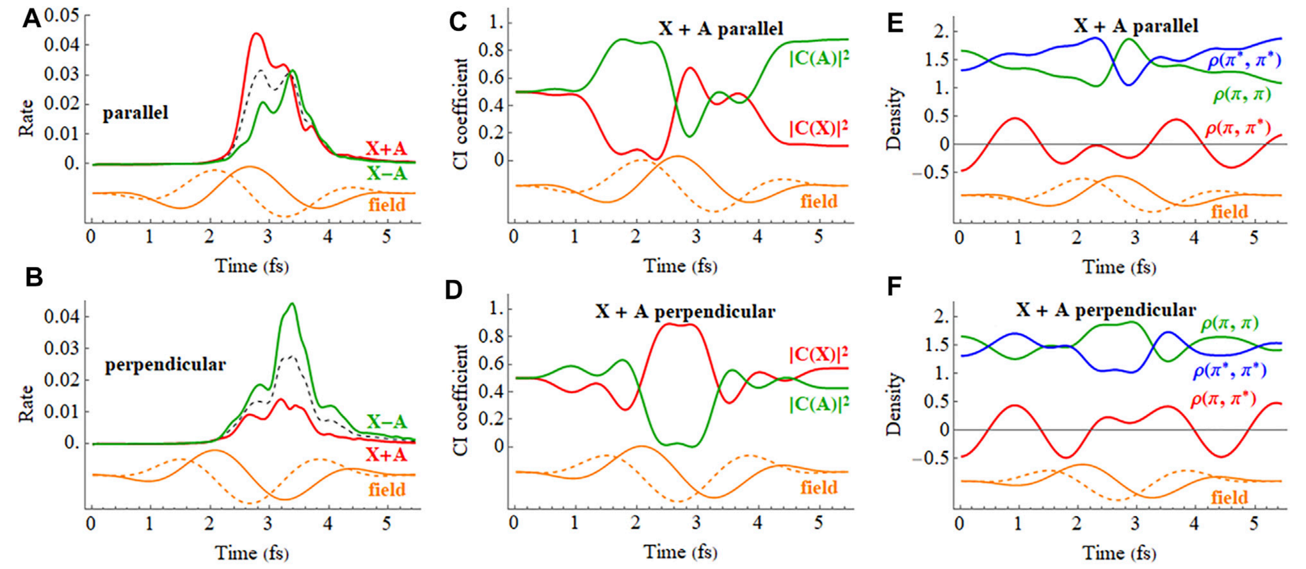

FIGURE 13 | (A,B) Ionization rate for X + A and X − A coherent superpositions for a 2 cycle, 800 nm circularly polarized pulse with $E_{max} = 0.0566$ au with the carrier envelope maximum parallel and perpendicular to the molecular axis (incoherent average of X and A in black dashed). **(C,D)** CI coefficients for the X and A configurations (red and green, resp.) in the normalized wavefunction for X + A with the carrier envelope maximum parallel and perpendicular to the molecular axis. **(E,F)** Density matrix elements for the π_x and π_x^* orbitals for X + A (the orange traces are proportional to the electric field). A movie of the hole density is available in **Supplementary Figure S3** of the Supporting Information.

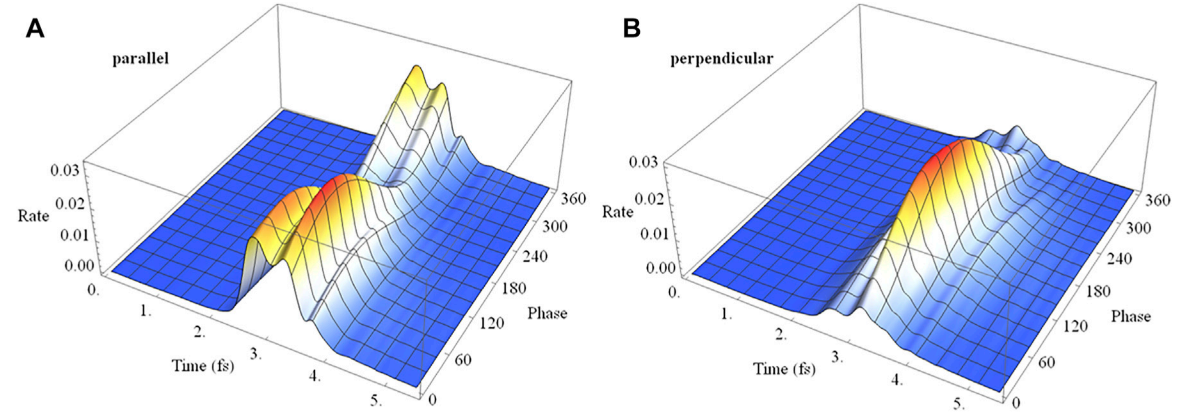

FIGURE 14 | Ionization rate as a function of time and the initial phase of the superposition (X + $e^{i\phi}$ A) for 2 cycle circularly polarized 800 nm pulse with E_{max} = 0.0530 au with the carrier envelope maximum **(A)** parallel and **(B)** perpendicular to the molecular axis.

shown) are essentially the same as the field-free case (**Figure 5**).

In a pump-probe experiment, the initial ionization of neutral HCCI by a pump pulse can produce a coherent superposition of the X and A cations. In the time delay between the pump and probe pulses, the phase of the superposition evolves with a field-free period of 1.87 fs. Thus, varying the pump-probe delay is equivalent to varying the initial phase of the superposition at the beginning of the probe pulse. **Figure 11** shows the time dependence of the ionization rate and as a function of the phase of the superposition (X + $e^{i\phi}$ A) for polarizations parallel and perpendicular to the molecular axis. The ionization rates show clear maxima and minima with the variation of the initial phase (equivalent to the variation of the pump-probe time delay). The total ionization yield also shows corresponding maxima and minima with the variation of the initial phase. For a pulse perpendicular to the molecular axis (**Figure 11B**), the electron density migrates at the field-free rate and the maximum in the ionization rate occurs when the electron density on iodine is highest at the peak in the field. For a pulse parallel to the molecular axis (**Figure 11A**), the density starts to migrate at the field-free rate but is increasingly driven by the laser field as the intensity grows. As a result, the peak in the ionization rate is shifted to a different initial value of the superposition phase.

The ionization rates for the X and A cations by a 2 cycle circularly polarized pulse are shown in **Figure 12**. The field rotates in the xz plane and the CEP is chosen so that the maximum in the field is either parallel to the molecular axis (*z* axis) with ionization from the iodine end or perpendicular to the molecular axis with the field rotating toward the iodine. **Figures 12C,D** indicate that the mixing between the X and A configurations is largest mid-pulse when the field is aligned with the molecular axis. There is some population transferred between the X and A configurations by the end of the pulse. The ionization rates for a coherent superposition of the X and A states in a circularly polarized pulse are plotted in **Figure 13**. Similar to a linear pulse, there is a significant difference in the peak ionization rate for the X + A and X − A superpositions. The CI coefficients and the density matrix elements show a combination of two oscillations, reflecting the frequency of the laser pulse and the intrinsic frequency of charge oscillation of the superposition.

Analogous to the linear case, ionization of a coherent superposition of the X and A states of $HCCI^+$ with a 2 cycle circularly polarized pulse varies with the initial phase of the superposition and with the carrier envelop phase, as shown in **Figure 14**. The rotating electric field drives the electron dynamics in a more complicated fashion than for a linearly polarized pulse. The variation can be understood with the help of the angular dependence of ionization in a static field discussed earlier. For the chosen parameters of the circularly polarized pulse, the electric field rotates in a clockwise direction for **Figures 3D**, **4D**. When the maximum in the carrier envelope phase is parallel to the molecular axis and ionization is from the iodine end, the rate is a maximum at rotations of the field 45° before and after the molecular axis. This accounts for the two ridges seen in **Figure 14A**. The location of the maximum rate with respect to the initial superposition phase is similar to the linear case, **Figure 11A**, and depends on the interaction between the intrinsic charge migration dynamics and the driving laser field. When the maximum in the carrier envelope phase is perpendicular to the molecular axis and the field is rotating toward the iodine, the ionization rate has only one primary ridge. This occurs approximately 45° after the maximum when the field is aligned with the iodine π-type lone pair orbital (see **Figures 3D**, **4D**). Because the electric field for the parallel and perpendicular cases affects the migration of the electron density differently, the maximum in the ionization rate occurs at different values for the initial superposition phases (corresponding to different pump-probe delay times).

SUMMARY

The electron dynamics and strong field ionization of HCCI neutral and cations in intense laser fields have been simulated using time-dependent configuration interaction with a complex absorbing potential. Ionization of neutral HCCI occurs from the π^* and π orbitals, producing the X and A states of the cation, respectively. Use of a static field reveals the 3-dimensional angular dependence of strong field ionization and the orbitals involved in producing the cations and dications. Ionization of the neutral by a pump pulse can produce a coherent superposition of the X and A cations which results in charge oscillation between the CC π orbital and the iodine π-type lone pair. This migration can be monitored by ionizing with ultrashort probe pulses. Under field-free conditions, the frequency of charge oscillation is determined by the energy separation of the X and A states. However, the oscillation of the electron density is affected by the subsequent strong field ionization of the cations to dications by intense probe pulses. For fields along the molecular axis, strong field ionization of the individual X and A states causes extensive mixing between the X and A configurations resulting in charge oscillation between the CC π orbital and the iodine π-type lone pair during the pulse. For a coherent superposition, the oscillation of the charge shows two frequencies–the driving frequency of the laser field and the intrinsic frequency due to the energy separation between the X and A states. Strong field ionizations with linear and circularly polarized pulses show marked differences in the ionization rates that depend on the initial phase of the superposition, the polarization direction and the carrier envelope phase. Scanning the initial phase of the superposition is analogous to changing the delay between the pump and probe pulses. The charge oscillation resulting from the coherent superposition of the X and A states is seen in the variation in the ionization yield as a function of the initial phase of the superposition. Linearly polarized probe pulses perpendicular to the molecular axis do not affect the superposition and the charge oscillation frequency is the same as the field-free case. For linearly polarized pulses parallel to the molecular axis and for circularly polarized pulses, there is strong polarization along the molecular axis and the dynamics of the charge oscillation depends on the driving laser field as well as the intrinsic frequency resulting from the coherent superposition.

Finally, we briefly comment on the feasibility of experimental implementation of using strong field ionization to probe electronic wave packets. The proposed two-cycle laser pulses are indeed practical as single- or sub-cycle (FWHM) pulses have been produced with either a hollow-core fiber compressor or pulse synthesizer. (Hassan et al., 2016; Liang et al., 2017; Timmers et al., 2017). Our calculations also utilized pulses with fixed carrier-envelop phases. A technique for measuring the absolute CEPs of ultrashort pulses has been recently developed. (Debrah et al., 2019). While the ionization yield variation detection might require orientation of the molecules in space, it is rather straightforward to achieve this with an electron-ion coincidence method (Winney et al., 2018) in which the recoil momentum of the dissociated ion can be used to measure the orientation of molecules. Therefore, all necessary techniques that are needed to implement the current study are now available. The advantage of the proposed approach lies in its superb time resolution as well as an extended delay range, which will be crucial for studying electron wave packet decoherence and recoherence dynamics.

DATA AVAILABILITY STATEMENT

The raw data supporting the conclusion of this article will be made available by the authors, without undue reservation.

AUTHOR CONTRIBUTIONS

HBS carried out the simulations and prepared the manuscript with the assistance of PH and WL.

ACKNOWLEDGMENTS

This work was supported by the National Science Foundation grant number CHE1856437 (HBS) and the U.S. Department of Energy (DOE), Office of Science, Basic Energy Sciences (BES), under Award # DE-SC0020994 (HBS and WL). We thank Wayne State University's computing grid for computer time.

SUPPLEMENTARY MATERIAL

The Supplementary Material for this article can be found online at: https://www.frontiersin.org/articles/10.3389/fchem.2022.866137/full#supplementary-material

REFERENCES

Allan, M., Kloster-Jensen, E., and Maier, J. P. (1977). Emission Spectra of Cl-C=C-H+, Br-C=C-H+and I-C=C-H+radical Cations: Ã2Π→X2Π Band Systems and the Decay of the Ã2Π States. *J. Chem. Soc. Faraday Trans. 2* 73, 1406–1416. doi:10.1039/f29777301406

Bandrauk, A. D., and Légaré, F. in *Progress in Ultrafast Intense Laser Science*. Editors K. Yamanouchi, M. Nisoli, and W. T. Hill (Springer-Verlag, Berlin/Heidelberg2012), 8, 29–46. ch. 2.

Bruner, A., Hernandez, S., Mauger, F., Abanador, P. M., LaMaster, D. J., Gaarde, M. B., et al. (2017). Attosecond Charge Migration with TDDFT: Accurate Dynamics from a Well-Defined Initial State. *J. Phys. Chem. Lett.* 8, 3991–3996. doi:10.1021/acs.jpclett.7b01652

Calegari, F., Ayuso, D., Trabattoni, A., Belshaw, L., De Camillis, S., Anumula, S., et al. (2014). Ultrafast Electron Dynamics in Phenylalanine Initiated by Attosecond Pulses. *Science* 346, 336–339. doi:10.1126/science.1254061

Chu, X., and Chu, S. I. (2001). Time-dependent Density-Functional Theory for Molecular Processes in strong fields: Study of Multiphoton Processes and Dynamical Response of Individual Valence Electrons of N-2 in Intense Laser fields. *Phys. Rev. A.* 64, 063404. doi:10.1103/physreva.64.063404

Chu, X. (2010). Time-dependent Density-Functional-Theory Calculation of strong-field Ionization Rates of H-2. *Phys. Rev. A.* 82, 023407. doi:10.1103/physreva.82.023407

Debrah, D. A., Stewart, G. A., Basnayake, G., Tisch, J. W. G., Lee, S. K., and Li, W. (2019). Direct *In-Situ* Single-Shot Measurements of the Absolute Carrier-Envelope Phases of Ultrashort Pulses. *Opt. Lett.* 44, 3582–3585. doi:10.1364/ol.44.003582

Ding, H., Jia, D., Manz, J., and Yang, Y. (2017). Reconstruction of the Electronic Flux during Adiabatic Attosecond Charge Migration in HCCI+. *Mol. Phys.* 115, 1813–1825. doi:10.1080/00268976.2017.1287967

Dunning, T. H. (1989). Gaussian Basis Sets for Use in Correlated Molecular Calculations. I. The Atoms boron through Neon and Hydrogen. *J. Chem. Phys.* 90, 1007–1023. doi:10.1063/1.456153

Eckle, P., Smolarski, M., Schlup, P., Biegert, J., Staudte, A., Schöffler, M., et al. (2008). Attosecond Angular Streaking. *Nat. Phys* 4, 565–570. doi:10.1038/nphys982

Frisch, M. J., Trucks, G. W., Schlegel, H. B., and Scuseria, G. E. (2019). *Gaussian Development Version*. Wallingford CT: Revision J.02.

Goings, J. J., Lestrange, P. J., and Li, X. S. (2018). Real-time Time-dependent Electronic Structure Theory. *Wiley Interdiscip. Rev.-Comput. Mol. Sci.* 8, e1341. doi:10.1002/wcms.1341

Golubeva, A. A., Pieniazek, P. A., and Krylov, A. I. (2009). A New Electronic Structure Method for Doublet States: Configuration Interaction in the Space of Ionized 1h and 2h1p Determinants. *J. Chem. Phys.* 130, 124113. doi:10.1063/1.3098949

Goulielmakis, E., Loh, Z.-H., Wirth, A., Santra, R., Rohringer, N., Yakovlev, V. S., et al. (2010). Real-time Observation of Valence Electron Motion. *Nature* 466, 739–743. doi:10.1038/nature09212

Greenman, L., Ho, P. J., Pabst, S., Kamarchik, E., Mazziotti, D. A., and Santra, R. (2010). Implementation of the Time-dependent Configuration-Interaction Singles Method for Atomic strong-field Processes. *Phys. Rev. A.* 82, 023406. doi:10.1103/physreva.82.023406

Hassan, M. T., Luu, T. T., Moulet, A., Raskazovskaya, O., Zhokhov, P., Garg, M., et al. (2016). Optical Attosecond Pulses and Tracking the Nonlinear Response of Bound Electrons. *Nature* 530, 66–70. doi:10.1038/nature16528

Hehenberger, M., McIntosh, H. V., and Brändas, E. (1974). Weyl's Theory Applied to the Stark Effect in the Hydrogen Atom. *Phys. Rev. A.* 10, 1494–1506. doi:10.1103/physreva.10.1494

Hellgren, M., Rasanen, E., and Gross, E. K. U. (2013). Optimal Control of strong-field Ionization with Time-dependent Density-Functional Theory. *Phys. Rev. A.* 88, 013414. doi:10.1103/physreva.88.013414

Hermann, M. R., and Fleck, J. A. (1988). Split-operator Spectral Method for Solving the Time-dependent Schrödinger Equation in Spherical Coordinates. *Phys. Rev. A.* 38, 6000–6012. doi:10.1103/physreva.38.6000

Hoerner, P., and Schlegel, H. B. (2017). Angular Dependence of Strong Field Ionization of CH3X (X = F, Cl, Br, or I) Using Time-dependent Configuration Interaction with an Absorbing Potential. *J. Phys. Chem. A.* 121, 5940–5946. doi:10.1021/acs.jpca.7b06108

Hoerner, P., and Schlegel, H. B. (2018). Angular Dependence of Strong Field Ionization of Haloacetylenes HCCX (X = F, Cl, Br, I), Using Time-dependent Configuration Interaction with an Absorbing Potential. *J. Phys. Chem. C* 122, 13751–13757. doi:10.1021/acs.jpcc.8b00619

Humphrey, W., Dalke, A., and Schulten, K. (1996). VMD: Visual Molecular Dynamics. *J. Mol. Graphics* 14, 33–38. doi:10.1016/0263-7855(96)00018-5

Ishikawa, K. L., and Sato, T. (2015). A Review on Ab Initio Approaches for Multielectron Dynamics. *IEEE J. Selected Top. Quan. Elect.* 21, 8700916. doi:10.1109/jstqe.2015.2438827

Jenkins, A. J., Spinlove, K. E., Vacher, M., Worth, G. A., and Robb, M. A. (2018). The Ehrenfest Method with Fully Quantum Nuclear Motion (Qu-Eh): Application to Charge Migration in Radical Cations. *J. Chem. Phys.* 149, 094108. doi:10.1063/1.5038428

Jia, D., Manz, J., and Yang, Y. (2019). De- and Recoherence of Charge Migration in Ionized Iodoacetylene. *J. Phys. Chem. Lett.* 10, 4273–4277. doi:10.1021/acs.jpclett.9b01687

Jia, D., Manz, J., and Yang, Y. (2019). Timing the Recoherences of Attosecond Electronic Charge Migration by Quantum Control of Femtosecond Nuclear Dynamics: A Case Study for HCCI+. *J. Chem. Phys.* 151, 244306. doi:10.1063/1.5134665

Jia, D., and Yang, Y. (2022). Systematic Investigation of the Reliability of the Frozen Nuclei Approximation for Short-Pulse Excitation: The Example of HCCI+. *Front. Chem.* 10, 857348. doi:10.3389/fchem.2022.857348

Kienberger, R., Goulielmakis, E., Uiberacker, M., Baltuska, A., Yakovlev, V., Bammer, F., et al. (2004). Atomic Transient Recorder. *Nature* 427, 817–821. doi:10.1038/nature02277

Klinkusch, S., Saalfrank, P., and Klamroth, T. (2009). Laser-induced Electron Dynamics Including Photoionization: A Heuristic Model within Time-dependent Configuration Interaction Theory. *J. Chem. Phys.* 131, 114304. doi:10.1063/1.3218847

Kosloff, R., and Kosloff, D. (1986). Absorbing Boundaries for Wave Propagation Problems. *J. Comput. Phys.* 63, 363–376. doi:10.1016/0021-9991(86)90199-3

Kraus, P. M., Mignolet, B., Baykusheva, D., Rupenyan, A., Horný, L., Penka, E. F., et al. (2015). Measurement and Laser Control of Attosecond Charge Migration in Ionized Iodoacetylene. *Science* 350, 790–795. doi:10.1126/science.aab2160

Krause, P., Klamroth, T., and Saalfrank, P. (2007). Molecular Response Properties from Explicitly Time-dependent Configuration Interaction Methods. *J. Chem. Phys.* 127, 034107. doi:10.1063/1.2749503

Krause, P., Klamroth, T., and Saalfrank, P. (2005). Time-dependent Configuration-Interaction Calculations of Laser-Pulse-Driven many-electron Dynamics: Controlled Dipole Switching in Lithium Cyanide. *J. Chem. Phys.* 123, 074105. doi:10.1063/1.1999636

Krause, P., and Schlegel, H. B. (2015). Angle-Dependent Ionization of Hydrides AHn Calculated by Time-dependent Configuration Interaction with an Absorbing Potential. *J. Phys. Chem. A.* 119, 10212–10220. doi:10.1021/acs.jpca.5b06481

Krause, P., and Schlegel, H. B. (2015). Angle-dependent Ionization of Small Molecules by Time-dependent Configuration Interaction and an Absorbing Potential. *J. Phys. Chem. Lett.* 6, 2140–2146. doi:10.1021/acs.jpclett.5b00929

Krause, P., Sonk, J. A., and Schlegel, H. B. (2014). Strong Field Ionization Rates Simulated with Time-dependent Configuration Interaction and an Absorbing Potential. *J. Chem. Phys.* 140, 174113. doi:10.1063/1.4874156

Lee, M. K., Li, W., and Schlegel, H. B. (2020). Angular Dependence of strong Field Sequential Double Ionization for Neon and Acetylene Simulated with Time-dependent Configuration Interaction Using CIS and CISD-IP. *J. Chem. Phys.* 152, 064106. doi:10.1063/1.5133659

Li, X., Govind, N., Isborn, C., DePrince, A. E., and Lopata, K. (2020). Real-Time Time-dependent Electronic Structure Theory. *Chem. Rev.* 120, 9951–9993. doi:10.1021/acs.chemrev.0c00223

Liang, H., Krogen, P., Wang, Z., Park, H., Kroh, T., Zawilski, K., et al. (2017). High-energy Mid-infrared Sub-cycle Pulse Synthesis from a Parametric Amplifier. *Nat. Commun.* 8, 141. doi:10.1038/s41467-017-00193-4

Lopata, K., and Govind, N. (2013). Near and above Ionization Electronic Excitations with Non-hermitian Real-Time Time-dependent Density Functional Theory. *J. Chem. Theor. Comput.* 9, 4939–4946. doi:10.1021/ct400569s

Mathematica 12 (2019). *Mathematica 12*. Champaign, IL: Wolfram Research, Inc..

Muga, J., Palao, J., Navarro, B., and Egusquiza, I. (2004). Complex Absorbing Potentials. *Phys. Rep.* 395, 357–426. doi:10.1016/j.physrep.2004.03.002

Nisoli, M., Decleva, P., Calegari, F., Palacios, A., and Martín, F. (2017). Attosecond Electron Dynamics in Molecules. *Chem. Rev.* 117, 10760–10825. doi:10.1021/acs.chemrev.6b00453

Ortiz, J. V. (1996). Partial Third-order Quasiparticle Theory: Comparisons for Closed-shell Ionization Energies and an Application to the Borazine Photoelectron Spectrum. *J. Chem. Phys.* 104, 7599–7605. doi:10.1063/1.471468

Palacios, A., and Martin, F. (2020). The Quantum Chemistry of Attosecond Molecular Science. *Wiley Interdiscip. Rev.-Comput. Mol. Sci.* 10, e1430. doi:10.1002/wcms.1430

Peterson, K. A., Figgen, D., Goll, E., Stoll, H., and Dolg, M. (2003). Systematically Convergent Basis Sets with Relativistic Pseudopotentials. II. Small-Core Pseudopotentials and Correlation Consistent Basis Sets for the post-d Group 16-18 Elements. *J. Chem. Phys.* 119, 11113–11123. doi:10.1063/1.1622924

Peterson, K. A., Shepler, B. C., Figgen, D., and Stoll, H. (2006). On the Spectroscopic and Thermochemical Properties of ClO, BrO, IO, and Their Anions. *J. Phys. Chem. A.* 110, 13877–13883. doi:10.1021/jp065887l

Posthumus, J. H. (2004). The Dynamics of Small Molecules in Intense Laser fields. *Rep. Prog. Phys.* 67, 623–665. doi:10.1088/0034-4885/67/5/r01

Provorse, M. R., and Isborn, C. M. (2016). Electron Dynamics with Real-Time Time-dependent Density Functional Theory. *Int. J. Quan. Chem.* 116, 739–749. doi:10.1002/qua.25096

Rohringer, N., Gordon, A., and Santra, R. (2006). Configuration-interaction-based Time-dependent Orbital Approach for Ab Initio Treatment of Electronic Dynamics in a strong Optical Laser Field. *Phys. Rev. A.* 74, 043420. doi:10.1103/physreva.74.043420

Sandor, P., Sissay, A., Mauger, F., Abanador, P. M., Gorman, T. T., Scarborough, T. D., et al. (2018). Angle Dependence of strong-field Single and Double Ionization of Carbonyl Sulfide. *Phys. Rev. A.* 98, 043425. doi:10.1103/physreva.98.043425

Santra, R., and Cederbaum, L. S. (2002). Complex Absorbing Potentials in the Framework of Electron Propagator Theory. I. General Formalism. *J. Chem. Phys.* 117, 5511–5521. doi:10.1063/1.1501903

Smirnova, O., Patchkovskii, S., Mairesse, Y., Dudovich, N., and Ivanov, M. Y. (2009). Strong-field Control and Spectroscopy of Attosecond Electron-Hole Dynamics in Molecules. *Proc. Natl. Acad. Sci. U.S.A.* 106, 16556–16561. doi:10.1073/pnas.0907434106

Sommerfeld, T., and Ehara, M. (2015). Complex Absorbing Potentials with Voronoi Isosurfaces Wrapping Perfectly Around Molecules. *J. Chem. Theor. Comput.* 11, 4627–4633. doi:10.1021/acs.jctc.5b00465

Timmers, H., Kobayashi, Y., Chang, K. F., Reduzzi, M., Neumark, D. M., and Leone, S. R. (2017). Generating High-Contrast, Near Single-Cycle Waveforms with Third-Order Dispersion Compensation. *Opt. Lett.* 42, 811–814. doi:10.1364/ol.42.000811

Tolstikhin, O. I., Morishita, T., and Madsen, L. B. (2011). Theory of Tunneling Ionization of Molecules: Weak-Field Asymptotics Including Dipole Effects. *Phys. Rev. A.* 84, 053423. doi:10.1103/physreva.84.053423

Tong, X. M., Zhao, Z. X., and Lin, C. D. (2002). Theory of Molecular Tunneling Ionization. *Phys. Rev. A.* 66, 033402. doi:10.1103/physreva.66.033402

Tremblay, J. C., Klinkusch, S., Klamroth, T., and Saalfrank, P. (2011). Dissipative many-electron Dynamics of Ionizing Systems. *J. Chem. Phys.* 134, 044311. doi:10.1063/1.3532410

Winney, A. H., Basnayake, G., Debrah, D. A., Lin, Y. F., Lee, S. K., Hoerner, P., et al. (2018). Disentangling strong-field Multielectron Dynamics with Angular Streaking. *J. Phys. Chem. Lett.* 9, 2539–2545. doi:10.1021/acs.jpclett.8b00028

Winney, A. H., Lee, S. K., Lin, Y. F., Liao, Q., Adhikari, P., Basnayake, G., et al. (2017). Attosecond Electron Correlation Dynamics in Double Ionization of Benzene Probed with Two-Electron Angular Streaking. *Phys. Rev. Lett.* 119, 123201. doi:10.1103/physrevlett.119.123201

Woon, D. E., and Dunning, T. H., Jr. (1993). Gaussian Basis Sets for Use in Correlated Molecular Calculations. III. The Atoms Aluminum through Argon. *J. Chem. Phys.* 98, 1358–1371. doi:10.1063/1.464303

Conflict of Interest: The authors declare that the research was conducted in the absence of any commercial or financial relationships that could be construed as a potential conflict of interest.

frontiers | Frontiers in Chemistry

ORIGINAL RESEARCH
published: 25 April 2022
doi: 10.3389/fchem.2022.859405

Intense Laser Pulse Interaction With Graphene and Graphene Ribbons

F. H. M. Faisal*

Department of Physics, Universität Bielefeld, Bielefeld, Germany

In this work we investigate quantum mechanically the interaction of an intense ultrashort laser pulse with the graphene monolayer as well as with the armchair graphene ribbons of different widths. We consider a tight binding (TB) Hamiltonian of the monolayer graphene and give two rules for deriving the dispersion relations of the armchair graphene *ribbons* of any width, N, from the TB eigenvalues of the *monolayer*. The band structure of the monolayer and the armchair ribbons of different widths are discussed with illustrations. The time-dependent wavefunctions of the systems and the expectation values of interest are determined by solving the coupled equations of the band amplitudes "exactly" (numerically). First, simulations are made for the *population* excitation in the conduction band (CB) from the valence band (BV), the VB-CB *inter*band *correlation* (or "coherence"), the *intra*band, the *inter*band and the total *currents* in the monolayer graphene. The graphene currents are compared with the corresponding currents induced in an armchair ribbon (width, N = 3). The change from the 2D monolayer to the 1D ribbon shows a remarkable transition of the dominance of the *intra*band current that leads to a near *steady* total current in the monolayer, to a dominance of the *inter*band current in the ribbon that induces an *oscillatory* current in the ribbon beyond the pulse duration. The difference observed might be a combined effect of the "confinement" in one dimention and a finite band-gap minimum in the case of the ribbon. However, this transition should be further investigated for better clarity. A brief comparison of the radiation spectra emitted from the monolayer and from the ribbon is also made. They show a grossly similar structure and a relative insensitivity with respect to the detailed structure of the targets chosen. This might be due to the dominance of virtual continuum-continuum transitions, to and from the bands states, that lie behind the fundamental quantum process of high harmonic emissions. Lastly, the dependence of the charge currents, induced in a *ribbon* of unit width (N = 1), on the carrier-envelope-phase (CEP) of the incident laser pulse is investigated. It is seen that the shape of the *main* part of the current produced in the ribbon can be fully reversed by changing the CEP of the ultrashort laser pulse from 0 to π. More generally, it is suggested that the pulse shape of the charge carriers in the ribbon could be designed by similarly tailoring the form of the *vector potential* of the incident laser pulse.

Keywords: graphene, ribbon, adiabatic-Hamiltonian, energy-bands, population, current, CEP, laser-pulse

Edited by:
Yuichi Fujimura,
Tohoku University, Japan

Reviewed by:
Tobias Boolakee,
University of Erlangen Nuremberg, Germany
Amlan Kusum Roy,
Indian Institute of Science Education and Research Kolkata, India

***Correspondence:**
F. H. M. Faisal
ffaisal@physik.uni-bielefeld.de

Specialty section:
This article was submitted to Physical Chemistry and Chemical Physics,
a section of the journal Frontiers in Chemistry

Received: *21 January 2022*
Accepted: *16 March 2022*
Published: *25 April 2022*

Citation:
Faisal FHM (2022) Intense Laser Pulse Interaction With Graphene and Graphene Ribbons.
Front. Chem. 10:859405.
doi: 10.3389/fchem.2022.859405

1 INTRODUCTION

Graphene is a two dimensional hexagonal one-atom-thin monolayer of carbon atoms that shows remarkable material, electrical and optical properties (e.g. Castro Neto et al. (2009)) with much potentials for future applications. The study of the interaction of intense laser light with monolayer graphene and theoretical and experimental investigations of the emission of high harmonic radiation from them began quite sometime ago (e.g., Faisal and Kaminski (1997); Ghimire et al. (2011); Faisal (2011); Faisal (2013); Schubert et al. (2014); Luu et al. (2015); Vampa et al. (2015); Liu et al. (2017); Sivis et al. (2017); Yoshikawa et al. (2017)). Investigations of the nature of electric currents in graphene generated by intense laser pulses have also made considerable progress (e.g. Kelardeh et al. (2015), Higuchi et al. (2017), Ernotte, et al. (2018), Heide et al. (2020). For example, ballistic electric currents and sub-optical cycle "Stueckelberg oscillations" in graphene monolayers induced by ultrashort lasers have been observed recently by Hommelhoff and collaborators (Higuchi et al. (2017); Heide et al. (2020)). A ramarkable progress had been reported recently by Karakachian et al. (2020) in synthesising high quality armchair graphene *ribbons* having finite widths. Their method makes use of the side walls of 6H-SiC mesa structures to epitaxially grow the armchair ribbons of different widths on them, while the ARPES technique was used to investigate the electronic structure of the sub-bands of armchair ribbons that revealed the presence of *band gaps* in most ribbons as well as a gapless pair of bands for ribbons of certain widths (see, below). This development opens up new prospects of further research on the effect of quantum *confinement* and of potential applications of the ribbons in semiconductor electronics, specially, where the monolayer graphene is not directly usable due to its missing band gap.

In this work we explore (quantum mechanically) the interactions of an intense ultrashort laser pulse with the monolayer graphene *and* with armchair graphene ribbons. To this end first we consider an analytical TB (tight binding) Hamiltonian in the reciprocal lattice space, determine its eigenvalues and eigenfunctions, give two simple rules for constructing the band-system of armchair ribbons (of any width) from the graphene bands and, briefly illustrate the lattice structure of the monolayer graphene and of the armchair ribbons. Next, the current and the transition dipole operators (relevant for the study of laser interactions) are constructed analytically from the TB Hamiltonian. The laser interaction is introduced using the *minimal coupling* prescription in the reciprocal lattice space and the time-dependent Schrödinger equation of the interacting system is obtained in the adiabatic representation (cf. Faisal (2011)). To solve the equation, we expand the total wavefunction in terms of the adiabatic eigenstates of the "instantaneous" Hamiltonian and construct a pair of coupled dynamical equations (cf. Faisal (2016)) for the occupation amplitudes of the valence band (VB) and the conduction band (CB) of the interacting system. The equations are integrated numerically "exactly" to simulate the transition probabilities and the expectation values of the observables of the present interest. They are used to investigate 1) the transfer of population from the VB to the CB, 2) the induced VB-CB correlation (or "coherence"), 3) the ultrashort charge-currents generated both in the monolayer graphene and in the armchair graphene ribbons, as well as, 4) the radiation emitted from the generated charge-currents. Finally, the possibility of controlling the shape of the generated ultrashort charge-currents by choosing the incident laser pulse suitably is also considered for the case of an armchair ribbon of unit width (N = 1). The results of the simulations for the monolayer and the ribbons are presented, compared and discussed, with graphical illustrations.

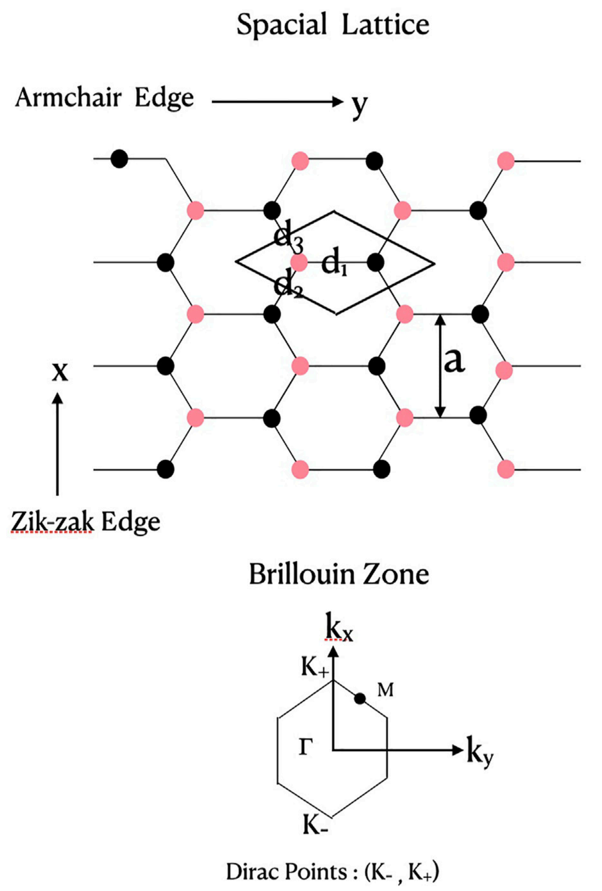

FIGURE 1 | Lattice structure of a graphene monolayer. The upper part shows a 2D hexagonal carbon lattice with two (red, black) interpenetrating triangular Bravais sub-lattices. The unit cell (rhombus) has two atoms per cell (red, black). The nearest neighbour distances from one atom (red) are ($\mathbf{d}_1$, $\mathbf{d}_2$, $\mathbf{d}_3$); a_{CC} is carbon-carbon bond length, $a = \sqrt{3}a_{CC}$ = lattice constant = 0.246 nm = 4.649 [a.u.]. Note the "armchair" structure along the horizontal axis and the "zik-zak" structure along the vertical axis. The lower part of the figure shows the first Brillouin zone with symmetry points (Γ, M) and the Dirac points (K_-, K_+).

2 THEORETICAL MODEL

The lattice structure of a two dimensional graphene monolayer is illustrated schematically in **Figure 1**. The upper part of the figure

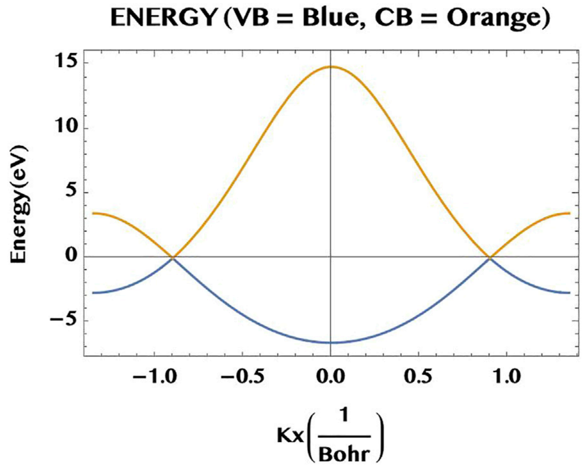

FIGURE 2 | A 1D cut of the band structure of graphene monolayer along the k_x-axis, with $k_y = 0$. The lower lying valence band (VB, blue) and the upper lying conduction band (CB, orange) are degenerate at the two Dirac points (along the k_x-axis at $\pm \frac{4\pi}{3a} = \pm\, 0.9 [\frac{1}{Bohr}]$, $1 Bohr = 0.0529$ nm). Note that for a non-vanishing overlap integral $s_0 = 0.129$, the bands are linear and symmetric near the Dirac point (but differ away from it).

shows the hexagonal honeycomb carbon lattice with two (red and black) interpenetrating triangular Bravais sub-lattices. A unit cell with two atoms per cell is also outlined (the rhombus in the figure). The 2D lattice vectors are defined by $\mathbf{a}_1 = \{a/2, \sqrt{3}\,a/2\}, \mathbf{a}_2 = \{a/2, -\sqrt{3}\,a/2\}$ where, $a = |\mathbf{a}_1| = |\mathbf{a}_2|$ is the lattice constant. The nearest neighbour (nn) distances from one atom (red) of the cell are $\mathbf{d}_1 = \{0, a/\sqrt{3}\}$, $\mathbf{d}_2 = \{a/2, -a/(2\sqrt{3})\}$, $\mathbf{d}_3 = \{-a/2, -a/(2\sqrt{3})\}$. They define the complex "geometric" factor $h(\mathbf{k}) = \sum_{j=1}^{3} e^{i\mathbf{k}\cdot\mathbf{d}_j}$ with, $|\mathbf{d}_1| = |\mathbf{d}_2| = |\mathbf{d}_2| = a_{CC}$, the carbon-carbon bond length, and, $\mathbf{K}_{\pm} = \pm\{4\pi/(3a), 0\}$ are the two non-equivalent "Dirac points" of band degeneracy (see, below). Note that the lattice constant $a = \sqrt{3}a_{CC}$. The lower part of the figure shows the first Brillouin zone, along with the symmetry points Γ and M, as well as the Dirac points (K_-, K_+). The "armchair" structure of the horizontal edge and the zik-zak structure of the vertical edge of the monolayer graphene sheet are to be noted here.

The graphene monolayer is often theoretically modelled by a symmetric TB Hamiltonian near the Dirac points where the energy dispersion relations and the energy bands are linear and symmetric (see, e.g. review Castro Neto et al. (2009)). Most responses of graphene to weak static and/or low frequency fields are dominated by this domain of the Brillouin Zone (BZ). We point out that also for the laser fields in the near infrared wavelength (800 nm) and at an intensity of 1 TW/cm^2, as used in this work, we tested (following the suggestion of an anonymous referee) and found *no* significant effect of the band asymmetry with non-zero overlap integral $s_0 = 0.129$, as in this work, and $s_0 = 0$ for the symmetric bands. This is apparently due to the high values of the dipole operator in the vicinity of the Dirac points (cf. **Figure 6**) where the bands are essentially symmetric and linear (cf. **Figure 2**).

Assuming two carbon atoms per unit cell (red and black dots in the rhombus of **Figure 1**), each described by a p_z-orbital oriented perpendicular to the graphene plane and, taking only the nearest neighbour (nn) interactions, the stationary wavefunction $\psi(\mathbf{k})$ of the graphene monolayer can be written as a linear combination of the two Bloch functions associated with the two p_z orbitals (per cell). We may then apply the variational principle as usual to construct the expectation value of the energy operator H^0, and arrive at the following 2 × 2 variational matrix equation (e.g. Saito et al. (1998); McCann (2012)) with respect to the two amplitudes associated with the two Bloch functions, $\psi(\mathbf{k}) = \{\psi_1(\mathbf{k}), \psi_2(\mathbf{k})\}$ as well as the energy of the least bound p_z orbital, ϵ_{2p}:

$$H^0(\mathbf{k})\psi(\mathbf{k}) = ES(\mathbf{k})\psi(\mathbf{k}) \tag{1}$$

where $H^0(\mathbf{k})$ is a 2 × 2 matrix with elements

$$\begin{aligned} H^0_{11}(\mathbf{k}) &= \epsilon_{2p} \\ H^0_{12}(\mathbf{k}) &= -g_0 h(\mathbf{k}) \\ H^0_{21}(\mathbf{k}) &= -g_0 h^*(\mathbf{k}) \\ H^0_{22}(\mathbf{k}) &= \epsilon_{2p} \end{aligned} \tag{2}$$

The complex geometric factor $h(\mathbf{k})$ can be expressed by its real amplitude f and phase χ as:

$$\begin{aligned} h(\mathbf{k}) &= f(\mathbf{k}) e^{i\chi(\mathbf{k})} \\ f(\mathbf{k}) &= \left(h_1^2(\mathbf{k}) + h_2^2(\mathbf{k})\right)^{1/2} \\ h_1(\mathbf{k}) &= 2\cos\left(\frac{k_y a}{2\sqrt{3}}\right)\cos(k_x a/2) \\ h_2(\mathbf{k}) &= \sin\left(k_y a/\sqrt{3}\right) - 2\sin\left(\frac{k_y a}{2\sqrt{3}}\right) cos(k_x a/2) \\ \chi(\mathbf{k}) &= \arctan\left(\frac{h_2(\mathbf{k})}{h_1(\mathbf{k})}\right) \end{aligned} \tag{3}$$

where, g_0 is the "hopping" integral (the nearest neighbour interaction matrix element); the lattice constant $a = \sqrt{3}a_{CC}$ and, a_{CC} is the carbon-carbon bond length. The 2 × 2 overlap matrix S is defined by its elements

$$\begin{aligned} S_{11} &= 1 \\ S_{12} &= s_0 h(\mathbf{k}) \\ S_{21} &= s_0 h^*(\mathbf{k}) \\ S_{22} &= 1 \end{aligned} \tag{4}$$

where, s_0 is the dimensionless overlap integral. In this work we have followed the convention (e.g. Saito et al. (1998); McCann (2012)) of fixing the energy origin for the bands by setting the unperturbed energy of the p_z-orbital $\epsilon_{2p} = 0$ (a possible limitation of this convention would be considered elsewhere); we also adopt the parameter values $g_0 = 3.033$ eV, $s_0 = 0.129$, and the C-C bond length $a_{CC} = 0.142$ nm, quoted therein (with the lattice constant $a = \sqrt{3}a_{CC} = 0.246$ nm).

Before proceeding further, we note that **Eq. 1** is not a proper Schrödinger equation, due to the fact that S is not a unit matrix and, hence, H^0 is not a proper Hamiltonian. We may, however, obtain a proper Hamiltonian by operating **Eq. 1** with the inverse of S, from the left, and define the present TB Hamiltonian by $H \equiv$

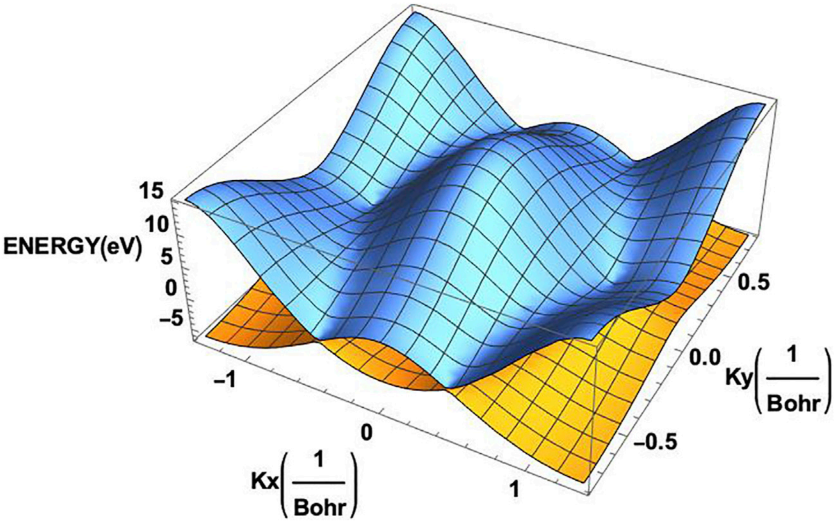

FIGURE 3 | Two dimensional band structure of the monolayer graphene. The valence band (orange) and the conduction band (blue) clearly exhibit the corners of the hexagonal Brillouin zone on them.

$S^{-1}H^0$. The associated Schrödinger equation of the system is then given by

$$H\psi_{\mathbf{k}} = E\psi_{\mathbf{k}} \tag{5}$$

where the elements of the 2 × 2 Hamiltonian matrix H

$$\begin{aligned} H_{11} &= \left(\epsilon_{2p} + g_0 s_0 f^2(\mathbf{k})\right) / \left(1 - s_0^2 f^2(\mathbf{k})\right) \\ H_{12} &= -g_0 f(\mathbf{k}) e^{i\chi(\mathbf{k})} / \left(1 - s_0^2 f^2(\mathbf{k})\right) \\ H_{21} &= -g_0 f(\mathbf{k}) e^{-i\chi(\mathbf{k})} / \left(1 - s_0^2 f^2(\mathbf{k})\right) \\ H_{22} &= \left(\epsilon_{2p} + g_0 s_0 f^2(\mathbf{k})\right) / \left(1 - s_0^2 f^2(\mathbf{k})\right) \end{aligned} \tag{6}$$

The eigenvalues and the eigenvectors of H are easily obtained analytically by diagonalisation:

$$\begin{aligned} E_1(\mathbf{k}) &= \left(\epsilon_{2p} - g_0 f(\mathbf{k})\right) / \left(1 + s_0 f(\mathbf{k})\right) \\ E_2(\mathbf{k}) &= \left(\epsilon_{2p} + g_0 f(\mathbf{k})\right) / \left(1 - s_0 f(\mathbf{k})\right) \end{aligned} \tag{7}$$

where, $\mathbf{k} = (k_x, k_y)$ is the 2D lattice-momentum in the (x, y)-plane of the monolayer graphene. The corresponding normalised eigenvectors are,

$$\begin{aligned} \psi_1(\mathbf{k}) &= \frac{1}{\sqrt{2}}\left(1, e^{-i\chi(\mathbf{k})}\right) \\ \psi_2(\mathbf{k}) &= \frac{1}{\sqrt{2}}\left(-1, e^{-i\chi(\mathbf{k})}\right) \end{aligned} \tag{8}$$

We note that although for graphene the square of $s_0 = 0.129$ is small compared to 1, it appears in the first order in the denominators in the eigenvalues (**7**) and so in principle should be retained. These eigenvalues were first obtained by Saito et al. (1998) from the variational equations (without requiring the Hamiltonian (**6**)). Note also that if the parameter s_0 is neglected (set equal to zero) then, one obtains a pair of symmetric energy bands. This is particularly so near the Dirac points where the interaction with the laser field is dominant. One may note that with $s_0 = 0.129$ the energy bands are generally asymmetric and the VB and CB have different band widths (cf. e.g. **Figure 2**). The Hamiltonian matrix, **Eq. 6**, allows us to obtain also the other physically relevant operators of the system analytically. For example, the current operator $\mathbf{J}_{op}$ or, the transition dipole operator $\mathbf{D}_{op}$, can be obtained in useful analytic forms (see, below).

Introduction of the laser-graphene interaction in the system is readily implemented within the present theory by the *minimal coupling* prescription (see, e.g., Section 1.2, Faisal (1987)) in the reciprocal **k**-space, which, in the dipole approximation, consists in merely changing the Hamiltonian (**6**) by the simple substitution

$$\mathbf{k} \rightarrow \mathbf{k}_t \equiv \left(\mathbf{k} - \frac{e}{\hbar c}\mathbf{A}(t)\right) \tag{9}$$

where, $\mathbf{A}(t)$ is the vector potential associated with the laser electric pulse $\mathbf{F}(t)$, and is given by the definition $\mathbf{A}(t) = -c\int_0^t \mathbf{F}(t')dt'$. Thus, the time-dependent Schrödinger equation governing the evolution of the interacting laser-graphene system can be written as,

$$i\hbar\frac{d}{dt}\Psi_{\mathbf{k}}(t) = H(\mathbf{k}_t)\Psi_{\mathbf{k}}(t) \tag{10}$$

To solve it, we may first expand the total wavefunction $\Psi_{\mathbf{k}}(t)$ in terms of the adiabatic (or,"instantaneous") basis states $\psi_1(\mathbf{k}_t)$ and $\psi_2(\mathbf{k}_t)$ of $H(\mathbf{k}_t)$ and write:

$$\Psi_{\mathbf{k}}(t) = c_1(\mathbf{k}, t)\psi_1(\mathbf{k}_t) + c_2(\mathbf{k}, t)\psi_2(\mathbf{k}_t) \tag{11}$$

We substitute it in **Eq. 10** and project on to the two orthonormalized basis states $|1\rangle \equiv \psi_1(\mathbf{k}_t)$ and $|2\rangle \equiv \psi_2(\mathbf{k}_t)$ from the left to get the pair of coupled equations for the time-dependent occupation amplitudes of the valence and the conduction bands, $c_1(\mathbf{k}, t)$ and $c_2(\mathbf{k}, t)$, respectively:

$$\begin{aligned} i\hbar\frac{d}{dt}c_1(\mathbf{k}, t) &= V_{11}(\mathbf{k}_t)c_1(\mathbf{k}, t) + V_{12}(\mathbf{k}_t)c_2(\mathbf{k}, t) \\ i\hbar\frac{d}{dt}c_2(\mathbf{k}, t) &= V_{21}(\mathbf{k}_t)c_1(\mathbf{k}, t) + V_{22}(\mathbf{k}_t)c_2(\mathbf{k}, t) \end{aligned} \tag{12}$$

with,

$$\begin{aligned} V_{11}(\mathbf{k}_t) &= \left(\epsilon_{2p} - g_0 f(\mathbf{k}_t)\right) \Big/ \left(1 + s_0 f(\mathbf{k}_t) - \frac{1}{2}\frac{d}{dt}\chi(\mathbf{k}_t)\right) \\ V_{12}(\mathbf{k}_t) &= \frac{1}{2}\frac{d}{dt}\chi(\mathbf{k}_t) \\ V_{21}(\mathbf{k}_t) &= \frac{1}{2}\frac{d}{dt}\chi(\mathbf{k}_t) \\ V_{22}(\mathbf{k}_t) &= \left(\epsilon_{2p} + g_0 f(\mathbf{k}_t)\right) \Big/ \left(1 - s_0 f(\mathbf{k}_t) - \frac{1}{2}\frac{d}{dt}\chi(\mathbf{k}_t)\right) \end{aligned} \tag{13}$$

Note that a common term, $-\frac{1}{2}\frac{d}{dt}\chi(\mathbf{k}_t)$, that appears in the diagonal matrix elements V_{11} and V_{22} above, can be transformed away by a unitary transformation of the amplitudes without affecting the probabilities and the expectation values calculated with respect to the total wavefunction of the system (and, so, are dropped in the sequel).

2.1 Velocity Operator, Dipole Operator, *Intra*band Current, *Inter*band Current and Total Current

The x and y components of the velocity operator are obtained in the present theory analytically from the Hamiltonian 6) by differentiation with respect to the components of the lattice-momentum $\mathbf{k} = (k_x, k_y)$,

$$\begin{aligned} u_x(\mathbf{k}_t) &= \frac{1}{\hbar}\frac{d}{dk_x}H(\mathbf{k}_t) \\ u_y(\mathbf{k}_t) &= \frac{1}{\hbar}\frac{d}{dk_y}H(\mathbf{k}(t)) \end{aligned} \tag{14}$$

The quantum mechanical current operator defined as $\mathbf{J}_{op} = e\mathbf{u}_{op}$ and the transition dipole operator can be obtained from the velocity operator using the Heisenberg equation of motion:

$$\mathbf{J}_{op} = \frac{d}{dt}\mathbf{D}_{op} = \frac{i}{\hbar}\left[H, \mathbf{D}_{op}\right] \tag{15}$$

Taking the matrix element of the above equation between a pair of eigenstates, $|\psi_1>$ and $|\psi_2>$, with the respective eigenvalues, E_1 and E_2, of H (**6**), one finds the useful relation,

$$\mathbf{D}_{21} = -i\hbar\mathbf{J}_{21} \big/ (E_2 - E_1) \tag{16}$$

For the applications, the incident laser field $\mathbf{F}(t)$ may be defined generally in the form $\mathbf{F}(t) = \hat{\mathbf{e}}_x F_x(t) + \hat{\mathbf{e}}_y F_y(t)$, where $(\hat{\mathbf{e}}_x, \hat{\mathbf{e}}_y)$ are unit polarisation vectors along the x and y axes, respectively; the associated vector potential is given by $\mathbf{A}(t) = -c\int_0^t \mathbf{F}(t')dt'$. The interaction Hamiltonian, in the adiabatic representation, for the transition dipole operator in the so-called "length gauge" is simply,

$$\begin{aligned} H_{int}(\mathbf{k}_t, t) &= \mathbf{D}(\mathbf{k}_t)\cdot\mathbf{F}(t) \\ &= D_x(\mathbf{k}_t)F_x(t) + D_y(\mathbf{k}_t)F_y(t) \end{aligned} \tag{17}$$

We point out in passing that the coupled dynamical **Eq. 12** derived here using the adiabatic basis representation and the minimal coupling prescription in the so-called "momentum gauge" are, in fact, gauge invariant (cf. Krieger and Iafrate (1986)). This can be ascertained by comparing the respective time-dependent coupled equations in the two gauges (in the present representation) and noticing that the off-diagonal coupling matrix elements V_{12} $(\mathbf{k}_t)$ and V_{21} $(\mathbf{k}_t)$ in **(13)** are equal to the transition matrix elements of the dipole interaction Hamiltonian above (on performing the simple differential operation, $\frac{1}{2}\frac{d}{dt} = \frac{1}{2}\left(F_x(t)\frac{\partial}{\partial k_x} + F_y(t)\frac{\partial}{\partial k_y}\right)$ on the phase function $\chi(\mathbf{k}_t)$ that appears in **Eq. 13**).

Finally, we give the expressions for the quantum mechanical *expectation value* of the "current" along the x and y axes, using the interacting total wavefunction of the system, $\Psi(\mathbf{k}, t)$, and summing over the $\mathbf{k}$-states of the first Brillouin zone (BZ) including the 2-fold spin- and valley-degeneracy of graphene, respectively $g_s = 2$, and $g_v = 2$:

$$\begin{aligned} \hat{e}\cdot\mathbf{J}(\mathbf{k}, t) = {} & g_s g_v \sum_{BZ} \langle\Psi(\mathbf{k}, t)|e\left(\hat{e}\cdot\mathbf{u}_{op}(\mathbf{k}_t)\right)|\Psi(\mathbf{k}, t)\rangle \\ = {} & g_s g_v \left(\frac{L}{2\pi}\right)^D \times \int_{BZ} d^D k\Big\{|c_1(\mathbf{k}, t)|^2\left(\Sigma_{i=x,y} e_i\langle 1|u_i(\mathbf{k}_t)|1\rangle\right) \\ & +c_2(\mathbf{k}, t)|^2\left(\Sigma_{i=x,y} e_i\langle 2|u_i(\mathbf{k}_t)|2\rangle\right) \\ & +2\mathrm{Re}\left[c_2^*(\mathbf{k}, t)c_1(\mathbf{k}, t)\left(\Sigma_{i=x,y} e_i\langle 2|u_i(\mathbf{k}_t)|1\rangle\right)\right]\Big\} \end{aligned} \tag{18}$$

where $\hat{\mathbf{e}} = (e_x, e_y)$ is the unit polarisation vector. $\sum_{BZ} \equiv \left(\frac{L}{2\pi}\right)^D \int_{BZ}(\cdots)d^D k$ stands for the state-sum in the $\mathbf{k}$-space and L^D, for the "volume" in the lattice-space (with D = 2 for the monolayer graphene and D = 1 for the armchair graphene ribbons).

We note that the first two sums on the right hand side above, that depend directly on the occupation probability of the valence band (VB = $|1\rangle$) and the conduction band (CB = $|2\rangle$), is often referred to as the *intra*band current, while the third sum that depends on the VB-CB correlation (or "coherence") term is referred to as the *inter*band current. It is convenient for most purposes to deal with the corresponding *normalised* currents (normalised per $g_s g_v\left(\frac{L}{2\pi}\right)^D$) as:

$$j^{total}(t) = j^{intra}(t) + j^{inter}(t) \tag{19}$$

$$\begin{aligned} j^{intra}(t) = \int_{BZ} & d^D k\Big\{|c_1(\mathbf{k}, t)|^2\left(\Sigma_{i=x,y} e_i\langle 1|u_i(k_t)|1\rangle\right) \\ & + \left|c_2(\mathbf{k}, t)\right|^2\left(\Sigma_{i=x,y} e_i\langle 2|u_i(\mathbf{k}_t)|2\rangle\right)\Big\} \end{aligned} \tag{20}$$

$$j^{inter}(t) = \int_{BZ} d^D k\Big\{2Re\left[c_2^*(\mathbf{k}, t)c_1(\mathbf{k}, t)\left(\Sigma_{i=x,y} e_i\langle 2|u_i(k_t)|1\rangle\right)\right]\Big\} \tag{21}$$

We note that the normalised currents are in a. u., with $[1a.u.] = \left(\frac{e}{t_0}\right)/a_0^{D-1} = 0.125\left(\frac{C}{s}\right)$/nm, for the monolayer (D = 2) and, = $6.624 \times 10^{-3}\left(\frac{C}{s}\right)$ for the ribbons (D = 1).

To complete the definitions we also give the matrix elements appearing above, explicitly:

$$\begin{aligned} \langle 1|u_i(\mathbf{k}_t)|1\rangle &= -\left(g_0 + e_{2p}s_0\right)\frac{\partial f(\mathbf{k}_t)}{\partial k_i}\left(1 + s_0 f(\mathbf{k}_t)\right)^2 \\ \langle 2|u_i(\mathbf{k}_t)|1\rangle &= i\left(g_0 + e_{2p}s_0\right)\partial\chi(\mathbf{k}(t))\partial k_i f(\mathbf{k}_t) \Big/ \left(1 - s_0^2 f^2(\mathbf{k}_t)\right) \\ \langle 1|u_i(\mathbf{k}_t)|2\rangle &= -i\left(g_0 + e_{2p}s_0\right)\partial\chi(\mathbf{k}_t)\partial k_i f(\mathbf{k}_t) \Big/ \left(1 - s_0^2 f^2(\mathbf{k}_t)\right) \\ \langle 2|u_i(\mathbf{k}_t)|2\rangle &= \left(g_0 + e_{2p}s_0\right)\frac{\partial f(\mathbf{k}_t)}{\partial k_i}\left(1 - s_0 f(\mathbf{k}_t)\right)^2, i = (x, y). \end{aligned} \tag{22}$$

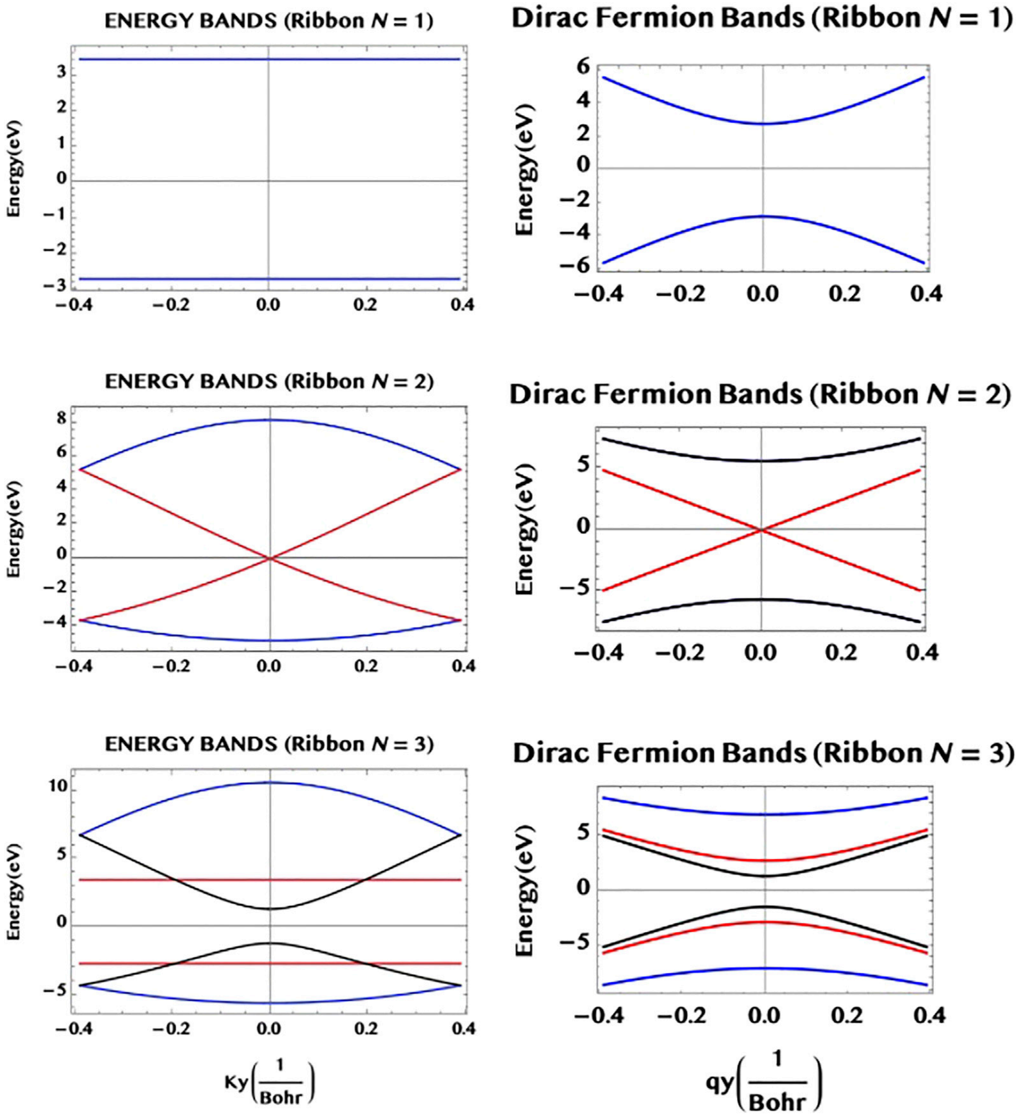

FIGURE 4 | The band structure of armchair graphene ribbons having widths N = 1, 2 and 3, are constructed using the two simple rules for the ribbons given in the text. The full bands from the TB theory (left hand side column), as well as the approximate bands from the Dirac fermion model (right hand side column) are shown. They agree near the middle of the bands (a Dirac point) as they should (but differ away from it). The N = 1 ribbon ("chain") has a single (r = 1, blue) pair of "flat" bands of constant separation along the armchair axis (horizontal *y*-axis); the N = 2 ribbon has two pairs of VB-CB bands, one pair (r = 2, red) is degenerate at the Dirac point; the N = 3 ribbon has three pairs of VB-CB bands, one pair (r = 2, red) has a constant separation (cf. N = 1), while another pair (r = 3, black) shows a finite band-gap minimum at the centre as in a 1D semiconductor. Note that they follow the "m-rules", for the occurrence of a degenerate and/or a "flat" pair of sub-bands, as given in the text.

For the simulations made in this work, we have solved the coupled **Eq. 12** numerically to obtain the amplitudes c_1 (**k**, t) and c_2 (**k**, t). They are used to determine the total wavefunction of the interacting system and to construct the expectation values to investigate first the excitation of the CB population and the *inter*band correlation (or "coherence"). Next, the *intra*band and the *inter*band currents as well as the total current are simulated for the case of graphene monolayer and an armchair ribbon (width, N = 3). Also simulated are the spectra of the radiation emitted from the monolayer and the ribbon currents. Lastly, the effect of the so-called carrier-envelope-phase (or, CEP) on the shape or symmetry of the current produced in a ribbon (width, N = 1) is studied. It is suggested that ultrashort charge-current pulses of desired shape or symmetry might be possible to design by tailoring the *vector potential* of the laser pulse similarly. The results of the simulations carried out are illustrated graphically, and are compared, and discussed in the next section.

3 RESULTS AND DISCUSSIONS

Unless stated explicitly otherwise, for the convenience of writing and the numerical simulations, in the rest of the work we have

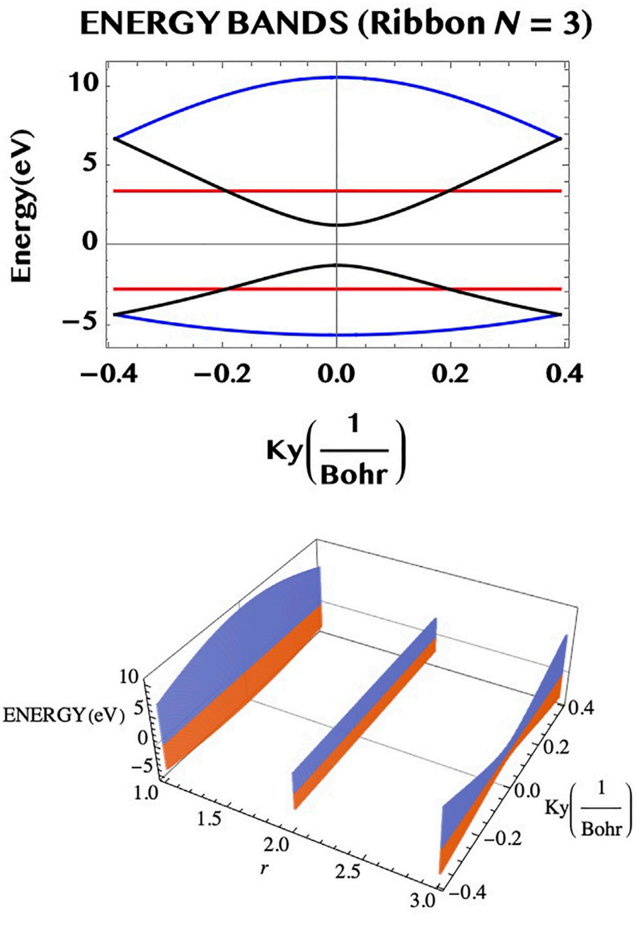

FIGURE 5 | The dispersion relation of the N = 3 armchair ribbon (upper part) may be seen from a different perspective (lower part) as consisting of three "channels" of VB–CB pairs (along the armchair axis), separated by unit widths in the transverse direction.

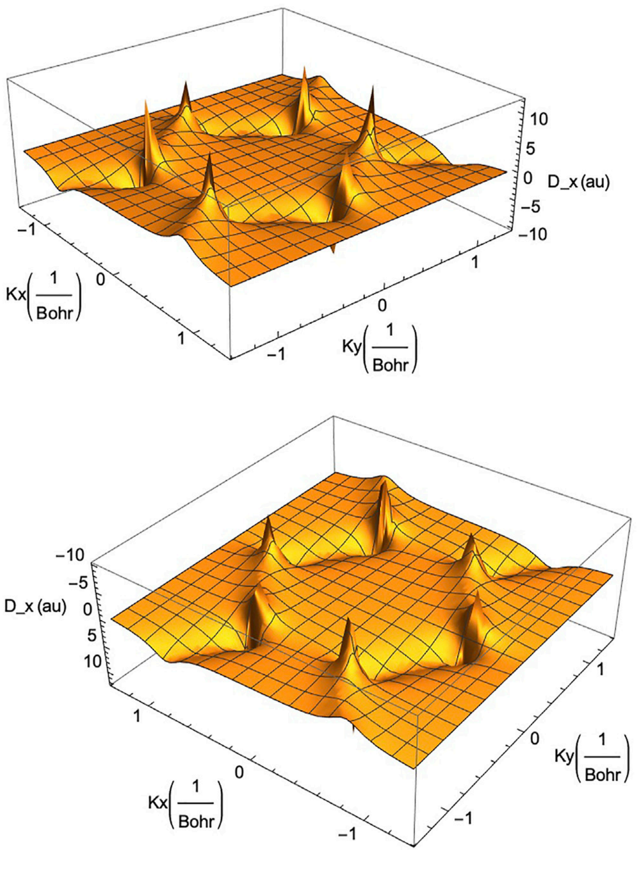

FIGURE 6 | The transition dipole moment operator for monolayer graphene along the *x*-axis, D_x (k_x, k_y), in the reciprocal space (k_x, k_y)-plane. Note the high positive values (upper part) and high negative values (lower part) at the corners of the Brillouin zone. A similar behaviour holds for the component of the dipole operator along the *y*-axis, D_y (k_x, k_y) (not shown here).

used the Hartree atomic units: $e = m = \hbar = 1$, $c = \alpha^{-1} = 137.036$. We note also that [1 a. u.] of length = a_0 = 1Bohr = 0.0519 nm [1 a. u.] of time = $t_0 = a_0/(\alpha c)$ = 24.19 as, and [1. a. u.] of e = 1.602×10^{-19} C.

3.1 Band Structure of Graphene and Armchair Graphene Ribbons

In **Figure 2**, we show a cut through the valence band (VB, blue) and the conduction band (CB, orange) of the monolayer graphene along the k_x-axis (for $k_y = 0$). The energy degeneracy of the two bands are seen to occurr at the Dirac points ($k_x = \pm \frac{4\pi}{3a} = \pm 0.9$ a. u.). Note that in the vicinity of the Dirac points the band dispersions are essentially linear. This is similar to the linear dispersion relation for a hypothetical relativistic free Dirac electron of "zero mass" (hence the nomenclature, "Dirac fermion"). If we neglect the finite overlap integral and set it to $s_0 = 0$, the present TB Hamiltonian naturally goes over to the usual TB dispersion relations with symmetric band widths of the VB and CB. In **Figure 3** we show the full 2D energy surface of graphene (for $s_0 = 0.129$) in the (k_x, k_y)-plane where one can also readily recognise the hexagonal structure of the Brillouin zone of the monolayer graphene. In this work, as indicated earlier, we also consider the armchair graphene ribbons cut along the armchair edge (*y*-axis) with a finite number of cell widths, N, along the transverse direction (*x*-axis) (cf. **Figure 1**). The *confinement* of the ribbon to a finite width along the *x*-axis in fact *quantises* the continuum k_x-states of the monolayer into a set of discrete values that depends on the width index N (the number of cells within the width of the "armchair ribbon") while the ribbon's length is assumed to extend freely along the armchair axis (*y*-axis).

3.1.1 Rules for Constructing Band Dispersion Relations for a Ribbon of a Given Width

We give below two simple, yet general, rules for obtaining the entire system of energy band dispersion relations of the sub-bands of the armchair graphene ribbons (of any width N):

Rule 1: An armchair ribbon of width N has N VB-CB band-pairs, r = 1, 2, . . . , up to N.

Rule 2: The *N* pairs of dispersion relations of the bands can be obtained from the eigenvalues of the monolayer graphene by the

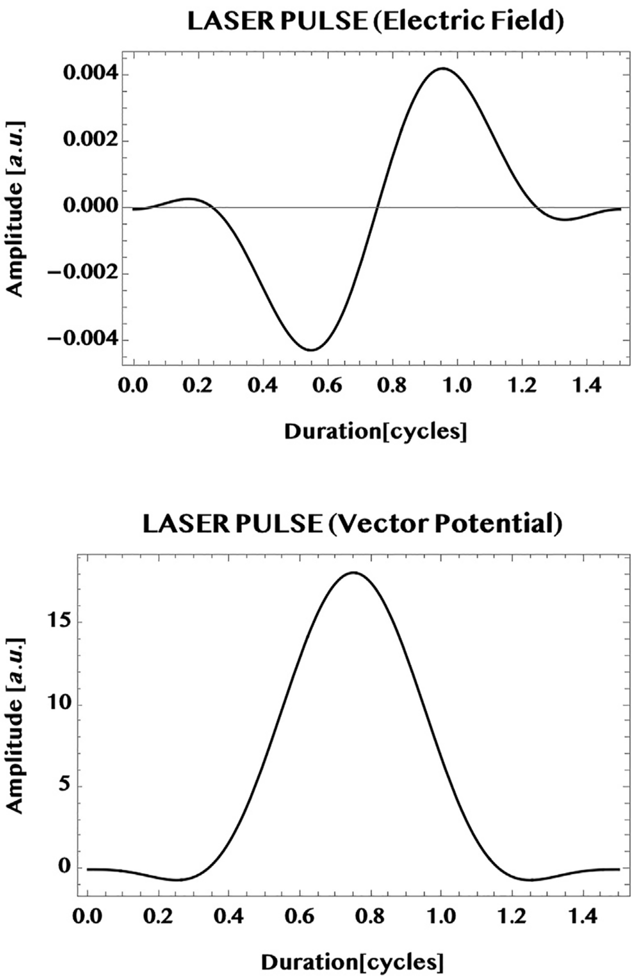

FIGURE 7 | Illustration of a typical ultrashort near-infrared laser pulse used for the simulations in this work (wavelength = 800 nm, peak intensity = 1 TW/cm^2, CEP = 0, pulse duration = 1.5 cycles). Shown in the upper part is the "sin^2-envelope" electric field and in the lower part, the corresponding vector potential. Vertical axis: pulse amplitude in a. u. (field strength [1 a. u.] = 514.22 V/nm), horizontal axis: pulse duration in cycles (1 cycle = T = $2\pi/\omega$): The pulse chosen is linearly polarised parallel to the armchair edge (y-axis): $\mathbf{F}(t) = \hat{\mathbf{e}}_y F_y(t) = \hat{\mathbf{e}}_y F_0 \sin^2(\pi \frac{t}{t_p}) \cos(\omega t + CEP)$, where $\hat{\mathbf{e}}$ = unit polarisation vector, F_0 = peak field strength, t_p = pulse duration, ω = circular frequency, CEP = carrier-envelope-phase. The corresponding vector potential is $A_y(t) = -c\int_0^t F_y(t')dt'$, c = speed of light in vacuum. For the simulations in this work generally CEP = 0 is used (except for **Figure 12**, where the CEP-dependence of the current in an armchair ribbon is investigated).

simple substitution: $k_x \rightarrow k_x[N, r] = (2/a)\,(r\pi/(N+1))$, where a is the graphene lattice constant).

They apply to the full TB dispersion relations as well as to the Dirac fermion model (applicable near the Dirac points **K**). Thus, for the Dirac fermion model of armchair ribbons we get the following simple dispersion relations of the rth pair of bands of a ribbon of width N:

$$E_{\pm}\left(N, r, q_y\right) = \pm\, v_F \sqrt{q_x[N, r]^2 + q_y^2},$$
$$q_x[N, r] \equiv \left(k_x[N, r] - \frac{4\pi}{3a}\right), q_y \equiv k_y \tag{23}$$

where, the Dirac fermion velocity $v_F \approx c/300$. It is also worth observing (cf. Karakachian et al. (2020)) that 1) for each N = 2m + 2 (for, m = 0, or, integer), there is a degenerate pair of VB-CB bands (with a zero band gap) and 2) for each N = 2m + 1 (m = 0, or, integer), there is a "flat" pair of VB-CB bands, for which the band-gap remains *constant* throughout the k_y-space. We may point out that such a ribbon with a flat pair of bands provides a large number of identical "two level" systems (rather analogous to the atomic "two level" systems but) in a robust and compact form of an armchair ribbon. This might be of interest for potential applications in digital/optical systems. In **Figure 4** we illustrate the band structure of the armchair ribbons of widths N = 1, 2, and 3, as constructed from the above rules applied to the TB eigenvalues for graphene monolayer (left hand side column) and compare them to the Dirac fermion model, **Eq. 23**, (right hand side column). It can be seen that both the models agree near the Dirac point, $q_y = 0$, as they should (but differ elsewhere). The system of VB-CB band pairs are colour coded as follows: (N = 1, r = 1) → blue; (N = 2, r = 1, 2) → (blue, red) and, (N = 3, r = 1, 2, 3) → (blue, red, black). For example, for N = 3, there are three VB-CB pairs of bands none of which is degenerate. However, one pair (red) shows a band-gap minimum, as in a 1D semiconductor. The "m-rules" 1) and 2) given above can be easily verified (for m = 0 or, 1) for the three ribbons of widths N = 1, 2, and 3, shown in the figure. (Not surprisingly, however, the Dirac fermion model, that applies near the Dirac point (q_y = near 0), does not maintain the parallel separation away from the band centre, $q_y = 0$, unlike the "flat" bands of the full TB model, that do.) We may add that the band structure of the armchair ribbons of width N may be also viewed as possessing N "conduction channels". **Figure 5** illustrates this for N = 3. The bands shown in the upper part of the figure viewed from an alternative perspective (lower part of the figure) helps to visualise the three "channels" along the armchair axis (for r = 1, 2, and three along the width axis).

3.2 Interaction With an Intense Ultrashort Laser Pulse

As we have seen above, the availability of the TB Hamiltonian in the analytic form **(6)** allows one to obtain the physically interesting current operator $\mathbf{J}_{op} = e\mathbf{u}_{op}$ (below, **Eq. 14**) and the dipole operator $\mathbf{D}_{op}$ **Eq. 16**) for the graphene system. They control the response of graphene and graphene ribbons to laser fields. In **Figure 6** we show an example of the x-component of the transition dipole operator of graphene as a function of the lattice momentum $\mathbf{k} = (k_x, k_y)$. It is clear from the figure that the strength of the transition moment is particularly strong near the corners of the hexagonal BZ (or the Dirac points) in both positive (upper part in the figure) and negative (lower part of the figure) signs of the strength.

For the simulations in this work we have generally restricted ourselves to an intensity of 1 TW/cm^2 (or, a peak field strength F_0 = 2.72 V/nm that is reasonably high but is below the damage threshold for a monolayer graphene Currie et al. (2011). More specifically, we have

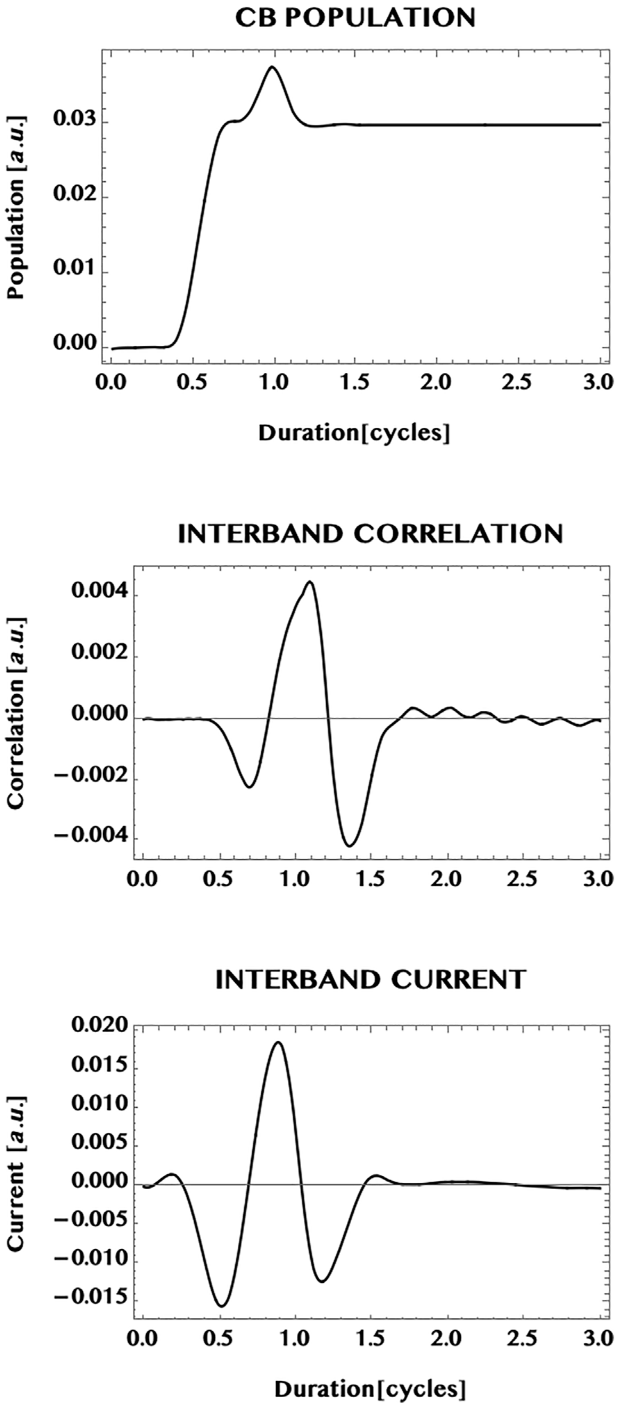

FIGURE 8 | Response of a graphene monolayer to an intense ultrashort laser pulse. Pulse parameters are: wavelength = 800 nm, peak intensity = 1 TW/cm^2, pulse duration = 1.5 cycles, CEP = 0; simulation period = 3 cycles. Top panel: normalised population excited in the conduction band (CB); middle panel: normalised *inter*band "coherence" (or correlation). Shown also is the normalised *inter*band current (bottom panel). Note the near steady population in the CB and an oscillatory *inter*band coherence after the pulse is over. The *inter*band current (being a 2D integrated sum of the *inter*band coherence *wighted* by the k-dependent current operator) shows only a mild modulation for the 2D monolayer (in comparison with a 1D ribbon that is confined along the width dimension (cf. also **Figures 9**, **10** below).

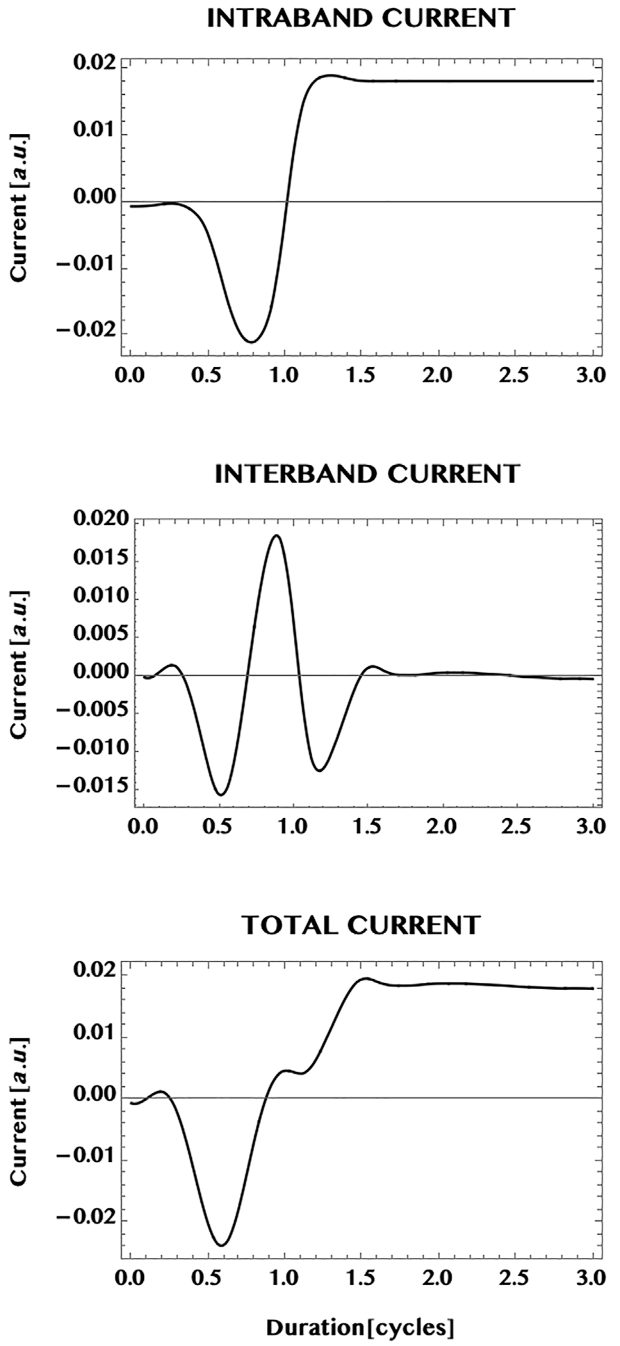

FIGURE 9 | Normalised currents induced in a monolayer graphene by an ultrashort laser pulse (with the same pulse parameters as in **Figure 7**). The upper panel: *intra*band current; the middle panel: *inter*band current. The total current is shown in the bottom panel. It is dominated by the *intra*band current that shows a near steady state by the end of the pulse, at 1.5 cycles, and after the pulse is over. The mild modulation seen to be present could be an effect of the reduced "coherence" (or correlation) of the *inter*band current by the 2D dispersion effect of the integrated sum of **k**-dependent *inter*band coherence weighted by the 2D current operator. This should be contrasted with the possible effects of "quantum confinement" along the width dimension and the band-gap minimum, in the case of the armchair ribbon (cf. **Figure 10**).

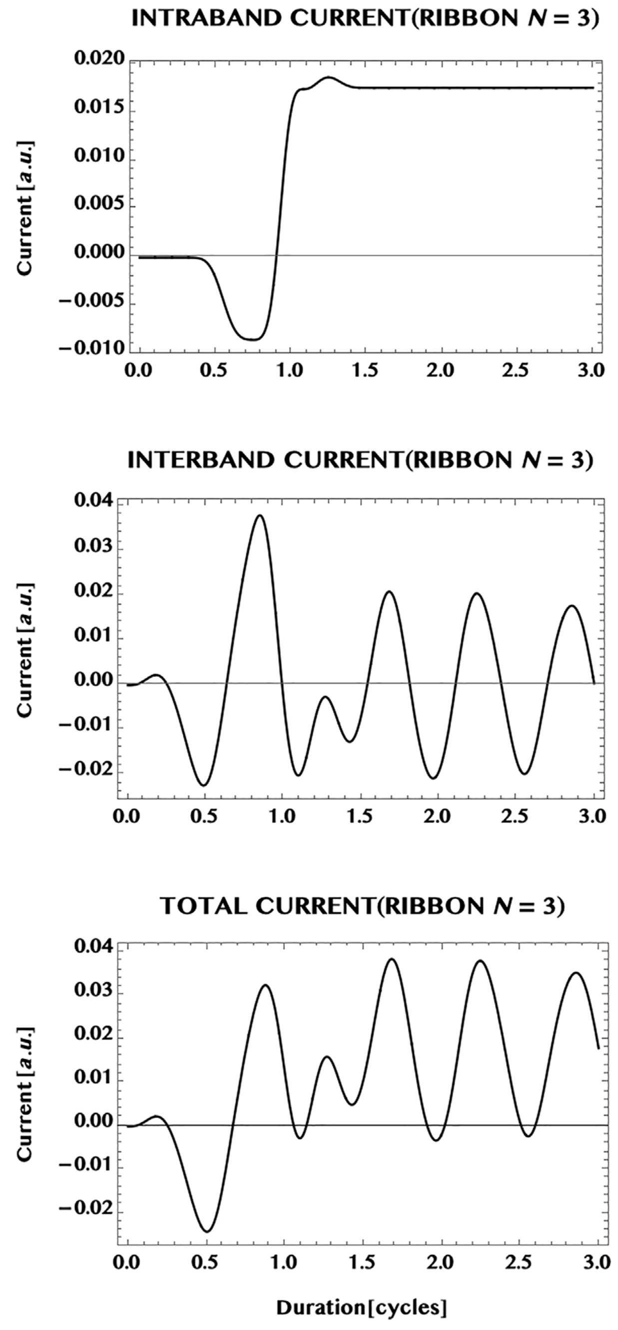

FIGURE 10 | Normalised current generated in an armchair ribbon (N = 3) by an ultrashort laser pulse (wavelength = 800 nm, intensity = 1 TW/cm^2, pulse duration = 1.5 cycles, CEP = 0; simulation period = 3 cycles). Top panel: *intra*band current; middle panel, *inter*band current; bottom panel: *total* current. Note that the total current is dominated by the *inter*band ("coherent") current that shows an oscillatory behaviour during and after the pulse. This might be understood as an effect of the *confinement* of the ribbon along the width dimension, resulting in a reduced band dispersion in the 1D ribbon compared to the fully open 2D monolayer.

chosen a "sin^2-envelope" for the electric field, $\mathbf{F}(t)$, polarised linearly and parallel to the "armchair edge" of graphene (the y-axis):

$$\mathbf{F}(t) = \hat{e}_y F_0 \sin^2\left(\pi \frac{t}{t_p}\right)\cos\left(\omega t + \phi_0\right) \tag{24}$$

where, F_0 is the peak electric field strength, t_p is the pulse duration, ω is the circular frequency and ϕ_0 is the carrier-envelope-phase (or CEP). The corresponding vector potential is given by,

$$\mathbf{A}(t) = -c\int_0^t \mathbf{F}(t')dt' \tag{25}$$

The pulse is illustrated graphically in **Figure 7** (upper panel: electric field, lower panel: vector potential; wavelength 800 nm, intensity one TW/cm^2, $t_p = 1.5$ cycles or, 4 fs).

Note that the duration of the simulation times are extended mostly up to twice the pulse duration (up to three cycles) with no field present in the last 1.5 cycles. This allows one to observe the residual response of the system *after* the pulse has ended. Simulations are made for the following quantities: 1) CB population, 2) "VB-CB correlation", and 3) "band currents", and the results are presented graphically below. They are *normalised*, as discussed above per unit "volume" (precisely, per $g_s g_v (\frac{L}{2\pi})^D$, where, $g_s = 2$, $g_v = 2$ are the spin and valley degeneracy factors of graphene; D = 2 for the monolayer and, D = 1 for the ribbons). As indicated above, the units of the quantities represented are in Hartree atomic units (a.u.) (with [1a.u.] of length = 0.0529 *nm* [1 a. u.] of time = 24.19 *as*, and [1 a. u.] of charge e = 1.602×10^{-19} C). The *normalised* population transfer to the CB and the VB-CB correlation are computed assuming an initially fully occupied VB and an empty CB. Similar initial conditions are assumed for the simulations of the normalised band currents. They are computed from the following normalised formulas (obtained from the general formulas given above).

1) Normalised CB population:

$$Population[t] = \int_{BZ} |c_2(\mathbf{k},t)|^2 d^D k[a.u.], \tag{26}$$

2) Normalised VB-CB correlation:

$$Correlation[t] = \int_{BZ} 2Re\left[c_2(\mathbf{k},t)^* c_1(\mathbf{k},t)\right] d^D k[a.u.], \tag{27}$$

The units for 1) and 2): $[1a.u.] = \frac{1}{a_0^D}$ or, 357.3 $\frac{1}{nm^2}$ for monolayer graphene (D = 2), and =18.904 $\frac{1}{nm}$ for the ribbons (D = 1).

3) The normalised Currents: They are simulated from the y-component of the formulas, **Eqs 19**, **20** and **21**. The units of the normalised currents are in a. u. with $[1a.u.] = \frac{e}{t_0 a_0^{(D-1)}}$; D = 2, monolayer, D = 1, ribbons; the conversion factors to S.I. are the same as given below **Eq. 21** above.

In **Figure 8** we show the population transferred to the CB of graphene (upper panel), the *inter*band correlation—or the VB-CB "coherence"—(middle panel), as well as the *inter*band current (bottom panel). The simulation duration is extended to twice the pulse duration (1.5 cycles) to 3.0 cycles. This allows one to observe the behaviour of the response after the pulse is over. The CB population is seen to increase considerably with the passage of the pulse and attains essentially a steady state superimposed by a mild modulation that persists after the end

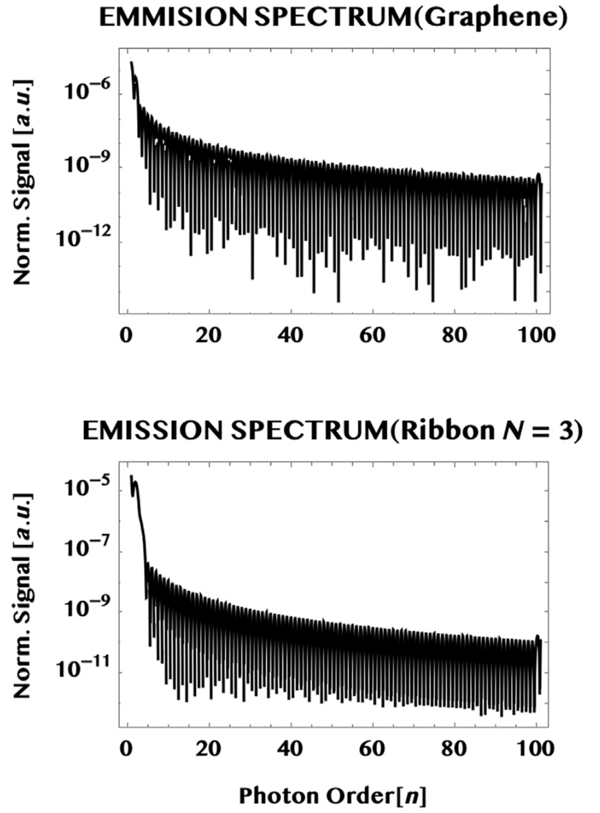

FIGURE 11 | Emission spectra radiated by the ultrashort charge-currents generated in the monolayer graphene (upper plot) and in a graphene ribbon (width, N = 3) (lower plot) by a 1.5 cycles, 800 nm, one TW/cm^2 laser pulse polarised linearly parallel to the armchair edge (y-axis). Notice that both the spectra exhibit similar characteristics i.e. a rapid fall in intensity within a few photon orders followed by a low but broad plateau that extends over many orders (over one hundred).

of the pulse. This is to be contrasted with the oscillatory behaviour of the *inter*band correlation (or the VB-CB "coherence") that shows a sub-cycle oscillation at the end of the pulse and beyond. We point out that sub-cycle oscillations and ballistic currents have been studied and observed experimentally earlier by Hommelhoff and collaborators (Higuchi et al. (2017); Heide et al. (2020)). Note that the *inter*band current—that corresponds to the *inter*band correlation *weighted* by the current operator—is seen here to show only a mild modulation about zero-current. The difference between the strong oscillation in the *inter*band coherence and the mild modulation of the *inter*band current might be an effect of the weighted dispersion in the two dimensional **k**-space for the *inter*band current compared to the un-weighted *inter*band correlation. In **Figure 9** we show the full current (bottom panel) in graphene as well as the individual contributions of the *intra*band current (upper panel) and the *inter*band current (middle panel). Conceptually, the *intra*band current is associated directly with the sum of the electron-current in the CB and the "hole"-current in the VB. The *inter*band current (middle panel) is associated with the *inter*band correlation or the VB-CB "coherence" (discussed above with respect to **Figure 8**). It can be seen here that the total current (bottom panel) is dominated by the *intra*band current (top panel) and reaches essentially a steady state with a mild modulation. Note that the mild modulation of the *inter*band current causes the mild modulation of the total current beyond the duration of the 1.5 cycle laser pulse.

Next, we compare the currents in the monolayer graphene with the current in an armchair graphene ribbon. In **Figure 10** we show the current generated in a ribbon of width N = 3, having three pairs of VB-CB bands or, three "conduction channels" (cf. **Figure 5**). The laser pulse chosen is the same as in the case of the monolayer i.e. a Ti-Sapphire laser pulse at 800 nm, with a peak intensity of one TW/cm^2, and a pulse duration of 1.5 cycles. In comparison with the monolayer case (**Figure 9**), the transition to the ribbon shows a remarkable change of the dominance from the *intra*band current in the 2D monolayer to a dominance of the *inter*band current in the 1D ribbon. The ribbon appears to reduce the possible influence of band dispersion in 1D compared to the open 2D monolayer. This difference might be a result of the confinement effect as well as of the difference in the band structure of the ribbon that has a finite band-gap minimum. However, the same transition from a steady state (with a mild modulation) in the monolayer current to the strong oscillation of the current in the ribbon does not hold universally for the ribbons (as can be seen (cf. **Figure 12**) from the steady zero-current, albeit at a much reduced laser intensity = 1 GW/cm^2, in a ribbon of unit width having a pair of "flat" bands with a wide separation, and needs further investigations for a greater clarity.

The induced currents in graphene and the graphene ribbon imply emissions of radiation. We, therefore, have also briefly considered the emission spectra radiated by them.

The normalised emission spectra computed here are defined by the frequency transform of the normalised currents as follows:

$$Signal\,(n) = |\frac{1}{t_p}\int_0^{t_p} j_y^{total}\,(t)e^{-in\omega t}dt|^2\,[a.u.], \tag{28}$$

where, t_p is the pulse duration. (We may add that the unit of the normalised emission signal in the figure is in [a.u.] and, in S.I. it is simply the square of the units of the normalised currents given earlier.) We show in **Figure 11** the normalised spectra of radiation emitted from a graphene monolayer as well as by an armchair ribbon (of width N = 3) interacting with a 1 TW/cm^2, 800 nm, 1.5 cycle laser pulse (as in **Figure 7**). The laser is assumed to be incident transversely to the monolayer and polarised linearly along the armchair edge (y-axis). It can be seen that both the spectra have similar qualitative characteristics—namely, a high signal for the low photon orders with a rapid fall in intensity followed by a low and *broad* plateau that extends to large orders (over a hundred) of the incident photon energy. They show a relative insensitivity to the detailed structure of the target chosen. This is reminiscent of the relative insensitivity also of the gross structure of the so-called "HHG" spectra of atoms/molecules. From the quantum point of view, this insensitivity

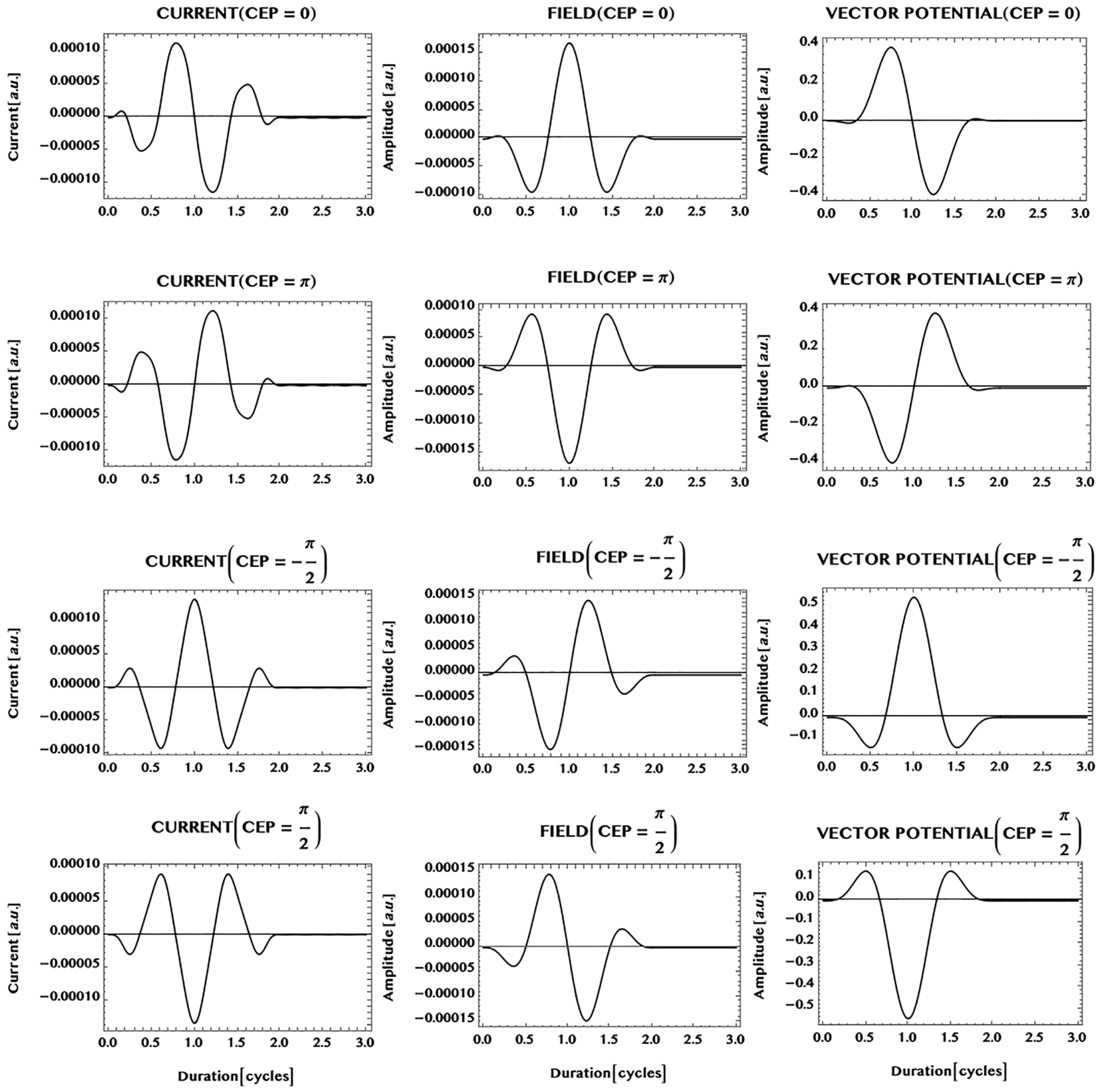

FIGURE 12 | Carrier-envelope-phase (or, CEP) dependence of an ultrashort charge-current generated in an armchair ribbon of unit width (N = 1) by an ultrashort laser pulse (wavelength = 800 nm, peak intensity = 1 GW/cm^2, pulse duration = 1.5 cycles, simulation period = 3 cycles). Shown are: charge-current (LHS column); electric field (middle column); the vector potential (RHS column). Note that CEP = 0 (row 1), CEP = π (row 2), CEP = -π/2 (row 3), and CEP = π/2 (row 4). It can be seen that the *phase* of the charge-current pulse is correlated with the CEP of the laser pulse. For example, the charge-current pulse is fully *reversed* by changing the CEP = 0 (row 1) to CEP = π (row 2). More generally, the shape or symmetry of the main portion of the current is seen to be similar to the shape or symmetry of the *vector potential* of the laser pulse. This suggests the possibility of shaping pulses of charge-carriers to a desired form by tailoring the *vector potential* of the laser pulse similarly.

of the gross structure of the spectra seen here might be due to the dominance of the virtual continuum-continuum transitions between the two band-continua, like that in the ionisation continuum of atoms/molecules that lie behind the fundamental HHG emission process [cf. e.g., review (Section 4.7), Becker and Faisal (2005)].

Finally, we consider the possibility of shaping the ultrashort current of charge carriers in an armchair graphene *ribbon* by tailoring the laser pulse. It has been found recently by Hommelhoff and collaborators that the electron dynamics in monolayer graphene can be controlled by choosing the field strength and the phase of the laser field. Thus, they have observed sub-cycle Stuekelberg oscillations and field dependent change of directions of the ballistic current in monolayer graphene (Higuchi et al. (2017); Heide et al. (2020)). Here we have made a brief study of the influence of the carrier-envelope-phase (CEP) of the laser pulse on the shape of the charge-current pulse generated in an *armchair ribbon*. The results of simulations of the currents (LHS column) are shown in **Figure 12**, along with the electric field (middle column) and the vector potential (RHS column), for four different carrier-envelope-phases of the laser pulse: CEP = 0, π, -π/2, and π/2. Comparing the top two rows of the figure, with CEP = 0 and CEP = π, it can be seen that the symmetry of the ultrashort current pulse is fully *reversed* on changing the CEP of the incident laser pulse from 0 to π. More generally, the results show that the *main* part of the currents for different CEPs in the ribbon follow the shape of the *vector potential* of the incident laser pulse. This suggests the possibility of shaping an ultrashort pulse of charge-carriers in the ribbon to a desired form by tailoring the *vector potential* of the incident laser pulse to mimic the form.

4 SUMMARY

A quantum mechanical investigation of the interaction of an ultra-short intense laser pulse with a two dimensional monolayer graphene *and* with armchair graphene ribbons of different widths is made. A TB model is used for the graphene bands and two simple rules for generating the system of sub-bands of the armchair graphene ribbons of any width, N, are given and the band structures are discussed with illustrations.

Simulations are carried out to investigate, first, the laser pulse excitation of the CB population, the VB-CB *inter*band "correlation" (or "coherence") and the currents generated in the monolayer graphene and in an armchair graphene ribbon (width, N = 3). It is found that the population transfer from an initially fully occupied valence band (VB) to an empty conduction band (CB), is seen to increase during the pulse and ends with a finite steady population, that persists after the pulse is over. In contrast the excitation of the *inter*band correlation or, the VB-CB "coherence", shows an oscillatory behaviour both during and after the passage of the pulse.

A comparison of the currents generated in the monolayer graphene with the current in an armchair ribbon (of width N = 3) shows that the former is dominated by the *intra*band component, that leads to a near steady rest-current with a mild modulation. The transition to the ribbon exhibits a remarkable change from the dominance of the *intra*band current in the monolayer to the dominance of the oscillatory *inter*band current in the ribbon. The ribbon appears to reduce the possible effect of band dispersion in 1D, compared to the open 2D monolayer. The difference seen could be a combined result of the quantum "confinement" effect to 1D as well as due to the difference in the band structure of the ribbon having a band-gap minimum. However, the transition to the oscillatory ribbon current does not hold universally for the ribbons of different widths and, thus, remains open to further investigations in the future for greater clarity.

A brief comparison of the radiation emitted by the currents in the monolayer graphene and the ribbon (N = 3) is also made. They show a gross similarity and a relative insensitivity to the detailed structure of the targets used. The emission spectra are found to be virtually continuous in frequency and fall off rapidly in intensity with the initial photon orders and reach a low but *broad* plateau that extends over many (over a hundred) orders of the incident photon energy. The form of the spectra are also rather insensitive to the target chosen. This is reminiscent of the gross structure and the relative insensitivity to the target chosen also for the well-known "HHG" spectra of atoms or molecules. From the quantum point of view, this insensitivity might be due to the dominance of the virtual continuum-continuum transitions between the two bands, not unlike the transitions in the ionisation continuum of atoms and molecules, that govern the fundamental HHG emission process.

Finally, the possibility of controlling the shape of the ultrashort current of the charge carriers in an armchair ribbon of unit width (N = 1) by the incident laser field is briefly studied. Simulations with different carrier-envelope-phase (CEP) of the incident laser pulse show, for example, that the symmetry of the current in the ribbon can be fully reversed by changing the CEP of the laser pulse from 0 to π. More generally, the result of the simulations made shows that the *main* part of the pulse of the charge-carriers in the ribbon follows the shape of the *vector potential* of the incident laser pulse. This suggests the possibility of *shaping* the ultrashort pulse of charge carriers in the ribbon to a desired form by tailoring the *vector potential* of the laser pulse to mimic the form.

DATA AVAILABILITY STATEMENT

The original contributions presented in the study are included in the article, further inquiries can be directed to the corresponding author.

AUTHOR CONTRIBUTIONS

The author confirms being the sole contributor of this work and has approved it for publication.

FUNDING

Support for the publication costs by the Open Access Publication Fund of Bielefeld University and the Deutsche Forschungsgemeinschaft (DFG).

REFERENCES

Becker, A., and Faisal, F. H. M. (2005). Intense-field many-bodyS-matrix Theory. *J. Phys. B: Mol. Opt. Phys.* 38, R1–R56. doi:10.1088/0953-4075/38/3/r01

Castro Neto, A. H., Guinea, F., Peres, N. M. R., Novoselov, K. S., and Geim, A. K. (2009). The Electronic Properties of Graphene. *Rev. Mod. Phys.* 81, 109–162. doi:10.1103/revmodphys.81.109

Currie, M., Caldwell, J. D., Bezares, F. J., Robinson, J., Anderson, T., Chun, H., et al. (2011). Quantifying Pulsed Laser Induced Damage to Graphene. *Appl. Phys. Lett.* 99, 211909. doi:10.1063/1.3663875

Ernotte, G., Hammond, T. J., and Taucer, M. (2018). A Gauge-Invariant Formulation of Interband and Intraband Currents in Solids. *Phys. Rev. B* 98, 235202. doi:10.1103/physrevb.98.235202

Faisal, F. H. M. (2011). Adiabatic Solutions of a Dirac Equation of a New Class of Quasi-Particles and High Harmonic Generation from Them in an Intense Electromagnetic Field. *J. Phys. B: Mol. Opt. Phys.* 44, 111001. doi:10.1088/0953-4075/44/11/111001

Faisal, F. H. M. (2011). Adiabatic Solutions of a Dirac Equation of a New Class of Quasi-Particles and High Harmonic Generation from Them in an Intense Electromagnetic Field. *J. Phys. B: Mol. Opt. Phys.* 44, 111001. doi:10.1088/0953-4075/44/11/111001

Faisal, F. H. M. (2016). Band-gap Generation and Excitation of Conduction Electrons in Graphene by THz Laser fields. *Mol. Phys.* 115, 7510. doi:10.1080/00268976.2016.1267410

Faisal, F. H. M., and Kamiński, J. Z. (1997). Floquet-Bloch Theory of High-Harmonic Generation in Periodic Structures. *Phys. Rev. A.* 56, 748–762. doi:10.1103/physreva.56.748

Faisal, F. H. M. (1987). *Theory of Multiphoton Processes*. New York: Plenum Press.

Ghimire, S., DiChiara, A. D., Sistrunk, E., Agostini, P., DiMauro, L. F., and Reis, D. A. (2011). Observation of High-Order Harmonic Generation in a Bulk crystal. *Nat. Phys* 7, 138–141. doi:10.1038/nphys1847

Heide, C., Boolakee, T., Higuchi, T., and Hommelhoff, P. (2020). *J. Phys. Photon.* 2, 24004. doi:10.1088/2515-7647/ab7d82

Higuchi, T., Heide, C., Ullmann, K., Weber, H. B., and Hommelhoff, P. (2017). Light-field-driven Currents in Graphene. *Nature* 550, 224–228. doi:10.1038/nature23900

Karakachian, H., Nguyen, T. T. N., Aprojanz, J., Zakharov, A. A., Yakimova, R., Rosenzweig, P., et al. (2020). One-dimensional Confinement and Width-dependent Bandgap Formation in Epitaxial Graphene Nanoribbons. *Nat. Commun.* 11. doi:10.1038/s41467-020-19051-x

Kelardeh, H. K., Apalkov, V., and Stockman, M. I. (2015). *Phys. Rev. B* 91, 045439. doi:10.1103/physrevb.91.045439

Krieger, J. B., and Iafrate, G. J. (1986). Time Evolution of Bloch Electrons in a Homogeneous Electric Field. *Phys. Rev. B* 33, 5494–5500. doi:10.1103/physrevb.33.5494

Liu, H., Li, Y., You, Y. S., Ghimire, S., Heinz, T. F., and Reis, D. A. (2017). High-harmonic Generation from an Atomically Thin Semiconductor. *Nat. Phys* 13, 262–265. doi:10.1038/nphys3946

Luu, T. T., Garg, M., Kruchinin, S. Y., Moulet, A., Hassan, M. T., and Goulielmakis, E. (2015). Extreme Ultraviolet High-Harmonic Spectroscopy of Solids. *Nature* 521, 498–502. doi:10.1038/nature14456

McCann, E. (2012). "Electronic Properties of Monolayer and Bilayer Graphene," in *Graphene Nanoelectronics: Metrology, Synthesis, Properties and Applications* (Heidelberg: Springer-Verlag Berlin), 237–275. doi:10.1007/978-3-642-22984-8_8

Saito, R., Dresselhaus, M. S., and Dresselhaus, G. (1998). *Physical Properties of Carbon Nanotubes*. London: Imperial College Press.

Schubert, O., Hohenleutner, M., Langer, F., Urbanek, B., Lange, C., Huttner, U., et al. (2014). Sub-cycle Control of Terahertz High-Harmonic Generation by Dynamical Bloch Oscillations. *Nat. Photon* 8, 119–123. doi:10.1038/nphoton.2013.349

Sivis, M., Taucer, M., Vampa, G., Johnston, K., Staudte, A., Naumov, A. Y., et al. (2017). Tailored Semiconductors for High-Harmonic Optoelectronics. *Science* 357, 303–306. doi:10.1126/science.aan2395

Vampa, G., Hammond, T. J., Thiré, N., Schmidt, B. E., Légaré, F., McDonald, C. R., et al. (2015). Linking High Harmonics from Gases and Solids. *Nature* 522, 462–464. doi:10.1038/nature14517

Yoshikawa, N., Tamaya, T., and Tanaka, K. (2017). High-harmonic Generation in Graphene Enhanced by Elliptically Polarized Light Excitation. *Science* 356, 736–738. doi:10.1126/science.aam8861

Conflict of Interest: The author declares that the research was conducted in the absence of any commercial or financial relationships that could be construed as a potential conflict of interest.

frontiers | Frontiers in Physics

ORIGINAL RESEARCH
published: 12 May 2022
doi: 10.3389/fphy.2022.880793

Fragmentation Dynamics of Fluorene Explored Using Ultrafast XUV-Vis Pump-Probe Spectroscopy

D. Garg[1,2†], J. W. L. Lee[1,3†], D. S. Tikhonov[1,4†], P. Chopra[1,4], A. L. Steber[1,4,5], A. K. Lemmens[6,7], B. Erk[1], F. Allum[3], R. Boll[8], X. Cheng[1,9], S. Düsterer[1], S. Gruet[1], L. He[9], D. Heathcote[3], M. Johny[2,5,9], M. M. Kazemi[1], H. Köckert[3], J. Lahl[10], D. Loru[1,4], S. Maclot[10,11], R. Mason[3], E. Müller[1], T. Mullins[9], P. Olshin[12], C. Passow[1], J. Peschel[10], D. Ramm[1], D. Rompotis[1,8], S. Trippel[5,9], J. Wiese[9,13], F. Ziaee[14], S. Bari[1], M. Burt[3], J. Küpper[2,5,9,13], A. M. Rijs[15], D. Rolles[14], S. Techert[1,16], P. Eng-Johnsson[10], M. Brouard[3], C. Vallance[3], B. Manschwetus[1] and M. Schnell[1,4]*

[1]Deutsches Elektronen-Synchrotron DESY, Hamburg, Germany, [2]Department of Physics, Universität Hamburg, Hamburg, Germany, [3]Chemistry Research Laboratory, Department of Chemistry, University of Oxford, Oxford, United Kingdom, [4]Institute of Physical Chemistry, Christian-Albrechts-Universität zu Kiel, Kiel, Germany, [5]Center for Ultrafast Imaging, Universität Hamburg, Hamburg, Germany, [6]Van't Hoff Institute for Molecular Sciences, University of Amsterdam, Amsterdam, Netherlands, [7]FELIX Laboratory, Radboud University, Nijmegen, Netherlands, [8]European XFEL, Schenefeld, Germany, [9]Center for Free-Electron Laser Science, Deutsches Elektronen-Synchrotron DESY, Hamburg, Germany, [10]Department of Physics, Lund University Lund, Sweden, [11]Physics Department, University of Gothenburg, Gothenburg, Sweden, [12]Department of Chemistry, College of Natural Sciences, Ulsan National Institute of Science and Technology, Ulsan, South Korea, [13]Department of Chemistry, Universität Hamburg, Hamburg, Germany, [14]J. R. Macdonald Laboratory, Department of Physics, Kansas State University, Manhattan, KS, United States, [15]Division of BioAnalytical Chemistry, Vrije Universiteit Amsterdam, Amsterdam, Netherlands, [16]Institute for X-Ray Physics, Georg-August-Universität, Göttingen, Germany

OPEN ACCESS

Edited by:
Yuichi Fujimura,
Tohoku University, Japan

Reviewed by:
Nigel John Mason,
University of Kent, United Kingdom
Aparna Shastri,
Bhabha Atomic Research Centre (BARC), India

***Correspondence:**
M. Schnell
melanie.schnell@desy.de

†These authors have contributed equally to this work and share first authorship

Specialty section:
This article was submitted to Physical Chemistry and Chemical Physics,
a section of the journal Frontiers in Physics

Received: 21 February 2022
Accepted: 27 April 2022
Published: 12 May 2022

Citation:
Garg D, Lee JL, Tikhonov DS, Chopra P, Steber AL, Lemmens AK, Erk B, Allum F, Boll R, Cheng X, Düsterer S, Gruet S, He L, Heathcote D, Johny M, Kazemi MM, Köckert H, Lahl J, Loru D, Maclot S, Mason R, Müller E, Mullins T, Olshin P, Passow C, Peschel J, Ramm D, Rompotis D, Trippel S, Wiese J, Ziaee F, Bari S, Burt M, Küpper J, Rijs AM, Rolles D, Techert S, Eng-Johnsson P, Brouard M, Vallance C, Manschwetus B and Schnell M (2022) Fragmentation Dynamics of Fluorene Explored Using Ultrafast XUV-Vis Pump-Probe Spectroscopy.
Front. Phys. 10:880793.
doi: 10.3389/fphy.2022.880793

We report on the use of extreme ultraviolet (XUV, 30.3 nm) radiation from the Free-electron LASer in Hamburg (FLASH) and visible (Vis, 405 nm) photons from an optical laser to investigate the relaxation and fragmentation dynamics of fluorene ions. The ultrashort laser pulses allow to resolve the molecular processes occurring on the femtosecond timescales. Fluorene is a prototypical small polycyclic aromatic hydrocarbon (PAH). Through their infrared emission signature, PAHs have been shown to be ubiquitous in the universe, and they are assumed to play an important role in the chemistry of the interstellar medium. Our experiments track the ionization and dissociative ionization products of fluorene through time-of-flight mass spectrometry and velocity-map imaging. Multiple processes involved in the formation of each of the fragment ions are disentangled through analysis of the ion images. The relaxation lifetimes of the excited fluorene monocation and dication obtained through the fragment formation channels are reported to be in the range of a few tens of femtoseconds to a few picoseconds.

Keywords: polycylic aromatic hydrocarbon (PAH), time-resolved spectroscopy, velocity-map imaging mass spectrometry, ultrafast dynamics of molecules, free electron laser

1 INTRODUCTION

The rich molecular inventory of the interstellar medium (ISM) includes polycyclic aromatic hydrocarbons (PAHs), which are estimated to constitute more than 10% of the total galactic carbon [1–4]. UV photons present in the ISM can be absorbed by the PAHs, which can lead to photodissociation, photoionization, photoemission, and photoelectron emission [5]. PAH molecules absorb UV photons, and they relax through IR photon emission [6]. PAHs also play an active role in the ISM through the photoelectric effect where the photoelectrons emitted from the PAH provide the energy to the gas and atoms in the ISM. It also has been suggested that near the photodissociation regions (PDRs), photolysis of these PAHs may lead to the formation of small hydrocarbons [3, 5]. The unidentified infrared bands (UIR), measured in the interstellar atomic hydrogen (H II) and planetary nebula regions of the ISM, are attributed to PAHs and their clusters in cationic or neutral form [5, 7–9] and are also referred to as Aromatic Infrared Bands (AIBs). With radio telescope observations, the support of laboratory experiments, and quantum chemical calculations, the first PAH (indene) and substituted PAHs (1-cyano-naphthalene and 2-cyano-naphthalene) have recently been identified in the ISM [10–12]. To understand the formation of these species, various mechanisms and hypotheses are proposed, involving small hydrocarbons or hydrogen as precursors. These small species might become available as the fragmentation products of other PAHs under harsh radiations [12–14]. Understanding the complex pathways leading to the formation of the detected carbon-containing species extending from small-sized PAHs to large carbonaceous species (e.g., C_{60}^{+} [15]) will provide guidance towards finding more molecules and exploring the constituents of the ISM in the presence of photons, ions, and electrons. One of the ways to look into the complex chemical reactions involved in the ISM is to study the interaction of the relevant molecules with radiation at well defined wavelengths and observing the dissociation products to provide insights into the possible species present in the ISM. Knowledge of the reaction products and the average relaxation lifetimes of the excited species will aid astrochemical evolution models [11].

Despite the remarkable stability of PAHs, they can undergo ionization, isomerization, fragmentation, and dissociative ionization when exposed to high-energy radiation [16–21]. Understanding these processes is challenging for both computational and experimental methods because a large number of nuclear and electronic degrees of freedom are strongly coupled when the system is highly excited and typically enters the non-adiabatic regime, in which the Born-Oppenheimer approximation breaks down [22–25]. The excited species then relax on ultrafast timescales, which can be investigated by pump-probe spectroscopy. Such ultrafast timescales have been observed and reported by several previous laboratory studies [16, 18, 21, 26].

Different experimental approaches exist to investigate the fragmentation products and the fragmentation dynamics of PAHs within different energy regimes (XUV, UV, Vis, IR) [16, 17, 20, 27–29]. The general fragmentation pattern after the interaction of these molecules with high energy photons (a few 10 eV) shows multiple hydrogen losses and a prominent carbon backbone fragmentation, which majorly involves an even number of carbon atoms, for example in the form of acetylene units. The interaction of the molecular beam with high energy photons may also lead to double ionization of the parent molecules, which then dissociate into two monocations involving the loss of zero or an even number of carbon atoms, as shown in photoelectron-photoion-photoion-coincidence (PEPIPICO) measurements [30, 31]. In a recent study employing recoil-frame covariance analysis of velocity-map imaging, we observed a similar behaviour [16]. In the ultraviolet regime, larger PAHs (more than 32 carbon atoms) show more dehydrogenation and less carbon-carbon fragmentation [5] than the small and medium-sized PAHs, which undergo fragmentation affecting the carbon skeleton. Fragmentation of the carbon skeleton could also provide information on the origin of potential species for the hydrogen abstraction and acetylene addition (HACA) model, which is widely suggested as a possible PAH growth mechanism in the photosphere of the asymptotic giant branch stars, where small hydrocarbons form large molecules and soot analogues in the ISM [5, 32].

Here, we present the results from an XUV-Vis pump-probe spectroscopy experiment on the PAH fluorene (FLU, $C_{13}H_{10}$, molecular mass = 166 a.m.u.), which contains two aliphatic hydrogen atoms. The fluorenyl cation, which is dehydrogenated singly ionized FLU, has been reported to be formed from various other PAHs [33–35], which points towards its considerable stability. In a previous study, FLU molecules were irradiated with visible light (593 nm) and their charged clusters were observed to undergo photo-dehydrogenation and photo-isomerization, resulting in the formation of bowl-type structures [36]. This "curling" mechanism was discussed as a bottom-up step to form the fullerene-type structures that are found in the interstellar medium [36]. The formation of stable large FLU clusters is also interesting in the context of the "grandPAH hypothesis," according to which only the most stable species are thought to survive in the photodissociation regions [37]. We investigate the interaction of FLU with XUV radiation centered at 30.3 nm (40.9 eV), which corresponds to the helium (He) II emission line. As the dynamics occur on femtosecond (fs) timescales, we use femtosecond XUV pulses generated from FLASH [38]. The resulting ionized system generated by the XUV radiation is then probed by 405 nm (3.1 eV) visible photons. The studies give insight into the relaxation, dissociation, and ionization dynamics of FLU under XUV conditions.

2 MATERIALS AND METHODS

2.1 Experiments

The experiments were performed using the CFEL-ASG Multi Purpose (CAMP) endstation [39] at the beamline BL1 at the FLASH1 branch of the free-electron laser with a double-sided velocity-map-imaging (VMI) spectrometer installed at the CAMP endstation. We used two pulsed beams (XUV and Vis), operated at a repetition rate of 10 Hz. The XUV pulses (λ = 30.3 nm, pulse duration 80–90 fs (FWHM), which is estimated from the pulse length of electrons [40] using the "LOLA instrument" [41]) were provided by FLASH1 with an average pulse energy of 14.5 μJ, which was then reduced to 1.4 μJ by two aluminium filters of thickness 100.9 nm (55% transmission) and 423.4 nm (28% transmission), and the five beamline mirrors (resultant transmission 62%). The second harmonic generation output of a Ti:Sapphire optical laser, obtained using one beta-barium borate (BBO) crystal, was used as

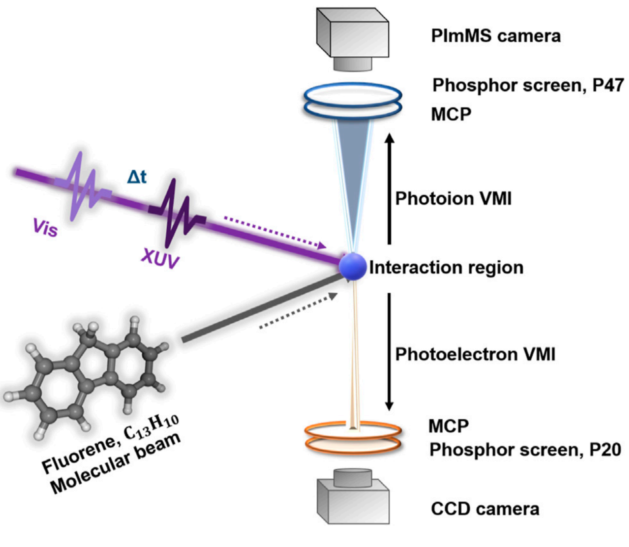

FIGURE 1 | Schematic of the experimental arrangement at the CAMP endstation at FLASH1 (excluding the ion optics for ion and electron extraction) [39]. The supersonically expanded molecular beam interacts with the XUV and Vis pulses (arriving with a delay time, Δt, between them). After interaction, ions and electrons were velocity-mapped on the ion detector assembly (at the top) and on the electron detector assembly (at the bottom). The paths followed by the beams after the interaction are not shown in the figure.

the Vis laser pulse (λ = 405 nm, pulse duration less than ~150 fs, which is estimated from the fundamental beam pulse duration) with a pulse energy up to ~390 μJ [42].

We used the VMI setup [43, 44] at the CAMP endstation [39] to obtain the ion yields and ion momenta of the FLU parent ions (mono-, di-, and trication) as well as fragment ions as a function of pump-probe delay time. FLU was purchased with 98% purity from Sigma-Aldrich and was used without any further purification. A brief description of the experimental procedure and setup (shown in **Figure 1**) is as follows. FLU with a melting point of 116°C was heated to 200°C to produce sufficient molecules in the gas phase. The molecular beam was produced *via* supersonic expansion through a high temperature Even-Lavie pulsed valve with opening times of a few 10 microseconds [45]. We used helium as a carrier gas at 1–2 bar backing pressure. After passing through a pair of skimmers, the well-collimated and internally cooled molecular beam, with the majority of the molecules in their vibrational ground state, entered the vacuum chamber and was irradiated by the two almost collinear beams (XUV and Vis pulses), which crossed each other at a small angle (~1.5°) with different delay times, Δt, between them. The two pulses interact with the neutral molecules perpendicularly. The ions and electrons produced by ionization or dissociative ionization of the neutral molecules were accelerated by an electric field along two diametrically opposed flight tubes and detected at the microchannel plate (MCP) detector/phosphor detector setups in the "top" and "bottom" detector assemblies, respectively. In this work, only the ion data is discussed.

The ion detector assembly consists of a dual MCP detector coupled to a P47 phosphor screen that converts the position information of each ion hit on the detector to light. A multi-mass imaging PImMS2 sensor in a PImMS camera [46, 47] recorded the velocity-mapped 2D ion images formed by the phosphor screen for all the fragments and parent ions in each interaction event. A high-resolution TOF spectrum was obtained by recording the total signal from the MCP using a 2-GHz analog to digital converter (model: ADQ2AC-4G-MTCA, company: SP Devices). Similar to the ion detector assembly, the electrons were simultaneously velocity-mapped onto a P20 phosphor screen and captured by a charged coupled device (CCD) camera. Each experiment involved scanning over the pump-probe delay time between the two laser pulses and recording the ion yield (intensities of the time-of-flight mass spectrum recorded) and ion momenta (extracted from the ion velocity map images) at each step. In this experiment, we scanned a range of 3 picoseconds (ps) of pump-probe delay time with 0.05 ps steps. At each delay value, ~250 measurements were acquired in order to obtain sufficient statistics.

2.2 Analysis

The 2D ion velocity-map images captured from the PImMS camera were fully symmetrized (top/bottom/left/right) and then Abel-inverted to obtain the central slices of the 3D product ion velocity distributions, using the onion peeling method implemented in the PyAbel package available in Python [48, 49]. Angular integration of these Abel-inverted velocity-map ion images generated the radial distribution (in pixels), which was converted to ion momentum using a calibration factor determined through SIMION ion trajectory simulations [50]. The momentum distributions were analyzed as a function of delay time, and the resulting pump-probe delay-time dependent ion yields were fitted using in-house developed open source libraries and scripts [51–53]. The fitting procedure is explained in detail in Refs. [54, 55].

The temporal overlap of the two laser pulses (t_0) was extracted after simultaneously fitting 18 different pump-probe delay time-dependent ion yield curves, which were recorded in the same dataset, and therefore have the same parameter t_0. The resulting t_0 with a fit error of 1 femtosecond was then used as a constraint parameter to fit time-dependent ion yields of other fragments, which were fit with multiple transient features as discussed below for the fragment $C_4H_x^+$. The pump-probe delay time values were corrected for the temporal overlap offset between the two pulses and for jitter in the XUV pulse arrival time that was measured by the beam arrival-time monitor (BAM) [56, 57]. The ion yield intensity was also corrected for shot-to-shot FEL pulse energy fluctuations that is described briefly in the **Supplementary Material**. Covariance analysis [58] was performed on both TOF and VMI results. The TOF measurements enabled us to calculate TOF-TOF partial covariance. The method is explained in detail in Ref. [59], and the results are shared in the **Supplementary Material**. The two-body recoil-frame covariance could be calculated from the VMI data, which are discussed in the results section.

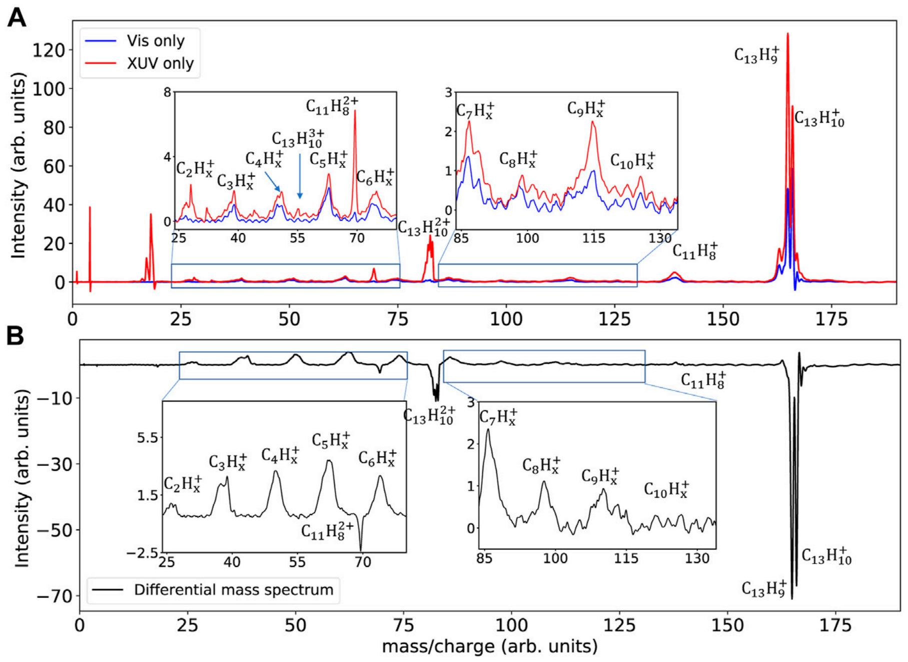

FIGURE 2 | (A) Mass spectra shown for two different conditions: XUV only (red) and Vis only (blue), which were measured using the MCP detector. The insets are the zoomed views of less intense fragments. **(B)** Differential mass spectrum calculated by subtracting the individual XUV only and Vis only spectra from the pump-probe delay-time averaged XUV-Vis mass spectrum in order to visualize the effect of the XUV and Vis pulses.

3 RESULTS

3.1 Time-Independent Results

3.1.1 Ionization and Fragmentation of FLU

Mass spectra obtained after the interaction of FLU with XUV (mass spectrum in red) and Vis (mass spectrum in blue) radiation are shown in **Figure 2A**. Subscript "x" depicts the number of hydrogen atoms attached to the fragments (ranges from 1 to 10). In the following section, we first discuss the effect of Vis and XUV photons on FLU separately before we evaluate their combined effects.

When FLU absorbs Vis photons, mostly single ionization (ionization potential: 7.88 ± 0.05 eV [60]) with loss of up to three hydrogen atoms (hydrogen dissociation energy: ~4 eV [16, 61]) and one acetylene (forming $C_{11}H_x^+$) is observed. The single hydrogen atom loss from FLU^+ is found to be the second most intense peak, FLU^+ being the most intense one. As the energy required for ionization and dissociative ionization is more than the single Vis photon energy (3.1 eV), multi-photon processes must be involved [16]. Consequently, several fragmentation channels are also accessible.

The absorption of XUV photons by FLU leads to single, double, and triple ionization. The singly and doubly charged FLU ions show loss of up to three and four hydrogen atoms, respectively. In the mass spectrum, the intensity of the fluorenyl cation $C_{13}H_9^+$ is observed to be higher than the intensity of $C_{13}H_{10}^+$. The major contribution of $C_{13}H_9^+$ to the mass spectrum can be attributed to the conversion of an sp^3 hybridized carbon to an sp^2 hybridized carbon after loss of an aliphatic hydrogen, which makes the molecule a fully conjugated system. Since a single XUV photon has enough energy to cause ionization and/or hydrogen dissociation, the production of the fluorenyl cation is observed to be more intense during XUV interaction than in the case of Vis pulse interaction that needs multiple photons to produce the fluorenyl cation. Low abundance of the fluorenyl cation is consistent to the observation in other studies with rather low ~4.1 eV photon energy [62] and proton

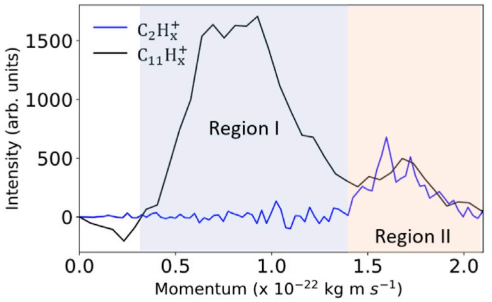

FIGURE 3 | The momentum profiles of $C_2H_x^+$ (blue curve) and $C_{11}H_x^+$ (black curve) fragments are shown for the XUV-only condition and were acquired from the velocity-mapped ion images. Regions I and II mark ions with low and high momentum, respectively. The momentum matches for the two ions, indicating their co-production, which is confirmed by recoil-frame covariance.

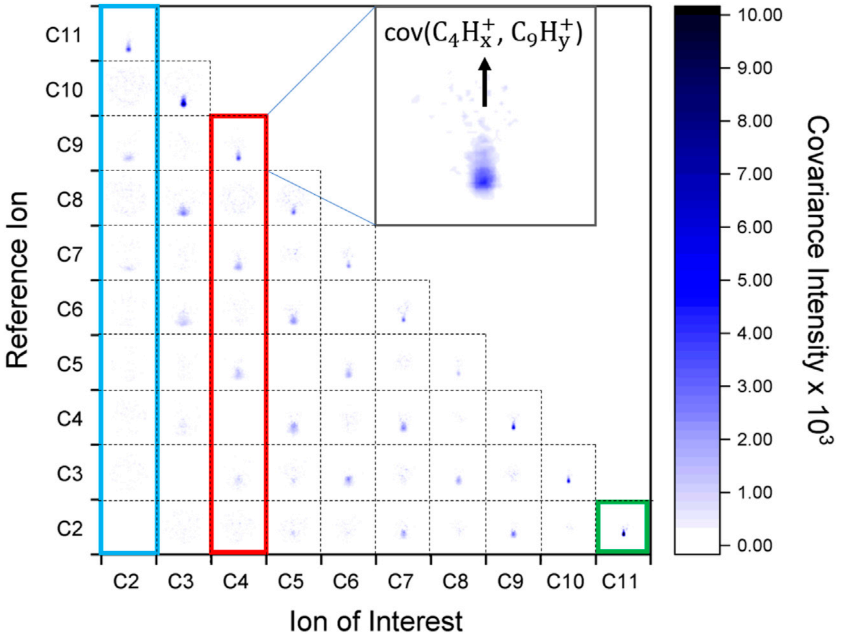

FIGURE 4 | Each square in the dotted grid represents a two-body recoil frame covariance map of the ion of interest with respect to the reference ion, for all the fragment ions, where the direction of the reference ion is vertically upward as also shown in the inset by the black arrow. Self-covariance of an ion with itself is omitted for clarity. Since FLU has 13 carbon atoms, the sum of carbon atoms of the dissociation products cannot exceed 13, and therefore no covariance is expected in the upper half. As an example, the zoomed covariance signal of $C_4H_x^+$ with the reference ion $C_9H_y^+$ is displayed in the inset. The additional subscript "y" depicts the number of hydrogen atoms attached to the fragment, which is the momentum partner of another fragment with the number of hydrogen atoms depicted with subscript "x". The blue rectangle depicts multiple possible ions with which $C_2H_x^+$ could be produced, similarly the red rectangle and green square highlight the possible partners of $C_4H_x^+$ and $C_{11}H_x^+$, respectively.

impact studies [19]. Acetylene loss from the parent monocation forming $C_{11}H_x^+$ and from the parent dication forming $C_{11}H_x^{2+}$ is also observed. The relative abundance of $C_{11}H_x^{2+}$ w.r.t $C_{13}H_x^{2+}$ is higher than that of $C_{11}H_x^+$ w.r.t $C_{13}H_x^+$, which points towards a facilitated acetylene loss from the parent dication than from the parent monocation. The possible dissociation pathways leading to the formation of $C_{11}H_x^+$ and $C_{11}H_x^{2+}$ and the energies involved in dissociation of the parent mono- and dication are summarized in the **Supplementary Material**.

A more prominent $C_2H_x^+$ peak is observed in the XUV-only case compared to the Vis-only condition. During interaction with XUV photons, both the parent monocation and the dication can dissociate to produce $C_2H_x^+$. For the parent monocation, both the formation of the charged acetylene unit, $C_2H_x^+$ (together with the neutral partners, e.g., $C_{11}H_y$, where the subscript "y" depicts the number of hydrogen atoms in this partner fragment), and formation of neutral C_2H_x (together with charged partners, e.g., $C_{11}H_x^+$) are feasible. The parent monocation dissociation will be reflected in the low momentum region, i.e., region I in **Figure 3**, since during the dissociation of the parent monocation, the charged fragments are recoiling from neutral fragments, whereas the parent dication produces $C_2H_x^+$ partnered by charged $C_{11}H_y^+$ resulting in higher momentum and increase the signal measured in region II in **Figure 3**. The co-production of these two fragment ions is indicated by the similar momentum profiles in region II, which is confirmed by the recoil-frame covariance (shown in **Figure 4**). Only a low amount of $C_2H_x^+$ is formed from FLU^+, while significant amounts are formed from the FLU^{2+}.

The differential mass spectrum is calculated by subtracting the individual ion yields observed in the XUV only and the Vis only condition from the XUV-Vis pump-probe delay-time averaged mass spectrum (shown in black in **Figure 2B**). The positive and negative intensity show the increase and decrease in the ion yield, respectively. The decrease in the ion yield of the large fragments or the parent ion species (for example for $C_{13}H_{10}^+$, $C_{13}H_{10}^{2+}$, and $C_{11}H_8^{2+}$) together with the substantial increase in the fragment intensity allude the dissociation of the large species into the smaller fragment ions as a result of the molecular beam interacting with the XUV and Vis pulses.

3.1.2 Ion Momenta and Covariance of Product Fragment Ions

Recoil-frame covariance analysis was performed on the multi-mass VMI data set to discern the correlated ions. The details of covariance mapping can be found in Refs. [63–66]. Briefly, recoil-frame covariance shows the velocity distribution of one ion (ion of interest) with respect to the recoil velocity vector of another ion (reference ion). **Figure 4** shows the covariances between all possible monocation pairs resulting from dissociation of FLU^{2+}. Generally, the intense spot directing opposite to the reference ion direction indicates that the two ions (the ion of interest and the reference ion) are created from the same parent molecule, in a simple two-body decay. Since recoil-frame

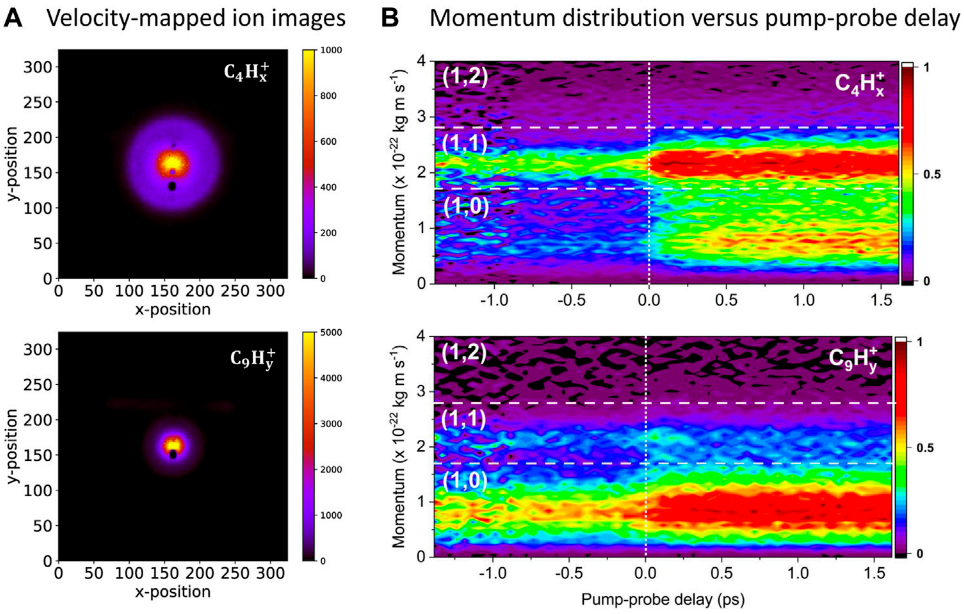

FIGURE 5 | Results for two of the fragments, $C_4H_x^+$ and $C_9H_y^+$: **(A)** 2D raw velocity-mapped ion images for the two fragments. The *x* and *y* axes denote the pixels of the PImMS camera (324 × 324). The black spots in the ion images are due to an artifact in the MCP detector. These images are later fully symmetrized and then Abel-inverted to obtain the central slice of the 3D velocity distribution. This central slice is angularly integrated, and the resultant momentum distribution is plotted as a function of delay time shown in **(B)**. **(B)** Momentum distribution as a function of pump-probe delay for two fragment ions showing momentum matching in the (1,1) channel, indicating their co-production in the same fragmentation reaction, which is verified by the two-body recoil frame covariance. The white vertical dotted line indicates the overlap of the two pulses at t_0.

covariance demonstrates the correlated motion of the two species, the blurred spots indicate that they are produced *via* a more complex mechanism along with other (neutral or charged) partners. It can be observed that $C_{11}H_x^+$ (green square) is only produced together with an acetylene ion, but that the acetylene ion can be produced with other monocations (blue rectangle). The TOF-TOF partial covariance map provides information on only three of the fragmentation channels involving dissociation of FLU^{2+} into $C_2H_x^+$ (with $C_{11}H_y^+$), $C_3H_x^+$ (with $C_{10}H_y^+$), and $C_4H_x^+$ (with $C_9H_y^+$), shown in the **Supplementary Material**. To summarize, the mass spectrum and the covariance analysis help us to identify a number of major fragmentation pathways of FLU molecules when subjected to Vis and XUV radiation. The time-dependent results are shown in the next section to understand the time evolution of the XUV-initiated dynamics in FLU molecules, probed using Vis photons.

3.2 Time-Resolved Results

3.2.1 Fragmentation Channels and Their Relative Intensities

We probed the dynamics and fragmentation pathways of fluorene initiated by the XUV photons at different delay times Δt using Vis photons. In the following, negative time delays ($\Delta t < 0$) denote Vis light irradiating the FLU molecules before the XUV pulse, and positive delays ($\Delta t > 0$) denote XUV pulses arriving earlier than Vis pulses, where the time at which the pulses coincide corresponds to $\Delta t = 0$. In the notation (i,j), "i" indicates the charge state of the ion of interest, and "j" depicts the charge state of the partner produced along with the ion of interest. The (1,0) channel would thus correspond to a monocation (ion of interest) recoiling against a neutral partner. Such products will have lower momentum than in the case of the (1,1) channel, where the monocation is recoiling against another monocation and experiences Coulomb repulsion, which is absent when recoiling against a neutral partner. We specify $C_2H_x^+$, $C_3H_x^+$, $C_4H_x^+$ as small fragments, $C_{10}H_x^+$ and $C_{11}H_x^+$ as large fragments, and the others are considered as medium fragments.

Figure 5A shows the delay-time averaged velocity-map ion images for two fragments $C_4H_x^+$ and $C_9H_y^+$. These images were processed to obtain the momentum distribution as a function of delay time shown in **Figure 5B**, which can be divided into three channels: (1,0), (1,1), and (1,2) to depict low, medium, and high momentum regions, respectively. The signal intensity is then integrated over the momentum coordinate to generate pump-probe delay time-dependent ion yields in these distinct channels (green points in **Figures 6C,D**).

FLU undergoes single and double ionization upon interaction with XUV photons, the resulting parent monocation and the dication interact with the Vis probe pulse and dissociate into the (1,0) and (1,1) channels of the fragment ions, respectively. This dissociation is evident by a sudden decrease in signal for the parent ions accompanied by an increase in the intensity of fragment ions after $\Delta t = 0$. For small fragments, the (1,1) channel is observed to be the most dominant amongst the (1,0), (1,1) and (1,2) channels as shown in **Figure 5B** for

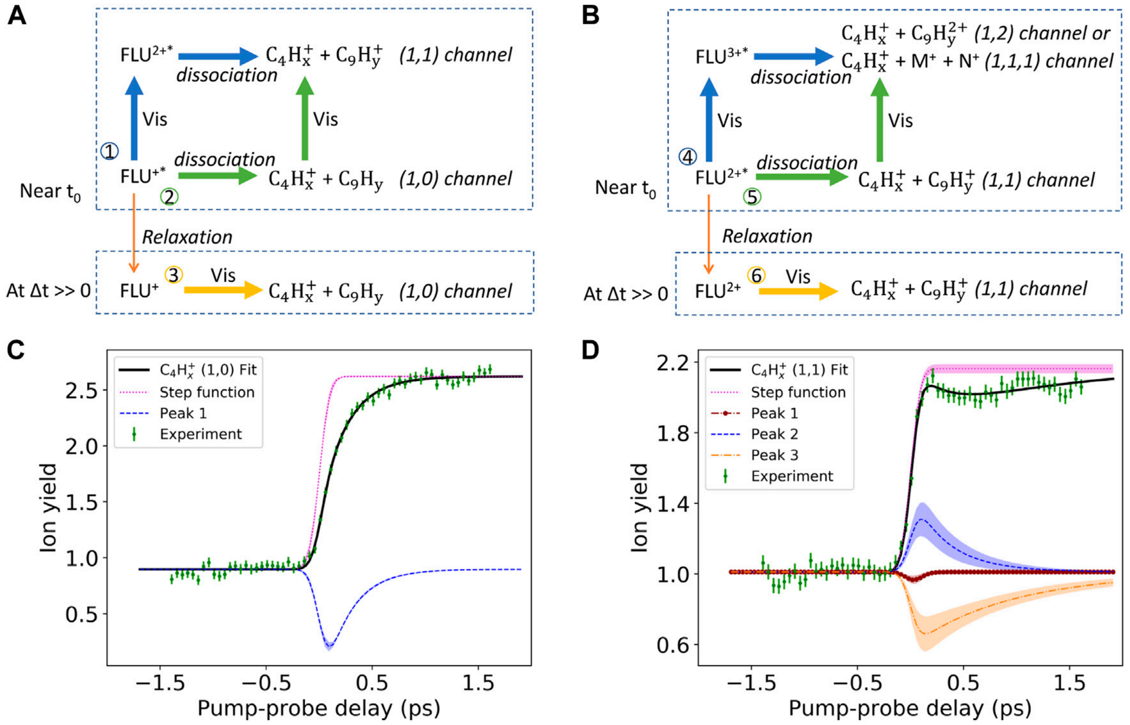

FIGURE 6 | Schematics of the XUV-pump, Vis-probe regime for the monocation and dication, **(A)** and **(B)**, respectively. The orange arrow depicts the relaxation of electronically excited ions over time. The letters M and N depict other possible fragments, which may be produced with the fragment $C_4H_x^+$. Ion yield dependences [in **(B)**] on the pump-probe delay time for the fragment ion $C_4H_x^+$ is shown for both (1,0) **(C)** and (1,1) channel **(D)**. The black curve is the final fitted curve, which is the result of transient peaks (blue, brown, and orange) and the step function (magenta curve). In all the curves the shaded area depicts the error. **(C)** The downward transient peak in the (1,0) channel depicts the transient depletion in the ion yield. **(D)** The (1,1) channel is fitted with three transient features, which comprises of two peaks showing transient decrease in the ion yields (peak 1 and peak 3) and one peak indicating transient increase (peak 2).

$C_4H_x^+$. On the contrary, the medium-sized fragments are observed to be mostly produced through the (1,0) channel, shown in **Figure 5B** for $C_9H_y^+$. The preference of the (1,0) channel and (1,1) channel by medium and small-sized ions, respectively, is explained as follows. During the dissociation of the parent monocation, the charge is mostly carried by the larger fragment than the smaller fragment due to higher ionization potential energy of the smaller fragment. As a result, the medium-sized fragments carry away the charges and are produced with neutrals in the (1,0) channel. The dissociation of the parent dication into the (1,1) channel is energetically favorable, which results in the production of small fragment ions in the (1,1) channel. Therefore, small charged ions are preferably produced with other medium-sized ions in the (1,1) channel than being produced in the (1,0) channel. Although the medium-sized ions are being produced through both channels (1,0) and (1,1), the (1,0) channel is observed to be more pronounced because of the larger production of the parent monocations as shown in **Figure 5B**. A similar trend in the preference of the channels is shown in the **Supplementary Material** for other small and medium-sized fragments.

3.2.2 Internal Relaxation Lifetimes

The experimental delay-time dependent ion yields are displayed with green points in **Figures 6C,D**. The black curve shows the final fit result, which has two major components, namely the step function (magenta curve) and transient peaks (blue, orange, and brown curves). The step function corresponds to the transition from the Vis-pump/XUV-probe (negative Δt) regime to the XUV-pump/Vis-probe (positive Δt) regime. The pronounced increase/decrease in the ion yields are depicted by transient peaks, which are observed in the positive Δt regions, i.e., we observed transient features when the FLU molecules are first pumped by the XUV photons to the singly and doubly ionized states, and the resulting parent monocations and dications dissociate through a number of fragmentation pathways after interaction with the Vis pulses. The various fragmentation channels arise from different ensembles of electronic states, giving rise to different relaxation lifetimes for each channel. In the following, we address the average electronic relaxation lifetimes of FLU monocation and dication obtained from the data on dissociation into $C_4H_x^+$ through the (1,0) and (1,1) channel. The $C_4H_x^+$ ion is highlighted as an example, which shows all the features observed across the other fragment ions.

FLU^{+*}: After absorbing an XUV photon, the FLU monocation may be formed in electronically excited states (FLU^{+*}), which relaxes over time to low-lying electronic states depicted as FLU$^+$. The relaxation process is probed using Vis pulses, as shown schematically in **Figure 6A**. Near t_0, FLU^{+*} may undergo two processes, denoted by pathways (1) and (2). The Vis pulse may induce dissociative ionization, promoting FLU^{+*} to FLU^{2+*} that dissociates into $C_4H_x^+$ and $C_9H_y^+$ [the (1,1) channel of $C_4H_x^+$], demonstrated by pathway (1) following the blue arrows. As a side note, $C_4H_x^+$ could also be produced with other monocations in a (1,1,0) channel with neutral co-fragments. Another possibility is that FLU^{+*} can spontaneously dissociate through the (1,0) channel of $C_4H_x^+$ before the arrival of the probe pulse. The Vis pulse can ionize the neutral fragments produced in the (1,0) channel of $C_4H_x^+$ and convert the (1,0) channel to a (1,1) channel as indicated by pathway (2) following the green arrows. During this conversion, the two charged fragments in the resulting (1,1) channel are still close enough to face a strong Coulombic repulsion and must appear in the (1,1) channel region of the momentum distribution. Upon arrival of the Vis pulse during the evolution of the system along pathway (2), the (1,0) channel can in principle also lead to a (2,0) channel, if the Vis pulse ionizes the charged fragment ($C_4H_x^+$) rather than the neutral C_9H_y, thus there may also be a conversion from the (1,0) to the (2,0) channel. Since double ionization of the small fragment has a comparable low probability and we do not observe this conversion, this process is not discussed here and is not included in the schematic. At longer delay, the FLU^{+*} electronically relaxes (orange arrow in **Figure 6A**), and the Vis pulses can only lead to dissociation of relaxed FLU^+ through the (1,0) channel [pathway (3)].

Overall, these three pathways contribute to the transient increase in the (1,1) channel of $C_4H_x^+$ (blue peak 2 in **Figure 6D**), which matches the transient decrease in the (1,0) channel of the $C_4H_x^+$ yield (blue peak 1 in **Figure 6C**) near time $\Delta t = 0$. The timescales of the transient peaks correspond to the relaxation lifetime of the FLU^{+*} electronic states, which lead to the formation of $C_4H_x^+$ in the channels described above. These lifetimes are found to be 249 ± 10 fs and 339 ± 77 fs, for the depletion of the (1,0) [pathway (3)] and increase in the (1,1) channel (pathways (1) and (2) in **Figure 6A**, respectively). In addition to relaxation *via* carbon loss fragmentation channels, the H-loss channel also shows a transient increase, with a relaxation lifetime of 136 ± 7 fs. All other fragments have similar transient increase and decrease features in their (1,1) and (1,0) channels, respectively, except $C_2H_x^+$, where the data had a significant N_2^+ contamination. These are shown in the **Supplementary Material**.

FLU^{2+*}: XUV photon absorption also forms FLU in an electronically excited dication state, FLU^{2+*}. Similar to the processes described above, near t_0 we probe a number of dissociative pathways. Pathway (4) demonstrates dissociative ionization of FLU^{2+*} after interaction with Vis photons forming FLU^{3+*}, which dissociates through either (1,2) or (1,1,1) channels (monocation recoiling against two other monocations), shown in **Figure 6B** following the blue arrows. The other pathway (5) depicts spontaneous dissociation of the FLU^{2+*} ions into the (1,1) channel, before the arrival of the Vis pulse. The Vis pulse may lead to the formation of the (1,2) or (1,1,1) channel of $C_4H_x^+$. If alternatively there is a sufficiently long delay time, the FLU^{2+*} molecules relax to FLU^{2+}, and promotion to the next ionization state by the Vis pulse is less favoured. The relaxed FLU^{2+} can then dissociate through the (1,1) channel upon arrival of the Vis pulse.

We observed two peaks depicting transient depletion in the ion yields in the (1,1) channel of $C_4H_x^+$, indicated as peak 1 (brown) and peak 3 (orange) in **Figure 6D**. The less intense peak 1 corresponds to a short lifetime of 30 ± 14 fs showing the depletion in the ion yield near t_0. This depletion is attributed to the corresponding transient increase in the (1,2) channel of $C_4H_x^+$. In our experiments, the signal for the (1,2) channel is very low, which could be due to the less intense probe pulse, and the corresponding increase in the (1,2) channel is not observed clearly. But the presence of the (1,2) channel for the fragment ion $C_3H_x^+$ was visible in a previous study with a different probe (810 nm), and a similar short lifetime of 17 ± 5 fs was reported [16]. Therefore, the peak 1 can be attributed to the shifting of population from the (1,1) channel to the (1,2) channel of $C_4H_x^+$ near t_0.

Peak 3 with a long lifetime of 1001 ± 204 fs can be attributed to the formation of the (1,1,1) channel. Formation of the (1,1,1) channel initiated by the Vis pulse involves production of three fragment ions, which can be produced at any time after the Vis pulse interaction. This leads to their production in a longer time span resulting in longer lifetime. The corresponding increase in the (1,1,1) channel can not be shown since this channel will have a large momentum distribution that could not be disentangled through the momentum maps. To summarize, the relaxation lifetime of FLU^{2+*} is determined *via* three pathways (4), (5), and (6), which result in transient depletion in the (1,1) channel resolvable for conversion into two dissociation channels, namely the (1,2) channel with a lifetime of 30 ± 14 fs and the (1,1,1) channel with a lifetime of 1001 ± 204 fs.

In addition to the FLU^{2+*} lifetimes obtained through the carbon skeleton fragmentation channels, we also obtained the relaxation lifetime of the FLU dication dissociating through the H-loss channel, which was found to be 117 ± 6 fs. The H-loss relaxation lifetimes of FLU^{2+*} and FLU^{+*} are similar and indicate that hydrogen loss from the parent ion, which involves σ-bond fission, is unaffected by the difference in the charge states that are mostly localized in the conjugated-π system. The lifetimes extracted from other fragments are tabulated in the **Supplementary Material**.

The fragment ions with higher masses than $C_6H_x^+$ were fitted with a single transient increase peak. The absence of multiple peaks in the (1,1) channels for these heavier mass fragments is attributed to the following two reasons. Firstly, the conversion from the (1,1) channel to the (1,2) channel for the higher masses might be inaccessible since the small partner ions of these large fragments are difficult to doubly ionize by the Vis pulse, due to the higher ionization potential compared to the larger fragments and even higher double ionization potential. Secondly, the (1,1,1) channel is formed by the dissociation of the FLU trication into smaller fragments, and hence this channel is likely to have a significantly smaller branching ratio due to the fact that one of the fragments is already large.

Relaxation lifetimes for near-ionization-threshold electronic states of FLU^{2+*} could also be extracted from the transient increase in the FLU trication signal. As depicted in process (4) in the schematic of **Figure 6B**, the Vis pulse absorption by FLU^{2+*} results in the formation of FLU trication, observed as a transient increase in the FLU^{3+} ion yield. This transient peak corresponds to a relaxation lifetime of 184 ± 44 fs, which was measured using 405 nm Vis photons as the probe pulse (~390 μJ pulse energy).

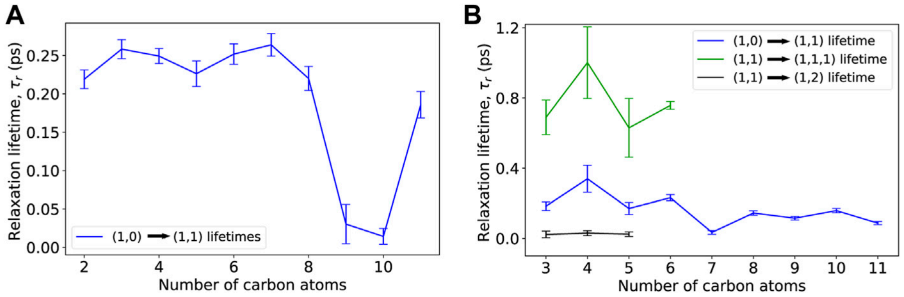

FIGURE 7 | Observed trends as a function of fragment size. **(A)** Relaxation lifetime of FLU^{+*} plotted as a function of the number of carbon atoms of the fragment, with which the relaxation lifetime is associated. This demonstrates the depletion of the (1,0) channel and the formation of the (1,1) channel. **(B)** Relaxation lifetime of FLU monocation and dication plotted as a function of the number of carbon atoms of the fragment obtained from the (1,1) channel, depicting three processes. First, conversion of the (1,0) channel to the (1,1) channel, which corresponds to the electronic relaxation lifetimes of the FLU monocation (blue curve). Second, conversion of the (1,1) channel to the (1,2) channel, which corresponds to the electronic relaxation lifetimes of the FLU dication (black curve). Third, conversion of the (1,1) channel to the (1,1,1) channel, which also corresponds to the electronic relaxation lifetimes of the FLU dication (green curve). The fragment ion $C_2H_x^+$ with a lifetime of 2.987 ± 0.006 ps, which would be on the blue curve, has been omitted for better visibility of the other fragments with much shorter lifetimes.

The relaxation lifetime was also determined before using XUV-IR (30.3 and 810 nm) [16] pump-probe studies to be 126 ± 16 fs, which is somewhat lower compared to the XUV-Vis studies reported here.

4 DISCUSSION

4.1 Effect of Fragment Size on the Observed Relaxation Lifetimes

The relaxation of the electronically excited FLU monocation and dication is probed *via* Vis pulses by inducing dissociation and/or dissociative ionization. Various fragment ions thus produced would show different relaxation lifetimes (τ_r) of FLU$^+$ and FLU^{2+}. The effect of the fragment ion's size on the τ_r can be observed in **Figures 7A,B**, where we plot the identified relaxation lifetimes as a function of the number of carbon atoms in the fragment ion. The respective τ_r of FLU^{+*} determined through the (1,0) channel and the (1,1) channel are depicted by the blue curves in **Figures 7A,B**. The small fragments with number of carbons atoms from two to eight indicate similar lifetimes (τ_r) whereas the large fragments $C_9H_x^+$ and $C_{10}H_x^+$ except $C_{11}H_x^+$ show longer τ_r.

The longer and shorter relaxation lifetimes for the small and large fragments, respectively, can be explained as follows: as can be inferred from the covariance maps (**Figure 4**), the smaller fragments have more possible dissociation partners, and hence more fragmentation pathways are associated with them. The relaxation of FLU^{+*} into these multiple pathways, involving the formation of a small fragment with various other partners, is not completely resolvable. The resultant transient peaks thus have contributions from all possible formation pathways, and hence longer lifetimes are observed compared to the large fragments having a relatively low number of formation pathways resulting in shorter lifetimes.

The longer lifetime corresponding to the $C_{11}H_x^+$ fragment ion is an exception to the lifetimes extracted from other large fragment ions. This exception is attributed to the fact that the formation pathway of $C_{11}H_x^+$ involves acetylene loss from the parent species. This pathway is thought to progress *via* a mechanism involving rearrangement of the rings to allow C_2H_2 loss described in Ref. [67], which is not the case for the C_3H_x loss or C_4H_x loss leading to the formation of other large fragments. This low-energy dissociative pathway forming $C_{11}H_x^+$ is likely to be initiated by the Vis pulse from a wide range of electronic states of FLU$^+$, which results in longer relaxation lifetimes. The relaxation lifetimes of FLU^{2+*} were obtained from the shift of population from the (1,1) channel to the (1,2) and (1,1,1) channels of small fragment ions. The absence of these features in the large fragments was explained in the previous section. The observation of similar lifetimes for small fragments is consistent here as depicted by the green and black curve in **Figure 7B**.

4.2 Effect of Probe Pulse on the Observed Relaxation Lifetimes

As reported in the results section, the relaxation lifetimes of FLU^{2+*} were found to be different when probed with IR and Vis pulses. This difference in the recorded lifetime with the Vis pulse is attributed to its higher probe energy, which is able to excite lower-lying states of FLU^{2+*} to FLU^{3+*}, resulting in an increase in the observed relaxation lifetimes.

5 SUMMARY AND CONCLUSION

We studied the interaction of FLU molecules with XUV radiation, which is present in the interstellar medium as He II emission line. FLU was observed to undergo numerous processes, involving single and double ionization, dominant single dehydrogenation post single ionization, and fragmentation into various carbon loss channels with acetylene loss being a major process. The fragments observed in the mass spectrum can be thought of as potential ions that would be present in the ISM as a result of UV induced photodissociation.

The recoil-frame covariance technique exhibited the primary, secondary, and tertiary fragmentation of the parent dication that have occurred from a high amount of residual energy given by the high-energy photons. The ultrafast pump-probe measurements with the 405 nm probe enabled us to investigate the ultrafast decay of electronically excited and highly energetic parent ions that are promoted to the next charge state dissociation and/or non-dissociation channels.

Interaction with high energy photons opened the possibility for parent ion dissociation through a large number of fragmentation pathways. The momentum resolution provided by the velocity map imaging made it possible to distinguish between several channels for the fragments, which we label as (1,0), (1,1) and (1,2) channels. A detailed analysis on the fragments showed the transient depletion and enhancement of the ion yields, as a result of the FLU^{+*} and FLU^{2+*} ions' temporal relaxation into different energy levels. It is interesting to observe the time-resolved shift of the population from one channel to another one of the observed fragments, revealing the lifetimes of the species they are formed from. The results enabled us to determine the dependence of the relaxation lifetimes on the fragment size. These relaxation lifetimes were reported to be in the range of 10 fs to a few ps. The range of the lifetimes is similar to the lifetimes that were reported to be in the range of 10–100 fs using XUV-IR pump-probe spectroscopy [16, 18, 26].

In this work, we used and discussed different experimental and analytical tools to investigate the fundamental photophysics and chemical processes engaged after the interaction of fluorene with XUV radiation. Through these processes, the relaxation lifetimes of the fluorene parent ions were extracted, which are beneficial to gaining a complete view of the timescales of small PAHs. All dissociation products from fluorene were found to have reaction pathways decaying on the sub-picosecond timescale, indicating non-adiabatic relaxation mediated by a high number of conical intersections. As PAHs typically have a high density of states, similar to fluorene, ultrafast relaxation across all charge states investigated might be expected amongst PAH molecules in general. Overall, exploring the possible reaction pathways of the fluorene cations in its non-radiative regime is advantageous for the fundamental femtochemistry and astrochemistry fields.

DATA AVAILABILITY STATEMENT

The original contributions presented in the study are included in the article/**Supplementary Material**, further inquiries can be directed to the corresponding author.

AUTHOR CONTRIBUTIONS

BM and MS conceived and designed the experiments. JWLL, PC, SM, AS, SG, FA, RB, XC, SD, BE, LH, DH, MJ, MK, HK, JL, AL, DL, RM, EM, TM, PO, CP, JP, DRa, DRom, STr, JW, FZ, SB, MBu, DRol, STe, PJ, BM, and MS performed the experiments. DG, JWLL, DT, PC, SM, AS, SG, and EM analyzed the data. DG, JWLL, DT, PC, AS, BE, FA, MBu, JK, AR, DRol, RB, PJ, MBr, CV, BM, and MS performed detailed discussions of the results. DG, JWLL, DT, and MS wrote the manuscript.

FUNDING

This work was supported by the ERC Starting Grant ASTROROT, grant number 638027, and the project CALIPSOplus under the grant agreement 730872 from the EU Framework Programme for Research and Innovation HORIZON 2020. The experimental parts of this research were carried out at beamline BL1 FLASH at DESY, a member of the Helmholtz Association (HGF). Beamtime was allocated for proposal F-20170540. We acknowledge the Max Planck Society for funding the development and the initial operation of the CAMP end-station within the Max Planck Advanced Study Group at CFEL and for providing this equipment for CAMP@ FLASH. The installation of CAMP@FLASH was partially funded by the BMBF grants 05K10KT2, 05K13KT2, 05K16KT3, and 05K10KTB from FSP-302. We acknowledge financial support by the European Union's Horizon 2020 research and innovation program under the Marie Skłodowska-Curie Grant Agreement 641789 "Molecular Electron Dynamics investigated by Intense Fields and Attosecond Pulses" (MEDEA), the Clusters of Excellence "Center for Ultrafast Imaging" (CUI, EXC 1074, ID 194651731), the "Advanced Imaging of Matter" (AIM, EXC 2056, ID 390715994) of the Deutsche Forschungsgemeinschaft (DFG), the European Research Council under the European Union's Seventh Framework Programme (FP7/2007–2013) through the Consolidator Grant COMOTION (614507), and the Helmholtz Gemeinschaft through the "Impuls- und Vernetzungsfonds". In addition, the project was supported by The Netherlands Organization for Scientific Research (NWO) and is part of the Dutch Astrochemistry Network (DAN) II (Project No. 648.000.029). PE-J, SM, and JP acknowledge support from the Swedish Research Council and the Swedish Foundation for Strategic Research. The authors are additionally thankful for the support from the following funding bodies: the UK EPSRC (MBR and CV-EP/L005913/1 and EP/V026690/1; MBU-EP/S028617/1), STFC (PNPAS award and mini-IPS Grant No. ST/J002895/1), the Chemical Sciences, Geosciences, and Biosciences Division, Office of Basic Energy Sciences, Office of Science, US Department of Energy (FZ—DE-FG02-86ER13491); the National Science Foundation (DR - PHYS-1753324); and the Helmholtz Initiative and Networking Fund through the Young Investigators Group Program (SB). We acknowledge the use of the Maxwell computational resources operated at Deutsches Elektronen-Synchrotron DESY, Hamburg, Germany.

SUPPLEMENTARY MATERIAL

The Supplementary Material for this article can be found online at: https://www.frontiersin.org/articles/10.3389/fphy.2022.880793/full#supplementary-material

REFERENCES

1. Ehrenfreund P, Sephton MA. Carbon Molecules in Space: from Astrochemistry to Astrobiology. *Faraday Discuss* (2006) 133:277. doi:10.1039/b517676j
2. Herbst E, van Dishoeck EF. Complex Organic Interstellar Molecules. *Annu Rev Astron Astrophys* (2009) 47:427–80. doi:10.1146/annurev-astro-082708-101654
3. Tielens AGGM. Interstellar Polycyclic Aromatic Hydrocarbon Molecules. *Annu Rev Astron Astrophys* (2008) 46:289–337. doi:10.1146/annurev.astro.46.060407.145211
4. Ziurys LM. The Chemistry in Circumstellar Envelopes of Evolved Stars: Following the Origin of the Elements to the Origin of Life. *Proc Natl Acad Sci U.S.A* (2006) 103:12274–9. doi:10.1073/pnas.0602277103
5. Tielens AGGM. The Aromatic Universe. In: *Molecular Astrophysics*. Cambridge: Cambridge University Press (2021). p. 567–628. doi:10.1017/9781316718490.013
6. Allamandola LJ, Tielens AGGM, Barker JR. Interstellar Polycyclic Aromatic Hydrocarbons: The Infrared Emission Bands, the Excitation/Emission Mechanism, and the Astrophysical Implications. *Astrophysical J Suppl Ser* (1989) 71:733. doi:10.1086/191396
7. Berné O, Joblin C, Rapacioli M, Thomas J, Cuillandre J-C, Deville Y. Extended Red Emission and the Evolution of Carbonaceous Nanograins in NGC 7023. *Astron Astrophysics* (2008) 479:L41–L44. doi:10.1051/0004-6361:20079158
8. Rapacioli M, Joblin C, Boissel P. Spectroscopy of Polycyclic Aromatic Hydrocarbons and Very Small Grains in Photodissociation Regions. *Astron Astrophysics* (2004) 429:193–204. doi:10.1051/0004-6361:20041247
9. Peeters E, Hony S, Van Kerckhoven C, Tielens AGGM, Allamandola LJ, Hudgins DM, et al. The Rich 6 to 9 $\vec\µ$m Spectrum of Interstellar PAHs. *Astron Astrophysics* (2002) 390:1089–113. doi:10.1051/0004-6361:20020773
10. Cernicharo J, Agúndez M, Cabezas C, Tercero B, Marcelino N, Pardo JR, et al. Pure Hydrocarbon Cycles in TMC-1: Discovery of Ethynyl Cyclopropenylidene, Cyclopentadiene, and Indene. *Astron Astrophysics* (2021) 649:L15. doi:10.1051/0004-6361/202141156
11. Burkhardt AM, Long Kelvin Lee K, Bryan Changala P, Shingledecker CN, Cooke IR, Loomis RA, et al. Discovery of the Pure Polycyclic Aromatic Hydrocarbon Indene (c-C9H8) with GOTHAM Observations of TMC-1. *ApJL* (2021) 913:L18. doi:10.3847/2041-8213/abfd3a
12. McGuire BA, Loomis RA, Burkhardt AM, Lee KLK, Shingledecker CN, Charnley SB, et al. Detection of Two Interstellar Polycyclic Aromatic Hydrocarbons via Spectral Matched Filtering. *Science* (2021) 371:1265–9. doi:10.1126/science.abb7535
13. Doddipatla S, Galimova GR, Wei H, Thomas AM, He C, Yang Z, et al. Low-temperature Gas-phase Formation of Indene in the Interstellar Medium. *Sci Adv* (2021) 7:4044. doi:10.1126/sciadv.abd4044
14. Kaiser RI, Parker DSN, Mebel AM. Reaction Dynamics in Astrochemistry: Low-Temperature Pathways to Polycyclic Aromatic Hydrocarbons in the Interstellar Medium. *Annu Rev Phys Chem* (2015) 66:43–67. doi:10.1146/annurev-physchem-040214-121502
15. Campbell EK, Holz M, Gerlich D, Maier JP. Laboratory Confirmation of C_{60}^{+} as the Carrier of Two Diffuse Interstellar Bands. *Nature* (2015) 523:322–3. doi:10.1038/nature14566
16. Lee JWL, Tikhonov DS, Chopra P, Maclot S, Steber AL, Gruet S, et al. Time-resolved Relaxation and Fragmentation of Polycyclic Aromatic Hydrocarbons Investigated in the Ultrafast XUV-IR Regime. *Nat Commun* (2021) 12:6107. doi:10.1038/s41467-021-26193-z
17. Robson L, Tasker AD, Ledingham KWD, McKenna P, McCanny T, Kosmidis C, et al. Ionisation and Fragmentation Dynamics of Laser Desorbed Polycyclic Aromatic Hydrocarbons Using Femtosecond and Nanosecond post-ionisation. *Int J Mass Spectrom* (2002) 220:69–85. doi:10.1016/s1387-3806(02)00823-0
18. Marciniak A, Despré V, Barillot T, Rouzée A, Galbraith MCE, Klei J, et al. XUV Excitation Followed by Ultrafast Non-adiabatic Relaxation in PAH Molecules as a Femto-Astrochemistry experiment. *Nat Commun* (2015) 6:8909. doi:10.1038/ncomms8909
19. Bagdia C, Biswas S, Mandal A, Bhattacharjee S, Tribedi LC. Ionization and Fragmentation of Fluorene upon 250 keV Proton Impact. *Eur Phys J D* (2021) 75:37. doi:10.1140/epjd/s10053-020-00001-7
20. Zhen J, Castillo SR, Joblin C, Mulas G, Sabbah H, Giuliani A, et al. Vuv Photo-Processing of PAH Cations: Quantitative Study on the Ionization versus Fragmentation Processes. *Astrophysical J* (2016) 822:113. doi:10.3847/0004-637x/822/2/113
21. Bazzi S, Welsch R, Vendrell O, Santra R. Challenges in XUV Photochemistry Simulations: A Case Study on Ultrafast Fragmentation Dynamics of the Benzene Radical Cation. *J Phys Chem A* (2018) 122:1004–10. doi:10.1021/acs.jpca.7b11543
22. Reddy VS, Ghanta S, Mahapatra S. First Principles Quantum Dynamical Investigation Provides Evidence for the Role of Polycyclic Aromatic Hydrocarbon Radical Cations in Interstellar Physics. *Phys Rev Lett* (2010) 104:111102. doi:10.1103/physrevlett.104.111102
23. Domcke W, Yarkony DR. Role of Conical Intersections in Molecular Spectroscopy and Photoinduced Chemical Dynamics. *Annu Rev Phys Chem* (2012) 63:325–52. doi:10.1146/annurev-physchem-032210-103522
24. Galbraith MCE, Scheit S, Golubev NV, Reitsma G, Zhavoronkov N, Despré V, et al. Few-femtosecond Passage of Conical Intersections in the Benzene Cation. *Nat Commun* (2017) 8:1018. doi:10.1038/s41467-017-01133-y
25. Curchod BFE, Martínez TJ. Ab Initio nonadiabatic Quantum Molecular Dynamics. *Chem Rev* (2018) 118:3305–36. doi:10.1021/acs.chemrev.7b00423
26. Hervé M, Despré V, Castellanos Nash P, Loriot V, Boyer A, Scognamiglio A, et al. Ultrafast Dynamics of Correlation Bands Following XUV Molecular Photoionization. *Nat Phys* (2020) 17:327–31. doi:10.1038/s41567-020-01073-3
27. Bernstein MP, Sandford SA, Allamandola LJ, Gillette JS, Clemett SJ, Zare RN. UV Irradiation of Polycyclic Aromatic Hydrocarbons in Ices: Production of Alcohols, Quinones, and Ethers. *Science* (1999) 283:1135–8. doi:10.1126/science.283.5405.1135
28. Boyer A, Hervé M, Despré V, Castellanos Nash P, Loriot V, Marciniak A, et al. Ultrafast Vibrational Relaxation Dynamics in XUV-Excited Polycyclic Aromatic Hydrocarbon Molecules. *Phys Rev X* (2021) 11:041012. doi:10.1103/physrevx.11.041012
29. Bouwman J, Cuppen HM, Steglich M, Allamandola LJ, Linnartz H. Photochemistry of Polycyclic Aromatic Hydrocarbons in Cosmic Water Ice. *Astron Astrophysics* (2011) 529:A46. doi:10.1051/0004-6361/201015762
30. Ruehl E, Price SD, Leach S. Single and Double Photoionization Processes in Naphthalene between 8 and 35 eV. *J Phys Chem* (1989) 93:6312–21. doi:10.1021/j100354a011
31. Leach S, Eland JHD, Price SD. Formation and Dissociation of Dications of Naphthalene-D8. *J Phys Chem* (1989) 93:7583–93. doi:10.1021/j100359a014
32. Lu J, Ren X, Cao L. Studies on Characteristics and Formation of Soot Nanoparticles in an Ethylene/air Inverse Diffusion Flame. *J Energ Eng.* (2016) 142:04015041. doi:10.1061/(asce)ey.1943-7897.0000305
33. Petrignani A, Vala M, Eyler JR, Tielens AGGM, Berden G, van der Meer AFG, et al. Breakdown Products of Gaseous Polycyclic Aromatic Hydrocarbons Investigated with Infrared Ion Spectroscopy. *Astrophysical J* (2016) 826:33. doi:10.3847/0004-637x/826/1/33
34. Güsten H, Klasinc L, Marsel J, Milivojević D. A Comparative Study of the Mass Spectra of Stilbene and Fluorene. *Org Mass Spectrom* (1972) 6:175–8. doi:10.1002/oms.1210060207
35. Bowie JH, Bradshaw TK. Electron Impact Studies. LVI. The Fluorenyl and Phenalenyl Cations. the Application of Metastable Characteristics. *Aust J Chem* (1970) 23:1431. doi:10.1071/ch9701431
36. Zhang W, Si Y, Zhen J, Chen T, Linnartz H, Tielens AGGM. Laboratory Photochemistry of Covalently Bonded Fluorene Clusters: Observation of an Interesting PAH Bowl-Forming Mechanism. *Astrophysical J* (2019) 872:38. doi:10.3847/1538-4357/aafe10
37. Andrews H, Boersma C, Werner MW, Livingston J, Allamandola LJ, Tielens AGGM. PAH Emission at the Bright Locations of PDRs: The grandPAH Hypothesis. *Astrophysical J* (2015) 807:99. doi:10.1088/0004-637x/807/1/99
38. Ackermann W, Asova G, Ayvazyan V, Azima A, Baboi N, Bähr J, et al. Operation of a Free-Electron Laser from the Extreme Ultraviolet to the Water Window. *Nat Photon* (2007) 1:336–42. doi:10.1038/nphoton.2007.76
39. Erk B, Müller JP, Bomme C, Boll R, Brenner G, Chapman HN, et al. CAMP@FLASH: an End-Station for Imaging, Electron- and Ion-Spectroscopy, and

Pump-Probe Experiments at the FLASH Free-Electron Laser. *J Synchrotron Radiat* (2018) 25:1529–40. doi:10.1107/s1600577518008585

40. Düsterer S, Rehders M, Al-Shemmary A, Behrens C, Brenner G, Brovko O, et al. Development of Experimental Techniques for the Characterization of Ultrashort Photon Pulses of Extreme Ultraviolet Free-Electron Lasers. *Phys Rev ST Accel Beams* (2014) 17:120702. doi:10.1103/physrevstab.17.120702
41. Behrens C, Gerasimova N, Gerth C, Schmidt B, Schneidmiller EA, Serkez S, et al. Constraints on Photon Pulse Duration from Longitudinal Electron Beam Diagnostics at a Soft X-ray Free-Electron Laser. *Phys Rev ST Accel Beams* (2012) 15:030707. doi:10.1103/physrevstab.15.030707
42. Redlin H, Al-Shemmary A, Azima A, Stojanovic N, Tavella F, Will I, et al. The FLASH Pump-Probe Laser System: Setup, Characterization and Optical Beamlines. *Nucl Instr Methods Phys Res Section A: Acc Spectrometers, Detectors Associated Equipment* (2011) 635:S88–S93. doi:10.1016/j.nima.2010.09.159
43. Eppink ATJB, Parker DH. Velocity Map Imaging of Ions and Electrons Using Electrostatic Lenses: Application in Photoelectron and Photofragment Ion Imaging of Molecular Oxygen. *Rev Scientific Instr* (1997) 68:3477–84. doi:10.1063/1.1148310
44. Parker DH, Eppink ATJB. Photoelectron and Photofragment Velocity Map Imaging of State-Selected Molecular Oxygen Dissociation/ionization Dynamics. *J Chem Phys* (1997) 107:2357–62. doi:10.1063/1.474624
45. Even U. "The Even-Lavie Valve as a Source for High Intensity Supersonic Beam". *EPJ Techn Instrum* (2015) 2:17. doi:10.1140/epjti/s40485-015-0027-5
46. Clark AT, Crooks JP, Sedgwick I, Turchetta R, Lee JWL, John JJ, et al. Multimass Velocity-Map Imaging with the Pixel Imaging Mass Spectrometry (PImMS) Sensor: An Ultra-fast Event-Triggered Camera for Particle Imaging. *J Phys Chem A* (2012) 116:10897–903. doi:10.1021/jp309860t
47. Amini K, Blake S, Brouard M, Burt MB, Halford E, Lauer A, et al. Three-dimensional Imaging of Carbonyl Sulfide and Ethyl Iodide Photodissociation Using the Pixel Imaging Mass Spectrometry Camera. *Rev Scientific Instr* (2015) 86:103113. doi:10.1063/1.4934544
48. Jaycen A. Open-source Software Compares Abel Transforms for Easy Use. *Scilight* (2019) 2019:260003. doi:10.1063/1.5111853
49. Van Rossum G, Drake FL, Jr. *Python Reference Manual*. Amsterdam, Netherlands: Centrum voor Wiskunde en Informatica Amsterdam (1995).
50. Dahl DA, Delmore JE, Appelhans AD. SIMION PC/PS2 Electrostatic Lens Design Program. *Rev Scientific Instr* (1990) 61:607–9. doi:10.1063/1.1141932
51. [Dataset] Tikhonov DS. *MCMCMCFitting* (2019). Available from: https://stash.desy.de/projects/cfa/repos/mcmcmcfitting/browse (Accessed February 1, 2022).
52. [Dataset] Steber A, Müller E. *PAH* (2016). Available from: https://stash.desy.de/projects/cs/repos/pah/browse (Accessed February 1, 2022).
53. [Dataset] Tikhonov DS. *Campfancyanalysis* (2019). Available from: https://stash.desy.de/projects/cfa/repos/campfancyanalysis/browse (Accessed February 1, 2022).
54. Pedersen S, Zewail A. Femtosecond Real-Time Probing of Reactions XXII. Kinetic Description of Probe Absorption, Fluorescence, Depletion and Mass Spectrometry. *Mol Phys* (1996) 89:1455–502. doi:10.1080/002689796173291
55. Tikhonov DS. *CAMPFancyAnalyis Home* (2019). Available from: https://confluence.desy.de/display/CFA/CAMPFancyAnalyis+Home (Accessed February 1, 2022).
56. Savelyev E, Boll R, Bomme C, Schirmel N, Redlin H, Erk B, et al. Jitter-correction for IR/UV-XUV Pump-Probe Experiments at the FLASH Free-Electron Laser. *New J Phys* (2017) 19:043009. doi:10.1088/1367-2630/aa652d
57. Schulz S, Grguraš I, Behrens C, Bromberger H, Costello JT, Czwalinna MK, et al. Femtosecond All-Optical Synchronization of an X-ray Free-Electron Laser. *Nat Commun* (2015) 6:6938. doi:10.1038/ncomms6938
58. Frasinski LJ, Codling K, Hatherly PA. Covariance Mapping: A Correlation Method Applied to Multiphoton Multiple Ionization. *Science* (1989) 246:1029–31. doi:10.1126/science.246.4933.1029
59. Tikhonov DS. *TOF-TOF Covariance Analysis* (2019). Available from: https://confluence.desy.de/display/CFA/TOF-TOF+covariance+analysis (Accessed February 1, 2022).
60. Dabestani R, Ivanov IN. A Compilation of Physical, Spectroscopic and Photophysical Properties of Polycyclic Aromatic Hydrocarbons. *Photochem Photobiol* (1999) 70:10–34. doi:10.1111/j.1751-1097.1999.tb01945.x
61. Holm AIS, Johansson HAB, Cederquist H, Zettergren H. Dissociation and Multiple Ionization Energies for Five Polycyclic Aromatic Hydrocarbon Molecules. *J Chem Phys* (2011) 134:044301. doi:10.1063/1.3541252
62. Vinitha MV, Nair AM, Ramanathan K, Kadhane UR. Understanding Dehydrogenation Sequence in Fluorene$^+$ by Multiphoton Ionisation-Excitation Processes. *Int J Mass Spectrom* (2022) 471:116704. doi:10.1016/j.ijms.2021.116704
63. Frasinski LJ. Covariance Mapping Techniques. *J Phys B: Mol Opt Phys* (2016) 49:152004. doi:10.1088/0953-4075/49/15/152004
64. Slater CS, Blake S, Brouard M, Lauer A, Vallance C, John JJ, et al. Covariance Imaging Experiments Using a Pixel-Imaging Mass-Spectrometry Camera. *Phys Rev A* (2014) 89:011401. doi:10.1103/physreva.89.011401
65. Slater CS, Blake S, Brouard M, Lauer A, Vallance C, Bohun CS, et al. Coulomb-explosion Imaging Using a Pixel-Imaging Mass-Spectrometry Camera. *Phys Rev A* (2015) 91:053424. doi:10.1103/physreva.91.053424
66. Vallance C, Heathcote D, Lee JWL. Covariance-map Imaging: A Powerful Tool for Chemical Dynamics Studies. *J Phys Chem A* (2021) 125:1117–33. doi:10.1021/acs.jpca.0c10038
67. West BJ, Lesniak L, Mayer PM. Why Do Large Ionized Polycyclic Aromatic Hydrocarbons Not Lose C_2H_2? *J Phys Chem A* (2019) 123:3569–74. doi:10.1021/acs.jpca.9b01879

Conflict of Interest: The authors declare that the research was conducted in the absence of any commercial or financial relationships that could be construed as a potential conflict of interest.

frontiers | Frontiers in Chemistry

ORIGINAL RESEARCH
published: 02 June 2022
doi: 10.3389/fchem.2022.899461

Molecular Free Electron Vortices in Photoionization by Polarization-Tailored Ultrashort Laser Pulses

*Tim Bayer and Matthias Wollenhaupt**

Ultrafast Dynamics Group, Institut für Physik, Carl von Ossietzky Universität Oldenburg, Oldenburg, Germany

Atomic and molecular free electron vortices (FEVs), characterized by their spiral-shaped momentum distribution, have recently attracted a great deal of attention due to their varied shapes and their unusual topological properties. Shortly after their theoretical prediction by the single-photon ionization (SPI) of He atoms using pairs of counterrotating circularly polarized attosecond pulses, FEVs have been demonstrated experimentally by the multiphoton ionization (MPI) of alkali atoms using single-color and bichromatic circularly polarized femtosecond pulse sequences. Recently, we reported on the analysis of the experimental results employing a numerical model based on the *ab initio* solution of the time-dependent Schrödinger equation (TDSE) for a two-dimensional (2D) atom interacting with a polarization-shaped ultrashort laser field. Here, we apply the 2D TDSE model to study molecular FEVs created by SPI and MPI of a diatomic molecule using polarization-tailored single-color and bichromatic femtosecond pulse sequences. We investigate the influence of the coupled electron-nuclear dynamics on the vortex formation dynamics and discuss the effect of CEP- and rotational averaging on the photoelectron momentum distribution. By analyzing how the molecular structure and dynamics is imprinted in the photoelectron spirals, we explore the potential of molecular FEVs for ultrafast spectroscopy.

Keywords: free electron vortices, polarization-tailored femtosecond laser pulses, diatomic molecules, multiphoton ionization, coupled electron-nuclear dynamics, polarization-shaped bichromatic fields, photoelectron momentum distribution

Edited by:
Yuichi Fujimura,
Tohoku University, Japan

Reviewed by:
Martin Centurion,
University of Nebraska-Lincoln, United States
Bernd Von Issendorff,
University of Freiburg, Germany

***Correspondence:**
Matthias Wollenhaupt
matthias.wollenhaupt@uol.de

Specialty section:
This article was submitted to Physical Chemistry and Chemical Physics,
a section of the journal Frontiers in Chemistry

Received: *18 March 2022*
Accepted: *06 May 2022*
Published: *02 June 2022*

Citation:
Bayer T and Wollenhaupt M (2022) Molecular Free Electron Vortices in Photoionization by Polarization-Tailored Ultrashort Laser Pulses. Front. Chem. 10:899461. doi: 10.3389/fchem.2022.899461

1 INTRODUCTION

Vortex beams, such as optical vortices (Babiker et al., 2002; Shen et al., 2019; Eickhoff et al. 2020b) and electron vortex beams (Verbeeck et al., 2010; Lloyd et al., 2017), which are characterized by their helical wave fronts, are currently attracting much attention both theoretically and experimentally. Recently, the analogies between free electron vortices (FEVs) in transmission electron microscopy and multiphoton ionization (MPI) have been pointed out (Eickhoff et al., 2020c). In photoionization, FEVs are created by ionizing a quantum system with tailored ultrashort circularly polarized laser pulse sequences. Introducing a time-delay τ between two counterrotating circularly polarized subpulses results in an “unusual kind of Ramsey interference” Ngoko Djiokap et al. (2015), which gives rise to an azimuthal interference pattern in the photoelectron momentum distribution (PMD) forming a multi-armed Archimedean spiral. Atomic FEVs have been studied theoretically employing different numerical methods, including the *ab initio* solution of the time-dependent Schrödinger equation (TDSE) (Ngoko Djiokap et al. 2015; Ngoko Djiokap et al., 2016; Djiokap and Starace., 2017; Ngoko Djiokap et al., 2017; Ivanov et al., 2017; Jia et al., 2019; Xiao et al., 2019; Bayer et al., 2020; Qin et al., 2020; Wang et al., 2020; Zhen et al., 2020; Geng et al., 2020; Maxwell et al., 2020; Djiokap et al., 2021; Geng et al., 2021), calculations based on the strong-field approximation (Hasović et al., 2016; Ivanov et al., 2017; Li M. et al., 2017; Li et al., 2018a; Li et al., 2018b; Gazibegović-Busuladžić et al., 2018; Kong et al., 2018; Li et al., 2019b; Xiao et al., 2019; Geng et al., 2020; Maxwell et al. 2020; Qin et al., 2020; Geng et al., 2021; Becker and Milošević, 2022), perturbative analytical approaches (Ngoko Djiokap et al., 2015; Ngoko Djiokap et al., 2016; Djiokap and Starace, 2017; Ngoko Djiokap et al., 2017; Djiokap et al., 2021), emerging techniques such as the $\mathcal{R}$-matrix with time-dependence theory (Clarke et al., 2018; Armstrong et al., 2019; Maxwell et al., 2020) and semi-classical Monte-Carlo methods (Ben et al., 2020). Current research topics comprise the creation of FEVs with odd rotational symmetry using bichromatic pulse sequences (Ngoko Djiokap et al., 2016), the study of electron-electron correlations in atomic double-ionization (Djiokap and Starace, 2017; Ngoko Djiokap et al, 2017), the influence of the AC-Stark effect on FEVs from strong-field ionization (Kong et al., 2018; Li et al., 2019a), the application of FEVs to probe electron displacement in strong-field ionization (Xiao et al., 2019), the detection of ring currents (Wang et al., 2020), the interferometric use of FEVs for quantum phase retrieval Qin et al. (2020) and unusual subjects such as multiphoton pair-production in single-color (Li Z. L. et al., 2017) and bichromatic (Li Z. L. et al., 2018) fields. A comparison between FEVs characterized by their spiral-shaped PMD and free electron vortex states (Bliokh et al., 2017) [also termed twisted electrons (Maxwell et al., 2020)] derived from the fluid-dynamical formulation of quantum mechanics (Madelung, 1927) is given in (Geng et al., 2020; Geng et al. 2021; Kerbstadt et al., 2020).

The first experimental demonstration of atomic FEVs was reported in (Pengel et al., 2017b). By MPI of potassium atoms with *single-color* time-delayed counterrotating circularly polarized pulse sequences, we observed FEVs with four-, six and eight-fold rotational symmetry (Pengel et al., 2017a; Pengel et al., 2017b). Subsequently, we demonstrated the creation of seven-fold rotationally symmetric FEVs by MPI of sodium atoms (Kerbstadt et al., 2019b) using time-delayed *bichromatic* sequences. In the same work, FEVs with odd rotational symmetry have been created using bichromatic fields in the limit $\tau \rightarrow 0$. In addition, we reported on crescent-shaped FEVs (Kerbstadt et al., 2019b; Eickhoff et al., 2020a; Eickhoff et al., 2021c) and a five-fold symmetric FEV (Eickhoff et al., 2021c) created by bichromatic MPI. In the strong-field ionization regime, Mancuso *et al.* observed crescent-shaped and three-fold symmetric FEVs using co- and counterrotating bichromatic fields, respectively (Mancuso et al., 2015, Mancuso et al., 2016). Similarly, Eckart *et al.* created three-fold symmetric FEVs (Eckart et al., 2016; Eckart et al., 2018) and measured the PMD using cold target recoil-ion momentum spectroscopy (Dörner et al., 2000; Ullrich et al., 2003). In our experiments, we applied photoelectron tomography (Wollenhaupt et al., 2009b; Wollenhaupt et al., 2013) to reconstruct the 3D PMD of the atomic FEVs (Pengel et al., 2017a; Pengel et al., 2017b; Kerbstadt et al., 2019b; Eickhoff et al., 2021c). Recently, this method has been developed further into a holographic scheme to reconstruct the photoelectron wave function by measuring interferograms in the PMD (Eickhoff et al., 2020a; Eickhoff et al., 2021b; Eickhoff et al., 2021c).

Meanwhile, the theoretical research focus has evolved from atomic FEVs towards the investigation of FEVs created on molecular systems. Bandrauk and coworkers were the first to recognize the potential of molecular FEVs as spectroscopic tools sensitive to the molecular geometry and ultrafast electron dynamics by investigating the MPI of H_2^+ (Yuan et al., 2016) and H_3^{2+} (Yuan et al., 2017) in co- and counterrotating circularly polarized bichromatic fields. Subsequently, Ngoko-Djiokap *et al.* reported on molecular FEVs in the double-ionization of H_2 created by single-photon ionization (SPI) (Djiokap et al., 2018) and resonance-mediated two-photon ionization (Djiokap and Starace, 2021). In an initial study of molecular FEVs in the tunneling regime, created by counterrotating circularly polarized bichromatic fields, Ke *et al.* reported on highly structured photoelectron holograms—commonly recorded using linearly polarized pulses (Huismans et al., 2011; Bian and Bandrauk, 2012)—which yielded rich information about the molecular structure and laser-driven electron dynamics (Ke et al., 2019). Spiral-shaped *nuclear* momentum distribution analogous to those of FEVs have been obtained for the fragments of the H_2^+ molecular ion after dissociation along different interfering pathways induced by a single circularly polarized laser pulse (Chen et al,. 2020; Chen and He, 2020). Using co- and counterrotating circularly polarized pulses sequences, Shu *et al.* recently exerted control on the interference of degenerate Zeeman states in the H_2^+ molecular ion, mapped into the PMD by an ionizing third pulse (Shu et al., 2020). Very recently, Guo *et al.* presented a numerical study on N_2 based on the *ab initio* solution of the two-dimensional (2D) TDSE, in which they studied the sensitivity of molecular FEVs to the laser parameters (Guo et al., 2021).

Building on our recent numerical study on atomic FEVs (Bayer et al., 2020), here we apply our 2D TDSE model to numerically investigate molecular FEVs created by photoionization of a diatomic molecular ion with polarization-tailored laser pulses. Using polarization-shaped pulses, at least 2D numerical simulations are required to describe the generally asymmetric polarization profiles. In many cases, the 2D approach is sufficient to capture the essential features of the PMD. Compared to a full 3D calculation, 2D simulations benefit from a greatly reduced computational cost. Recently, we employed the 2D TDSE model to accurately reproduce atomic FEVs created experimentally by MPI of alkali atoms (Bayer et al., 2020) to validate our numerical approach. Considering a molecule aligned in the laser polarization plane, the 2D model is expected to yield similarly realistic results for molecular FEVs. The central inset to **Figure 1A** illustrates the 2D laser-molecule interaction by showing a counterrotating circularly polarized pulse sequence impinging on a diatomic molecule aligned in the laser polarization-plane along with the created 2D PMD. Compared to a full 3D calculation, the polar information of the

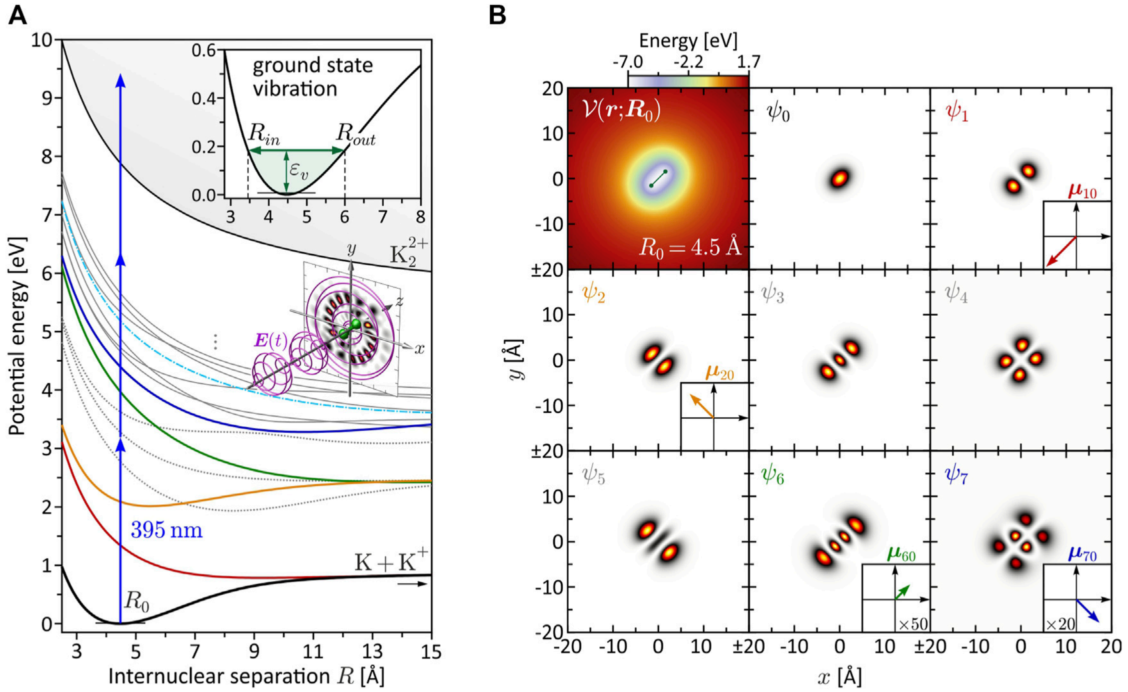

FIGURE 1 | (Color online.) Characterization of the bound molecular system. **(A)** BO potential energy curves $V_n(R)$. The equilibrium distance in the electronic ground state is found at $R_0 = 4.48$ Å. Among the eight lowest states, only $V_1(R)$ (red), $V_2(R)$ (yellow), $V_6(R)$ (green) and $V_7(R)$ (blue) are dipole-coupled to the ground state. These states are relevant for the investigated MPI schemes. Especially state $V_6(R)$ plays a prominent role in the dynamic three-photon ionization scenario (see **Section 3.2.2**), because it becomes near-resonant with a pulse of central wavelength $\lambda_0 = 395$ nm at the outer turning point $R_{out} = 6.0$ Å of the vibration (see inset). **(B)** Molecular potential $\mathcal{V}(\boldsymbol{r};\boldsymbol{R})$ and first eight electronic eigenfunctions $\psi_n(\boldsymbol{r};\boldsymbol{R})$ for $R = R_0$. The eigenfunctions are used to determine the transition dipole moments $\boldsymbol{\mu}_{n0}$, coupling the states ψ_n ($n \geq 1$) to the ground state ψ_0, and to calculate the bound state population dynamics in the MPI scenarios.

PMD is lost. However, in the case of FEVs, this information is generally less relevant, since the characteristic spiral pattern is an azimuthal feature of the PMD which is fully contained in a central section parallel to the polarization plane. We note that, although the description in 2D "flatland" is considered an approximation of real space, 2D approaches are relevant for confined condensed matter systems such as surfaces, interfaces or monolayers of e.g., graphene (Novoselov et al., 2012) or transition-metal dichalcogenides (Li et al., 2022). In this contribution, we focus on three aspects of molecular FEVs which are relevant for the design of future experiments and provide insights into the rich variety of physical mechanisms behind the generation of molecular FEVs by polarization-shaped pulses. First, we compare the PMD from different ionization regimes, i.e., SPI vs. MPI, at a range of fixed internuclear separations. Besides the influence of the increased angular momentum transfer in MPI, we investigate to which extend intermediate resonances are involved in the formation of the FEVs. Second, we identify the fingerprints of the coupled electron-nuclear dynamics in the interference structures of the FEVs. To this end, we compare the PMDs from photoionization of a rigid and a vibrating molecule and study the interaction between nuclear motion and electronic ionization dynamics. Specifically, we discuss the role of transient electronic resonances arising during the vibration for FEVs created by MPI and examine signatures of non-adiabatic bound state dynamics in the PMD. Third, we investigate molecular FEVs in the molecular frame vs. laboratory frame by considering molecular rotation and optical phase averaging. We analyze the sensitivity of the PMD to the experimental parameters and define optimal conditions to observe the molecular FEVs in the experiment.

The paper is organized as follows. After the introduction of the numerical model and the characterization of the molecular system in **Section 2**, we start in **Section 3.1** by investigating a rigid molecule interacting with laser pulses of different polarization in the SPI and MPI regime. In **Section 3.2**, we consider a vibrating molecule and focus on the creation of molecular FEVs *via* SPI and MPI in the presence of coupled electron-nuclear dynamics. **Section 3.3** addresses different experimental averaging mechanisms which we discuss on a molecular FEV from bichromatic two- vs. three-photon ionization. In **Section 4**, we conclude the paper and give a brief outlook.

2 PHYSICAL SYSTEM

In this section, we provide the theoretical background to describe the interaction of a diatomic molecule with a polarization-shaped laser field in two dimensions, and present the numerical methods used to solve the 2D TDSE. The 2D TDSE model is based on established numerical techniques (Tannor, 2007; Bauer, 2017) and has been described in more detail in Bayer et al. (2020) for the generation of atomic FEVs. Here we focus on the extension of the model from an atomic to a molecular system. In particular, we describe our semi-classical approach to incorporate the vibrational nuclear dynamics into the 2D TDSE model, in order to investigate the interplay between the nuclear motion and the electronic excitation, i.e., the coupled electron-nuclear dynamics.

2.1 Theoretical Description

We consider the interaction of a diatomic molecular ion with a polarization-shaped ultrashort laser pulse propagating in the z-direction. The two atoms are arranged in the x-y-plane which coincides with the laser polarization plane. Their nuclei are separated by $\boldsymbol{R} = R\,\boldsymbol{e}_R$, with $\boldsymbol{e}_R$ being a unit vector parallel to the internuclear axis. Throughout this paper, we consider a homonuclear molecule. The x-y-coordinate frame is chosen such that $\boldsymbol{e}_R = (\boldsymbol{e}_x + \boldsymbol{e}_y)/\sqrt{2}$ is aligned along the positive diagonal and the nuclei are situated at $\pm\,\boldsymbol{R}/2$. Furthermore, we assume a single active valence electron. The molecular system is described by the screened Coulomb potential introduced by Sprik and Klein (1988), Shin and Metiu (1995), Shin and Metiu (1996), Erdmann et al. (2004).

$$\mathcal{V}(\boldsymbol{r};\boldsymbol{R}) = -\frac{e^2}{4\pi\varepsilon_0}\left[\frac{z\,\mathrm{erf}\left(|\boldsymbol{r}+\boldsymbol{R}/2|/a\right)}{|\boldsymbol{r}+\boldsymbol{R}/2|} + \frac{z\,\mathrm{erf}\left(|\boldsymbol{r}-\boldsymbol{R}/2|/a\right)}{|\boldsymbol{r}-\boldsymbol{R}/2|} - \frac{z^2}{R}\right], \tag{1}$$

with $\boldsymbol{r} = (x, y)$ and erf denoting the error function. Motivated by our recent experiments on potassium atoms (Pengel et al., 2017b) and dimers (Bayer et al., 2013), we choose an effective nuclear charge of $z = 0.9085$ and a softcore parameter of $a = 2.3065$ Å (Eickhoff et al., 2021c) to mimic the singly charged potassium dimer K_2^+ for the study of molecular FEVs. **Figure 1A** shows the first 15 Born-Oppenheimer (BO) potential energy curves $V_n(R)$ obtained by solving the time-independent Schrödinger equation

$$\left[-\frac{\hbar^2}{2m_e}\Delta + \mathcal{V}(\boldsymbol{r};\boldsymbol{R})\right]\psi_n(\boldsymbol{r};\boldsymbol{R}) = V_n(R)\,\psi_n(\boldsymbol{r};\boldsymbol{R}), \tag{2}$$

with m_e being the mass of the electron, for different values of R. The higher-lying Rydberg states are mainly characterized by Coulomb repulsion between the two nuclei and converge to the repulsive double-ionization potential $V_i(R)$ (thin black line). The BO potentials aid us in the design of specific excitation scenarios and, in particular, serve to identify intermediate resonances encountered along the MPI pathways. The color coding among the lowest eight states ψ_n indicates their dipole-coupling to the electronic ground state ψ_0. States plotted as gray dotted lines are not coupled to the ground state. The transition dipole moments $\boldsymbol{\mu}_{n0} = -e\langle\psi_n|\boldsymbol{r}|\psi_0\rangle$, with the electron charge $-e$, are determined using the electronic eigenfunctions $\psi_n(\boldsymbol{r};\boldsymbol{R})$. The eigenfunctions $\psi_n(\boldsymbol{r};\boldsymbol{R}_0)$ at the equilibrium distance $R_0 = 4.48$ Å are shown in **Figure 1B**, along with the molecular potential $\mathcal{V}(\boldsymbol{r};\boldsymbol{R}_0)$. The insets depict the non-vanishing transition dipole moments; their R-dependence is shown in **Figure 6C** and addressed in **Section 3.2.1**. In addition to the determination of dipole-couplings, the eigenfunctions are used to calculate the bound state population dynamics $p_n(t) = |\langle\psi_n|\psi(t)\rangle|^2$ (see **Figure 4**) in order to unravel the ionization dynamics in the various MPI scenarios.

The temporal laser electric field is described in the spherical basis (Wollenhaupt et al., 2009a; Bayer et al., 2019; Kerbstadt et al., 2019b). We consider a bichromatic double pulse sequence of the general form (Eickhoff et al., 2021a; Eickhoff et al., 2021c).

$$\begin{aligned}\boldsymbol{E}^+(t) = {} & \mathcal{E}_1\,g(t-\tau_1)\,e^{i\left(\omega_1 t+\varphi_1+\varphi_{ce}\right)}\,\boldsymbol{e}_{q_1} \\ & + \mathcal{E}_2\,g(t-\tau_2)\,e^{i\left(\omega_2 t+\varphi_2+\varphi_{ce}\right)}\,\boldsymbol{e}_{q_2}.\end{aligned} \tag{3}$$

Each subpulse $n = 1, 2$ is characterized by an individual peak amplitude $\mathcal{E}_n$, time-delay τ_n, central frequency ω_n, relative phase φ_n and polarization state $\boldsymbol{e}_{q_n}$ ($q_n = \pm 1$). The latter can either be left-handed circularly polarized (LCP), described by $\boldsymbol{e}_1 = -(\boldsymbol{e}_x + i\boldsymbol{e}_y)/\sqrt{2}$, or right-handed circularly polarized (RCP), described by $\boldsymbol{e}_{-1} = -(\boldsymbol{e}_x - i\boldsymbol{e}_y)/\sqrt{2}$. Common to both subpulses is the carrier-envelope phase (CEP) φ_{ce} and the Gaussian-shaped envelope $g(t)$ with unit amplitude and a duration of Δt (full width at half maximum of the intensity). In the single-color schemes discussed in **Sections 3.1**, **3.2**, we use $\omega_0 \coloneqq \omega_1 = \omega_2$ as central frequency and $\lambda_0 = 2\pi c/\omega_0$ as the corresponding central wavelength. The real-valued field is given by $\boldsymbol{E}(t) = \Re[\boldsymbol{E}^+(t)]$.

The laser-molecule interaction is described in the dipole approximation. Initially, we consider a rigid molecule with fixed internuclear separation $\boldsymbol{R}$. As a consequence, the nuclear kinetic energy vanishes. The corresponding TDSE for the wave function $\psi(\boldsymbol{r};\boldsymbol{R},t)$ of the valence electron in the length gauge reads

$$i\hbar\frac{\partial}{\partial t}\psi(\boldsymbol{r};\boldsymbol{R},t) = \left[-\frac{\hbar^2}{2m_e}\Delta + \mathcal{V}(\boldsymbol{r};\boldsymbol{R}) + e\,\boldsymbol{r}\cdot\boldsymbol{E}(t)\right]\psi(\boldsymbol{r};\boldsymbol{R},t). \tag{4}$$

The TDSE is solved numerically using established methods described in **Section 2.2.** The *ab initio* TDSE calculation inherently includes all intermediate states, which are relevant for the MPI schemes discussed in **Sections 3.2.2**, **3.3**. Therefore, no further approximations concerning the electronic structure of the molecule are required, as confirmed in Bayer et al. (2020). In our model, the electron dynamics is treated quantum mechanically, whereas the slower dynamics of the nuclei is treated classically, which is an established strategy to reduce the dimensionality of the calculation (Carrasco et al., 2022). Specifically, we model the vibrational nuclear dynamics by inserting a time-dependent function $R = R(t)$ into the electronic potential $\mathcal{V}[\boldsymbol{r};\boldsymbol{R}(t)]$, which periodically modulates the potential along the internuclear axis. The function $R(t)$ is obtained by solving the Newtonian equation of motion $\mu\ddot{R} = -dV_0/dR$ for the ground state BO potential $V_0(R)$. The reduced mass μ of the nuclear system serves us as a parameter to design specific vibration scenarios for our studies of coupled electron-nuclear dynamics in **Section 3.2**. In particular, μ is adapted such that the vibrational period T_v is compatible with the employed laser pulses, i.e., in the order of several times the pulse duration Δt. In the experiment, the duration and timing of the pulses need to be adapted to the molecular dynamics (Bayer et al. 2013). The vibrational energy is set to $\varepsilon_v = 180$ meV. As depicted in the inset to **Figure 1A**, this vibrational excitation corresponds to a mildly anharmonic nuclear oscillation between R_{in} = 3.45 Å (inner turning point) and R_{out} = 6.0 Å (outer turning point). The choice of the vibrational energy is a trade-off between the amplitude and the period of the oscillation. The vibration amplitude should be sufficiently large to energetically disentangle the photoelectron signals generated at the inner and outer turning point (cf. **Section 3.2.1**). This condition sets a lower limit on ε_v. On the other hand, the vibration period should not be too large, otherwise the radial interference pattern of the FEVs created by a sequence of two time-delayed laser pulses locked to different turning points (cf. **Section 3.2.2**) becomes too dense to be resolved energetically. This condition sets an upper limit on ε_v. The chosen value of $\varepsilon_v = 180$ meV was found to be suitable for all vibration scenarios discussed in **Sections 3.2**, **3.3**.

2.2 Numerical Methods

The TDSE in **Eq. 4** is solved numerically on a discrete 2D spatial grid. The wave function of the active electron is propagated in time according to

$$\psi(\boldsymbol{r};\boldsymbol{R},t+\delta t) = e^{-i\frac{\delta t}{\hbar}\mathcal{H}(\boldsymbol{r};\boldsymbol{R},t)}\psi(\boldsymbol{r};\boldsymbol{R},t), \qquad (5)$$

where $\mathcal{H}(\boldsymbol{r};\boldsymbol{R},t)$ is the Hamiltonian, written in square brackets on the right-hand side of **Eq. 4**. The propagator is calculated using a Fourier-based split-operator technique (Feit et al., 1982; Bandrauk and Shen, 1993; Rice and Zhao, 2000; Wollenhaupt et al., 2005; Tannor, 2007; Bauer, 2017; Grossmann, 2018). The time propagation is performed in two consecutive stages. The first stage, starting at the initial time $t_i < 0$ and ranging up to $T = -t_i$, is the interaction with the laser pulse centered around $t = 0$. In this stage, the photoelectron wave packets are created. The second stage ranging up to the final time t_f is the field-free propagation of the wave packets under the influence of the long-ranged Coulomb-type molecular potential. Throughout both stages, we use the same temporal step size of $\delta t = 10$ as. The wave function is propagated on a square spatial grid with boundaries $(x_{\max}, y_{\max}) = -(x_{\min}, y_{\min}) = (500, 500)$ Å. The spatial resolution is chosen to be $\delta x = \delta y = 1$ Å. The molecule is initiated in the electronic ground state $\psi(\boldsymbol{r}; \boldsymbol{R}, t_i) = \psi_0(\boldsymbol{r}; \boldsymbol{R})$. Starting from the solution of the time-independent Schrödinger equation **Eq. 2**, obtained on a smaller spatial grid using the Fourier grid Hamiltonian method (Marston and Balint-Kurti, 1989), the ground state wave function is refined by imaginary-time propagation (Tal-Ezer and Kosloff, 1986). In order to minimize unphysical reflections of the wave function at the spatial boundaries, we use absorbing boundary conditions (Kosloff and Kosloff, 1986; Santra, 2006) implemented by adding an artificial spherically symmetric imaginary potential $\mathcal{U}(r) \propto -i\,r^{16}$ to the molecular potential $\mathcal{V}(\boldsymbol{r};\boldsymbol{R})$ in **Eq. 1**. After the interaction with the laser pulse, the wave function is propagated until the free photoelectron wave packets have detached from the bound part, which remains localized at the two nuclei, but not yet reached the absorbing boundaries. Then the free part of the electron wave function is separated from the bound part by application of a spherically symmetric splitting filter of the form $f(r) = 1 - e^{-\ln(2)\left(\frac{r}{\Delta r}\right)^4}$, similar to Heather and Metiu (1987). The PMD $\mathcal{P}(\boldsymbol{k})$ is proportional to the modulus square of the momentum space wave function $\tilde{\psi}_f(\boldsymbol{k})$ of the free part,

$$\mathcal{P}(\boldsymbol{k}) \propto \left|\tilde{\psi}_f(\boldsymbol{k})\right|^2 = \left|\mathcal{F}\left[f(r)\,\psi\big(\boldsymbol{r};\boldsymbol{R},t_f\big)\right](\boldsymbol{k})\right|^2, \qquad (6)$$

where $\mathcal{F}$ denotes the Fourier transform. For $t_f > T$, the right-hand side of **Eq. 6** rapidly converges towards the final (far field) PMD (Wollenhaupt et al., 2002; Bayer et al., 2020).

3 RESULTS

Motivated by recent attosecond studies on molecular FEVs (Yuan et al., 2016; Djiokap et al., 2018; Guo et al., 2021), we start in **Section 3.1** by considering a rigid diatomic molecule interacting with various standard pulse shapes, including simple linearly and circularly polarized pulses as well as counterrotating circularly polarized double pulse sequences (Pengel et al., 2017b). For a selection of fixed internuclear separations, we analyze the PMD resulting from SPI and MPI to identify the basic physical mechanisms in the creation of molecular FEVs. Molecular vibration is introduced in **Section 3.2**, where we study the influence of the nuclear motion on the electronic excitation for SPI and MPI. In **Section 3.3**, we address different types of spatial averaging in view of the experimental implementation of molecular FEV scenarios. For this purpose, we consider a CEP-sensitive bichromatic two- vs. three-photon ionization scenario to compare the calculated molecular frame PMD with the PMD measured in the laboratory frame. In particular, we investigate the influence of molecular rotation averaging and CEP-averaging, both of which play a crucial role in molecular photoionization experiments.

3.1 Rigid Molecule

To get a first idea of the ionization dynamics of diatomic molecules, especially when ionized with polarization shaped pulses, we start with a rigid diatomic molecule whose nuclei are fixed in space. This so-called static nuclear frame represents a particularly good approximation for the interaction of molecules with attosecond pulses (Yuan et al., 2016; Djiokap et al., 2018; Guo et al., 2021), because the nuclei are virtually frozen on the attosecond timescale. For our purpose, freezing the nuclei serves as a simplification to provide a clear physical picture of the various interference mechanisms involved in molecular photoionization. The influence of the nuclear motion is investigated next in **Section 3.2**. In the following, two types of perturbative ionization processes are compared. First, we study SPI by XUV/UV pulses with central wavelengths in the range of λ_0 = 113–210 nm and a fixed pulse duration of $\Delta t = 2$ fs. Second, we study MPI by UV/VIS pulses with central wavelengths of λ_0 = 353–680 nm and a duration of $\Delta t = 5$ fs. The pulse duration in the MPI scheme is chosen slightly larger than in the SPI scheme, because the photoelectron signal from (non-resonant) perturbative N-photon ionization is determined by the N-th order optical spectrum (Meshulach and Silberberg, 1999). For

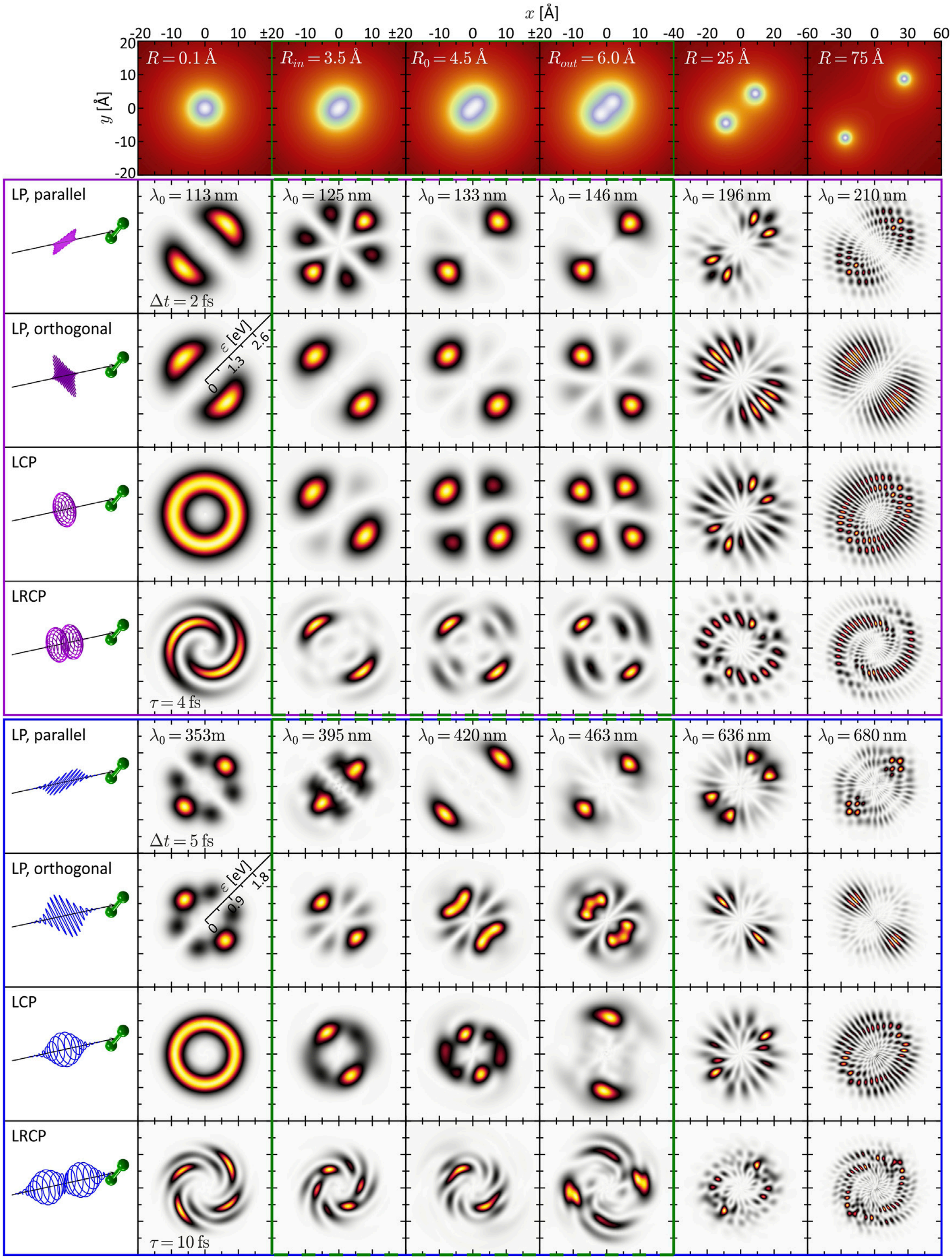

FIGURE 2 | (Color online.) Gallery of calculated and energy-calibrated PMDs created by photoionization of the rigid molecule at different internuclear separations (columns) with different types of laser pulses (rows). The corresponding molecular potentials are shown in the top row. The laser pulses are illustrated on the left-hand side. The upper part (magenta frame) shows the PMDs resulting from one-photon ionization, the PMDs in the lower part (blue frame) result from three-photon ionization. The green frames (second to fourth column) indicate the vibration window.

a Gaussian-shaped pulse, the signal is spectrally broadened by a factor of $\sqrt{N}$. The effective pulse duration of the 5 fs pulse in the three-photon ionization scheme discussed in **Sections 3.1.2**, **3.2.2** is hence $\Delta t_{eff} = \Delta t/\sqrt{3} = 2.9$ fs, which is close to the pulse duration in the SPI scheme. Also, with this choice, the XUV and the VIS pulses have approximately the same number of optical cycles. In general, the results from SPI are conceptually more transparent and easier to interpret than the MPI results, because SPI is not influenced by intermediate bound state resonances and dipole selection rules for the absorption of multiple photons. On the other hand, MPI schemes are more amenable to the experimental implementation, since polarization-shaped ultrafast VIS and UV laser sources are readily available in the lab. We investigate the PMD created by photoionization of the potassium molecular ion (cf. **Section 2.1**) by standard types of polarization-shaped laser pulses at different internuclear separations R. **Figure 2** shows a gallery of the numerical results in kinetic energy representation. Different rows correspond to the results obtained for different pulse shapes, including linearly polarized (LP) single pulses with their polarization vector aligned either parallel or orthogonal to the internuclear axis, left-handed circularly polarized (LCP) single pulses and double pulse sequences consisting of an LCP first pulse and a right-handed circularly polarized (RCP) second pulse (LRCP sequence) separated by $\tau = \tau_2 - \tau_1 = 2\Delta t$. The results obtained for different R are organized in columns, with the related molecular potentials $\mathcal{V}(\boldsymbol{r};\boldsymbol{R})$ shown in the top frames. Three distinct R-regions are selected. The first column corresponds to the atomic limit, $R \ll R_0$, where the potential resembles that of a single atom. The second to fourth column (green frame) corresponds to the vibration window $R_{in} \leq R \leq R_{out}$ discussed in the following sections, including the equilibrium distance $R = R_0$ (third column). The fifth column represents the transition to the dissociation limit, $R \gg R_0$, which is covered in the last column. Because the ionization potential depends on R, the central wavelength λ_0 is adapted in each column such that the PMD is centered in the same kinetic energy window, i.e., [0, 2.6] eV in the SPI scheme (magenta frame) and [0, 1.8] eV in the MPI scheme (blue frame).

3.1.1 Static One-Photon Ionization

We start by inspecting the results from the SPI scheme. In the limit $R \to 0$ (first column of **Figure 2**), the PMDs are straightforwardly described in an atomic picture. The potential becomes approximately spherically symmetric entailing an $|s,\ m = 0\rangle$-type ground state wave function. In accordance with the dipole selection rules, SPI by an LP laser pulse therefore creates a $|p,\ 0\rangle$-type, dumbbell-shaped photoelectron wave packet aligned along the polarization direction. Similarly, an LCP pulse produces a $|p,\ 1\rangle$-type, torus-shaped wave packet. In general, the superposition principle applies to perturbative SPI, i.e., the free electron wave packet from photoionization with a superposition of laser fields is given by the coherent superposition of the partial waves from the individual fields (Wollenhaupt et al., 2002). For example, the photoelectron wave packets created by an LCP pulse are a coherent superposition of the wave packets created by the corresponding LP pulses parallel and orthogonal to the internuclear axis. SPI by a time-delayed LRCP sequence yields an FEV in the shape of a two-armed Archimedean spiral with a counterclockwise sense of rotation (Ngoko Djiokap et al., 2015). This spiral-shaped PMD is understood in the framework of the perturbative ionization model presented in Pengel et al. (2017a), Pengel et al. (2017b) applied to one-photon ionization. According to the model, the two-armed FEV arises from the superposition of the $\tilde{\psi}_{p,1}(\boldsymbol{k})$- and $\tilde{\psi}_{p,-1}(\boldsymbol{k})$-type partial waves created by the LCP and RCP pulse, respectively. Due to the free time evolution during the time τ between both pulses, the initial wave packet acquires an energy-dependent phase of $-\varepsilon(k)\tau/\hbar$, where $\varepsilon(k) = \hbar^2k^2/(2m_e)$ is the photoelectron kinetic energy. The PMD of the two-armed FEV thus reads $\mathcal{P}(\boldsymbol{k}) = |\tilde{\psi}_{p,1}(\boldsymbol{k})e^{-i\varepsilon(k)\tau/\hbar} + \tilde{\psi}_{p,-1}(\boldsymbol{k})|^2$. The number of spiral arms is determined by the difference between the magnetic quantum numbers of the involved partial waves. The rotational sense depends on the pulse ordering and is inverted for an RLCP sequence.

Next, we consider the PMD from SPI in the dissociation limit $R \gg R_0$. The PMDs shown in the last column of **Figure 2** exhibit the same coarse (average) structure as in the atomic limit but are modulated by an intricate interference pattern. Some of the PMDs resemble the trilobite states currently discussed in the context of long-range Rydberg molecules (Shaffer et al., 2018; Eiles, 2019) and initially reported in (Greene et al., 2000). The observed pattern results from the interplay between two interference mechanisms already discussed by Cohen and Fano (1966) and reviewed recently in Yuan and Bandrauk (2015). The first mechanism is two-center interference, i.e., the superposition of partial waves emitted from the individual nuclei—hence both being of similar shape as in the atomic limit—spatially displaced by R. The second mechanism is Coulomb diffraction of each partial wave at the potential of the neighboring nucleus. Both mechanisms are illustrated in **Figure 3** on the example of the two-armed FEV from ionization with an LRCP sequence. Panel (a) shows the spiral-shaped PMD $|\tilde{\psi}(\boldsymbol{k})|^2$ in the atomic limit, $R = 0.1$ Å, in energy and momentum representation (inset). Panel (b) shows the result of a simple two-center interference model based on the superposition of two replica of the atomic wave function from (a) with spatial origins displaced by $R_d = 75$ Å. According to the Fourier shift theorem, the spatial displacement gives rise to a relative linear phase in momentum space $-\boldsymbol{R}_d\cdot\boldsymbol{k}$ between the two partial waves in the direction of the internuclear axis. The resulting PMD $|\tilde{\psi}(\boldsymbol{k}) + \tilde{\psi}(\boldsymbol{k})e^{-i\boldsymbol{R}_d\cdot\boldsymbol{k}}|^2 = 2|\tilde{\psi}(\boldsymbol{k})|^2[1 + \cos(\boldsymbol{R}_d\cdot\boldsymbol{k})]$, shown in the inset of (b), exhibits a cosine modulation along the positive grid-diagonal. The nodal lines are aligned parallel to the negative diagonal (grey dotted line in the inset). The energy calibration $k \mapsto \varepsilon(k)$ of the PMD bends the linear nodal lines and focuses them towards the center, as indicated by the grey dotted curves in the energy representation. The full calculation result for $R = 75$ Å is shown in panel (c). In the second (II) and fourth (IV) quadrant of the grid, i.e., lateral to the internuclear axis, the fringe-type interference pattern indeed resembles that of the two-center interference model. However, in axial direction, i.e., in the first (I) and third (III) quadrant, the full calculation exhibits a

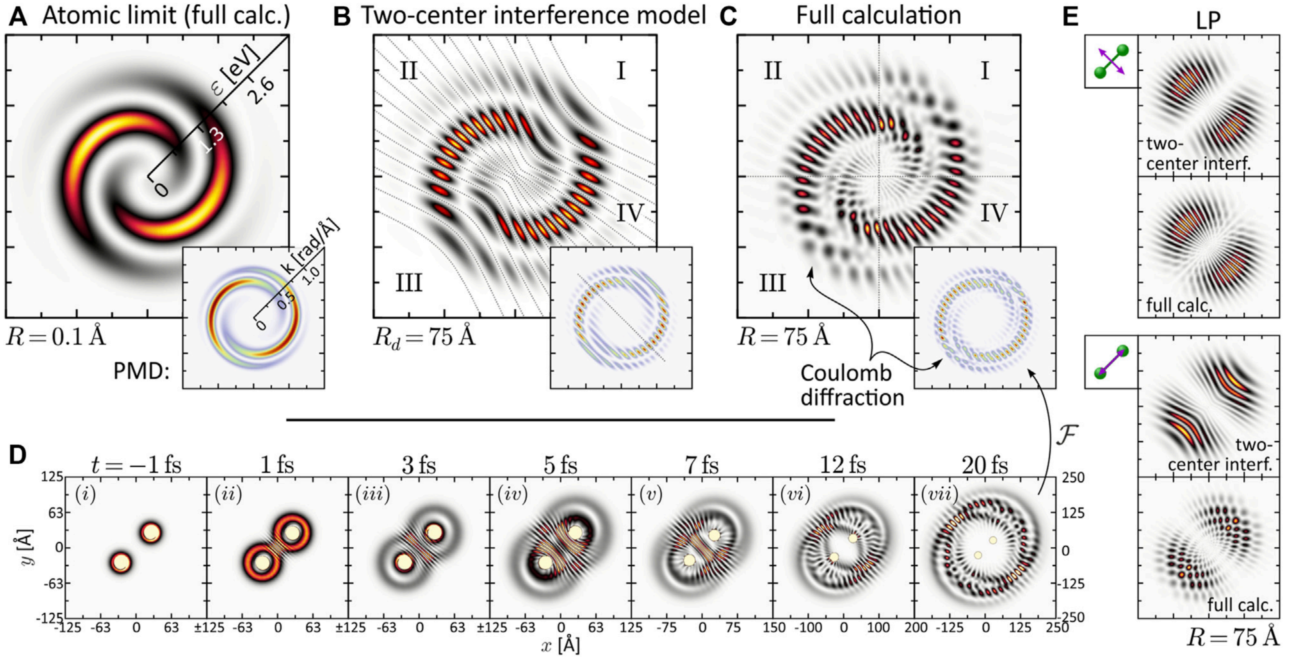

FIGURE 3 | (Color online.) Discussion of interference mechanisms on the example of the two-armed FEV created by one-photon ionization with an LRCP pulse sequence (cf. **Panel 2**). The two pulses are centered at $\tau_1 = -\tau_2 = -2$ fs. **(A)** Energy-calibrated PMD of the FEV in the atomic limit $R = 0.1$ Å. The inset shows the actual PMD in momentum representation. **(B)** Two-center interference model based on the superposition of two atomic partial wave packets with origins displaced by $R_d = 75$ Å. **(C)** Full calculation of the two-armed FEV in the dissociation limit $R = 75$ Å. **(D)** Time series of the electron density $|\psi(\boldsymbol{r}; \boldsymbol{R}, t)|^2$ illustrating the diffraction of the partial wave packets emitted from one nucleus at the Coulomb potential of the neighboring nucleus. **(E)** Comparison between two-center interference model and full calculation for the LP single-pulse scenarios orthogonal and parallel to the internuclear axis.

speckle-type interference pattern. This speckle pattern is a superposition of the two-center interference pattern emanating laterally from the internuclear axis, and a second pattern emanating in axial direction. The latter arises from the diffraction of the partial waves emitted from either nucleus at the Coulomb potential of the neighboring nucleus. Panel (d) illustrates the Coulomb diffraction process by a time series of the coordinate space density $|\psi(\boldsymbol{r};\ \boldsymbol{R},\ t)|^2$ (note the different grid ranges). The series begins with the creation of the $|p, 1\rangle$-type partial waves by the initial LCP pulse centered at $\tau_1 = -2$ fs (frame (*i*)). Both partial waves evolve rapidly into torus shapes which overlap and interfere in between the two nuclei (frame (*ii*)). By the time the $|p, -1\rangle$-type partial waves are created by the time-delayed RCP pulse (frame (*iii*)), the initial waves have already arrived at the neighboring nuclei. Frames (*iii*)–(*v*) capture their diffraction at the attractive Coulomb potentials which focus them towards the internuclear axis. The time-delayed partial waves undergo the same diffraction process in frame (*vi*). Eventually, all partial waves have passed the two nuclei and depart from the molecule [frame (*vii*)], dispersing asymptotically into their own PMD (Winter et al., 2006; Bayer et al., 2020). To highlight the different contributions of two-center interference and Coulomb diffraction to the PMD, panel (e) compares full calculation and two-center interference model for the LP scenarios parallel and orthogonal to the internuclear axis (see first and second frame of last column in **Figure 2**). In the orthogonal case (top), where the PMD is aligned lateral to the molecular axis, the agreement of the model and calculation is quite convincing. In the parallel case (bottom), however, where the PMD is aligned along the molecular axis, the deviations are substantial, emphasizing the strong influence of Coulomb diffraction on the interference pattern in this direction. In summary, besides Coulomb diffraction, the seemingly complicated molecular FEV in **Figure 3C** can be understood as a result an interplay of three types of interference: (1) The interference of the two atomic wave packets $\tilde{\psi}_{p,\pm 1} \propto e^{\pm im\phi}$, created by the two counterrotating circularly polarized subpulses, determines the azimuthal structure of the PMD, (2) by virtue of the time delay τ, the two pulses act as a *temporal double slit* due to the free time-evolution phase factor $e^{-i\varepsilon\tau/\hbar}$, which results in the radial fringe pattern in the PMD (Wollenhaupt et al., 2002), and (3) the spatial displacement $\boldsymbol{R}$ of the two atoms along the molecular axis, associated with the phase factor $e^{-i\boldsymbol{k}\cdot\boldsymbol{R}}$, causes a lateral fringe pattern in the PMD, reminiscent of a *spatial double slit*. We note, that this physical picture allows us to extract the internuclear separation directly from the lateral fringe pattern in the PMD.

While the interpretation of the PMDs in the atomic and the dissociation limit is quite transparent, the analysis of the PMDs in the intermediate regime, presented in the central columns of **Figure 2**, is more demanding. The penultimate column, with R = 25 Å, represents the transition between the two limits. Here the PMDs are already characterized by the two interference mechanisms, the main difference being the lower modulation frequency of the two-center interference fringes in comparison to the last column. Around the equilibrium distance R_0 = 4.48 Å (third column; see also **Figure 1A**) of the molecule, however, the two mechanisms are less meaningful for the interpretation of the PMDs. In this regime, the internuclear separation is difficult to extract directly from the PMD but could be retrieved by comparison to an analytical model of the photoelectron wave function (Fernández et al., 2009) or by application of a machine learning procedure (Shvetsov-Shilovski and Lein, 2022). Some general features of the PMDs, which we confirmed numerically, can be identified. For example, the PMDs created by LCP and RCP pulses (the latter are not shown) are mirror images of one another, when reflected at the internuclear axis or orthogonal to this axis. Mirroring the field at one of these axes inverts its rotational sense and transforms an LCP into an RCP pulse and vice versa. Currently, the mirror symmetry of LCP and RCP pulses is also referred to when discussing chiro-optical effects, such as photoelectron circular dichroism (Hergenhahn et al., 2004; Powis, 2008; Lux et al., 2012). Altogether, the second (R = 3.45 Å), third and fourth (R = 6.0 Å) column correspond to the nuclear vibration window which will be investigated in the following **Section 3.2**. The PMDs shown here build the basis for the discussion of the vibrational dynamics.

3.1.2 Static Three-Photon Ionization

Unlike SPI, MPI depends not only on the initial state and the final state in the continuum, but is also highly sensitive to intermediate resonances. Moreover, the absorption of multiple photons opens up numerous ionization pathways leading to target continuum states characterized by superpositions of angular momenta that are generally larger than in SPI. As a consequence, PMDs created by MPI have a richer structure than those created by SPI. The simulation results shown in the bottom part of **Figure 2** (blue frame) are based on three-photon ionization of the potassium molecular ion, motivated by recent experimental studies on potassium atoms (Wollenhaupt et al., 2009a; Pengel et al., 2017a; Pengel et al., 2017b) and molecules (Bayer et al., 2013; Braun et al., 2014). The PMDs in the first column are again well understood in an atomic picture invoking the dipole selection rules. Accordingly, three-photon ionization of the $|s, 0\rangle$-type ground state by an LP pulse creates an $|f, 0\rangle$-type photoelectron wave packet aligned in laser polarization direction (Wollenhaupt et al., 2009a). Analogously, the LCP pulse creates an $|f, 3\rangle$-type, torus-shaped wave packet, slightly more confined in radial direction compared to the SPI scheme. The radial width of the PMD in the MPI scheme is determined by the bandwidth of the third-order spectrum of the 5 fs pulse, which is actually smaller than the fundamental bandwidth of the 2 fs pulse. The LRCP sequence creates a six-armed FEV with counterclockwise sense of rotation, as observed and discussed in detail in Pengel et al. (2017a), Pengel et al. (2017b).

In the dissociation limit (last column), we recognize the same interference mechanisms at play as in the SPI scheme (cf. **Section 3.1.1**). Again, the average structure of the PMDs is the same as in the atomic limit (first column). Along the internuclear axis, however, the PMDs are modulated by speckle-shaped interference patterns due to the combined effect of Coulomb diffraction and two-center interference, whereas in lateral direction, we observe the fringe-type patterns characteristic for almost pure two-center interference.

The interpretation of the intermediate R-regime is more involved. The PMDs shown in the central columns depend strongly on the central wavelength λ_0, which indicates the presence of intermediate resonances. Also, a comparison of the different PMDs within each row shows that the shape of the PMDs changes drastically with the internuclear separation. In contrast, in the SPI scheme, where resonances of the bound system play no role, the PMDs in the vibration window (green frame) are qualitatively similar and change smoothly with R. Another indication of intermediate resonances is the rotation of the PMDs in the circularly polarized scenarios, discernible e.g., by the angular alignment of the main lobes in the 2D plane. Resonances introduce additional ionization phases in the photoelectron wave packet (Eickhoff et al., 2022) which, in the circularly polarized case, translate into an azimuthal rotation of the PMD (Eickhoff et al., 2020a). The observed rotation is particularly pronounced in the PMDs from LCP and LRCP ionization in the fourth column, i.e., for $R = R_{out}$ = 6.0 Å. The excitation scheme in **Figure 1A** suggests that at this internuclear separation the transition from the ground state to state ψ_6 (green line in **Figure 1A**) becomes near-resonant with a pulse of central wavelength λ_0 = 463 nm (see also **Figure 6B**).

The quantitative analysis of the bound state population dynamics $p_n(t)$ for the lowest eight electronic states is shown in **Figure 4**. At the equilibrium distance R_0 and λ_0 = 420 nm (third column), shown in panel (a), we see the transient population of states ψ_1 and ψ_2 by a few percent, followed by a population return to the ground state. This result confirms the non-resonant character of the interaction and verifies the perturbative interaction conditions. Panel (b) shows the dynamics at R_{out} and the same central wavelength. In this case, we observe an efficient population transfer to state ψ_6 of about 10%. The induced electronic coherence results in a pronounced charge oscillation in the bound molecular system along the internuclear axis. This dynamics is illustrated in the insets to (b) which show the time-dependent electron density $|\psi(\boldsymbol{r}; \boldsymbol{R}, t)|^2$ over one half-cycle of the charge oscillation after the interaction. These findings confirm the above assumption of a resonance-enhanced multiphoton ionization (REMPI) process at R_{out} *via* state ψ_6. Our simulations show that the exact resonance at R_{out} is found around λ_0 = 413 nm. At λ_0 = 463 nm, as in the fourth column, we still register about 1% population transfer due to the broad bandwidth of the pulses. Additional high-lying resonances are expected at the two-photon level, due to the high density of Rydberg states, but their analysis is beyond the scope of this paper. The resonance $\psi_0 \rightarrow \psi_6$ at R_{out}, however, will also be relevant in the discussion of coupled vibrational and electronic (vibronic) MPI dynamics in **Sections 3.2.2**, **3.3**.

3.2 Vibrating Molecule

The coupled electron-nuclear dynamics in molecules has been studied extensively on the femtosecond timescale, as reviewed for example in Gatti (2014), Bircher et al. (2017), and very recently on the attosecond timescale (Nisoli et al., 2017; Cattaneo et al., 2018).

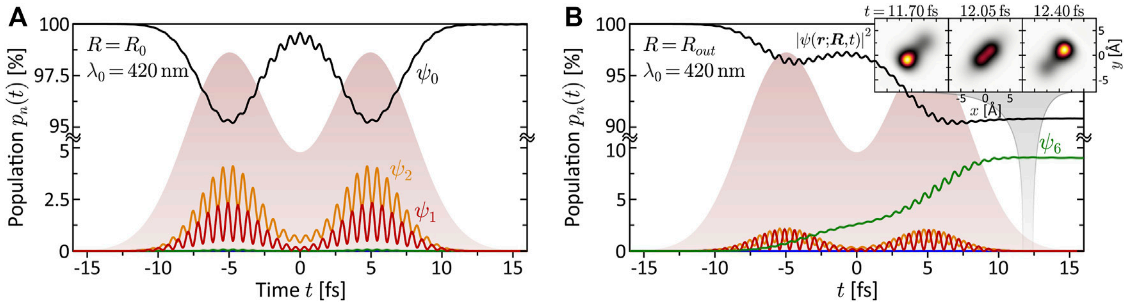

FIGURE 4 | (Color online.) Bound state population dynamics of the rigid molecule excited by the LRCP sequences (shaded background) from the MPI scheme. Shown are the time-dependent populations of the eight lowest electronic states ψ_n (cf. **Panel 1B**). **(A)** Non-resonant excitation at the equilibrium distance $R_0 = 4.48$ Å using a central wavelength of $\lambda_0 = 420$ nm. Only states ψ_1 and ψ_2 are transiently populated, mediating the MPI process. Finally, almost the entire population returns to the ground state. **(B)** Resonant excitation of state ψ_6 at the outer turning point $R_{out} = 6.0$ Å, using the same central wavelength $\lambda_0 = 420$ nm as in **(A)**. The coherent superposition of states ψ_0 and ψ_6 corresponds to an efficient ultrafast charge oscillation in the bound molecular system, illustrated in the inset by a time series of the electron density $|\psi(\boldsymbol{r};\, \boldsymbol{R},\, t)|^2$.

Experimentally, the coupled electron-nuclear dynamics of potassium dimers has been investigated in Bayer et al. (2013), Braun et al. (2014). In this section, we account for the vibration of the nuclei along the internuclear axis and study the coupling between the nuclear motion and the electronic ionization dynamics. To this end, we initialize the molecule in a vibrationally excited state of the electronic ground state potential $V_0(R)$, which we can think of as being prepared, e.g., by stimulated Raman excitation. We use LRCP sequences to study the creation of FEVs by ionization of the vibrating molecule. Femtosecond double pulse sequences are well-established in femtochemistry and the time-resolved investigation of molecular dynamics (Zewail, 1995), being the basis of pump-probe techniques (Zewail, 2000). Here, however, the focus is not primarily on time-resolved imaging of the dynamics, but on exploring their signatures imprinted in the photoelectron spirals. In the following, we design specific vibration-scenarios *via* the timing of the pulse sequence. Specifically, we lock the two pulses to distinct stages of the nuclear oscillation, i.e., the inner and the outer turning point. The resulting PMD is analyzed for both the SPI and the MPI scheme (cf. **Section 3.1**).

3.2.1 Dynamic One-Photon Ionization

The timescale of the vibrational dynamics depends, amongst others, on the reduced mass μ of the nuclear system. For the purpose of this study, μ is chosen such that the nuclear timescale is adapted to the laser pulses employed in **Section 3.1.1**, which yields the most transparent results. Specifically, μ is adapted such that the period of the vibration (cf. top inset to **Figure 1**) is $T_v = 13.7$ fs. This value is compatible with the laser pulse duration of $\Delta t = 2$ fs. The laser central wavelength is fixed to $\lambda_0 = 125$ nm as in the second column of **Figure 2** (magenta frame). The variation parameter is the time-delay τ between the two subpulses of the LRCP sequence.

Two distinct scenarios are investigated. First, the pulses are separated by half a vibrational cycle, $\tau = T_v/2 = 6.84$ fs, and locked to *different* turning points. Second, the pulses are separated by $\tau = T_v$ and locked to the *same* turning point of two consecutive vibration cycles. The numerical results are presented in **Figure 5**. The top frames show the nuclear motion $R(t)$ (green curve) together with the x-component of the circularly polarized laser field $\boldsymbol{E}(t)$ (magenta curve). During the most intense part of the pulses, i.e. within Δt, the nuclei move by about 0.2 Å at the inner and 0.1 Å at the outer turning point. The calculated photoelectron spectra are shown below in different representations, including the 2D PMD $\mathcal{P}(\varepsilon, \phi)$ in a Cartesian and a spherical coordinate frame, the energy-integrated angular distribution $\mathcal{A}(\phi)$ (blue polar plot) and the angle-integrated energy spectrum $\mathcal{S}(\varepsilon)$ (bottom right frame). We notice that the photoelectron signal is spread out over a much larger energy region than in the rigid case (cf. **Section 3.1.1**). This spreading, which is best discernible in the energy spectra $\mathcal{S}(\varepsilon)$, is particularly apparent in panels (a) and (c). In these scenarios, the ionizing field probes the nuclear dynamics over a full vibrational cycle. In the static molecular frame, the photoelectrons are created in a fixed kinetic energy window, the width of which is essentially determined by the spectral bandwidth of the laser pulses. In the dynamic case, however, the ionization maps the nuclear motion into different energy windows *via* the R-dependent ionization potential $\Delta V(R) = V_i(R) - V_0(R)$. According to Mulliken's difference potential analysis (Mulliken, 1971), a photoelectron created at the internuclear separation R by absorption of a photon with frequency ω_0 receives a kinetic energy of $\varepsilon_{1\omega}(R) = \hbar\omega_0 - \Delta V(R)$. Thus, the different stages of the vibrational dynamics are energetically disentangled in the energy spectrum, which is the basis for the time-resolved mapping of ultrafast vibrational wave packets by femtosecond photoelectron spectroscopy (Baumert et al., 1991; Assion et al., 1996; Wollenhaupt et al., 2003; Bayer et al., 2013; Braun et al., 2014). In a full quantum mechanical treatment of the vibrational dynamics, the photoelectron energy spectrum is additionally broadened due to the finite width of the vibrational wave packet. The latter describes a distribution of internuclear separations at which the ionization takes place. To estimate this additional broadening, the entire vibrational wave packet needs to be mapped onto the photoelectron energy axis *via* the difference potential. The result of the difference potential

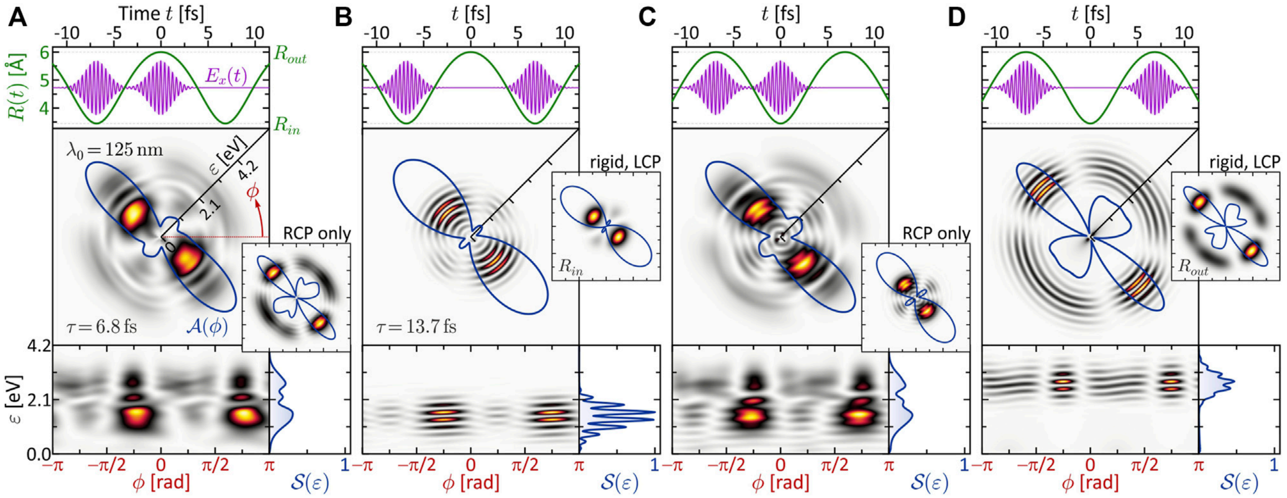

FIGURE 5 | One-photon ionization of the vibrating molecule by single-color LRCP sequences locked to the two turning points of the nuclear vibration $R(t)$. The 2D PMD in energy representation $\mathcal{P}(\varepsilon, \phi)$ is shown in Cartesian (central frames) and spherical representation (bottom frames). In addition, the energy-integrated angular distributions $\mathcal{A}(\phi)$ are shown as polar plots (blue curves) and the angle-integrated energy spectra $\mathcal{S}(\varepsilon)$ are shown in the bottom right frames. In **(A,C)**, the two subpulses are locked to different turning points, while in **(B)**, both pulses ionize the molecule at the inner and in **(D)** at the outer turning point.

analysis applied to the SPI scheme is shown as magenta curve in **Figure 6A**. Taking into account the laser bandwidth in addition, depicted in the left frame, the kinetic energy range of the released photoelectrons is $\varepsilon \in [0; 4.2\,\mathrm{eV}]$.

Specifically, the inner turning point is mapped to an energy of $\varepsilon_{1\omega}(R_{in}) = 1.4\,\mathrm{eV}$, while the outer turning point is mapped to $\varepsilon_{1\omega}(R_{out}) = 2.9\,\mathrm{eV}$. This mapping gives rise to the localized rings observed in **Figures 5B,D**. In these SPI scenarios, the laser pulses probe the nuclear dynamics at two consecutive inner and outer turning points, respectively. The enhancement of the photoelectron amplitude in these regions indicates the increased probability of finding the nuclei at one of the two turning points, in analogy to a classical oscillator. The corresponding angular distributions $\mathcal{A}(\phi)$ are almost identical to the result obtained in the rigid case. For comparison, the PMDs created by SPI of the rigid molecule using a single LCP pulse is shown in the respective insets. Note that, in the single pulse scenarios, the side lobes of the angular distribution are not symmetric. This asymmetry is compensated in the LRCP scenarios by the contribution of the time-delayed RCP pulse, which is mirrored at the internuclear axis (see also discussion in **Section 3.1.1**). The delicate radial fringe patterns observed in the LRCP scenarios results from the interference of the two partial wave packets created by the LCP and the RCP subpulse, enabled by their energetic overlap. The fringe spacing is determined by the time-delay as $\Delta\varepsilon = h/\tau$ (Wollenhaupt et al., 2002; Pengel et al., 2017b). In the polar representation of the 2D PMD (bottom left frames), we recognize that the fringes are slightly sloped, suggesting a spiral-shaped interference pattern analogous to that of atomic FEVs (Ngoko Djiokap et al,. 2015; Pengel et al., 2017b). In contrast to the atomic case, however, the spiral arms of these molecular FEVs evolve non-linearly in the polar plane. This non-linear ϕ-dependence of the interference pattern, which is neither fully resolved in the energy spectrum $\mathcal{S}(\varepsilon)$ nor visible in the angular distribution $\mathcal{A}(\phi)$, encodes spectroscopic information about the structure and the dynamics of the molecule.

In panels (a) and (c) of **Figure 5**, we observe no such regular interference pattern as in (b) and (d). Here, the two partial wave packets are mapped into different energy windows and interfere only in a narrow overlap region around $\varepsilon = 2.1\,\mathrm{eV}$ (see left frame of **Figure 6A**), where indeed some interference fringes are observed. The energetic disentanglement of the free electron wave packets is also indicated by the slight asymmetry of the side lobes in the angular distribution $\mathcal{A}(\phi)$. These side lobes reflect mainly the side lobes of the low-energy wave packet created at the inner turning point, i.e., by the LCP subpulse in panel (a) and the RCP subpulse in panel (c). A more striking difference between the PMDs in panel (a) and (c) is the weak fringe pattern which is observed in the low-energy region $\varepsilon \lesssim 2.1\,\mathrm{eV}$ in (c) and absent in (a). This difference is seemingly counterintuitive, since the underlying physical scenarios are—at first glance—very similar. A closer numerical investigation revealed that the fringe pattern arises due to non-adiabatic dynamics of the electronic ground state wave function induced by the vibrating nuclei. While the ground state electron density $|\psi(\boldsymbol{r}; \boldsymbol{R}, t)|^2$ adapts almost adiabatically to the nuclear motion, the corresponding wave function acquires a saddle-shaped phase aligned along the internuclear axis. Signatures of this phase emerge as the radial fringe pattern in the PMD in (c). To confirm this analysis, we examined the PMD created by the time-delayed RCP pulse only, i.e., without the initial LCP subpulse. The resulting PMD, shown in the inset to (c) exhibits the same fringe pattern as the full calculation. The same procedure applied to the scenario in (a) yields the PMD shown in the inset to (a). Evidently, the wave packet created by the RCP pulse at the outer turning point also exhibits a fringe structure reflecting the vibrational history of the molecule, albeit

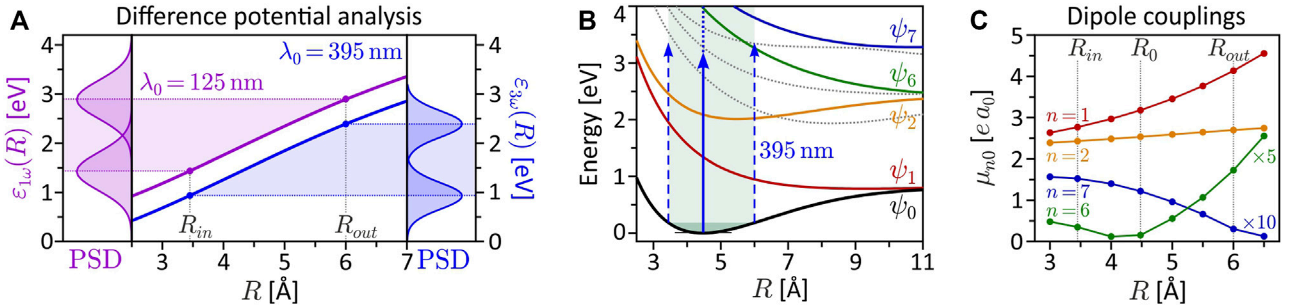

FIGURE 6 | (Color online.) Derived quantities to characterize the interdependence of electronic and nuclear dynamics. **(A)** Difference potential analysis for the SPI scheme (magenta curve) and the MPI scheme (blue curve). The left frame depicts the power spectral density (PSD) of the 125 nm, 2 fs pulse mapped at the inner and outer turning point of the vibration. The right frame shows the PSD of the third order spectrum of the 395 nm, 5 fs pulse. **(B)** Excitation scheme of the vibrating molecule interacting with the 395 nm pulse employed in the MPI scheme. At the outer turning point, state ψ_6 is excited resonantly from the ground state. **(C)** R-dependent transition dipole moments $\mu_{n0}(R) = |e\langle\psi_n|\boldsymbol{r}|\psi_0\rangle|$ for ground state transitions to the seven lowest bound electronic states (vanishing dipole couplings are not shown). At the outer turning point R_{out}, the coupling of the ground state to the resonant state ψ_6 is one order of magnitude larger than at the equilibrium distance R_0.

less pronounced as in (c) and therefore less visible in the full calculation. In both cases, we find for the fringe spacing $\Delta\varepsilon$ = 334 meV. This value corresponds to a time constant of $\tau = h/\Delta\varepsilon$ = 12.4 fs, approximately matching the time interval from the initiation of the vibration at $t_i = -11.5$ fs to the arrival of the RCP pulse at $t = 0$. These findings demonstrate that the interference structures in the photoelectron spectrum are highly sensitive to non-adiabatic electron-nuclear dynamics in molecules. The results once again underscore that differential detection of photoelectron wave packets is essential to reveal the subtle changes in the bound electronic wave function, which are otherwise not detected.

3.2.2 Dynamic Three-Photon Ionization

The results obtained in the dynamic MPI scheme are especially rich in information. Not only is MPI sensitive to intermediate resonances, but unlike the static case, in the presence of nuclear dynamics, electronic resonances may occur at certain internuclear distances and be absent in others. To study the signatures of such transient resonances in the PMD, we again lock two pulses, which are short compared to the vibrational period of the molecule, to different stages of the nuclear dynamics. The vibrational dynamics are adapted to the longer pulse duration of Δt = 5 fs used in **Section 3.1.2** by choosing the reduced mass of the nuclei such that the vibration period is increased to T_v = 30.6 fs. We employed the LRCP sequences from **Section 3.1.2** with a central wavelength of λ_0 = 395 nm (second column of **Figure 2**). This central wavelength is very close to the one-photon resonance $\psi_0 \rightarrow \psi_6$ at the outer turning point R_{out} of the vibration, as illustrated in the excitation scheme shown in **Figure 6B** (see also **Section 3.1.2**). At the inner turning point R_{in} and at the equilibrium distance R_0, however, the field is far detuned from any one-photon resonance, since the states ψ_3, ψ_4 and ψ_5 (gray dashed curves) are not dipole-coupled to the ground state. Consequently, we expect the transient resonance $\psi_0 \rightarrow \psi_6$ to play a prominent role in the scenarios involving MPI at the outer turning point. The R-dependent transition dipole moments plotted in **Figure 6C** show that the coupling between the ground state and the ψ_6-state (green curve) at the outer turning point is one order of magnitude larger than at the equilibrium distance (cf. **Figure 1B**). In general, the variation of a transition dipole moment along a nuclear coordinate can be indicative of a change of the electronic structure in this direction (Wollenhaupt et al., 2003). However, in this case, the variation of the dipole coupling is attributed to the R-dependent contributions of the inner and outer lobes of ψ_6 to the matrix element (cf. **Figure 1B**). In the vicinity of R_0, at $R \approx 4.2$ Å, these contributions cancel each other and the matrix element vanishes. The numerical results are presented in **Figure 7**, with the same organization as in **Figure 5** to facilitate the comparison. We start with the discussion of panel (b), where both pulses ionize the vibrating molecule at the inner turning point. This is the only scenario, where the above-mentioned resonance is not crucial. According to the difference potential analysis in **Figure 6A** (blue curve), the inner turning point is mapped to an energy of $\varepsilon_{3\omega}(R_{in}) = 3\hbar\omega_0 - \Delta V(R_{in}) = 0.9$ eV. This energy is marked by a blue arrow in the bottom right frame of **Figure 7B**. In fact, the calculated PMD is red-shifted towards a kinetic energy of ε = 0.6 eV, best seen in the energy spectrum $\mathcal{S}(\varepsilon)$. An examination of the bound state population dynamics (not shown) confirmed that the excitation is fully perturbative, ruling out the AC Stark effect to explain the observed energy shift, and non-resonant at the one-photon level. The angular distribution $\mathcal{A}(\phi)$ is similar but not identical to that of the static LRCP scenario shown in the inset. The slight rotation between both, indicating the acquisition of an additional phase in the REMPI process (Eickhoff et al., 2022), hints towards the influence of another resonance encountered during the vibration on the two-photon level. The analysis of the population dynamics yields that the high-lying state ψ_{11}, plotted as cyan dashed-dotted line in **Figure 1A**, 1is excited near-resonantly by both subpulses—albeit with a population transfer of less than 1%. However, the population stored in ψ_{11} by the first subpulse is efficiently mapped by one photon of the second subpulse into an energy window around ε = 0.5 eV, consistent with the observed energy shift. A closer inspection of the 2D PMD reveals an intricate interference pattern. The pattern

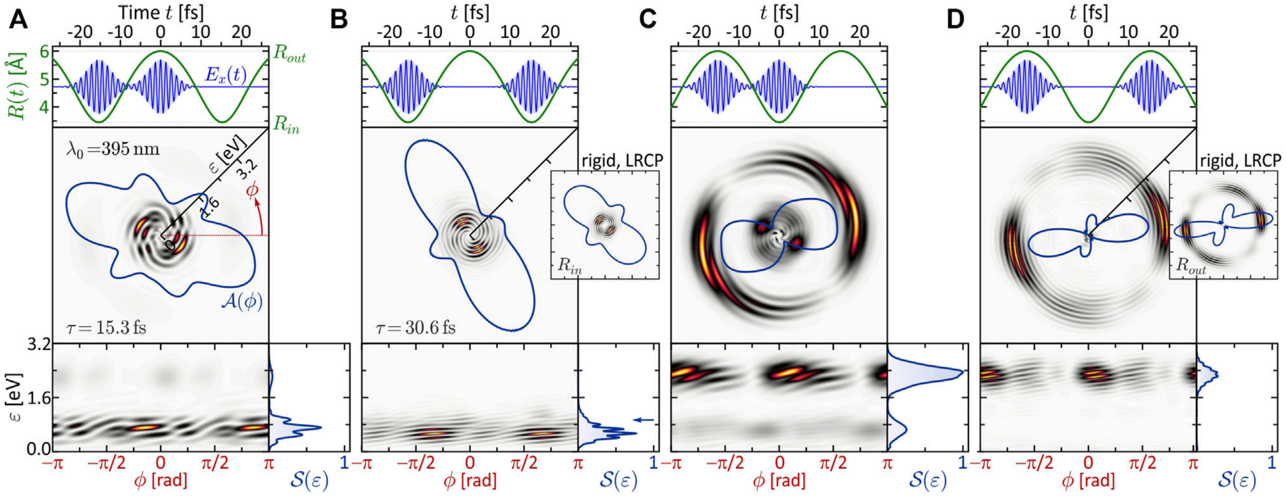

FIGURE 7 | (Color online.) Three-photon ionization of the vibrating molecule by single-color LRCP sequences locked to the two turning points of the nuclear vibration *R*(*t*). The organization of panels **(A–D)** is analogous to **Figure 5**. Striking differences to the SPI scheme are observed, especially in panels **(A,C)**, which are attributed to the occurrence of transient intermediate resonances.

starts out as a six-arm spiral, as expected for three-photon ionization with LRCP pulses (Pengel et al., 2017b). With increasing energy, however, the pattern becomes more and more intertwined, indicating a beating of the six-armed FEV with a another contribution. Because this beating pattern is not observed in the rigid case (see inset), we conclude that the second contribution arises from an interplay of the non-adiabatic (but near-diabatic) dynamics of the ground state wave function (see discussion in **Section 3.2.1**) and the time-delayed mapping of the two-photon resonance ψ_{11} by the second subpulse.

A similar beating pattern is observed in **Figure 7D**, where both pulses ionize the molecule at the outer turning point. The created photoelectron wave packets are localized energetically around $\varepsilon_{3\omega}(R_{out})$ = 2.4 eV, in accordance with the difference potential analysis in **Figure 6A**. Both pulses excite the ψ_6-state near-resonantly driving a (1 + 2) REMPI process, which we verified numerically by evaluation of the population dynamics (not shown) similar to **Figure 4**. Our results show that the first subpulse transfers about 5% of population from the ground state to the resonant ψ_6-state. Hence, the second pulse finds the molecule in a coherent superposition of states ψ_0 and ψ_6 and maps both into the continuum, the former by three- and the latter by two-photon ionization. One might suspect that the additional photoelectron contribution from state ψ_6 is responsible for the observed beating pattern in the PMD. However, since the beating—unlike the $\psi_0 \rightarrow \psi_6$ resonance—is absent in the static LRCP scenario shown in the inset, we conclude that the beating is indeed a signature of the non-adiabatic ground state dynamics. The same alignment of the angular distributions in the static and the dynamic LRCP scenario confirms the absence of additional resonances in the course of the nuclear vibration.

In the scenarios of panels (a) and (c), we expect again a broader energy distribution of the photoelectrons, because the laser field ionizes the molecule at both turning points. In fact, the PMD in panel (c) displays a bimodal energy spectrum $\mathcal{S}(\varepsilon)$ with significant contributions around $\varepsilon_{3\omega}(R_{in})$ and $\varepsilon_{3\omega}(R_{out})$. The first subpulse is locked to the outer turning point and hence induces (1 + 2) REMPI *via* the ψ_6-state. The created photoelectron wave packet is centered energetically in the high-energy window around 2.4 eV. The second subpulse, locked to the inner turning point, creates a wave packet in the low-energy window around ε = 0.7 eV by direct (2 + 1) REMPI from the ground state *via* state ψ_{11}. Again, the subtle radial fringe pattern superimposed on this contribution reveals the non-adiabatic phase dynamics of the bound state wave function. Due to our classical implementation of the nuclear dynamics, the high-energy contribution exhibits an additional spiral pattern. This pattern reflects the interference of the initial wave packet, created by the first subpulse directly, with another contribution created by time-delayed two-photon ionization of the ψ_6-state by the second subpulse. However, in a quantum mechanical description of the vibrational dynamics, the ψ_6-population excited by the first subpulse would follow the repulsive BO potential $V_6(R)$. Here, the second subpulse maps the ψ_6-state coincidentally into the high-energy window around ε = 2.4 eV, such that the created wave packet overlaps with the first wave packet. This observation shows that, in order to account for the full dynamics of multiple vibrational wave packets in electronic superposition states, our numerical model needs to be refined towards a full quantum mechanical treatment of the coupled electron-nuclear dynamics.

Eventually, in panel (a), the role of the two subpulses is exchanged. The first subpulse ionizes the molecule at the inner turning point *via* direct (2 + 1) REMPI, creating a low-energy wave packet around ε = 0.9 eV and transferring some population to ψ_{11}. At the outer turning point, the second subpulse therefore ionizes the molecule by direct (1 + 2) REMPI *via* the resonant ψ_6-state, creating a high-energy wave packet around ε = 2.4 eV and, in addition, maps the ψ_{11}-state into the continuum, creating another wave packet centered around ε = 0.5 eV. The interference of the two low-energy wave packets gives rise to the pronounced vortex structure observed in the low-energy region. We note that, although the different intensities of slow and fast electrons in **Figures 7A,C** suggest a ground state depletion by the first pulse of each scenario, the ionization is indeed perturbative. In both cases, the first pulse depopulates the ground state only by several %, comparable to **Figure 4B**.

The results presented in this section demonstrate that the coupled electron-nuclear dynamics leaves distinct fingerprints in the spiral-shaped PMDs of molecular FEVs. For example, the striking difference between **Figures 7A,C**, as well as the comparison between the PMD from the vibrating and the rigid molecule, clearly reveal that, in molecular MPI, the interplay between nuclear dynamics and electronic resonances is of great importance. Therefore, model calculations that predict the fully differential PMDs are invaluable tools to decipher the sophisticated structures of the PMD and identify the multiple interference phenomena underlying the creation of molecular FEVs. However, the results also show, that more refined models including the quantum mechanical description of nuclear dynamics are needed to accurately predict the fine details of the coupled electron-nuclear dynamics. Given the high degree of complexity of the interference patterns, further processing and analysis of the PMDs will in practice be necessary to extract detailed information on the underlying molecular dynamics. Experimentally, the creation and differential detection of molecular FEVs promises to be a highly-sensitive spectroscopic technique to probe molecular structure and dynamics, provided the delicate interference patterns are not averaged out by the experimental conditions—an issue which we will address in the following section.

3.3 Molecular Rotation and CEP-Averaging

So far, we have considered the laser-molecule interaction in the molecular frame, i.e., for a fixed alignment of the molecule in space. In addition, we have assumed a phase-stable wave form and polarization profile of the laser field with a fixed orientation relative to the molecular axis in the experiment. Any deviation from these idealizations will, in general, wash out the intricate interference patterns observed in the molecular frame PMD. For example, measurements are typically performed on isotropic ensembles of molecules. The PMD measured in the laboratory frame is then a rotational average of all molecular alignments relative to the laser propagation direction. In addition, the measured PMD is typically accumulated over multiple laser shots and locations within the laser focus introducing wave form averaging *via* phase fluctuations of the laser and the Gouy phase (Hoff et al., 2017; Bayer et al., 2020). While these phase fluctuations might be less significant in the case of a single multi-cycle pulse, they become crucial in the case of few-cycle pulses, multi-pulse sequences and combinations thereof. Specifically, a variation of the relative phase between the subpulses in the LRCP sequences used here for the creation of molecular FEVs rotates the spiral-shaped interference pattern in the molecular frame PMD (Pengel et al., 2017a). As a result, fluctuating relative phases blur the interference pattern in the angular direction. Since bichromatic LRCP sequences, consisting of two subpulses with commensurable central frequencies, control the rotation of the PMD *via* the relative phase and the CEP (Kerbstadt et al., 2019b; Eickhoff et al., 2020a), even CEP fluctuations wash out the observable interference pattern in the bichromatic case.

In this section, we investigate the influence of the different averaging mechanisms on the PMD in a single test scenario. Besides the averaging over the molecular alignment, we examine CEP-averaging. Unlike the relative optical phase, which can be controlled experimentally with zeptosecond precision (Köhler et al., 2011), the CEP is generally more difficult to stabilize and inherently varies over the laser focus due to the Gouy-phase (Hoff et al., 2017). Under perturbative conditions, however, FEVs created by *single-color* pulses are CEP-insensitive (Pengel et al., 2017b). Therefore, we consider a molecular FEV created by dynamic two- vs. three-photon ionization using a bichromatic (2ω: 3ω) LRCP pulse sequence, which is highly sensitive to the CEP (Kerbstadt et al., 2019b; Eickhoff et al., 2021c). The pulses are separated by a full vibrational cycle, $\tau = T_\nu$, and locked to consecutive instants of the nuclei traversing the equilibrium distance R_0, heading outwards. Thus, both pulses probe the same vibrational stage and a maximum range of internuclear separations. Maintaining a pulse duration of $\Delta t = 5$ fs as in **Sections 3.1.2**, **3.2.2**, we adapted the reduced mass such that the vibrational period is $T_\nu = 18.0$ fs to fully separate both pulses in time and minimize photoelectron contributions due to frequency mixing between the two colors (Kerbstadt et al., 2017a; Eickhoff et al., 2021c). The initial LCP subpulse has a central wavelength of $\lambda_1 = 395$ nm as in the MPI scheme discussed in the previous sections. The time-delayed RCP subpulse has a central wavelength of $\lambda_2 = 2\lambda_1/3 = 263$ nm to ensure the energetic overlap of two- and three-photon ionization pathways at $2\hbar\omega_2 = 3\hbar\omega_1$. The amplitude ratio of the two subpulses is chosen such that in a static MPI scenario with $R = R_0$ both produce the same photoelectron yield. This procedure, which is also followed in the experiments (Kerbstadt et al., 2019b; Eickhoff et al., 2020a), generally optimizes the interference contrast between the two partial wave packets in the full LRCP scenario.

The numerical results are presented in **Figure 8**. Panel (a) shows the PMD in the molecular frame for a fully stabilized pulse. We observe a structured five-armed FEV consistent with the perturbative ionization model applied to two- vs. three-photon ionization. The FEV is localized in the low-energy region around $\varepsilon = 0.75$ eV. The reason for the enhancement of the photoelectron signal near the ionization threshold is the resonant excitation of the ψ_6-state by the first subpulse (cf. discussion in **Section 3.2.2**), which is then mapped into the continuum around $\varepsilon = 0.75$ eV by absorption of another photon from the second subpulse. The inset shows the PMD obtained in the atomic limit (rigid molecule with $R = 0.1$ Å). Compared to the dynamic case, it displays a more regularly shaped five-armed Archimedean spiral, similar to the result obtained recently for the 2D model of a single potassium atom (Eickhoff et al., 2021c). **Figures 8B–D** show three types of rotational averaging procedures. In panel (b), both the molecule and the laser field are rotated by 360°, in 16 steps of $\delta\phi = 22.5°$, keeping their relative orientation locked. In an experiment, this procedure corresponds to a rotation of the detector around an aligned molecule interacting with a phase-stable field. As

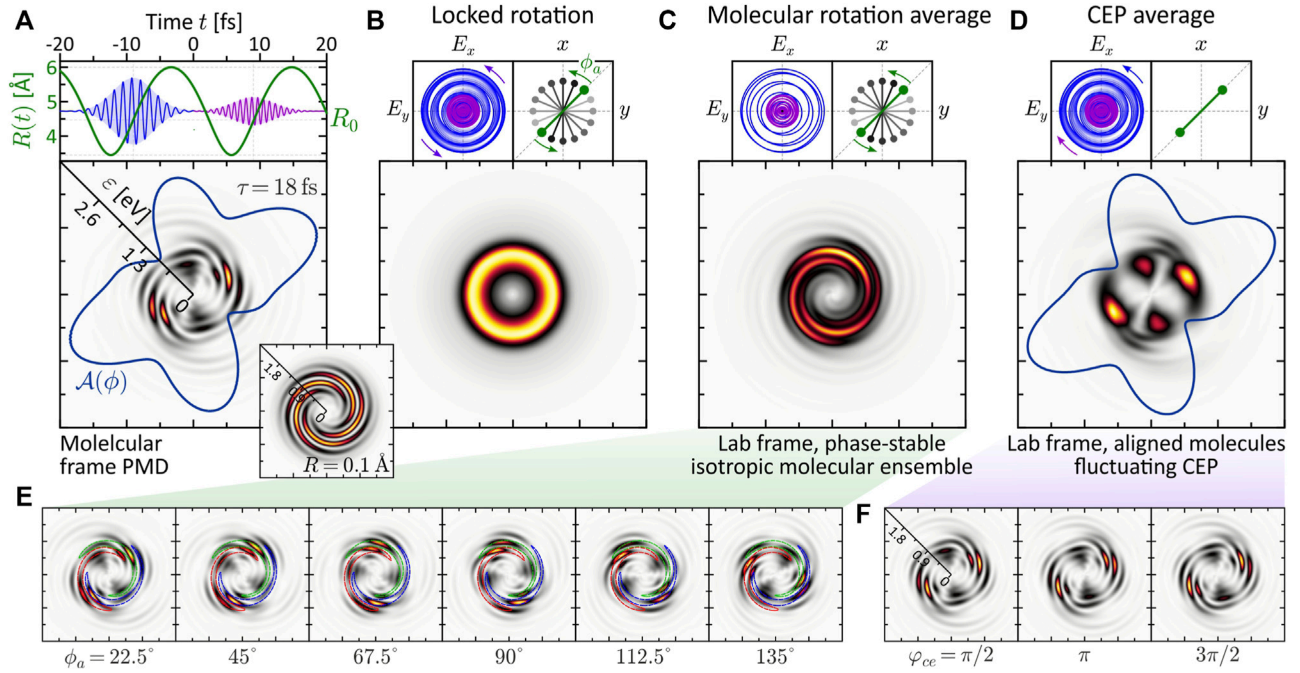

FIGURE 8 | (Color online.) Influence of experimental conditions on a molecular FEV created by dynamic two- vs. three-photon ionization using an LRCP bichromatic (2ω: 3ω) pulse sequence. All frames show energy-calibrated 2D PMDs. **(A)** The molecular frame PMD created by a phase-stable field exhibits an intricate five-armed spiral pattern. **(B)** Rotating both the molecule and the field about the laser propagation direction washes out the interference pattern completely and yields an isotropic, torus-shaped PMD in the lab frame. **(C)** Lab frame PMD obtained for an isotropic molecular ensemble and a phase-stable pulse sequence. Surprisingly, the highly structured five-armed FEV transforms into a regularly shaped three-armed Archimedean spiral. **(D)** Lab frame PMD obtained for an ensemble of aligned molecules and a fluctuating CEP. The CEP controls the rotation of the bichromatic field. **(E,F)** show selected subsets of molecular frame PMDs underlying the molecular rotation averaging and the CEP-averaging procedure, respectively.

expected, the average result is an isotropic, torus-shaped PMD which serves as a reference for the other two—experimentally more relevant—averaging studies.

Panel (c) shows the effect of molecular rotation averaging on the PMD. This type of averaging is relevant when measuring on an ensemble of unaligned molecules. In contrast to the real 3D space, where the molecule has two angular degrees of freedom (polar and azimuthal), in 2D we consider the rotation about the azimuthal angle ϕ. Due to the reflection symmetry of the homonuclear dimer, only rotations up to an angle of $\phi_a = 180°$ need to be considered. The alignment angle ϕ_a is taken relative to the positive grid-diagonal in counterclockwise direction. Keeping the laser field fixed, we calculated 16 molecular frame PMDs in which we successively rotated the molecule in steps of $\delta\phi_a = 11.25°$. A subset of these calculations is shown in panel (e). Surprisingly, the five-armed spiral pattern is not completely washed out by the molecular rotation, but evolves into a three-armed Archimedean spiral. To rationalize the formation of the three-armed spiral in the lab frame PMD, the series of images in panel (e) illustrates how the maxima of the five-armed spiral shift along a contour of the three-armed spiral of the averaged PMD under the molecular rotation. So far, the exact mechanism behind the counterintuitive transformation of the five-armed spiral into a three-armed spiral upon averaging has not been fully analyzed. Clearly, in order to obtain averaged PMDs that can be compared with experimental results, rotation averaging needs to be performed in 3D. It is quite possible that 3D averaging also blurs other features of the PMD. The results from the 2D model presented here are a natural first step in this direction and serve to compare rotational vs. CEP averaging.

Panel (d) shows the influence of CEP-averaging on the PMD. This type of averaging is especially relevant in bichromatic MPI schemes based on the interference of photoelectron wave packets of different parity (Kerbstadt et al., 2018; Kerbstadt et al., 2019b). In the case of MPI with a bichromatic LRCP sequence, the CEP controls the rotation of the field in the polarization plane and therefore determines the relative orientation between field and molecule. Here, we considered an aligned molecule ($\phi_a = 0$) and varied the CEP from $\varphi_{ce} = 0$ to 2π in 16 steps of $\delta\varphi_{ce} = \pi/8$. As a result, the fine five-armed spiral pattern observed in the phase-stable scenario (a) is averaged out. The main lobes of the angular distribution $\mathcal{A}(\phi)$, however, are maintained because the lobe structure is governed by the molecular structure and alignment rather than the phase of the circularly polarized pulses.

The above results show, that both the molecular alignment and the stability of the optical phase are required for the observation of the fine details characterizing the molecular FEVs. Hence, the retrieval of the rich structural and dynamical information encoded in the PMD from laboratory measurements requires optimal experimental conditions including molecular alignment and phase stability. An alternative to the alignment of molecules is the use of coincidence detection techniques (Ullrich et al., 2003) and post-selection of ionization events corresponding to a specific molecular alignment.

4 SUMMARY AND CONCLUSION

Free electron vortices (FEVs) created by photoionization of *atoms* with ultrashort polarization-tailored laser pulse sequences already exhibit a great variety of shapes, as recently reviewed in (Kerbstadt et al., 2019a; Kerbstadt et al., 2020, Eickhoff et al., 2021c). The photoelectron momentum distribution (PMD) of atomic FEVs is characterized by a regularly shaped multi-armed Archimedean spiral (in energy representation) (Pengel et al., 2017b), with controllable symmetry, rotational sense and spiral arm pitch (Kerbstadt et al., 2019b). However, *molecular* FEVs, studied in this contribution, display an even richer structure than their atomic counterparts, resulting from the interplay of three key features. The basic characteristic is the spiral-shaped interference pattern, fully analogous to that of atomic FEVs. This vortex shape is superimposed by a structural feature, due to the broken spherical symmetry of the molecule as opposed to an atom. Finally, a dynamical feature arises due to the nuclear degrees of freedom and the coupling between the electron and nuclear dynamics. The interplay of all these features results in a wide variety of details in the PMD and opens the door to the emerging field of molecular FEVs.

In this numerical study, we have explored the rich structures in the molecular FEVs and studied multiple interference phenomena underlying the ionization dynamics. Our strategy was based on the *ab initio* solution of the 2D time-dependent Schrödinger equation (TDSE) for a diatomic molecular ion with a single active electron, aligned in the polarization plane of a polarization-shaped ultrashort laser pulse. The molecular system was thoroughly characterized by the calculation of the Born-Oppenheimer potentials, eigenfunctions and transition dipole moments. The 2D TDSE model for the light-induced coupled electron-nuclear dynamics was employed to study the PMD created by a number of established laser pulse shapes (Eickhoff et al., 2021a), focusing on the creation of molecular FEVs by counterrotating circularly polarized double pulse sequences. We compared the results from single-photon ionization (SPI) and multiphoton ionization (MPI). The SPI findings were easier to interpret than the MPI results because the latter give rise to multiple ionization pathways (Eickhoff et al., 2021c) and are highly sensitive to intermediate resonances in the bound system. The physical properties of the molecular FEVs were analyzed taking into account various observables, including the fully differential 2D PMD, the (angle-integrated) energy spectrum and the (energy-integrated) angular distribution. In addition, we followed the time evolution of the electron density $|\psi|^2$ in coordinate space, to reveal the ionization dynamics in the bound molecular system and rationalize the vortex formation dynamics in the continuum. In the investigated MPI schemes, the evaluation of the bound state population dynamics allowed us to unambiguously identify intermediate resonances and unravel their signatures imprinted in the PMD.

Specifically, we presented three interrelated studies. In the first study, we explored the influence of the nuclear configuration on the molecular FEVs. For this purpose, we considered the interaction of a *rigid* molecule with different standard pulse shapes, already used for experiments on MPI of atoms, and analyzed the created PMDs for different internuclear separations R. In the limit $R \to 0$, the findings reproduced the experimental atomic FEV results and were well-understood in an atomic picture. In the limit $R \to \infty$, complex interference patterns were observed in the PMD, which were created by an interplay of two-center interference and Coulomb diffraction. In the intermediate R-regime, around the equilibrium distance R_0, the structure of the PMDs was found to be more intricate and more difficult to explain in a simple picture. This regime was relevant for the second study, in which we considered the interaction of a *vibrating* molecule with specifically designed counterrotating circularly polarized pulse sequences. By synchronization of the two subpulses to the molecular vibration, we investigated the interplay between the nuclear motion and the electronic excitation dynamics and identified signatures of the coupled electron-nuclear dynamics in the PMD of the molecular FEVs. First, we found that the nuclear dynamics result in a bimodal photoelectron kinetic energy spectrum, rationalized by Mullikan's difference potential analysis. Second, we observed the fingerprint of non-adiabatic phase dynamics of the ground state wave function, which manifested in a subtle but clearly visible radial modulation of the PMD. The latter finding demonstrates the high sensitivity of the PMD to non-adiabatic electron-nuclear dynamics in molecules and underscores the power of highly differential photoelectron detection techniques to reveal even subtle changes in the bound electronic wave function. Further characteristic features of the FEVs created by MPI could be attributed to the influence of two intermediate resonances, which were excited during different stages of the molecular vibration. All these results highlight the great importance of the interplay between the nuclear dynamics and electronic resonances in molecular MPI. The third study was relevant in view of the experimental implementation of molecular FEV scenarios. On the example of bichromatic two- vs. three-photon ionization, we compared the PMD obtained in the molecular frame to the PMD measured in the laboratory which is, in general, subject to different types of averaging. Specifically, we studied the influence of molecular rotation averaging and CEP-averaging. We found that in both cases, some of the fine details of the molecular FEVs were washed out. In order to retrieve the rich structural and dynamical information encoded in the PMD, it is essential to align the molecules prior to photoionization, or detect the momentum of the photoions in coincidence and post-select the events corresponding to a specific molecular alignment, and to stabilize the phase of the laser pulses.

In perspective, our 2D TDSE model will be refined towards the inclusion of quantum mechanical nuclear wave packet dynamics, i.e., a full quantum treatment of the coupled electron-nuclear dynamics. The refined model will allow more accurate simulation of the molecular FEVs generated by MPI in the presence of intermediate resonances. The numerical study presented here provides first insights into the rich variety of relevant physical mechanisms involved in the generation of molecular FEVs with shaped laser pulses and serves as preparatory work for the experimental implementation in the laboratory. The combination of white-light polarization pulse shaping (Pengel et al., 2017a; Kerbstadt et al., 2017b) with photoelectron tomography (Wollenhaupt et al., 2009b; Kerbstadt et al., 2019a) will enable the use of molecular FEVs as powerful spectroscopic tools to probe molecular structure and dynamics.

DATA AVAILABILITY STATEMENT

The original contributions presented in the study are included in the article/supplementary material, further inquiries can be directed to the corresponding author.

AUTHOR CONTRIBUTIONS

Building on previous experimental studies by both authors, TB and MW proposed to study the physics of molecular vortices by direct simulation of the two-dimensional TDSE. They developed the concept and structure of the manuscript and interpreted the results. In close cooperation with MW, TB prepared the figures, performed the numerical calculations, and wrote the manuscript. TB and MW contributed to the revision of the manuscript, read and approved the submitted version.

FUNDING

This research was funded by the Deutsche Forschungsgemeinschaft (DFG) *via* the priority program SPP1840 QUTIF.

REFERENCES

Armstrong, G. S. J., Clarke, D. D. A., Benda, J., Wragg, J., Brown, A. C., and van der Hart, H. W. (2019). Modeling Tomographic Measurements of Photoelectron Vortices in Counter-Rotating Circularly Polarized Laser Pulses. *Phys. Rev. A* 100, 063416. doi:10.1103/physreva.100.063416

Assion, A., Geisler, M., Helbing, J., Seyfried, V., and Baumert, T. (1996). Femtosecond Pump-Probe Photoelectron Spectroscopy: Mapping of Vibrational Wave-Packet Motion. *Phys. Rev. A* 54, R4605–R4608. doi:10.1103/physreva.54.r4605

Babiker, M., Bennett, C. R., Andrews, D. L., and Dávila Romero, L. C. (2002). Orbital Angular Momentum Exchange in the Interaction of Twisted Light with Molecules. *Phys. Rev. Lett.* 89, 143601. doi:10.1103/physrevlett.89.143601

Bandrauk, A. D., and Shen, H. (1993). Exponential Split Operator Methods for Solving Coupled Time-dependent Schrödinger Equations. *J. Chem. Phys.* 99, 1185–1193. doi:10.1063/1.465362

Bauer, D. (2017). *Computational Strong-Field Quantum Dynamics: Intense Light-Matter Interactions*, 1. Berlin/Boston: De Gruyter.

Baumert, T., Buehler, B., Grosser, M., Thalweiser, R., Weiss, V., Wiedenmann, E., et al. (1991). Femtosecond Time-Resolved Wave Packet Motion in Molecular Multiphoton Ionization and Fragmentation. *J. Phys. Chem.* 95, 8103–8110. doi:10.1021/j100174a019

Bayer, T., Braun, H., Sarpe, C., Siemering, R., von den Hoff, P., de Vivie-Riedle, R., et al. (2013). Charge Oscillation Controlled Molecular Excitation. *Phys. Rev. Lett.* 110, 123003. doi:10.1103/physrevlett.110.123003

Bayer, T., Gräfing, D., Kerbstadt, S., Pengel, D., Eickhoff, K., Englert, L., et al. (2019). Time-resolved 3d Imaging of Ultrafast Spin-Orbit Wave Packet Dynamics. *New J. Phys.* 21, 033001. doi:10.1088/1367-2630/aafb87

Bayer, T., Philipp, C., Eickhoff, K., and Wollenhaupt, M. (2020). Atomic Photoionization Dynamics in Ultrashort Cycloidal Laser Fields. *Phy. Rev. A* 102, 013104. doi:10.1103/physreva.102.013104

Becker, W., and Milošević, D. B. (2022). Elliptic Dichroism in Strong-Field Ionization of Atoms Subjected to Tailored Laser Fields. *Phys. Chem. Chem. Phys.* 24, 7014–7027. doi:10.1039/d1cp05209h

Ben, S., Chen, S., Bi, C.-R., Chen, J., and Liu, X.-S. (2020). Investigation of Electron Vortices in Time-Delayed Circularly Polarized Laser Pulses with a Semiclassical Perspective. *Opt. Express* 28, 29442–29454. doi:10.1364/oe.400846

Bian, X. B., and Bandrauk, A. D. (2012). Attosecond Time-Resolved Imaging of Molecular Structure by Photoelectron Holography. *Phys. Rev. Lett.* 108, 263003. doi:10.1103/physrevlett.108.263003

Bircher, M. P., Liberatore, E., Browning, N. J., Brickel, S., Hofmann, C., Patoz, A., et al. (2017). Nonadiabatic Effects in Electronic and Nuclear Dynamics. *Struct. Dyn.* 4, 061510. doi:10.1063/1.4996816

Bliokh, K. Y., Ivanov, I. P., Guzzinati, G., Clark, L., Van Boxem, R., Béché, A., et al. (2017). Theory and Applications of Free-Electron Vortex States. *Phys. Rep.* 690, 1–70. doi:10.1016/j.physrep.2017.05.006

Braun, H., Bayer, T., Sarpe, C., Siemering, R., Vivie-Riedle, R., Baumert, T., et al. (2014). Coupled Electron-Nuclear Wavepacket Dynamics in Potassium Dimers. *J. Phys. B* 47, 124015. doi:10.1088/0953-4075/47/12/124015

Carrasco, S., Rogan, J., Valdivia, J. A., Chang, B. Y., Malinovsky, V. S., and Sola, I. R. (2022). Circularly Polarized Light-Induced Potentials and the Demise of Excited States. *Phys. Chem. Chem. Phys.* 24, 2966–2973. doi:10.1039/d1cp04523g

Cattaneo, L., Vos, J., Bello, R. Y., Palacios, A., Heuser, S., Pedrelli, L., et al. (2018). Attosecond Coupled Electron and Nuclear Dynamics in Dissociative Ionization of H2. *Nat. Phys.* 14, 733–738. doi:10.1038/s41567-018-0103-2

Chen, Z., and He, F. (2020). Interference of Nuclear Wave Packets Carrying Different Angular Momenta in the Dissociation of H_2^+ in Strong Circularly Polarized Laser Pulses. *Phys. Rev. A* 102, 033107. doi:10.1103/physreva.102.033107

Chen, Z., He, P.-L., and He, F. (2020). Spiral Nuclear Momentum Distribution for the Dissociation of H_2^+ in a Circularly Polarized Laser Pulse. *Phys. Rev. A* 101, 033406. doi:10.1103/physreva.101.033406

Clarke, D. D. A., Armstrong, G. S. J., Brown, A. C., and van der Hart, H. W. (2018). R-matrix-with-time-dependence Theory for Ultrafast Atomic Processes in Arbitrary Light Fields. *Phys. Rev. A* 98, 053442. doi:10.1103/physreva.98.053442

Cohen, H. D., and Fano, U. (1966). Interference in the Photo-Ionization of Molecules. *Phys. Rev.* 150, 30–33. doi:10.1103/physrev.150.30

Djiokap, J. M. N., and Starace, A. F. (2017). Doubly-excited State Effects on Two-Photon Double Ionization of Helium by Time-Delayed, Oppositely Circularly-Polarized Attosecond Pulses. *J. Opt.* 19, 124003. doi:10.1088/2040-8986/aa8fc0

Djiokap, J. M. N., and Starace, A. F. (2021). Temporal Coherent Control of Resonant Two-Photon Double Ionization of the Hydrogen Molecule via Doubly Excited States. *Phys. Rev. A* 103, 053110. doi:10.1103/physreva.103.053110

Djiokap, J. M. N., Meremianin, A. V., Manakov, N. L., Madsen, L. B., Hu, S. X., and Starace, A. F. (2018). Dynamical Electron Vortices in Attosecond Double Photoionization of H_2. *Phys. Rev. A* 98, 063407. doi:10.1103/physreva.98.063407

Djiokap, J. M. N., Meremianin, A. V., and Manakov, N. L. (2021). Electron Interference in Atomic Ionization by Two Crossing Polarized Ultrashort Pulses. *Phys. Rev. A* 103, 023103. doi:10.1103/physreva.103.023103

Dörner, R., Mergel, V., Jagutzki, O., Spielberger, L., Ullrich, J., Moshammer, R., et al. (2000). Cold Target Recoil Ion Momentum Spectroscopy: a 'momentum Microscope' to View Atomic Collision Dynamics. *Phys. Rep.* 330, 95–192. doi:10.1016/s0370-1573(99)00109-x

Eckart, S., Richter, M., Kunitski, M., Hartung, A., Rist, J., Henrichs, K., et al. (2016). Nonsequential Double Ionization by Counterrotating Circularly Polarized Two-Color Laser Fields. *Phys. Rev. Lett.* 117, 133202. doi:10.1103/physrevlett.117.133202

Eckart, S., Kunitski, M., Ivanov, I., Richter, M., Fehre, K., Hartung, A., et al. (2018). Subcycle Interference upon Tunnel Ionization by Counter-rotating Two-Color Fields. *Phys. Rev. A* 97, 041402. doi:10.1103/physreva.97.041402

Eickhoff, K., Kerbstadt, S., Bayer, T., and Wollenhaupt, M. (2020a). Dynamic Quantum State Holography. *Phys. Rev. A* 101, 013430. doi:10.1103/physreva.101.013430

Eickhoff, K., Köhnke, D., Feld, L.-C., Englert, L., Bayer, T., and Wollenhaupt, M. (2020b). Tailored Holograms for Superimposed Vortex States. *New J. Phys.* 22, 123015. doi:10.1088/1367-2630/abc8b0

Eickhoff, K., Rathje, C., Köhnke, D., Kerbstadt, S., Englert, L., Bayer, T., et al. (2020c). Orbital Angular Momentum Superposition States in Transmission Electron Microscopy and Bichromatic Multiphoton Ionization. *New J. Phys.* 22, 103045. doi:10.1088/1367-2630/abbe54

Eickhoff, K., Englert, L., Bayer, T., and Wollenhaupt, M. (2021a). Multichromatic Polarization-Controlled Pulse Sequences for Coherent Control of Multiphoton Ionization. *Front. Phys.* 9, 444. doi:10.3389/fphy.2021.675258

Eickhoff, K., Feld, L., Köhnke, D., Bayer, T., and Wollenhaupt, M. (2021b). Trichromatic Shaper-Based Quantum State Holography. *Phys. Rev. A* 104, 052805. doi:10.1103/physreva.104.052805

Eickhoff, K., Feld, L., Köhnke, D., Englert, L., Bayer, T., and Wollenhaupt, M. (2021c). Coherent Control Mechanisms in Bichromatic Multiphoton Ionization. *J. Phys. B Atomic, Mol. Opt. Phys.* 54, 164002. doi:10.1088/1361-6455/ac11a0

Eickhoff, K., Köhnke, D., Feld, L., Bayer, T., and Wollenhaupt, M. (2022). *Determination of Atomic Multiphoton Ionization Phases by Trichromatic Multichannel Wave Packet Interferometry*. *Phys. Rev. A* 105, 053113.

Eiles, M. T. (2019). Trilobites, Butterflies, and Other Exotic Specimens of Long-Range Rydberg Molecules. *J. Phys. B* 52, 113001. doi:10.1088/1361-6455/ab19ca

Erdmann, M., Gross, E. K. U., and Engel, V. (2004). Time-dependent Electron Localization Functions for Coupled Nuclear-Electronic Motion. *J. Chem. Phys.* 121, 9666–9670. doi:10.1063/1.1806812

Feit, M. D., Fleck, J. A., and Steiger, A. (1982). Solution of the Schrödinger Equation by a Spectral Method. *J. Comp. Phys.* 47, 412–433. doi:10.1016/0021-9991(82)90091-2

Fernández, J., Yip, F. L., Rescigno, T. N., McCurdy, C. W., and Martín, F. (2009). Two-center Effects in One-Photon Single Ionization of H_2^+, H_2, and Li_2^+ with Circularly Polarized Light. *Phys. Rev. A* 79, 043409. doi:10.1103/physreva.79.043409

Gatti, F. (2014). *Molecular Quantum Dynamics: From Theory to Applications*. Berlin Heidelberg: Springer.

Gazibegović-Busuladžić, A., Becker, W., and Milošević, D. B. (2018). Helicity Asymmetry in Strong-Field Ionization of Atoms by a Bicircular Laser Field. *Opt. Express* 26, 12684–12697. doi:10.1364/oe.26.012684

Geng, L., Cajiao, V., F., Kamiński, J. Z., Peng, L.-Y., and Krajewska, K. (2020). Vortex Structures in Photodetachment by Few-Cycle Circularly Polarized Pulses. *Phys. Rev. A* 102, 043117. doi:10.1103/physreva.102.043117

Geng, L., Cajiao Vélez, F., Kamiński, J. Z., Peng, L.-Y., and Krajewska, K. (2021). Structured Photoelectron Distributions in Photodetachment Induced by Trains of Laser Pulses: Vortices versus Spirals. *Phys. Rev. A* 104, 033111. doi:10.1103/physreva.104.033111

Greene, C. H., Dickinson, A. S., and Sadeghpour, H. R. (2000). Creation of Polar and Nonpolar Ultra-long-range Rydberg Molecules. *Phys. Rev. Lett.* 85, 2458–2461. doi:10.1103/physrevlett.85.2458

Grossmann, F. (2018). *Theoretical Femtosecond Physics: Atoms and Molecules in Strong Laser Fields*. Berlin Heidelberg: Springer.

Guo, J., Zhang, S. Q., Zhang, J., Zhou, S. P., and Guan, P. F. (2021). Exploration of Electron Vortices in the Photoionization of Diatomic Molecules in Intense Laser Fields. *Laser Phys.* 31, 065301. doi:10.1088/1555-6611/abfb73

Hasović, E., Becker, W., and Milošević, D. B. (2016). Electron Rescattering in a Bicircular Laser Field. *Opt. Express* 24, 6413–6424. doi:10.1364/OE.24.006413

Heather, R., and Metiu, H. (1987). An Efficient Procedure for Calculating the Evolution of the Wave Function by Fast Fourier Transform Methods for Systems with Spatially Extended Wave Function and Localized Potential. *J. Chem. Phys.* 86, 5009–5017. doi:10.1063/1.452672

Hergenhahn, U., Rennie, E. E., Kugeler, O., Marburger, s., Lischke, T., Powis, I., et al. (2004). Photoelectron Circular Dichroism in Core Level Ionization of Randomly Oriented Pure Enantiomers of the Chiral Molecule Camphor. *J. Chem. Phys.* 120, 4553–4556. doi:10.1063/1.1651474

Hoff, D., Kruger, M., Maisenbacher, L., Sayler, A. M., Paulus, G. G., and Hommelhoff, P. (2017). Tracing the Phase of Focused Broadband Laser Pulses. *Nat. Phys.* 13, 947. doi:10.1038/nphys4185

Huismans, Y., Rouzée, A., Gijsbertsen, A., Jungmann, J. H., Smolkowska, A. S., Logman, P., et al. (2011). Time-resolved Holography with Photoelectrons. *Science* 331, 61–64. doi:10.1126/science.1198450

Ivanov, I. A., Nam, C. H., and Kim, K. T. (2017). Photoionization in the Presence of Circularly Polarized Fundamental and Odd-Order Harmonic Fields. *Phys. Rev. A* 95, 053401. doi:10.1103/physreva.95.053401

Jia, J., Cui, H., Zhang, C., Shao, J., Ma, J., and Miao, X. (2019). Investigation of the Photoionization Process of Helium Ion in Bichromatic Circularly Xuv Fields with Different Time Delays. *Chem. Phys. Lett.* 725, 119–123. doi:10.1016/j.cplett.2019.04.008

Ke, Q., Zhou, Y., Tan, J., He, M., Liang, J., Zhao, Y., et al. (2019). Two-dimensional Photoelectron Holography in Strong-Field Tunneling Ionization by Counter Rotating Two-Color Circularly Polarized Laser Pulses. *Opt. Express* 27, 32193–32209. doi:10.1364/oe.27.032193

Kerbstadt, S., Pengel, D., Johannmeyer, D., Englert, L., Bayer, T., and Wollenhaupt, M. (2017a). Control of Photoelectron Momentum Distributions by Bichromatic Polarization-Shaped Laser Fields. *New J. Phys.* 19, 103017. doi:10.1088/1367-2630/aa83a4

Kerbstadt, S., Timmer, D., Englert, L., Bayer, T., and Wollenhaupt, M. (2017b). Ultrashort Polarization-Tailored Bichromatic Fields from a CEP-Stable White Light Supercontinuum. *Opt. Express* 25, 12518. doi:10.1364/oe.25.012518

Kerbstadt, S., Pengel, D., Englert, L., Bayer, T., and Wollenhaupt, M. (2018). Carrier-envelope-phase Control of Asymmetries in the Multiphoton Ionization of Xenon Atoms by Ultrashort Bichromatic Fields. *Phys. Rev. A* 97, 063402. doi:10.1103/physreva.97.063402

Kerbstadt, S., Eickhoff, K., Bayer, T., and Wollenhaupt, M. (2019a). Control of Free Electron Wave Packets by Polarization-Tailored Ultrashort Bichromatic Laser Fields. *Adv. Phys. X* 4, 1672583. doi:10.1080/23746149.2019.1672583

Kerbstadt, S., Eickhoff, K., Bayer, T., and Wollenhaupt, M. (2019b). Odd Electron Wave Packets from Cycloidal Ultrashort Laser Fields. *Nat. Comm.* 10, 658. doi:10.1038/s41467-019-08601-7

Kerbstadt, S., Eickhoff, K., Bayer, T., and Wollenhaupt, M. (2020). *Bichromatic Control of Free Electron Wave Packets*. Cham, Switzerland: Springer, 43–76. book section 3. doi:10.1007/978-3-030-47098-2_3

Köhler, J., Wollenhaupt, M., Bayer, T., Sarpe, C., and Baumert, T. (2011). Zeptosecond Precision Pulse Shaping. *Opt. Express* 19, 11638–11653. doi:10.1364/oe.19.011638

Kong, X., Zhang, G., Li, M., Wang, T., Ding, X., and Yao, J. (2018). Odd-fold-symmetric Spiral Momentum Distributions and Their Stark Distortions in Hydrogen. *JOSA B* 35, 2163–2168. doi:10.1364/josab.35.002163

Kosloff, R., and Kosloff, D. (1986). Absorbing Boundaries for Wave Propagation Problems. *J. Comp. Phys.* 63, 363–376. doi:10.1016/0021-9991(86)90199-3

Li, M., Zhang, G., Zhao, T., Ding, X., and Yao, J. (2017a). Electron Vortices in Photoionization by a Pair of Elliptically Polarized Attosecond Pulses. *Chin. Opt. Lett.* 15, 120202. doi:10.3788/col201715.120202

Li, Z. L., Li, Y. J., and Xie, B. S. (2017b). Momentum Vortices on Pairs Production by Two Counter-rotating Fields. *Phys. Rev. D.* 96, 076010. doi:10.1103/physrevd.96.076010

Li, M., Zhang, G., Ding, X., and Yao, Y. (2018a). Symmetric Electron Vortices of Hydrogen Ionized by Orthogonal Elliptical Fields. *IEEE Photonics J.* 10, 1–9. doi:10.1109/jphot.2018.2854237

Li, M., Zhang, G., Kong, X., Wang, T., Ding, X., and Yao, J. (2018b). Dynamic Stark Induced Vortex Momentum of Hydrogen in Circular Fields. *Opt. Express* 26, 878–886. doi:10.1364/oe.26.000878

Li, Z. L., Xie, B. S., and Li, Y. J. (2018c). Vortices in Multiphoton Pair Production by Two-Color Rotating Laser Fields. *J. Phys. B* 52, 025601. doi:10.1088/1361-6455/aaf3f9

Li, M., Zhang, G., Ding, X., and Yao, J. (2019a). Ac Stark Effect on Vortex Spectra Generated by Circularly Polarized Pulses. *IEEE Photonics J.* 11, 1–11. doi:10.1109/jphot.2019.2916106

Li, M., Zhang, G. Z., Ding, X., and Yao, J. Q. (2019b). Carrier Envelope Phase Description for an Isolated Attosecond Pulse by Momentum Vortices. *Chin. Phys. Lett.* 36, 063201. doi:10.1088/0256-307x/36/6/063201

Li, D., Shan, H., Rupprecht, C., Knopf, H., Watanabe, K., Taniguchi, T., et al. (2022). Hybridized exciton-photon-phonon states in a transition metal dichalcogenide van der waals heterostructure microcavity. *Phys. Rev. Lett.* 128, 087401. doi:10.1103/PhysRevLett.128.087401

Lloyd, S. M., Babiker, M., Thirunavukkarasu, G., and Yuan, J. (2017). Electron Vortices: Beams with Orbital Angular Momentum. *Rev. Mod. Phys.* 89, 035004. doi:10.1103/revmodphys.89.035004

Lux, C., Wollenhaupt, M., Bolze, T., Liang, Q., Köhler, J., Sarpe, C., et al. (2012). Circular Dichroism in the Photoelectron Angular Distributions of Camphor and Fenchone from Multiphoton Ionization with Femtosecond Laser Pulses. *Angew. Chem. Int. Ed.* 51, 5001–5005. doi:10.1002/anie.201109035

Madelung, E. (1927). Quantentheorie in Hydrodynamischer Form. *Z. Phys.* 40, 322–326. doi:10.1007/bf01400372

Mancuso, C. A., Hickstein, D. D., Grychtol, P., Knut, R., Kfir, O., Tong, X. M., et al. (2015). Strong-field Ionization with Two-Color Circularly Polarized Laser Fields. *Phys. Rev. A* 91, 031402R. doi:10.1103/physreva.91.031402

Mancuso, C. A., Hickstein, D. D., Dorney, K. M., Ellis, J. L., Hasovic, E., Knut, R., et al. (2016). Controlling Electron-Ion Rescattering in Two-Color Circularly Polarized Femtosecond Laser Fields. *Phys. Rev. A* 93, 053406. doi:10.1103/physreva.93.053406

Marston, C. C., and Balint-Kurti, G. G. (1989). The Fourier Grid Hamiltonian Method for Bound State Eigenvalues and Eigenfunctions. *J. Chem. Phys.* 91, 3571–3576. doi:10.1063/1.456888

Maxwell, A., Armstrong, G. S. J., Ciappina, M., Pisanty, E., Kang, Y., Brown, A., et al. (2020). Manipulating Twisted Electrons in Strong Field Ionization. *Faraday Discuss.* 228, 394–412. doi:10.1063/1.1675522

Meshulach, D., and Silberberg, Y. (1999). Coherent Quantum Control of Multiphoton Transitions by Shaped Ultrashort Optical Pulses. *Phys. Rev. A* 60, 1287–1292. doi:10.1103/physreva.60.1287

Mulliken, R. S. (1971). Role of Kinetic Energy in the Franck-Condon Principle. *J. Chem. Phys.* 55, 309–314. doi:10.1063/1.1675522

Ngoko Djiokap, J. M., Hu, S. X., Madsen, L. B., Manakov, N. L., Meremianin, A. V., and Starace, A. F. (2015). Electron Vortices in Photoionization by Circularly Polarized Attosecond Pulses. *Phys. Rev. Lett.* 115, 113004. doi:10.1103/physrevlett.115.113004

Ngoko Djiokap, J. M., Meremianin, A. V., Manakov, N. L., Hu, S. X., Madsen, L. B., and Starace, A. F. (2016). Multistart Spiral Electron Vortices in Ionization by Circularly Polarized Uv Pulses. *Phys. Rev. A* 94, 013408. doi:10.1103/physreva.94.013408

Ngoko Djiokap, J. M., Meremianin, A. V., Manakov, N. L., Hu, S. X., Madsen, L. B., and Starace, A. F. (2017). Kinematical Vortices in Double Photoionization of Helium by Attosecond Pulses. *Phys. Rev. A* 96, 013405. doi:10.1103/physreva.96.013405

Nisoli, M., Decleva, P., Calegari, F., Palacios, A., and Martín, F. (2017). Attosecond Electron Dynamics in Molecules. *Chem. Rev.* 117, 10760–10825. doi:10.1021/acs.chemrev.6b00453

Novoselov, K. S., Fal'ko, V. I., Colombo, L., Gellert, P. R., Schwab, M. G., and Kim, K. (2012). A Roadmap for Graphene. *Nature* 490, 192–200. doi:10.1038/nature11458

Pengel, D., Kerbstadt, S., Englert, L., Bayer, T., and Wollenhaupt, M. (2017a). Control of Three-Dimensional Electron Vortices from Femtosecond Multiphoton Ionization. *Phys. Rev. A* 96, 043426. doi:10.1103/physreva.96.043426

Pengel, D., Kerbstadt, S., Johannmeyer, D., Englert, L., Bayer, T., and Wollenhaupt, M. (2017b). Electron Vortices in Femtosecond Multiphoton Ionization. *Phys. Rev. Lett.* 118, 053003. doi:10.1103/PhysRevLett.118.053003

Powis, I. (2008). Photoelectron Circular Dichroism in Chiral Molecules. *Adv. Chem. Phys.* 138, 267–329. doi:10.1002/9780470259474.ch5

Qin, Y. N., Li, M., Feng, Y., Luo, S., Zhou, Y., and Lu, P. (2020). Extracting the Phase Distribution of the Electron Wave Packet Ionized by an Elliptically Polarized Laser Pulse. *Front. Phys.* 16, 32502. doi:10.1007/s11467-020-1017-x

Rice, S. A., and Zhao, M. (2000). *Optical Control of Molecular Dynamics*. New York: Wiley.

Santra, R. (2006). Why Complex Absorbing Potentials Work: A Discrete-Variable-Representation Perspective. *Phys. Rev. A* 74, 034701. doi:10.1103/physreva.74.034701

Shaffer, J. P., Rittenhouse, S. T., and Sadeghpour, H. R. (2018). Ultracold Rydberg Molecules. *Nat. Comm.* 9, 1965. doi:10.1038/s41467-018-04135-6

Shen, Y., Wang, X., Xie, Z., Min, C., Fu, X., Liu, Q., et al. (2019). Optical Vortices 30 Years on: Oam Manipulation from Topological Charge to Multiple Singularities. *Light Sci. Appl.* 8, 1–29. doi:10.1038/s41377-019-0194-2

Shin, S., and Metiu, H. (1995). Nonadiabatic Effects on the Charge Transfer Rate Constant: A Numerical Study of a Simple Model System. *J. Chem. Phys.* 102, 9285–9295. doi:10.1063/1.468795

Shin, S., and Metiu, H. (1996). Multiple Time Scale Quantum Wavepacket Propagation: Electron-Nuclear Dynamics. *J. Phys. Chem.* 100, 7867–7872. doi:10.1021/jp952498a

Shu, C.-C., Guo, Y., Yuan, K.-J., Dong, D., and Bandrauk, A. D. (2020). Attosecond All-Optical Control and Visualization of Quantum Interference between Degenerate Magnetic States by Circularly Polarized Pulses. *Opt. Lett.* 45, 960–963. doi:10.1364/ol.386879

Shvetsov-Shilovski, N. I., and Lein, M. (2022). Deep Learning for Retrieval of the Internuclear Distance in a Molecule from Interference Patterns in Photoelectron Momentum Distributions. *Phys. Rev. A* 105, L021102. doi:10.1103/physreva.105.l021102

Sprik, M., and Klein, M. L. (1988). Optimization of a Distributed Gaussian Basis Set Using Simulated Annealing: Application to the Adiabatic Dynamics of the Solvated Electron. *J. Chem. Phys.* 89, 1592–1607. doi:10.1063/1.455156

Tal-Ezer, H., and Kosloff, R. (1986). A Direct Relaxation Method for Calculating Eigenfunctions and Eigenvalues of the Schr Odinger Equation. *Chem. Phys. Lett.* 127, 223.

Tannor, D. (2007). *Introduction to Quantum Mechanics: A Time-dependent Perspective*. Sausalito: University Science Books.

Ullrich, J., Moshammer, R., Dorn, A., Dörner, R., Schmidt, L. P. H., and Schmidt-Böcking, H. (2003). Recoil-ion and Electron Momentum Spectroscopy: Reaction-Microscopes. *Rep. Prog. Phys.* 66, 1463–1545. doi:10.1088/0034-4885/66/9/203

Verbeeck, J., Tian, H., and Schattschneider, P. (2010). Production and Application of Electron Vortex Beams. *Nature* 467, 301. doi:10.1038/nature09366

Wang, R., Zhang, Q., Ran, C., Cao, W., and Lu, P. (2020). Proposal for Detecting Ring Current via Electron Vortices. *Opt. Lett.* 45, 1383–1386. doi:10.1364/ol.388516

Winter, M., Wollenhaupt, M., and Baumert, T. (2006). Coherent Matter Waves for Ultrafast Laser Pulse Characterization. *Opt. Comm.* 264, 285–292. doi:10.1016/j.optcom.2005.12.079

Wollenhaupt, M., Assion, A., Liese, D., Sarpe-Tudoran, C., Baumert, T., Zamith, S., et al. (2002). Interferences of Ultrashort Free Electron Wave Packets. *Phys. Rev. Lett.* 89, 173001. doi:10.1103/physrevlett.89.173001

Wollenhaupt, M., Assion, A., Graefe, O., Liese, D., Sarpe-Tudoran, C., Winter, M., et al. (2003). Changes of the Electronic Structure along the Internuclear Coordinate Studied by Ultrafast Photoelectron Spectroscopy: the $2^1\ \Sigma_u^+$ Na_2 Double Minimum State. *Chem. Phys. Lett.* 376, 457–464. doi:10.1016/s0009-2614(03)00994-1

Wollenhaupt, M., Engel, V., and Baumert, T. (2005). Femtosecond Laser Photoelectron Spectroscopy on Atoms and Small Molecules: Prototype Studies in Quantum Control. *Annu. Rev. Phys. Chem.* 56, 25–56. doi:10.1146/annurev.physchem.56.092503.141315

Wollenhaupt, M., Krug, M., Köhler, J., Bayer, T., Sarpe-Tudoran, C., and Baumert, T. (2009a). Photoelectron Angular Distributions from Strong-Field Coherent Electronic Excitation. *Appl. Phys. B* 95, 245–259. doi:10.1007/s00340-009-3431-1

Wollenhaupt, M., Krug, M., Köhler, J., Bayer, T., Sarpe-Tudoran, C., and Baumert, T. (2009b). Three-dimensional Tomographic Reconstruction of Ultrashort Free Electron Wave Packets. *Appl. Phys. B* 95, 647–651. doi:10.1007/s00340-009-3513-0

Wollenhaupt, M., Lux, C., Krug, M., and Baumert, T. (2013). Tomographic Reconstruction of Designer Free-Electron Wave Packets. *Chem. Phys. Chem.* 14, 1341–1349. doi:10.1002/cphc.201200968

Xiao, X.-R., Wang, M.-X., Liang, H., Gong, Q., and Peng, L.-Y. (2019). Proposal for Measuring Electron Displacement Induced by a Short Laser Pulse. *Phys. Rev. Lett.* 122, 053201. doi:10.1103/PhysRevLett.122.053201

Yuan, K.-J., and Bandrauk, A. D. (2015). Electron Interference in Molecular Circular Polarization Attosecond Xuv Photoionization. *Photonics* 2, 71–92. doi:10.3390/photonics2010071

Yuan, K.-J., Chelkowski, S., and Bandrauk, A. D. (2016). Photoelectron Momentum Distributions of Molecules in Bichromatic Circularly Polarized Attosecond UV Laser Fields. *Phys. Rev. A* 93, 053425. doi:10.1103/physreva.93.053425

Yuan, K. J., Lu, H. Z., and Bandrauk, A. D. (2017). Photoionization of Triatomic Molecular Ions H_3^{2+} by Intense Bichromatic Circularly Polarized Attosecond Uv Laser Pulses. *J. Phys. B* 50, 124004.

Zewail, A. H. (1995). *Femtochemistry: Concepts and Applications*. Weinheim: VCH Verlagsgesellschaft mbH, 15–130.

Zewail, A. H. (2000). Femtochemistry: Atomic-Scale Dynamics of the Chemical Bond Using Ultrafast Lasers. *Angew. Chem. Int. Ed.* 39, 2586–2631. doi:10.1002/1521-3773(20000804)39:15<2586::aid-anie2586>3.0.co;2-o

Zhen, Q., Zhang, H.-D., Zhang, S.-Q., Ji, L., Han, T., and Liu, X.-S. (2020). Generation of Electron Vortices in Photoionization by Counter-rotating Circularly Polarized Attosecond Pulses. *Chem. Phys. Lett.* 738, 136885. doi:10.1016/j.cplett.2019.136885

Conflict of Interest: The authors declare that the research was conducted in the absence of any commercial or financial relationships that could be construed as a potential conflict of interest.

frontiers | Frontiers in Chemistry

ORIGINAL RESEARCH
published: 05 August 2022
doi: 10.3389/fchem.2022.942633

Nuclear–Electron Correlation Effects and Their Photoelectron Imprint in Molecular XUV Ionisation

Karl Michael Ziems[1,2], Jakob Bruhnke[1], Volker Engel[3] and Stefanie Gräfe[1,2,4,5]*

[1]Institute of Physical Chemistry, Friedrich Schiller University Jena, Jena, Germany, [2]Max Planck School of Photonics, Jena, Germany, [3]Institut für Physikalische und Theoretische Chemie, Universität Würzburg, Würzburg, Germany, [4]Abbe Center of Photonics, Friedrich Schiller University, Jena, Germany, [5]Fraunhofer Institute for Applied Optics and Precision Engineering, Jena, Germany

The ionisation of molecules by attosecond XUV pulses is accompanied by complex correlated dynamics, such as the creation of coherent electron wave packets in the parent ion, their interplay with nuclear wave packets, and a correlated photoelectron moving in a multi-centred potential. Additionally, these processes are influenced by the dynamics prior to and during the ionisation. To fully understand and subsequently control the ionisation process on different time scales, a profound understanding of electron and nuclear correlation is needed. Here, we investigate the effect of nuclear–electron correlation in a correlated two-electron and one-nucleus quantum model system. Solving the time-dependent Schrödinger equation allows to monitor the correlation impact pre, during, and post-XUV ionisation. We show how an initial nuclear wave packet displaced from equilibrium influences the post-ionisation dynamics by means of momentum conservation between the target and parent ion, whilst the attosecond electron population remains largely unaffected. We calculate time-resolved photoelectron spectra and their asymmetries and demonstrate how the coupled electron–nuclear dynamics are imprinted on top of electron–electron correlation on the photoelectron properties. Finally, our findings give guidelines towards when correlation resulting effects have to be incorporated and in which instances the exact correlation treatment can be neglected.

Keywords: ultrafast phenomena, XUV, attosecond dynamics, photoionisation, TDSE, correlation effects, entanglement, photoelectron spectrum

Edited by:
Yuichi Fujimura,
Tohoku University, Japan

Reviewed by:
Nadia Rega,
University of Naples Federico II, Italy
Sabyashachi Mishra,
Indian Institute of Technology Kharagpur, India

Correspondence:
Stefanie Gräfe
s.graefe@uni-jena.de

Specialty section:
This article was submitted to Physical Chemistry and Chemical Physics,
a section of the journal Frontiers in Chemistry

Received: *12 May 2022*
Accepted: *20 June 2022*
Published: *05 August 2022*

Citation:
Ziems KM, Bruhnke J, Engel V and Gräfe S (2022) Nuclear–Electron Correlation Effects and Their Photoelectron Imprint in Molecular XUV Ionisation.
Front. Chem. 10:942633.
doi: 10.3389/fchem.2022.942633

1 INTRODUCTION

The fact that, if formerly non-interacting particles have interacted at some time, their wave function can no longer be expressed in a simple product form (Blum, 2012), has far-reaching consequences in many particle systems. For example, this situation appears in electronic structure calculations and there is termed electron–electron correlation (Kutzelnigg, 1994). The latter determines—to a great deal—the structure and behaviour of matter. In the field of quantum information, this correlation effect is associated with the entanglement of particles (Nielson and Chuang, 2000; Horodecki et al., 2009). As for molecules, not only electron–electron but also electron–nuclear and nuclear–nuclear interactions are of importance. Here, nuclear geometry deformations, in general, lead to the modification of the electronic density, which is responsible for chemical bonding.

The interaction of molecules with strong and ultrashort laser pulses leads, besides many other strong-field phenomena (Wolter et al., 2015; Pukhov, 2002; Krausz and Ivanov, 2009; Corkum and Krausz, 2007; Joachain et al., 2012), to single or multiple ionisation. A single XUV pulse is able to directly produce photoelectrons with different kinetic energies. With respect to the particle correlations mentioned previously, several questions arise where some of these are: What does a coupled electronic–nuclear motion look like during and after the ionisation process? Can features appearing in photoelectron spectra be related to electron–electron and electron–nuclear correlation? What characteristics appear in the post-ionisation dynamics of the charged particles?

Such fundamental issues will be taken up in the present work. Naturally, regarding the complexity of a molecule possessing many electronic and nuclear degrees of freedom, a complete quantum description of a field-triggered ionisation is simply out of reach today. One may then search for physically reasonable models to address the questions posed. It should be clear that they have to go beyond single active electron approximations and include the motion of the nuclei, most desirably on the same level as the electrons. In an early study, Lein et al. (2002) studied the single and double ionisation of the hydrogen molecule involving the motion of all particles in a single dimension and Sukiasyan et al. (2012) described the one-electron photoionisation for a 1D-Helium atom with two active electrons. To understand the impact of ionisation on the parent ion dynamics in real molecules, approximated quantum chemical methods neglecting the explicit ionisation pump can be applied and are powerful tools to unravel electron dynamics post ionisation (Ayuso et al., 2017; Nisoli et al., 2017) and study the nuclear decoherence effect on electronic wave packets (Vacher et al., 2015, 2017).

A useful model to study electron–nuclear correlation effects is the so-called Shin–Metiu model (Shin and Metiu, 1995, 1996). It consists of an electron and a nucleus that move in one dimension in an additional field of two positive charges. Originally devised to describe charge-transfer processes, it was later used to illustrate features of, e.g., coupled electronic–nuclear quantum (Hader et al., 2017; Albert et al., 2017; Schaupp and Engel, 2019b, 2022) and classical dynamics (Schaupp and Engel, 2019a) or two-dimensional coherent femtosecond spectroscopy (Albert et al., 2015). The model was also used to study photoionisation (Falge et al., 2011, 2012a, 2017).

The simple Shin–Metiu model was later extended to include the motion of a second electron, which made it possible to introduce time-dependent electron localisation functions (ELF) and characterise the influence of nuclear motion on these (Erdmann et al., 2004). Also, the wave-packet dynamics in spin-coupled electronic states could be described (Falge et al., 2012b).

Here, we extend our work on XUV ionisation in a molecular model system comprised of fully correlated two electrons and one nucleus (Fröbel et al., 2020). We study the impact of electron–nuclear correlation upon electron–electron correlation on the complete XUV ionisation process monitoring the influence pre, during, and post ionisation. Consequently, we dissect the effects on the parent ion, as well as on the photoelectron. Finally, we report on an imprint of the two-electron correlated bound dynamics on the photoelectron spectrum's asymmetry, thus yielding an observable to measure the electrons' density behaviour caused by nuclear correlation. This is a natural extension of our former work limited to a single active electron system (Falge et al., 2012a, 2017) and shows that the concept also holds for more complex systems. Moreover, by thoroughly dissecting the different effects present in a full quantum dynamical study with correlated particles, we provide guidance for future investigations resting on more approximated methods.

This study is organised as follows: In **Section 2**, we briefly introduce the model system, its potential energy surface, the numerical details for solving the time-dependent Schrödinger equation (TDSE), and different analysis tools. In presenting our results, we start by introducing the laser-free non-equilibrium dynamics and, subsequently, report on the impact of correlation effects on 1) the attosecond electron dynamics during ionisation, 2) the post-ionisation dynamics in the parent ions, and 3) the photoelectron. In the last section, we discuss how the asymmetry of the integrated photoelectron spectra shows imprints of resonance dependencies into the continuum and the coupled electron–nuclear dynamics.

2 THEORETICAL BACKGROUND

In the following, we briefly describe the model system and numerical procedure. For more details, we refer to our recent work (Fröbel et al., 2020), where we introduce the model in the context of ionisation. Atomic units are used throughout the study.

2.1 Molecular Model System

2.1.1 Full Three-Dimensional Model

To capture electron–nuclear and electron–electron correlation in molecular XUV ionisation, we use the one-dimensional extended Shin–Metiu model system, which includes two electrons (x, y) and a central nucleus with coordinate R (Shin and Metiu, 1995, 1996; Erdmann et al., 2004). Furthermore, two fixed nuclear point charges (Z_1, Z_2) at $\pm L/2$ define the outer potential barriers. The particle configuration is sketched in **Figure 1A**. The molecular Hamiltonian reads:

$$\mathcal{H}_0 = \frac{\hat{P}^2}{2M} + \frac{\hat{p}_x^2}{2} + \frac{\hat{p}_y^2}{2} + \hat{V}^{2e}(x, y, R), \tag{1}$$

where M is the nuclear mass, $\hat{P}$ the nuclear momentum operator, and $\hat{p}_x, \hat{p}_y$ the electron momentum operators. The potential is defined as:

$$\begin{aligned}\hat{V}^{2e}(x, y, R) = {} & \frac{Z_1 Z}{|L/2 - R|} + \frac{Z_2 Z}{|L/2 + R|} - \frac{Z \operatorname{erf}(|R - y|/R_c)}{|R - y|} \\ & - \frac{Z_1 \operatorname{erf}\left(|L/2 - y|/R_f\right)}{|L/2 - y|} - \frac{Z_2 \operatorname{erf}\left(|L/2 + y|/R_f\right)}{|L/2 + y|} \\ & - \frac{Z \operatorname{erf}(|R - x|/R_c)}{|R - x|} - \frac{Z_1 \operatorname{erf}\left(|L/2 - x|/R_f\right)}{|L/2 - x|} \\ & - \frac{Z_2 \operatorname{erf}\left(|L/2 + x|/R_f\right)}{|L/2 + x|} + \frac{\operatorname{erf}(|x - y|/R_e)}{|x - y|}.\end{aligned} \tag{2}$$

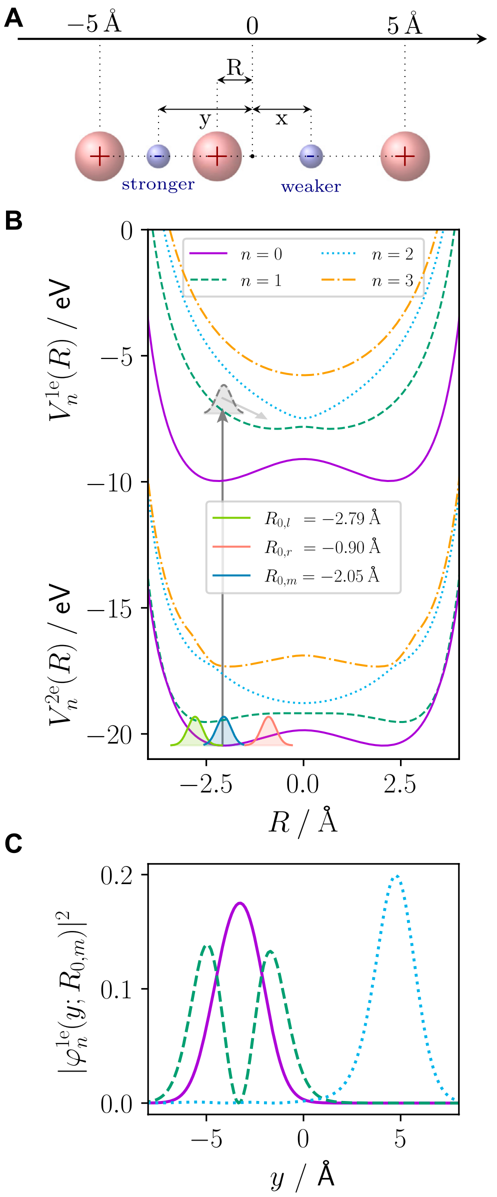

FIGURE 1 | (A) Extended Shin–Metiu model system: two electrons (x, y) and one nucleus l move in one dimension in the field of the two outer fixed (point charge) nuclei (R). For $R < 0$ as in the focus of investigation here, the left electron (here: y) is stronger bound, while the right electron (here: x) is weaker bound. The electrons are indistinguishable and are just given defined labels here for visualisation purposes. **(B)** PECs of the 2e system, $V_n^{2e}(R)$, and the 1e parent ion, $V_n^{1e}(R)$. The vertical line indicates one-photon ionisation and the population of the parent ion states. As an example, the nuclear wave packet in the $n = 1$ ion state is shown together with the gradient exerted by the PEC on it (grey shaded Gaussian). In the 2e system ground state ($n = 0$), the three different initial nuclear wave packets investigated in this work are shown. The nuclear wave packet near the equilibrium position of $R_{0,m} = -2.05$ Å (blue shaded Gaussian), and the two non-equilibrium starting wave packets starting at the isopotential turning points left, $R_{0,l} = -2.79$ Å (green shaded Gaussian), and right, $R_{0,r} = -0.90$ Å (red shaded Gaussian), of the equilibrium. **(C)** The absolute square of the first three 1e parent ion wave functions shows that $n = 2$ (blue dotted) is located at $y > 0$ (weaker bound).

Here, we set the charges $Z_1 = Z_2 = Z = 1$, M to the proton mass, the screening parameters $R_c = R_f = R_e = 1.5$ Å and $L = 10$ Å for the outer point charges. The potential contains soft Coulomb interactions between the moving particles, parameterised by error functions (erf). The model mimics a generic molecular system leading to a qualitative description of processes. It does not represent a specific class of molecules, such as linear molecules, especially since the central moving nucleus has unscreened interactions with the outer fixed nuclei preventing dissociation. Such effect would be essential for strong-field interactions with seemingly similar linear triatomic systems, but they are not in the scope of this work. Moreover, we are restricted to one nuclear degree of freedom, thus, not investigating nuclear–nuclear correlation. Since the model is one-dimensional, effects of the orbital angular momentum of the electrons are not regarded. We note that the system is already of ionic type. Nevertheless, in what follows, we will refer to the removal of an electron by the external field as an ionisation process.

While the reduced dimensionality of the model allows for solving the dynamics of all three particles, for interpretation, it is useful to obtain the electronic eigenstates and the potential energy curves (PECs) of the two-electron (2e) system. Therefore, we solve the time-independent electronic Schrödinger equation:

$$\left[\frac{\hat{p}_x^2}{2} + \frac{\hat{p}_y^2}{2} + \hat{V}^{2e}(x, y, R)\right]\varphi_n^{2e}(x, y; R) = V_n^{2e}(R)\,\varphi_n^{2e}(x, y; R). \tag{3}$$

where $\hat{p}_x$ and $\hat{p}_y$ are the electronic momentum operators. This yields the adiabatic electronic eigenstates $\varphi_n^{2e}(x, y; R)$ and the potentials $V_n^{2e}(R)$. All our calculations are restricted to the singlet case, i.e., the appearing wave functions are symmetric upon exchanging x and y. Upon removal of an electron through the XUV interaction, the remaining one-electron (1e) parent ion system has the potential:

$$\begin{aligned}\hat{V}^{1e}(y, R) = {} & \frac{Z_1 Z}{|L/2 - R|} + \frac{Z_2 Z}{|L/2 + R|} - \frac{Z\,\mathrm{erf}(|R - y|/R_c)}{|R - y|} \\ & - \frac{Z_1\,\mathrm{erf}\left(|L/2 - y|/R_f\right)}{|L/2 - y|} - \frac{Z_2\,\mathrm{erf}\left(|L/2 + y|/R_f\right)}{|L/2 + y|}.\end{aligned} \tag{4}$$

The respective electronic eigenstates ($\varphi_n^{1e}(y; R)$) and the PECs ($V_n^{1e}(R)$) are determined by the time-independent electronic Schrödinger equation

$$\left[\frac{\hat{p}_y^2}{2} + \hat{V}^{1e}(y, R)\right]\varphi_n^{1e}(y; R) = V_n^{1e}(R)\,\varphi_n^{1e}(y; R). \tag{5}$$

The PECs of both the 2e and 1e systems are shown in **Figure 1B** for the lowest four electronic eigenstates. It is important to point out that for the 1e system (parent ion), and $R < 0$ (which is the case throughout this work), the electron resides either left, at negative y values (stronger bound), or right, at positive y values (weaker bound), of the central nucleus depending on its electronic state. For the $n = 2$ 1e state, the electronic eigenfunction's probability density, $|\varphi_2^{1e}(y;R)|^2$, is located at the weaker bound site. The other 1e states shown in **Figure 1C** are located left of the central nucleus (stronger bound site).

We define the initial wave function as the product of the 2e adiabatic ground state ($n = 0$) and a Gaussian-shaped vibrational wave packet, $\chi(R)$:

$$\chi(R) = N_0\, e^{-\beta_R \left(R - R_{0,l/m/r}\right)^2}, \tag{6}$$

$$\Psi(x, y, R, t_0) = \varphi_0^{2e}(x, y; R)\,\chi(R), \tag{7}$$

with the normalisation constant N_0 and $\beta_R = 7.14$ Å^{-2}. As shown in **Figure 1B**, we regard three different initial vibrational wave packets, which differ with respect to the centre of the Gaussian in **Eq. 6**. In particular, we use the equilibrium configuration $R_{0,m} = -2.05$ Å (blue shaded Gaussian), and two non-equilibrium configurations, where one is placed to the left $R_{0,l} = -2.79$ Å (green shaded Gaussian) and the other to the right $R_{0,r} = -0.90$ Å (red shaded Gaussian) of $R_{0,m}$. The two non-equilibrium positions were chosen isopotentially.

The system interacts with a linearly polarised XUV pulse defined via its vector potential, $\mathcal{A}(t)$, with polarisation aligned along with the molecular axis of the model:

$$\mathcal{A}(t) = \frac{E_0}{\omega}\, g(t + t_0)\, \sin(\omega(t + t_0)). \tag{8}$$

We use an electric field strength of $E_0 = 0.169$ a.u. (corresponding to an intensity of $I = 10^{15}$ W/cm^2), an angular frequency of $\omega = 0.570$ a.u. ($\lambda = 80$ nm $= 15.5$ eV), and a full-width at half-maximum (FWHM) of $\tau = 5$ fs for the Gaussian pulse envelope function $g(t)$. The comparatively long FWHM was chosen to avoid possible few-cycle effects leading to pulse-dependent intrinsic asymmetries in the photoelectron spectrum (PES). For the parameters chosen here, the light pulse does not influence the asymmetry of the PES, and despite the high field strength, the simple one-photon picture of energy conservation between light pulse, parent ion, and photoelectron holds. The different pulse interaction times t_0, for different simulation setups are discussed and introduced as follows: the propagation starts at $t = t_0 - 2\tau$. The full time-dependent Hamiltonian in velocity gauge and dipole approximation reads:

$$\mathcal{H}(t) = \frac{\hat{P}^2}{2M} + \frac{\hat{p}_x^2}{2} + \frac{\hat{p}_y^2}{2} + \hat{V}^{2e}(x, y, R) + e\,\mathcal{A}(t)\left(-\frac{\hat{P}}{M} + \hat{p}_x + \hat{p}_y\right), \tag{9}$$

2.1.2 Approximations: Frozen and Single Point Charge Nucleus

In order to understand the role of the nuclear degree-of-freedom in the quantum dynamical simulations, we compare the complete electron–nuclear dynamics to the case of *1*) a frozen nuclear wave packet and *2*) a single point charge calculation. In the frozen nuclear wave packet approximation, *1*), the nuclear dimension becomes parametric and is only used to sample the nuclear wave packet on the grid by several 2D simulations of the electronic degrees of freedom. Hence, the Hamiltonian, **Eq. 9**, is missing the nuclear kinetic energy and XUV interaction term. The R-dimension in the potential and the wave function becomes parametric. The single point calculation, *2*), completely neglects the wave packet nature of the central nucleus and treats the central nucleus as a point charge at a fixed position leading to a single 2D simulation of the electronic degrees of freedom. This leaves the Hamiltonian of **Eq. 9** without any explicit or parametric R dependence, yielding a two-dimensional wave function depending on x, y.

2.2 Numerical Details

The time-dependent Schrödinger equation is as follows:

$$i\frac{\partial}{\partial t}\Psi(x, y, R, t) = \mathcal{H}(t)\Psi(x, y, R, t), \tag{10}$$

with the Hamiltonian defined in **Eq. 9** is solved numerically on a grid of dimensions $[-240, 240]$Å with 1,024 grid points for x and y (electronic dimensions) and $[-4.99, 4.99]$Å with 128 grid points for R (nuclear dimension). The integration is performed with a time step of 5as using the split-operator technique (Feit et al., 1982) and the FFTW three libraries (Frigo and Johnson, 1998) for Fourier transforms. This setup is used for all calculations unless stated otherwise. The time-independent 2e and 1e Schrödinger equations defined in **Eqs. (3)** and **(5)**, respectively, are numerically solved with the relaxation method, solving the TDSE in imaginary time (Kosloff and Tal-Ezer, 1986).

To avoid grid reflection, cut-off functions are applied each time step to the full wave function in the asymptotic region of the molecular potential

$$f(x, y) = \left[1 + e^{\zeta_1\,(|x| - \zeta_2)}\right]^{-1}\left[1 + e^{\zeta_1\,(|y| - \zeta_2)}\right]^{-1} \tag{11}$$

with the parameters $\zeta_1 = 0.085$ a.u. and $\zeta_2 = 492$ a.u. (Heather and Metiu, 1987).

In the following, we introduce three analysis tools of the full-wave function, $\Psi(x, y, R, t)$, in order to arrive at a deeper understanding of the ionisation dynamics. The exact ionised wave function comprised of having one electron in the continuum, whilst the other electron is still bound in the parent ion is unknown for such molecular, many-particle, and multi-centred systems. The following approaches circumvent this problem by using grid-based functions and projection operators.

2.2.1 Outer Wave Functions, $\Psi_{\mathrm{out}}^{\mathrm{fwd/bwd}}(p_x, y, R, t)$, Long-Time Limit

To obtain the part of the wave function representing the ionised system at long times, the outgoing parts of the wave function in x direction are collected. Since the wave function is fully mirror symmetric in x and y, we arbitrarily choose x as a dimension of ionisation, while y characterises the bound electron in the parent ion. To this end, we define a mask function in forward (fwd), $x > 0$, and backward (bwd), $x < 0$, direction using the same values of ζ_1, ζ_2 as mentioned previously.

$$\tilde{f}^{\mathrm{fwd}}(x,y) = \left(1 - \left[1 + \mathrm{e}^{\zeta_1\,(x-\zeta_2)}\right]^{-1}\right)\Theta\left(25\,\text{Å} - |y|\right), \tag{12}$$

$$\tilde{f}^{\mathrm{bwd}}(x,y) = \left(1 - \left[1 + \mathrm{e}^{\zeta_1\,(-x-\zeta_2)}\right]^{-1}\right)\Theta\left(25\,\text{Å} - |y|\right), \tag{13}$$

where the Heaviside function restricts the outer wave function to grid values of $-25\,\text{Å} < y < 25\text{Å}$, thus, neglecting double ionisation. At each time step, $\tilde{f}^{\mathrm{fwd/bwd}}(x,y)$ is applied to the total wave function, Fourier-transformed (FT) with respect to the electronic coordinate x and added coherently to the parts already localised in the outer regions in order to yield the outer wave functions:

$$\Psi_{\mathrm{out}}^{\mathrm{fwd/bwd}}(p_x,y,R,t) = \Psi_{\mathrm{out}}^{\mathrm{fwd/bwd}}(p_x,y,R,t-\Delta t) + \mathcal{FT}_x\left[\tilde{f}^{\mathrm{fwd/bwd}}(x,y)\Psi(x,y,R,t)\right]. \tag{14}$$

Consequently, $\Psi_{\mathrm{out}}^{\mathrm{fwd/bwd}}(p_x,y,R,t)$ is only propagated in momentum space in x dimension. The outer wave functions are used to calculate the PESs, state resolved to particular 1e states in the parent ion, $\sigma_n^{\mathrm{fwd/bwd}}(p_x)$, and to obtain the total integrated asymmetry A. The former is obtained by projection on the adiabatic 1e states at the end of the time propagation, in the limit $t \to \infty$

$$\sigma_n^{\mathrm{fwd/bwd}}(p_x) = \int\left|\int \varphi_n^{1e}(y;R)\Psi_{\mathrm{out}}^{\mathrm{fwd/bwd}}(p_x,y,R,t\to\infty)\,\mathrm{d}y\right|^2\mathrm{d}R. \tag{15}$$

The total integrated asymmetry of the PES is calculated as

$$A = \sum_n \int \frac{\sigma_n^{\mathrm{fwd}}(p_x) - \sigma_n^{\mathrm{bwd}}(p_x)}{\sigma_n^{\mathrm{fwd}}(p_x) + \sigma_n^{\mathrm{bwd}}(p_x)}\mathrm{d}p_x. \tag{16}$$

2.2.2 Channel Wave Functions, $\Psi_{\mathrm{ch}}^{\mathrm{fwd/bwd}}(x,y,R,t)$, Intermediate Times

In order to investigate the ionised system at intermediate times in fwd and bwd directions, we define the channel wave functions.

$$\Psi_{\mathrm{ch}}^{\mathrm{fwd}}(x,y,R,t) = \Theta\left(-25\,\text{Å} + x\right)\Theta\left(25\,\text{Å} - |y|\right)\Psi(x,y,R,t), \tag{17}$$

$$\Psi_{\mathrm{ch}}^{\mathrm{bwd}}(x,y,R,t) = \Theta\left(-25\,\text{Å} - x\right)\Theta\left(25\,\text{Å} - |y|\right)\Psi(x,y,R,t). \tag{18}$$

Again, these wave functions represent the ionised system and monitor the parent ion electron (y) located in the grid range $-25\,\text{Å} < y < 25\,\text{Å}$, while the photoelectron (x) is at larger position values on the grid, $|x| > 25\,\text{Å}$.

2.2.3 Bound/Continuum Wave Function, $\Psi_{1b/1c}(x,y,R,t)$, Early Times

Additionally, to understand the attosecond electron dynamics at early times during XUV pulse interaction, the exact 1e-bound/1e-continuum (1b/1c) wave function is needed. For this, we define a bound/continuum wave function, i.e., 1e-bound/1e-continuum, by projecting out the 2e bound states at each time step

$$\Psi_{1b/1c}(x,y,R,t) = \Psi(x,y,R,t) - \sum_{n=0}^{19}\left(\iint \varphi_n^{2e}(x',y';R)\Psi(x',y',R,t)\mathrm{d}x'\,\mathrm{d}y'\right)\varphi_n^{2e}(x,y;R). \tag{19}$$

This procedure is computationally very demanding and, therefore, limited to the early few femtoseconds. A maximum of 20 2e bound states has shown to be sufficient to obtain convergence. The as such calculated wave function can be used to identify trends in the integrated asymmetry of the PES without having to propagate the full wave function for long times. This is achieved by integrating the bound/continuum wave function once over positive (fwd) and once over negative (bwd) x direction, yielding the asymmetry as:

$$n^{\mathrm{fwd}}(t) = \int_0^{120\,\text{Å}}\mathrm{d}x\iint\Theta\left(25\,\text{Å} - |y|\right)\left|\Psi_{1b/1c}(x,y,R,t)\right|^2\mathrm{d}y\,\mathrm{d}R, \tag{20}$$

$$n^{\mathrm{bwd}}(t) = \int_{-120\,\text{Å}}^{0}\mathrm{d}x\iint\Theta\left(25\,\text{Å} - |y|\right)\left|\Psi_{1b/1c}(x,y,R,t)\right|^2\mathrm{d}y\,\mathrm{d}R, \tag{21}$$

$$\tilde{A}(t) = \frac{n^{\mathrm{fwd}}(t) - n^{\mathrm{bwd}}(t)}{n^{\mathrm{fwd}}(t) + n^{\mathrm{bwd}}(t)}. \tag{22}$$

Hereby, the grid boundaries and grid points of the electronic grid where halved to reduce the computational costs. Because this procedure is only performed to investigate the very early attosecond dynamics, the shorter grid is sufficient to get an insight into the early ionisation dynamics. As will be seen, the asymmetry defined by **Eq. 22** produces quantitatively similar results to the asymmetry given by **Eq. 16**.

3 RESULTS

3.1 Laser-Free Dynamics

In **Figures 2A,B**, we show the nuclear coordinate and momentum expectation values obtained for the three different initial nuclear wave packet starting positions $R_{0,l/m/r}$. In 3), the corresponding mean electron momentum is displayed. Starting with the nuclear case, we see that for R_r an oscillating dynamics within the left potential well takes place (recall **Figure 1B**) with the nuclear momentum behaving accordingly. For R_l, there is partial nuclear density transfer to the right potential well after approximately $t > 25$ fs, destroying the simple oscillatory motion of the nucleus. This is due to higher momenta being present in the nuclear wave packet that originate from the steep gradient left of the centre of $R_{0,l}$. The electron response, i.e., the electron density's momentum $\langle\Psi(t)|p_x|\Psi(t)\rangle$, follows qualitatively the nuclear momentum, $\langle\Psi(t)|P|\Psi(t)\rangle$, however, with small discrepancies. For both non-equilibrium starting positions, the maximum nuclear and electron momentum expectation value is reached

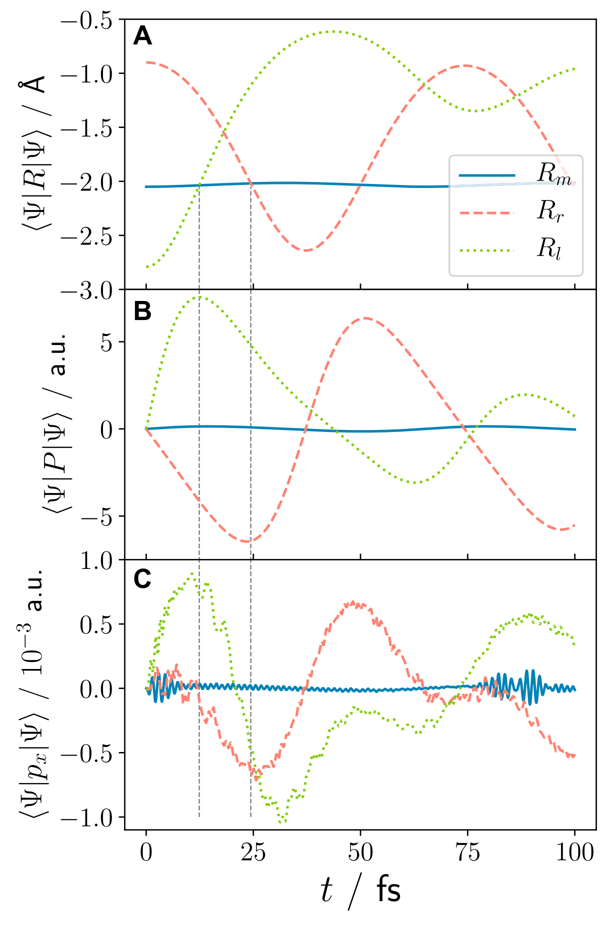

FIGURE 2 | Laser-free dynamics in the 2e ground state for different initial wave functions (see **Eq. 7**): R_m for starting in equilibrium position $R_{0,m}$ = −2.05 Å (blue), R_l and R_r for starting in non-equilibrium positions $R_{0,l}$ = −2.79 Å (green) and $R_{0,r}$ = −0.90 Å (red), respectively. **(A)** Nuclear coordinate expectation values, **(B)** nuclear momentum expectation values, and **(C)** electron momentum expectation values. The vertical dashed lines indicate the time when the nuclear wave packets reach the equilibrium position. This corresponds to the time of maximum nuclear and electron momentum, and the times around which the XUV pulse is centred in **Subsection 3.2** and following.

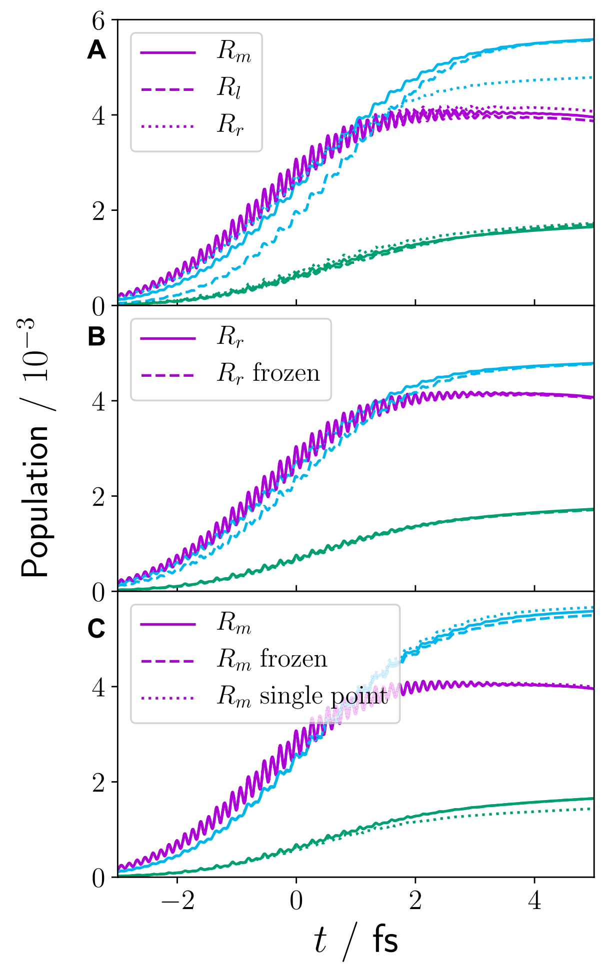

FIGURE 3 | Population, $a_n^{1e}(t)$, of the first three parent ion states, $\varphi_n^{1e}(y;R)$ (n = 0 (violet), n = 1 (green), n = 2 (blue)), during the XUV ionisation, **Eq. 23**. Panel **(A)** shows the comparison of equilibrium (solid lines), i.e., zero nuclear and electron momentum at time of ionisation, and non-equilibrium configuration (dashed/dotted lines), i.e., R_l/R_r: positive/negative nuclear and electron momentum at time of ionisation. **(B)** comparison of R_r and frozen nucleus R_r, i.e., no quantum mechanical nuclear degree-of-freedom but sampled nuclear wave packet (see **Subsection 2.1.2**). **(C)** comparison of R_m, frozen nucleus R_m, and a single 2D purely electronic calculation with a point charge central nucleus at $R_{0,m}$.

when the nucleus passes the minimum of the potential well, as indicated with the vertical, dashed lines in **Figure 2**.

3.2 Attosecond Dynamics

We aim at investigating the impact of nuclear motion and nuclear–electron correlation on the ultrafast ionisation dynamics. For this, we compare the ionisation process of the nuclear equilibrium configuration ($R_{0,m}$) with ionisation of the initial non-equilibrium nuclear configuration ($R_{0,\mathrm{l/r}}$) with the pulse centred around the time of equilibrium passage, i.e., when $\langle R_{\mathrm{l/r}}(t_0)\rangle = R_{0,m}$. These times are indicated previously in **Figure 2** with the dashed vertical lines and correspond to a maximum positive (negative) nuclear and electron momentum for R_l(R_r). The times are t_0 = 12.30 fs for $R_{\mathrm{l}}(t_0) = R_{0,m}$ and t_0 = 24.405 fs for $R_{\mathrm{r}}(t_0) = R_{0,m}$. From now on, referring to R_l and R_r implicates this procedure, while $R_{0,\mathrm{l/r/m}}$ refers to the initial nuclear positions.

First, we analyse the attosecond dynamics during the XUV pulse interaction leading to the population of the parent ion states, $\varphi_n^{1\mathrm{e}}(y;R)$. Thus, we project the 1e states on the bound/continuum wave function

$$a_n^{1\mathrm{e}}(t) = \iint \left| \int \varphi_n^{1\mathrm{e}}(y;R)\Psi_{1\mathrm{b}/1\mathrm{c}}(x,y,R,t)\,\mathrm{d}y \right|^2 \mathrm{d}x\,\mathrm{d}R. \qquad (23)$$

Figure 3A shows the population of the first three electronic parent ion states for the equilibrium and non-equilibrium cases (R_l, R_r). It can be seen that the previously discussed

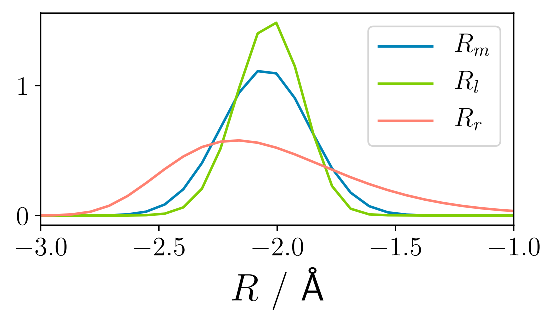

FIGURE 4 | Nuclear wave packet at the time of ionisation, t_0, for $R_m(t_0)$, $R_l(t_0)$, $R_r(t_0)$, see text.

dynamics prior to ionisation, which leads to non-zero electron momentum at the time of ionisation, have almost no impact on the attosecond electronic population dynamics. The only small difference is visible for the $n = 2$ state in the case of R_r (blue dotted line). However, this difference does not originate from the nuclear–electron correlation but is rather due to the deformation of the nuclear wave packet prior to ionisation, see **Figure 4**, depicting the nuclear wave packet at the time of ionisation for $R_m(t_0)$, $R_l(t_0)$, and $R_r(t_0)$. The deformation of the R_r nuclear wave packet, caused by the anharmonic PEC, leads to a small change in resonance conditions into the 1e-bound/1e-continuum and, consequently, to a slight change in the 1e state population. This becomes also evident by comparing the attosecond dynamics of R_r with a frozen nucleus calculation using the nuclear wave packet obtained at the time of ionisation from the 3D R_r simulation (recall **Subsection 2.1.2**, see **Figure 3B**). Although in the frozen nuclear wave packet simulation no nuclear or electron momentum is present, it shows identical attosecond dynamics. The frozen nuclear wave packet calculation without intrinsic quantum mechanical nuclear dimension reproduces the attosecond dynamics also for the other two investigated cases (R_m, R_r). More so, **Figure 3C** shows that for R_m, a single 2D calculation with the classical point charge nucleus centred at −2.05 Å (the centre of the R_m wave packet) is sufficient to reproduce the attosecond dynamics and population of ionic states.

In other words, to describe the correct attosecond dynamics of the parent ion population upon ionisation, the quantum mechanical description of the nuclear degree of freedom can be neglected—a frozen nucleus approach of sampling the nuclear wave packet is sufficient. Moreover, if the nuclear dynamics prior to ionisation only proceeded on a harmonic PEC, leading to a compact Gaussian-like nuclear wave packet, a purely electronic TDSE simulation is able to reproduce the correct behaviour. This is an important finding for future approximations in the field of attosecond ionisation dynamics.

3.3 Momentum Conservation in Parent Ion Dynamics

As seen in the previous section, within the first 4 fs upon XUV pulse interaction, the population in the parent ion is created and reaches stable values. Subsequently, in the parent ion, the nuclear wave packet moves on the corresponding PECs contained in the electronic wave packet acquiring momenta determined by the PEC's gradients. In particular, the nuclear wave packet propagating on $n = 2$ and moving towards $R = 0$ undergoes a pronounced non-adiabatic transition with $n = 1$. Passing through $R = 0$ will lead to a change in the population of the parent ion states in the electronic wave packet. If ionisation into $n = 2$ and the subsequent nuclear relaxation would be independent of the initial nuclear momentum at t_0, $P^{2e}(t_0)$, gained during propagation in the 2e electronic ground state (cf. **Figure 2**), the crossing at $R = 0$ would always be reached approximately 17fs after ionisation. However, if this initial nuclear momentum is retained upon ionisation, this will become visible through the timing of the non-adiabatic transition. Thus, the time at which the non-adiabatic crossing occurs is a direct measurement for pre-ionisation momentum dynamics. **Figure 5** shows the parent ion state-resolved population obtained in bwd direction using the channel wave function

$$b_n^{1e}(t) = \iint \left| \int \varphi_n^{1e}(y;R)\Psi_{\mathrm{ch}}^{\mathrm{bwd}}(x,y,R,t)\mathrm{d}y \right|^2 \mathrm{d}x\,\mathrm{d}R \qquad (24)$$

for R_m, R_l, and R_r. The non-adiabatic transition leading to depopulation of $n = 2$ and population of $n = 1$ is clearly visible for all three cases. Moreover, the time of the transition is shifted to earlier (later) times for R_l (R_r) demonstrating that the pre-ionisation momentum acquired by the nuclear wave packet propagating in the electronic ground state is retained upon ionisation. This is even more evident in **Table 1** where the nuclear momentum expectation value of the individual nuclear

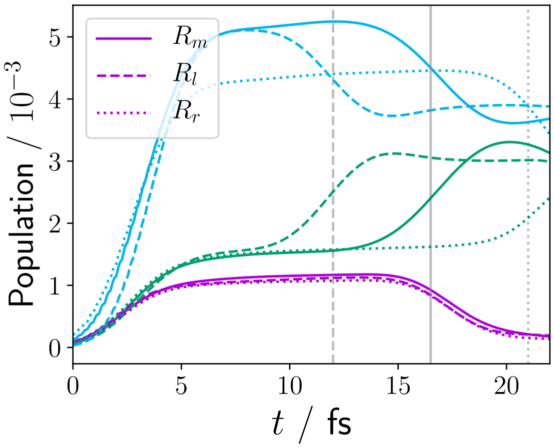

FIGURE 5 | Population of parent ion 1e states using the bwd channel wave function (**Eq. 24**) to visualise the timing of the non-adiabatic transition between the $n = 2$ (blue) and $n = 1$ (green) state for R_m (solid lines), R_l (dashed lines), and R_r (dotted lines). The $n = 0$ population (violet) decreases as the channel wave function for this ion ground state with corresponding highest photoelectron momenta reaches the absorber after 15 fs. The difference in population of the $n = 2$ state for R_r compared to R_m is based on the nuclear wave packet deformation as discussed in the text for the bound/continuum wave function.

TABLE 1 | Nuclear momentum expectation value of the different nuclear wave packets on different parent ion states, see **Eq. 26**, for the three different initial nuclear positions (first to third row). The fourth and fifth rows show the difference of non-equilibrium to equilibrium momentum, emphasising momentum conservation upon ionisation.

Starting position	$P_0^{1e}(t_0 + 2.5\ \text{fs})$	$P_1^{1e}(t_0 + 2.5\ \text{fs})$	$P_2^{1e}(t_0 + 2.5\ \text{fs})$
R_m	−0.24	2.92	5.42
R_l	6.95	10.23	12.87
R_r	−6.38	−3.57	−1.28
$R_l - R_m$	7.18	7.30	7.45
$R_r - R_m$	−6.15	−6.49	−6.70

wave packet propagating on one of the first three parent ion states is shown at $t = t_0 + 2.5$ fs for the three initial starting positions. This is calculated by projecting bwd channel wave function on the corresponding ionic state and calculating the momentum expectation value:

$$\Psi_{\text{ch, n}}^{\text{bwd, 1e}}(x, R, t) = \int \varphi_n^{1\text{e}}(y; R)\Psi_{\text{ch}}^{\text{bwd}}(x, y, R, t)\text{d}y, \tag{25}$$

$$P_n^{1\text{e}}(t) = \iint \Psi_{\text{ch, n}}^{\text{bwd, 1e}\,*}(x, R, t)\, P\, \Psi_{\text{ch, n}}^{\text{bwd, 1e}}(x, R, t)\text{d}R\, \text{d}x. \tag{26}$$

It can be gathered from **Table 1** that the nuclear momentum is different depending on the PEC the nuclear wave packet evolves on, e.g., for R_m (first row) the momentum is negative for $n = 0$, while it is positive for $n = 1$ and further increased for $n = 2$ as expected from the PEC gradients (**Figure 1**). Second, the momenta for the non-equilibrium cases R_l (R_r) (second and third row) are uniformly shifted to higher (lower) momentum values. The lower rows, R_l–R_m and R_r–R_m, quantify the difference to the equilibrium case (no initial momentum). These concur with the momentum in the bound 2e system at time of ionisation, which is for R_l: $P^{2\text{e}}(t_0) = 7.6$ a.u. and for R_r: $P^{2\text{e}}(t_0) = -6.4$ a.u (seen vertical dashed lines in **Figure 2B**). Therefore, we have unambiguously shown that the nuclear momentum in the bound 2e system is conserved upon ionisation manifesting itself in a change in timing for the non-adiabatic transition.

3.4 Photoelectron Spectra and Asymmetry

We now investigate to which extent these nuclear–electron correlation dynamics impact the PES. It has been reported that for simple one active electron systems, the coupled nuclear–electron dynamics are imprinted in the integrated photoelectron asymmetry (Falge et al., 2012a, 2017). So far, it is an open question, whether this also holds for multi-electron systems.

3.4.1 Resonance Condition

The major difference to our previous work using single active electron systems is that upon ionisation, there is no ionisation into a single continuum state but rather complex transitions into several 1e-bound/1e-continuum states depending on the XUV pulse's central frequency. Moreover, ionisation into these different states features varying resonance conditions for the various ion states. The resonance conditions are visualised in **Figure 6A** as a function of the parametric nuclear position

$$\text{IP}_n(R) = V_0^{2\text{e}}(R) - V_n^{1\text{e}}(R). \tag{27}$$

For the three initial nuclear positions ($R_{0,m}$, $R_{0,l}$, $R_{0,r}$), respectively, 3, 2, or 4 parent ion states are energetically accessible for the XUV pulse used in this work ($\hbar\omega = 15.5$ eV). **Figures 6D–F** show the respective PES with exactly those 3, 2, or 4 peaks. Additionally, ionisation in these ionic states comes together with static and dynamic electron–electron correlation effects on top of any electron–nuclear correlation due to coupled dynamics. Therefore, depending on the position of the nuclear wave packet at the time of ionisation, there is a state-intrinsic inherent fwd/bwd asymmetry independent of any nuclear–electron coupling, originating from electron–electron interaction. Thus, each peak in the PES has a unique fwd/bwd asymmetry (see **Figures 6D–F**) leading to the overall photoelectron integrated asymmetry. The origin of the asymmetry for each peak is rooted in the different ionisation processes that lead to its population and are purely based on electron-electron interaction as reported in Fröbel et al. (2020) (see scheme in **Figure 6C**): $n = 0$ is predominantly populated via direct ionisation of the weaker bound electron (right of the central nucleus), which is favourable in fwd direction since it does not have to pass the other electron. $n = 2$ is the respective direct ionisation of the stronger bound electron (left of nucleus), which proceeds predominantly into bwd direction. $n = 1$ is in a bwd direction dominated knock-up ionisation process with smaller parts as knock-down process in fwd direction. As for different (parametric) R values, a different number of ionic states is accessible, with each of them featuring this intrinsic preference in the emission direction of the photoelectron, this leads to the overall parametric R-dependent asymmetry behaviour shown in **Figure 6B**. These results have been obtained by frozen nucleus calculations using **Eq. 16** to calculate the asymmetry, thus, showing that it is a purely electron-electron correlation driven inherent asymmetry. Its R-dependency can be easily understood: starting from $R_{0,m}$, the asymmetry rises for more negative R positions since the bwd-dominated $n = 2$ state becomes energetically inaccessible (**Eq. 27**). Equally, the overall asymmetry rises for larger R as the fwd/bwd neutral $n = 3$ state becomes energetically accessible. For a nuclear wave packet rather than a point-like R-value (see **Figure 1**) these two effects are smeared.

3.4.2 Nuclear–Electron Correlation Imprint

The procedure to visualise the imprint of pre-ionisation nuclear–electron correlation dynamics on the photoelectron is the following: we start at $R_{0,r}$ and probe the integrated asymmetry by scanning the time delay of the XUV pulse interaction from $T = [7, 100]$fs in 1 fs interval steps. We start the integrated asymmetry calculation earliest at 7 fs to ensure sufficient time for the 5 fs broad XUV pulse. $R_{0,r}$ was chosen as a starting point since the nuclear dynamics are constricted to the left potential well exhibiting a more distinct dynamics with larger imprinted momenta (see **Figure 2**). During the propagation, the nuclear

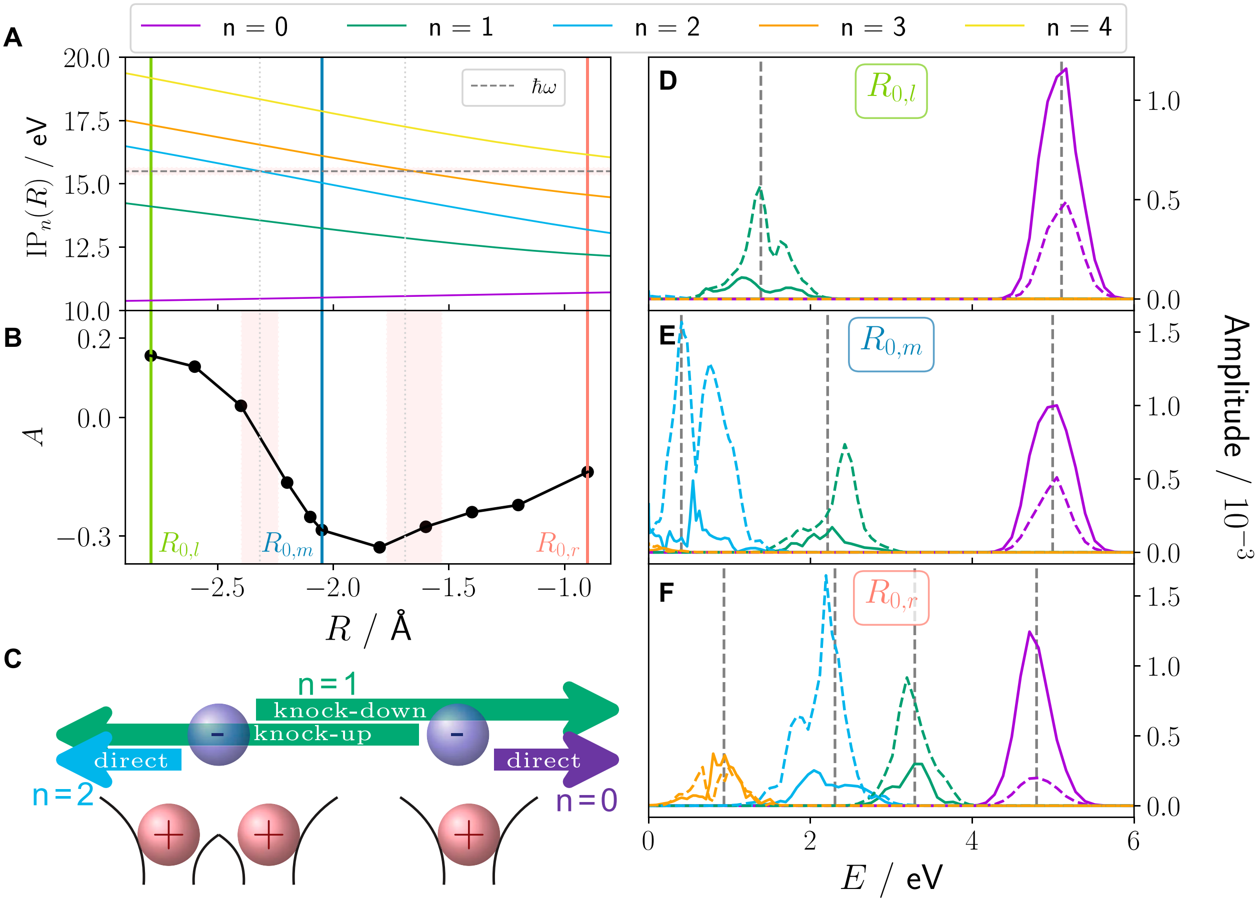

FIGURE 6 | (A) Ionisation potential (**Eq. 27**) for different parent ion states and XUV pulse energy $\hbar\omega$ =15.5 eV (horizontal dashed line) with FWHM in light red. Vertical green, blue and red lines indicate the three initial nuclear positions, $R_{0,m}$, $R_{0,l}$, and $R_{0,r}$, respectively. **(B)** Asymmetry is calculated with frozen nucleus simulation at different parametric R values (**Eq. 16**). **(C)** Scheme of the relevant ionisation pathways and the resulting ion state: direct ionisation of the weaker (stronger) bound electron dominant in fwd (bwd) direction leads to population of $n = 0$ (violet) ($n = 2$ (blue)) parent ion state; $n = 1$ parent ion state is populated via knock-up of weaker bound electron in bwd direction or via knock-down of stronger bound electron in fwd direction. Panels **(D)**, **(E)**, and **(F)** show the PES (solid lines: fwd, dashed lines: bwd) for frozen nucleus calculations at $R_{0,m}$, $R_{0,l}$, and $R_{0,r}$, respectively. The dashed vertical lines indicate the expected peak position based on the resonance condition $E = \hbar\omega - \mathrm{IP}_n(R_{0,l/m/r})$.

wave packet propagates on the 2e electronic ground state PEC from the inner turning point $R_{0,r}$ (right) to the outer turning point $R_{0,l}$ (left) and back to $R_{0,r}$, corresponding to the time-delay intervals of T = [7, 37]fs and T = [37, 74]fs, respectively (see **Figures 1**, **2**). To save computational cost, we calculate the asymmetry from the bound/continuum wave function using **Eq. 22**, since it allows us to obtain converged asymmetries with fewer time steps and compare with some selected calculations using **Eq. 16** that require propagation for long times. As is seen in **Figure 6B**, due to the changing resonance conditions, the inherent electron–electron correlation-based asymmetry varies for different parametric nuclear positions. The nuclear–electron correlation-based asymmetry is, thus, imprinted on top of the inherent electron–electron correlation-based asymmetry. Consequently, to extract the nuclear–electron correlation-based asymmetry, a "baseline" of the electron–electron correlation-based asymmetry during the nuclear propagation is required. This is carried out here in two approaches whose merits and shortcomings we will discuss shortly: *1)* a mean baseline is obtained from relating the asymmetry from forth and back movement of the nucleus (right to left vs left to right, **Figure 7A**). *2)* A baseline is calculated for each interval step using frozen nuclear wave packet calculations with the nucleus set to its position at the time of ionisation. Approach *1)* resembles more an experimental setup where a nuclear wave packet could be propagated forth and back in a potential, whereas a baseline by frozen nucleus calculations (approach *2)* cannot be obtained in the experimental setup, however, is not restricted to a forth and back movement of the nucleus in the same potential.

Figure 7A shows how the nuclear–electron correlation-based asymmetry is imprinted on top of the purely electron–electron correlation-based inherent asymmetry baseline that shows the same behaviour as shown in **Figure 6B**. The right to left (blue) and left to right (orange) curves are obtained by relating the corresponding time intervals T = [7, 37]fs and T = [37, 74]fs to the R value at the time of ionisation. In **Figure 7B**, the difference of the asymmetry to the two baselines 1*)* mean (dashed) and *2)* frozen (dotted) is shown with

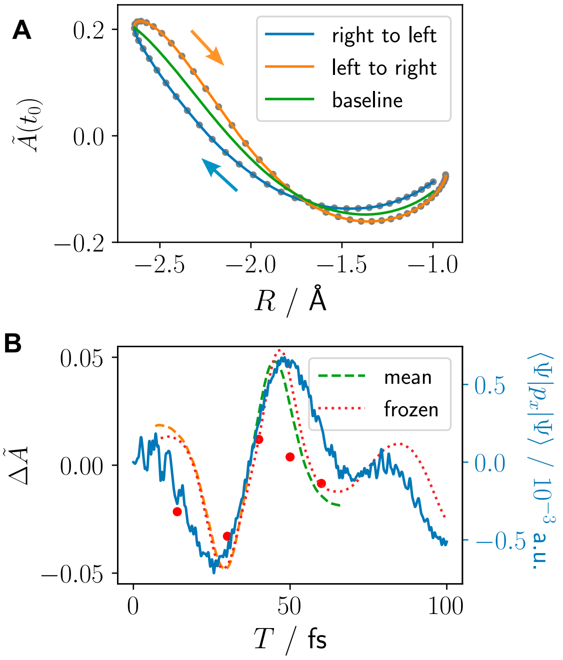

FIGURE 7 | Imprint of nuclear–electron correlation in the asymmetry of the PES for a non-equilibrium starting position of $R_{0,r}$ probed by a XUV pulse at different time-delays T: **(A)** Asymmetry calculated according to **Eq. 22** at time of ionisation in dependence of the nuclear position R at time of ionisation, t_0. Right to left and left to right refer to the time-delay intervals of T = [7,37]fs and T = [37,74]fs, respectively. The baseline is calculated using approach *1*) explained in the text as mean between left to right and right to left. **(B)** The nuclear–electron correlation-based asymmetry, $\Delta\tilde{A}$, as a function of the time delay T obtained with the mean baseline (*1*, dashed) and the calculated frozen nucleus baseline (*2*, dotted). As explained in the text, the mean basline can only be obtained if forth and back propagation in the same potential is available (T = [7,37]fs and T = [37,74]fs), whereas the frozen nucleus baseline is available for all time delay points. The red dots stem from the asymmetry calculated with the more computationally demanding **Eq. 16**. The electron mean momentum is also shown, for comparison (solid blue line).

respect to the time-delay T. Comparison with the electron density's momentum in the 2e bound system (solid blue line) shows very good agreement.

This means that starting the nucleus in a non-equilibrium position, which experimentally could be realised, e.g., by a first pump pulse, leads to coupled nuclear–electron bound dynamics that are imprinted on the electron density's momentum. That, in turn, is imprinted on the photoelectron spectrum. Thus, we have demonstrated here that imprints of both, nuclear–electron and electron–electron correlated dynamics, are visible in the photoelectron spectra and the asymmetry of the photoelectron emission direction. We have generalised previous work and analysis on single-electron systems for the here investigated correlated system involving two electrons.

4 SUMMARY

We set out to answer questions of particle correlation in molecular XUV ionisation and shed light on how these effects manifest in observables. To this end, we have employed a fully correlated molecular quantum model system comprised of two active electrons and one active nucleus that mimics a generic molecular system and allows us to report qualitative effects.

First, we examine what a coupled electronic–nuclear motion looks like in the bound system and showed the adiabatic imprint of the nuclear motion on the electronic momentum. Next, we focused on the implication of these coupled dynamics on the molecular XUV ionisation process, in particular to answer the question regarding characteristics in the attosecond population dynamics and post-ionisation dynamics. We report that the nuclear momentum is conserved during the XUV ionisation from the target to the parent ion and impacts the post-ionisation dynamics. On the other hand, the attosecond electron population dynamics are largely unaffected by the coupled nuclear–electron dynamics in the bound system. Finally, we turned towards features appearing in the photoelectron spectra and their relation to electron–electron and electron–nuclear correlation. The results drastically show how all particles are strongly correlated and imprint each other's properties. Each photoelectron peak has an inherent asymmetry rooted in its electron–electron correlation-based ionisation pathways with its bound counterpart. The underlying complex bound/continuum resonances change when the nucleus is displaced leading to a change in electron–electron correlation-based photoelectron properties. On top of this, the initial coupled nuclear–electron momentum in the bound system is imprinted on the entangled photoelectron via its spectrum's asymmetry and could be used as an experimental observable. While we have seen that correlation impacts pre, during, and post ionisation in various ways, well-designed approximations can be introduced at different stages depending on the intended outcome of the simulation. For example, the attosecond population dynamics are only influenced by a deformation of the nuclear wave packet pre-ionisation, which is not based on nuclear–electron correlation and can be reproduced by a sampling approach to the nuclear wave packet. In the case of harmonic PECs yielding a compact Gaussian-like nuclear wave packet, the nuclear degree of freedom can be safely ignored and a purely electronic description of the system with single-point nuclei reproduces the correct electronic parent ion wave packet population. Moreover, the momentum conservation in the nuclei between target and parent ion can be incorporated into classical approximations. Combining these ideas will be the subject of future research. The photoelectron asymmetries are purely based on the correlation effects of all particles and, thus, can only be observed when treating all particles quantum dynamically and with the corresponding exact correlation. However, approximated methods could be used to calculate the effect that is imprinted in the photoelectron asymmetry rather than the full correlated XUV ionisation process. For example, approximate theories can calculate the change in continuum resonances that lead to a change in the electron–electron correlation-based asymmetry, or the nuclear dynamics in the bound state that are imprinted on the spectrum via nuclear–electron correlation.

We are confident that our findings not only widen our understanding of fundamental correlation-driven processes in XUV ionisation but will also guide future experiments and approximated theory towards which effects have to be taken into account to properly describe correlation in molecular ionisation.

DATA AVAILABILITY STATEMENT

The raw data supporting the conclusion of this article will be made available by the authors, without undue reservation.

AUTHOR CONTRIBUTIONS

KMZ and JB performed simulations and data analysis. KMZ and SG conceived and designed the study. VE and SG supervised the research. All authors discussed the research and contributed to manuscript revision, read, and approved the submitted version.

FUNDING

KMZ and SG are part of the Max Planck School of Photonics supported by BMBF, Max Planck Society, and Fraunhofer Society. JB would like to acknowledge generous funding by the “Honours Programme for Future Researchers” of the Friedrich-Schiller-Universität Jena. SG acknowledges the ERC Consolidator Grant QUEM-CHEM (grant number 772676).

ACKNOWLEDGMENTS

All calculations have been performed at the Universitätsrechenzentrum of the Friedrich Schiller University Jena.

REFERENCES

Albert, J., Falge, M., Gomez, S., Sola, I. R., Hildenbrand, H., and Engel, V. (2015). Communication: Vibrational and Vibronic Coherences in the Two Dimensional Spectroscopy of Coupled Electron-Nuclear Motion. *J. Chem. Phys.* 143, 041102. doi:10.1063/1.4927396

Albert, J., Hader, K., and Engel, V. (2017). Coupled Electron-Nuclear Quantum Dynamics through and Around a Conical Intersection. *J. Chem. Phys.* 147, 064302. doi:10.1063/1.4989780

Ayuso, D., Palacios, A., Decleva, P., and Martín, F. (2017). Ultrafast Charge Dynamics in glycine Induced by Attosecond Pulses. *Phys. Chem. Chem. Phys.* 19, 19767–19776. doi:10.1039/C7CP01856H

Blum, K. (2012). *Density Matrix Theory and Applications*. third edn. Heidelberg: Springer.

Corkum, P. B., and Krausz, F. (2007). Attosecond Science. *Nat. Phys.* 3, 381–387. doi:10.1038/nphys620

Erdmann, M., Gross, E. K. U., and Engel, V. (2004). Time-dependent Electron Localization Functions for Coupled Nuclear-Electronic Motion. *J. Chem. Phys.* 121, 9666–9670. doi:10.1063/1.1806812

Falge, M., Engel, V., and Gräfe, S. (2012a). Fingerprints of Adiabatic versus Diabatic Vibronic Dynamics in the Asymmetry of Photoelectron Momentum Distributions. *J. Phys. Chem. Lett.* 3, 2617–2620. doi:10.1021/jz3009826

Falge, M., Engel, V., and Gräfe, S. (2011). Time-resolved Photoelectron Spectroscopy of Coupled Electron-Nuclear Motion. *J. Chem. Phys.* 134, 184307. doi:10.1063/1.3585692

Falge, M., Engel, V., Lein, M., Vindel-Zandbergen, P., Chang, B. Y., and Sola, I. R. (2012b). Quantum Wave-Packet Dynamics in Spin-Coupled Vibronic States. *J. Phys. Chem. A* 116, 11427–11433. doi:10.1021/jp306566x

Falge, M., Fröbel, F. G., Engel, V., and Gräfe, S. (2017). Time-resolved Photoelectron Spectroscopy of IR-Driven Electron Dynamics in a Charge Transfer Model System. *Phys. Chem. Chem. Phys.* 19, 19683–19690. doi:10.1039/C7CP01832K

Feit, M. D., Fleck, J. A., and Steiger, A. (1982). Solution of the Schrödinger Equation by a Spectral Method. *J. Comput. Phys.* 47, 412–433. doi:10.1016/0021-9991(82)90091-2

Frigo, M., and Johnson, S. (1998). “FFTW: an Adaptive Software Architecture for the FFT,” in *Proceedings of the 1998 IEEE International Conference on Acoustics, Speech and Signal Processing, ICASSP ’98 (Cat. No.98CH36181)* (Seattle, WA, USA: IEEE), Vol. 3, 1381–1384. doi:10.1109/ICASSP.1998.681704

Fröbel, F. G., Ziems, K. M., Peschel, U., Gräfe, S., and Schubert, A. (2020). The Impact of Electron-Electron Correlation in Ultrafast Attosecond Single Ionization Dynamics. *J. Phys. B At. Mol. Opt. Phys.* 53, 144005. doi:10.1088/1361-6455/ab8c21

Hader, K., Albert, J., Gross, E. K. U., and Engel, V. (2017). Electron-nuclear Wave-Packet Dynamics through a Conical Intersection. *J. Chem. Phys.* 146, 074304. doi:10.1063/1.4975811

Heather, R., and Metiu, H. (1987). An Efficient Procedure for Calculating the Evolution of the Wave Function by Fast Fourier Transform Methods for Systems with Spatially Extended Wave Function and Localized Potential. *J. Chem. Phys.* 86, 5009–5017. doi:10.1063/1.452672

Horodecki, R., Horodecki, P., Horodecki, M., and Horodecki, K. (2009). Quantum Entanglement. *Rev. Mod. Phys.* 81, 865–942. doi:10.1103/RevModPhys.81.865

Joachain, C. J., Kylstra, N. J., and Potvliege, R. M. (2012). *Atoms in Intense Laser Fields*. Cambridge: Cambridge University Press.

Kosloff, R., and Tal-Ezer, H. (1986). A Direct Relaxation Method for Calculating Eigenfunctions and Eigenvalues of the Schrödinger Equation on a Grid. *Chem. Phys. Lett.* 127, 223–230. doi:10.1016/0009-2614(86)80262-7

Krausz, F., and Ivanov, M. (2009). Attosecond Physics. *Rev. Mod. Phys.* 81, 163–234. doi:10.1103/revmodphys.81.163

Kutzelnigg, W. (1994). *Einführung in die Theoretische Chemie, Band 2*. Weinheim: VCH.

Lein, M., Gross, E., Kreibich, T., and Engel, V. (2002). Strong-Field Ionization Dynamics of a Model H2 Molecule. *Phys. Rev. A* 65, 033403. doi:10.1103/physreva.65.033403

[Dataset] Nielson, M. A., and Chuang, I. L. (2000). *Quantum Computation and Quantum Information*.

Nisoli, M., Decleva, P., Calegari, F., Palacios, A., and Martín, F. (2017). Attosecond Electron Dynamics in Molecules. *Chem. Rev.* 117, 10760–10825. doi:10.1021/acs.chemrev.6b00453

Pukhov, A. (2002). Strong Field Interaction of Laser Radiation. *Rep. Prog. Phys.* 66, 47–101. doi:10.1088/0034-4885/66/1/202

Schaupp, T., and Engel, V. (2019a). A Classical Ride through a Conical Intersection. *J. Chem. Phys.* 150, 034301. doi:10.1063/1.5080399

Schaupp, T., and Engel, V. (2022). Correlated Three-Dimensional Electron-Nuclear Motion: Adiabatic Dynamics vs Passage of Conical Intersections. *J. Chem. Phys.* 156, 074302. doi:10.1063/5.0082597

Schaupp, T., and Engel, V. (2019b). Electronic and Nuclear Flux Dynamics at a Conical Intersection. *J. Chem. Phys.* 151, 084309. doi:10.1063/1.5111922

Shin, S., and Metiu, H. (1996). Multiple Time Scale Quantum Wavepacket Propagation: Electron–Nuclear Dynamics. *J. Phys. Chem.* 100, 7867–7872. doi:10.1021/jp952498a

Shin, S., and Metiu, H. (1995). Nonadiabatic Effects on the Charge Transfer Rate Constant: A Numerical Study of a Simple Model System. *J. Chem. Phys.* 102, 9285–9295. doi:10.1063/1.468795

Sukiasyan, S., Ishikawa, K. L., and Ivanov, M. (2012). Attosecond Cascades and Time Delays in One-Electron Photoionization. *Phys. Rev. A* 86, 033423. doi:10.1103/physreva.86.033423

Vacher, M., Bearpark, M. J., Robb, M. A., and Malhado, J. P. (2017). Electron Dynamics upon Ionization of Polyatomic Molecules: Coupling to Quantum

Nuclear Motion and Decoherence. *Phys. Rev. Lett.* 118, 083001. doi:10.1103/PhysRevLett.118.083001

Vacher, M., Steinberg, L., Jenkins, A. J., Bearpark, M. J., and Robb, M. A. (2015). Electron Dynamics Following Photoionization: Decoherence Due to the Nuclear-Wave-Packet Width. *Phys. Rev. A* 92, 040502. doi:10.1103/physreva.92.040502

Wolter, B., Pullen, M. G., Baudisch, M., Sclafani, M., Hemmer, M., Senftleben, A., et al. (2015). Strong-Field Physics with Mid-ir Fields. *Phys. Rev. X* 5, 021034. doi:10.1103/physrevx.5.021034

Conflict of Interest: The authors declare that the research was conducted in the absence of any commercial or financial relationships that could be construed as a potential conflict of interest.

frontiers | Frontiers in Chemistry

TYPE Original Research
PUBLISHED 13 September 2022
DOI 10.3389/fchem.2022.982120

Time-dependent optimized coupled-cluster method with doubles and perturbative triples for first principles simulation of multielectron dynamics

Himadri Pathak[1], Takeshi Sato[1,2,3]* and Kenichi L. Ishikawa[1,2,3]

[1]Department of Nuclear Engineering and Management, School of Engineering, The University of Tokyo, Tokyo, Japan, [2]Photon Science Center, School of Engineering, The University of Tokyo, Tokyo, Japan, [3]Research Institute for Photon Science and Laser Technology, The University of Tokyo, Tokyo, Japan

EDITED BY
Yuichi Fujimura,
Tohoku University, Japan

REVIEWED BY
Xiaowei Sheng,
Anhui Normal University, China
Shu Ohmura,
Nagoya Institute of Technology, Japan

*CORRESPONDENCE
Takeshi Sato,
sato@atto.t.u-tokyo.ac.jp

SPECIALTY SECTION
This article was submitted to Physical Chemistry and Chemical Physics, a section of the journal Frontiers in Chemistry

RECEIVED 30 June 2022
ACCEPTED 09 August 2022
PUBLISHED 13 September 2022

CITATION
Pathak H, Sato T and Ishikawa KL (2022), Time-dependent optimized coupled-cluster method with doubles and perturbative triples for first principles simulation of multielectron dynamics. *Front. Chem.* 10:982120.
doi: 10.3389/fchem.2022.982120

We report the formulation of a new, cost-effective approximation method in the time-dependent optimized coupled-cluster (TD-OCC) framework [T. Sato *et al.*, J. Chem. Phys. 148, 051101 (2018)] for first-principles simulations of multielectron dynamics in an intense laser field. The method, designated as TD-OCCD(T), is a time-dependent, orbital-optimized extension of the "gold-standard" CCSD(T) method in the ground-state electronic structure theory. The equations of motion for the orbital functions and the coupled-cluster amplitudes are derived based on the real-valued time-dependent variational principle using the fourth-order Lagrangian. The TD-OCCD(T) is size extensive and gauge invariant, and scales as $O(N^7)$ with respect to the number of active orbitals N. The pilot application of the TD-OCCD(T) method to the strong-field ionization and high-order harmonic generation from a Kr atom is reported in comparison with the results of the previously developed methods, such as the time-dependent complete-active-space self-consistent field (TD-CASSCF), TD-OCC with double and triple excitations (TD-OCCDT), TD-OCC with double excitations (TD-OCCD), and the time-dependent Hartree-Fock (TDHF) methods.

KEYWORDS

multielectron dynamics, time-dependent optimized coupled-cluster, high harmonic generation, strong laser field, strong field ionization

1 Introduction

Recent years witnessed unprecedented progress in laser technologies, which made it possible to observe the motions of electrons at the attosecond time scale (Itatani et al. (2004); Corkum and Krausz (2007); Krausz and Ivanov (2009); Baker et al. (2006)). On the other hand, various theoretical and numerical methods have been developed for interpreting, understanding, and predicting the experiments.

The multi-configuration time-dependent Hartree-Fock (MCTDHF) method (Caillat et al. (2005); Kato and Kono (2004); Nest et al. (2005); Haxton et al. (2011); Hochstuhl and Bonitz (2011)), and the time-dependent complete-active-space self-consistent-field (TD-CASSCF) method (Sato and Ishikawa (2013); Sato et al. (2016); Sato et al. (2018a)) are the most rigorous approaches to solve time-dependent Schrödinger equation (TDSE) of many-electron systems, where the wavefunction is given by the full configuration interaction (FCI) expansion,

$$\Psi(t) = \sum_I C_I(t)\Phi_I(t), \tag{1}$$

with both CI coefficients $\{C_I(t)\}$ and orbital functions $\{\psi_p(t)\}$ constituting Slater determinants $\{\Phi_I(t)\}$ are propagated in time according to the time-dependent variational principle (TDVP). The TD-CASSCF method broadens the applicability of the MCTDHF method by flexibly classifying the orbital subspace into frozen-core, dynamical-core, and active. Unfortunately, the factorial computational scaling impedes large-scale applications. There are reports of various affordable size-inextensive methods (Miyagi and Madsen (2013, 2014); Haxton and McCurdy (2015); Sato and Ishikawa (2015)) developed by limiting the CI expansion of the wavefunction. Alternatively, the size-extensive coupled-cluster method, which relies on an exponential wavefunction, is a superior choice to address these problems with a polynomial cost-scaling (Kümmel (2003); Shavitt and Bartlett (2009)). We have developed an explicitly time-dependent coupled-cluster method considering optimized orthonormal orbitals within the flexibly chosen active space, called the time-dependent optimized coupled-cluster (TD-OCC) method, (Sato et al. (2018b)) including double (TD-OCCD) and double and triple excitation amplitudes (TD-OCCDT). Our method is a time-dependent formulation of the stationary optimized coupled-cluster method (Scuseria and Schaefer (1987); Sherrill et al. (1998); Krylov et al. (1998)). Kvaal (Kvaal (2012)) also developed an orbital adaptive time-dependent coupled-cluster (OATDCC) method using biorthogonal orbitals. We take note of a few reports on the time-dependent coupled-cluster methods (Huber and Klamroth (2011); Pigg et al. (2012); Nascimento and DePrince (2016)), using time-independent orbitals, and their interpretation (Pedersen and Kvaal (2019); Pedersen et al. (2021)), including the very initial attempts (Schonhammer (1978); Hoodbhoy and Negele (1978, 1979)).

The TD-OCCDT scales as $O(N^8)$ (N= the number of active orbitals), not ideally suited for applications to larger chemical systems. Therefore, we have developed a few lower cost methods in the TD-OCC framework (Pathak et al. (2020b,c,a, 2021)). We find triple excitations are necessary, including perfect optimization of the orbitals. Therefore, we are interested in developing affordable TD-OCC methods retaining a part of the triples. The most popular coupled-cluster method that treats the triple excitation amplitudes approximately is called CCSD(T) (Raghavachari et al. (1989); Watts et al. (1993)). Bozkaya *et al*, (Bozkaya and Schaefer (2012)) included various symmetric and asymmetric triple excitation corrections to their optimized double (OD) method.

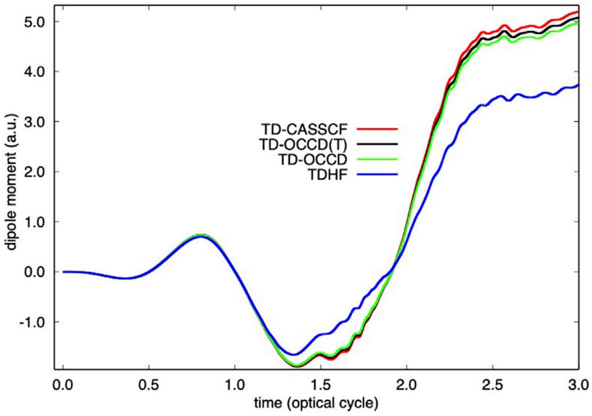

FIGURE 1
Time evolution of dipole moment of Kr irradiated by a laser pulse with a wavelength of 800 nm and a peak intensity of 2 × 10^{14} W/cm^2 calculated with TDHF, TD-OCCD, TD-OCCD(T), and TD-CASSCF methods.

In this communication, we report the formulation and implementation of the CCSD(T) method in the time-dependent optimized coupled-cluster framework, TD-OCCD(T). Following our previous works (Sato et al. (2018b); Pathak et al. (2020b,c, 2021)), we exclude single excitation amplitudes but optimize the orbitals according to time-dependent variational principle (TDVP). As the first application of this method, we study electron dynamics in Kr using intense near-infrared laser fields.

2 Methods

The second quantization representation of the Hamiltonian, including the laser field, is as follows,

$$\hat{H} = h^{\mu}_{\nu}(t)\hat{c}^{\dagger}_{\mu}\hat{c}_{\nu} + \frac{1}{2}u^{\mu\gamma}_{\nu\lambda}\hat{c}^{\dagger}_{\mu}\hat{c}^{\dagger}_{\gamma}\hat{c}_{\lambda}\hat{c}_{\nu} \tag{2}$$

where $\hat{c}^{\dagger}_{\mu}$ ($\hat{c}_{\mu}$) represents a creation (annihilation) operator in a complete, orthonormal set of $2n_{\text{bas}}$ time-dependent spin-orbitals $\{\psi_\mu(t)\}$. n_{bas} is the number of basis functions used for expanding the spatial part of ψ_μ, which, in the present real-space implementation, corresponds to the number of grid points, and

$$h^{\mu}_{\nu}(t) = \int dx_1 \psi^*_{\mu}(x_1)[h_0 + V_{ext}]\psi_{\nu}(x_1), \tag{3}$$

$$u^{\mu\gamma}_{\nu\lambda} = \iint dx_1 dx_2 \frac{\psi^*_{\mu}(x_1)\psi^*_{\gamma}(x_2)\psi_{\nu}(x_1)\psi_{\lambda}(x_2)}{|\boldsymbol{r}_1 - \boldsymbol{r}_2|}, \tag{4}$$

where $x_i = (\boldsymbol{r}_i, \sigma_i)$ represents a composite spatial-spin coordinate. h_0 is the field free one-electronic Hamiltonian and $V_{ext} = A(t)p_z$

in the velocity gauge, $A(t) = -\int^t E(t')dt'$ is the vector potential, with $E(t)$ being the laser electric field linearly polarized along the z axis.

The complete set of $2n_{\mathrm{bas}}$ spin-orbitals (labeled with $\mu, \nu, \gamma, \lambda$) is divided into n_{occ} *occupied* (o, p, q, r, s) and $2n_{\mathrm{bas}} - n_{\mathrm{occ}}$ *virtual* spin-orbitals. The coupled-cluster (or CI) wavefunction is constructed only with occupied spin-orbitals, which are time-dependent in general, and virtual spin-orbitals form the orthogonal complement of the occupied spin-orbital space. The occupied spin-orbitals are classified into n_{core} *core* spin-orbitals, which are occupied in the reference Φ and kept uncorrelated, and $N = n_{\mathrm{occ}} - n_{\mathrm{core}}$ *active* spin-orbitals (t, u, v, w) among which the active electrons are correlated. The active spin-orbitals are further split into those in the *hole* space (i, j, k, l) and the *particle* space (a, b, c, d), which are defined as those occupied and unoccupied, respectively, in the reference Φ. The core spin-orbitals can further be split into *frozen-core* space (i'', j''), fixed in time and the *dynamical-core* space (i', j'), propagated in time (Sato and Ishikawa (2013)) (See. Figure 1 in Sato et al. (2018b) for a pictorial illustration).

The real action formulation of the TDVP with orthonormal orbitals is our guiding principle, (Sato et al. (2018b))

$$S = \mathrm{Re}\int_{t_0}^{t_1} L dt = \frac{1}{2}\int_{t_0}^{t_1} (L + L^*) dt, \tag{5}$$

$$L = \langle\Phi|\left(1 + \hat{\Lambda}\right)e^{-\hat{T}}\left(\hat{H} - i\frac{\partial}{\partial t}\right)e^{\hat{T}}|\Phi\rangle, \tag{6}$$

$$\hat{T} = \hat{T}_2 + \hat{T}_3 \cdots = \tau_{ij}^{ab}\hat{E}_{ij}^{ab} + \tau_{ijk}^{abc}\hat{E}_{ijk}^{abc}\cdots, \tag{7}$$

$$\hat{\Lambda} = \hat{\Lambda}_2 + \hat{\Lambda}_3 \cdots = \lambda_{ab}^{ij}\hat{E}_{ab}^{ij} + \lambda_{abc}^{ijk}\hat{E}_{abc}^{ijk}\cdots, \tag{8}$$

where $\tau_{ij\cdots}^{ab\cdots}$ $(\lambda_{ab\cdots}^{ij\cdots})$ are (de-)excitation amplitudes, and $\hat{E}_{ij\cdots}^{ab\cdots} = \hat{c}_a^\dagger\hat{b}_b^\dagger\cdots\hat{c}_j\hat{c}_i$. The stationary conditions, $\delta S = 0$, with respect to the variation of the parameters of the wavefunction ($\delta\tau_{ij\cdots}^{ab\cdots}$, $\delta\lambda_{ab\cdots}^{ij\cdots}$, and $\delta\psi_\mu$) gives us the corresponding equations of motions (EOMs), $\delta\psi_\mu$ is orthonormality-conserving orbital variation.

For deriving the TD-OCCD(T) method, we first construct a fourth-order Lagrangian defined in Pathak et al. (2021). We make a further approximation to the Lagrangian and write separating it into two parts,

$$L_{\mathrm{CCD(T)}}^{(4)} = L_0 + \langle\Phi|\left(1 + \hat{\Lambda}_2\right)\left[(\bar{f} + \hat{v})e^{\hat{T}_2}\right]_c|\Phi\rangle - i\lambda_{ab}^{ij}\dot{\tau}_{ij}^{ab} \tag{9a}$$

$$+\langle\Phi|\hat{\Lambda}_2\left[(\bar{f} + \hat{v})\hat{T}_3\right]_c|\Phi\rangle + \langle\Phi|\hat{\Lambda}_3\left(\bar{f}\hat{T}_3\right)_c|\Phi\rangle$$

$$+\langle\Phi|\hat{\Lambda}_3\left(\hat{v}\hat{T}_2\right)_c|\Phi\rangle - i\lambda_{abc}^{ijk}\dot{\tau}_{ijk}^{abc}, \tag{9b}$$

where $\bar{f} = \hat{f} - i\hat{X}$, $\hat{f} = (h_q^p + v_{qj}^{pj})\{\hat{E}_q^p\}$, $\hat{v} = v_{qs}^{pr}\{\hat{E}_{qs}^{pr}\}/4$, and $v_{qs}^{pr} = u_{qs}^{pr} - u_{sq}^{pr}$, $\hat{X} = X_\nu^\mu\hat{E}_\nu^\mu$, and $X_\nu^\mu = \langle\psi_\mu|\dot{\psi}_\nu\rangle$ is anti-Hermitian. The double amplitudes are obtained by making $L_{\mathrm{CCD(T)}}^{(4)}$ of Eq. 9a stationary with respect to $\delta S/\delta\lambda_{ab}^{ij}(t) = 0$, $\delta S/\delta\tau_{ij}^{ab}(t) = 0$, the triples by making Eq. 9b stationary with respect to $\delta S/\delta\lambda_{abc}^{ijk}(t) = 0$, and $\delta S/\delta\tau_{ijk}^{abc}(t) = 0$,

$$\begin{aligned} i\dot{\tau}_{ij}^{ab} = {} & v_{ij}^{ab} - p(ij)\bar{f}_j^k\tau_{ik}^{ab} + p(ab)\bar{f}_c^a\tau_{ij}^{cb} \\ & + \frac{1}{2}v_{cd}^{ab}\tau_{ij}^{cd} + \frac{1}{2}v_{ij}^{kl}\tau_{kl}^{ab} + p(ij)p(ab)v_{ic}^{ak}\tau_{kj}^{cb} \\ & - \frac{1}{2}p(ij)\tau_{ik}^{ab}\tau_{jl}^{cd}v_{cd}^{kl} + \frac{1}{2}p(ab)\tau_{ij}^{bc}\tau_{kl}^{ad}v_{cd}^{kl} \\ & + \frac{1}{4}\tau_{kl}^{ab}\tau_{ij}^{cd}v_{cd}^{kl} + \frac{1}{2}p(ij)p(ab)\tau_{il}^{bc}\tau_{jk}^{ad}v_{cd}^{kl} \end{aligned} \tag{10}$$

$$\begin{aligned} -i\dot{\lambda}_{ab}^{ij} = {} & v_{ab}^{ij} - p(ij)\bar{f}_k^i\lambda_{ab}^{kj} + p(ab)\bar{f}_a^c\lambda_{cb}^{ij} \\ & + \frac{1}{2}v_{ab}^{cd}\lambda_{cd}^{ij} + \frac{1}{2}v_{kl}^{ij}\lambda_{ab}^{kl} + p(ij)p(ab)v_{kb}^{cj}\lambda_{ac}^{ik} \\ & - \frac{1}{2}p(ij)\lambda_{cd}^{ik}\tau_{kl}^{cd}v_{ab}^{jl} + \frac{1}{2}p(ab)\lambda_{bc}^{kl}\tau_{kl}^{cd}v_{ad}^{ij} \\ & + \frac{1}{4}\lambda_{ab}^{kl}\tau_{kl}^{cd}v_{cd}^{ij} + \frac{1}{2}p(ij)p(ab)\lambda_{ac}^{jk}\tau_{kl}^{cd}v_{bd}^{il} \\ & - \frac{1}{2}p(ij)\lambda_{ab}^{ik}\tau_{kl}^{cd}v_{cd}^{jl} \\ & + \frac{1}{2}p(ab)\lambda_{bc}^{ij}\tau_{kl}^{cd}v_{ad}^{kl} + \frac{1}{4}\lambda_{cd}^{ij}\tau_{kl}^{cd}v_{ab}^{kl} \end{aligned} \tag{11}$$

$$\begin{aligned} i\dot{\tau}_{ijk}^{abc} = {} & p(k/ij)p(a/bc)v_{dk}^{bc}t_{ij}^{ad} - p(i/jk)p(c/ab)v_{jk}^{lc}t_{il}^{ab} \\ & - p(k/ij)\bar{f}_k^l\tau_{ijl}^{abc} + p(c/ab)\bar{f}_d^c\tau_{ijk}^{abd}, \end{aligned} \tag{12}$$

$$\begin{aligned} -i\dot{\lambda}_{abc}^{ijk} = {} & p(k/ij)p(a/bc)v_{bc}^{dk}\lambda_{ad}^{ij} - p(c/ab)p(i/jk)v_{lc}^{jk}\lambda_{ab}^{ij} \\ & + p(c/ab)\bar{f}_c^d\lambda_{abd}^{ijk} - p(k/ij)\bar{f}_l^k\lambda_{abc}^{ijl} \\ & + p(i/jk)p(a/bc)\bar{f}_a^i\lambda_{bc}^{jk}, \end{aligned} \tag{13}$$

where $p(\mu\nu)$ and $p(\mu|\nu\gamma)$ are the permutation operators; $p(\mu\nu)$ $A_{\mu\nu} = A_{\mu\nu} - A_{\nu\mu}$, and $p(\mu/\nu\gamma) = 1 - p(\mu\nu) - p(\mu\gamma)$.

The EOM for the orbitals can be written down in the following form Sato et al. (2016),

$$i|\dot{\psi}_p\rangle = \left(\hat{1} - \hat{P}\right)\hat{F}|\psi_p\rangle + i|\psi_q\rangle X_p^q, \tag{14}$$

where $\hat{1} = \sum_\mu|\psi_\mu\rangle\langle\psi_\mu|$ is the identity operator within the space spanned by the given basis, $\hat{P} = \sum_q|\psi_q\rangle\langle\psi_q|$ is the projector onto the occupied spin-orbital space, and

$$\hat{F}|\psi_p\rangle = \hat{h}|\psi_p\rangle + \hat{W}_s^r|\psi_q\rangle P_{or}^{qs}\left(D^{-1}\right)_p^o, \tag{15}$$

where D and P are Hermitialized one- (1RDM) and two- (2RDM) particle reduced density matrices defined in Sato et al. (2018b), and W_s^r is the mean-field operator (Sato and Ishikawa (2013)). The matrix element X_p^q includes orbital rotations among various subspaces. Non-redundant orbital rotations are determined by $i(\delta_b^a D_i^j - D_b^a\delta_i^j)X_j^b = F_p^a D_i^p - D_p^a F_p^{i*} - \frac{i}{8}\dot{\tau}_{ijk}^{abc}\lambda_{bc}^{jk} - \frac{i}{8}\tau_{ijk}^{abc}\dot{\lambda}_{bc}^{jk}$. Redundant orbital rotations $\{X_{j'}^{i'}\}$, $\{X_j^i\}$, and $\{X_b^a\}$ can be arbitrary antiHermitian matrix elements. The general expressions for the RDMs are the same as in the TD-OCCDT(4) method (Pathak et al. (2021)).

3 Numerical results and discussion

Our numerical implementation has an interface with the Gaussian09 program (Frisch et al. (2009)) for checking ground state energy with the standard Gaussian basis results. We study BH molecule with double-ζ plus polarization (DZP). We have

TABLE 1 Comparison of the ground state energy of BH (r_e=2.4 bohr) molecule in DZP basis[a].

Method	This work	References	
OCCD[b]	− 25.225 591 67	− 25.225 592	Bozkaya and Schaefer (2012)
OCCD(T)[b]	− 25.226 913 29	− 25.226 913	Bozkaya and Schaefer (2012)
OCCD[c]	− 25.178 285 70	− 25.178 286	Krylov et al. (1998)
OCCD(T)[c]	− 25.178 301 00		

[a] Gaussian09 program (Frisch et al. (2009)) is used to generate the required one-electron, two-electron, and overlap integrals, required for the imaginary time propagation of EOMs in the orthonormalized Gaussian basis. A convergence cut-off of 10^{-15} Hartree of energy difference is chosen in subsequent time steps.

[b] Six electrons correlated within the full basis set.

[c] Six electrons correlated within the six optimized active orbitals.

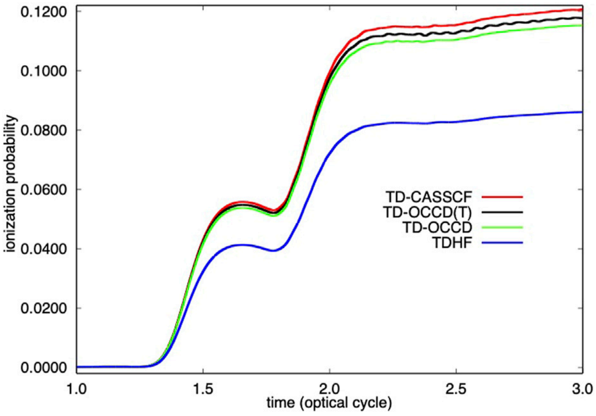

FIGURE 2
Time evolution of single ionization probability of Kr irradiated by a laser pulse with a wavelength of 800 nm and a peak intensity of 2×10^{14} W/cm^2 calculated with TDHF, TD-OCCD, TD-OCCD(T), and TD-CASSCF methods.

reported ground state energy computed by propagating in the imaginary time for OCCD and OCCD(T) methods in Table 1 and compared those with the optimized double and asymmetric triple excitation corrections for the orbital-optimized doubles method of Bozkaya *et al.*, Bozkaya and Schaefer (2012). We also compare our OCCD ground state energy result with Krylov *et al.*,Krylov et al. (1998) within the chosen active space of six electrons correlated among the six optimized active orbitals. We obtained a perfect agreement for all available values.

We have used a spherical-finite-element-discrete-variable representation (FEDVR) basis for representing orbital functions, Sato et al. (2016); Orimo et al. (2018) $\chi_{klm}(r,\theta,\psi) = \frac{1}{r} f_k(r) Y_{lm}(\theta,\phi)$ where Y_{lm} and $f_k(r)$ are spherical harmonics and the normalized radial-FEDVR basis function, respectively. The expansion of the spherical harmonics continued up to the maximum angular momentum $L_{\max}$, and the radial FEDVR basis supports the range of radial coordinate $0 \le r \le R_{\max}$, with cos$^{1/4}$ mask function used as an absorbing boundary for avoiding unphysical reflection from the wall of the simulation box. We have used $l_{\max} = 72$, and the FEDVR basis supporting the radial coordinate $0 < r < 300$ using 78 finite elements each containing 25 DVR functions. The absorbing boundary is switched on at $r = 180$ in all our simulations. The Fourth-order exponential Runge-Kutta method (Hochbruck and Ostermann (2010)) is used to propagate the EOMs with 20000 time steps for each optical cycle. We run the simulations for a further 6,000 time steps after the end of the pulse. In all correlation calculations, eight electrons of 4*s*4*p* orbitals are considered as active and correlated among thirteen active orbitals. We report simulation results computed using a three-cycle laser pulse with a central wavelength of 800 nm having intensity 2×10^{14} W/cm^2 and a period of $T = 2\pi/\omega_0 \sim 2.67$ fs.

We report the time evolution of dipole moment of Kr in Figure 1 and in Figure 2 single electron ionization probability. Time-dependent dipole moment is evaluated as a trace $\langle\psi_p|\hat{z}|\psi_q\rangle D^q_p$ using 1RDMs. For the single electron ionization probability, we computed the probability of finding an electron outside a sphere of a radius of 20 a.u. using RDMs defined in Refs. 19; 20; 37. We compare the results of TD-CASSCF, TD-OCCD(T), TD-OCCD, and TDHF methods.

We observe a substantial underestimation (both in Figure 1, and Figure 2) by the TDHF method due to the lack of correlation treatment. All correlation methods perform according to their ability to treat electron correlation. We also computed results using the TD-OCCDT method but not reported here since those results are not identifiable from the TD-CASSCF results within the graphical resolution.

Next, we report high-harmonic generation in Figure 3. It is calculated by squaring the modulus $I(\omega) = |a(\omega)|^2$ of the Fourier transform of the expectation value of the dipole acceleration with a modified Ehrenfest expression (Sato et al. (2016)). In panel (c) of Figure 3, we plot the absolute relative deviation ($\delta(\omega)$, of the spectral amplitude $a(\omega)$ from the TD-CASSCF value for each method. All methods qualitatively predict similar HHG spectra with TDHF underestimates the spectral intensity. The relative deviation of results from TD-CASSCF ones follows the general trend TDHF > TD-OCCD > TD-OCCD(T) > TD-OCCDT, the same as what we observe for the time-dependent dipole moment and single ionization probability. We also simulated results with lower and higher intensity. However, the trend remains the same.

Finally, we make a tally of computational costs for all the methods considered in this article. All simulations performed using an Intel(R) Xeon(R) Gold 6,230 central processing unit (CPU) with 40 processors with a clock speed of 2.10 GHz, and report total simulations time in Table 2. Further, we report a reduction in the computational cost for various TD-OCC methods relative to the TD-CASSCF. We see a massive 63% cost reduction for the TD-OCCD(T) method, which is larger

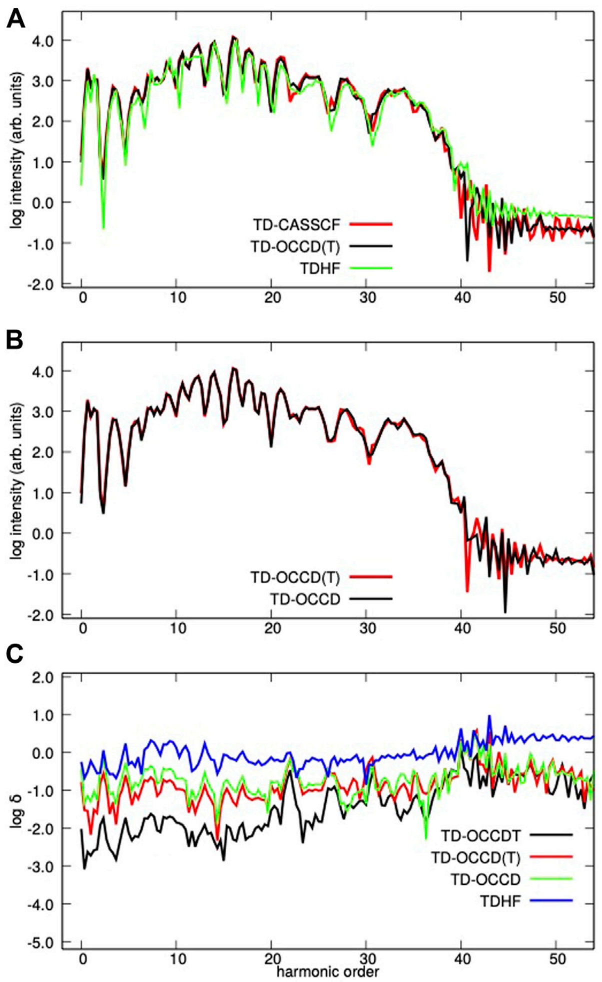

FIGURE 3
The HHG spectra **(A,B)** and the relative deviation **(C)** of the spectral amplitude from the TD-CASSCF spectrum from Kr irradiated by a laser pulse with a wavelength of 800 nm and a peak intensity of 2 × 10^{14} W/cm^2 with various methods.

TABLE 2 Comparison of the total simulation time[a] (in min) spent for TD-CASSCF, TD-OCCDT, TDCCD(T), and TD-OCCD methods.

Method	Time (min)	Cost reduction (%)
TD-CASSCF	47303	. . .
TD-OCCDT	19697	58
TD-OCCD(T)	17504	63
TD-OCCD	17494	63

[a] Time spent for the simulation of Kr atom for 66000 time steps ($0 \le t \le 3.3T$) of a real-time simulation ($I_0 = 2 \times 10^{14}$ W/cm^2 and $\lambda = 800$ nm), using an Intel(R) Xeon(R) Gold 6230 CPU with 40 processors having a clock speed of 2.10 GHz.

than for the TD-OCCDT method (58%), and a minimal increase from the TD-OCCD method.

4 Concluding remarks

We have reported the formulation and implementation of the TD-OCCD(T) method. As the first application, we employed this method to study laser-driven dynamics in Kr exposed to an intense near-infrared laser pulse. We observe a 63% cost reduction in comparison to the TD-CASSCF method without losing much accuracy. Therefore, we conclude that TD-OCCD(T) method will certainly be beneficial in exploring highly accurate *ab initio* simulations of electron dynamics in larger chemical systems.

Data availability statement

The raw data supporting the conclusion of this article will be made available by the authors, without undue reservation.

Author contributions

HP and TS formulated the method. HP numerically implemented the method and performed simulations. All the authors analyzed the results and contributed to the submitted version of the manuscript.

Funding

This research was supported in part by a Grant-in-Aid for Scientific Research (Grants No. JP18H03891 and No. JP19H00869) from the Ministry of Education, Culture, Sports, Science and Technology (MEXT) of Japan. This research was also partially supported by JST COI (Grant No. JPMJCE1313), JST CREST (Grant No. JPMJCR15N1), and by MEXT Quantum Leap Flagship Program (MEXT Q-LEAP) Grant Number JPMXS0118067246.

Conflict of interest

The authors declare that the research was conducted in the absence of any commercial or financial relationships that could be construed as a potential conflict of interest.

Publisher's note

References

Baker, S., Robinson, J. S., Haworth, C., Teng, H., Smith, R., Chirilă, C., et al. (2006). Probing proton dynamics in molecules on an attosecond time scale. *Science* 312, 424–427. doi:10.1126/science.1123904

Bozkaya, U., and Schaefer, H. F., III (2012). Symmetric and asymmetric triple excitation corrections for the orbital-optimized coupled-cluster doubles method: Improving upon ccsd (t) and ccsd (t) λ: Preliminary application. *J. Chem. Phys.* 136, 204114. doi:10.1063/1.4720382

Caillat, J., Zanghellini, J., Kitzler, M., Koch, O., Kreuzer, W., and Scrinzi, A. (2005). Correlated multielectron systems in strong laser fields: A multiconfiguration time-dependent Hartree-Fock approach. *Phys. Rev. A . Coll. Park.* 71, 012712. doi:10.1103/physreva.71.012712

Corkum, P. á., and Krausz, F. (2007). Attosecond science. *Nat. Phys.* 3, 381–387. doi:10.1038/nphys620

[Dataset] Frisch, M., Trucks, G., Schlegel, H., Scuseria, G., Robb, M., Cheeseman, J., et al. (2009). *Gaussian 09, revision d. 01*.

Haxton, D. J., Lawler, K. V., and McCurdy, C. W. (2011). Multiconfiguration time-dependent Hartree-Fock treatment of electronic and nuclear dynamics in diatomic molecules. *Phys. Rev. A . Coll. Park.* 83, 063416. doi:10.1103/physreva.83.063416

Haxton, D. J., and McCurdy, C. W. (2015). Two methods for restricted configuration spaces within the multiconfiguration time-dependent Hartree-Fock method. *Phys. Rev. A . Coll. Park.* 91, 012509. doi:10.1103/physreva.91.012509

Hochbruck, M., and Ostermann, A. (2010). Exponential integrators. *Acta Numer.* 19, 209–286. doi:10.1017/s0962492910000048

Hochstuhl, D., and Bonitz, M. (2011). Two-photon ionization of helium studied with the multiconfigurational time-dependent Hartree–Fock method. *J. Chem. Phys.* 134, 084106. doi:10.1063/1.3553176

Hoodbhoy, P., and Negele, J. W. (1978). Time-dependent coupled-cluster approximation to nuclear dynamics. i. application to a solvable model. *Phys. Rev. C* 18, 2380–2394. doi:10.1103/physrevc.18.2380

Hoodbhoy, P., and Negele, J. W. (1979). Time-dependent coupled-cluster approximation to nuclear dynamics. ii. general formulation. *Phys. Rev. C* 19, 1971–1982. doi:10.1103/physrevc.19.1971

Huber, C., and Klamroth, T. (2011). Explicitly time-dependent coupled cluster singles doubles calculations of laser-driven many-electron dynamics. *J. Chem. Phys.* 134, 054113. doi:10.1063/1.3530807

Itatani, J., Levesque, J., Zeidler, D., Niikura, H., Pépin, H., Kieffer, J. C., et al. (2004). Tomographic imaging of molecular orbitals. *Nature* 432, 867–871. doi:10.1038/nature03183

Kato, T., and Kono, H. (2004). Time-dependent multiconfiguration theory for electronic dynamics of molecules in an intense laser field. *Chem. Phys. Lett.* 392, 533–540. doi:10.1016/j.cplett.2004.05.106

Krausz, F., and Ivanov, M. (2009). Attosecond physics. *Rev. Mod. Phys.* 81, 163–234. doi:10.1103/revmodphys.81.163

Krylov, A. I., Sherrill, C. D., Byrd, E. F., and Head-Gordon, M. (1998). Size-consistent wave functions for nondynamical correlation energy: The valence active space optimized orbital coupled–cluster doubles model. *J. Chem. Phys.* 109, 10669–10678. doi:10.1063/1.477764

Kümmel, H. G. (2003). A biography of the coupled cluster method. *Int. J. Mod. Phys. B* 17, 5311–5325. doi:10.1142/s0217979203020442

Kvaal, S. (2012). *Ab initio* quantum dynamics using coupled-cluster. *J. Chem. Phys.* 136, 194109. doi:10.1063/1.4718427

Miyagi, H., and Madsen, L. B. (2013). Time-dependent restricted-active-space self-consistent-field theory for laser-driven many-electron dynamics. *Phys. Rev. A . Coll. Park.* 87, 062511. doi:10.1103/physreva.87.062511

Miyagi, H., and Madsen, L. B. (2014). Time-dependent restricted-active-space self-consistent-field theory for laser-driven many-electron dynamics. ii. extended formulation and numerical analysis. *Phys. Rev. A . Coll. Park.* 89, 063416. doi:10.1103/physreva.89.063416

Nascimento, D. R., and DePrince, A. E., III (2016). Linear absorption spectra from explicitly time-dependent equation-of-motion coupled-cluster theory. *J. Chem. Theory Comput.* 12, 5834–5840. doi:10.1021/acs.jctc.6b00796

Nest, M., Klamroth, T., and Saalfrank, P. (2005). The multiconfiguration time-dependent Hartree–Fock method for quantum chemical calculations. *J. Chem. Phys.* 122, 124102. doi:10.1063/1.1862243

Orimo, Y., Sato, T., Scrinzi, A., and Ishikawa, K. L. (2018). Implementation of the infinite-range exterior complex scaling to the time-dependent complete-active-space self-consistent-field method. *Phys. Rev. A. Coll. Park.* 97, 023423. doi:10.1103/physreva.97.023423

Pathak, H., Sato, T., and Ishikawa, K. L. (2020a). Study of laser-driven multielectron dynamics of ne atom using time-dependent optimised second-order many-body perturbation theory. *Mol. Phys.* 118, e1813910. doi:10.1080/00268976.2020.1813910

Pathak, H., Sato, T., and Ishikawa, K. L. (2021). Time-dependent optimized coupled-cluster method for multielectron dynamics iv: Approximate consideration of the triple excitation amplitudes. *J. Chem. Phys.* 154, 234104. doi:10.1063/5.0054743

Pathak, H., Sato, T., and Ishikawa, K. L. (2020b). Time-dependent optimized coupled-cluster method for multielectron dynamics. ii. a coupled electron-pair approximation. *J. Chem. Phys.* 152, 124115. doi:10.1063/1.5143747

Pathak, H., Sato, T., and Ishikawa, K. L. (2020c). Time-dependent optimized coupled-cluster method for multielectron dynamics. iii. a second-order many-body perturbation approximation. *J. Chem. Phys.* 153, 034110. doi:10.1063/5.0008789

Pedersen, T. B., Kristiansen, H. E., Bodenstein, T., Kvaal, S., and Schøyen, Ø. S. (2021). Interpretation of coupled-cluster many-electron dynamics in terms of stationary states. *J. Chem. Theory Comput.* 17, 388–404. doi:10.1021/acs.jctc.0c00977

Pedersen, T. B., and Kvaal, S. (2019). Symplectic integration and physical interpretation of time-dependent coupled-cluster theory. *J. Chem. Phys.* 150, 144106. doi:10.1063/1.5085390

Pigg, D. A., Hagen, G., Nam, H., and Papenbrock, T. (2012). Time-dependent coupled-cluster method for atomic nuclei. *Phys. Rev. C* 86, 014308. doi:10.1103/physrevc.86.014308

Raghavachari, K., Trucks, G. W., Pople, J. A., and Head-Gordon, M. (1989). A fifth-order perturbation comparison of electron correlation theories. *Chem. Phys. Lett.* 157, 479–483. doi:10.1016/s0009-2614(89)87395-6

Sato, T., Ishikawa, K. L., Březinová, I., Lackner, F., Nagele, S., and Burgdörfer, J. (2016). Time-dependent complete-active-space self-consistent-field method for atoms: Application to high-order harmonic generation. *Phys. Rev. A . Coll. Park.* 94, 023405. doi:10.1103/physreva.94.023405

Sato, T., and Ishikawa, K. L. (2013). Time-dependent complete-active-space self-consistent-field method for multielectron dynamics in intense laser fields. *Phys. Rev. A . Coll. Park.* 88, 023402. doi:10.1103/physreva.88.023402

Sato, T., and Ishikawa, K. L. (2015). Time-dependent multiconfiguration self-consistent-field method based on the occupation-restricted multiple-active-space model for multielectron dynamics in intense laser fields. *Phys. Rev. A . Coll. Park.* 91, 023417. doi:10.1103/physreva.91.023417

Sato, T., Orimo, Y., Teramura, T., Tugs, O., and Ishikawa, K. L. (2018a). "Time-dependent complete-active-space self-consistent-field method for ultrafast intense laser science," in *Progress in ultrafast intense laser science XIV* (Berlin, Germany: Springer), 143–171.

Sato, T., Pathak, H., Orimo, Y., and Ishikawa, K. L. (2018b). Communication: Time-dependent optimized coupled-cluster method for multielectron dynamics. *J. Chem. Phys.* 148, 051101. doi:10.1063/1.5020633

Schonhammer, K., and Gunnarsson, O. (1978). Time-dependent approach to the calculation of spectral functions. *Phys. Rev. B* 18, 6606. doi:10.1103/physrevb.18.6606

Scuseria, G. E., and Schaefer, H. F., III (1987). The optimization of molecular orbitals for coupled cluster wavefunctions. *Chem. Phys. Lett.* 142, 354–358. doi:10.1016/0009-2614(87)85122-9

Shavitt, I., and Bartlett, R. J. (2009). *Many-body methods in chemistry and physics: MBPT and coupled-cluster theory*. Cambridge: Cambridge University Press.

Sherrill, C. D., Krylov, A. I., Byrd, E. F., and Head-Gordon, M. (1998). Energies and analytic gradients for a coupled-cluster doubles model using variational brueckner orbitals: Application to symmetry breaking in o 4+. *J. Chem. Phys.* 109, 4171–4181. doi:10.1063/1.477023

Watts, J. D., Gauss, J., and Bartlett, R. J. (1993). Coupled-cluster methods with noniterative triple excitations for restricted open-shell Hartree–Fock and other general single determinant reference functions. energies and analytical gradients. *J. Chem. Phys.* 98, 8718–8733. doi:10.1063/1.464480

frontiers | Frontiers in Chemistry

TYPE Original Research
PUBLISHED 28 September 2022
DOI 10.3389/fchem.2022.983342

OPEN ACCESS

EDITED BY
Yuichi Fujimura,
Tohoku University, Japan

REVIEWED BY
Tobias Brixner,
Julius Maximilian University of Würzburg, Germany
Artur Nenov,
University of Bologna, Italy

*CORRESPONDENCE
Patrick Nuernberger,
patrick.nuernberger@ur.de

SPECIALTY SECTION
This article was submitted to Physical Chemistry and Chemical Physics, a section of the journal Frontiers in Chemistry

RECEIVED 30 June 2022
ACCEPTED 23 August 2022
PUBLISHED 28 September 2022

CITATION
Wortmann S, Kutta RJ and Nuernberger P (2022), Monitoring the photochemistry of a formazan over 15 orders of magnitude in time.
Front. Chem. 10:983342.
doi: 10.3389/fchem.2022.983342

Monitoring the photochemistry of a formazan over 15 orders of magnitude in time

Svenja Wortmann, Roger Jan Kutta and Patrick Nuernberger*

Institut für Physikalische und Theoretische Chemie, Universität Regensburg, Regensburg, Germany

2,3,5-triphenyltetrazolium chloride (TTC) may convert into phenyl-benzo[c] tetrazolocinnolium chloride (PTC) and 1,3,5-triphenylformazan (TPF) under irradiation with light. The latter reaction, albeit enzymatically rather than photochemically, is used in so-called TTC assays indicating cellular respiration and cell growth. In this paper, we address the photochemistry of TPF with time-resolved spectroscopy on various time scales. TPF is stabilized by an intramolecular hydrogen bond and switches photochemically *via* an E-Z isomerization around an N=N double bond into another TPF-stereoisomer, from which further isomerizations around the C=N double bond of the phenylhydrazone group are possible. We investigate the underlying processes by time-resolved spectroscopy in dependence on excitation wavelength and solvent environment, resolving several intermediates over a temporal range spanning 15 orders of magnitude (hundreds of femtoseconds to hundreds of seconds) along the reaction path. In a quantum-chemical analysis, we identify 16 stable ground-state isomers and discuss which ones are identified in the experimental data. We derive a detailed scheme how these species are thermally and photochemically interconnected and conclude that proton transfer processes are involved.

KEYWORDS

formazan, photoisomerization, transient absorption, femtochemistry, streak camera, excited-state dynamics, proton transfer, ground-state dynamics

1 Introduction

Formazans comprise an azo group (–N=N–) and a hydrazone group (–C=N–N–), with both being capable to isomerize at the double bond upon excitation with visible light. The most investigated representative is 1,3,5-triphenylformazan (TPF, Figure 1). TPF can be generated by a photochemical conversion of 2,3,5-triphenyltetrazolium chloride (TTC), accompanied by a color change of the solution from colorless to red (Hausser et al., 1949a; Grummt and Langbein, 1981). TPF exhibits a unique photochromism which depends on the excitation conditions and the solvent environment. We investigated in an earlier study to which extent the thermal back relaxation around the C=N double bond is sensitive to the polarity and the hydrogen-bond donating ability of the solvent (Wortmann et al., 2022). While polar solvents with a higher polarity result in a decrease of the activation barrier of the anti-syn isomerization around the C=N bond, hydrogen bonding has an oppositely directed effect and can stabilize the trans-anti isomer under certain conditions. Due to its distinct photochromism and this high sensitivity toward external influences, but mostly because of its enzymatic formation from TTC, TPF is found in a wide field of applications. These are found in biological assays to indicate cellular respiration and cell growth (Ziegler, 1953; Mosmann, 1983; Berridge et al., 2005), in agriculture to verify the germinability of seeds (Lakon, 1942; Smith, 1951), in medicine, especially in cancer research (Carmichael et al., 1987; Alley et al., 1988; Scudiere et al., 1988), but also in areas like dosimetry (Kovács et al., 1996), chemical synthesis (Neugebauer and Russell, 1968; Lipunova et al., 2019), or as chelating agents in organometallic chemistry (Lipunova et al., 2019; Gilroy and Otten, 2020). In general, most of these applications rely on the reduction of the colorless tetrazolium salt TTC to TPF, so that a colorless solution turns red (Hausser et al., 1949a). The photochemistry of the precursor TTC has already been explored in detail with various techniques (Pechmann and Runge, 1894; Hausser et al., 1949b; Nineham, 1955; Neugebauer and Russell, 1968; Umemoto, 1985; Gonzalez and San Roman, 1989; Kovács et al., 1996; Kanal et al., 2015; Bolze et al., 2018). Despite several studies with a focus on quantum-chemical calculations (Buemi et al., 1998; Buemi and Zuccarello, 2002; King and Murrin, 2004; Tezcan and Tokay, 2010; Sherif, 2015), luminescence (Turkoglu et al., 2015), solvatochromism (Sherif, 1997; Kumar et al., 2014; Wortmann et al., 2022), Raman and infrared studies (Schiele, 1965; Otting and Neugebauer, 1968; Otting and Neugebauer, 1969; Lewis and Sandorfy, 1983; Hiura and Takahashi, 1989a; Hiura and Takahashi, 1989b; Tezcan and Ozkan, 2003), or electrochemical properties (Gökçe et al., 2005; Sherif, 2015; Turkoglu et al., 2015) of formazans, also investigated under temperature (Kuhn and Weitz, 1953; Langbein, 1979; Grummt and Langbein, 1981; Sueishi and Nishimura, 1983) or pressure variation (Sueishi and Nishimura, 1983), the interplay of light-induced processes which set in on an ultrafast time scale and extend to minutes has not been comprehensively studied for TPF. With regard to the involved intermediate species of TPF, several photoisomerization mechanisms of TPF are discussed in literature, with the one proposed by Grummt and Langbein which was derived from laser flash photolysis experiments (Grummt and Langbein, 1981) being in closest accordance to the one inferred in our recent study (Wortmann et al., 2022). Note that also the orientation of the single bonds adjacent to the double bonds are sometimes drawn differently (Lewis and Sandorfy, 1983; Veas-Arancibia, 1986) and lead to further stable isomers, as we will discuss in detail in Section 4. The energetically most-stable isomer is the trans-syn form (also called "red I", Figure 1), which is stabilized by an intramolecular hydrogen bond, forming a quasi-aromatic heterocycle. Illumination with visible light leads to an isomerization around the N=N double bond, yielding a cis-syn isomer ("red II", Figure 1). For this species, an intramolecular hydrogen bonding can occur as well. Afterwards, thermal isomerization around both N=N and C=N leads to the trans-anti analogue ("yellow I", Figure 1), which is accompanied by a color change of the solution from red to yellow. Spectroscopically, a hypsochromic shift from around 490 nm to 405 nm is observable in toluene solutions (Kuhn and Weitz, 1953; Langbein, 1979; Grummt and Langbein, 1981; Atabekyan et al., 2011; Wortmann et al., 2022). Under dark conditions, the trans-anti isomer relaxes back into the energetically-favored trans-syn form *via* an anti-syn isomerization around the C=N double bond. However, when absorbing visible light, the trans-anti isomer may follow another pathway, yielding a second yellow species, the cis-anti analogue ("yellow II", Figure 1). Both yellow forms can be characterized by absorption spectra with different extinction coefficients (Hausser et al., 1949a; Langbein, 1979; Grummt and Langbein, 1981) and a broader absorption band for yellow II.

Here, we address three aspects of the light-induced reactions of TPF. First, we want to monitor all relevant time scales, from the primary steps occurring in sub-ps to the slowest thermal equilibrations occurring within minutes. Several different pump-probe setups were used to monitor this extended time window, that is fs to ns transient absorption (TA) based on femtosecond lasers, ns to ms TA with ns excitation pulses, and ms up to minutes with pulsed light-emitting diodes (LEDs) as pump source. Second, we reassess the assignment of the involved isomers by DFT and TD-DFT calculations. Third, we discuss the role of proton transfer to the thermal interconversion of the isomers.

2 Materials and methods

TPF was purchased from Sigma-Aldrich, used without further purification, and dissolved in anhydrous acetonitrile (Sigma-Aldrich) or methanol (Uvasol, Merck) of spectroscopic grade. UV-Vis absorption spectra were recorded on a spectrophotometer (Cary60, Agilent) which could be combined with LED excitation in a perpendicular arrangement in order to record ms to min TA data with a time increment of 12.5 ms. For some of the employed LEDs, a different spectrophotometer (UV 1800, Shimadzu) was employed for the same purpose, with a time increment of 480 ms. The LED temporal rectangular pulse width was also set to 12.5 or 480 ms, respectively. The sample (250 µL) was inside a rectangular quartz cuvette (Starna, 10 mm × 2 mm) and the absorption was monitored over the 10 mm optical path length, while the LED was adjusted to illuminate the entire sample, thus aiming at a homogeneous illumination over the 2 mm path length.

For ns to ms TA, a Nd:YAG laser (Surelite II, Continuum) in combination with an optical parametric oscillator (Surelite OPO Plus, Continuum) generated the pump pulses, while the broadband probe light originated from a Xenon flash lamp (MSP-05, Müller Elektronik-Optik). A streak camera (C7700, Hamamatsu Photonics) with spectrograph and CCD camera (ORCA-CR, Hamamatsu

Photonics) was employed for detection [see (Kutta et al., 2013; Dick et al., 2019) for further details on the experimental implementation]. The sample was circulated through the 2 mm (excitation path) × 10 mm (probe path) quartz cuvette from an external reservoir of 4 mL.

For fs to ns TA, a Ti:Sa amplifier system (Libra, Coherent) generated laser pulses at a repetition rate of 1 kHz centered at 800 nm that were used to pump an optical parametric amplifier (TOPAS-C, Light Conversion), yielding pulses at 530 nm or (after a further nonlinear process) 330 nm used for excitation of the sample. For the probe beam, parts of the 800 nm were used to pump a home-built noncollinear optical parametric amplifier adjusted to ca. 500 nm that then was focused into a moving calcium fluoride plate generating a white-light supercontinuum (Dobryakov et al., 2010). This was split into a reference bypassing the sample and a probe beam traversing the sample. These two beams were independently imaged onto two home-built grating spectrographs, and their spectra were recorded with photodiode arrays (S3901-512Q, Hamamatsu, 512 pixels) at 1.5 nm resolution. The polarizations of pump and probe beams were set to the magic angle (Megerle et al., 2009; Schott et al., 2014) before reaching the 2 mm × 10 mm quartz cuvette. The temporal resolution was around 100 fs, and the temporal delay was introduced by a cornercube retroreflector on a delay stage (M-531.2S, Physik Instrumente) placed in the pump beam. More details on the employed setup are given in (Brandl et al., 2020).

Quantum-mechanical calculations on all stable TPF conformers were performed using the Orca package (Neese, 2012; Neese, 2018). All ground-state structures were optimized on the level of restricted closed shell density functional theory (RHF-DFT) using the B3LYP functional and the def2-TZVP basis set with D4 dispersion correction. Potential barriers connecting the individual conformers were roughly estimated (as DFT is not able to correctly describe the bond rotation around double bonds) from the crossing points for the relaxed potential energy surfaces along the rotational motion around a corresponding bond starting from each stable conformer using B3LYP/def2-TZVP level of theory.

3 Experimental results and discussion

The steady-state UV-Vis absorption spectra of TPF detected in methanol and acetonitrile solution are nearly identical, with two main absorption bands peaking around 300 and 480 nm, of which the latter comprises a weak shoulder on its red edge (see Figure 2). In unsubstituted formazan, the lowest electronic transition is of $n-\pi^*$ character (Buemi et al., 1998). The same is found for TPF, albeit with a negligible oscillator strength, so that the major absorption band in the visible is dominated by a $\pi-\pi^*$ transition (Avramenko and Stepanov, 1974; Nădejde et al., 2009) to the second excited state S_2 (see also Supplementary Figure S6 with corresponding DFT calculations). For the TPF absorption spectrum in toluene solution, a small spectral shift of the low-frequency $\pi-\pi^*$ transition band by ~10 nm is observed. Under irradiation with visible light, the formation of the yellow isomeric species was reported to occur in acetonitrile (Wilhite, 1991) as well as in toluene/benzene solutions (Kuhn and Weitz, 1953; Langbein, 1979; Grummt and Langbein, 1981; Atabekyan et al., 2011) and is manifested by an increased absorption around 400 nm. Constantly illuminating TPF in methanol solution with 520 nm light also leads to the formation of the yellow species (Figure 2). In comparison to toluene, where the equilibrium is nearly fully shifted under these conditions, in acetonitrile and methanol a distinct amount of TPF molecules is observed in its initial conformation, indicated by both the lower absorption around 400 nm (yellow I) and the remaining contribution at 500 nm (compare black/red dashed curves in Figure 2 with the blue dashed curve).

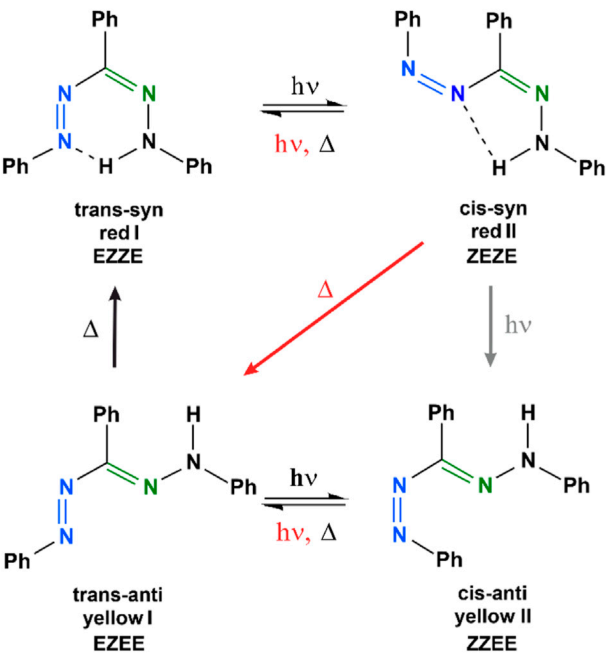

FIGURE 1
The two most prominent photoisomerization schemes of TPF after excitation, as introduced by Kuhn and Weitz (Kuhn and Weitz, 1953) and by Grummt and Langbein (Grummt and Langbein, 1981). Black arrows and symbols indicate pathways present in both models, while gray elements are only found in the Kuhn-Weitz scheme and red elements only in the Grummt-Langbein scheme, respectively. The nomenclature, e.g., trans-syn, corresponds to the N=N double bond (blue) and the C=N double bond (green). The orientation of the adjacent C−N and N−N single bonds will be discussed in Section 4.

3.1 fs-ns transient absorption of 1,3,5-triphenylformazan

The initial photodynamics of TPF were followed by recording the TA on a fs to ns time scale after excitation either at 530 or 330 nm. Transient absorption spectra of TPF are shown in

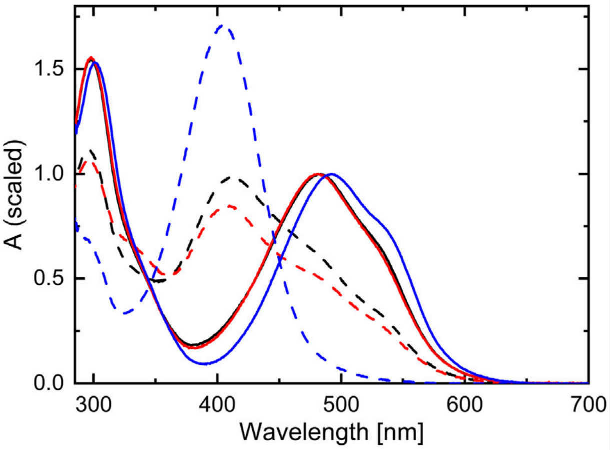

FIGURE 2
Steady-state absorption spectra of TPF dissolved in methanol (black), acetonitrile (red), and toluene (blue). The solid curves display the ground-state absorption spectra (normalized to the maximum around 500 nm), while the dashed spectra correspond to the photostationary state under illumination with 520 nm light.

Figures 3A,C for methanol solution. In both cases, two regions of increased absorption around 400 and 600 nm are observed, together with the ground-state bleach (GSB) in the spectral region around 500 nm. Whereas the overall signal intensity decreases with time, a contribution persists beyond the experimental time window of 2 ns (Kanal et al., 2015). The decay-associated difference spectra (DADS), resulting from a global multiexponential fit to the data matrices with four time constants, are displayed in Figures 3B,D, respectively [contributions for modelling the coherent artefact (Megerle et al., 2009) are not shown for clarity].

The fastest process, with decay time τ_1 being 0.3 and 0.2 ps, respectively, for the two excitation wavelengths, may be assigned to isomerization dynamics connected to the azo group. For trans-azobenzene, the excited-state dynamics directly towards a conical intersection exhibit a decay time around 0.3 ps (Nägele et al., 1997; Lu et al., 2002; Satzger et al., 2003; Satzger et al., 2004; Pancur et al., 2005; Quick et al., 2014; Nenov et al., 2018), with similar values reported for related compounds (Siewertsen et al., 2011; Slavov et al., 2016; Grimmelsmann et al., 2017). However, there is also a further excited-state motion in trans-azobenzene on a time scale of 1–3 ps, assigned to diffusion-type motion (Nägele et al., 1997) or the passage of a barrier in the excited state (Quick et al., 2014). Along these lines, the positive signals around 400 and 600 nm (red DADS in Figure 3B,D) may indicate absorption features of molecules still in an excited state that depopulates with decay time τ_2 mainly into the ground state configuration that was present prior to excitation, as can be seen by the negative contribution in the red DADS. We link the more pronounced excited state absorption (ESA) for excitation at 330 nm compared to 530 nm to the excess energy introduced by the higher photon energy. The DADS with τ_3 (green DADS) may reflect relaxation dynamics accompanied by vibrational cooling of molecules either in the excited state or already in the ground state all ending in the most stable conformer that was initially excited. Although the dominant fraction of excited molecules returns to the initial ground state configuration, a GSB at 480 nm and a product absorption around 330 nm remains on a time scale > 2 ns (see also blue DADS) substantiating the formation of another stable photoisomer. Note that TPF is in an equilibrium of two ground state conformers with predominantly red I but also a few red II conformers, so that the TA data observed after excitation at 330 nm resemble the superposed dynamics of both isomers which explains the small differences in the absorption strength and dynamics compared to the situation when exciting at 530 nm. This aspect will become more evident on a longer time scale (vide infra).

The TA data in the fs-ns time range of TPF in the solvent acetonitrile are very similar and can be analyzed and interpreted accordingly (see Supplementary Figure S1). Only time constant τ_3 assigned to vibrational cooling is by a factor of two larger compared to the situation in methanol. The more rapid vibrational cooling in methanol compared to acetonitrile was reported for other systems and is related to intermolecular hydrogen-bonding in protic environments aggravating energy transfer from the solute to the solvent (Middleton et al., 2007; Ghosh et al., 2019).

There is an alternative rationale for the dynamics on the ps time scale. From resonance Raman studies it was concluded that the initial photoinduced process is an excited-state intramolecular proton transfer (ESIPT) (Lewis and Sandorfy, 1983). Since the isomer red I that predominates in solution is a hydrogen-bonded quasi-aromatic heterocycle, there is a striking congruence with intramolecularly H-bonded ß-diketones which have been studied with laser flash photolysis (Veierov et al., 1977; Kobayashi et al., 2013) and ultrafast spectroscopy approaches (Xu et al., 2004; Poisson et al., 2008; Verma et al., 2014; Verma et al., 2015; Verma et al., 2016). The latter revealed that ESIPT occurs within less than 0.1 ps, followed by relaxation to the lowest excited state in a few ps, and subsequent depopulation of the excited state on a time scale of 10 ps both by relaxation to the hydrogen-bonded ground-state isomer and the formation of other isomers by rotation around a single or double bond. Given the similarity of the molecular system and of the detected time scales, an analogous assignment of processes to the observed dynamics is plausible as well.

A quantitative analysis of our data assuming a fully branched model, in which each transient species is partially converting into each other and partially converting back into the ground-state species, gave a value of 7% for the quantum yield of product formation [see (Kutta et al., 2013), also containing detailed discussion on the general analysis of global fit data]. This is significantly lower than both isomer formation after ESIPT in ß-ketones [e.g., 36% for acetylacetone in acetonitrile (Verma et al., 2014)] and N=N isomerization in *trans*-azobenzene [31% for $n - \pi*$ and 15% for $\pi - \pi*$ excitation in acetonitrile, slightly different yields in other solvents (Quick et al., 2014)], so that an

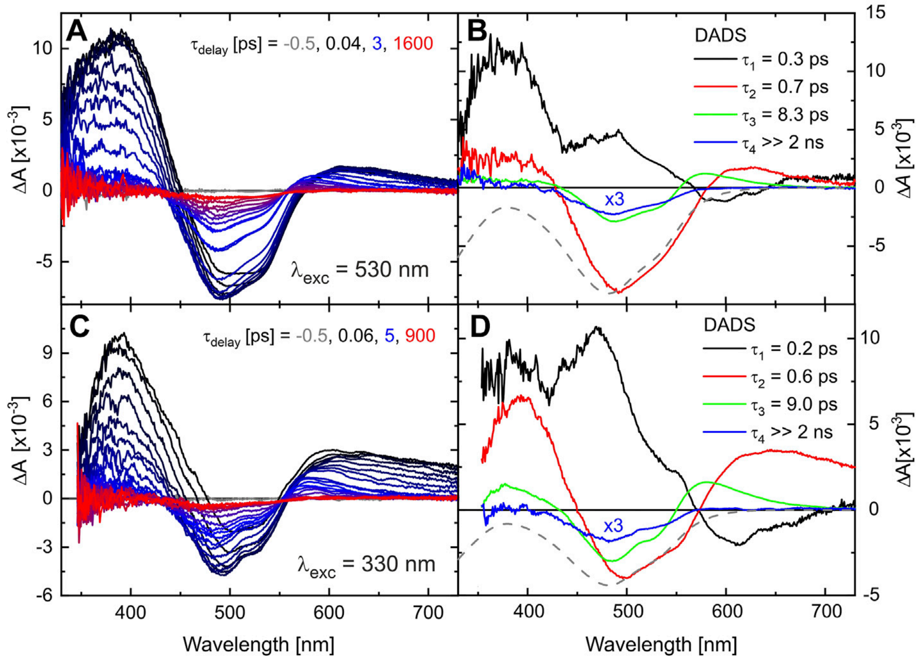

FIGURE 3
Transient absorption of TPF in methanol after excitation at 530 nm **(A)** and 330 nm **(C)** after defined delay times on a fs-ns time scale. The corresponding DADS from a global exponential fit to the data are given in **(B,D)**. The scaled and inverted absorption spectrum of the initial sample is given by a gray-dashed line for comparison.

identification of the initial reaction step is not unambiguous from the TA data but will be further analyzed in Section 4. The rather low quantum yield could be related to the significant $\pi - \pi*$ character (delocalized over the entire molecular framework) of the initially excited S_2 in TPF (see Supplementary Figure S6), but might also originate from the intramolecular hydrogen bond stabilizing the planar configuration of the six-membered chelated ring, thereby disfavoring an out-of-plane motion required for photoisomerization. Nonetheless, our TA data corroborates that although the vast majority of excited red I molecules returns to the red I configuration, the decision along which reaction pathway the system evolves involving several thermal isomerizations (vide infra) is already made within the first few ps.

3.2 ns-ms transient absorption of 1,3,5-triphenylformazan

In order to follow the reaction dynamics further on a ns to ms time scale, the TA of TPF after exciting at 532 or 355 nm was recorded with a pump-flashlamp-probe spectrometer using a streak camera as detection unit. The TA data recorded for TPF in methanol after excitation at 532 nm consist of one absorption band around 340 nm and the GSB at 480 nm. Both features rise faster than the temporal resolution of the used setup, which agrees with the formation of these two TA features within a few ps as determined in Section 3.1, and persist beyond the time window of 1 ms. Hence, a global monoexponential model yielding one DADS (magenta curve in Figure 4A) is sufficient to fully describe the data, and this DADS matches the one for τ_4 of the fs-ns TA measurements (blue-dotted curve in Figure 4A).

When exciting at 355 nm, the same absorption band at 340 nm is observed as after 532 nm excitation. However, the GSB is broader in this case, ranging from 350 nm up to 600 nm. Comparing the DADS with the absorption spectrum of TPF under 520 nm illumination (black-dashed line in Figure 2) reveals the origin for this behavior. The intense Xe-flashlamp of ms duration used as probe source in the ns-ms TA experiment is sufficient to prepare a mixture of red I and yellow I isomers prior to the excitation of the system by the intense pump pulse so that exciting at 532 nm leaves the yellow isomers unaffected, whereas exciting at 355 nm allows the excitation of both isomers, causing a GSB signal comprising the spectral signature of both. To note, in the fs-ns TA experiment (blue-dashed line in Figure 4B) no accumulation of a probe-light induced photostationary equilibrium between forms red I and yellow I is observed due to significantly shorter and less intense probe pulses.

Again, the ns-ms TA data obtained for TPF in acetonitrile (Supplementary Figure S2) are very similar to the ones recorded in methanol.

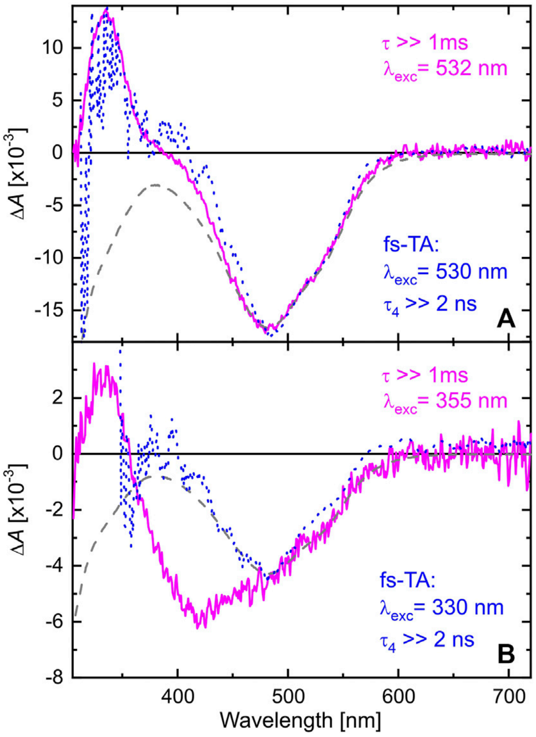

FIGURE 4
DADS of TPF in methanol after excitation at 532 nm **(A)** and 355 nm **(B)**. The magenta DADS result from a global monoexponential fit to the data on a 1 ms time window. The blue dashed curves are the DADS corresponding to τ_4 of the fs-ns TA experiments (blue curves in Figures 3B,D) scaled to match the negative contribution at around 500 nm. The inverted absorption spectrum of the initial sample also scaled to the negative contribution at around 500 nm is given by a gray-dashed line for comparison.

3.3 ms–min transient absorption of 1,3,5-triphenylformazan

The preceding two TA measurement series have shown that the species absorbing around 340 nm is formed on an ultrafast time scale and persists well beyond 1 ms. Hence, ms to min TA measurements were performed exciting TPF either at 390, 405, 455, or 530 nm. The maximal time window of all four measurements was set to 1 min, sufficient for detecting the full recovering process to the initial ground state situation of TPF in methanol. All data matrices were analyzed by a global biexponential fit, yielding the DADS shown in Figure 5.

The cyan DADS corresponding to τ_4 exhibits a positive absorption peaking around 340 nm for all excitation wavelengths. Comparison to the DADS from the ns-ms TA measurements (pink curve in Figures 5A,D) confirms that the same dynamics that were monitored up to 1 ms can now be followed completely. This absorption band was already identified in toluene solution (Wortmann et al., 2022) and assigned to the red II form of TPF, in accordance with the isomerization scheme of Figure 1. The DADS furthermore comprises negative contributions around 500 nm and around 405 nm. These negative amplitudes resemble spectral features of red I and yellow I, respectively, and thus give evidence that photochemically formed red II thermally relaxes back to red I and to yellow I with a decay time of a few hundred milliseconds. The typical absorption feature of formed yellow I is seen at 405 nm in the orange DADS corresponding to τ_5. Thus, the slowest dynamics observed after 530 nm excitation are described by the orange DADS, which shows the spectral features of red I as a negative amplitude (compare the gray-dashed inverted ground-state absorption spectrum) and the absorption feature of yellow I as a positive amplitude, demonstrating the thermally activated back relaxation to red I on a time scale of 10 s (Figure 5A).

Figure 5B shows a similar experiment, but with 455 nm excitation. As red I and red II both absorb at 455 nm, here contributions of both isomers show up in the data. The observed dynamics can nonetheless be interpreted on the lines of the 530 nm excitation experiment in Figure 5A, as the additional contribution of excited red II are rather low.

The situation changes when exciting TPF at 405 nm (Figure 5C). Now, only a small amount of red I is excited, again giving rise to the dynamics described by the cyan DADS that is very similar to the two situations with 530 or 455 nm excitation, respectively. However, since in the dark also yellow I contributes to a small amount to the ground state equilibrium (see Figure 1) it is excited by 405 nm light giving rise to yellow II formation. This is substantiated by the second DADS (orange) that shows a positive absorption feature of yellow II at around 500 nm that decays with a lifetime of ca. 7 s (Figure 5C) back into yellow I identified by the characteristic negative amplitude at 405 nm. The data recorded with 390 nm excitation (Figure 5D) agrees with this interpretation, because at this wavelength, red I can be excited even worse, whereas yellow I still has a high extinction coefficient, so that the cyan DADS (mostly representing relaxation after generation of red II from red I) becomes smaller whereas the orange DADS (comprising yellow II photogenerated from yellow I) gains in relative intensity.

In comparison to the kinetics in methanol, the ground-state processes of TPF on a ms to min time scale are slower in acetonitrile (see Supplementary Figure S3), but much faster than in toluene solution (Wortmann et al., 2022). There, it was shown that the solvent's ability to participate in hydrogen bonds is decisive for how fast the equilibration proceeds.

In the following, we try to develop a line of reasoning with the help of quantum-chemical calculations for how the isomers are interconnected, explaining the slow processes observed for TPF after photoexcitation.

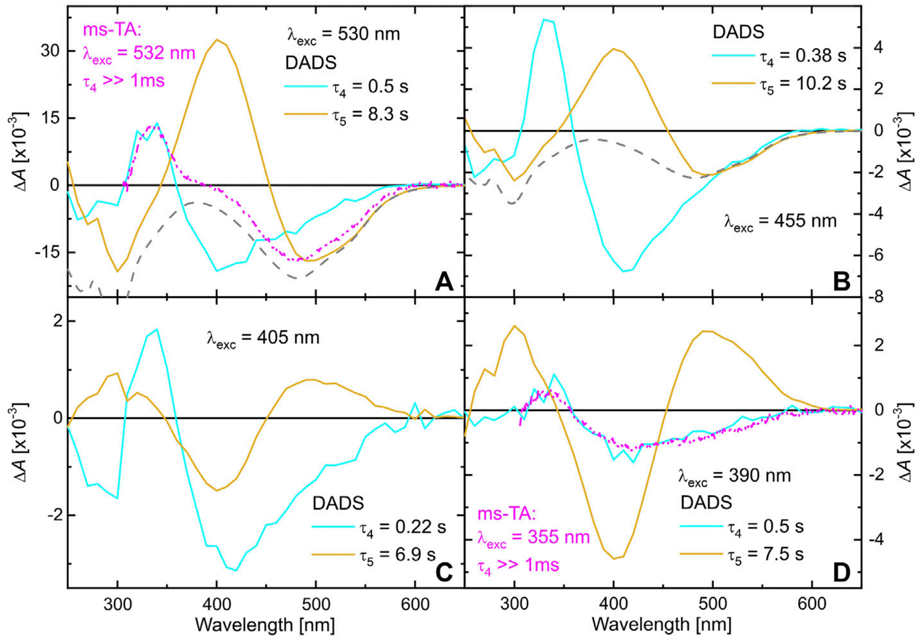

FIGURE 5
DADS of TPF dissolved in methanol, obtained by a global biexponential fit to the data matrices detected after excitation at 530 nm **(A)**, 455 nm **(B)**, 405 nm **(C)** and 390 nm **(D)**. The gray-dashed line represents the absorption spectrum of the solution, while the pink DADS are taken from Figure 4 for comparison.

4 Analysis of reaction pathways

4.1 Simulation of ground-state conformers

Most of the previous experimental studies on the photochemical processes of TPF do not differentiate possible rotamers beyond the four isomers obtained from the cis-trans isomerizations around the N=N and the C=N double bond, resulting in the trans-syn nomenclature also displayed in Figure 1. Theoretical studies [e.g., (Buemi et al., 1998; King and Murrin, 2004)] have addressed further rotamers, as we will also do in the following. For our discussion of the reaction pathways, we further take into account the rotations around the two adjacent single bonds, so that each of the four isomers labelled in Figure 1 may lead to four distinguishable conformers. Our calculations at the B3LYP/def2-TZVP/D4 level of theory indeed result in 16 corresponding ground-state minima, i.e., 16 potentially stable conformers, which however strongly differ in energy and the height of the barriers connecting them.

The optimized structures of the 16 conformers are plotted in Figure 6, together with the absorption spectra obtained from the calculations. For a systematic description, we use the E/Z nomenclature and start from the N=N double bond. Thus, the most stable isomer (red I, trans-syn) with the intramolecular hydrogen bond is the EZZE conformer, reflecting the E (trans) configuration with regard to the N=N double bond, Z with regard to N–C, Z (syn) for C=N, and E for the N–N single bond, respectively. Each row of panels in Figure 6 represents a variation of a single bond, as indicated on the left, whereas each column represents an isomerization of a double bond.

The absorption spectra, even within one column and hence only due to rotation around single bonds, vary substantially (for a comparison with calculations using the CAM-B3LYP functional and including a conductor-like polarizable continuum model, see Supplementary Figures S4, S5). To allow a comparison to experiment, the lowest row of panels in Figure 6 gives experimental absorption spectra, where always one isomeric species is dominating. Starting on the left with the absorption spectrum of the solution in the dark (corresponding to red I), followed by the spectrum of red II derived from spectra of intermediates in time-resolved experiments, additionally to the spectrum of yellow I measured directly after illumination and the spectrum of yellow II obtained in the photostationary state. In the visible spectral range, the simulated spectra of EZZE and EEZE are very similar and match best with the experimental spectrum corresponding to red I, although the experimental data is red-shifted and exhibits a shoulder at longer wavelengths not reproduced in the simulations. Both aspects might be related to a significant stabilization effect caused by the intramolecular hydrogen bond, which the calculations might underestimate. The spectrum of the intermediate red II matches best with ZZZE or

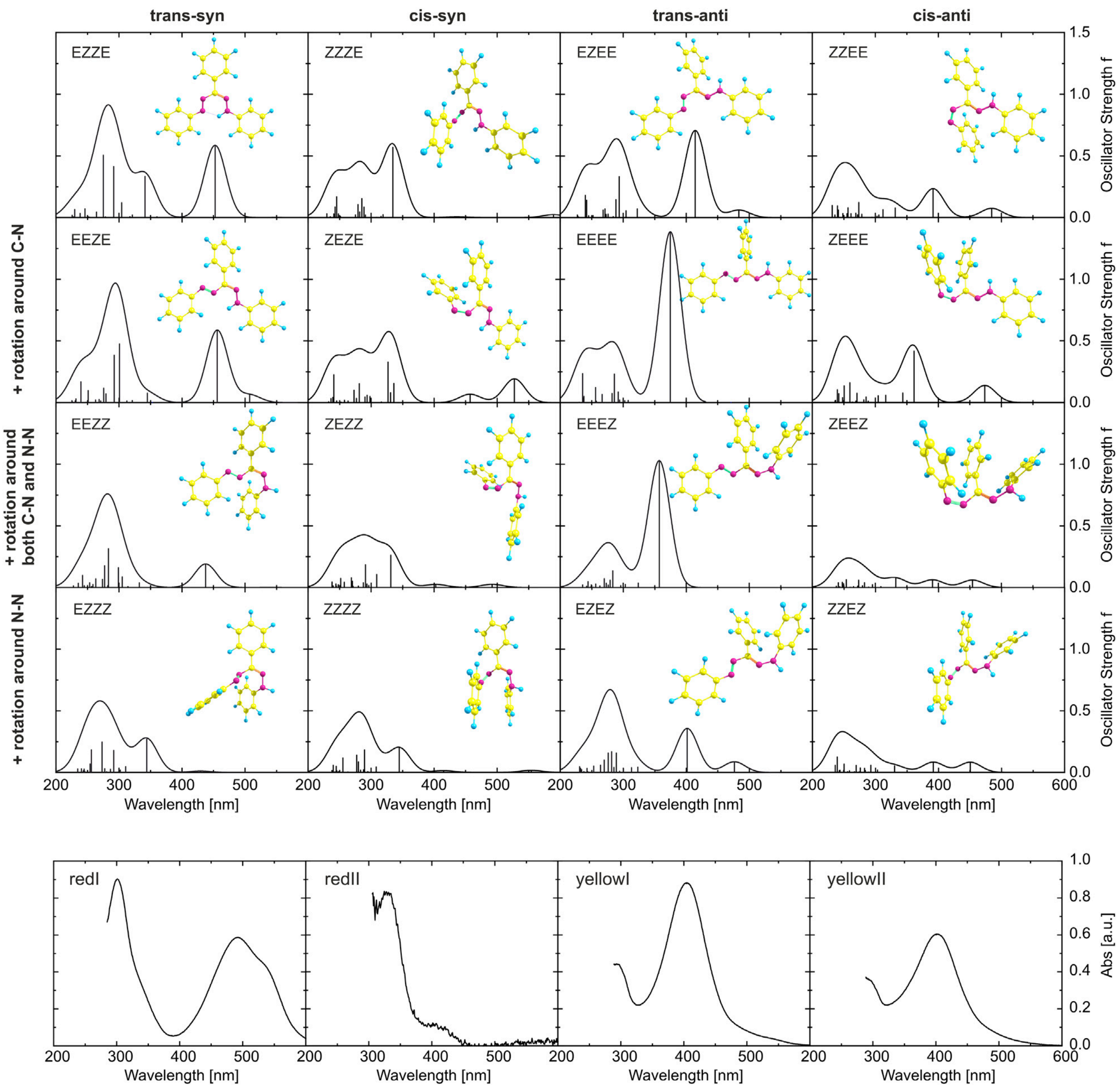

FIGURE 6
Top 16 panels: Results from DFT calculations for the 16 isomers considered in this study. The optimized ground-state geometries are displayed together with the calculated absorption spectra (the oscillator strengths at the corresponding transition energies are given as stick spectrum convoluted each with a Gaussian of a 40 nm width at half maximum). The orientations with respect to the N=N and C=N double bonds are identical within each column, whereas the ones with respect to the C–N and N–N single bond are the same for each row. Bottom 4 panels: Experimentally determined spectra of the four isomers corresponding to the double-bond orientations given at the top of each column. The red I spectrum is the ground-state absorption spectrum of a toluene solution, yellow I was measured directly after illumination with 455 nm of a toluene solution, yellow II corresponds to the photostationary state in toluene induced by 455 nm light (Wortmann et al., 2022), and red II is estimated by subtracting the GSB from the pink DADS in Figure 4A.

ZEZE, substantiating that the initial process after photoexcitation involves a trans-cis isomerization around the N=N double bond. Comparing the experimental and theoretical spectra, also the assignment of EZEE as the yellow I species is confirmed. Furthermore, a comparison of the experimental spectrum of yellow II with the calculated spectra in the right-hand column yields the best agreement for the ZZEE conformer, whose absorption peaks around 400 and 490 nm might not be identifiable as separate peaks in the experimental spectrum.

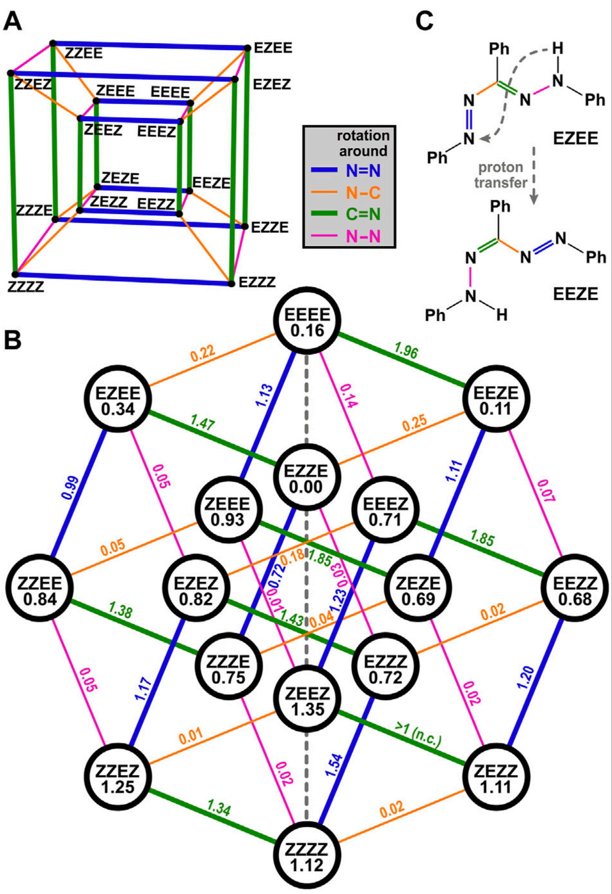

FIGURE 7
Reaction pathways illustrated as Schlegel diagram **(A)** or hypercube graph **(B)**. The isomers' calculated energies, referenced to the energetically most stable geometry EZZE, are written in the circles, barrier heights are shown above the reaction pathway; all values are in eV. The final single point energies of the individual isomers were optimized by DFT calculations on the B3LYP/def2-TZVP level of theory. The energy barriers between two adjacent isomeric species of TPF are roughly estimated by relaxed surface scans along a fixed torsional angle. The stated values along the possible pathways always describe the amount of energy to overcome the energy barrier from the energetically higher lying isomer to the energetically more favored species. The performed calculations are summarized in Supplementary Figure S8. Note that in case of one barrier height the calculation did not converge (n.c.). **(C)** exemplarily displays that a proton transfer from the phenylhydrazone to the azo group is associated with the formation of an isomer with reversed nomenclature.

While the juxtaposition of the theoretical with the experimental spectra from time-resolved measurements confirms the involvement of the four species initially included in the Kuhn-Weitz and Grummt-Langbein reaction schemes (see Figure 1), the actual sequence of transformations cannot be deduced. Especially, the thermal process from red II (ZEZE) to yellow I (EZEE) in the Grummt-Langbein scheme (diagonal arrow in Figure 1) formally necessitates isomerization around both the N=N and the C=N double bond. Experiments indicated that this might be a bimolecular process and that two TPF molecules are required (Grummt and Langbein, 1981). In the following section, we provide an analysis for identifying which conformers are involved.

4.2 Interconnection among isomers

For merocyanine systems in which eight cis/trans isomers can occur, it is illustrative to represent them as the corners of a cube, so that each edge of the cube corresponds to a change of one orientation from cis to trans or vice versa (Ernsting et al., 1990). For an analogous treatment of TPF and the 16 structures shown in Figure 6, a four-dimensional hypercube, often called tesseract, would be required, which has 16 corners (i.e., isomers) and 32 edges (i.e., reaction pathways involving one rotation). In order to plot it in two dimensions, the tesseract can be represented for instance by its Schlegel diagram (a perspective 3D view, with the fourth dimension pointing inwards, Figure 7A) or by an orthogonal projection (Coxeter, 1948), from which the hypercube graph Q_4 is obtained (Maehara, 2016; Hammack and Kainen, 2021). Transferred to the TPF isomer manifold (Figure 7B), each of the 16 isomers is thus connected to four other isomers by a line. As follows from the properties of hypercube graphs (Hammack and Kainen, 2021), the lines can be separated into 4 groups, which correspond to the 4 possible rotational degrees of freedom in TPF as indicated by the color in Figure 7B. Note that each isomer is connected to one line of each color (as there are four possible rotations), and lines of identical color are parallel in this representation.

We have further calculated the energy of the 16 isomers (given in the circles together with the abbreviation of the isomer) as well as the 32 barriers (values given above the lines representing the rotation) to go from one isomer to another. In this way, one can visualize nicely how the reaction might proceed.

The EZZE (red I) isomer is the energetically most favorable one, and all four possible rotations to reach another isomer are energetically uphill, exhibit a significant barrier, or both. As inferred from the experiments, EZZE performs a trans/cis isomerization around the N=N bond (i.e., it follows the blue line in Figure 7B) upon photoexcitation, reaching ZZZE. Looking at the possible pathways of ZZZE, one can deduce that an almost barrierless and slightly downhill pathway is possible by rotation around the N–C bond (orange line), yielding ZEZE (isomer red II). From there, no further rotation is plausible, because of too high barriers and energetically disfavored isomers.

So how is it possible that a thermal process leads from ZEZE (red II) to EZEE (yellow I) without any detectable intermediates? In chelated formazan isomers exhibiting an intramolecular hydrogen bond, intramolecular proton transfer was reported to occur in the ground state (Fischer et al., 1968; Hutton and Irving, 1980; Hutton and Irving, 1982; Grummt et al., 1984), and also IR spectra in solution and in the solid state point towards this pathway (Otting and Neugebauer, 1968; Otting and Neugebauer, 1969). A combined IR and resonance Raman study, also of unsymmetrical derivates of TPF, found evidence for this tautomerism even in the photochemical generation of non-chelated isomers and interpreted the transfer step to occur in the excited state (Lewis and Sandorfy, 1983). Owing to the symmetry of the TPF molecule, transferring a proton from the phenylhydrazone to the azo group reverts the order of single and double bonds. Thus, the nomenclature is reverted, as exemplarily shown in Figure 7C. In the hypercube graph of Figure 7B, this means that such a proton transfer eventually is equivalent to a reflection on the central vertical line (dashed in gray).

Hence, for chelated isomer ZEZE (red II), the next step might be a proton transfer, resulting in the formation of EZEZ, which will immediately relax to the energetically lower-lying EZEE (yellow I). Therefore, we infer that for the thermal process from red II to yellow I in Figure 1, it is not necessary to isomerize around both double bonds, but only to transfer a proton.

The same rationale can also explain how the reaction proceeds further. From EZEE (yellow I), a return to the most stable isomer EZZE (red I) formally necessitates a thermal rotation around the C=N double bond. If the proton is transferred, EEZE is obtained, from where it is much easier to reach EZZE because only a rotation around the N–C single bond is required.

While for chelated isomers, the proton transfer may proceed directly, for other isomers the distance between the donating and the accepting nitrogen atom is too far. In principle, also an intermediate [as is of relevance in formazan synthesis (Hegarty and Scott, 1966; Hegarty and Scott, 1967; King and Murrin, 2004)] with two azo groups and the H atom at the interjacent C atom is conceivable, but much less stable than the formazan tautomers (Buemi et al., 1998) (see also Supplementary Figure S7). However, the transfer might occur *via* a proton wire mechanism, i.e., in a Grotthuss-type fashion (Agmon, 1995; Miyake and Rolandi, 2015; Adams et al., 2021) as was found in water but also identified in other protic solvents (Stoyanov et al., 2008; Fujii et al., 2018; Long et al., 2020). Hence, the isomerization involving proton transfer should only be possible in protic solvents or in aprotic solvents containing at least traces of protic cosolvents. Indeed, the thermal isomerization from EZEE (yellow I) to EZZE (red I) occurs extremely slow in thoroughly dried toluene, and values up to 138.9 h (Kuhn and Weitz, 1953) are reported for the half-life of EZEE. Addition of slight amounts of protic solvents drastically accelerate the reaction (Kuhn and Weitz, 1953; Sueishi and Nishimura, 1983), and in case of alcohols as a cosolvent, a correlation with the H-bonding donating ability of the alcohol was found (Wortmann et al., 2022). Hence, while hydrogen bonding to nitrogen atoms being part of a double bond may also facilitate a ground-state isomerization, in the case of TPF an actual proton transfer might contribute to a significant extent.

5 Summary and conclusion

The primary reaction step when exciting TPF with light is an isomerization around the N=N double bond through which the electronic ground state is reached on an ultrafast time scale. Our combined experimental and theoretical study unveiled that the initially excited conformer EZZE (red I) thus turns into ZZZE and from there directly to ZEZE. The low barrier found for the latter step might even imply that the excited-state isomerization and rotation around the N–C single bond might proceed in a concerted fashion. Following spectroscopically the evolution of the newly formed ZEZE (red II), it was shown that the next reaction step occurs on a time scale of hundreds of milliseconds, yielding EZEE (yellow I). For this reaction step, we propose that an intramolecular proton transfer significantly contributes, so that no isomerization around a double bond is necessary. Along these lines, the reaction step from EZEE back to EZZE might also include a proton transfer and proceed *via* EEZE, so that again no rotation around a double bond is required.

The above conclusion are supported by observations in different solvents and interpreted in the context of a Grotthuss-type mechanism, also explaining the remarkably high decay times reported for the last step of the TPF photocycle in dried aprotic solvents. It might be worthwhile to investigate whether also in molecules with a larger separation between the azo and the hydrazone group, a similar acceleration of the ground-state equilibration is found in protic solvent environments. These aspects could also be of interest in the field of organocatalysis, where hydrazone compounds find increased attention (Müller and List, 2009; Landge et al., 2011; Müller et al., 2011; de Gracia Retamosa et al., 2016; Aprahamian, 2017; Cvrtila et al., 2017; Mader et al., 2022; Žabka and Gschwind, 2022).

Data availability statement

The raw data supporting the conclusion of this article will be made available by the authors, without undue reservation.

Author contributions

SW with support in setting up experiments by RJK performed experiments and calculations; PN conceived and supervised the project; all authors analysed and discussed the data and participated in writing the manuscript.

Funding

Deutsche Forschungsgemeinschaft (DFG, German Research Foundation)—RTG 2620 “Ion Pair Effects in Molecular Reactivity”, Project 426795949.

Acknowledgments

We are grateful to Sebastian Bergwinkl for setting up some of the utilized equipment, and to him as well as to Sylvia Schloeglmann and Matthias Kawalek for their support during some of the measurements. We further thank Florian Kanal and Domenik Schleier (both formerly at Universität Würzburg) for preliminary measurements on TPF.

Conflict of interest

Publisher's note

Supplementary material

The Supplementary Material for this article can be found online at: https://www.frontiersin.org/articles/10.3389/fchem.2022.983342/full#supplementary-material

References

Adams, E. M., Hao, H., Leven, I., Rüttermann, M., Wirtz, H., Havenith, M., et al. (2021). Proton traffic jam: Effect of nanoconfinement and acid concentration on proton hopping mechanism. *Angew. Chem. Int. Ed.* 60, 25419–25427. doi:10.1002/anie.202108766

Agmon, N. (1995). The Grotthuss mechanism. *Chem. Phys. Lett.* 244, 456–462. doi:10.1016/0009-2614(95)00905-J

Alley, M. C., Scudiere, D. A., Monks, A., Hursey, M. L., Czerwinski, M. J., Fine, D. L., et al. (1988). Feasibility of drug screening with panels of human tumor cell lines using a microculture tetrazolium assay. *Cancer Res.* 48, 589–601.

Aprahamian, I. (2017). Hydrazone switches and things in between. *Chem. Commun.* 53, 6674–6684. doi:10.1039/C7CC02879B

Atabekyan, L. S., Barachevskii, V. A., Melkozerov, S. A., Lipunova, G. N., Perova, I. G., Lipunov, I. N., et al. (2011). Laser photolysis study of 1-aryl-3-methyl-5-(benzothiazole-2-yl) formazan phototransformation. *High. Energy Chem.* 45, 52–56. doi:10.1134/S0018143911010036

Avramenko, G. V., and Stepanov, B. I. (1974). Tautomerism and nature of the electronic spectra of triaryl formazans. *Zhurnal Obshchei Khimii J. Gen. Chem. USSR* 44, 1298–1302.

Berridge, M. V., Herst, P. M., and Tan, A. S. (2005). Tetrazolium dyes as tools in cell biology: New insights into their cellular reduction. *Biotechnol. Annu. Rev.* 11, 127–152. doi:10.1016/S1387-2656(05)11004-7

Bolze, T., Wree, J-L., Kanal, F., Schleier, D., and Nuernberger, P. (2018). Ultrafast dynamics of a fluorescent tetrazolium compound in solution. *ChemPhysChem* 19, 138–147. doi:10.1002/cphc.201700831

Brandl, F., Bergwinkl, S., Allacher, C., and Dick, B. (2020). Consecutive photoinduced electron transfer (conPET): The mechanism of the photocatalyst rhodamine 6G. *Chem. Eur. J.* 26, 7946–7954. doi:10.1002/chem.201905167

Buemi, G., and Zuccarello, F. (2002). Is the intramolecular hydrogen bond energy valuable from internal rotation barriers? *J. Mol. Struct. THEOCHEM* 581, 71–85. doi:10.1016/S0166-1280(01)00745-X

Buemi, G., Zuccarello, F., Venuvanalingam, P., Ramalingam, M., and Salai Cheettu Ammal, S. (1998). *Ab initio* study of formazan and 3-nitroformazan. *Faraday Trans.* 94, 3313–3319. doi:10.1039/a806334f

Carmichael, J., DeGraff, W. G., Gazdar, A. F., Minna, J. D., and Mitchell, J. B. (1987). Evaluation of a tetrazolium-based semiautomated colorimetric assay: Assessment of chemosensitivity testing. *Cancer Res.* 47, 936–942.

Coxeter, H. S. M. (1948). *Regular polytopes*. London: Methuen & Co., Ltd.

Cvrtila, I., Fanlo-Virgós, H., Schaeffer, G., Monreal Santiago, G., and Otto, S. (2017). Redox control over acyl hydrazone photoswitches. *J. Am. Chem. Soc.* 139, 12459–12465. doi:10.1021/jacs.7b03724

de Gracia Retamosa, M., Matador, E., Monge, D., Lassaletta, J. M., and Fernández, R. (2016). Hydrazones as singular reagents in asymmetric organocatalysis. *Chem. Eur. J.* 22, 13430–13445. doi:10.1002/chem.201602430

Dick, B., Kensy, U., and Kutta, R. J. (2019). Transient absorption with a streak camera. *Phys. Sci. Rev.* 4, 20170179. doi:10.1515/psr-2017-0179

Dobryakov, A. L., Kovalenko, S. A., Weigel, A., Pérez-Lustres, J. L., Lange, J., Müller, A., et al. (2010). Femtosecond pump/supercontinuum-probe spectroscopy: Optimized setup and signal analysis for single-shot spectral referencing. *Rev. Sci. Instrum.* 81, 113106. doi:10.1063/1.3492897

Ernsting, N. P., Dick, B., and Arthen-Engeland, T. (1990). The primary photochemical reaction step of unsubstituted indolino-spiropyrans. *Pure Appl. Chem.* 62, 1483–1488. doi:10.1351/pac199062081483

Fischer, P. B., Kaul, B. L., and Zollinger, H. (1968). Untersuchungen über die Struktur von Formazanen I. ^{15}N-H-Kopplung des Chelatwasserstoffatoms. *Helv. Chim. Acta* 51, 1449–1451. doi:10.1002/hlca.19680510629

Fujii, A., Sugawara, N., Hsu, P-J., Shimamori, T., Li, Y-C., Hamashima, T., et al. (2018). Hydrogen bond network structures of protonated short-chain alcohol clusters. *Phys. Chem. Chem. Phys.* 20, 14971–14991. doi:10.1039/C7CP08072G

Ghosh, R., Mora, A. K., and Nath, S. (2019). Disentangling time scales of vibrational cooling, solvation, and hydrogen bond reorganization dynamics using ultrafast transient infrared spectroscopy of formylperylene. *J. Phys. Chem. B* 123, 4408–4414. doi:10.1021/acs.jpcb.9b01920

Gilroy, J. B., and Otten, E. (2020). Formazanate coordination compounds: Synthesis, reactivity, and applications. *Chem. Soc. Rev.* 49, 85–113. doi:10.1039/C9CS00676A

Gökçe, G., Durmus, Z., Tezcan, H., Kiliç, E., and Yilmaz, H. (2005). Electrochemical investigation of 1, 3, 5-triphenylformazan and its nitro derivatives in dimethyl sulfoxide. *Anal. Sci.* 21, 685–688. doi:10.2116/analsci.21.685

Gonzalez, M. C., and San Roman, E. (1989). Photochemistry of aqueous solutions of triphenyltetrazolium chloride. *J. Phys. Chem.* 93, 3536–3540. doi:10.1021/j100346a035

Grimmelsmann, L., Marefat Khah, A., Spies, C., Hättig, C., and Nuernberger, P. (2017). Ultrafast dynamics of a triazene: Excited-state pathways and the impact of binding to the minor groove of DNA and further biomolecular systems. *J. Phys. Chem. Lett.* 8, 1986–1992. doi:10.1021/acs.jpclett.7b00472

Grummt, U-W., and Langbein, H. (1981). A flash photolysis investigation of photochromic triphenylformazan. *J. Photochem.* 15, 329–334. doi:10.1016/0047-2670(81)80007-X

Grummt, U-W., Langbein, H., Nöske, R., and Röbisch, G. (1984). Photochromic properties of 3-methylthio-1, 5-diphenylformazan. *J. Photochem.* 24, 53–63. doi:10.1016/0047-2670(84)80006-4

Hammack, R. H., and Kainen, P. C. (2021). A new view of hypercube genus. *Am. Math. Mon.* 128, 352–359. doi:10.1080/00029890.2020.1867472

Hausser, I., Jerchel, D., and Kuhn, R. (1949). Ein blau fluorescierendes Bestrahlungsprodukt von Triphenyl-tetrazolium-chlorid. *Chem. Ber.* 82, 195–199. doi:10.1002/cber.19490820302

Hausser, I., Jerchel, D., and Kuhn, R. (1949). Über die Rot $\rightleftharpoons$ Gelb-Umlagerung von Formazanen im Licht; Grenzfragen von Mesomerie und Isomerie. *Chem. Ber.* 82, 515–527. doi:10.1002/cber.19490820612

Hegarty, A. F., and Scott, F. L. (1967). Kinetics and mechanism of the formation of formazans by diazonium ion attack on hydrazones. *J. Org. Chem.* 32, 1957–1963. doi:10.1021/jo01281a057

Hegarty, A. F., and Scott, F. L. (1966). The mechanism of formazan formation. *Chem. Commun.* 1966, 622–623. doi:10.1039/C19660000622

Hiura, H., and Takahashi, H. (1989). Resonance Raman and absorption studies of the configurations of photochromic 3-alkyl-substituted 1, 5-diphenylformazans: Steric effect of the substituent. *J. Mol. Struct.* 212, 221–233. doi:10.1016/0022-2860(89)85079-3

Hiura, H., and Takahashi, H. (1989). Study of the configurations of 3-aryl-substituted 1, 5-diphenylformazans by resonance Raman and absorption spectroscopy: Steric and conjugation effects of the substituent. *J. Mol. Struct.* 212, 235–245. doi:10.1016/0022-2860(89)85080-X

Hutton, A. T., and Irving, H. M. N. H. (1982). Isomers of 3-methylthio-1, 5-diarylformazans and their interconversion in solution. *J. Chem. Soc. Perkin Trans.* 2, 1117–1121. doi:10.1039/P29820001117

Hutton, A. T., and Irving, H. M. N. H. (1980). X-Ray crystallographic and spectroscopic study of the configurations of isomeric 3-methylthio-1, 5-diarylformazans and their interconversion in solution. *J. Chem. Soc. Chem. Commun.* 1980, 763–765. doi:10.1039/C39800000763

Kanal, F., Schleier, D., and Nuernberger, P. (2015). Ultrafast photogeneration of a tetrazolinyl radical. *ChemPhysChem* 16, 3143–3146. doi:10.1002/cphc.201500628

King, R. A., and Murrin, B. (2004). A computational study of the structure and synthesis of formazans. *J. Phys. Chem. A* 108, 4961–4965. doi:10.1021/jp0400622

Kobayashi, A., Yamaji, M., Nakajima, S., Akiyama, K., Tero-Kubota, S., Kato, S., et al. (2013). Photochemical behaviors of a tethered 1, 3-diketone derivative studied by transient absorption and time-resolved EPR measurements. *Chem. Phys. Lett.* 555, 101–105. doi:10.1016/j.cplett.2012.10.067

Kovács, A., Wojnárovits, L., McLaughlin, W. L., Eid, S. E. E., and Miller, A. (1996). Radiation-chemical reaction of 2, 3, 5-triphenyl-tetrazolium chloride in liquid and solid state. *Radiat. Phys. Chem.* 47, 483–486. doi:10.1016/0969-806X(95)00144-M

Kuhn, R., and Weitz, H. M. (1953). Photochemie des Triphenylformazans. *Chem. Ber.* 86, 1199–1212. doi:10.1002/cber.19530860927

Kumar, S., Sharma, R., Kumar, S., and Nitika (2014). Solvatochromic behaviour of formazans and contribution of Kamlet-Taft coefficients towards spectral shifts of formazans in different organic solvents. *Chem. Sci. Trans.* 3, 919–928. doi:10.7598/cst2014.836

Kutta, R-J., Langenbacher, T., Kensy, U., and Dick, B. (2013). Setup and performance of a streak camera apparatus for transient absorption measurements in the ns to ms range. *Appl. Phys. B* 111, 203–216. doi:10.1007/s00340-012-5320-2

Lakon, G. (1942). Topographischer Nachweis der Keimfähigkeit der Getreidefrüchte durch Tetrazoliumsalze. *Berichte Dtsch. Bot. Ges.* 60, 299–305.

Landge, S. M., Tkatchouk, E., Benítez, D., Lanfranchi, D. A., Elhabiri, M., Goddard, W. A., et al. (2011). Isomerization mechanism in hydrazone-based rotary switches: Lateral shift, rotation, or tautomerization? *J. Am. Chem. Soc.* 133, 9812–9823. doi:10.1021/ja200699v

Langbein, H. (1979). Tieftemperaturuntersuchungen zur Photochromie von Triphenylformazan. *J. Prakt. Chem.* 321, 655–664. doi:10.1002/prac.19793210418

Lewis, J. W., and Sandorfy, C. (1983). Infrared absorption and resonance Raman scattering of photochromic triphenylformazans. *Can. J. Chem.* 61, 809–816. doi:10.1139/v83-148

Lipunova, G. N., Fedorchenko, T. G., and Chupakhin, O. N. (2019). New aspects of the chemistry of formazans. *Russ. J. Gen. Chem.* 89, 1225–1245. doi:10.1134/S1070363219060203

Long, Z., Atsango, A. O., Napoli, J. A., Markland, T. E., and Tuckerman, M. E. (2020). Elucidating the proton transport pathways in liquid imidazole with first-principles molecular dynamics. *J. Phys. Chem. Lett.* 11, 6156–6163. doi:10.1021/acs.jpclett.0c01744

Lu, Y-C., Chang, C-W., and Diau, E. W-G. (2002). Femtosecond fluorescence dynamics of trans-azobenzene in hexane on excitation to the $S_1(n, \pi^*)$ state. *J. Chin. Chem. Soc.* 49, 693–701. doi:10.1002/jccs.200200103

Mader, S., Sudan Maji, M., Atodiresei, I., and Rueping, M. (2022). Brønsted acid catalyzed enantioselective addition of hydrazones to 3-indolylmethanols. *Org. Chem. Front.* 9, 4466–4471. doi:10.1039/D2QO00840H

Maehara, H. (2016). Orthogonal projections of cubes and regular simplices into a plane. *J. Geom.* 107, 567–577. doi:10.1007/s00022-015-0289-8

Megerle, U., Pugliesi, I., Schriever, C., Sailer, C. F., and Riedle, E. (2009). Sub-50 fs broadband absorption spectroscopy with tunable excitation: Putting the analysis of ultrafast molecular dynamics on solid ground. *Appl. Phys. B* 96, 215–231. doi:10.1007/s00340-009-3610-0

Middleton, C. T., Cohen, B., and Kohler, B. (2007). Solvent and solvent isotope effects on the vibrational cooling dynamics of a DNA base derivative. *J. Phys. Chem. A* 111, 10460–10467. doi:10.1021/jp0740595

Miyake, T., and Rolandi, M. (2015). Grotthuss mechanisms: From proton transport in proton wires to bioprotonic devices. *J. Phys. Condens. Matter* 28, 023001. doi:10.1088/0953-8984/28/2/023001

Mosmann, T. (1983). Rapid colorimetric assay for cellular growth and survival: Application to proliferation and cytotoxicity assays. *J. Immunol. Methods* 65, 55–63. doi:10.1016/0022-1759(83)90303-4

Müller, S., and List, B. (2009). A catalytic asymmetric 6π electrocyclization: Enantioselective synthesis of 2-pyrazolines. *Angew. Chem. Int. Ed.* 48, 9975–9978. doi:10.1002/anie.200905035

Müller, S., Webber, M. J., and List, B. (2011). The catalytic asymmetric Fischer indolization. *J. Am. Chem. Soc.* 133, 18534–18537. doi:10.1021/ja2092163

Nădejde, C., Creangă, D., Filip, E., and Dorohoi, D-O. (2009). Spectral investigation of triphenylformazan derivatives in ultraviolet light. *Romanian J. Phys.* 54, 649–657.

Nägele, T., Hoche, R., Zinth, W., and Wachtveitl, J. (1997). Femtosecond photoisomerization of cis-azobenzene. *Chem. Phys. Lett.* 272, 489–495. doi:10.1016/S0009-2614(97)00531-9

Neese, F. (2018). Software update: The ORCA program system, version 4.0. *WIREs Comput. Mol. Sci.* 8, e1327. doi:10.1002/wcms.1327

Neese, F. (2012). The ORCA program system. *WIREs Comput. Mol. Sci.* 2, 73–78. doi:10.1002/wcms.81

Nenov, A., Borrego-Varillas, R., Oriana, A., Ganzer, L., Segatta, F., Conti, I., et al. (2018). UV-Light-Induced vibrational coherences: The key to understand Kasha rule violation in trans-azobenzene. *J. Phys. Chem. Lett.* 9, 1534–1541. doi:10.1021/acs.jpclett.8b00152

Neugebauer, F. A., and Russell, G. A. (1968). Tetrazolinyl radicals. *J. Org. Chem.* 33, 2744–2746. doi:10.1021/jo01271a029

Nineham, A. W. (1955). The chemistry of formazans and tetrazolium salts. *Chem. Rev.* 55, 355–483. doi:10.1021/cr50002a004

Otting, W., and Neugebauer, F. A. (1968). IR-spektroskopische Untersuchungen an NH- und ND-Formazanen. *Z. Naturforsch. B* 23, 1064–1071. doi:10.1515/znb-1968-0809

Otting, W., and Neugebauer, F. A. (1969). IR-Spektroskopische Untersuchungen zur Frage der Isomerie bei Formazanen und Tetrazoliumsalzen. *Chem. Ber.* 102, 2520–2529. doi:10.1002/cber.19691020805

Pancur, T., Renth, F., Temps, F., Harbaum, B., Krüger, A., Herges, R., et al. (2005). Femtosecond fluorescence up-conversion spectroscopy of a rotation-restricted azobenzene after excitation to the S_1 state. *Phys. Chem. Chem. Phys.* 7, 1985–1989. –1989. doi:10.1039/B419236B

Pechmann, H. V., and Runge, P. (1894). Oxydation der Formazylverbindungen. II. Mittheilung. *Ber. Dtsch. Chem. Ges.* 27, 2920–2930. doi:10.1002/cber.18940270352

Poisson, L., Roubin, P., Coussan, S., Soep, B., and Mestdagh, J-M. (2008). Ultrafast dynamics of acetylacetone (2, 4-pentanedione) in the S_2 state. *J. Am. Chem. Soc.* 130, 2974–2983. doi:10.1021/ja0730819

Quick, M., Dobryakov, A. L., Gerecke, M., Richter, C., Berndt, F., Ioffe, I. N., et al. (2014). Photoisomerization dynamics and pathways of trans- and cis-azobenzene in solution from broadband femtosecond spectroscopies and calculations. *J. Phys. Chem. B* 118, 8756–8771. doi:10.1021/jp504999f

Satzger, H., Root, C., and Braun, M. (2004). Excited-state dynamics of trans- and cis-azobenzene after UV excitation in the ππ* band. *J. Phys. Chem. A* 108, 6265–6271. doi:10.1021/jp049509x

Satzger, H., Spörlein, S., Root, C., Wachtveitl, J., Zinth, W., and Gilch, P. (2003). Fluorescence spectra of trans- and cis-azobenzene – emission from the Franck–Condon state. *Chem. Phys. Lett.* 372, 216–223. doi:10.1016/S0009-2614(03)00364-6

Schiele, C. (1965). IR- und UV-VIS-spektroskopische Untersuchungen am System Tetrazoliumsalz/Formazan. *Ber. Bunsenges. Phys. Chem.* 69, 308–318. doi:10.1002/bbpc.19650690409

Schott, S., Steinbacher, A., Buback, J., Nuernberger, P., and Brixner, T. (2014). Generalized magic angle for time-resolved spectroscopy with laser pulses of arbitrary ellipticity. *J. Phys. B At. Mol. Opt. Phys.* 47, 124014. doi:10.1088/0953-4075/47/12/124014

Scudiere, D. A., Shoemaker, R. H., Paul, K. D., Monks, A., Tierney, S., Nofziger, T. H., et al. (1988). Evaluation of a soluble tetrazolium/formazan assay for cell growth and drug sensitivity in culture using human and other tumor cell lines. *Cancer Res.* 48, 4827–4833.

Sherif, O. E. (2015). DFT calculations, electrical and thermal properties of unsubstituted triphenylformazan. *Int. J. Electrochem Sci.* 10, 15.

Sherif, O. E. (1997). Effect of solvents on the electronic absorption spectra of some substituted diarylformazans. *Monatsh. Chem.* 128, 981–990. doi:10.1007/BF00806964

Siewertsen, R., Boyke Schönborn, J., Hartke, B., Renth, F., and Temps, F. (2011). Superior Z → E and E → Z photoswitching dynamics of dihydrodibenzodiazocine, a bridged azobenzene, by S_1 (n π*) excitation at λ = 387 and 490 nm. *Phys. Chem. Chem. Phys.* 13, 1054–1063. doi:10.1039/C0CP01148G

Slavov, C., Yang, C., Schweighauser, L., Boumrifak, C., Dreuw, A., Wegner, H. A., et al. (2016). Connectivity matters – ultrafast isomerization dynamics of bisazobenzene photoswitches. *Phys. Chem. Chem. Phys.* 18, 14795–14804. doi:10.1039/C6CP00603E

Smith, F. E. (1951). Tetrazolium salt. *Science*. doi:10.1126/science.113.2948.751.b

Stoyanov, E. S., Stoyanova, I. V., and Reed, C. A. (2008). IR spectroscopic properties of H(MeOH)n^+ clusters in the liquid phase: Evidence for a proton wire. *Chem. Eur. J.* 14, 3596–3604. doi:10.1002/chem.200701746

Sueishi, Y., and Nishimura, N. (1983). Kinetic pressure and substituent effects on the thermal isomerization of triphenylformazans. *Bull. Chem. Soc. Jpn.* 56, 2598–2604. doi:10.1246/bcsj.56.2598

Tezcan, H., and Ozkan, N. (2003). Substituent effects on the spectral properties of some 3-substituted formazans. *Dyes Pigm.* 56, 159–166. doi:10.1016/S0143-7208(02)00131-6

Tezcan, H., and Tokay, N. (2010). A computational study of the absorption spectra of 1-substituted phenyl-3, 5-diphenylformazans. *Int. J. Quantum Chem.* 110, 2140–2146. doi:10.1002/qua.22639

Turkoglu, G., Berber, H., and Kani, I. (2015). Synthesis, crystal structure, optical and electrochemical properties of novel diphenylether-based formazan derivatives. *New J. Chem.* 39, 2728–2740. doi:10.1039/C4NJ02353F

Umemoto, K. (1985). Reduction mechanism of 2, 3, 5-triphenyltetrazolium chloride and 1, 3, 5-triphenylformazan. *Bull. Chem. Soc. Jpn.* 58, 2051–2055. doi:10.1246/bcsj.58.2051

Veas-Arancibia, C. (1986). *Spectroscopy and photochromism of triphenyl–formazan and its derivatives.* PhD thesis. Baton Rouge, United States: Louisiana State University. doi:10.31390/gradschool_disstheses.4213

Veierov, D., Bercovici, T., Fischer, E., Mazur, Y., and Yogev, A. (1977). Photoisomerization of the enol form of 1, 3-dicarbonyl compounds. *J. Am. Chem. Soc.* 99, 2723–2729. doi:10.1021/ja00450a053

Verma, P. K., Koch, F., Steinbacher, A., Nuernberger, P., and Brixner, T. (2014). Ultrafast UV-induced photoisomerization of intramolecularly H-bonded symmetric β-diketones. *J. Am. Chem. Soc.* 136, 14981–14989. doi:10.1021/ja508059p

Verma, P. K., Steinbacher, A., Koch, F., Nuernberger, P., and Brixner, T. (2015). Monitoring ultrafast intramolecular proton transfer processes in an unsymmetric β-diketone. *Phys. Chem. Chem. Phys.* 17, 8459–8466. doi:10.1039/C4CP05811A

Verma, P. K., Steinbacher, A., Schmiedel, A., Nuernberger, P., and Brixner, T. (2016). Excited-state intramolecular proton transfer of 2-acetylindan-1, 3-dione studied by ultrafast absorption and fluorescence spectroscopy. *Struct. Dyn.* 3, 023606. doi:10.1063/1.4937363

Wilhite, E. (1991). *The spectroscopy of neutral and ionic forms of triphenylformazan derivatives.* PhD thesis. Baton Rouge, United States: Louisiana State University. doi:10.31390/gradschool_disstheses.5156

Wortmann, S., Schloeglmann, S., and Nuernberger, P. (2022). Sensitivity of isomerization kinetics of 1, 3, 5-triphenylformazan on cosolvents added to toluene. *J. Org. Chem.* 87, 1745–1755. doi:10.1021/acs.joc.1c01928

Xu, S., Park, S. T., Feenstra, J. S., Srinivasan, R., and Zewail, A. H. (2004). Ultrafast electron diffraction: Structural dynamics of the elimination reaction of acetylacetone. *J. Phys. Chem. A* 108, 6650–6655. doi:10.1021/jp0403689

Žabka, M., and Gschwind, R. M. (2022). Substrate photoswitching for rate enhancement of a organocatalytic cyclization reaction. *Eur. J. Org. Chem.* 2022, e202200048. doi:10.1002/ejoc.202200048

Ziegler, H. (1953). Über die Reduktion des Tetrazoliumchlorids in der Pflanzenzelle und über den Einfluß des Salzes auf Stoffwechsel und Wachstum. *Z. Naturforsch. B* 8, 662–667. doi:10.1515/znb-1953-1109

frontiers | Frontiers in Chemistry

TYPE Original Research
PUBLISHED 12 January 2023
DOI 10.3389/fchem.2022.1006637

OPEN ACCESS

EDITED BY
Yuichi Fujimura,
Tohoku University, Japan

REVIEWED BY
Tomoyuki Endo,
National Institues for Quantum and Radiological Science and Technology (QST), Japan
Manabu Kanno,
Tohoku University, Japan

*CORRESPONDENCE
Debabrata Goswami,
✉ dgoswami@iitk.ac.in

SPECIALTY SECTION
This article was submitted to Physical Chemistry and Chemical Physics, a section of the journal Frontiers in Chemistry

RECEIVED 29 July 2022
ACCEPTED 28 December 2022
PUBLISHED 12 January 2023

CITATION
Goswami D (2023), Intense femtosecond optical pulse shaping approaches to spatiotemporal control.
Front. Chem. 10:1006637.
doi: 10.3389/fchem.2022.1006637

Intense femtosecond optical pulse shaping approaches to spatiotemporal control

Debabrata Goswami[1,2]*

[1]Department of Chemistry, Indian Institute of Technology Kanpur, Kanpur, India, [2]Center for Lasers and Photonics, Indian Institute of Technology Kanpur, Kanpur, India

For studying any event, measurement can never be enough; "control" is required. This means mere passive tracking of the event is insufficient and being able to manipulate it is necessary. To maximize this capability to exert control and manipulate, both spatial and temporal domains need to be jointly accounted for, which has remained an intractable problem at microscopic scales. Simultaneous control of dynamics and position of an observable event requires a holistic combination of spatial and temporal control principles, which gives rise to the field of spatiotemporal control. For this, we present a novel femtosecond pulse-shaping approach. We explain how to achieve spatiotemporal control by spatially manipulating the system through trapping and subsequently or simultaneously exerting temporal control using shaped femtosecond pulses. By leveraging ultrafast femtosecond lasers, the prospect of having temporal control of molecular dynamics increases, and it becomes possible to circumvent the relaxation processes at microscopic timescales. Optical trapping is an exemplary demonstration of spatial control that results in the immobilization of microscopic objects with radiation pressure from a tightly focused laser beam. Conventional single-beam optical tweezers use continuous-wave (CW) lasers for achieving spatial control through photon fluxes, but these lack temporal control knobs. We use a femtosecond high repetition rate (HRR) pulsed laser to bypass this lack of dynamical control in the time domain for optical trapping studies. From a technological viewpoint, the high photon flux requirement of stable optical tweezers necessitates femtosecond pulse shaping at HRR, which has been a barrier until the recent Megahertz pulse shaping developments. Finally, recognizing the theoretical distinction between tweezers with femtosecond pulses and CW lasers is of paramount interest. Non-linear optical (NLO) interactions must be included *prima facie* to understand pulsed laser tweezers in areas where they excel, like the two-photon-fluorescence-based detection. We show that our theoretical model can holistically address the common drawback of all tweezers. We are able to mitigate the effects of laser-induced heating by balancing this with femtosecond laser-induced NLO effects. An interesting side-product of HRR femtosecond-laser-induced thermal lens is the development of femtosecond thermal lens spectroscopy (FTLS) and its ability to provide sensitive molecular detection.

KEYWORDS

femtosecond pulse shaping, pulsed optical tweezers, coherent control, kerr effect, thermal lens spectroscopy, convection, microheterogeneity, interface

1 Introduction

For a spectroscopist, typical light-matter interactions are kept at perturbative levels, with active attempts to minimize all possible interactions with light so as to recover as much information as possible about the system under study. The experimenter is a passive observer in such studies. However, when one wants to participate in and control light-matter processes, for example, out of a desire to enhance chemical selectivity or reaction yields in photochemical processes, the passive viewer approach of a spectroscopist is not sufficient. The desire to selectively enhance chemical processes gave rise to the dream of “controlling chemistry” (Warren et al., 1993), way back in the 1960s, since the first practical demonstration of lasers.

The most general investigation and manipulation of light-induced processes require simultaneous control over temporal and spatial properties of the electromagnetic radiation on femtosecond time and nanometer length scales (Aeschlimann et al., 2010; Froula et al., 2018; Schmidt et al., 2021). Most vibrational transitions occur within a few femtoseconds, and these are responsible for chemical transformations that make new bonds and break old bonds. The coherent nature of an ultrafast pulsed laser is crucial for manipulating electronic and nuclear motions, and this gave birth to the concept of “coherent control” involving the manipulation of molecular states coherently and, therefore, circumventing the limits of the uncertainty principle for ultrashort laser pulses (Dantus and Lozovoy, 2004). Though coherent control is an exciting principle, it often involves exotic experimental and laboratory conditions with limited success since practical implementations require that we have control and execution within ultra-short timescales. Thus, the most celebrated and successful aspects of control have been under highly specialized circumstances (Hikosaka et al., 2019). For example, in the gas phase, the system is mostly isolated under molecular beam conditions, where a single isolated molecule undergoes the coveted light-matter interaction for the controlled activity, often referred to as the “active control”; or the “passive control” that can be performed in some designer reactions with conditions based on the specific choice of reactants where predictable pathways can be modulated through light (de Vivie-Riedle et al., 2001). We have shown that more generalizability can be achieved for the “active control” methodology with the help of programmable ultrafast pulse shaping approaches. However, under the abovementioned conditions, the requirement of having a single isolated system interacting with light remains important (Kumar and Goswami, 2014).

We propose, in this paper, the idea of a novel laser-directed experimental environment that could work under standard laboratory conditions. This would, therefore, be more of an open laboratory situation where one does not need, e.g., a beam chamber or other isolated environments with ultracold temperatures or specialized conditions for the cold atoms. The idea of generating such situations in a spatially and temporally controlled environment is an interesting mix of the thermal and non-linear processes arising from several aspects, including femtosecond laser interactions. We want to create a programmable and reproducible environment that will still work under relatively open conditions, which forms our basic promise. Though possibilities of using directed and optimal control can also exist (Rice and Zhao, 2000; Arnold, 2017), the approach presented here is distinctly different. We present our approach that uses a pulsed optical tweezers setup for spatiotemporal control, which is different from the usual optical tweezers with continuous-wave (CW) lasers. The inception of pulsed optical tweezers was initiated to alleviate the fact that all CW tweezers have thermal complications destabilizing the trap for extended timescale operations. Currently, this development has led to championing of spatiotemporal control (De and Goswami, 2011), which stems from the fact that it has only recently become a close reality. These include the specific developments taking into account the recent crucial developments in variegated fields of pulsed optical tweezers (De et al., 2009), the understanding and control of thermal aspects even with ultrashort pulses due to their high repetition rates (Bandyopadhyay et al., 2021) as well as rapid pulse shaping demonstration into megahertz timescales (Dinda et al., 2019). These diverse developments have been essential as ultrafast pulsed lasers with varying repetition rates have become critical for light-matter interactions and their control.

As always, the practical limitations of generalized control approaches have been that we have control over processes only within the ultra-short coherent timescales of light-matter interactions (Boyd, 2003). Unfortunately, whenever we go to ultra-short timescales, non-linear interactions are unavoidable. When isolated environments cannot be guaranteed, the additional spatial control knob is crucial, though this begets a non-negligible thermal effect at long timescales (Kumar et al., 2014). We will show how we can convert these vices of thermal effects and non-linearities into virtues. At the very outset, however, for clarity and in keeping with the earlier developments, we begin with the importance of temporal aspects from a control perspective.

2 Temporal control

For practical implementations of temporal control, it is important to use ultrafast laser pulses, preferably in the femtosecond time domain, which pertains to the vibrational period of most molecules. This ensures the photophysical event can occur before the characteristic natural decay timescales. The ultrashort pulses, however, contain large spectral bandwidths making it challenging to generate selective excitations. For example, even a standard commercial 20 fs laser centered at 800 nm has a large bandwidth of ~47 nm, and its second harmonic at 400 nm will have a bandwidth of ~23 nm. In fact, an excitation process with ultrashort pulses, though devoid of relaxation complications, will generate a mixture of many states and not a single state, which is often difficult to control. To circumvent this limitation, we devised the approach of selective excitation using linearly chirped pulses under adiabatic conditions. The adiabatic rapid passage principle ensures a robust, smooth selective excitation for isolated molecules (Melinger et al., 1994). Figure 1 shows that even the femtosecond linear pulse shaping scheme can show predictable control based on the sign of the chirp in the fragmentation of dicyclopentadiene to cyclopentadiene under molecular beam conditions (Goswami et al., 2013).

A noticeable improvement in the coherent control scenario involves programmable pulse shaping with a feedback loop, which ensures that control can be attained for isolated molecules (Bergt et al., 2001). Since most individual molecular dynamics are completed within microseconds, a millisecond repetition rate is often ideal. Amplified laser pulse shaping at kHz repetition has thus flourished

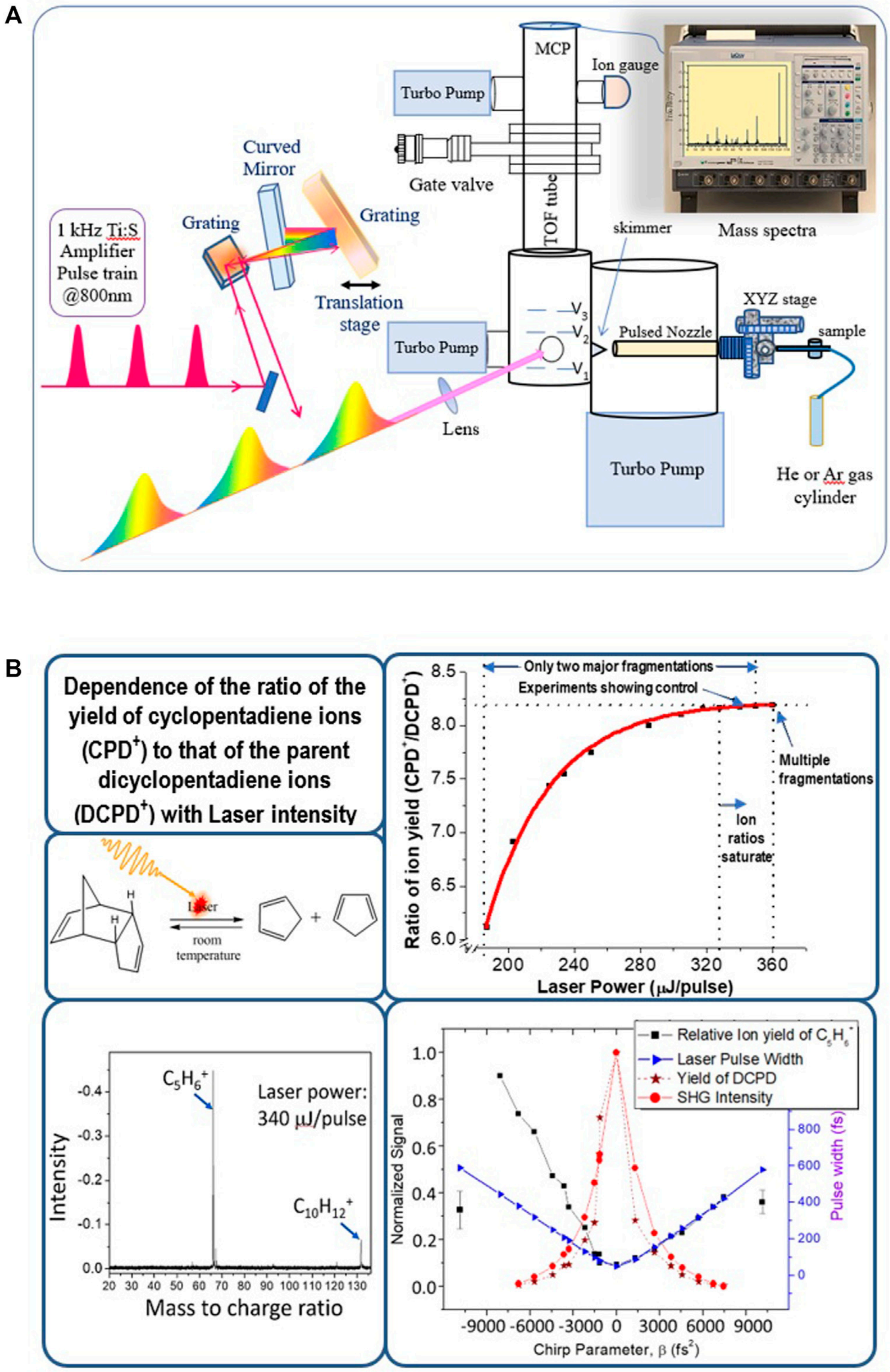

FIGURE 1
(A) Schematic diagram of control experiments with molecular beams with linearly shaped amplified laser pulses. In **(B)**, the specific case of laser photo-fragmentation control of dicyclopentadiene is shown. The data here show that the negatively chirped laser pulses (with negative chirp parameter, β) enhance the fragmentation of dicyclopentadiene to cyclopentadiene.

(Fetterman et al., 1998), and individually shaped pulses at such repetition rates have become routine (Figure 2).

This scenario changes for the case of control in the condensed phase, where under experimental conditions, the principle of an individual isolated molecule interacting with laser cannot be applied. This is because, for condensed matter, unlike molecular beam conditions or low temperature diluted doped crystals, there is always a non-negligible statistical interaction

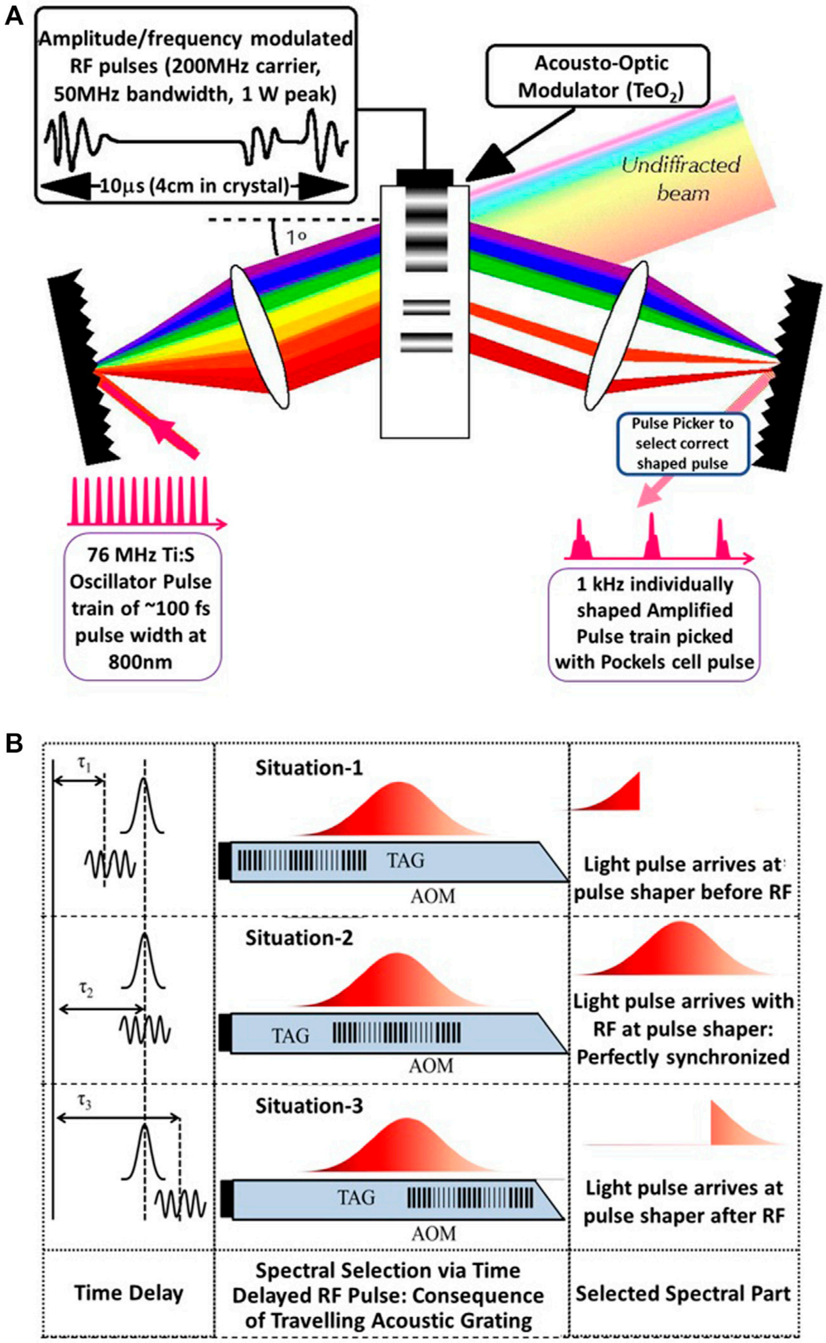

FIGURE 2
(A) Schematic of the Fourier Domain Pulse Shaping approach. For ultrashort pulses, the two lenses can be replaced with curved mirrors. **(B)** Low repetition rate femtosecond pulse shaping in the Fourier domain involves the selection of the desired shaped pulse, which is achieved by the Pockels Cell pulse picker in a 1 kHz amplified pulse shaping process. If needed, each pulse at 1 kHz can have a distinct shape. The control in the Fourier domain is possible by controlling the microsecond radio-frequency (RF) driving the acousto-optic modulator (AOM).

with surrounding molecules. The focus of single-beam optical tweezers is appropriate for spatially controlling their degrees of freedom or their center of mass motion. However, to ensure the possible implementation of simultaneous temporal control, the single-beam optical tweezer setup necessitated augmentations using pulsed lasers resulting in the advancement of pulsed optical tweezers. In this context, we discuss our ultrafast pulsed laser optical tweezers developments.

3 Spatial control with ultrafast optical tweezers

As Arthur Ashkin, (1970) proposed optical tweezers with CW lasers are based on force balancing principles with the laser photon flux, which can be modeled as a Simple Harmonic Oscillator potential well, and calibrated for sensitive measurements accordingly (Ashkin and Ebrary, 2006). The scattering force on

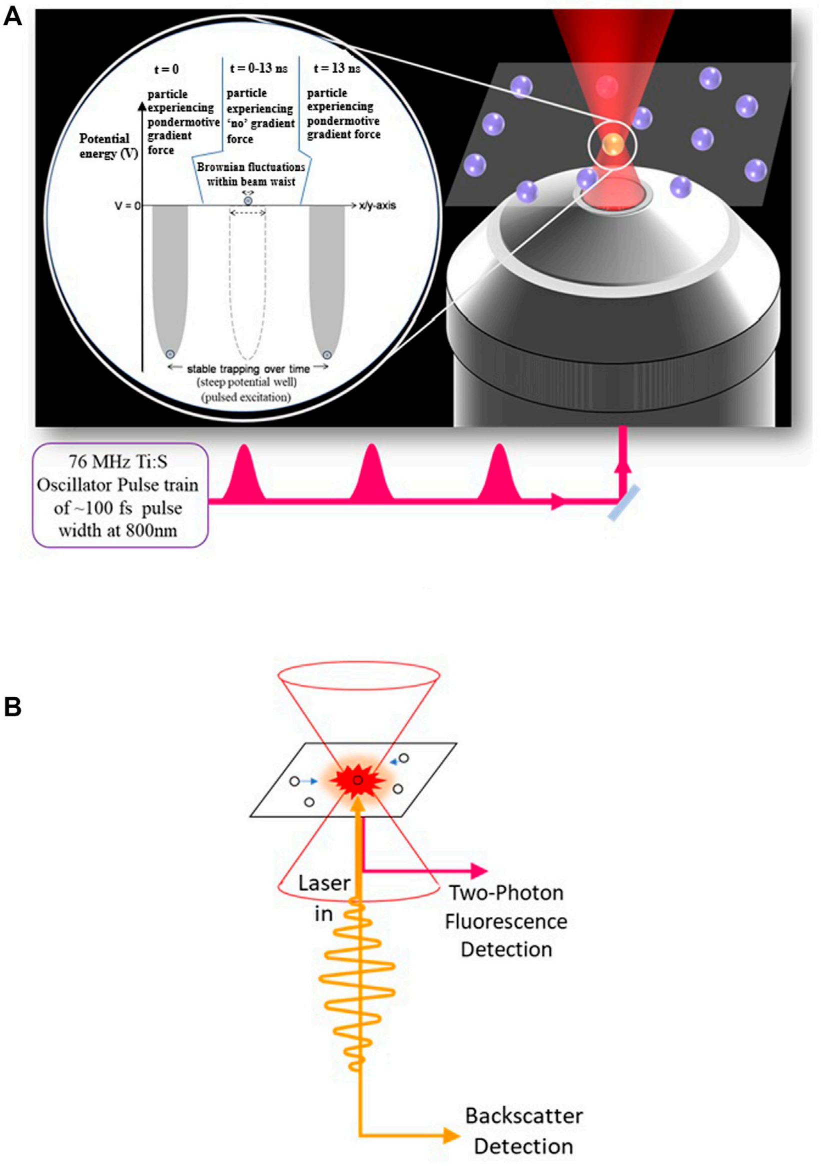

FIGURE 3
(A) Schematic diagram of the Femtosecond pulsed optical tweezers (FOT) and **(B)** its enhanced detection scheme due to the Two-Photon Fluorescence (TPF) detection.

the particle can be balanced by the gradient force generated from the photon flux. Such a balance is achieved for a sharply focused Gaussian beam profile, which is the working principle behind CW optical trapping. For a pulsed laser, however, the gradient force will only be present during the pulse and not otherwise. Nevertheless, pulsed laser optical tweezers have worked reliably with high repetition rate (HRR) lasers operating at several MHz frequencies (Figure 3). This is because even the fastest possible naturally occurring process of scattering, the Brownian motion in liquids, would require about a microsecond for the particle to move away from the laser's focal point. Thus, subsequent pulses from an HRR laser would sample the same object, and the necessary force balancing for optical tweezers remains viable. Optical tweezers are very sensitive to their immediate environments and, in fact, once calibrated, they are very effective in probing microenvironments and any changes thereof with high sensitivity (Goswami, 2015; Mondal and Goswami, 2015; Mondal et al., 2016).

An immediate advantage of using ultrashort pulses for optical tweezers lies in the capability of inducing non-linear processes that can enhance the detection of optically trapped particles through, say, the TPF effect (De et al., 2011). Enhanced detection sensitivity with TPF has also enabled the observation of smaller trapped particles because it gives rise to resolution enhancement as it is much smaller than the focusing wavelength (De and Goswami, 2011). As shown in Figure 4, this high signal-to-noise ratio (SNR) with TPF has also enabled the visualization of the optically induced aggregation effects (Mondal and Goswami, 2016; Roy et al., 2016; Roy, Mondal, and Goswami, 2016) in femtosecond optical tweezers (FOT). In fact, FOT is more optimized for Rayleigh particles that behave as point dipoles, which would be the limiting case for approaching the single-molecule domain.

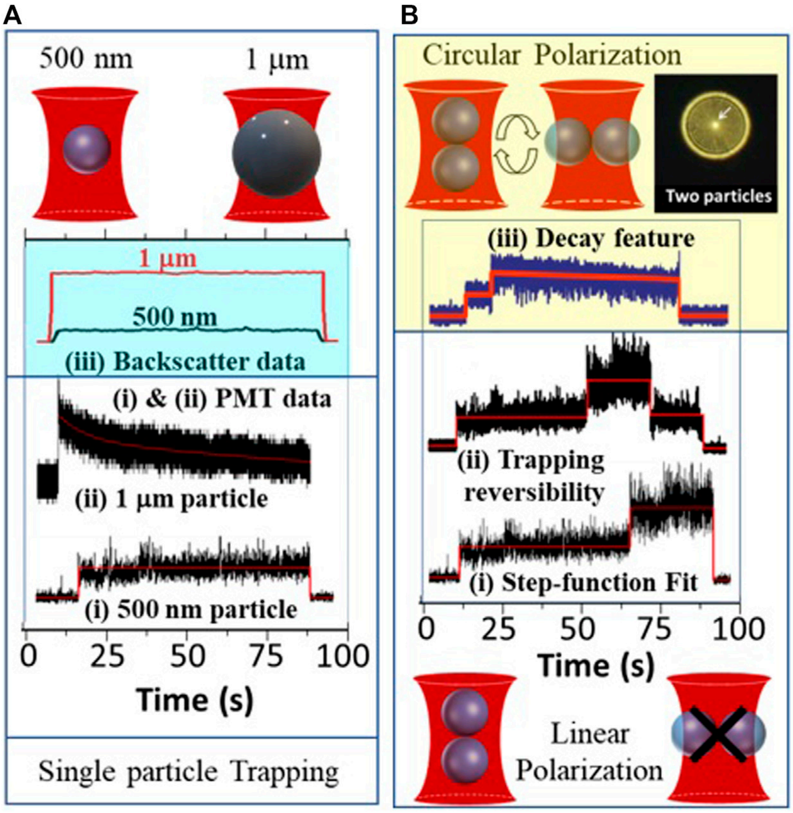

FIGURE 4
Highlighting the characteristics of FOT: **(A)** Size-dependent TPF signal decay in FOT as shown for (i) 500 nm *versus* (ii) 1-micron fluorophore-coated-bead through photo-multiplier tube (PMT) detection, which shows the importance of total *versus* partial illumination of the tweezed particle. (iii) Same study for backscatter data acquisition does not show any characteristic decay. Given this distinction of FOT, it can be used for determining the orientation of multiply trapped beads: **(B)** Use of linear *versus* circular polarization in the TPF data acquisition (i), (ii), and (iii) respectively, for determining the possible orientation of the two co-trapped 500 nm beads.

Another critical aspect of ultrafast pulsed optical tweezers lies in their superior management of the thermal elements of optical tweezers (Bandyopadhyay et al., 2021), which we will discuss in detail after covering the spatiotemporal aspects of the ultrafast optical tweezers. In fact, the background advancements discussed above have led us to a discussion on the development of ultrafast pulse shaping at MHz repetition rates which would be critical for implementing simultaneous temporal control with the ultrafast single-beam optical tweezer.

4 HRR femtosecond pulse shaping

Most of the programmable femtosecond pulse shaping approaches are based on Fourier Transform (FT) techniques (Goswami, 2003), as femtosecond timescales are too short for direct time-domain modulations. At a kHz repetition rate, femtosecond arbitrary pulse shaping has been successfully demonstrated by selecting and amplifying the shaped pulses through an AOM (Figure 2), acting as a traveling grating in the Fourier domain (Hillegas et al., 1994). However, it is almost impossible for the HRR femtosecond lasers to generate and select a single "correct" shape through the Fourier approach alone due to the finite refresh rate and transit time of a traveling wave grating through an AOM. Fortunately, since a phase change in the Fourier domain translates to a time delay in the inverse Fourier domain, we used this approach of complex pulse shaping [both amplitude and phase modulation (Yang et al., 1998)] to demonstrate HRR femtosecond pulse shaping at MHz repetition rates. The specific demonstration is shown in Figure 5, where individually shaped pulses at ~10-MHz repetition rates were generated that were temporarily shifted from the 76-MHz incident laser pulses from the Coherent MIRA 900F© femtosecond Ti:Sapphire laser using the Fourier delay principle (Dinda et al., 2019).

Such MHz repetition rate pulse shaping, as shown in Figure 5, would be suitable for pulsed optical tweezers applications, as mentioned in the previous section. Given this possibility of using shaped pulse FOT, let us now revisit the theoretical aspects of FOT that arise when faced with NLO in addition to the thermal issues of optical trapping.

5 FOT: Subtle balancing of thermal effects with NLO effects

Thermal problems are omnipresent in optical tweezer experiments, irrespective of whether CW or pulsed lasers are generating them. In general, thermal effects for CW lasers are understood in terms of "thermal lens" generation due to changes in the refractive index

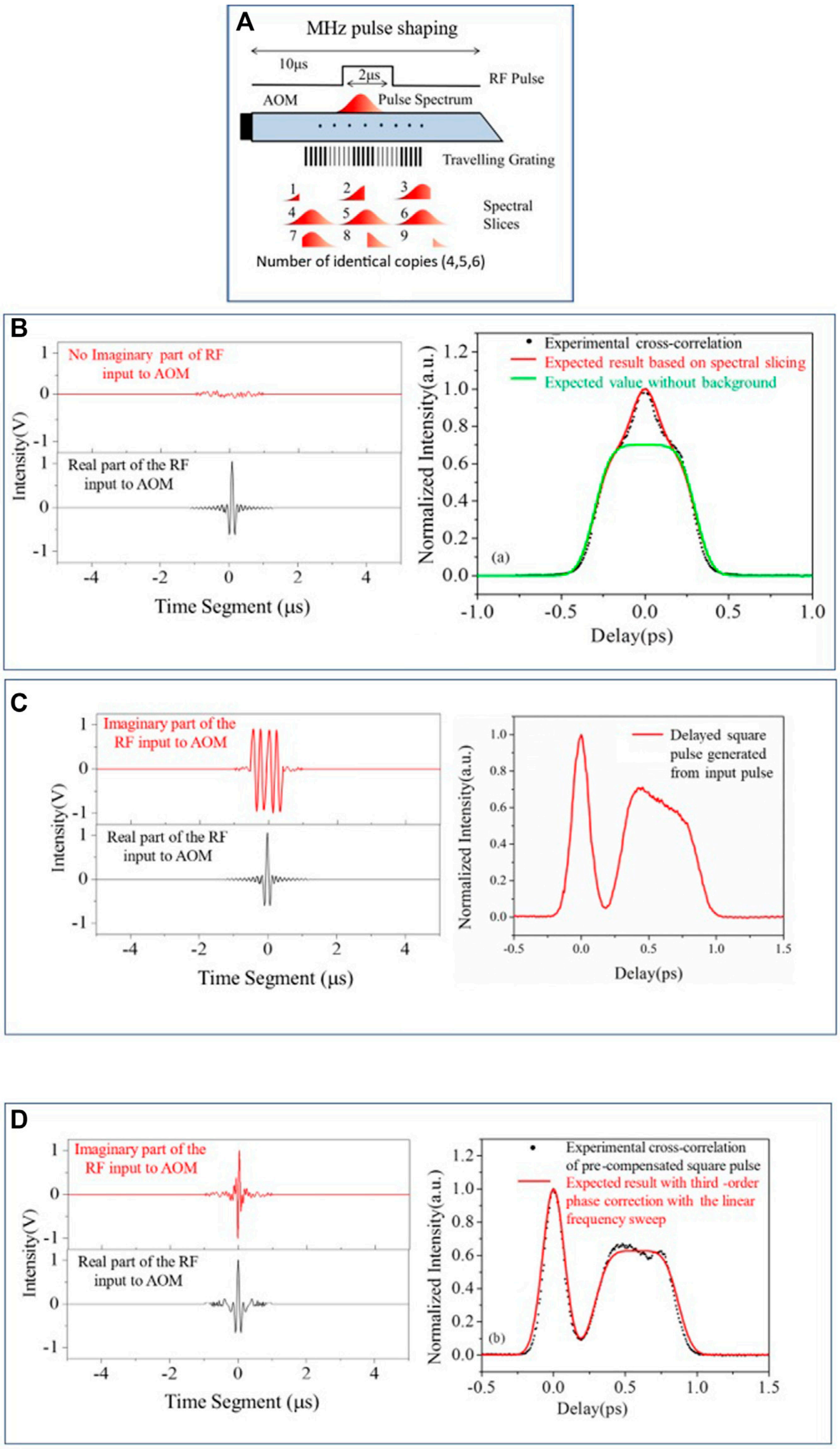

FIGURE 5
Megahertz repetition rate femtosecond pulse shaping: **(A)** Schematic representation showing that spectral slicing is the key in this MHz pulse shaping scheme in contrast to pulse picking for the low repetition method. **(B)** Since each pulse at 76 MHz cannot be shaped, there is a background of the original pulses (incident from the laser) in this pulse shaping approach. **(C)** Application of the Fourier phase provides the requisite time delay to separate the shaped pulses from the unshaped background. **(D)** Finally, distortion compensation by pre-compensating the RF by adding a third-order phase with the linear frequency sweep, which generates the correct individually shaped square pulses at ~10 MHz.

arising from the thermally induced heat load (Català et al., 2017). Most systems expand on heating. As a consequence, a reduction of the refractive index occurs. Thus, the thermal lens (TL) is primarily a diverging lens. Due to the high disparity in timescales for a single femtosecond laser pulse, the thermal effect is insignificant. However, for HHR femtosecond lasers, which is the requirement for, say, an optical tweezer, cumulative thermal effects occur as well (Singh et al., 2021). Additionally, the use of femtosecond pulses for optical trapping also invokes NLO processes. Much of the NLO effect induced is a result of the Kerr non-linearity. Interestingly, ultrafast-laser-induced non-linearities can offset thermal effects in femtosecond optical tweezers since the refractive index changes due to TL and the ones due to the Kerr effect have opposite signs for many systems over varying conditions for the laser parameters (Goswami, 2021). This result is of significant benefit (Figure 6) as it is an important aspect of control that can be achieved through the manipulation of several light-matter interactions depending on the tweezing particle's size and environment as well as the tweezer laser's characteristics like its beam size and shape, laser pulse width, center wavelength, phase, etc., As shown in Figure 6, we define an important parameter in this context, the "escape potential," which can effectively be used to quantify the stability of the optical trap.

A further important aspect of this pragmatic developmental approach to control is that it does not ignore or oversimplify the practical ubiquity of thermal effects, which also interfere with NLO measurements; this is evident from the discussion above. There have been multiple attempts to minimize or avoid thermal effects with varying levels of success (Singhal et al., 2017; Maurya et al., 2019). Interestingly, FOT can also measure with high precision at micron resolution the impact of laser-induced thermal effects that result in temperature and viscosity changes (Mondal, Mathur, Goswami, 2016). For studying a perfectly uniform system, it is best to use a sufficiently rapid moving or flowing design to circumvent thermal effects by effectively regenerating the sample. However, the most important fallout of this recognition of thermal effects, even with femtosecond lasers at HRR, is perhaps the development of femtosecond thermal lens spectroscopy (FTLS) (Bhattacharyya et al., 2010), which we will discuss next.

6 The FTLS: Transforming vice to virtue

In general, thermal effects always interfere with the measurement process. However, there are circumstances like the one presented in the previous section where thermal effects may be beneficial to offset NLO effects in femtosecond optical tweezers. Similarly, FTLS has been developed and proven to be an incredibly versatile technique (Bhattacharyya et al., 2010; Singhal and Goswami, 2019). Though each femtosecond laser pulse provides an almost negligible energy load to the sample, the cumulative effect of HRR femtosecond pulses results in a significant thermal load (Kumar et al., 2014). Such an accumulative effect with minuscule heating capability is even suitable for highly volatile systems and a smooth transition into out-of-equilibrium conditions without other delirious effects under

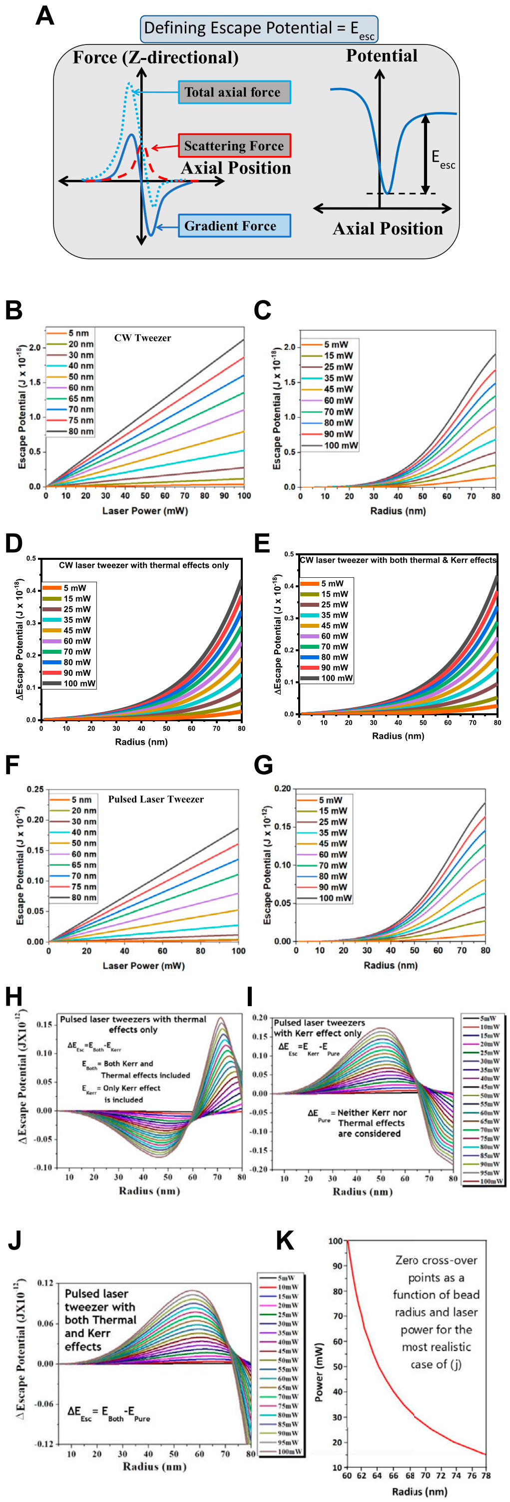

FIGURE 6
A theoretical model of optical tweezers for both CW and pulsed lasers: **(A)** Schematic of the force balancing used for the calculations. For CW tweezers, as shown in **(B)**, the calculated escape potentials scale linearly with increasing laser powers, which also depends on the trapped bead radius. However, as shown in **(C)**, the trapped bead radius dependence on the calculated escape potentials is not linear. A more useful approach is to use the difference in the escape potentials for **(D)** thermal effects only and **(E)** both thermal and Kerr effects, compared to the case with neither effect present. Note that **(D)** and **(E)** is essentially the same since the Kerr effect is not induced with CW lasers. For pulsed tweezers, **(F)** the calculated escape potentials are about 5-orders in *(Continued)*

FIGURE 6 (Continued)
magnitude higher due to high peak powers and still scale linearly with increasing laser powers. **(G)** For the simplest case without any thermal or Kerr effect, the bead radius dependence on the calculated escape potentials is also like that of the CW laser case except for the higher magnitude. However, the dependence of trapping bead radius on the difference in the escape potentials looks much more complicated with **(H)** only the Kerr effect and with **(I)** only the thermal effect compared to the cases when neither effect is incorporated. **(J)** We also have the distinct case where both thermal and Kerr effects are present, which is the most realistic case for femtosecond pulsed laser optical tweezers. **(K)** Finally, since the thermal and Kerr effects often impact in opposite ways on non-linear refractive index, they can balance each other as a function of trapping bead radius.

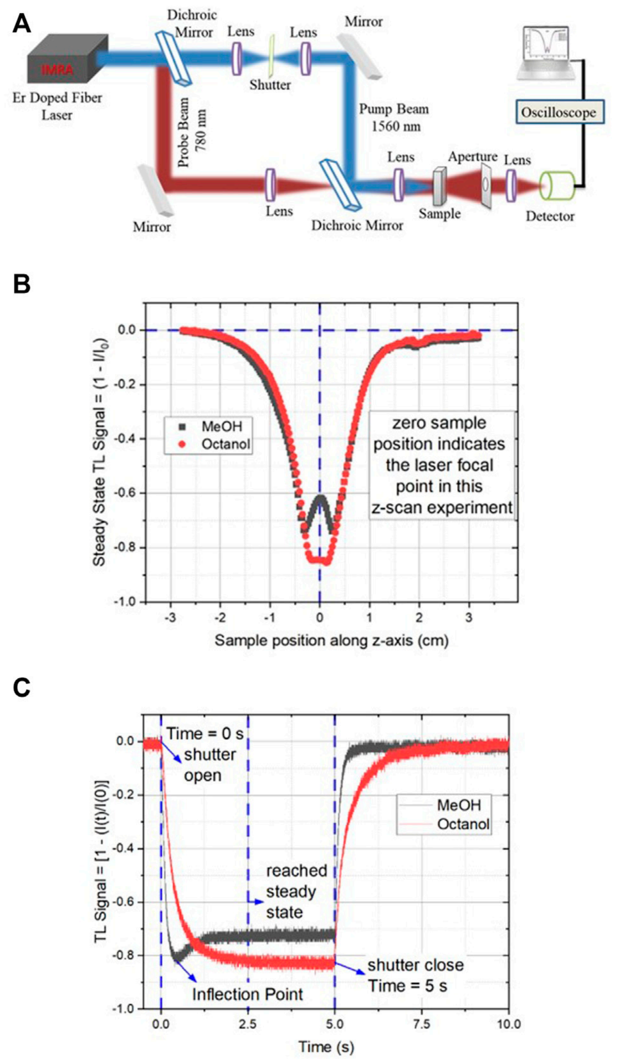

FIGURE 7
Femtosecond thermal lens (TL) spectroscopy with dual laser beams: **(A)** Experimental setup for both stationary as well as time-resolved TL measurements with high-repetition-rate lasers in a dual-beam experimental configuration. **(B)** Typical steady-state TL signals for dual-beam experiments for two different samples were collected as a function of sample position across the focal point of the TL-inducing laser. Drastic molecular dependence of TL is evident between methanol and octanol. **(C)** The corresponding time-resolved TL signal shows the molecular distinction in femtosecond TL. The inflection point indicates the importance of convection effects in addition to the conduction models that are molecule insensitive.

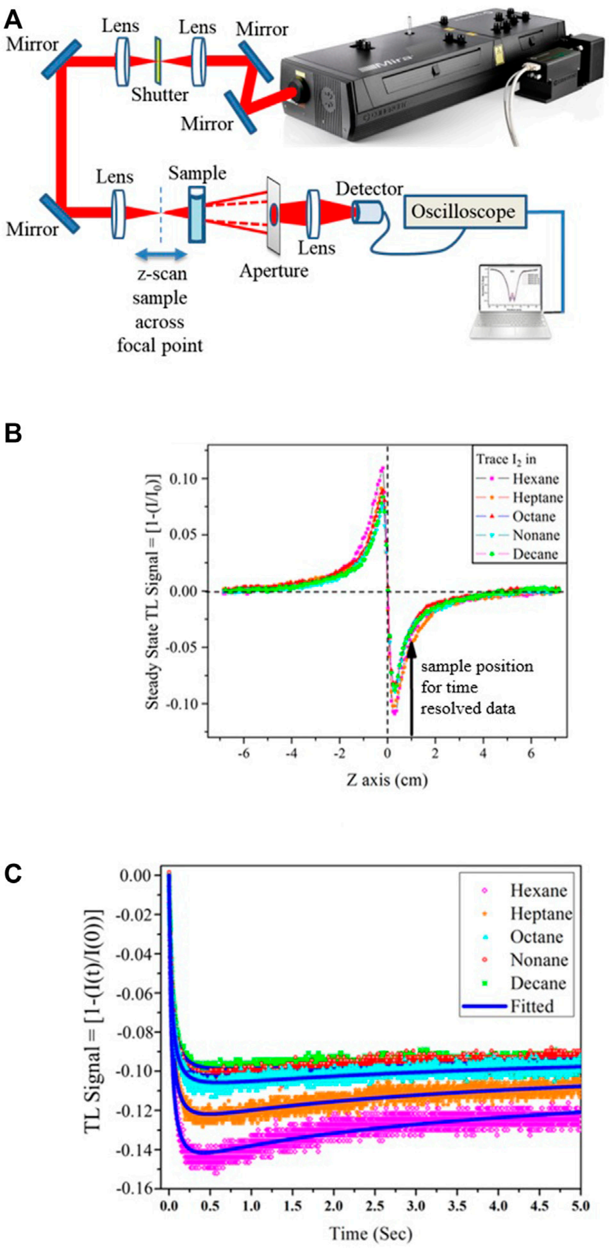

FIGURE 8
Femtosecond thermal lens (TL) spectroscopy with single laser beam: **(A)** Experimental setup for both stationary as well as time-resolved single beam femtosecond TL studies. **(B)** Typical steady-state TL signals for single-beam experiments as a function of sample position across the focal point of the TL-inducing laser for various samples showing zero-crossing at the focal point. For time-resolved TL collection, a position other than the focal point indicated by the arrow is chosen. **(C)** Time-resolved TL signals for Single beam femtosecond TL studies for the same shutter opening window. The early-time diagnostics of the shutter open part shows the importance of early time versus steady state. Note that for alkane samples, where the thermal effect is low, I_2 was added to keep the extent of TL generation steady across different samples. Fitting of the data is possible with Eq. 2, as discussed in the text.

reasonable experimental conditions (Kumar et al., 2014). The heat load generated is maximum at the center of the beam resulting in a temperature gradient leading to the creation of a refractive index gradient and results in the "thermal lens," a lens-like optical element in the sample (Leite et al., 1964; Roess, 1966; Osterink and Foster, 1968; Foster and Osterink, 1970). Subsequently, various heat dissipation dynamics arise, *viz.*, thermal conduction, convection, and radiative relaxation, all of which work together to equilibrate the heat generated in the sample. Amongst these, thermal convection plays a significant role for fluids primarily associated with molecular movement and is, thus, found to be strongly correlated to molecular properties. Previous studies involving continuous irradiation focused on thermal effects of small magnitudes, where it sufficed only to consider the conductive dissipation effects (Shen et al., 1992; Shen et al., 1995; Marcano et al., 2002; Marcano et al., 2006) to be able to derive exhibited phenomenological and bulk characteristics. The inclusion of thermal convection for ultrafast laser thermal processes, which correlates with molecular properties, has driven the development of ultrafast laser-induced thermal processes for sensitive spectroscopy (Figure 7, 8). Figure 7 represents the dual beam high repetition rate experimental setup where both the steady-state and time-resolved experiments can be carried out.

The experimental data collected can be effectively modeled and fitted by understanding the temperature distribution in space and time created as a result of the excitation laser heat deposition and dissipation. The uniqueness of the FTLS lies in the cumulative nature of the heat deposition process, as discussed.

A single laser beam high repetition rate experimental setup with high sensitivity has, in fact, also been established (Figure 8), where both the steady-state and time-resolved experiments can be carried out (Singhal and Goswami, 2020). The crucial aspect in the experimental design of the single beam technique (Figure 8A) lies in realizing that the stationary sample position for time-resolved measurements cannot be the focal point of the TL-generating laser. This is because there is no TL signal at the focus, so we choose the stationary sample position for time-resolved measurements as indicated by an arrow in Figure 8B, which is quite unlike the dual beam setup.

The TL model that includes both the conduction and convection terms involves a coupled differential equation that can be solved using the dimensionless parameter known as the Peclet number, P_E, which is the ratio of convective to conductive heat transfer rates (Bergman, 2019), where the laser beam size, ω_e, itself imposes the characteristic TL length. Mathematically,

$$\text{Peclet Number } (P_E) = \frac{\text{Rate of convection}}{\text{Rate of conduction}} = \frac{\omega_e v_x}{4D} \tag{1}$$

where, D is the thermal diffusivity and v_x is the convection velocity through the region of investigation. This can result in the TL fitting model that uses both conduction and convection (Singhal and Goswami, 2020):

$$\text{TL Signal} = \left|1 - \frac{j\theta}{4}\left[\begin{array}{l} -\left(1+\frac{P_E^2}{2}\frac{(1+jV+2m)^2}{2m(1+jV)}\right)\left(2j\tan^{-1}\left\{\frac{2mV}{\left[(1+2m)^2+V^2\right](t_c/2t)+1+2m+V^2}\right\}\right. \\ \qquad\qquad\qquad\left. +ln\left\{\frac{\left[1+2m/(1+2t/t_c)\right]^2+V^2}{(1+2m)^2+V^2}\right\}\right) \\ -P_E^2\left[\frac{2m}{(1+jV)}ln\left(1+\frac{2t}{t_c}\right)+\left(\frac{2t/t_c}{1+2t/t_c}\right)\right] \end{array}\right]\right|^2 \tag{2}$$

The real nature of the TL signal arises from the mod square as shown in the above complex expression involving: $j = \sqrt{-1}$. The absorbance coefficient, α, and the beam divergence angles are small for the propagating laser with wavevector, k, and wavelength, λ_p. This allows us to consider the exciting laser beam power and beam radius, ω_e, to be taken as constant within the cell of path length l. The phase change of the collimated probe laser beam, which could be the same as the exciting laser beam, results in the generation of the TL due to a variation in the refractive index (dn/dt) of the medium (Sheldon et al., 1982; Shen et al., 1992). Thus, Eq. 2 has fitted the experimental data well for the experimental results as shown in Figure 8C. If the exiting and probe beams are not the same, the probe beam is collimated and overfills the exciting beam. We define the parameter, m, to be related to the ratio of the two beam waists as: $m = (\omega_{1p}^2/\omega_e^2)$. Consequently, the terms: $\theta = -P_e \alpha l dn/dt/k\lambda_p$ and $t_c = \omega_e^2/4D$, relate to different physical properties of the sample responsible for the formation of a thermal lens in the laser interaction volume V in such a way that its magnitude is directly related to the strength of the thermal lens.

When $P_E = 0$, Eq. 2 reduces to the Shen et al., (1992) equation, which corresponds to situations arising from considering only the conductive mode of heat transfer as below:

$$\text{TL Signal} = \left[1 - \frac{\theta}{2}\tan^{-1}\left(\frac{2mV}{\left[(1+2m)^2+V^2\right](t_c/2t)+(1+2m+V^2)}\right)\right]^2 + \left[\frac{\theta}{4}ln\left\{\frac{(1+2m/(1+2t/t_c))^2+V^2}{(1+2m)^2+V^2}\right\}\right]^2 \tag{3}$$

Most literature involving the Shen model has a very low heat load. Therefore, the first term of Eq. 3 suffices, which can then be reduced to the popular mathematical expression for the Shen model (Shen et al., 1992; Shen et al., 1995) given by:

$$\text{TL Signal} = \left[1 - \frac{\theta}{2}\tan^{-1}\left(\frac{2mV}{\left[(1+2m)^2+V^2\right](t_c/2t)+(1+2m+V^2)}\right)\right]^2 \tag{4}$$

Thus, FTLS can distinguish between molecules within fluids based on both size and shape (Kumar et al., 2014; Kumar et al., 2014). Similarly, the differentiation of isomers and isotopes in fluids is also effectively possible with FTLS (Bhattacharyya et al., 2014; Kumar et al., 2014). Additionally, FTLS is also sensitive to changes in intermolecular interactions, which would lead to phase separations (Goswami et al., 2019), interfaces (Singhal and Goswami, 2020), and several other physical interactions (Maurya et al., 2016; Rawat et al., 2021). Cumulative thermal processes fall in the domain of weak perturbations that do not require strong absorption or any exact resonant excitation conditions. Consequently, they work over a broad range of wavelengths as well as laser pulse widths. Thus, FTLS is an astoundingly versatile technique (Goswami et al., 2021), which is continuously being unveiled to date.

7 Conclusion

We have presented the pragmatic aspect of intense laser-induced light-matter control that can circumvent practical experimental constraints. The concept of spatiotemporal control that simultaneously manipulates the position and time dynamics has been discussed in the context of femtosecond optical trapping and is further enabled through the Megahertz repetition rate femtosecond pulse shaping. While the presence of non-linear interactions with femtosecond lasers has been shown to offset the omnipresent thermal effects in optical tweezers, it has also been shown to attain a better signal-to-noise ratio through two-photon fluorescence detection of trapping. As an additional outcome, we have demonstrated how the omnipresent thermal effects can be turned around for cumulatively accumulating minuscule femtosecond induced heat load into an interesting femtosecond laser thermal lens setup for Megahertz repetition rate femtosecond lasers and provide sensitive molecular detection. Such developments in spatiotemporal control with intense femtosecond optical pulse shaping approaches thus promise myriad applications with continuous advancements.

Data availability statement

The original contributions presented in the study are included in the article/Supplementary Material, further inquiries can be directed to the corresponding author.

Author contributions

The author confirms being the sole contributor of this work and has approved it for publication.

Funding

The author acknowledges the funding support of this research from MEITY, SERB, STC ISRO of the Govt. of India as well as IIT Kanpur for all the infrastructure support.

Acknowledgments

The author thanks all his present and past students for their hard work over the years, enabling the present state-of-the-art experiments and explorations possible. The author is also highly thankful to S. Goswami for proofreading, language correction, and editing.

Conflict of interest

Publisher's note

References

Aeschlimann, M., Bauer, M., Bayer, D., Brixner, T., Cunovic, S., Dimler, F., et al. (2010). Spatiotemporal control of nanooptical excitations. *Proc. Natl. Acad. Sci.* 107 (12), 5329–5333. doi:10.1073/pnas.0913556107

Arnold, F. H. (2017). Directed evolution: Bringing new chemistry to life. *Angew. Chem. Int. Ed.* 57 (16), 4143–4148. doi:10.1002/anie.201708408

Ashkin, A. (1970). Acceleration and trapping of particles by radiation pressure. *Phys. Rev. Lett.* 24 (4), 156–159. doi:10.1103/physrevlett.24.156

Ashkin, A., and Ebrary, I. (2006). *Optical trapping and manipulation of neutral particles using lasers*. Hackensack, NJ, USA: World Scientific.

Bandyopadhyay, S. N., Gaur, T., and Goswami, D. (2021). Comparative study of the real-time optical trapping in the Rayleigh regime for continuous and femtosecond pulsed lasers. *Opt. Laser Technol.* 136, 106770. doi:10.1016/j.optlastec.2020.106770

Bergman, T. L. (2019). *Fundamentals of heat and mass transfer*, wileyplus blackboard card S L. Hoboken, NJ, USA: John Wiley.

Bergt, M., Brixner, T., Kiefer, B., Strehle, M., and Gerber, G. (2001). Control of quantum dynamics by adaptive femtosecond pulse shaping. *Ultrafast Phenom.* 12, 19–23. doi:10.1007/978-3-642-56546-5_4

Bhattacharyya, I., Kumar, P., and Goswami, D. (2014). Effect of isotope substitution in binary liquids with Thermal-Lens spectroscopy. *Chem. Phys. Lett.* 598, 35–38. doi:10.1016/j.cplett.2014.02.056

Bhattacharyya, I., Kumar, P., and Goswami, D. (2010). Probing intermolecular interaction through thermal-lens spectroscopy. *J. Phys. Chem. B* 115 (2), 262–268. doi:10.1021/jp1062429

Boyd, R. W. (2003). *Nonlinear optics*. 3rd Edition. Amsterdam, Netherlands: Elsevier Science.

Català, F., Marsà, F., Montes-Usategui, M., Farré, A., and Martín-Badosa, E. (2017). Influence of experimental parameters on the laser heating of an optical trap. *Sci. Rep.* 7 (1), 16052. doi:10.1038/s41598-017-15904-6

Dantus, M., and Lozovoy, V. V. (2004). Experimental coherent laser control of physicochemical processes. *Chem. Rev.* 104 (4), 1813–1860. doi:10.1021/cr020668r

De, A. K., and Goswami, D. (2011). Towards controlling molecular motions in fluorescence microscopy and optical trapping: A spatiotemporal approach. *Int. Rev. Phys. Chem.* 30 (3), 275–299. doi:10.1080/0144235x.2011.603237

De, A. K., Roy, D., Dutta, A., and Goswami, D. (2009). Stable optical trapping of latex nanoparticles with ultrashort pulsed illumination. *Appl. Opt.* 48 (31), G33. doi:10.1364/ao.48.000g33

De, A. K., Roy, D., and Goswami, D. (2011). Two-photon fluorescence diagnostics of femtosecond laser tweezers. *Curr. Sci.* 101 (7), 935–945. https://www.jstor.org/stable/24079130.

de Vivie-Riedle, R., Kurtz, L., and Hofmann, A. (2001). Coherent control for ultrafast photochemical reactions. *Pure Appl. Chem.* 73 (3), 525–528. doi:10.1351/pac200173030525

Dinda, S., Bandyopadhyay, S. N., and Goswami, D. (2019). Rapid programmable pulse shaping of femtosecond pulses at the MHz repetition rate. *OSA Contin.* 2 (4), 1386. doi:10.1364/osac.2.001386

Fetterman, M. R., Goswami, D., Keusters, D., Yang, W., Rhee, J.-K., and Warren, W. S. (1998). Ultrafast pulse shaping: Amplification and characterization. *Opt. Express* 3 (10), 366. doi:10.1364/oe.3.000366

Foster, J. D., and Osterink, L. M. (1970). Thermal effects in a Nd:YAG laser. *J. Appl. Phys.* 41 (9), 3656–3663. doi:10.1063/1.1659488

Froula, D. H., Turnbull, D., Davies, A. S., Kessler, T. J., Haberberger, D., Palastro, J. P., et al. (2018). Spatiotemporal control of laser intensity. *Nat. Photonics* 12 (5), 262–265. doi:10.1038/s41566-018-0121-8

Goswami, D. "Demonstrating a nano viscometer using femtosecond laser induced photo-thermal effect," in Proceedings of the 2015 Workshop on Recent Advances in Photonics (WRAP), Bangalore, India, December 2015. doi:10.1109/wrap.2015.7806018

Goswami, D. (2003). Optical pulse shaping approaches to coherent control. *Phys. Rep.* 374 (6), 385–481. doi:10.1016/s0370-1573(02)00480-5

Goswami, D. (2021). Understanding femtosecond optical tweezers: The critical role of nonlinear interactions. *J. Phys. Conf. Ser.* 1919 (1), 012013. doi:10.1088/1742-6596/1919/1/012013

Goswami, S., Singhal, S., Banerjee, A., and Goswami, D. "Sensitive detection of phase separation with femtosecond thermal lens spectroscopy," in Proceedings of the 2019 Workshop on Recent Advances in Photonics (WRAP), Guwahati, India, December 2019. doi:10.1109/wrap47485.2019.9013833

Goswami, S., Singhal, S., and Goswami, D. (2021). "Detecting *in-situ* phase separation with Femtosecond thermal lens spectroscopy to map COVID-19 transmission," *OSA Optical Sensors and Sensing Congress 2021 (AIS, FTS, HISE, SENSORS, ES)*. Editor S. Buckley, F. Vanier, K. Shi, I. Walker, S. Coddington, S. Paine, et al. (OSA Technical Digest (Optica Publishing Group, 2021)). paper AM2D.6

Goswami, T., Das, D. K., and Goswami, D. (2013). Controlling the femtosecond laser-driven transformation of dicyclopentadiene into cyclopentadiene. *Chem. Phys. Lett.* 558, 1–7. doi:10.1016/j.cplett.2012.10.054

Hikosaka, Y., Kaneyasu, T., Fujimoto, M., Iwayama, H., and Katoh, M. (2019). Coherent control in the extreme ultraviolet and attosecond regime by synchrotron radiation. *Nat. Commun.* 10 (1), 4988. doi:10.1038/s41467-019-12978-w

Hillegas, C. W., Tull, J. X., Goswami, D., Strickland, D., and Warren, W. S. (1994). Femtosecond laser pulse shaping by use of microsecond radio-frequency pulses. *Opt. Lett.* 19 (10), 737. doi:10.1364/ol.19.000737

Kumar, P., Dinda, S., Chakraborty, A., and Goswami, D. (2014). Unusual behavior of thermal lens in alcohols. *Phys. Chem. Chem. Phys.* 16 (24), 12291–12298. doi:10.1039/c4cp00895b

Kumar, P., Dinda, S., and Goswami, D. (2014). Effect of molecular structural isomers in thermal lens spectroscopy. *Chem. Phys. Lett.* 601, 163–167. doi:10.1016/j.cplett.2014.03.095

Kumar, P., and Goswami, D. (2014). Importance of molecular structure on the thermophoresis of binary mixtures. *J. Phys. Chem. B* 118, 14852–14859. doi:10.1021/jp5079604

Kumar, P., Khan, A., and Goswami, D. (2014). Importance of molecular heat convection in time resolved thermal lens study of highly absorbing samples. *Chem. Phys.* 441, 5–10. doi:10.1016/j.chemphys.2014.06.008

Leite, R. C. C., Moore, R. S., and Whinnery, J. R. (1964). Low absorption measurements by means of the thermal lens effect using an He–Ne laser. *Appl. Phys. Lett.* 5 (7), 141–143. doi:10.1063/1.1754089

Marcano, A., Cabrera, H., Guerra, M., Cruz, R. A., Jacinto, C., and Catunda, T. (2006). Optimizing and calibrating a mode-mismatched thermal lens experiment for low absorption measurement. *J. Opt. Soc. Am. B* 23 (7), 1408. doi:10.1364/josab.23.001408

Marcano, A., Loper, C., and Melikechi, N. (2002). Pump–probe mode-mismatched thermal-lens Z scan. *J. Opt. Soc. Am. B* 19 (1), 119. doi:10.1364/josab.19.000119

Maurya, S. K., Das, D., and Goswami, D. (2016). Probing intermolecular interactions in binary liquid mixtures using femtosecond laser-induced self-defocusing. *Appl. Spectrosc.* 70 (10), 1655–1661. doi:10.1177/0003702816643547

Maurya, S. K., Yadav, D., and Goswami, D. (2019). Effect of femtosecond laser pulse repetition rate on nonlinear optical properties of organic liquids. *PeerJ Phys. Chem.* 1, e1. doi:10.7717/peerj-pchem.1

Melinger, J. S., Gandhi, S. R., Hariharan, A., Goswami, D., and Warren, W. S. (1994). Adiabatic population transfer with frequency swept laser pulses. *J. Chem. Phys.* 101 (8), 6439–6454. doi:10.1063/1.468368

Mondal, D., and Goswami, D. (2016). Controlling and tracking of colloidal nanostructures through two-photon fluorescence. *Methods Appl. Fluoresc.* 4 (4), 044004. doi:10.1088/2050-6120/4/4/044004

Mondal, D., and Goswami, D. (2015). Controlling local temperature in water using femtosecond optical tweezer. *Biomed. Opt. Express* 6 (9), 3190. doi:10.1364/boe.6.003190

Mondal, D., Mathur, P., and Goswami, D. (2016). Precise control and measurement of solid–liquid interfacial temperature and viscosity using dual-beam femtosecond optical tweezers in the condensed phase. *Phys. Chem. Chem. Phys.* 18 (37), 25823–25830. doi:10.1039/c6cp03093a

Osterink, L. M., and Foster, J. D. (1968). Thermal effects and transverse mode control in a Nd:YAG laser. *Appl. Phys. Lett.* 12 (4), 128–131. doi:10.1063/1.1651922

Rawat, A. K., Chakraborty, S., Mishra, A. K., and Goswami, D. (2021). Unraveling molecular interactions in binary liquid mixtures with time-resolved thermal-lens-spectroscopy. *J. Mol. Liq.* 336, 116322. doi:10.1016/j.molliq.2021.116322

Rice, Stuart Alan, and Zhao, Meishan (2000). *Optical control of molecular dynamics*. New York, NY, USA: John Wiley.

Roess, D. (1966). Analysis of a room temperature cw ruby laser of 10 mm resonator length: The ruby laser as a thermal lens. *J. Appl. Phys.* 37 (9), 3587–3594. doi:10.1063/1.1708908

Roy, D., Mondal, D., and Goswami, D. (2016). Structure and dynamics of optically directed self-assembly of nanoparticles. *Sci. Rep.* 6 (1), 23318. doi:10.1038/srep23318

Roy, D., Mondal, D., and Goswami, D. (2016). Two-photon fluorescence tracking of colloidal clusters. *J. Fluoresc.* 26 (4), 1271–1277. doi:10.1007/s10895-016-1814-3

Schmidt, R., Weihs, T., Wurm, C. A., Jansen, I., Rehman, J., Sahl, S. J., et al. (2021). MINFLUX nanometer-scale 3D imaging and microsecond-range tracking on a common fluorescence microscope. *Nat. Commun.* 12 (1), 1478. doi:10.1038/s41467-021-21652-z

Sheldon, S. J., Knight, L. V., and Thorne, J. M. (1982). Laser-induced thermal lens effect: A new theoretical model. *Appl. Opt.* 21 (9), 1663. doi:10.1364/ao.21.001663

Shen, J., Lowe, R. D., and Snook, R. D. (1992). A model for cw laser induced mode-mismatched dual-beam thermal lens spectrometry. *Chem. Phys.* 165 (2-3), 385–396. doi:10.1016/0301-0104(92)87053-c

Shen, J., Soroka, A. J., and Snook, R. D. (1995). A model for cw laser induced mode mismatched dual beam thermal lens spectrometry based on probe beam profile image detection. *J. Appl. Phys.* 78 (2), 700–708. doi:10.1063/1.360329

Singh, A., Bandyopadhyay, S. N., Singh, K. K., Kumar, D., and Goswami, D. "Experimental comparison of conventional and femtosecond optical tweezers," in Proceeding of the 2021Conference on Lasers and Electro-Optics, San Jose, CA, USA, May 2021. doi:10.1364/cleo_at.2021.jw1a.153

Singhal, S., Dinda, S., and Goswami, D. (2017). Measurement of pure optical nonlinearity in carbon disulfide with a high-repetition-rate femtosecond laser. *Appl. Opt.* 56 (3), 644. doi:10.1364/ao.56.000644

Singhal, S., and Goswami, D. (2019). Thermal lens study of NIR femtosecond laser-induced convection in alcohols. *ACS Omega* 4 (1), 1889–1896. doi:10.1021/acsomega.8b02956

Singhal, S., and Goswami, D. (2020). Unraveling the molecular dependence of femtosecond laser-induced thermal lens spectroscopy in fluids. *Analyst* 145 (3), 929–938. doi:10.1039/c9an01082c

Warren, W. S., Rabitz, H., and Dahleh, M. (1993). Coherent control of quantum dynamics: The dream is alive. *Science* 259 (5101), 1581–1589. doi:10.1126/science.259.5101.1581

Yang, W., Keusters, D., Goswami, D., and Warren, W. S. (1998). Rapid ultrafine-tunable optical delay line at the 155-μm wavelength. *Opt. Lett.* 23 (23), 1843. doi:10.1364/ol.23.001843

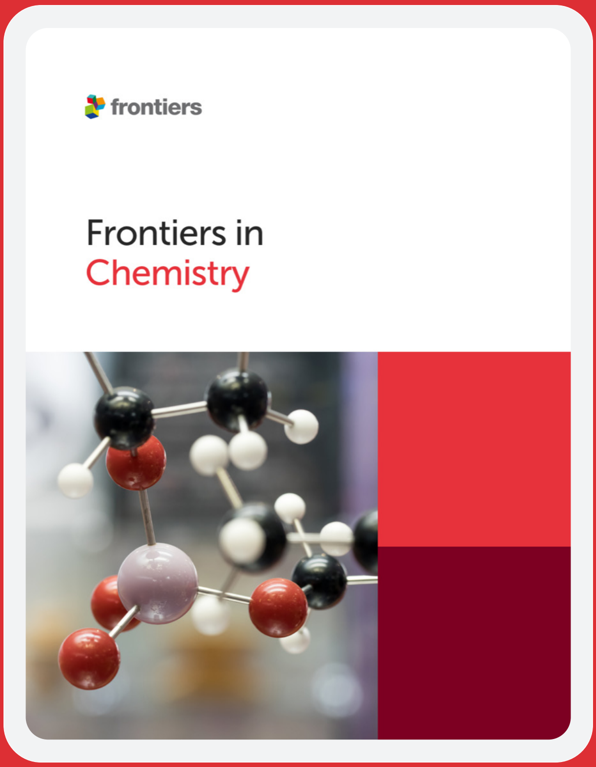

frontiers

Frontiers in
Chemistry